THE UNIVERSITY
of EDINBURGH

This thesis has been submitted in fulfilment of the requirements for a postgraduate degree (e.g. PhD, MPhil, DClinPsychol) at the University of Edinburgh. Please note the following terms and conditions of use:

This work is protected by copyright and other intellectual property rights, which are retained by the thesis author, unless otherwise stated.
A copy can be downloaded for personal non-commercial research or study, without prior permission or charge.
This thesis cannot be reproduced or quoted extensively from without first obtaining permission in writing from the author.
The content must not be changed in any way or sold commercially in any format or medium without the formal permission of the author.
When referring to this work, full bibliographic details including the author, title, awarding institution and date of the thesis must be given.

Search for the Standard Model Higgs boson produced in association with a vector boson and decaying to a b-quark pair with the ATLAS detector

Ben Harry Smart

A thesis submitted in fulfilment of the requirements
for the degree of Doctor of Philosophy
to the
University of Edinburgh
February 2015

Abstract

An important question at present in particle physics is whether the recently discovered boson with a mass of about 125 GeV is the Standard Model Higgs boson. A Standard Model Higgs boson with a mass of 125 GeV will predominantly decay to b-quark pairs. This work presents the author's contribution to the search with the ATLAS detector for a Standard Model Higgs boson produced in association with a W or Z boson and decaying to b-quark pairs. In order to search for the decay modes $ZH \to \nu\nu b\bar{b}$, $WH \to \ell\nu b\bar{b}$ and $ZH \to \ell\bar{\ell}b\bar{b}$, where ℓ is either an electron or muon, events with zero, one or two electrons or muons are considered in 20.3 fb^{-1} of 8 TeV LHC data. A Standard Model Higgs boson is not observed decaying to b-quark pairs, although neither is this decay mode ruled out. A Standard Model Higgs boson with a mass of between 110 GeV and 115 GeV is excluded. For $m_H = 125$ GeV the observed (expected) upper limit on the cross-section times the branching ratio is found to be 2.16 (1.07) times the Standard Model prediction. For a Standard Model Higgs boson with a mass of 125 GeV, the best fit signal strength is $\mu = 1.09\ ^{+0.43}_{-0.42}$ (stat) $^{+0.44}_{-0.37}$ (syst) $= 1.09\ ^{+0.61}_{-0.56}$. The combined results are consistent with a Standard Model Higgs boson with a mass of 125 GeV. The author's own work is presented, including estimation of systematic uncertainties on $WH \to \ell\nu b\bar{b}$ modelling, and future ATLAS data selection methods for $WH \to \ell\nu b\bar{b}$ searches. Overviews of underlying theoretical matters and the experimental facilities used are given.

Declaration

Except where otherwise stated, the research undertaken in this thesis was the unaided work of the author. Where the work was done in collaboration with others, a significant contribution was made by the author.

B.H. Smart
February 2015

Acknowledgements

I would like to record my thanks to all those who have helped me in the course of this work. In particular, the following:

Dr. Victoria Martin

Dr. Thomas Binoth

Prof. Phil Clark

Dr. Andy Buckley

Dr. Heather Gray, Dr. Tim Scanlon and Dr. Gabriel Facini

Sara Alderweireldt

Jack Medley and Richard Ruiz, for stimulating discussions on and patient help with all manner of theoretical matters.

The S.T.F.C. for financial support.

My parents, for their encouragement and support throughout.

Jane Patterson

And the coffee shops of Edinburgh, for fuelling me.

Contents

List of Figures

List of Tables

Chapter 1

Introduction

In 'Timaeus' by Plato, the natural philosopher Timaeus argues that the universe was created according to an underlying and eternal set of rules, mathematical in nature. He states that everything on earth is composed of fundamental particles, of which there are four types. These four types he associates with earth, air, fire, and water. He adds though, that these fundamental particles are only representations of the underlying laws as we see them, and that the deeper truth is known only by the creator [1].

In more recent times, mankind has used the scientific method to probe the nature of the universe, leading to great advances in human understanding. Still, we believe that the universe is composed of fundamental particles obeying underlying laws. Humanity's current best understanding of the universe in terms of these fundamental particles is represented by The Standard Model of particle physics [2]. The Standard Model includes all currently-known fundamental particles, and describes three of the four known fundamental forces. By studying proton-proton collisions with experiments such as the ATLAS experiment we can probe the Standard Model further, and look for new physics in order to better understand the universe around us.

In 2012 the ATLAS and CMS scientific collaborations announced the discovery of a new particle with a mass of about 125 GeV [3, 4], believed to be a Higgs boson, a fundamental particle predicted in the Standard Model and first proposed by Professor Peter Higgs in 1964 [5]. An important question at present in particle physics is whether this recently discovered particle is the Standard Model Higgs boson. A Standard Model Higgs boson with a mass of 125 GeV will predominantly

decay to b-quark pairs (the branching ratio for this decay is predicted to be 58%). This work presents the author's contribution to the search with the ATLAS detector for a Standard Model Higgs boson produced in association with a W or Z boson and decaying to a b-quark pair.

The following documents the author's work presented in this thesis, where the materials presented are entirely the work of the author, and where they represent work performed jointly with other members of the ATLAS collaboration as part of the 'Higgs Sub-Group 5' (HSG5) ATLAS research group. HSG5 is the ATLAS research group focussed on the search for a Standard Model Higgs boson produced in association with a W or Z boson and decaying to a b-quark pair.

Section 4.2 - Signal And Background Processes

The author has contributed to writing configuration scripts for the production of Higgs boson Monte Carlo samples, as well as validating such samples. The author co-wrote Rivet [6] analysis routines for such validation that he and others used. This work was done as part of a larger effort by the HSG5 group and ATLAS collaboration.

Section 4.3 - Physics Objects

The author implemented alternative hadronic jet selection in the $WH \to \ell\nu$ analysis framework. The author, working with other members of HSG5, investigated and compared available jet selection options, leading towards the jet selection discussed in this thesis.

Section 4.4 - Event Selection

The author developed, implemented, and validated the $WH \to \ell\nu$ analysis framework event selection. This was done in collaboration with HSG5 colleagues.

Section 4.6 - Systematic Uncertainties

The author estimated systematic uncertainties for the $WH \to \ell\nu$ signal process, as discussed in chapter 5.

Section 4.8 - Results

Results produced by the author are presented in chapter 6.

Chapter 5

The work done in this chapter was done entirely by the author. The author

generated all Monte Carlo samples used, writing all configuration scripts to do so. The author also wrote all analysis code used.

Chapter 6

The author produced the results presented in this chapter himself, using as inputs the uncertainties he calculated and presented in chapter 5. These results make use of the fitting code written by colleagues in HSG5.

Chapter 7

The author produced the results presented in this chapter himself, using and adapting the $WH \to \ell\nu$ analysis framework developed in collaboration with HSG5 colleagues. The proposals for future ATLAS $WH \to \ell\nu$ trigger configurations were proposed and developed by the author.

Chapter 2

The Theory of The Standard Model of Particle Physics

2.1 Introduction

Currently, humanity's best understanding of the universe on a subatomic scale is represented by The Standard Model (SM) of particle physics. It combines all fundamental particles that have been discovered with three of the four known fundamental forces. By studying proton-proton collisions at the ATLAS detector we can probe the Standard Model and look for new physics in order to better understand the universe around us.

In the Standard Model, matter and forces are described as fields. The quanta of these fields are fundamental particles. All currently known fundamental particles of the Standard Model, along with some of their properties, are shown in figure 2.1.

2.1.1 Fundamental Particles of Matter

Matter in the universe is described in the SM as being made up of particles called fermions. Fermions are defined as particles with half-integer spin.

For each fermion in the SM, there is an antifermion. As fermions make up matter, so antifermions make up antimatter. An antifermion shares the same properties as its partner fermion, except that it has opposite charges. It is currently unknown though whether neutrinos and their partner antineutrinos

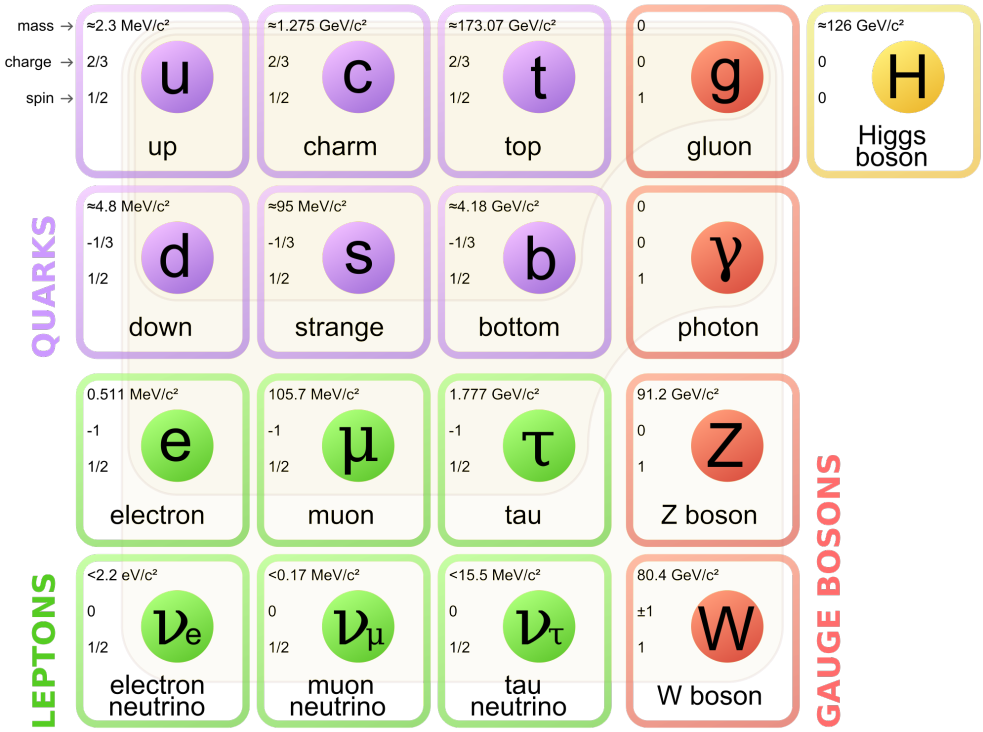

Figure 2.1: Particles of the Standard Model of Particle Physics. From [7].

are different particles (the 'Dirac' formulation, after Paul Dirac [8]), or whether neutrinos are their own antiparticles (whether they are 'Majorana' particles, after Ettore Majorana [9]). Further possible differences between matter and antimatter are currently an area of active research [10, 11, 12].

Fermions are divided into two categories: leptons and quarks. Quarks have colour charge (see section 2.1.2 for an explanation of colour charge) whereas leptons do not. All fermions have weak hypercharge, related to the weak force (section 2.1.2). The fermions are also grouped into three 'generations'. Each generation contains two quarks, one with $+\frac{2}{3}$ electric charge and the other with $-\frac{1}{3}$, one -1 electrically charged lepton, and one electrically neutral neutrino. Here, as in figure 2.1, electric charge is given in units of electron charge magnitude, 1.6×10^{-19} Coulombs. It is currently not known why the fermions are arranged into such generations, although theoretical and experimental results [13] suggest that there are three and only three generations.

Almost all matter surrounding us in our day to day lives is comprised of particles from the first generation of fermions: up and down quarks forming the

protons (two up quarks and one down quark) and neutrons (one up quark and two down quarks) of atomic nuclei, and electrons combining with those nuclei to form atoms.

2.1.2 Fundamental Forces

There are four 'fundamental' forces that humanity has knowledge of: electromagnetism, the weak force, the strong force, and gravity. Gravity is not included in the SM and is instead best described by Einstein's theory of General Relativity [14].

The SM describes forces as interactions mediated by particles called bosons, defined as particles with integer spin. A vector boson is a boson with non-zero spin. A scalar boson is a boson with zero spin.

The Electromagnetic Force

Particles with electric charge are affected by the electromagnetic force, mediated by the photon. The photon does not have electric charge or mass. As the photon does not have electric charge, it is not affected by the electromagnetic force, so the electromagnetic force decreases in strength proportional to $\frac{1}{r^2}$, where r is the distance between interacting electrically charged particles.

The Weak Force

The weak force is mediated by three massive particles, the W^+ boson, the Z boson, and the W^- boson. The W bosons only couple to particles that have weak isospin: left-handed fermions, right-handed anti-fermions, and bosons. Here left handed means that the particle's spin and momentum point in opposite directions. Right-handed means that they point in the same direction. The Z boson couples to particles with weak hypercharge or weak isospin. Weak hypercharge (Y), the third component of weak isospin (T_3), and electric charge (Q) are related by $Q = T_3 + Y/2$. The W^+ and W^- bosons have $+1$ and -1 electric charge respectively. The Z boson is electrically neutral. Due to their mass, these particles are short-lived, resulting in the weak force being short-ranged.

The Strong Force

The strong force is mediated by gluon exchange between particles with colour charge and particles with anti-colour charge. There are three colour charges, red, green, and blue, and three corresponding anti-colour charges. Quarks carry colour charge, while anti-quarks carry anti-colour charge. The gluon is massless and has a superposition of both colour and anti-colour charge, so not only mediates the strong force but is also affected by it.

α_s

α_s is defined as,

$$\alpha_s(Q) \equiv \frac{g_s^2(Q)}{4\pi} \tag{2.1}$$

for an interaction involving a momentum transfer of Q GeV. It quantifies the strength of the strong interaction coupling constant g_s. The strength of the strong interaction decreases asymptotically as the energy of the interaction increases. This dependence is known as asymptotic freedom, and for its discovery David J. Gross, H. David Politzer, and Frank Wilczek were awarded the 2004 Nobel Prize in physics [15]. This dependence can be thought of as being due to higher-order terms in a QCD interaction: loops, as shown in figure 2.2. Additional loops alter the effective coupling strength and cause it to be interaction-energy dependent.

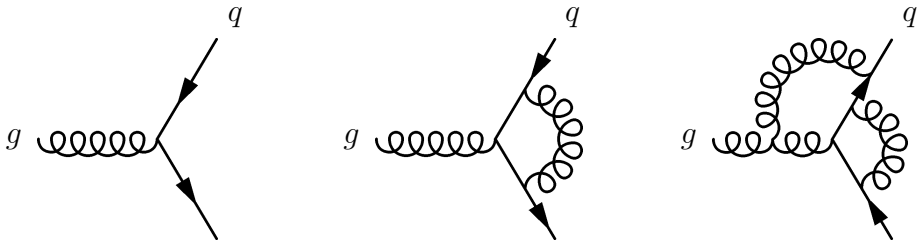

Figure 2.2: Examples of QCD interactions. Leading order (left), one-loop (middle), two-loop (right).

The order of the $\alpha_s(Q)$ function used in calculations must be chosen. Additionally, the function must be defined at some energy. Typically this is done by fixing $\alpha_s(m_Z)$, the value of α_s at the Z boson mass. Global fits to data

have been performed to extract the most likely value of $\alpha_s(m_Z)$ giving a value of $\alpha_s(m_Z) = 0.1184 \pm 0.0007$ [16]

2.1.3 The Higgs Boson

The Higgs boson, also a fundamental particle, is central to this thesis and will be discussed in section 2.3.

2.2 The Lagrangian Formalism Of The Standard Model

The Standard Model as a mathematical model can be described by a single Lagrangian density $\mathcal{L}$, given in equation 2.2.

$$\begin{aligned} \mathcal{L} &= -\frac{1}{4}\mathrm{F}^{\mathcal{A}}_{\mu\nu}\mathrm{F}^{\mathcal{A}\mu\nu} \\ &+ i\bar{\psi}\not{D}\psi + h.c. \\ &+ \psi_i y_{ij}\psi_j\phi + h.c. \\ &+ |D_\mu\phi|^2 - V(\phi) \end{aligned} \tag{2.2}$$

The terms in equation 2.2 are defined below.

h.c. is the hermitian conjugate of the preceding term.

$\mathrm{F}^{\mathcal{A}}_{\mu\nu} = \partial_\mu B^{\mathcal{A}}_\nu - \partial_\mu B^{\mathcal{A}}_\nu - g' f'^{\mathcal{ABC}} B^{\mathcal{B}}_\mu B^{\mathcal{C}}_\nu$
where $\mathcal{A} = 0$. This is the field strength tensor of U(1).

$\mathrm{F}^{\mathcal{A}}_{\mu\nu} = \partial_\mu W^{\mathcal{A}}_\nu - \partial_\mu W^{\mathcal{A}}_\nu - g f^{\mathcal{ABC}} W^{\mathcal{B}}_\mu W^{\mathcal{C}}_\nu$
where $\mathcal{A} = 1,\ldots,3$. This is the field strength tensor of SU(2).

$\mathrm{F}^{\mathcal{A}}_{\mu\nu} = \partial_\mu G^{\mathcal{A}}_\nu - \partial_\mu G^{\mathcal{A}}_\nu - g_s f_s^{\mathcal{ABC}} G^{\mathcal{B}}_\mu G^{\mathcal{C}}_\nu$
where $\mathcal{A},\mathcal{B},\mathcal{C} = 4,\ldots,11$, for the eight independent gluon colour states, or the eight linearly independent Gell-Mann matrices/generators of SU(3). This is the field strength tensor of SU(3) (QCD).

$B^{\mathcal{A}}_\mu$ is the spin-1 U(1) field, where $\mathcal{A} = 0$.

$W^{\mathcal{A}}_\mu$ is the spin-1 SU(2) field, where $\mathcal{A} = 1,\ldots,3$.

$G^{\mathcal{A}}_\mu$ is the spin-1 SU(3) (gluon) field, where $\mathcal{A} = 4,\ldots,11$.

g' is the U(1) gauge coupling constant.

g is the SU(2) gauge coupling constant.

g_s is the SU(3) gauge coupling constant.

and where,

$f'^{\mathcal{ABC}}$, $f^{\mathcal{ABC}}$, **and** $f_s^{\mathcal{ABC}}$
: are the structure constants of the, respectively, U(1), SU(2), and SU(3) groups.

$\not{D} = \gamma^\mu D_\mu$

γ^μ : are the Dirac gamma matrices, where $\mu = 0,\ldots,3$.

$D_\mu = \partial_\mu - ig\frac{1}{2}\sigma^a W_{\mu a} - ig'\frac{1}{2}YB_\mu$
: This is the covariant derivative in the case of SU(2) $\times$ U(1).

$(D_\mu)_{\alpha\beta} = \partial_\mu\delta_{\alpha\beta} - ig_s(t^{\mathcal{C}}A_\mu^{\mathcal{C}})_{\alpha\beta}$
: This is the covariant derivative in the case of SU(3), when acting on a triplet field. α and β are indices of the quark fields ψ_α, where α,$\beta = 1, 2, 3$.

$(D_\mu)_{\mathcal{AB}} = \partial_\mu\delta_{\mathcal{AB}} - ig_s(T^{\mathcal{C}}A_\mu^{\mathcal{C}})_{\mathcal{AB}}$
: This is the covariant derivative in the case of SU(3), when acting on an octet field.

t **and** T
: These are, respectively, matrices in the triplet (fundamental) and octet (adjoint) representations of SU(3).

$[t^{\mathcal{A}}t^{\mathcal{B}}] = if_s^{\mathcal{ABC}}t^{\mathcal{C}}$

$[T^{\mathcal{A}}T^{\mathcal{B}}] = if_s^{\mathcal{ABC}}T^{\mathcal{C}}$

σ^a : are the Pauli matrices

Y : is Weak hypercharge.

y_{ij} : are the Yukawa couplings between the fermion and Higgs fields.

ϕ : is the complex scalar Higgs field, a doublet in the SM.

$V(\phi) = \mu^2|\phi|^2 + \lambda|\phi|^4$
: is the Higgs potential. μ and λ are scalar real-valued constants.

One can additionally define the spin-1 photon field, (see equation 2.20):

$$A_\mu = \frac{1}{\sqrt{g^2 + g'^2 Y^2}}(gW_{3\mu} + g'Y B_\mu) \tag{2.3}$$

where ψ_i is the fermion field spinor for fermions of type i. This then allows the above field strength tensors to be rearranged to extract,

$$\mathrm{F}_{\mu\nu} = \partial_\mu A_\nu - \partial_\nu A_\mu \tag{2.4}$$

which is the field strength tensor of QED.

2.3 The Higgs Boson

If one only considers the first two lines of equation 2.2 then gauge invariance requires all particles in the SM to be massless. Yet we know objects to have mass. If we include the 3rd and 4th lines of equation 2.2, the mechanism of electroweak symmetry breaking proposed by by Brout, Englert, Higgs, Kibble, Hagen, and Guralnik [5, 17, 18, 19, 20, 21], then the fundamental particles can be shown to acquire their masses. A consequence of this mechanism is the existence of a complex scalar field ϕ, which leads to the existence of a scalar (spin 0) particle. The existence of this particle was first proposed in 1964 by Peter Higgs [5], and is therefore referred to as the Higgs boson.

On the 4th of July 2012, the discovery of a scalar boson consistent with the Standard Model Higgs boson was announced by the ATLAS and CMS collaborations [3, 4]. Subsequently Peter Higgs and François Englert were awarded the 2013 Nobel Prize for Physics [22].

2.3.1 Electroweak Symmetry Breaking

In the SM, the Higgs potential, ϕ, is a complex scalar doublet:

$$\phi = \begin{pmatrix} \phi^+ \\ \phi^0 \end{pmatrix} = \begin{pmatrix} \phi_1 + i\phi_2 \\ \phi_3 + i\phi_4 \end{pmatrix} \tag{2.5}$$

If we consider the last line of equation 2.2:

$$\begin{aligned} \mathcal{L}_{\text{Higgs}} &= |D_\mu \phi|^2 - V(\phi) \\ &= |D_\mu \phi|^2 - \mu^2 |\phi|^2 - \lambda |\phi|^4 \end{aligned} \tag{2.6}$$

the minima of this potential can be computed, giving,

$$\left. \frac{dV(\phi)}{d\phi} \right|_{\phi=\phi_0} = 2\mu^2 \phi_0 + 4\lambda \phi_0^3 = 0 \tag{2.7}$$

If μ and λ are real positive, then we have the trivial solution of $\phi_0 = 0$.

However, if $\mu^2 < 0$ then we have,

$$\phi_0 = \frac{1}{\sqrt{2}} \begin{pmatrix} 0 \\ v \end{pmatrix} \qquad \text{with} \qquad v = \sqrt{\frac{-\mu^2}{\lambda}} \tag{2.8}$$

It should be noted that we are free to choose the form of ϕ_0 such that $\phi^+ = 0$ and $\phi^0 = \frac{1}{\sqrt{2}}v$, since the potential ϕ is invariant under rotations in the (ϕ^+, ϕ^0) plane, that is to say ϕ is invariant under SU(2).

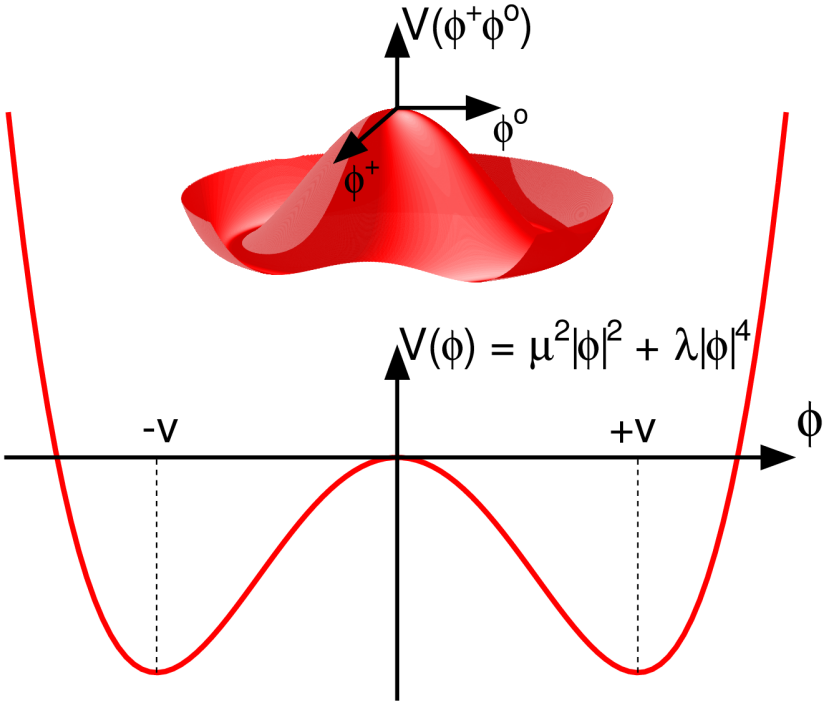

Figure 2.3: The Standard Model Higgs potential. Based on [23]

The Higgs potential can then be written as,

$$\phi = \frac{1}{\sqrt{2}} \begin{pmatrix} \phi_1 + i\phi_2 \\ v + H + i\phi_4 \end{pmatrix} \tag{2.9}$$

The Higgs potential, as shown in figure 2.3, has a non-zero ground state, or vacuum expectation energy, $E_{\text{vev}} = v$. In fixing this ground state we have broken the SU(2) symmetry

Oscillations around the minimum ϕ_0 then become the Higgs boson H and

three remaining fields of the Higgs potential known as Goldstone bosons [24]. These Goldstone bosons are massless unphysical fields.

To investigate what effect choosing this particular ϕ_0 has on the fields of SU(2)×U(1), let us evaluate equation 2.6 at ϕ_0,

$$\begin{aligned}\mathcal{L}_{\text{Higgs}} &= |D_\mu \phi_0|^2 - V(\phi_0) \\ &= (D_\mu \phi_0)^\dagger D^\mu \phi_0 - V(\phi_0)\end{aligned} \tag{2.10}$$

where,

$$D^\mu \phi_0 = \frac{1}{\sqrt{2}} \left(\partial^\mu - ig\frac{1}{2}\sigma^a W_a^\mu - ig'\frac{1}{2} Y B^\mu \right) \begin{pmatrix} 0 \\ v + H \end{pmatrix} \tag{2.11}$$

and,

$$\begin{aligned}\sigma^a W_a^\mu &= \sigma^1 W^{1\mu} + \sigma^2 W^{2\mu} + \sigma^3 W^{3\mu} \\ &= \begin{pmatrix} W^{3\mu} & W^{1\mu} - iW^{2\mu} \\ W^{1\mu} + iW^{2\mu} & -W^{3\mu} \end{pmatrix}\end{aligned} \tag{2.12}$$

therefore,

$$\begin{aligned}D^\mu \phi_0 = \frac{1}{\sqrt{2}} \Bigg(& \partial^\mu \begin{pmatrix} 1 & 0 \\ 0 & 1 \end{pmatrix} - ig\frac{1}{2} \begin{pmatrix} W^{3\mu} & W^{1\mu} - iW^{2\mu} \\ W^{1\mu} + iW^{2\mu} & -W^{3\mu} \end{pmatrix} \\ & -ig'\frac{1}{2} Y B^\mu \begin{pmatrix} 1 & 0 \\ 0 & 1 \end{pmatrix} \Bigg) \begin{pmatrix} 0 \\ v + H \end{pmatrix} \\ = \frac{1}{\sqrt{2}} & \left(\begin{pmatrix} 0 \\ \partial^\mu H \end{pmatrix} - i\frac{1}{2} \begin{pmatrix} g(W^{1\mu} - iW^{2\mu}) \\ g' Y B^\mu - g W^{3\mu} \end{pmatrix} (v + H) \right)\end{aligned} \tag{2.13}$$

$$
\begin{aligned}
(D_\mu\phi_0)^\dagger &= \phi_0^\dagger D_\mu^\dagger \\
&= \frac{1}{\sqrt{2}}\begin{pmatrix}0 & v+H\end{pmatrix} \\
&\quad \times \left(\partial_\mu \begin{pmatrix}1 & 0\\ 0 & 1\end{pmatrix} + ig\frac{1}{2}\begin{pmatrix}W_\mu^3 & W_\mu^1 - iW_\mu^2\\ W_\mu^1 + iW_\mu^2 & -W_\mu^3\end{pmatrix} + ig'\frac{1}{2}YB_\mu\begin{pmatrix}1 & 0\\ 0 & 1\end{pmatrix}\right) \\
&= \frac{1}{\sqrt{2}}\left(\begin{pmatrix}0 & \partial_\mu H\end{pmatrix} + i\frac{1}{2}\begin{pmatrix}g(W_\mu^1 + iW_\mu^2) & g'YB_\mu - gW_\mu^3\end{pmatrix}(v+H)\right)
\end{aligned}
\tag{2.14}
$$

and,

$$
\begin{aligned}
V(\phi_0) &= \mu^2|\phi_0|^2 + \lambda|\phi_0|^4 \\
&= -v^2\lambda\frac{1}{2}(v+H)^2 + \lambda\frac{1}{4}(v+H)^4 \\
&= -v^2\lambda\frac{1}{2}(v^2+H^2+2vH) + \lambda\frac{1}{4}(H^4+4vH^3+6v^2H^2+4v^3H+v^4) \\
&= -v^2\lambda\frac{1}{2}v^2 + \lambda\frac{1}{4}v^4 + (\lambda\frac{1}{4}4v^3 - v^2\lambda\frac{1}{2}2v)H \\
&\quad + (\lambda\frac{1}{4}6v^2 - v^2\lambda\frac{1}{2})H^2 + \lambda\frac{1}{4}4vH^3 + \lambda\frac{1}{4}H^4 \\
&= \lambda\frac{1}{2}v^4 + \lambda v^2H^2 + \lambda\frac{1}{4}4vH^3 + \lambda\frac{1}{4}H^4
\end{aligned}
\tag{2.15}
$$

so,

$$
\begin{aligned}
\mathcal{L}_{\text{Higgs}} &= (D_\mu\phi_0)^\dagger D^\mu\phi_0 - V(\phi_0) \\
&= \frac{1}{2}\left(\begin{pmatrix}0 & \partial_\mu H\end{pmatrix} + i\frac{1}{2}\begin{pmatrix}g(W^1_\mu + iW^2_\mu) & g'YB_\mu - gW^3_\mu\end{pmatrix}(v+H)\right) \\
&\quad \times \left(\begin{pmatrix}0\\ \partial^\mu H\end{pmatrix} - i\frac{1}{2}\begin{pmatrix}g(W^{1\mu} - iW^{2\mu})\\ g'YB^\mu - gW^{3\mu}\end{pmatrix}(v+H)\right) - V(\phi_0) \\
&= \frac{1}{2}\left((\partial H)^2 + \frac{1}{4}\left(g^2(W^{1\mu} - iW^{2\mu})(W^1_\mu + iW^2_\mu) + (g'YB^\mu - gW^{3\mu})^2\right)(v+H)^2\right) \\
&\quad + \mathcal{O}(\partial H) - V(\phi_0) \\
&= \frac{1}{2}(\partial H)^2 + \frac{1}{8}v^2g^2(W^{1\mu} - iW^{2\mu})(W^1_\mu + iW^2_\mu) + \frac{1}{8}v^2(g'YB^\mu - gW^{3\mu})^2 \\
&\quad + \frac{1}{4}vHg^2(W^{1\mu} - iW^{2\mu})(W^1_\mu + iW^2_\mu) + \frac{1}{4}vH(g'YB^\mu - gW^{3\mu})^2 \\
&\quad + \frac{1}{8}H^2g^2(W^{1\mu} - iW^{2\mu})(W^1_\mu + iW^2_\mu) + \frac{1}{8}H^2(g'YB^\mu - gW^{3\mu})^2 \\
&\quad + \mathcal{O}(\partial H) - \lambda\frac{1}{2}v^4 - \lambda v^2H^2 - \lambda\frac{1}{4}4vH^3 - \lambda\frac{1}{4}H^4
\end{aligned} \tag{2.16}
$$

From this we can see that the Higgs Lagrangian density above describes a number of linear combinations of fields, which can be interpreted as new fields corresponding to massive particles. We have neglected kinetic $\mathcal{O}(\partial H)$ terms above as they do not contribute to the masses of particles or their interactions with one another. These new physical fields are linear combinations of the SU(2), U(1) and Higgs potential fields. From the Higgs Lagrangian density then let us define these fields:

$$W^+_\mu = \frac{1}{\sqrt{2}}\left(W^1_\mu - iW^2_\mu\right) \tag{2.17}$$

$$W^-_\mu = \frac{1}{\sqrt{2}}\left(W^1_\mu + iW^2_\mu\right) \tag{2.18}$$

$$Z_\mu = \frac{1}{\sqrt{g^2 + g'^2Y^2}}(gW_{3\mu} - g'YB_\mu) \tag{2.19}$$

Where we have included the normalisations $\frac{1}{\sqrt{2}}$ and $\frac{1}{\sqrt{g^2+g'^2Y^2}}$.

Since we have the two fields $W_{3\mu}$ and B_μ combining to form the Z_μ field, we must also have a second field which must be a combination of the $W_{3\mu}$ and B_μ

fields but must be orthogonal to the Z_μ field:

$$A_\mu = \frac{1}{\sqrt{g^2 + g'^2 Y^2}}(gW_{3\mu} + g'YB_\mu) \tag{2.20}$$

Let us then rewrite the Higgs Lagrangian density in terms of these new fields:

$$\begin{aligned}\mathcal{L}_{\text{Higgs}} = &\frac{1}{2}(\partial H)^2 + \frac{1}{4}v^2 g^2 W^{+\mu}W^-_\mu + \frac{1}{8}v^2\left(g^2 + g'^2Y^2\right)(Z_\mu)^2 \\ &+ \frac{1}{2}vHg^2W^{+\mu}W^-_\mu + \frac{1}{4}vH\left(g^2 + g'^2Y^2\right)(Z_\mu)^2 \\ &+ \frac{1}{4}H^2g^2W^{+\mu}W^-_\mu + \frac{1}{8}H^2\left(g^2 + g'^2Y^2\right)(Z_\mu)^2 \\ &+ \mathcal{O}(\partial H) - \lambda\frac{1}{2}v^4 - \lambda v^2H^2 - \lambda\frac{1}{4}4vH^3 - \lambda\frac{1}{4}H^4\end{aligned} \tag{2.21}$$

From this we can now read off the masses of the physical field. The mass term for a field is quadratic in that field (and that field alone), such that the term is equal to $\frac{1}{2}m^2\theta^2$ for a neutral field θ, or $m^2\theta^+\theta^-$ for charged fields.

$$m_H = \sqrt{2\lambda}v \tag{2.22}$$

$$m_{W^+} = \frac{1}{2}gv \tag{2.23}$$

$$m_{W^-} = \frac{1}{2}gv \tag{2.24}$$

$$m_Z = \frac{1}{2}v\sqrt{g^2 + g'^2Y^2} \tag{2.25}$$

The field A_μ has no quadratic term in the Higgs Lagrangian density, which is equivalent to saying that the coefficient of its mass term is zero, thus it is massless.

$$m_A = 0 \tag{2.26}$$

The vacuum expectation energy v is determined precisely from muon decay measurements [25, 26, 27], giving a value of $v = 246$ GeV [28].

The mass of the Higgs boson is the only parameter that can not be calculated using other measurable parameters as it is dependent on λ. It is therefore a free parameter in the SM, and must be measured independently. From measurements

by the ATLAS experiment, $m_H = 125.36 \pm 0.37$ (stat) ± 0.18 (syst) GeV $= 125.36 \pm 0.41$ GeV [29]. From measurements by the CMS experiment, $m_H = 125.02\ ^{+0.26}_{-0.27}$ (stat) $^{+0.14}_{-0.15}$ (syst) GeV [30].

Other (non-constant) terms proportional to multiple fields in the Higgs Lagrangian density describe the interactions between these different fields, and so describe interactions between different particles. For example the term $\frac{1}{2}vHg^2W^{+\mu}W^-_\mu$ describes the interaction of a Higgs boson with a W^+ boson and a W^- boson. We can modify the term such that it describes a H interacting with any two W bosons, W_μ and W_ν, thusly: $\frac{1}{2}vHg^2g^{\mu\nu}W_\mu W_\nu$, where $g^{\mu\nu}$ is the metric. The interaction strength is then the coefficient of the fields, $\frac{1}{2}vg^2g^{\mu\nu}$, and we can multiply this by i to obtain the Feynman rule for this interaction vertex, $i\frac{1}{2}vg^2g^{\mu\nu}$, as given in figure 2.4.

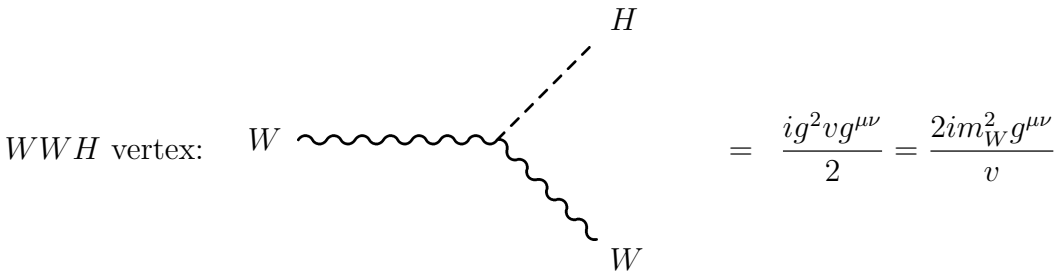

Figure 2.4: HWW Feynman diagram and Feynman rule, where the mass of the W boson has been used to rewrite the Feynman rule in an alternative form.

We can change from a basis of $(W_{3\mu}, B_\mu)$ to a basis of (Z_μ, A_μ) through a rotation of angle θ_W:

$$\begin{pmatrix} Z_\mu \\ A_\mu \end{pmatrix} = \begin{pmatrix} \cos\theta_W & -\sin\theta_W \\ \sin\theta_W & \cos\theta_W \end{pmatrix} \begin{pmatrix} W_{3\mu} \\ B_\mu \end{pmatrix} \tag{2.27}$$

θ_W is known as the 'weak mixing angle'.

We can then use definitions 2.19 and 2.20 to equate,

$$\cos\theta_W = \frac{g}{\sqrt{g^2 + g'^2Y^2}} \tag{2.28}$$

$$\sin\theta_W = \frac{g'}{\sqrt{g^2 + g'^2Y^2}} \tag{2.29}$$

From equations 2.23, 2.25, and 2.28 we can then write,

$$\cos\theta_W = \frac{m_W}{m_Z} \tag{2.30}$$

Equation 2.30 however is only correct to leading order in QCD. θ_W scales with interaction energy, as shown in figure 2.5. θ_W is determined through Z-pole observables, the W mass, and low-energy precision measurements of weak neutral current interactions [28, 31].

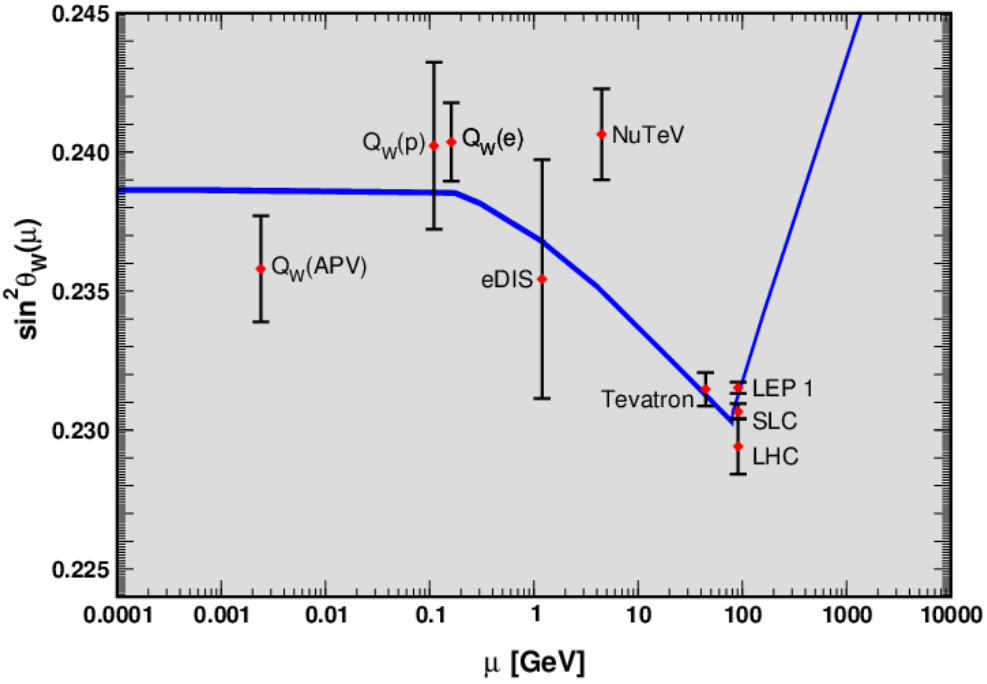

Figure 2.5: $\sin^2(\theta_W)$ against interaction energy μ. Results of experimental measurements of $\sin^2(\theta_W)$ are shown. Theoretical predictions of $\sin^2(\theta_W)$ are shown as a blue band. From [28].

We have thus seen how the Higgs Lagrangian density term (equation 2.6) in the SM Lagrangian density (equation 2.2) causes the system to take on a non-zero ground state value, thus breaking the symmetry of the SU(2) × U(1) × ϕ electroweak system, 'electroweak symmetry breaking', and causing previously massless fields of this system to transform into physical fields with mass. We can equate these physical fields with known massive SM particles: the W^+, the W^-, the Z, and the Higgs boson. The massless A_μ field is the SM photon.

Let us also consider the Goldstone bosons that were mentioned in equation

2.9. If we consider degrees of freedom, the massless SU(2) fields W^1, W^2, and W^3 each have 2 transverse polarisations (they do not have longitudinal polarisations due to being massless and thus travelling at the speed of light), and thus each has 2 degrees of freedom. Likewise the massless U(1) field also has 2 transverse polarisations and thus 2 degrees of freedom. The Higgs potential has 4 scalar fields. One becoming the scalar Higgs boson with one degree of freedom, leaving 3 fields remaining, the Goldstone bosons, each with one degree of freedom. This adds up to a total of 12 degrees of freedom. Once the physical gauge bosons have acquired mass through the electroweak symmetry breaking mechanism, the W^+, W^-, and Z each have 3 polarisations and thus 3 degrees of freedom. The photon remains massless and so has 2 transverse polarisations and thus 2 degrees of freedom. The Higgs boson is a scalar and thus has 1 degree of freedom. This again adds up to a total of 12 degrees of freedom. No degrees of freedom have therefore been gained or lost. In becoming massive, W^+, W^-, and Z have thus absorbed the degrees of freedom provided by the Goldstone bosons. The Goldstone bosons are therefore said to have been 'eaten' by the massive gauge bosons to become longitudinal polarisations.

2.3.2 Higgs Production

Prominent Higgs boson production modes at the LHC are shown in Feynman diagrams 2.6, and their cross-sections for different Higgs boson masses are shown in figure 2.7.

2.3.3 Higgs Decay

The Higgs boson is an unstable particle in the SM. A SM Higgs boson with a mass of 125 GeV is predicted to have a total width Γ_{TOT} of 4.07 MeV [32]. The mean lifetime τ of a particle is given by $\tau = \frac{\hbar}{\Gamma_{\mathrm{TOT}}}$, therefore the mean lifetime of a 125 GeV SM Higgs boson is 1.62×10^{-22} s. This means that a Higgs boson will never be directly observed in a particle detector such as the ATLAS detector. To search for evidence of the existence of a Higgs boson, one must therefore search for the products of its decay. The SM Higgs boson decays into a number of different final states. These final states are shown, along with their associated branching ratios (BR) for different Higgs boson masses, in figure 2.8.

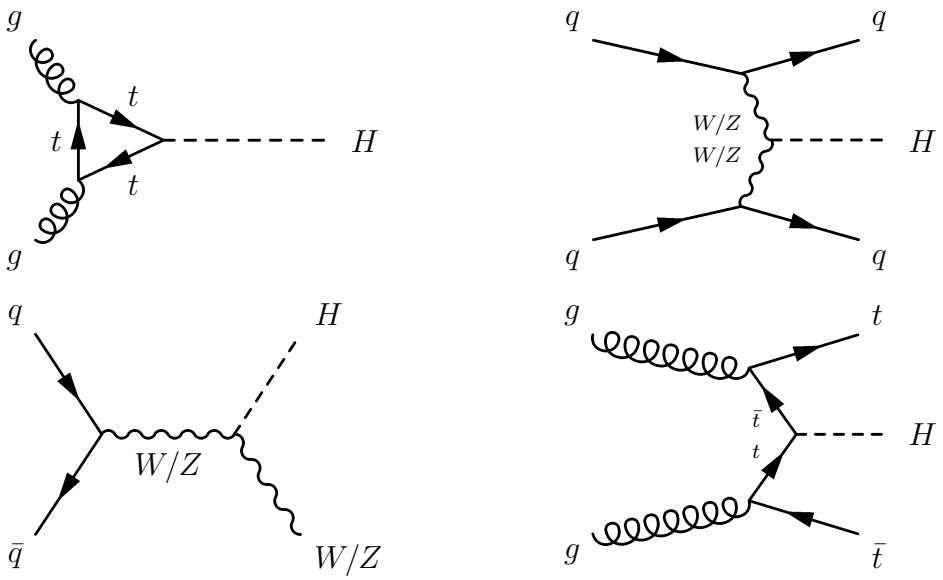

Figure 2.6: Feynman diagrams of Higgs boson production in proton-proton collisions at the LHC. Top left: gluon-gluon fusion via a top-quark loop. Top right: vector boson fusion. Bottom left: associated production. Bottom right: top-quark fusion.

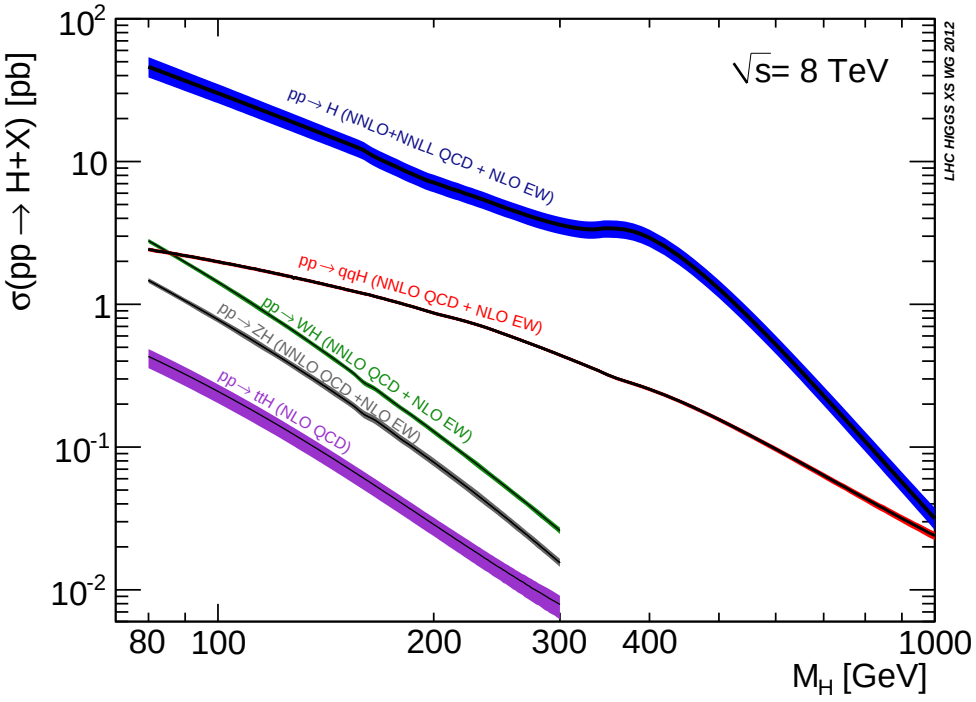

Figure 2.7: Cross sections of Higgs boson production modes in proton-proton collisions at $\sqrt{s} = 8$ TeV. From [32]

.

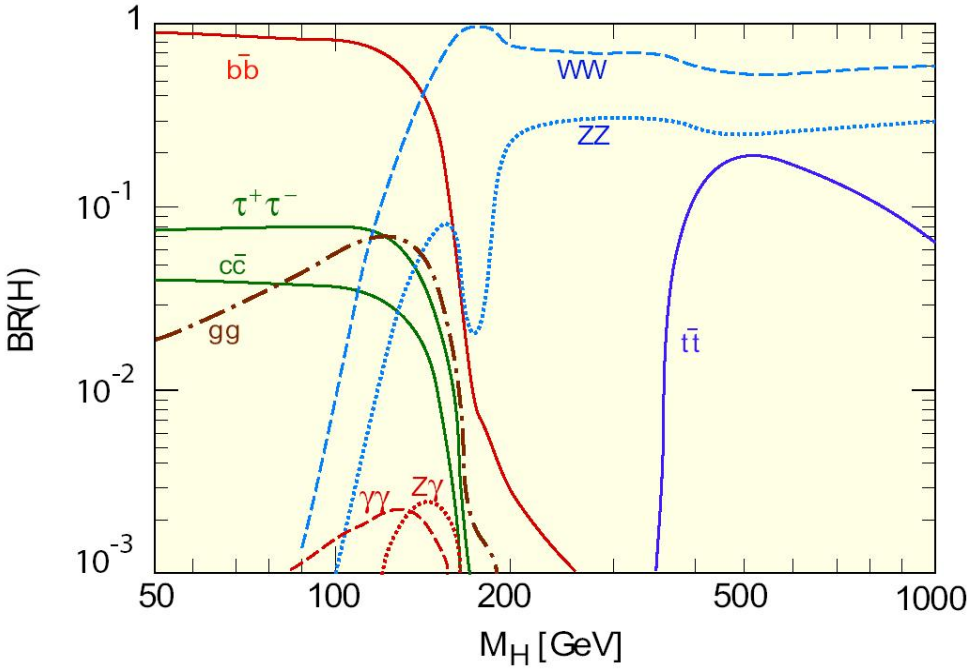

Figure 2.8: Branching ratios of the SM Higgs boson against Higgs boson mass. From [32]

.

2.3.4 Production Cross-Sections And Parton Density Functions

The cross-section (σ) of a given process at colliders such at the Large Hadron Collider (LHC) is a measure of the rate at which the process occurs. The number of times a given process will occur (N) in particle collisions is given by,

$$N = \sigma \int L \, \mathrm{d}t \tag{2.31}$$

where,

N = Number of times a given process will occur

σ = Cross-section of given process

L = Instantaneous luminosity. See equation 3.1

t = Time

$\int L \, \mathrm{d}t$ = Integrated Luminosity

Parton Density Functions

At the LHC (see chapter 3 section 3.2), for the collisions relevant to this thesis, the colliding particles are protons. Since protons are hadrons, composed of multiple quarks and gluons (partons), the cross-section of a process can be described, using the factorisation theorem, in terms of the theoretical cross section of the process where the colliding particles are partons, and the 'parton density functions' (PDFs) of the colliding hadrons. PDFs describe the densities of the different partons inside a hadron.

$$\begin{aligned}\sigma(\text{proton-proton} \to \text{X}) = \sum_{\text{parton flavours}} \int \mathrm{d}x_1 \, \mathrm{d}x_2 \\ \times \ \text{PDF}_1(x_1, Q^2, f_1) \ \text{PDF}_2(x_2, Q^2, f_2) \\ \times \ \hat{\sigma}(\text{parton-parton} \to \text{X})\end{aligned} \tag{2.32}$$

where,

$\sigma(\text{proton-proton} \to \text{X})$ = Cross-section of a given process when considering the incoming particles to be protons.

x_1 = Bjorken x of parton 1. It is the fraction of the 1st proton's momentum carried by parton 1.

x_2 = Bjorken x of parton 2. It is the fraction of the 2nd proton's momentum carried by parton 2.

f_1 and f_2 = The flavours of partons 1 and 2. Up-quark, down-quark, gluon, etc.

Q = The energy scale of the interaction.

$\text{PDF}_1(x_1, Q^2, f_1)$ and $\text{PDF}_2(x_2, Q^2, f_2)$ = The probability of finding a parton of flavour f_1 (f_2) with a fraction x_1 (x_2) of the 1st (2nd) proton's momentum, at energy scale Q^2

$\hat{\sigma}(\text{parton-parton} \to \text{X})$ = Cross-section of a given process when considering the incoming particles to be partons.

The forms of PDFs are determined from theoretical considerations and fits to data, and therefore have uncertainties associated with them. A number of groups have produced PDFs, including the CTEQ Collaboration [33] as shown in figure 2.10, the MSTW Collaboration [34] as shown in figure 2.11, and the NNPDF Collaboration [35] as shown in figure 2.12. PDFs are typically derived using data from deep-inelastic scattering, vector boson production, vector boson rapidity distributions, vector boson charge asymmetry, and inclusive jet production [36, 37, 38].

PDFs are made available in PDF 'sets'. A PDF set consists of a 'central member' PDF, and a PDF 'error set' containing n PDFs. This is shown diagrammatically in figure 2.9. For the CT10nlo PDF set, $n = 52$. For the MSTW2008 PDF set, $n = 40$. For the NNPDF2.3 PDF sets, $n = 100$. A PDF error set is a set of PDFs suitable for estimating the uncertainty on the central member PDF. Each PDF is fitted for a specific value of $\alpha_s(m_Z)$. All PDF sets, except CTEQas, are fitted for a specific value of $\alpha_s(m_Z)$. The CTEQas PDF set contains no error set, so can not be used to estimate PDF uncertainties. It

does however contain 11 central member PDFs, each fitted for a different value of $\alpha_s(m_Z)$, ranging from $\alpha_s(m_Z) = 0.113$ to 0.123 in steps of 0.001. Table 2.1 lists the PDF sets used in this thesis. PDF error sets used are one of two types: Hessian or Replicas.

Hessian-type PDF error sets

Hessian error sets represent variations of orthonormal PDF free parameter eigenvectors: free parameters in the PDFs are diagonalised and rescaled into a set of orthonormal eigenvectors. This is a change of basis from the original parameter basis to an orthonormal eigenvector basis. Each PDF in an error set represent a variation of one eigenvector up or down by a specified confidence level (one sigma for MSTW2008, a 90% C.L. for CT10nlo). For example, the CT10nlo PDFs have 26 free parameters, thus they have 26 eigenvectors. The CT10nlo error set therefore contains 52 PDFs. The first PDF in the error set has the first eigenvector varied up (by an amount corresponding to a 90% C.L.), with all other eigenvectors kept the same as in the central member PDF. The second PDF in the error set has the first eigenvector varied down. These PDFs therefore form a pair for the variation of the first eigenvector. All other error set PDFs form pairs, corresponding to variations of the other eigenvectors. The central member of each PDF set with a Hessian error set is the best-fit to data, ie. with all eigenvectors in their nominal (unvaried) positions.

Replica-type PDF error sets

Replica error sets consist of equally valid PDFs resulting from independent fits to data. The central member of each PDF set with a replica error set is the average of all the PDFs making up the error set.

$$\left\{ \Big[CM\Big], \Big[E_1, E_2, \ldots, E_n\Big] \right\}$$

Figure 2.9: Diagram of a PDF set. CM is the central member PDF. The n E_i PDFs make up the PDF error set.

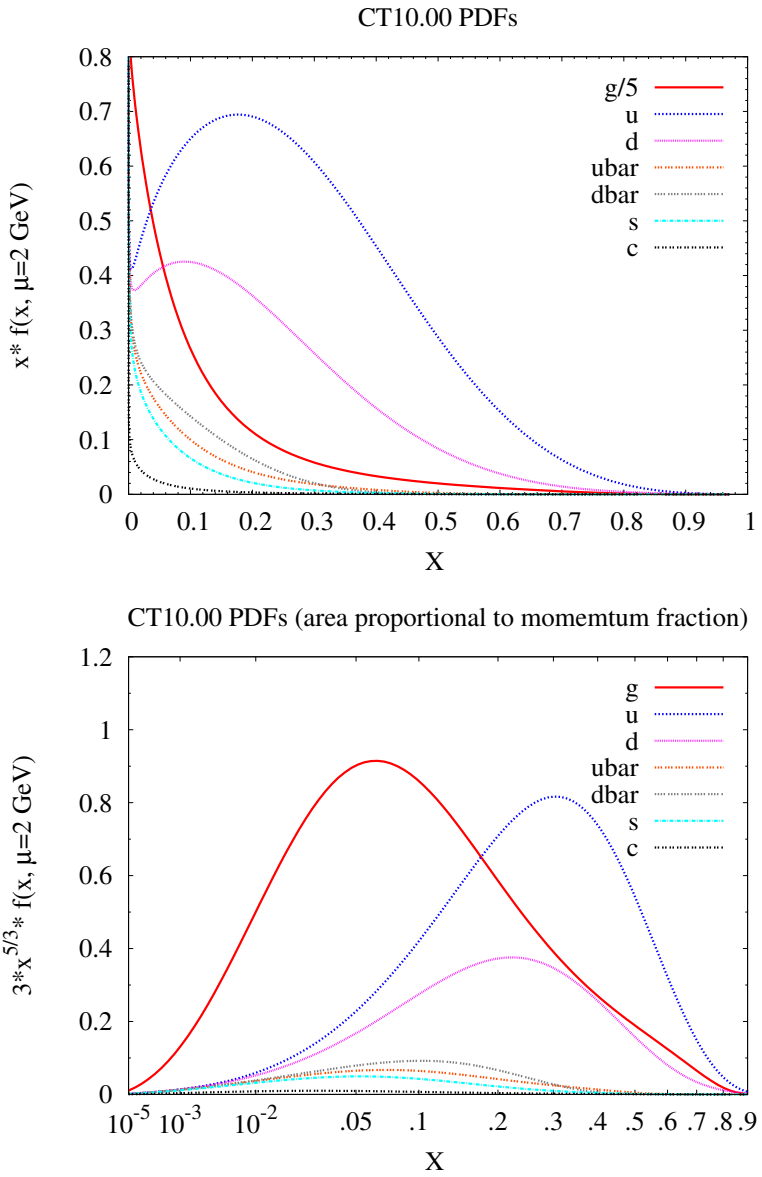

Figure 2.10: CT10 parton density functions (PDFs) for protons, produced by the CTEQ Collaboration. From [33] and [36]. The x and $f(x,\mu)$ of the y-axis variables plotted are the Bjorken x and PDF(x, Q^2, f) of equation 2.32. $Q^2 \equiv \mu^2 = 4$ GeV^2.

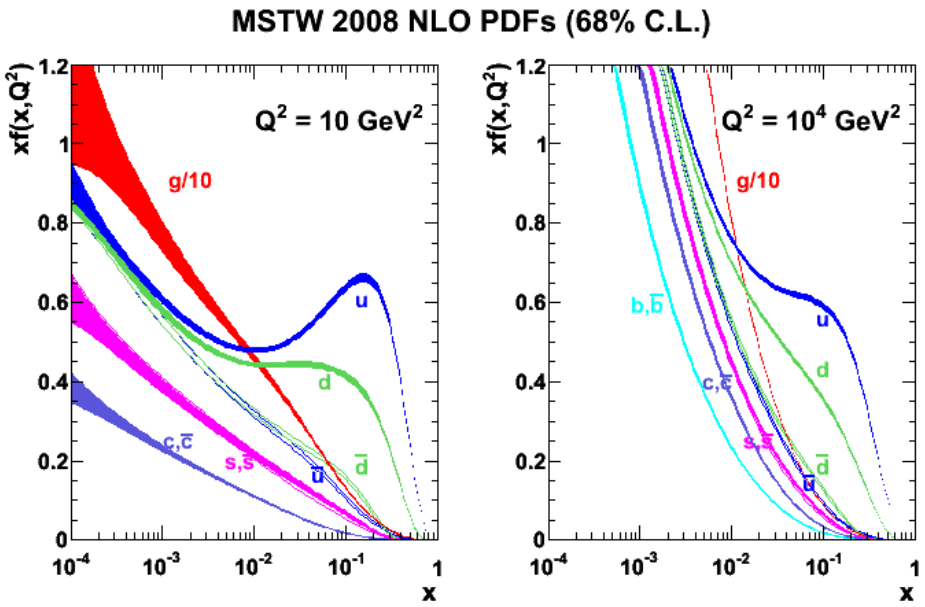

Figure 2.11: MSTW2008 parton density functions (PDFs) for protons, produced by the MSTW Collaboration. From [34]. The x and $f(x, Q^2)$ of the y-axis variables plotted are the Bjorken x and PDF(x, Q^2, f) of equation 2.32. $Q^2 = 10$ GeV^2.

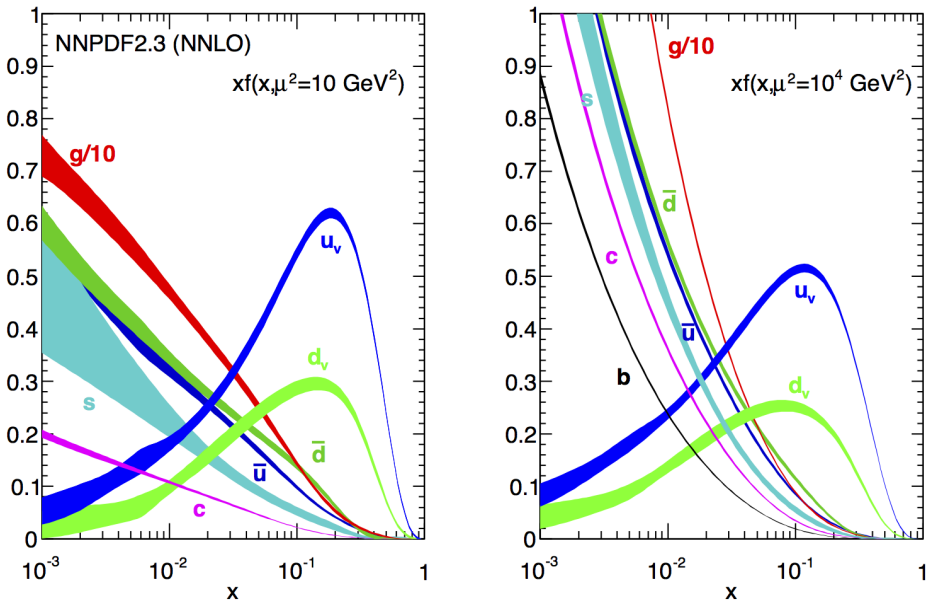

Figure 2.12: NNPDF2.3 parton density functions (PDFs) for protons, produced by the NNPDF Collaboration. From [35]. The x and $f(x, \mu)$ of the y-axis variables plotted are the Bjorken x and PDF(x, Q^2, f) of equation 2.32. $Q^2 \equiv \mu^2 = 10$ GeV^2.

PDF set	Collaboration	QCD order	$\alpha_s(m_Z)$	Error set	Number of PDFs	Error set type
cteq6l1	CTEQ	LO	0.130	No	1	N/A
CT10nlo	CTEQ	NLO	0.118	Yes	1+52	Hessian
CT10as	CTEQ	NLO	0.113 to 0.123	No	11	N/A
MSTW2008nlo68cl	MSTW	NLO	0.120179	Yes	1+40	Hessian
MSTW2008nlo68cl_asmz-68cl	MSTW	NLO	0.11867	Yes	1+40	Hessian
MSTW2008nlo68cl_asmz+68cl	MSTW	NLO	0.12140	Yes	1+40	Hessian
NNPDF23_nlo_as_0114	NNPDF	NLO	0.114	Yes	1+100	Replicas
NNPDF23_nlo_as_0115	NNPDF	NLO	0.115	Yes	1+100	Replicas
NNPDF23_nlo_as_0116	NNPDF	NLO	0.116	Yes	1+100	Replicas
NNPDF23_nlo_as_0117	NNPDF	NLO	0.117	Yes	1+100	Replicas
NNPDF23_nlo_as_0118	NNPDF	NLO	0.118	Yes	1+100	Replicas
NNPDF23_nlo_as_0119	NNPDF	NLO	0.119	Yes	1+100	Replicas
NNPDF23_nlo_as_0120	NNPDF	NLO	0.120	Yes	1+100	Replicas
NNPDF23_nlo_as_0121	NNPDF	NLO	0.121	Yes	1+100	Replicas
NNPDF23_nlo_as_0122	NNPDF	NLO	0.122	Yes	1+100	Replicas
NNPDF23_nlo_as_0123	NNPDF	NLO	0.123	Yes	1+100	Replicas
NNPDF23_nlo_as_0124	NNPDF	NLO	0.124	Yes	1+100	Replicas

Table 2.1: PDF sets used in this thesis.

2.3.5 *WH* Production At The Large Hadron Collider

The WH channel is central to this thesis. For more details on this, see chapter 4. Let us consider this channel and its production at the LHC. The full cross-section for this process $\sigma(pp \to WH)$ is given by,

$$\begin{aligned}\sigma(pp \to WH) = \sum_{\text{parton flavours}} \int \mathrm{d}x_1 \, \mathrm{d}x_2 \\ \times \ \mathrm{PDF}_1(x_1, Q^2, f_1) \ \mathrm{PDF}_2(x_2, Q^2, f_2) \\ \times \ \hat{\sigma}(q\bar{q} \to WH)\end{aligned} \tag{2.33}$$

where pp refers to proton-proton collisions, and $q\bar{q}$ refers to quark-antiquark annihilation.

In this chapter the partonic cross-section $\hat{\sigma}(q\bar{q} \to WH)$ will be calculated.

The leading order processes that contribute to the WH channel are shown in figure 2.13. A generic form of these two diagrams is shown in figure 2.14.

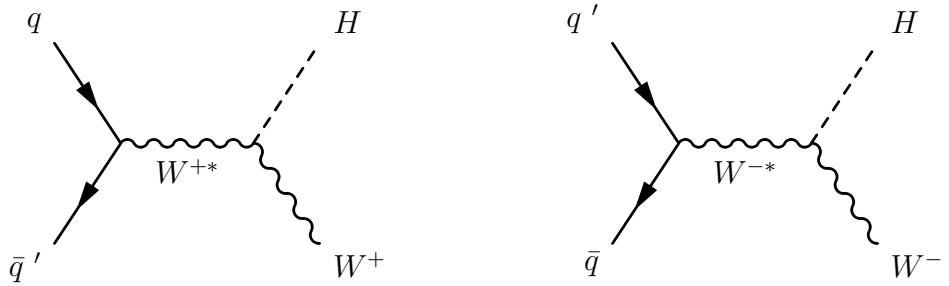

Figure 2.13: Leading order Feynman diagrams of Higgs boson production in association with a W boson.

where,

$u^s(p_1)$ = The Dirac spinor of the incoming quark with four-momentum p_1

$\bar{v}^s(p_2)$ = The Dirac spinor of the incoming anti-quark with four-momentum p_2

p_3 = The four-momentum of the outgoing Higgs boson

$\epsilon^*_\sigma(p_4)$ = The polarisation vector of the outgoing W boson with four-momentum p_4

k = The four-momentum of the intermediate virtual W boson

v_1 = The $q\ \bar{q}\ W$ boson vertex

v_2 = The $W\ W$ Higgs boson vertex

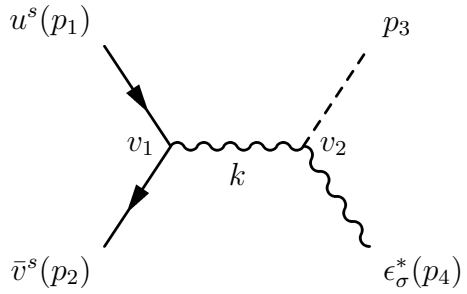

Figure 2.14: Leading order Feynman diagram of Higgs boson production in association with a W boson.

The cross-section of the $q\bar{q} \to WH$ process to leading order is given by equation 2.34 (see [39]):

$$\begin{aligned} \mathrm{d}\hat{\sigma}(q\bar{q} \to WH) = & \frac{1}{4\sqrt{(p_1 \cdot p_2)^2 - p_1^2 p_2^2}} \left(\prod_f \frac{\mathrm{d}^3 p_f}{(2\pi)^3} \frac{1}{2E_f} \right) \\ & \times (2\pi)^4 \delta^{(4)}(p_1 + p_2 - p_3 - p_4) \sum_\lambda |\overline{\mathcal{M}}(q\bar{q} \to WH)|^2 \end{aligned} \tag{2.34}$$

where,

$\sum_\lambda$ = Sum over final states.

$\hat{\sigma}(q\bar{q} \to WH)$ = Cross-section for the $q\bar{q} \to WH$ process.

$\overline{\mathcal{M}}(q\bar{q} \to WH)$ = The matrix element for the $q\bar{q} \to WH$ process, averaged over initial states.

$\prod_f$ = Product over the final state particles. $f = \{3, 4\}$.

The matrix element can be computed from the Feynman diagram 2.14. $\frac{1}{4\sqrt{(p_1 \cdot p_2)^2 - p_1^2 p_2^2}} \left(\prod_f \frac{\mathrm{d}^3 p_f}{(2\pi)^3} \frac{1}{2E_f} \right) (2\pi)^4 \delta^{(4)}(p_1 + p_2 - p_3 - p_4)$ is the Lorentz-invariant phase space for a 2 to 2 process.

Given that this is a 2 to 2 interaction, and we move to the centre of mass frame such that $\vec{p_1} = -\vec{p_2}$, where $\vec{p_n}$ is the three-momentum component of the

four-momentum p_n, we can simplify the Lorentz-invariant phase space to give,

$$\mathrm{d}\hat{\sigma}(q\bar{q} \to WH) = \frac{1}{4\sqrt{\hat{s}}|\vec{p_1}|}\left(\frac{\mathrm{d}\Omega_{cm}}{4\pi}\frac{1}{8\pi}\frac{2|\vec{p}|}{\sqrt{\hat{s}}}\right)\sum_{\lambda}|\overline{\mathcal{M}}(q\bar{q} \to WH)|^2 \qquad (2.35)$$

where,

Ω_{cm} = Solid angle in the centre of momentum frame.

$\hat{s} = (E_1 + E_2)^2$ where E_1 and E_2 are the energy of the q and $\bar{q}$ respectively.

$\vec{p}$ = The three-momentum of either outgoing particle in the centre of mass frame.

To calculate the matrix element $\mathcal{M}(q\bar{q} \to WH)$ we can consider the Feynman diagram 2.14, where each element of the diagram contributes a term to the matrix element. These terms, in the unitary gauge, are as follows:

Incoming q: 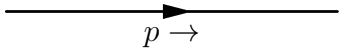

$= \quad u^s(p)$

Incoming $\bar{q}$: 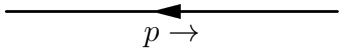

$= \quad \bar{v}^s(p)$

Outgoing W: 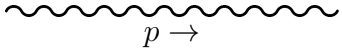

$= \quad \epsilon^*_\sigma(p)$

Outgoing H: 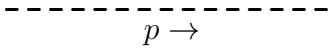

$= \quad 1$

W propagator: 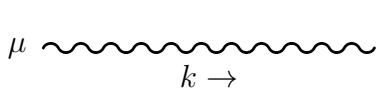

$= \dfrac{-i\left(g_{\mu\nu} - \frac{k_\mu k_\nu}{m_W^2}\right)}{k^2 - m_W^2}$

$q\bar{q}W$ vertex: 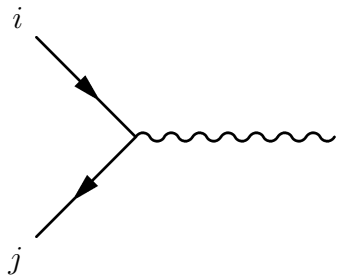

$= \dfrac{im_W}{\sqrt{2}v_{\text{vev}}}\gamma^\mu(1-\gamma^5)V_{ij}^{\text{CKM}}$

WWH vertex: 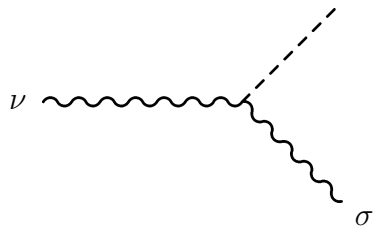

$= \dfrac{2im_W^2 g^{\nu\sigma}}{v_{\text{vev}}}$

where V^{CKM} is the CKM matrix. V_{ij}^{CKM} is the element of the CKM matrix for quarks of type i and j.

The matrix element $\mathcal{M}(q\bar{q} \to WH) \equiv \mathcal{M}$ is then given by:

$$\mathcal{M} = \bar{v}^s(p_2)\frac{im_W}{\sqrt{2}v_{\text{vev}}}\gamma^\mu(1-\gamma^5)V^{\text{CKM}}u^s(p_1)\frac{-i\left(g_{\mu\nu} - \frac{k_\mu k_\nu}{m_W^2}\right)}{k^2 - m_W^2}\frac{2im_W^2 g^{\nu\sigma}}{v_{\text{vev}}}\epsilon_\sigma^*(p_4) \tag{2.36}$$

Since $m_q \ll m_W$ we can take the limit where the quarks are massless. In this limit, the $E - |\vec{p}|$ terms in the spinors $u^s(p_1)$ and $\bar{v}^s(p_2)$ vanish:

$$u^s(p_1) = \begin{pmatrix} \sqrt{E_1 - \lambda|\vec{p_1}|}\ \chi_\lambda(\hat{p_1}) \\ \sqrt{E_1 + \lambda|\vec{p_1}|}\ \chi_\lambda(\hat{p_1}) \end{pmatrix} \tag{2.37}$$

$$\bar{v}^s(p_2) = \begin{pmatrix} -\sqrt{E_2 + \lambda|\vec{p_2}|}\ \chi_{-\lambda}(\hat{p_2}) \\ \sqrt{E_2 - \lambda|\vec{p_2}|}\ \chi_{-\lambda}(\hat{p_2}) \end{pmatrix}^\dagger \gamma^0 \tag{2.38}$$

where $\lambda = \pm 1$ is twice the helicity, and,

$$\chi_+(\hat{p}) = \begin{pmatrix} 1 \\ 0 \end{pmatrix} \quad \text{and} \quad \chi_-(\hat{p}) = \begin{pmatrix} 0 \\ 1 \end{pmatrix} \tag{2.39}$$

Since we are in the centre of mass frame, $\vec{k} = 0$. Thus $\bar{v}^s(p_2)u^s(p_1)k_\mu k_\nu = 0$ and we can neglect the $\frac{k_\mu k_\nu}{m_W^2}$ term in the W boson propagator. Therefore:

$$\begin{aligned}
\mathcal{M} &= \bar{v}^s(p_2)\frac{im_W}{\sqrt{2}v_{\text{vev}}}\gamma^\mu(1-\gamma^5)V^{\text{CKM}}u^s(p_1)\frac{-ig_{\mu\nu}}{k^2-m_W^2}\frac{2im_W^2 g^{\nu\sigma}}{v_{\text{vev}}}\epsilon^*_\sigma(p_4) \\
&= \frac{-\sqrt{2}im_W^3 V^{\text{CKM}}}{v_{\text{vev}}^2}\frac{1}{k^2-m_W^2}\bar{v}^s(p_2)\gamma_\nu(1-\gamma^5)u^s(p_1)\epsilon^{*\nu}(p_4) \\
&= A(k)\bar{v}^s(p_2)\gamma_\nu(1-\gamma^5)u^s(p_1)\epsilon^{*\nu}(p_4) \\
&= A(k)\bar{v}^s(p_2)\Gamma u^s(p_1)
\end{aligned} \tag{2.40}$$

where,

$$A(k) = \frac{-\sqrt{2}im_W^3 V^{\text{CKM}}}{v_{\text{vev}}^2}\frac{1}{k^2-m_W^2} \tag{2.41}$$

$$\Gamma = \gamma_\nu(1-\gamma^5)\epsilon^{*\nu}(p_4) \tag{2.42}$$

We then require,

$$\begin{aligned}
\sum_\lambda |\overline{\mathcal{M}}(q\bar{q}\to WH)|^2 &\equiv \sum_\lambda |\overline{\mathcal{M}}|^2 \\
&= \sum_\lambda \frac{1}{N_c N_s}\sum_c\sum_s |A(k)|^2 \left(\bar{v}^s(p_2)\Gamma u^s(p_1)\right)\left(\bar{u}^s(p_1)\bar{\Gamma}v^s(p_2)\right) \\
&= \sum_\lambda \frac{1}{6}\sum_s |A(k)|^2 \left(\bar{v}^s(p_2)\Gamma u^s(p_1)\right)\left(\bar{u}^s(p_1)\bar{\Gamma}v^s(p_2)\right)
\end{aligned} \tag{2.43}$$

where the $\frac{1}{N_c N_s}\sum_c\sum_s = \frac{1}{6}\sum_s$ term is an average over initial colours and spins, since the incoming quark can have either red, green, or blue colour charge, and can be either spin-up or spin-down. The anti-quark must have the colour anticharge of the quark, and the same spin as the quark, in order to create a

colour-charge neutral, spin-one W boson. This can be written as:

$$\begin{aligned}\sum_{\lambda}|\overline{\mathcal{M}}|^2 &= \sum_{\lambda}\frac{1}{6}\sum_{s}|A(k)|^2\ \mathrm{Tr}\left[\bar{v}^s(p_2)\Gamma u^s(p_1)\bar{u}^s(p_1)\bar{\Gamma}v^s(p_2)\right]\\ &= \sum_{\lambda}\frac{1}{6}\sum_{s}|A(k)|^2\ \mathrm{Tr}\left[\Gamma u^s(p_1)\bar{u}^s(p_1)\bar{\Gamma}v^s(p_2)\bar{v}^s(p_2)\right]\end{aligned} \tag{2.44}$$

where we have used the cyclic property of traces (known in this example as "Casimir's trick"). Additionally,

$$\begin{aligned}\bar{\Gamma} &= \gamma^0\Gamma^\dagger\gamma^0\\ &= \gamma^0\left(\gamma_\rho(1-\gamma^5)\epsilon^{*\rho}(p_4)\right)^\dagger\gamma^0\\ &= \gamma^0\epsilon^\rho(p_4)(1-\gamma^5)^\dagger\gamma_\rho^\dagger\gamma^0\\ &= \gamma^0\epsilon^\rho(p_4)(1-\gamma^5)\gamma^0\gamma_\rho\gamma^0\gamma^0\\ &= \epsilon^\rho(p_4)(1+\gamma^5)\gamma_\rho\end{aligned} \tag{2.45}$$

since $(\gamma^5)^\dagger=\gamma^5$, $(\gamma^\rho)^\dagger=\gamma^0\gamma^\rho\gamma^0$, $\gamma^\alpha\gamma^\beta=-\gamma^\beta\gamma^\alpha$, and $(\gamma^0)^2=I_4$.

We can then use the following spin-sum relations:

$$\sum_s u^s(p)\bar{u}^s(p) = (\not{p}+m) \tag{2.46}$$

$$\sum_s v^s(p)\bar{v}^s(p) = (\not{p}-m) \tag{2.47}$$

to give,

$$\sum_{\lambda}|\overline{\mathcal{M}}|^2 = \sum_{\lambda}\frac{1}{6}|A(k)|^2\ \mathrm{Tr}\left[\Gamma(\not{p}_1+m_q)\bar{\Gamma}(\not{p}_2-m_{\bar{q}})\right] \tag{2.48}$$

Furthermore, we can treat the quark masses as negligible, such that $m_q\to 0$

and $m_{\bar{q}} \to 0$, giving,

$$\begin{aligned}\sum_{\lambda} |\overline{\mathcal{M}}|^2 &= \sum_{\lambda} \frac{1}{6} |A(k)|^2 \ \mathrm{Tr}\left[\Gamma \not{p}_1 \bar{\Gamma} \not{p}_2\right] \\ &= \sum_{\lambda} \frac{1}{6} |A(k)|^2 \ \mathrm{Tr}\Big[\gamma_\nu (1-\gamma^5) \epsilon^{*\nu}(p_4) \not{p}_1 \epsilon^{\rho}(p_4) (1+\gamma^5) \gamma_\rho \not{p}_2\Big] \\ &= \sum_{\lambda} \frac{1}{6} |A(k)|^2 \ \mathrm{Tr}\Big[\ \epsilon^{*\nu}(p_4)\ p_{1\alpha}\ \epsilon^{\rho}(p_4)\ p_{2\beta}\ \gamma_\nu (1-\gamma^5) \gamma^\alpha (1+\gamma^5) \gamma_\rho \gamma^\beta\Big]\end{aligned} \tag{2.49}$$

Since we are interested in an unpolarised cross-section, we can sum over all three polarisation states of the outgoing W boson and use the Ward identity [39] to give,

$$\sum_{\text{polarisations}} \epsilon^{*\nu}(p_4) \epsilon^{\rho}(p_4) = -g^{\nu\rho} + \frac{p_4^\nu p_4^\rho}{m_W^2} \tag{2.50}$$

Including this in the sum over final states gives,

$$\sum_{\lambda} = \sum_{\text{processes}} \sum_{\text{polarisations}} = 2\left(-g^{\nu\rho} + \frac{p_4^\nu p_4^\rho}{m_W^2}\right) \tag{2.51}$$

where the factor of two accounts for the possible final states W^+H and W^-H. Then,

$$\begin{aligned}\sum_{\lambda} |\overline{\mathcal{M}}|^2 = \frac{1}{3} |A(k)|^2 \ \mathrm{Tr}\Bigg[&\left(\left(-g^{\nu\rho} + \frac{p_4^\nu p_4^\rho}{m_W^2}\right)\ p_{1\alpha}\ p_{2\beta}\right) \\ &\times \left(\gamma_\nu (1-\gamma^5) \gamma^\alpha (1+\gamma^5) \gamma_\rho \gamma^\beta\right)\Bigg] \\ = \frac{1}{3} |A(k)|^2 \ \mathrm{Tr}\Bigg[&\left(\left(-g^{\nu\rho} + \frac{p_4^\nu p_4^\rho}{m_W^2}\right)\ p_{1\alpha}\ p_{2\beta}\right) \\ &\times \Big(\left(\gamma_\nu \gamma^\alpha \gamma_\rho \gamma^\beta\right) \\ &\quad - \left(\gamma_\nu \gamma^5 \gamma^\alpha \gamma^5 \gamma_\rho \gamma^\beta\right) \\ &\quad - \left(\gamma_\nu \gamma^5 \gamma^\alpha \gamma_\rho \gamma^\beta\right) \\ &\quad + \left(\gamma_\nu \gamma^\alpha \gamma^5 \gamma_\rho \gamma^\beta\right)\Big)\Bigg]\end{aligned} \tag{2.52}$$

Let us then remove terms with an odd number of gamma matrices, since the trace of an odd number of gamma matrices equals zero. Let us also use $(\gamma^5)^2 = I_4$.

$$\begin{aligned}\sum_\lambda |\overline{\mathcal{M}}|^2 &= \frac{2}{3}|A(k)|^2 \ \mathrm{Tr}\left[\left(\left(-g^{\nu\rho} + \frac{p_4^\nu p_4^\rho}{m_W^2} \right) \ p_{1\alpha} \ p_{2\beta} \right) \left(\gamma_\nu \gamma^\alpha \gamma_\rho \gamma^\beta \right) \right] \\ &= \frac{2}{3}|A(k)|^2 \ \mathrm{Tr}\left[\left(\ p_{1\alpha} \ p_{2\beta} \right) \left(\left(\gamma^\rho \gamma^\alpha \gamma^\beta \gamma_\rho \right) + \frac{p_4^\nu p_4^\rho}{m_W^2} \left(\gamma_\nu \gamma^\alpha \gamma_\rho \gamma^\beta \right) \right) \right]\end{aligned} \tag{2.53}$$

We can then use $p^\rho \gamma_\rho = \not{p} = p_\rho \gamma^\rho$, the gamma matrix contraction $\gamma^\rho \gamma^\alpha \gamma^\beta \gamma_\rho = 4g^{\alpha\beta}$, and $\mathrm{Tr}\left(\gamma^\nu \gamma^\alpha \gamma^\rho \gamma^\beta\right) = 4\left(g^{\nu\alpha} g^{\rho\beta} - g^{\nu\rho} g^{\alpha\beta} + g^{\nu\beta} g^{\alpha\rho}\right)$, to give:

$$\begin{aligned}\sum_\lambda |\overline{\mathcal{M}}|^2 &= \frac{2}{3}|A(k)|^2 \left(\ p_{1\alpha} \ p_{2\beta} \right) \left(\left(4g^{\alpha\beta} \right) + \left(\frac{p_{4\nu} p_{4\rho}}{m_W^2} g^{\nu\alpha} g^{\rho\beta} - g^{\nu\rho} g^{\alpha\beta} + g^{\nu\beta} g^{\alpha\rho} \right) \right) \\ &= \frac{2}{3}|A(k)|^2 \left(\ p_{1\alpha} \ p_{2\beta} \right) \left(\left(4g^{\alpha\beta} \right) + \left(\frac{p_4^\alpha p_4^\beta}{m_W^2} - \frac{p_4^\rho p_{4\rho}}{m_W^2} g^{\alpha\beta} + \frac{p_4^\beta p_4^\alpha}{m_W^2} \right) \right) \\ &= \frac{2}{3}|A(k)|^2 \left(4 \ p_{1\alpha} \ p_2^\alpha + 2\frac{p_{1\alpha} \ p_{2\beta} \ p_4^\alpha \ p_4^\beta}{m_W^2} - \frac{p_{1\alpha} \ p_2^\alpha \ p_4^\rho \ p_{4\rho}}{m_W^2} \right) \\ &= \frac{2}{3}|A(k)|^2 \left(4(p_1 \cdot p_2) + 2\frac{(p_1 \cdot p_4)(p_2 \cdot p_4)}{m_W^2} - \frac{(p_1 \cdot p_2)(p_4 \cdot p_4)}{m_W^2} \right)\end{aligned} \tag{2.54}$$

We can then insert this into equation 2.35:

$$\begin{aligned}\mathrm{d}\hat{\sigma}(q\bar{q} \to WH) &= \frac{1}{4\sqrt{\hat{s}}|\vec{p_1}|} \left(\frac{\mathrm{d}\Omega_{cm}}{4\pi} \frac{1}{8\pi} \frac{2|\vec{p}|}{\sqrt{\hat{s}}} \right) \frac{2}{3}|A(k)|^2 \\ &\quad \times \left(4(p_1 \cdot p_2) + 2\frac{(p_1 \cdot p_4)(p_2 \cdot p_4)}{m_W^2} - \frac{(p_1 \cdot p_2)(p_4 \cdot p_4)}{m_W^2} \right) \\ &= \frac{2m_W^6 |V^{\mathrm{CKM}}|^2 |\vec{p}|}{3\hat{s} v_{\mathrm{vev}}^4 |\vec{p_1}|} \left(\frac{\mathrm{d}\Omega_{cm}}{4\pi} \frac{1}{8\pi} \right) \left(\frac{1}{k^2 - m_W^2} \right)^2 \\ &\quad \times \left(4(p_1 \cdot p_2) + 2\frac{(p_1 \cdot p_4)(p_2 \cdot p_4)}{m_W^2} - \frac{(p_1 \cdot p_2)(p_4 \cdot p_4)}{m_W^2} \right)\end{aligned} \tag{2.55}$$

Since we are in the centre of mass frame $\vec{p_1} = -\vec{p_2}$ and $\vec{p_3} = -\vec{p_4}$. We can also equate $k^2 = \hat{s}$. Therefore,

$$\begin{aligned} |\vec{p_3}| = |\vec{p_4}| = |\vec{p}| &= \frac{\sqrt{\left(\hat{s} - \left(m_W + m_H\right)^2\right)\left(\hat{s} - \left(m_W - m_H\right)^2\right)}}{2\sqrt{\hat{s}}} \\ &= \frac{\sqrt{\hat{s}^2 + m_W^4 + m_H^4 - 2m_W^2 m_H^2 - 2\hat{s}m_W^2 - 2\hat{s}m_H^2}}{2\sqrt{\hat{s}}} \end{aligned} \tag{2.56}$$

and so,

$$\begin{aligned} |\vec{p}|^2 &= \frac{\hat{s}^2 + m_W^4 + m_H^4 - 2m_W^2 m_H^2 - 2\hat{s}m_W^2 - 2\hat{s}m_H^2}{4\hat{s}} \\ &= \frac{\hat{s}}{4}\left(1 + \frac{(m_W^2 - m_H^2)^2}{\hat{s}^2} - 2\frac{m_W^2 + m_H^2}{\hat{s}}\right) \end{aligned} \tag{2.57}$$

giving,

$$\begin{aligned} |\vec{p}| &= \frac{\sqrt{\hat{s}}}{2}\sqrt{1 + \frac{(m_W^2 - m_H^2)^2}{\hat{s}^2} - 2\frac{m_W^2 + m_H^2}{\hat{s}}} \\ &= \frac{\sqrt{\hat{s}}}{2}\sqrt{\lambda_{WH}} \end{aligned} \tag{2.58}$$

where,

$$\lambda_{WH} = 1 + \frac{(m_W^2 - m_H^2)^2}{\hat{s}^2} - 2\frac{m_W^2 + m_H^2}{\hat{s}} \tag{2.59}$$

Likewise,

$$\begin{aligned} |\vec{p_1}| = |\vec{p_2}| &= \frac{\sqrt{\hat{s}}}{2}\sqrt{1 + \frac{(m_q^2 - m_{\bar{q}}^2)^2}{\hat{s}^2} - 2\frac{m_q^2 + m_{\bar{q}}^2}{\hat{s}}} \\ &= \frac{\sqrt{\hat{s}}}{2} \end{aligned}$$

since the incoming quark masses $m_q \ll \hat{s}$ and are therefore negligible. Neglecting the incoming quark masses also leads to,

$$m_q^2 = E^2 - |\vec{p}|^2 = 0 \tag{2.60}$$

therefore,

$$\begin{aligned} p_1 \cdot p_2 &= E_1 E_2 + |\vec{p_1}||\vec{p_2}| \\ &= 2|\vec{p_1}||\vec{p_2}| \\ &= \frac{\hat{s}}{2} \end{aligned} \tag{2.61}$$

Also,

$$p_4 \cdot p_4 = E_4^2 - |\vec{p_4}|^2 = m_W^2 \tag{2.62}$$

therefore,

$$E_4^2 = m_W^2 + |\vec{p_4}|^2 \tag{2.63}$$

Furthermore,

$$p_1 \cdot p_4 = E_1 E_4 - |\vec{p_1}||\vec{p_4}| \cos(\theta) \tag{2.64}$$

where θ is the angle between the quark four-momentum (p_1) and the W boson four-momentum (p_4), and,

$$\begin{aligned} p_2 \cdot p_4 &= E_2 E_4 - |\vec{p_2}||\vec{p_4}| \cos(\pi - \theta) \\ &= E_2 E_4 + |\vec{p_2}||\vec{p_4}| \cos(\theta) \end{aligned} \tag{2.65}$$

so,

$$\begin{aligned} (p_1 \cdot p_4)(p_2 \cdot p_4) &= (E_1 E_4 - |\vec{p_1}||\vec{p_4}| \cos(\theta))(E_2 E_4 + |\vec{p_2}||\vec{p_4}| \cos(\theta)) \\ &= (E_1 E_4 - |\vec{p_1}||\vec{p_4}| \cos(\theta))(E_1 E_4 + |\vec{p_1}||\vec{p_4}| \cos(\theta)) \\ &= E_1^2 E_4^2 - |\vec{p_1}|^2 |\vec{p_4}|^2 \cos^2(\theta) \\ &= |\vec{p_1}|^2 (m_W^2 + |\vec{p_4}|^2) - |\vec{p_1}|^2 |\vec{p_4}|^2 \cos^2(\theta) \\ &= |\vec{p_1}|^2 m_W^2 + |\vec{p_1}|^2 |\vec{p_4}|^2 (1 - \cos^2(\theta)) \\ &= |\vec{p_1}|^2 m_W^2 + |\vec{p_1}|^2 |\vec{p_4}|^2 \sin^2(\theta) \\ &= \frac{\hat{s}}{4} m_W^2 \left(1 + \frac{\hat{s}\lambda_{WH}}{4m_W^2} \sin^2(\theta)\right) \end{aligned} \tag{2.66}$$

Inserting these relations into equation 2.55 gives,

$$\begin{aligned}
\mathrm{d}\hat{\sigma}(q\bar{q} \to WH) &= \frac{2m_W^6 |V^{\mathrm{CKM}}|^2}{3\hat{s}v_{\mathrm{vev}}^4} \frac{2}{\sqrt{\hat{s}}} \frac{\sqrt{\hat{s}}\sqrt{\lambda_{WH}}}{2} \left(\frac{\mathrm{d}\Omega_{cm}}{4\pi}\frac{1}{8\pi}\right) \left(\frac{1}{\hat{s}-m_W^2}\right)^2 \\
&\quad \times \left(2\hat{s} + \frac{\hat{s}}{2}\left(1 + \frac{\hat{s}\lambda_{WH}}{4m_W^2}\sin^2(\theta)\right) - \frac{\hat{s}}{2}\right) \\
&= \frac{4m_W^6 |V^{\mathrm{CKM}}|^2 \sqrt{\lambda_{WH}}}{3v_{\mathrm{vev}}^4} \left(\frac{\mathrm{d}\Omega_{cm}}{4\pi}\frac{1}{8\pi}\right) \left(\frac{1}{\hat{s}-m_W^2}\right)^2 \\
&\quad \times \left(1 + \frac{\hat{s}\lambda_{WH}}{16m_W^2}\sin^2(\theta)\right) \qquad (2.67)
\end{aligned}$$

We can also write the solid angle integration as an integration in spherical coordinates: $\mathrm{d}\Omega_{cm} = \sin\theta \ \mathrm{d}\theta \ \mathrm{d}\phi$. Integrating over a full sphere gives,

$$\int_{\theta=0}^{\pi}\int_{\phi=0}^{2\pi} \sin\theta \ \mathrm{d}\theta \ \mathrm{d}\phi = 4\pi$$

and,

$$\int_{\theta=0}^{\pi}\int_{\phi=0}^{2\pi} \sin^3\theta \ \mathrm{d}\theta \ \mathrm{d}\phi = \frac{8}{3}\pi$$

Therefore,

$$\mathrm{d}\hat{\sigma}(q\bar{q} \to WH) = \frac{m_W^6 |V^{\mathrm{CKM}}|^2 \sqrt{\lambda_{WH}}}{6\pi v_{\mathrm{vev}}^4} \left(\frac{1}{\hat{s}-m_W^2}\right)^2 \left(1 + \frac{\hat{s}\lambda_{WH}}{24m_W^2}\right) \qquad (2.68)$$

Alternatively, if we only integrate over ϕ, and change variables from θ to $\eta = -\frac{1}{2}\ln(\tan(\frac{\theta}{2}))$, then we have,

$$\begin{aligned}
\frac{\mathrm{d}\hat{\sigma}(q\bar{q} \to WH)}{\mathrm{d}\eta} &= \frac{m_W^6 |V^{\mathrm{CKM}}|^2 \sqrt{\lambda_{WH}}}{6\pi v_{\mathrm{vev}}^4} \mathrm{sech}^2(2\eta) \left(\frac{1}{\hat{s}-m_W^2}\right)^2 \\
&\quad \times \left(1 + \frac{\hat{s}\lambda_{WH}}{24m_W^2}\mathrm{sech}^2(2\eta)\right) \qquad (2.69)
\end{aligned}$$

2.3.6 *W* Boson Branching Ratios

The W bosons can only decay to fermions due to mass and charge constraints. All fermionic W boson decays then can be described by the Feynman diagram given in figure 2.15:

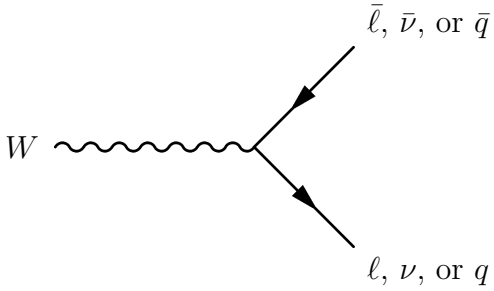

Figure 2.15: Leading order Feynman diagram of W boson decay.

Let us consider the Feynman rules that will contribute to the matrix element of figure 2.15:

Outgoing ℓ, ν or q: 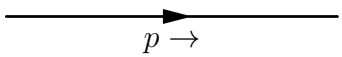 $= \bar{u}^s(p)$

Outgoing $\bar{\ell}, \bar{\nu}$ or $\bar{q}$: 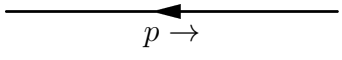 $= v^s(p)$

Incoming W: 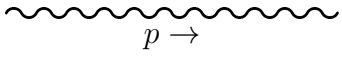 $= \epsilon(p)$

$Wf\bar{f}$ vertex 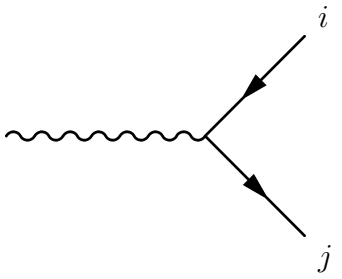 $= \frac{im_W}{\sqrt{2}v_{\text{vev}}}\gamma^\mu(1-\gamma^5)V_{ij}^{\text{CKM}}$

where $Wf\bar{f}$ refers to a W-fermion-antifermion interaction. If the fermions are leptons then we can take the V_{ij}^{CKM} term to be equal to 1, provided that charge and lepton flavour are conserved at the vertex.

The matrix element $\mathcal{M}$ for all W boson decays will then take the form:

$$\mathcal{M} = \bar{u}^s(p_2)\epsilon(p_1)\frac{im_W}{\sqrt{2}v_{\text{vev}}}\gamma^\mu(1-\gamma^5)V^{\text{CKM}}v^s(p_3) \tag{2.70}$$

The partial width Γ for any W boson decay has the form,

$$\mathrm{d}\Gamma = \frac{S}{2m_W}\left(\prod_f \frac{\mathrm{d}^3p_f}{(2\pi)^3}\frac{1}{2E_f}\right)(2\pi)^4\delta^{(4)}(p_W - \sum p_f)\sum_\lambda |\overline{\mathcal{M}}|^2 \tag{2.71}$$

For a two-body final state in the centre of mass frame, the Lorentz-invariant phase space can be simplified to give,

$$\mathrm{d}\Gamma = \frac{S}{2m_W}\left(\frac{\mathrm{d}\Omega_{cm}}{4\pi}\frac{1}{8\pi}\frac{2|\vec{p}|}{E_{cm}}\right)\sum_\lambda |\overline{\mathcal{M}}|^2 \tag{2.72}$$

but, for this decay,

$$\sum_\lambda |\overline{\mathcal{M}}|^2 = N_c|\mathcal{M}|^2 \tag{2.73}$$

so,

$$\mathrm{d}\Gamma = \frac{SN_c}{2m_W}\left(\frac{\mathrm{d}\Omega_{cm}}{4\pi}\frac{1}{8\pi}\frac{2|\vec{p}|}{E_{cm}}\right)|\mathcal{M}|^2 \tag{2.74}$$

where N_c is the number of colour charges of the interacting fermions. $N_c = 1$ for leptons and $N_c = 3$ for quarks. S is a statistical factor to avoid double counting. $S = \sum_i^N \frac{1}{n_i!}$ where n_i is the number of decay-product particles of type i. $S = 1$ in a two-body decay where the daughter particles are of different types, $W^+ \to e\bar{\nu}$ or $W^+ \to q_u\bar{q_d}$ for example. $S = \frac{1}{2}$ in a two-body decay where the daughter particles are of the same type, $H \to q_b\bar{q}_b$ for example.

This can be further simplified to give,

$$\Gamma = \frac{SN_c|\vec{p}|}{8\pi m_W^2}|\mathcal{M}|^2 \tag{2.75}$$

As the mass of a W boson is much larger than any of the fermion masses, we can neglect the fermion masses in the matrix element. Also, for all W boson

decays $S = 1$. We can then write the partial width Γ for any W boson decay as,

$$\Gamma = N_c |V^{\mathrm{CKM}}|^2 C_w \tag{2.76}$$

where C_W is a constant.

The total width of a particle is $\Gamma_{\mathrm{TOT}} = \sum_X \Gamma_X$, where the sum is over all possible decay channels. For the W^+ boson, these decay channels are shown in table 2.2 with their corresponding values of $N_c|V^{\mathrm{CKM}}|^2$. These numbers are the same for the W^- boson, with the particle-antiparticle pairs swapped to maintain the correct charge.

W^+ boson decay products	$N_c\|V^{\mathrm{CKM}}\|^2$
$e\bar{\nu_e}$	1
$\mu\bar{\nu_\mu}$	1
$\tau\bar{\nu_\tau}$	1
$q_u\bar{q_d}$	$3 \times (0.97427)^2 = 2.84761$
$q_c\bar{q_s}$	$3 \times (0.97343)^2 = 2.84276$
$q_u\bar{q_s}$	$3 \times (0.22536)^2 = 0.15236$
$q_c\bar{q_d}$	$3 \times (0.22522)^2 = 0.15217$
$q_u\bar{q_b}$	$3 \times (0.00355)^2 = 0.00004$
$q_c\bar{q_b}$	$3 \times (0.04140)^2 = 0.00514$

Table 2.2: W^+ boson decay channels with corresponding $N_c|V^{\mathrm{CKM}}|^2$ values. V^{CKM} from [28]

The W bosons can not decay to top-quarks due to mass constraints.

The total width of a W boson is therefore,

$$\begin{aligned}\Gamma_{\mathrm{TOT}} &= C_W \times (1 + 1 + 1 + 2.84761 + 2.84276 + 0.15236 + 0.15217 + 0.00004 + 0.00514) \\ &= 9\ C_W \end{aligned} \tag{2.77}$$

For a given particle decay $W \to X$, the branching ratio of this decay will be given by $\mathrm{BR}_X = \frac{\Gamma_X}{\Gamma_{\mathrm{TOT}}}$.

If we wish to consider the decay modes $W \to e\nu_e$ and $W \to \mu\nu_\mu$, then the corresponding branching ratios for these decays will be,

$$\mathrm{BR}_{e\nu_e} = \frac{\Gamma_{e\nu_e}}{\Gamma_{\mathrm{TOT}}} = \frac{1C_W}{9C_W} = \frac{1}{9} \approx 11\% \tag{2.78}$$

and,

$$\mathrm{BR}_{\mu\nu_\mu} = \frac{\Gamma_{\mu\nu_\mu}}{\Gamma_{\mathrm{TOT}}} = \frac{1C_W}{9C_W} = \frac{1}{9} \approx 11\% \tag{2.79}$$

Therefore the total branching ratio for a W boson decaying leptonically with either an electron or muon in the final state will be $\frac{2}{9} \approx 22\%$. This branching ratio has been experimentally measured to be $21.34 \pm 0.22\%$ [28].

2.3.7 Higgs Boson Branching Ratios

To calculate SM Higgs boson branching ratios of interest, we must calculate the total width Γ_{TOT} of the Higgs boson. For this we shall consider the decay modes $H \to b\bar{b}$, $H \to WW^*$, $H \to gg$, $H \to \tau^-\tau^+$, and $H \to ZZ^*$. Other decay modes are predicted for a SM Higgs boson: $H \to \gamma\gamma$, $H \to Z\gamma$, and $H \to \mu^-\mu^+$, however they will not be dealt with here as their contribution to the total width is negligible in the SM.

$H \to b\bar{b}$ Partial Width

The leading order Feynman diagram for a $H \to b\bar{b}$ decay is shown in figure 2.16:

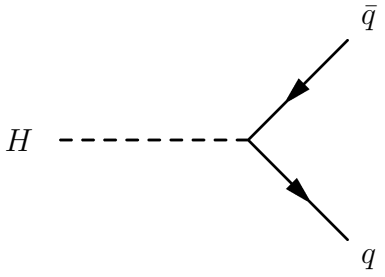

Figure 2.16: Leading order Feynman diagram for a Higgs boson decay to a $b\bar{b}$ pair.

The partial width for this decay is given by,

$$\mathrm{d}\Gamma_{H\to b\bar{b}} = \frac{S}{2m_H}\left(\prod_f \frac{\mathrm{d}^3 p_f}{(2\pi)^3}\frac{1}{2E_f}\right)(2\pi)^4\delta^{(4)}(p_1 - p_2 - p_3)\sum_\lambda |\overline{\mathcal{M}}(H \to b\bar{b})|^2 \tag{2.80}$$

but, for this decay,

$$\sum_{\lambda} |\overline{\mathcal{M}}|^2 = N_c |\mathcal{M}|^2 \tag{2.81}$$

so,

$$\mathrm{d}\Gamma_{H\to b\bar{b}} = \frac{SN_c}{2m_H} \left(\prod_f \frac{\mathrm{d}^3 p_f}{(2\pi)^3} \frac{1}{2E_f} \right) (2\pi)^4 \delta^{(4)}(p_1 - p_2 - p_3) |\mathcal{M}(H \to b\bar{b})|^2 \tag{2.82}$$

where,

$\Gamma_{H\to b\bar{b}}$ = Partial width for the $H \to b\bar{b}$ process.

$\mathcal{M}(H \to b\bar{b})$ = The matrix element for the $H \to b\bar{b}$ process.

N_c = The number of colour charges of the decay product quarks.

$N_c = 3$ for quarks.

S = A statistical factor to avoid double counting.

$S = \frac{1}{2}$ for the $H \to b\bar{b}$ process.

Given that this process has a two-body final state, we can move to the rest frame of the decaying Higgs boson and simplify the Lorentz-invariant phase space to give,

$$\mathrm{d}\Gamma_{H\to b\bar{b}} = \frac{N_c}{4m_H} \left(\frac{\mathrm{d}\Omega_{cm}}{4\pi} \frac{1}{8\pi} \frac{2|\vec{p}|}{E_{cm}} \right) |\mathcal{M}(H \to b\bar{b})|^2 \tag{2.83}$$

Furthermore, if we integrate over the solid angle $\mathrm{d}\Omega_{cm}$ and use $E_{cm} = m_H c^2 = m_H$ then we have,

$$\Gamma_{H\to b\bar{b}} = \frac{N_c |\vec{p}|}{16\pi m_H^2} |\mathcal{M}(H \to b\bar{b})|^2 \tag{2.84}$$

where,

$$|\vec{p}| = \frac{\sqrt{m_H^2 - 4m_f^2}}{2} = \frac{m_H}{2}\sqrt{1 - 4\frac{m_f^2}{m_H^2}} \tag{2.85}$$

Let us then write,

$$\Gamma_{H\to b\bar{b}} = \frac{N_c \beta}{32\pi m_H} |\mathcal{M}(H \to b\bar{b})|^2 \tag{2.86}$$

where,

$$\beta = \sqrt{1 - 4\frac{m_f^2}{m_H^2}} \tag{2.87}$$

where m_f is the mass of each of the fermions in the decay. In this case it is equal to the mass of the b-quark.

The Feynman rules contributing to the Feynman diagram 2.16 for the matrix element $\mathcal{M}(H \to b\bar{b})$ are as follows:

Outgoing q: 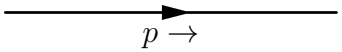

$= \quad \bar{u}^s(p)$

Outgoing $\bar{q}$: 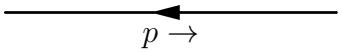

$= \quad v^s(p)$

Incoming H: 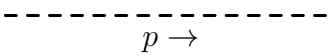

$= \quad 1$

$Hq\bar{q}$ vertex: 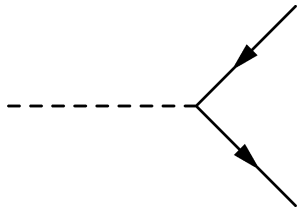 $= \quad \dfrac{im_f}{v_{\text{vev}}}$

The matrix element squared, $|\mathcal{M}(H \to b\bar{b})|^2$, is then given by,

$$\begin{aligned}
|\mathcal{M}(H \to b\bar{b})|^2 &= \mathcal{M}\mathcal{M}^\dagger \\
&= \sum_s \bar{u}^s(p_2)\frac{im_f}{v_{\text{vev}}}v^s(p_3)\bar{v}^s(p_3)\frac{(-i)m_f}{v_{\text{vev}}}u^s(p_2) \\
&= \text{Tr}[\bar{u}^s(p_2)\frac{im_f}{v_{\text{vev}}}v^s(p_3)\bar{v}^s(p_3)\frac{(-i)m_f}{v_{\text{vev}}}u^s(p_2)] \\
&= \text{Tr}[\frac{m_f^2}{v_{\text{vev}}^2}v^s(p_3)\bar{v}^s(p_3)u^s(p_2)\bar{u}^s(p_2)] \\
&= \text{Tr}[\frac{m_f^2}{v_{\text{vev}}^2}(\not{p}_3 - m_f)(\not{p}_2 + m_f)] \\
&= \text{Tr}[\frac{m_f^2}{v_{\text{vev}}^2}(\gamma^\mu\gamma^\nu p_{3\mu}p_{2\nu} - m_f\gamma^\nu p_{2\nu} + \gamma^\mu p_{3\mu}m_f - m_f^2)] \\
&= \frac{m_f^2}{v_{\text{vev}}^2}(4g^{\mu\nu}p_{3\mu}p_{2\nu} - m_f^2) \\
&= \frac{m_f^2}{v_{\text{vev}}^2}(4p_3 \cdot p_2 - m_f^2)
\end{aligned} \tag{2.88}$$

and,

$$\begin{aligned}
p_3 \cdot p_2 &= E_2E_3 - \vec{p_2} \cdot \vec{p_3} \\
&= E_2E_3 + |\vec{p}||\vec{p}|
\end{aligned} \tag{2.89}$$

Since $m_f^2 \ll m_H^2$, we can set $m_f^2 = E_n^2 - \vec{p_n}^2 = 0$, so $E_n = \vec{p_n}$. This then gives,

$$\begin{aligned} p_3 \cdot p_2 &= 2|\vec{p}||\vec{p}| \\ &= \frac{m_H^2}{2}\beta^2 \end{aligned} \tag{2.90}$$

therefore,

$$\begin{aligned} |\mathcal{M}(H \to b\bar{b})|^2 &= \frac{m_f^2}{v_{\text{vev}}^2}\left(4\left(\frac{m_H^2}{2}\beta^2\right) - m_f^2\right) \\ &= \frac{2m_f^2 m_H^2 \beta^2}{v_{\text{vev}}^2} - \frac{m_f^4}{v_{\text{vev}}^2} \end{aligned} \tag{2.91}$$

The $\frac{m_f^4}{v_{\text{vev}}^2}$ term can be neglected as $m_f^4 \ll v_{\text{vev}}^2$. We then have,

$$|\mathcal{M}(H \to b\bar{b})|^2 = \frac{2m_f^2 m_H^2 \beta^2}{v_{\text{vev}}^2} \tag{2.92}$$

which we can insert into equation 2.86 to give,

$$\begin{aligned} \Gamma_{H\to b\bar{b}} &= \frac{N_c \beta}{32\pi m_H}\frac{2m_f^2 m_H^2 \beta^2}{v_{\text{vev}}^2} \\ &= \frac{N_c m_f^2 m_H \beta^3}{16\pi v_{\text{vev}}^2} \end{aligned} \tag{2.93}$$

where,

$$\beta = \sqrt{1 - 4\frac{m_f^2}{m_H^2}} \tag{2.94}$$

If we insert the values $N_c = 3$, $m_H = 125$ GeV, $m_f = 4.18$ GeV, and $v_{\text{vev}} = 246$ GeV into equation 2.93, then we get,

$$\begin{aligned} \Gamma_{H\to b\bar{b}} &= \frac{N_c m_f^2 m_H \beta^3}{16\pi v_{\text{vev}}^2} \\ &= 2.14 \text{ MeV} \end{aligned} \tag{2.95}$$

$H \to \tau^- \tau^+$ Partial Width

To calculate the partial width for the $H \to \tau^- \tau^+$ decay, we can use equation 2.93:

$$\Gamma_{H \to \tau^- \tau^+} = \frac{N_c m_f^2 m_H \beta^3}{16\pi v_{\text{vev}}^2} \tag{2.96}$$

where,

$$\beta = \sqrt{1 - 4\frac{m_f^2}{m_H^2}} \tag{2.97}$$

If we insert the values $N_c = 1$, $m_H = 125$ GeV, $m_f = 1.78$ GeV, and $v_{\text{vev}} = 246$ GeV into equation 2.93, then we get,

$$\Gamma_{H \to \tau^- \tau^+} = 0.13 \text{ MeV} \tag{2.98}$$

$H \to WW^*$ Partial Width

The $H \to WW^*$ partial width is quoted directly [40, 41, 42]:

$$\Gamma_{H \to WW^*} = \frac{3 m_W^4 m_H}{32\pi^3 v_{\text{vev}}^4} F\left(\frac{m_w}{m_H}\right) \tag{2.99}$$

where,

$$\begin{aligned} F(x) = &-|1 - x^2| \left(\frac{47}{2}x^2 - \frac{13}{2} + \frac{1}{x^2}\right) + 3(1 - 6x^2 + 4x^4)|\ln(x)| \\ &+ 3\frac{1 - 8x^2 + 20x^4}{\sqrt{4x^2 - 1}} \cos^{-1}\left(\frac{3x^2 - 1}{2x^3}\right) \end{aligned} \tag{2.100}$$

If we insert the values $m_W = 80.4$ GeV, $m_H = 125$ GeV, and $v_{\text{vev}} = 246$ GeV into equation 2.99, then we get,

$$\Gamma_{H \to WW^*} = 0.78 \text{ MeV} \tag{2.101}$$

$H \to ZZ^*$ Partial Width

The $H \to ZZ^*$ partial width is quoted directly [40, 41, 42]:

$$\Gamma_{H\to ZZ^*} = \frac{m_W^4 m_H}{128(1-\sin^2(\theta_W))\pi^3 v_{\text{vev}}^4} \times \left(7 - \frac{40}{3}\sin^2(\theta_W) + \frac{160}{9}\sin^4(\theta_W)\right) F\left(\frac{m_Z}{m_H}\right) \tag{2.102}$$

where θ_W is the weak mixing angle, and as with $H \to WW^*$, $F(x)$ is given in equation 2.100.

If we insert the values $m_W = 80.4$ GeV, $m_Z = 91.2$ GeV, $m_H = 125$ GeV, $\theta_W = cos^{-1}\left(\frac{m_W}{m_Z}\right) = 28.2°$, and $v_{\text{vev}} = 246$ GeV into equation 2.102, then we get,

$$\Gamma_{H\to ZZ^*} = 0.07 \text{ MeV} \tag{2.103}$$

$H \to gg$ Partial Width

The SM Higgs boson decays to gluon pairs via a quark loop. Each possible quark loop contributes to the $H \to gg$ partial width with a term proportional to the mass of the quark squared. The $H \to gg$ partial width is therefore dominated by the top-quark loop. As an approximation, we can take the limit in which the top-quark mass goes to infinity: $m_t \to \infty$. The $H \to gg$ partial width then becomes [40, 41, 43]:

$$\Gamma_{H\to gg} = \frac{\alpha_s^2 m_H^2}{72 v_{\text{vev}}^2 \pi^3} \tag{2.104}$$

If we insert the values $m_H = 125$ GeV, $\alpha_s = 0.118$, and $v_{\text{vev}} = 246$ GeV into equation 2.104, then we get,

$$\Gamma_{H\to gg} = 0.20 \text{ MeV} \tag{2.105}$$

H Boson Branching Ratios

Partial widths for the decays of a SM Higgs boson with $m_H = 125$ GeV have been calculated in equations 2.95 2.98, 2.101, 2.103, and 2.105. The total width of the

Decay mode	Branching ratio
$H \to b\bar{b}$	64.5 %
$H \to WW^*$	23.5 %
$H \to gg$	6.1 %
$H \to \tau^-\tau^+$	3.9 %
$H \to ZZ^*$	2.0 %

Table 2.3: Branching ratios for the dominant $m_H = 125$ GeV SM Higgs boson decay modes, as calculated in this thesis.

Decay mode	Branching ratio
$H \to b\bar{b}$	58 %
$H \to WW^*$	22 %
$H \to gg$	9 %
$H \to \tau^-\tau^+$	6 %
$H \to ZZ^*$	3 %
$H \to \gamma\gamma$	0.2 %
$H \to Z\gamma$	0.2 %
$H \to \mu^-\mu^+$	10^{-4} %

Table 2.4: Branching ratios for $m_H = 125$ GeV SM Higgs boson decay modes. From [32]

Higgs boson is the sum of the partial widths, $\Gamma_{\text{TOT}} = \sum_X \Gamma_X$.

$$\begin{aligned} \Gamma_{\text{TOT}} &= 2.14 + 0.13 + 0.78 + 0.07 + 0.20 \\ &= 3.32 \text{ MeV} \end{aligned} \tag{2.106}$$

For comparison, the most precisely known value of the Higgs boson width is $\Gamma_{\text{TOT}} = 4.07$ MeV [32].

For a given particle decay $H \to X$, the branching ratio of this decay will be given by $\text{BR}_X = \frac{\Gamma_X}{\Gamma_{\text{TOT}}}$. The branching ratios for Higgs boson decay channels calculated in this thesis are shown in table 2.3. For comparison, the most precisely known values of branching ratios of Higgs boson decay channels, as given in [32], are shown in table 2.4.

2.3.8 The $WH \to \ell\nu b\bar{b}$ Channel

The leading-order partonic cross-section for the SM $q\bar{q} \to WH$ process has been calculated in equation 2.68.

The branching ratio of a W boson decaying leptonically with either an electron or muon in the final state has been calculated to be $\frac{2}{9} \approx 22\%$ from equations 2.78 and 2.79.

The partial width of a SM H boson decaying to a $b\bar{b}$ pair has been calculated in equation 2.95, as well as the partial widths for the decay modes $H \to \tau^-\tau^+$ (equation 2.98), $H \to WW^*$ (equation 2.101), $H \to ZZ^*$ (equation 2.103), and $H \to gg$ (equation 2.105). For a SM Higgs boson with $m_H = 125$ GeV, this gives a total width of $\Gamma_{\text{TOT}} = 3.32$ MeV (equation 2.106). The resulting branching ratios are shown in table 2.3. The branching ratio for a SM Higgs boson with $m_H = 125$ GeV decaying to a $b\bar{b}$ pair is found to be 64.5%.

To calculate values for $\hat{\sigma}(q\bar{q} \to WH)$, we assume that at least one interacting quark is a valence quark of its parent proton. For proton-proton collisions as at the LHC we then have the possible quark combinations shown in table 2.5, along with the corresponding value of V_{ij}^{CKM}.

Quark-antiquark combination	V_{ij}^{CKM}
$q_u\bar{q}_d$	0.97427
$q_u\bar{q}_s$	0.22536
$q_u\bar{q}_b$	0.00355
$q_d\bar{q}_u$	0.97427
$q_d\bar{q}_c$	0.22522
$q_d\bar{q}_t$	0.00886

Table 2.5: $q\bar{q}$ combinations where at least one quark is a valance quark of the proton, with corresponding V_{ij}^{CKM} from [28]

To calculate the partonic cross section $\hat{\sigma}(q\bar{q} \to WH)$ we will then sum over these $|V_{ij}^{\text{CKM}}|^2$:

$$\begin{aligned}\sum_{ij} |V_{ij}^{\text{CKM}}|^2 &= (0.97427)^2 + (0.22536)^2 + (0.00355)^2 + (0.97427)^2 + (0.22522)^2 + (0.00886)^2 \\ &= 2 \end{aligned} \tag{2.107}$$

Using this, and where required the values listed in table 2.6, $\hat{\sigma}(q\bar{q} \to WH)$

can then be plotted against $\sqrt{\hat{s}}$. This is shown in figure 2.17. For $\sqrt{\hat{s}} = 8$ TeV collisions, $\hat{\sigma}(q\bar{q} \to WH) = 0.154$fb.

Variable	Value
m_H	125 GeV
m_W	80.4 GeV
m_Z	91.2 GeV
v_{vev}	246 GeV
$\sqrt{\hat{s}}$	8 TeV
$\lvert V^{\text{CKM}}\rvert^2$	2
m_b	4.18 GeV
m_τ	1.78 GeV
α_s	0.118
θ_W	28.2°

Table 2.6: Values used, where required, in the calculations of distributions shown in section 2.3.8.

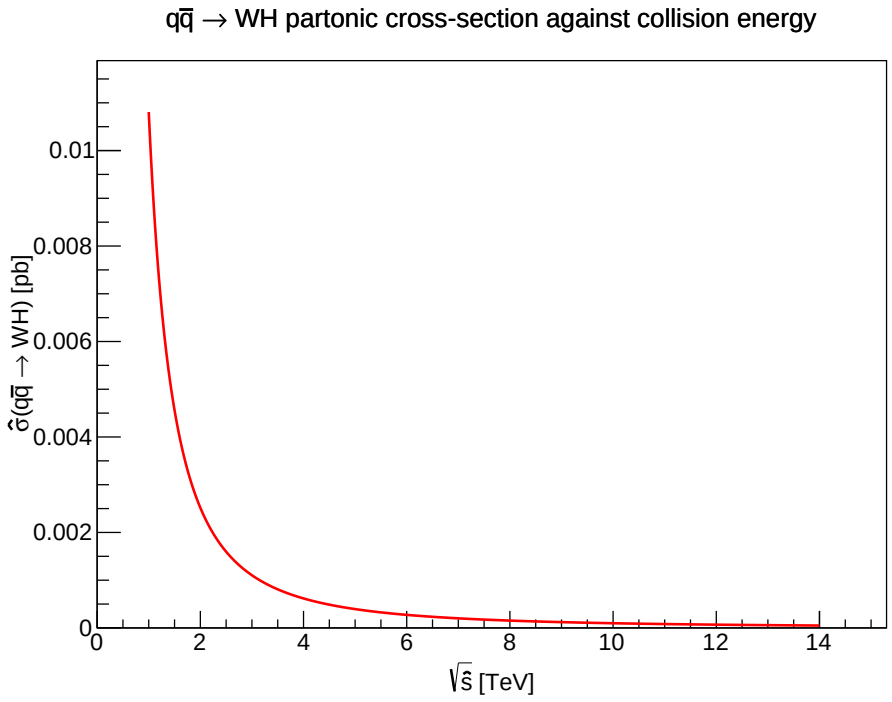

Figure 2.17: $\sqrt{\hat{s}}$-dependence of $\hat{\sigma}(q\bar{q} \to WH)$.

$\hat{\sigma}(q\bar{q} \to WH)$ can also be plotted against SM Higgs boson mass m_H. This is shown in figure 2.18.

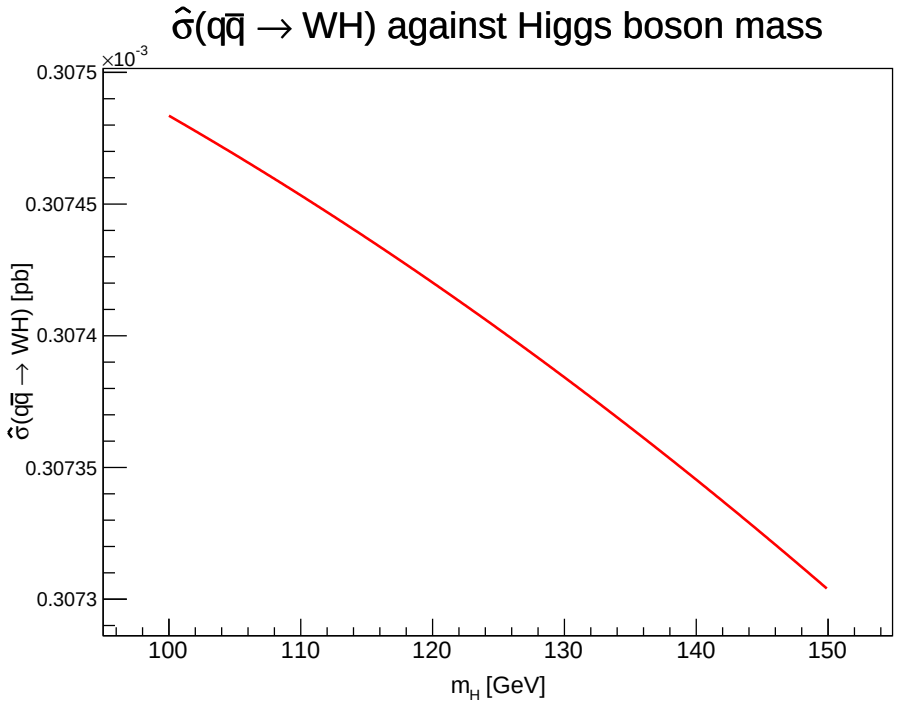

Figure 2.18: m_H-dependence of $\hat{\sigma}(q\bar{q} \to WH)$.

Using equation 2.69, the η-dependence of $\hat{\sigma}(q\bar{q} \to WH)$ can be plotted. This is shown in figure 2.19.

The total width of the SM Higgs boson is dependent on the mass of the Higgs boson. This is shown in figure 2.20.

The resulting SM Higgs boson branching ratios are shown in figure 2.21.

$\hat{\sigma}(q\bar{q} \to WH \to \ell\nu b\bar{b})$ can then be plotted against SM Higgs boson mass m_H. This is shown in figure 2.22.

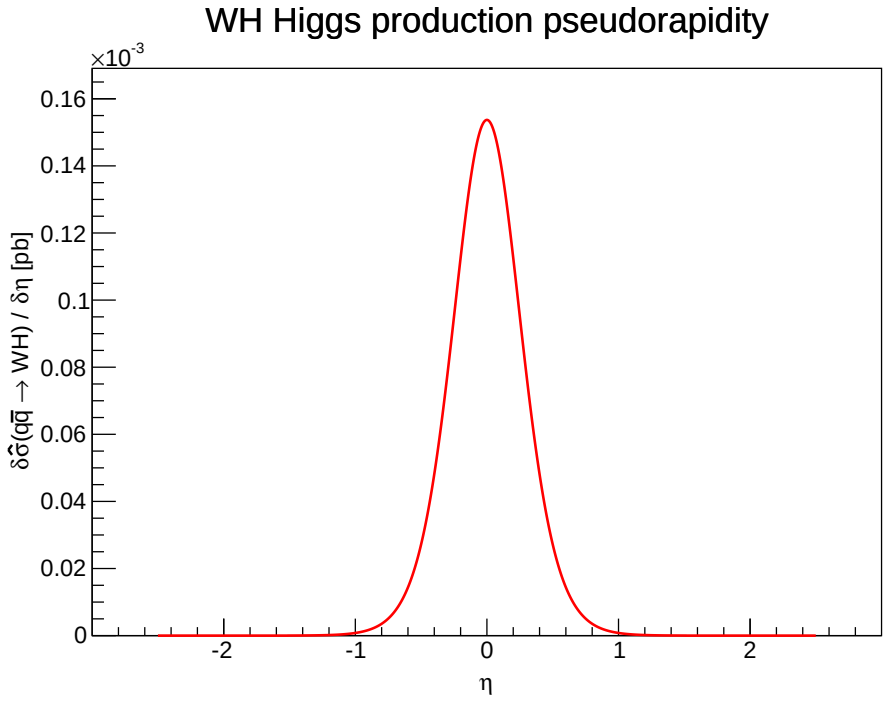

Figure 2.19: η-dependence of $\hat{\sigma}(q\bar{q} \to WH)$.

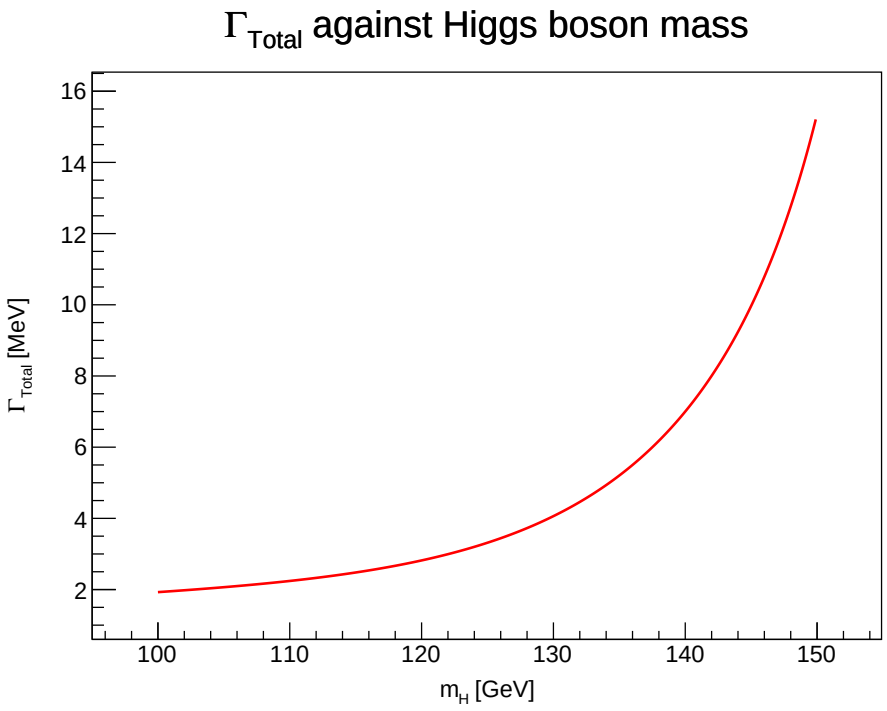

Figure 2.20: m_H-dependence of Γ_{TOT}.

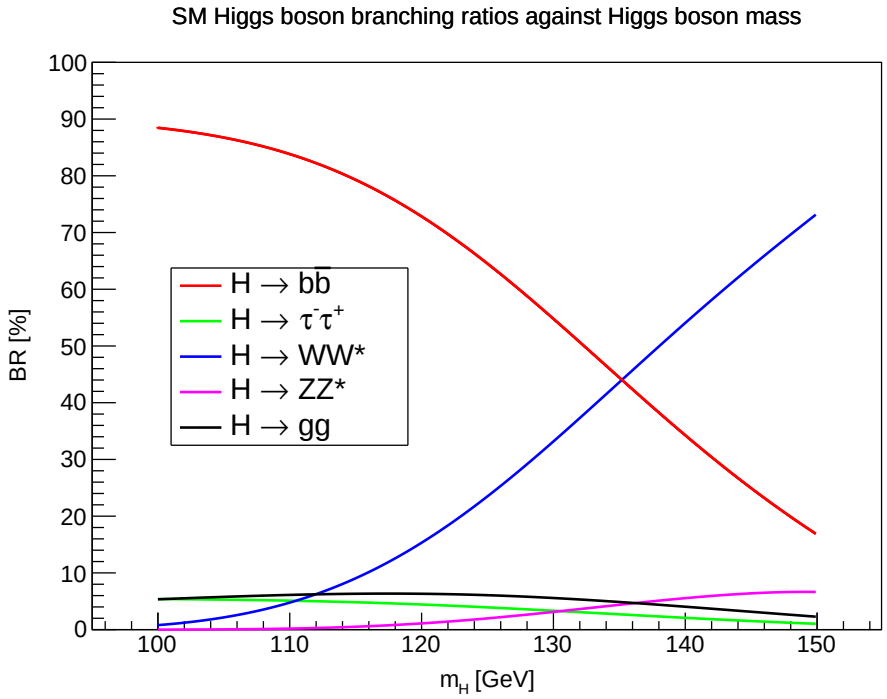

Figure 2.21: m_H-dependence of SM Higgs boson branching ratios.

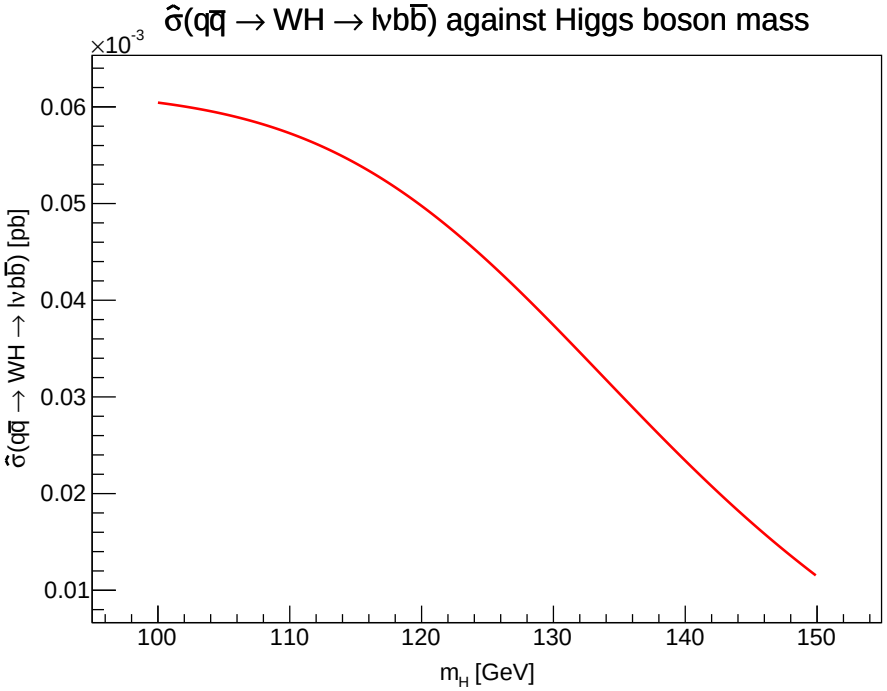

Figure 2.22: m_H-dependence of $\hat{\sigma}(q\bar{q} \to WH \to \ell\nu b\bar{b})$.

2.4 Summary

The Standard Model of particle physics has been discussed, with focus on electroweak symmetry breaking and the Higgs boson. The mechanism of electroweak symmetry breaking has been derived in section 2.3.1.

As a demonstration of the underlying theory of the process, the cross-section of the $q\bar{q} \to WH$ process, for $\sqrt{\hat{s}} = 8$ TeV collisions, and for a SM Higgs boson with a mass of $m_H = 125$ GeV, has been calculated in section 2.3.8, where it is found to be $\hat{\sigma}(q\bar{q} \to WH) = 0.154$fb. However, this calculation is for the partonic process, and so does not include PDF effects. It is also calculated to leading order in the perturbative expansion of QCD. It is therefore not used further in this thesis. For all cross sections used further in this thesis, full proton-proton cross-sections, so including PDF effects, are used. Where a specific Monte Carlo event generator (or combination of generators) is used to generate a process, the cross-section for that process as calculated by the generator(s) is used. Table 4.1 in chapter 4 shows the cross-sections of different processes, as used in the analysis discussed in this thesis and detailed in chapter 4.

Likewise, as a demonstration of the underlying theory of the process, the $H \to b\bar{b}$ branching ratio, for a SM Higgs boson with a mass of $m_H = 125$ GeV, has been calculated in section 2.3.7, where it is found to be 64.5%. This calculation however is to leading order in the perturbative expansion of QCD. More accurate estimates of the branching ratios of a SM Higgs boson with a mass of $m_H = 125$ GeV have been calculated [32], as shown in table 2.4. These values are used where required in the remainder of this thesis.

Chapter 3

The ATLAS Experiment

3.1 Introduction

The ATLAS (**A** **T**oroidal **L**HC **A**pparatu**S**) Experiment [44] is a high energy particle physics experiment for studying proton-proton collisions at never-before observed energies. It is referred to as a 'general purpose' experiment as it is designed to be able to study a wide range of particle physics topics, from probing the Standard Model (SM) to searching for the Higgs boson, supersymmerty (SUSY), and extra dimensions. The ATLAS Experiment consists of the ATLAS detector, described in more detail later in this chapter, and the ATLAS Collaboration - a group of over 3000 scientists from 38 countries and 177 different institutes working together to design, build and run the ATLAS detector, as well as to study the data it produces. Although the members of the ATLAS Collaboration are based all around the world, the home of the collaboration is CERN (the European Organisation for Nuclear Research) just outside Geneva Switzerland, where the ATLAS detector is located, as well as the Large Hadron Collider (LHC) [45, 46, 47] that provides high energy proton collisions for ATLAS.

3.2 The Large Hadron Collider

3.2.1 Introduction

The Large Hadron Collider (LHC) [45, 46, 47] is a particle accelerator situated at CERN outside Geneva, Switzerland. It is roughly circular in shape and 27 km in circumference, built into a tunnel about 100 m underground that previously housed the Large Electron-Positron (LEP) Collider [48, 49]. The location of the LHC can be seen in figure 3.1 and a diagram of some of the underground facilities can be seen in figure 3.3. The LHC is designed to collide protons at center-of-mass energies of up to 14 TeV and lead ions at center-of-mass energies of up to 5.5 TeV. These energies, being higher than any previous particle accelerator has achieved, allow the exploration of new physics around the 1 TeV scale.

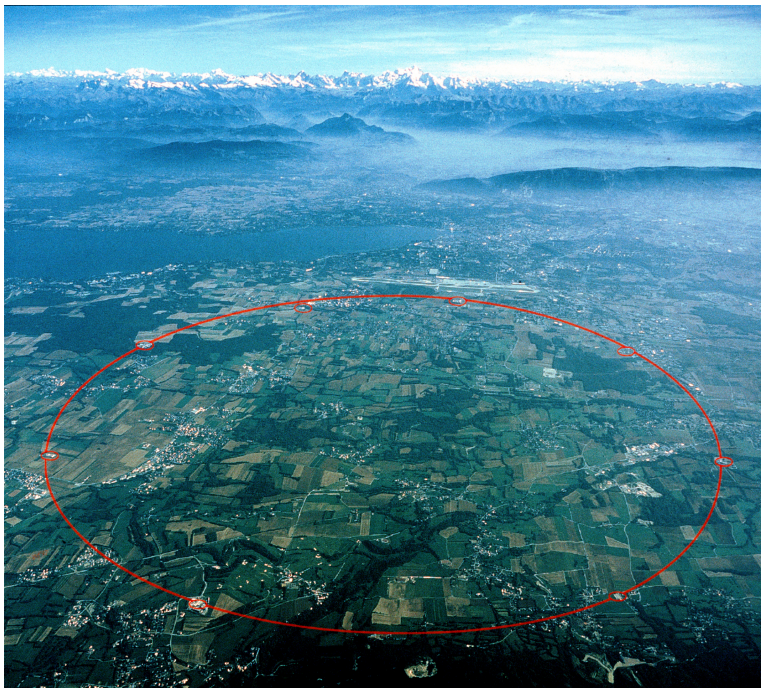

Figure 3.1: An aerial view of the location of the LHC to give a sense of scale. Geneva airport runway is the white horizontal line above the large red ring that marks the location of the LHC. From [50].

The LHC is also designed to create collisions (referred to as 'events') at higher luminosities than have previously been achieved at other accelerators. Instantaneous luminosity [45, 46, 47] (see equation 3.1) is a measure of number of events per second per unit of cross-section, with units of $\mathrm{cm}^{-2}\ \mathrm{s}^{-1}$.

$$L = \frac{n_p^2 n_b f \gamma F}{4\pi \epsilon_n \beta^*} \tag{3.1}$$

where,

L is the instantaneous luminosity

n_p is the number of protons in a bunch

n_b is the number of proton bunches in the LHC

f is the frequency of collisions

γ is the relativistic gamma factor for the protons

F is a geometric factor relating to the crossing angle of the proton bunches

ϵ_n is the normalised transverse beam emittance, a measure of the transverse spatial spread of the beams

β^* is the β function of the beams at the collision point, a measure of the spread in momentum space of the beams

The LHC is designed to collide protons at a center-of-mass energy of 14 TeV with a peak instantaneous luminosity of 10^{34} cm^{-2} s^{-1}. The cross-sections (σ) for various processes of interest as a function of center-of-mass collision energy ($\sqrt{s}$) are shown in figure 3.2.

Particles are accelerated in two separate beams around the LHC, one clockwise and the other anticlockwise. The beams are collided head-on at four points around the LHC ring. At each of these points a detector has been built to study these collisions. Two of these detectors, ATLAS and CMS, are general purpose detectors designed to study a wide range of physics topics. LHCb is a detector specialising in the study of B-hadron decays and matter-antimatter asymmetry. ALICE is a detector designed to focus on the study of heavy ion collisions. A diagram of the locations underground of the different detectors around the LHC can be seen in figure 3.3.

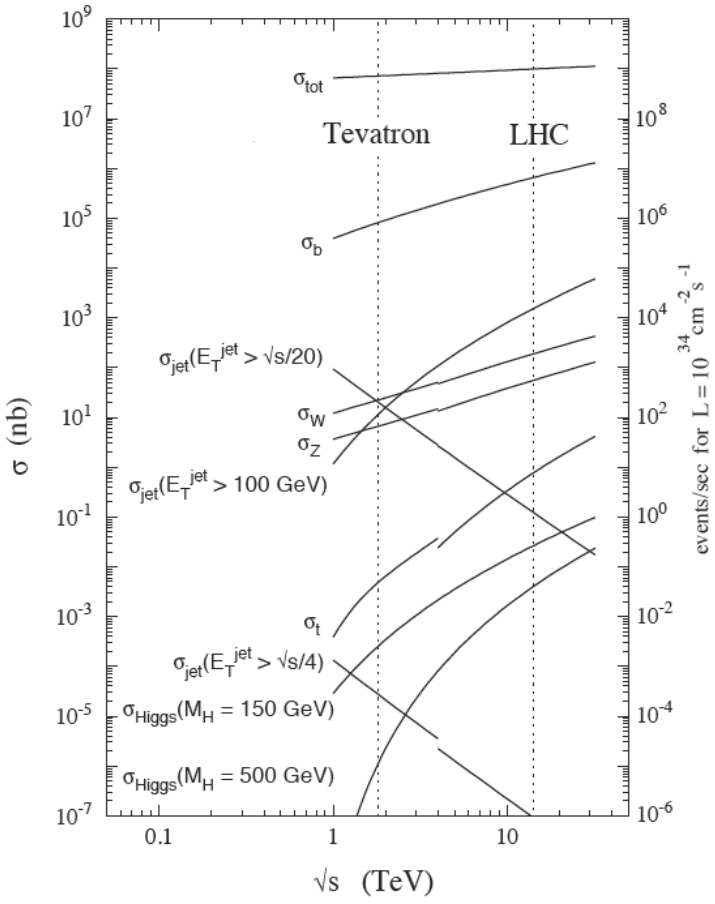

Figure 3.2: Cross-sections for various processes in proton-(anti)proton collisions as a function of center-of-mass collision energy. From [51].

3.2.2 Components

The LHC is designed to accelerate protons from an energy of 450 GeV to up to 7 TeV per beam (14 TeV center-of-mass collision energy). Therefore before entering the LHC protons must first be accelerated from stationary up to 450 GeV. This is done by a series of smaller accelerators as shown in figure 3.4.

A bottle of Hydrogen gas is used as the source of protons for the LHC. An electric field is used to separate the protons and electrons of the Hydrogen. The protons are then accelerated in Linac 2, a linear accelerator, up to an energy of 50 MeV. They are then fed into the first circular accelerator in the accelerator chain, the Proton Synchrotron Booster (PSB), which increases their energy to

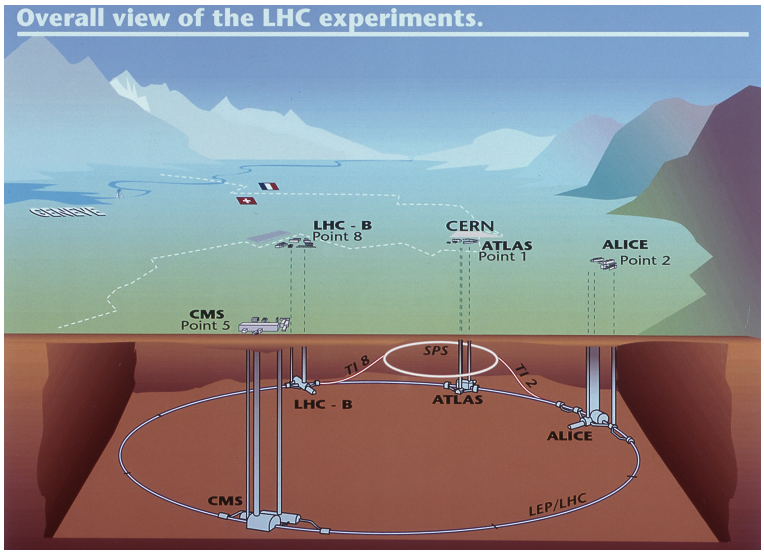

Figure 3.3: A diagram of the LHC ring to show its location and the four main experiments around it. From [50].

1.4 GeV. Next they are fed into the Proton Synchrotron (PS) and accelerated to 25 GeV, then passed into the Super Proton Synchrotron (SPS) where they are accelerated to 450 GeV before being directed into the LHC.

For heavy ions a different chain of accelerators is used. Vaporised lead is stripped of its electrons and the remaining nuclei are accelerated in Linac 3 to an energy of 4.2 MeV. They are then passed into the Low Energy Ion Ring (LEIR) where they are collected and accelerated to 72 MeV. After this they are passed into the PS and follow the same subsequent path as protons to the LHC.

The particle beams inside the accelerators are not continuous beams but are separated into 'bunches'. The LHC is designed so that each proton beam can contain up to 2808 bunches, with each bunch consisting of 1.5×10^{11} protons, and bunches from opposite beams colliding every 25 ns.

The LHC itself consist of a number of different components. There are 9300 magnets, of which 1232 are superconducting dipole magnets, each 15m long and weighing 40 tonnes, that bend the beams around the LHC ring. The dipoles operate at a temperature of 1.9 K and reach a peak magnetic field strength of 8.33 T. A diagram of a dipole magnet as used in the LHC is shown in diagram 3.5.

The other 8068 magnets are of higher order (quadrupoles up to dodecapoles) and are used to focus and stabilise the beams. The beams are focused as they

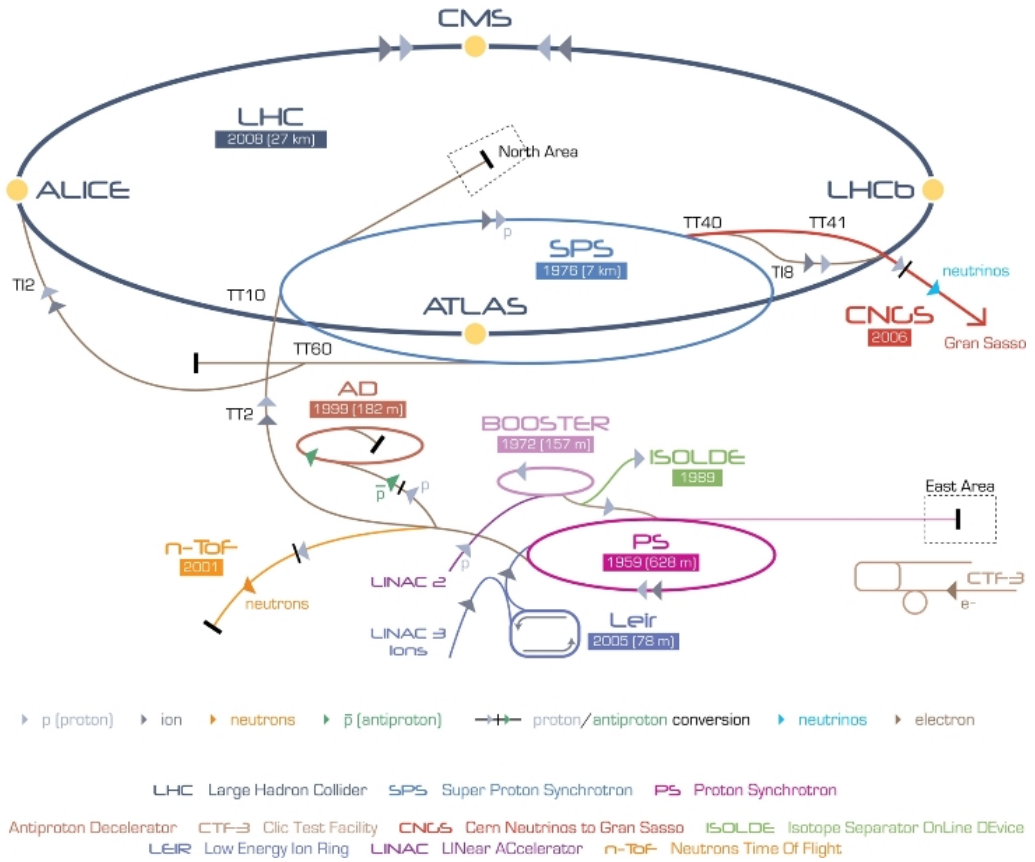

Figure 3.4: The beam production chain for the LHC and other experiments at CERN. From [52].

enter collision points so as to increase the luminosity of the collisions and are then defocused after each collision point to make them easier to control as they pass around the LHC ring.

At one point around the LHC the beams pass through radio-frequency (RF) cavities to accelerate them. The RF cavities also help constrain the protons in a bunch by forcing them to sit in the energetically favourable minima of the RF (called being in a 'bucket').

At other points around the LHC ring the beams pass through collimators [53]. These are devices where physical objects (usually blocks of carbon composites) are moved close to the beams. Any protons that are unacceptably divergent from the center of the beam-line will hit the collimators and scatter, so being removed from the beam. In this way the lateral dimensions of the LHC beams can be limited, thereby protecting equipment from being damaged by being hit by stray

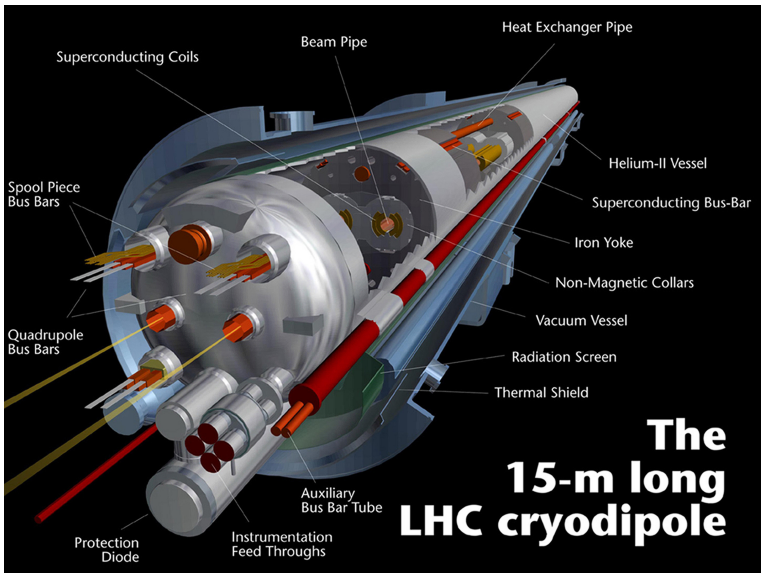

Figure 3.5: A diagram of a superconducting dipole magnet used in the LHC. From [50].

beam protons.

When it is desired to remove beams from the LHC, either as part of routine operation or in the case of something going wrong, the beams can be 'dumped'. This consists of steering the aborted beams out of the LHC ring and into graphite blocks that act as beam stops. The beams are deflected out of the LHC ring by 'kicker magnets' that take 3 μs to ramp up to full field strength. Each LHC beam must therefore contain an 'abort gap' of at least 3 μs between a pair of bunches to ensure that no particles pass through the kicker magnets as they ramp on, as this could result in beams being directed into equipment resulting in damage. The beams are defocused before reaching the beam stops and are 'painted' across the surface of the beams stops, as shown in figure 3.6. This reduces the energy deposited at any one point on a beam stop, resulting in less damage to the beam stops and a more effective stopping of the beams. A little fact that I believe should be documented for posterity is that every time the LHC beams are 'dumped' the noise of a toilet flushing is automatically played in the ATLAS Control Room.

3.2.3 Operational Timeline

Proton beams were first circulated in the LHC on the 10th of September 2008. Nine days later however a serious technical fault occurred resulting in damage to

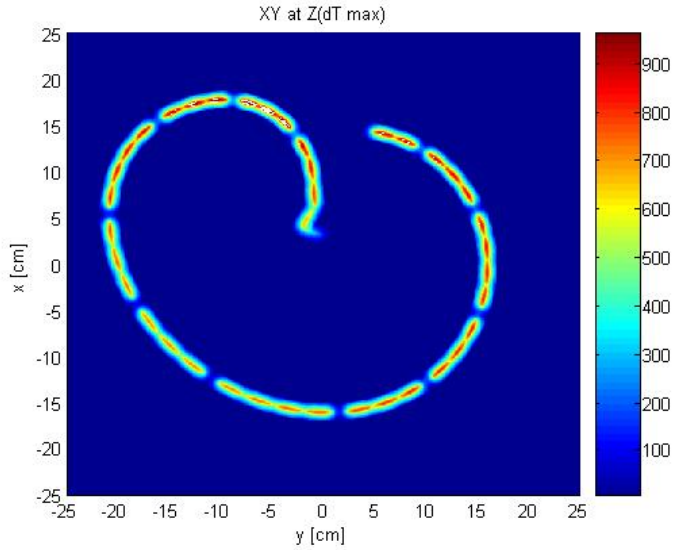

Figure 3.6: Energy deposited on the surface of a graphite beam stop during a proton beam dump at the LHC. The beam is 'painted' across the surface of the beam stop by using magnets to deflect it in the pattern shown as it is being dumped. From [54].

a large section of the LHC. In an electrical join between two dipole magnets a lack of solder between two superconducting wires resulted in electrical resistance. During high current testing a sufficient voltage built up across the join to form an electrical arc that burnt a hole in the side of the liquid helium cryostat of one of the dipole magnets. The resulting escape of helium created enough force to move several of the magnets by a large enough distance to rupture the beam pipe (normally under a vacuum). As a result soot was sucked along several kilometres of the beam pipe. Repairs were carried out involving fixing, cleaning or replacing 53 of the dipole magnets and redesigning safety systems to avoid a similar failure in the future. Proton beams were once again circulated in the LHC on the 20th of November 2009. Three days later the first proton-proton collisions in the LHC were achieved at a center-of-mass energy of 900 GeV.

In 2010 the proton beam energy was increased and on the 30th of March 2010 collisions with a center-of-mass energy of 7 TeV were achieved. During 2010 the LHC delivered 48.9 pb^{-1} of integrated luminosity of proton-proton collisions to the ATLAS detector, of which 45 pb^{-1} was recorded by the ATLAS detector.

In 2011 the LHC continued to collide protons at a center-of-mass collision energy of 7 TeV. The peak luminosity of the LHC increased as the year went on,

as shown in figure 3.7. By the end of 2011 the LHC had delivered 5.61 fb^{-1} of integrated luminosity of proton-proton collisions to the ATLAS detector, of which 5.25 fb^{-1} was recorded. The integrated luminosity against time for proton-proton collisions in 2011 is shown in figure 3.8.

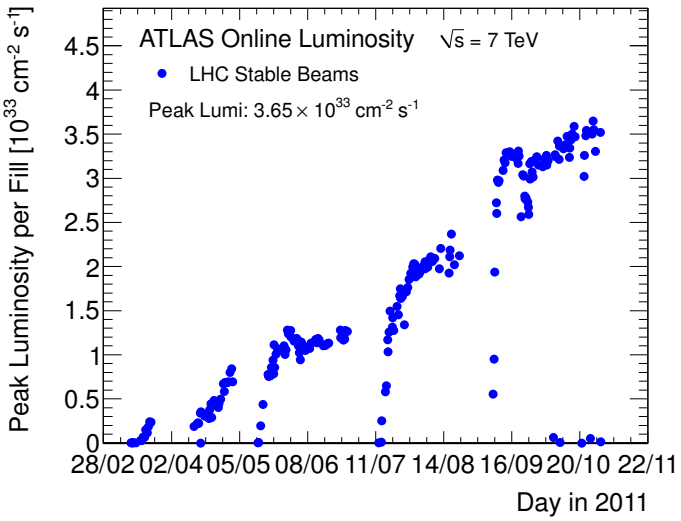

Figure 3.7: Maximum instantaneous luminosity versus day in 2011, delivered to the ATLAS detector. From [55].

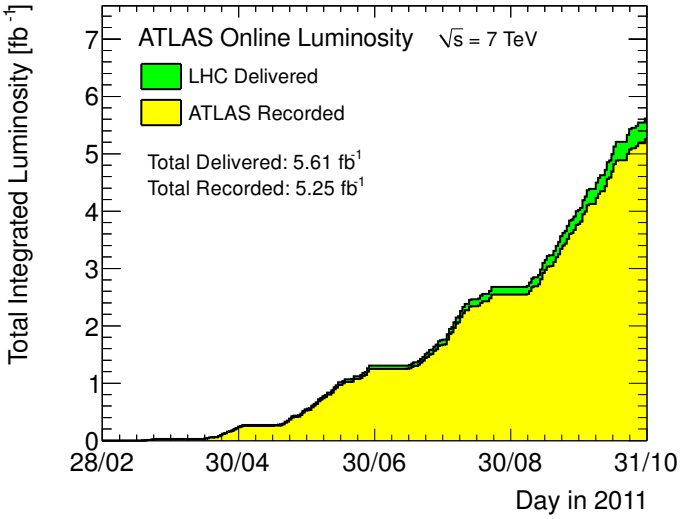

Figure 3.8: Cumulative luminosity versus day delivered to (green), and recorded by (yellow) the ATLAS detector in 2011. From [55].

In 2012 the energy of the LHC proton beams was raised to 4 TeV per beam,

resulting in a center-of-mass collision energy of 8 TeV. Over the course of 2012 the LHC delivered 23.3 fb^{-1} of integrated luminosity of proton-proton collisions to the ATLAS detector, of which 21.7 fb^{-1} was recorded. The integrated luminosity against time for proton-proton collisions in 2012 is shown in figure 3.9.

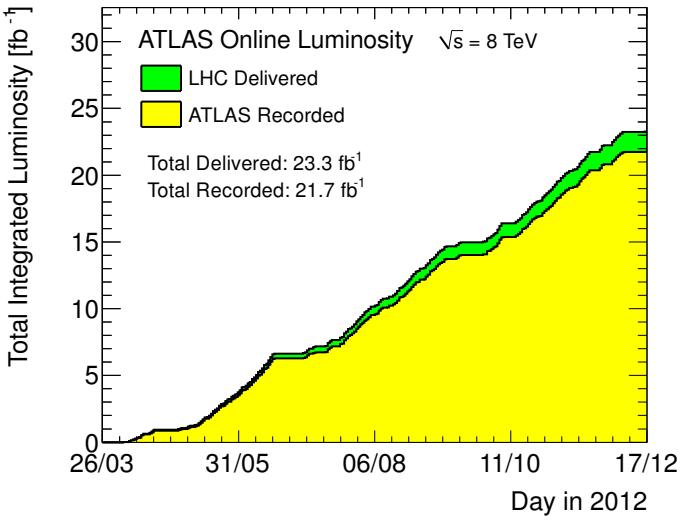

Figure 3.9: Cumulative luminosity versus day in 2012, delivered to the ATLAS detector. From [55].

The Integrated luminosity against time for proton-proton collisions in 2010, 2011 and 2012 is shown in figure 3.10 showing the increase in performance of the LHC from one year to the next.

The LHC was then shut down in early 2013 in order to upgrade various components of both the LHC and the detectors attached to it. The LHC will be switched back on in 2015 with an intended proton-proton center-of-mass collision energy of 13 TeV.

For the analysis detailed in this thesis proton-proton collision data from 2011 and 2012 was used.

3.2.4 Anatomy Of A Run

Once protons are injected into the LHC at 450 GeV the LHC 'ramps up' in energy, increasing the energy of the proton beams to the desired value (3.5 GeV per beam in 2011, and 4 TeV per beam in 2012). The beams are then adjusted and the bunches are 'squeezed' in the transverse plane in order to increase collision

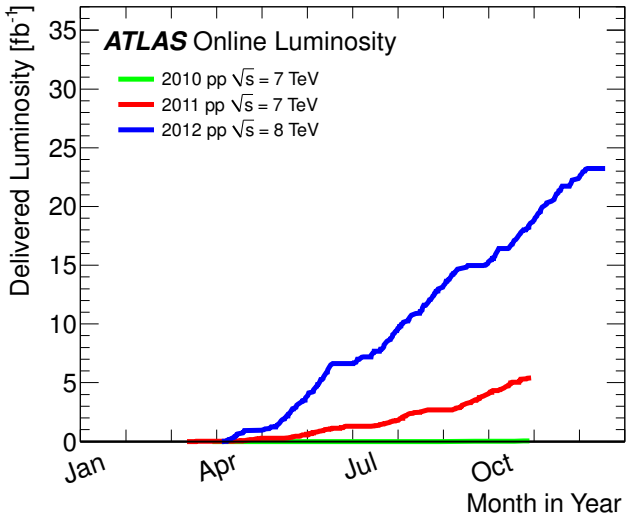

Figure 3.10: Cumulative luminosity versus day delivered to the ATLAS detector for proton-proton collisions in 2010, 2011 and 2012. From [55].

luminosity. Liouville's theorem [56] states that the density of particles in phase space remains constant. Reducing the size of the bunches in the transverse plane therefore results in increasing their length. The bunches roughly double in length, reducing intra-bunch interactions and so reducing beam losses. The bunches correspondingly decrease in transverse size by a factor of roughly $\frac{1}{\sqrt{2}}$. Next the beams are steered into each other at the four collision points around the LHC. Once collisions have begun the LHC declares 'stable beams' which allows the detectors to make final preparations and start recording collision data. The peak luminosity in a run is achieved at the start of the run. As the number of protons in the beams decreases over time due to protons colliding, the luminosity of collisions decreases. Once the luminosity has decreased by $\frac{1}{e}$ more data can be collected by dumping the beams, refilling the LHC with more protons and starting collisions again. The beams are therefore dumped and the LHC energy is 'ramped down' in energy, ready to accept new protons at 450 GeV. This whole process is described as a 'run'. During operation, runs with collisions lasting 10-15 hours were achieved. From the dumping of beams at the end of one run to 'stable beams' being declared as part of the next run a time as short as 45 minutes was required.

3.3 The ATLAS Detector

3.3.1 Introduction

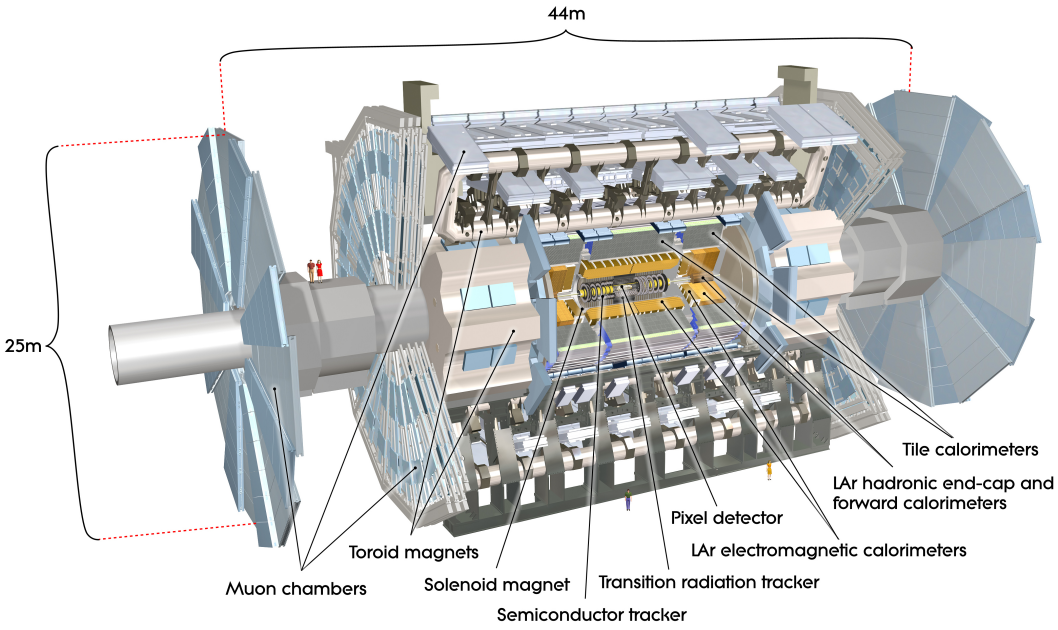

Figure 3.11: The ATLAS detector and its main subsystems. From [50].

The ATLAS detector is the largest particle detector ever built at 44 m long, 25 m wide and weighing roughly 7000 tonnes [44]. Particle collisions provided by the LHC occur at almost exactly the geometric center of ATLAS. The detector is made up of different subsystems arranged to identify and measure the particles that come out of these collisions. It is shown in figure 3.11.

3.3.2 Coordinate System

The ATLAS detector uses a right handed coordinate system. In Cartesian coordinates the x-axis is horizontal, with the positive direction pointing towards the center of the LHC ring. The y-axis is vertical with the positive direction pointing upwards. The z-axis is along the beam line with the positive direction pointing anticlockwise around the LHC ring. A cylindrical coordinate system is also commonly used in which the radius R is defined as $R = \sqrt{x^2 + y^2}$. The azimuthal coordinate ϕ is defined such that $\phi = 0$ corresponds to the positive direction of the x-axis. Instead of a polar angle θ, the pseudorapidity η is used

where $\eta = -\frac{1}{2}\ln(\tan(\frac{\theta}{2}))$. $\eta = 0$ corresponds to the x-y plane perpendicular to the beam line z-axis. Differences in rapidity, $y = \frac{1}{2}\ln(\frac{E+p_z}{E-p_z})$, are invariant with respect to Lorentz boosts along the z-axis. This results in reasonably uniform distributions in rapidity of particles from inelastic collisions. Pseudorapidity is rapidity in the limit of massless particles.

Quantities are often referred to in terms of their transverse component: their component in the x-y detector plane. Transverse momentum, p_{T}, is therefore the component of an object's momentum perpendicular to the beam axis. Transverse quantities are used as the initial transverse momentum of the colliding-protons system can be taken to be zero, whereas the total momentum of the colliding-protons system can not. This is due to proton movement within a bunch being negligible in the transverse plane, but non-negligible along the beam axis. Additionally, we do not know the Bjorken x of the colliding partons (Bjorken x is the fraction of the parent proton's momentum that a parton carries), thus can not know the longitudinal momenta of the partons.

3.3.3 Detector Components

Magnets

Magnetic fields are used in ATLAS to bend the paths of charged particles. By measuring the direction and curvature of the path of a particle the charge and momentum of that particle can be determined. The transverse momentum p_{T} of a particle in GeV is given by $p_{\mathrm{T}} = 0.2998 * B * r$ where B is the magnetic field strength in Tesla and r is the radius of curvature in metres of the particle's path in the plane perpendicular to the magnetic field.

The ATLAS detector contains two magnetic field systems. One is a solenoid surrounding the inner detector and providing a 2 T magnetic field. The second is a toroidal system placed outside the inner detector, calorimeters and part of the muon spectrometer. It consists of toroidal end-caps and a central toroid barrel. The toroid magnet system has a magnetic field strength of 4 T at the magnets. All the magnets in ATLAS are superconducting, and collectively store an energy of 1.6 GJ [44].

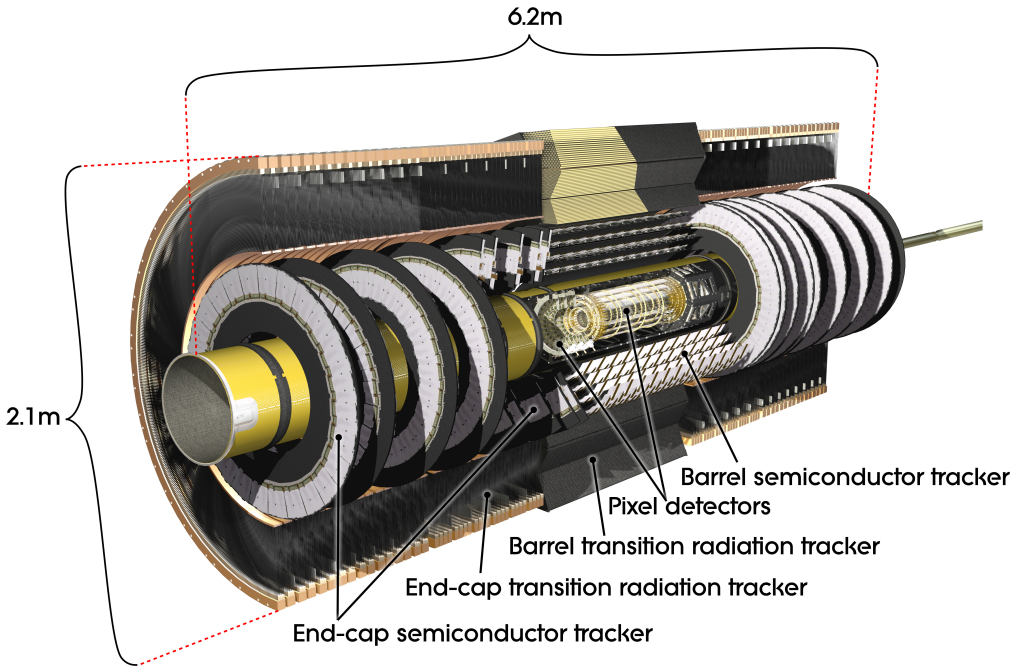

Figure 3.12: The ATLAS Inner Detector and its main subsystems. From [50].

The Inner Detector

The Inner Detector (ID), shown in figure 3.12, is designed to identify and measure the paths of particles (a process known as tracking). It allows for the reconstruction of paths of particles within $|\eta| < 2.5$, and the measurement of their momenta using the properties of the 2 T magnetic field it is immersed. Using multiple particle paths (tracks), the vertices from which particles have originated can also be identified.

The ID is made up of three sub-sections: the Pixel Detector, the SemiConductor Tracker (SCT), and the Transition Radiation Tracker (TRT), each utilising a different design. See tables 3.1 and 3.2.

The Pixel Detector is the closest to the interaction point of the three ID subsections and has the highest sensor granularity. Its sensors consist of silicon semiconductors 'modules' that are 250 µm thick and are divided into pixels 50 µm wide and 400 µm long. The modules are arranged into three layers in the barrel and three end-cap disks at each end of the barrel. In total there are 1744 modules, each with 47232 pixels, leading to over 80 million pixels in the Pixel Detector. The resulting spatial resolution of the Pixel Detector is 10 µm in

ID sub-section	Number of channels	Approximate operational fraction
Pixel	80 M	95.0 %
SCT	6.3 M	99.3 %
TRT	350 k	97.5 %

Table 3.1: Number of read out channels and approximate operational fraction at the end of 2012 for different sub-sections of the ATLAS Inner Detector.

$R\phi$ and 115 μm in z. When a charged particle passes through a pixel it deposits energy by energising electrons in the silicon to create electron-hole pairs, (usually in several adjacent pixels, which are then referred to as a 'cluster'). This energy can be measured and recorded as a 'hit' with a given location.

The SCT uses silicon semiconductor sensors in strips surrounding the Pixel Detector. Each strip is 80 μm wide and 12 cm long, and some strips are glued together in two layers. The layers are offset by a small angle (40 mrad) in order to improve the spatial resolution of the SCT. The resulting spatial resolution of the SCT is 16 μm in $R\phi$ and 580 μm in z.

The TRT is situated outside the SCT and consists of tubes, 4 mm in diameter, filled with a mixture of xenon, CO_2 and O_2. As changed particles pass through the gas mixture they ionise some of the gas. Each tube is wrapped in a gold wire and has a second gold wire running down the center of the tube, between which a voltage of up to 500 V is applied [57]. This allows the charge from the ionised gas to be collected. By measuring the time taken to collect the charge the position of the track perpendicular to the tube can be determined. It is not possible to determine the position of the track parallel to the tube, which is z in the barrel and R in the end-caps.

Over time the sensors of the ID have suffered from radiation damage as well as occasional errors in the read-out electronics modules. Monitoring for errors in read-out modules was performed and most errors were able to be automatically fixed by reconfiguring any module found to be in error. All SCT read-out modules were also reconfigured roughly every 30 minutes as a precaution against errors [58]. By the end of 2012 though only a fraction of sensors in the ID were still operational. This is shown in table 3.1.

A summary of coverage, resolution and typical number of hits per track is

ID sub-section	Coverage	Spatial resolution [μm]	Typical hits per track
Pixel barrel	$\|\eta\| < 2.5$	10 ($R\phi$), 115 (z)	3
Pixel end-caps	$2.0 < \|\eta\| < 2.5$	10 ($R\phi$), 115 (z)	3
SCT barrel	$\|\eta\| < 1.5$	16 ($R\phi$), 580 (z)	8
SCT end-caps	$1.3 < \|\eta\| < 2.5$	16 ($R\phi$), 580 (z)	8
TRT barrel	$\|\eta\| < 1.0$	130	>30
TRT end-caps	$0.8 < \|\eta\| < 2.0$	130	>30

Table 3.2: Summary of coverage, resolution and typical number of hits per track for different sub-sections of the ATLAS Inner Detector.

shown in table 3.2.

Calorimeters

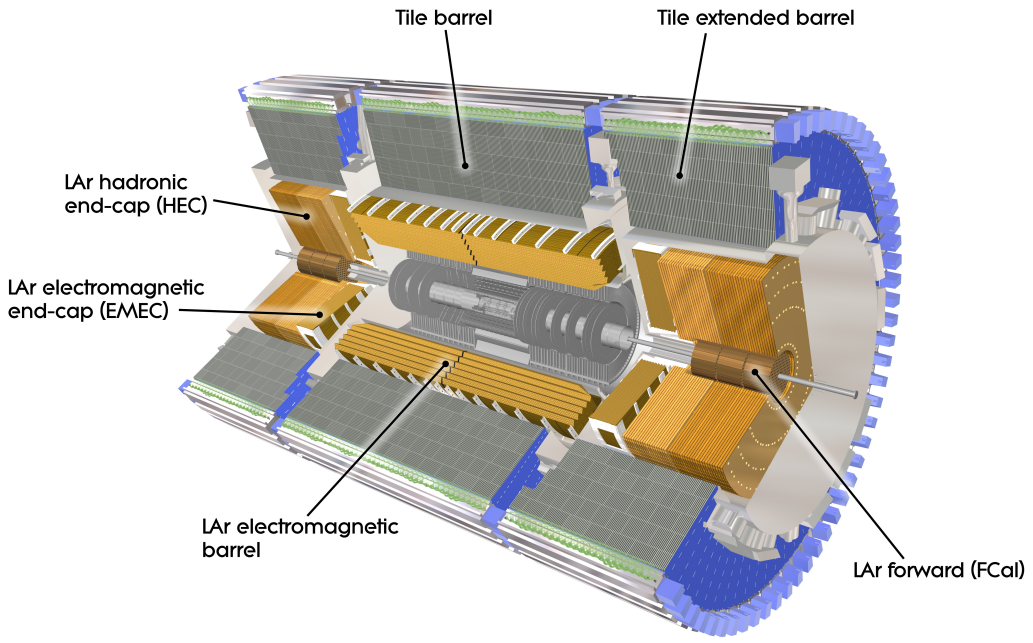

Figure 3.13: The ATLAS Calorimeters and their main subsystems. From [50].

The ATLAS Calorimeters are designed to absorb and measure the energy of certain particles that pass through them. They are segmented, allowing them to record the position in the detector of particles and physics objects they

detect. Typically a physics object will deposit energy into several adjacent calorimeter segments, creating a calorimeter 'cluster'. The calorimeters are split up into two sub-systems. The Electromagnetic (EM) Calorimeters are designed to contain and measure the energy of electromagnetic particles such as electrons and photons. The Hadronic calorimeters are used in conjunction with the EM Calorimeters to measure the properties of hadronic showers. The EM Calorimeters are made up of the Electromagnetic Barrel (EMB) and Electromagnetic End Caps (EMEC). The Hadronic Calorimeters are made up of the Hadronic End Cap (HEC), the Forward Calorimeters (FCal) and the Tile Calorimeters. The layout of the ATLAS Calorimeters is shown in figure 3.13.

The calorimeters use alternating layers of materials to absorb and measure the energy of particles. The absorber, is made of a material that is inert but has a short radiation length X_0 for EM calorimetery or interaction length λ_I for hadronic calorimetery, meaning that it is very good at absorbing the energy of incident particles. By including layers of absorber material the overall size and cost of the calorimeters can be kept within desired limits. The active medium, also absorbs some energy from incident particles, although not as much as the absorber. It does however allow for the measurement of the energy that it has absorbed. Two kinds of active medium are used in the ATLAS detector: Liquid Argon and plastic scintilator. In liquid Argon (LAr) the Argon is ionised by passing particles. This ionisation is then collected on electrodes in the presence of an electric field, where it can be measured and converted into a digital signal to be read out of the detector. In plastic scintilator, incident particles cause photons to be emitted by the scintilator. These photons can be guided onto photomultiplier tubes in order to generate an electrical signal that can be read out.

Different particles incident on the calorimeters behave in different ways, resulting in different 'physics objects' being identifiable. Electrons and positrons will emit photons via bremsstrahlung. The radiation length X_0 of a material is the mean distance over which an electron will lose all but 1/e of its energy this way. Photons will produce pairs of electrons and positrons as they pass through the calorimeters. The mean free path for pair production by a photon is 7/9ths of the X_0 of the material it is passing through. By a sequence of these processes incident electrons and photons will produce extended objects known as

Calorimeter sub-system	Coverage	Active medium	Absorber
EMB	$\lvert\eta\rvert < 1.457$	LAr	Pb
EMEC	$1.375 < \lvert\eta\rvert < 3.2$	LAr	Pb
HEC	$1.5 < \lvert\eta\rvert < 3.2$	LAr	Cu
FCal	$\lvert\eta\rvert < 1.475$	LAr	Cu/W
Tile	$\lvert\eta\rvert < 1.7$	Scintillating plastic	Steel

Table 3.3: Summary of coverage and materials of ATLAS calorimeter sub-systems.

electromagnetic showers. Hadronic objects will lose energy in the calorimeters by hadronic decay and inelastic nuclear interactions, with the mean distance travelled by a hadron before it undergoes inelastic nuclear interaction being given by the λ_I of the material it is passing though. By these processes hadronic objects produce extended physics objects known as hadronic showers or hadronic jets.

A summary of the coverage of, and materials used in, calorimeter sub-systems is shown in table 3.3.

Muon Spectrometer

A muon will typically pass through all components of the ATLAS detector, resulting in a single track. In order to measure the curvature of this track a large detector system is required (since higher-p_{T} tracks have less curvature, and it becomes harder to measure the curvature of a track as that curvature decreases). The Muon Spectrometer (MS) performs this task, as well as helping to differentiate between muons and other physics objects. It is immersed in the magnetic field of the toroid magnet (see section 3.3.3) and is comprised of 'muon chambers' arranged into several different sections: in the central barrel region ($|\eta| < 1.0$) the muon chambers are arranged in three cylindrical layers. In the end-caps ($1.4 < |\eta| < 2.7$) they form three vertical disks. In the transition region ($1.0 < |\eta| < 1.4$) there are four layers of muon chambers.

The layout of the ATLAS Muon Spectrometer is shown in figure 3.14.

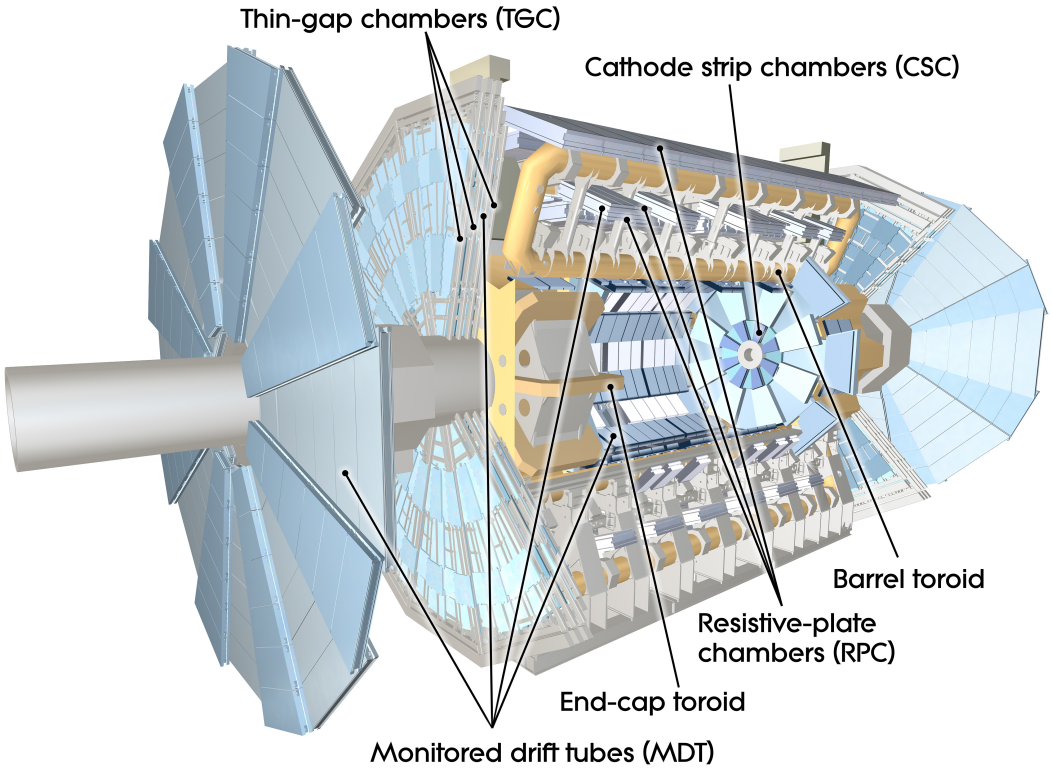

Figure 3.14: The ATLAS Muon Spectrometer and its main subsystems. From [50].

Physics Objects

Different physics objects are identified and reconstructed in the ATLAS detector using different algorithms [44]. They correspond to fundamental particles passing through the detector, or extended objects such as hadronic jets. This is shown in figure 3.15. By using the location information of all the hits in the ID in an event, the tracks of charged particles can be determined [59]. All physics objects, except neutrinos, will deposit energy in the calorimeters, which will allow for the measurement of their energy, and also assist in the determination of their position. The position of a physics object is determined in the detector coordinates of η and ϕ.

Electrons

Electrons create hits in the ID, and deposit energy in the calorimeters. This information is used to reconstruct their tracks, and measure their position, energy and momentum. Typically their mass is neglected, such that their

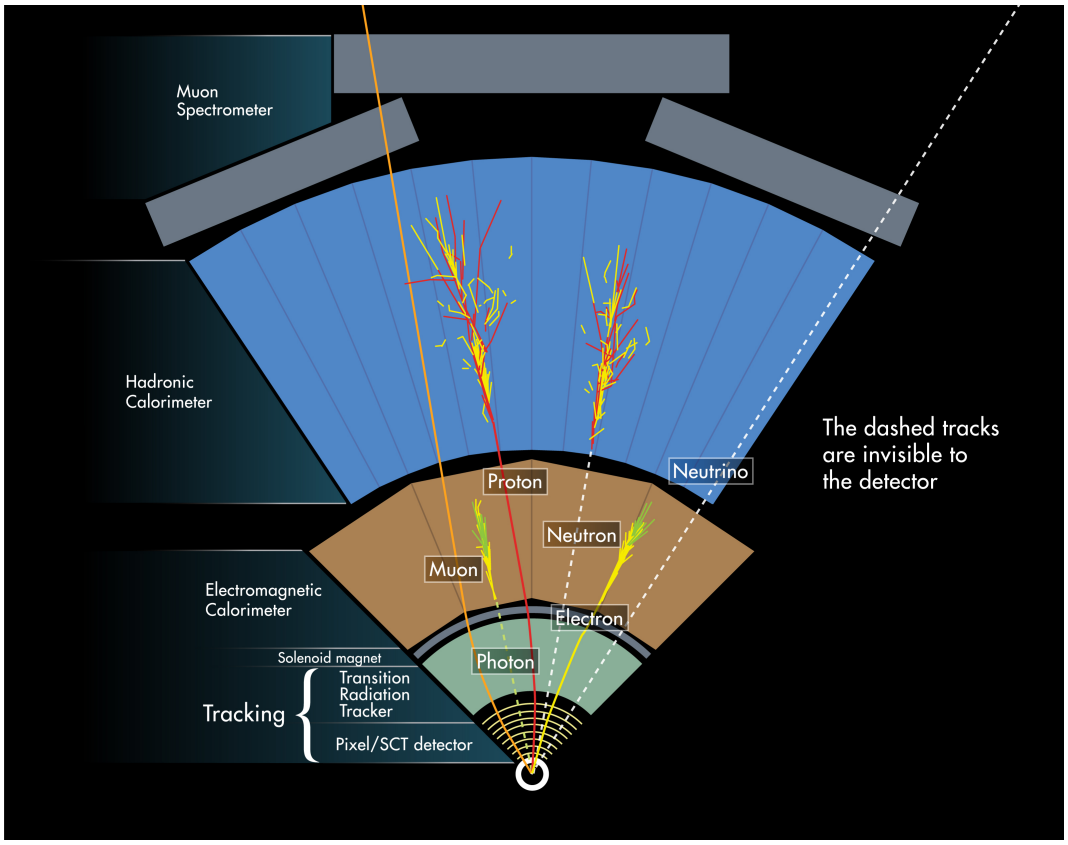

Figure 3.15: A cross-section of the ATLAS detector, showing how different types of particles interact with different detector components. From [50].

energy and momentum are equal.

Muons

Muons create hits in the ID and the muon spectometer. These hits from both subsystems are used to reconstruct their tracks [60]. With these tracks, and the little energy they deposit in the calorimeters, their position, energy and momentum are measured.

Hadronic jets

Jets deposit energy in the calorimeters. They may also cause hits in the ID, leading to tracks being reconstructed and associated with the jet. This allows for their energy and position to be determined, where the position is determined from the centre of the energy cluster in η and ϕ.

Neutrinos - Missing transverse energy

Neutrinos can not be detected by the ATLAS detector. Instead, only the sum of all undetected momenta (including the momenta of neutrinos) can be determined from conservation of energy and momentum in the x-y plane. This is referred to as 'missing transverse energy'.

Data Acquisition And Triggering

The LHC was designed to achieve a bunch-crossing rate of 40 MHz. Given that for a single event the ATLAS detector produces 1.5 MB of data, to store all the data for 40 M events per second would require 60 TB of data to be processed and recorded every second, far beyond the limits of current computing technology. In addition to this, subsystems in the ATLAS detector are not all able to produce data at a rate of 40 MHz. Some require 'dead time', time during which they cannot record data, in order to 'reset' and be able to once again record data. Typically this involves reading out and clearing memory buffers built into the detector components. Finally, not all collisions that occur in the ATLAS detector will be interesting to physics studies being performed by the collaboration.

The ATLAS detector therefore requires a system to select which events to save to disk. This system is the trigger system of ATLAS. The trigger system is split into three levels of decision-making processes.

The first level, level 1 (L1), is a hardware-based system built into the ATLAS detector itself. It is designed to very rapidly (within 2.5 μs) decide if something interesting has happened after a bunch-crossing has occurred. It does this based on very basic information from the calorimeters and muon systems: If part of the detector is found to have energy deposited, where that energy is above a certain configurable threshold and contained within a region of a certain configurable size, then that part of the detector is identified as a 'Region Of Interest' (ROI). If suitable ROIs are found by the L1 trigger then they are passed on to the next level of the decision-making process; the level 2 (L2) trigger. The L1 trigger passes events to L2 at a rate of about 100 kHz.

The L2 trigger is software based, located on machines in a cavern adjacent to the ATLAS cavern. It has access to data from all of the ATLAS detector, although it processes data based on the ROI passed to it from the L1. It gives a more complete picture of an event than the L1 trigger gives, although in the interests of speed it does not do a full event reconstruction. Based on a configurable trigger

'menu', the L2 will decide to pass an event on to the next stage in the trigger system if it finds that the event has criteria that match one or more possible options in the menu. The next stage in the trigger system is the Event Filter (EF) to which the L2 passes events at a rate of about 2.5 kHz.

The EF is also a software based trigger, located on the same group of machines as the L2. Given that it has fewer events per second to process than the L2 it can perform a more detailed reconstruction of each event, allowing for more detailed trigger menus to be used, and more accurate measurements of physics objects to be used in trigger decisions. The EF outputs events at a rate of about 80 Hz, equivalent to about 200 MB/s. These events are then written to disk.

The L2 and EF are collectively known as the High Level Trigger (HLT). Since they run on the same group of machines, each machine can be individually configured to run either L2 or EF software, allowing the computing power for each stage in the HLT to be adjusted as required based on the trigger menus being used at the time.

A further consideration for each level in the trigger system as to whether to pass an event on to the next stage is the limitation of output bandwidth. If more events pass trigger requirements at a certain stage than it is possible for that stage to output, or if more events pass a certain trigger menu item's requirements than we desire to dedicate our bandwidth to, then a certain fraction of those events will have to be rejected. To do this each individual trigger menu item can be 'prescaled' meaning that only a certain fraction of the events that pass that trigger menu item's criteria will be output to the next stage in the trigger system. For example, say that we have a trigger menu item that says we should accept events that contain a hadronic jet with a p_{T} greater than 50 GeV. It may be that more events occur per second that pass this requirement than we want to record (as they would otherwise use up too much bandwidth, say). We can then prescale this trigger so that only an acceptable fraction of the events that pass this trigger are passed on to the next stage in the trigger system. A prescale of 100 would mean that only one in 100 events that pass this trigger would be passed on to the next stage in the trigger system. This is done by randomly selecting applicable events with a probability of 1 %.

Data that is saved to disk is then later fully reconstructed offline.

Chapter 4

Search For The Standard Model Higgs Boson In The $WH \to \ell\nu b\bar{b}$ Channel

4.1 Introduction

The Brout, Englert, Higgs (BEH) mechanism and the associated Higgs boson were first proposed in 1964 [5] and incorporated into the Standard Model by Weinberg in 1967 [2]. For many years since then the Higgs boson has been searched for [61, 62], however it was not until 2012 that a particle with properties consistent with a Standard Model Higgs boson was first found by the ATLAS and CMS collaborations at CERN [3, 4]. Further measurements of this newly-discovered particle have strengthened the hypothesis that it is a SM Higgs boson with a mass, as measured by the ATLAS collaboration, of $m_H = 125.36 \pm 0.37(\text{stat}) \pm 0.18(\text{syst})$ GeV $= 125.36 \pm 0.41$ GeV [29]. The CMS collaboration measures its mass to be $m_H = 125.02\ ^{+0.26}_{-0.27}$ (stat) $^{+0.14}_{-0.15}$ (syst) GeV [30]. Not all properties of a SM Higgs boson have been observed or excluded from possibility in this new-found particle however. For example, a SM Higgs boson with a mass of 125 GeV is expected to have a branching ratio to b-quark pairs of 58 % [32]. This new-found particle has not yet been observed decaying to $b\bar{b}$ pairs. Nor has it been shown to not decay to this final state. Furthermore, it has not been observed decaying to any types of fermions, although there is evidence for Higgs boson to tau-pair decays [63]. It is therefore important to search for this decay mode in order to further ascertain whether this new-found particle is indeed consistent with a SM

Higgs boson. Additionally, observation of Higgs to b-quark pair decays would allow for the measurement of the coupling strength of Higgs boson to b-quarks. This would be an important test of whether the Higgs boson couples to fermions as the Standard Model predicts.

A search for $H \to b\bar{b}$ is not straightforward however. b-quarks hadronise to produce hadronic jets. It is possible to estimate, with a given efficiency, whether a given hadronic jet has originated from a b-quark. This is known as 'b-jet tagging' or just 'b-tagging'. However, even with this identification procedure there is still a large background from QCD multijet production, (this background has a cross-section of roughly 5×10^7 times the expected cross-section of a SM Higgs boson signal [64, 51]). In order to reduce contributions from backgrounds, features of the production of a Higgs boson can be used: if a Higgs boson is produced in association with a vector boson (see chapter 2, section 2.3.2) then the decay of this vector boson can be searched for. This extra requirement on the event topology reduces contribution from QCD background processes by a factor of roughly $\frac{1}{190}$.

In the ATLAS search for $H \to b\bar{b}$ decays in association with a vector boson both the production of a Higgs boson in association with a W boson and in association with a Z boson are considered and targeted. The search is split into three orthogonal channels, with final states containing either zero, one, or two electrons or muons. These target, respectively, the vector boson decay modes $Z \to \nu\bar{\nu}$, $W \to \ell\nu$, and $Z \to \ell\bar{\ell}$, with $\ell = e$ or μ. These three channel are referred to as the '0-lepton', '1-lepton', and '2-lepton' channels, respectively.

The search is also split into bins of vector boson p_{T} (p_{T}^V), number of jets in the final state, b-jet tagging likelihood, and b-jet pair invariant mass ($m_{b\bar{b}}$). Bins with larger p_{T}^V typically have larger signal-to-background ratios, but fewer events. This binning allows the analysis to be optimised separately in each bin, and increases the overall sensitivity of the analysis.

In this chapter a cut-based search for the Standard Model Higgs boson in the $WH \to \ell\nu b\bar{b}$ process with the ATLAS detector will be presented. The combination of this result with the $ZH \to \nu\nu b\bar{b}$ and $ZH \to \ell\ell b\bar{b}$ cut-based searches [65] will also be presented in this chapter. The combination of these searches is referred to as $VH \to b\bar{b}$ for brevity, where V refers to a vector boson, either a W or Z boson. Where there are differences between the WH and ZH cut-based searches, these will be presented in this chapter.

4.2 Signal And Background Processes

Signal and background processes occurring in this analysis are listed in table 4.1. Also shown in this table are the Monte Carlo event generator programs used to model the processes. For more information on background modelling see section 4.5. The cross-section for each sample generated, as well as the number of Monte Carlo events generated, are also shown.

Process	Event Generator Used	σ	Number of Events
$q\bar{q} \to WH$	Pythia 8	704.6 fb	3 M
$q\bar{q} \to ZH$	Pythia 8	382.8 fb	6 M
$gg \to ZH$	Powheg_Box + Pythia 8	32.46 fb	800 k
W + jets	Sherpa 1.4.1	12.07 nb	390 M
Z + jets	Sherpa 1.4.1	7.95 nb	164 M
WW	Powheg_Box + Pythia 8	52.44 pb	10 M
WZ	Powheg_Box + Pythia 8	9.241 pb	15 M
ZZ	Powheg_Box + Pythia 8	3.171 pb	15 M
QCD multijet	Derived from data	-	-
Top-quark:			
$t\bar{t}$	Powheg_Box + PYTHIA6	256.89 pb	100 M
t-channel	AcerMC + PYTHIA6	87.76 pb	9 M
s-channel	Powheg_Box + PYTHIA6	5.61 pb	6 M
Wt-channel	Powheg_Box + PYTHIA6	22.37 pb	20 M
Total generated background	-	20.46 nb	729 M

Table 4.1: Signal and background processes of the $VH \to b\bar{b}$ analysis, with event generators used to generate corresponding Monte Carlo samples, cross-section for each sample as reported by the event generator used, and the number of Monte Carlo events generated. For signal processes, only numbers for the $m_H = 125$ GeV mass point are listed. However, signal Monte Carlo samples were created for Higgs mass points of $m_H = 100$ to 150 GeV in 5 GeV intervals.

In the 0-lepton channel, the main backgrounds are Zbb and $t\bar{t}$, with a smaller contribution from Wbb. The $t\bar{t}$ background contributes predominantly in the lower p_{T}^V bins. In the 1-lepton channel, the main backgrounds are Wbb and

$t\bar{t}$. There are also contributions from the QCD multijet and single-top-quark backgrounds (mostly Wt for the latter). While contributions from $t\bar{t}$ tend to decrease with increasing p_{T}^{V}, contributions from Wbb tend to increase with increasing p_{T}^{V}. In the 2-lepton channel, the main background is Zbb, with a smaller, but still significant, contribution from $t\bar{t}$ in the lower p_{T}^{V} bins.

20.3 fb^{-1} [66] of $\sqrt{s} = 8$ TeV proton proton collision data was analysed in this $H \to b\bar{b}$ search. The collisions were provided by the LHC in 2012 with stable beam conditions. The data was collected with the ATLAS detector where all subsystems were running and providing high-quality data.

4.3 Physics Objects

Physics objects (see section 3.3.3) are items identified and reconstructed in the ATLAS detector such that they can be used in physics analyses [44].

4.3.1 Particle Tracks

Tracks of charged particles with a $p_{\mathrm{T}} > 400$ MeV are reconstructed and as such are available for further physics analysis.

4.3.2 The Primary Vertex

The primary vertex, the interaction point identified as the origin for physics processes of interest in an event, is chosen to be the reconstructed vertex with the highest sum of associated-track transverse momenta squared, $\sum p_{\mathrm{T}}^2$, and is required to have at least three reconstructed tracks associated with it.

4.3.3 Electrons And Muons

Electrons and muons in this analysis [67, 68, 69] are split into three categories, known as loose, medium, and tight leptons, in order of increasing accuracy of measurement and likelihood of correct identification of the leptons.

Loose leptons are required to have transverse energy $E_{\mathrm{T}} > 7$ GeV. Additionally, an isolation requirement is applied: the scalar sum of the p_{T} of tracks within $\Delta R = \sqrt{(\Delta\eta)^2 + (\Delta\phi)^2} = 0.2$ of the lepton-candidate track, excluding the lepton-candidate track, must be less than 10 % of the p_{T} of the lepton-candidate track. Loose electrons must be within $|\eta| < 2.47$, the coverage of the ATLAS inner detector. They must also pass likelihood identification criteria known as 'very loose likelihood' [68]. Loose muons are split into three categories to maximise acceptance. The first category consists of muons reconstructed in both the inner detector and the muon spectrometer. These requirements limit these muons to $0.1 < |\eta| < 2.5$. These muons must also have impact parameters with respect to the primary vertex, the distance of closest approach of the muon-track to the primary vertex, of less than 1 mm along the ATLAS detector z-axis (the beam line), and less than 0.1 mm in the x-y plane. Muons in the second category must have $p_{\mathrm{T}} > 20$ GeV, have a track in the inner detector within $|\eta| < 0.1$,

and be identified in the calorimeters. They must also have impact parameters with respect to the primary vertex of less than 1 mm along the z-axis, and less than 0.1 mm in the transverse x-y plane. Muons in the third category must have $|\eta| > 2.5$ and be reconstructed in the muon spectrometer.

Medium leptons must pass all the criteria for loose leptons, but must also have $p_{\mathrm{T}} > 25$ GeV. In addition, medium muons must be reconstructed in both the inner detector and the muon spectrometer, thus they must be within $0.1 < |\eta| < 2.5$.

Tight leptons must fulfil the medium-lepton criteria. Additionally, a tighter isolation requirement is applied:, the sum of energy deposited in the calorimeters within $\Delta R = 0.3$ of the lepton candidate, excluding energy associated with the lepton candidate, must be less than 4 % of the lepton candidate energy. Also, the scalar sum of the p_{T} of tracks within $\Delta R = \sqrt{(\Delta\eta)^2 + (\Delta\phi)^2} = 0.2$ of the lepton-candidate track, excluding the lepton-candidate track, must be less than 4 % of the p_{T} of the lepton-candidate track. Finally, tight electrons are also required to pass 'very tight likelihood' identification criteria [68].

4.3.4 Hadronic Jets

Hadronic jets are reconstructed [70] using an anti-k_t algorithm [71] with a radius parameter of 0.4. Jets are corrected for detector and multiple-collision ('pile-up') effects [72, 73, 74]. Jets must have $p_{\mathrm{T}} > 20$ GeV and $|\eta| < 4.5$. Additionally, for jets with $p_{\mathrm{T}} > 50$ GeV and $|\eta| < 2.4$, the scalar sum of p_{T} of tracks matched to the jet and originating from the primary vertex must be at least 50 % of the scalar sum of p_{T} of all tracks matched to the jet.

4.3.5 *b*-Tagged Jets

For each hadronic jet with $|\eta| < 2.5$ in an event, the likelihood of that jet having originated from a b-quark is estimated. This is referred to as b-jet tagging, or b-tagging. An ATLAS-specific algorithm, MV1c, is used in this analysis for b-tagging. It is an improved version of the MV1 algorithm [75, 76, 77] with better c-jet (jets originating from charm-quarks) rejection. The MV1c algorithm has been chosen as it allows for improved suppression of the $t\bar{t}$ background. At low p_{T}^{V} the $t\bar{t}$ background predominantly contains bb events (events containing two b-

jets), but at high p_{T}^{V} the $t\bar{t}$ background predominantly contains bc events (events containing one b-jet and one c-jet). The analysis is most sensitive at higher p_{T}^{V}, so the MV1c algorithm allows for better suppression of the $t\bar{t}$ background in this high-sensitivity analysis region. The MV1c algorithm uses a neural network with inputs from various algorithms based on track impact parameters or the reconstruction of b-hadron or c-hadron decay vertices. It then outputs a weight, w, that can have a value between 0 and 1, related to the probability that the jet in question originated from a b-quark. Three 'operating points' for the output weight of the MV1c algorithm have been calibrated, corresponding to average b-jet identification efficiencies of 50 %, 70 %, and 80 %. These operating points are, respectively, referred to as 'loose', 'medium', and 'tight'. Table 4.2 details the w values corresponding to these operating points. For the MV1c algorithm, the rejection factors for c-jets and light jets at different operating points are shown in table 4.3, where a rejection factor is the inverse of an efficiency, as shown in equation 4.1. For details on how these operating points are used to define signal and control regions in the analysis, see section 4.4.

Operating point	b-tagging efficiency [%]	MV1c w value
Loose	80	0.4050
Medium	70	0.7028
	60	0.8353
Tight	50	0.9237

Table 4.2: Operating points of the MV1c b-jet tagging algorithm, with corresponding b-jet tagging efficiencies, and w values, where w is the output of the MV1c algorithm.

$$\text{rejection factor} = \frac{\text{total number of jets}}{\text{number of jets tagged as } b\text{-jets}} \tag{4.1}$$

Monte Carlo samples are corrected for differences between b-tagging efficiencies in data and in Monte Carlo samples, and also for differences in b-tagging efficiencies between different Monte Carlo samples. For this, MV1c w distributions are calibrated separately for b-jets (using $t\bar{t}$ events [78],[76]), c-jets (using D^* events [79]), and for light jets (using dijet events [80]). These calibrations are used to determine scale factors by which Monte Carlo events

Operating point	b-tagging efficiency [%]	c-jet rejection factor	Light jet rejection factor
Loose	80	3	29
Medium	70	5	136
	60	10	454
Tight	50	26	1388

Table 4.3: Rejection factors of the MV1c b-jet tagging algorithm, for c-jets and light jets, at different operating points. 'Rejection factor' is defined in equation 4.1, and is the inverse of an efficiency.

are reweighted to match the b-tagging efficiencies found in data. Scale factors are binned in jet MC-truth-flavour, p_{T}, η, and w. For Monte-Carlo-to-data corrections, the PYTHIA6 events generator is used. Separate scale factors are determined for other event generators, to correct their MV1c w distributions, and thus their b-tagging efficiencies, to match the PYTHIA6 distributions. Monte-Carlo-to-data scale factors, before global fits to data (see section 4.7 for details of the global fit), and unfolded from distributions after global fits to data, are shown in figure 4.1.

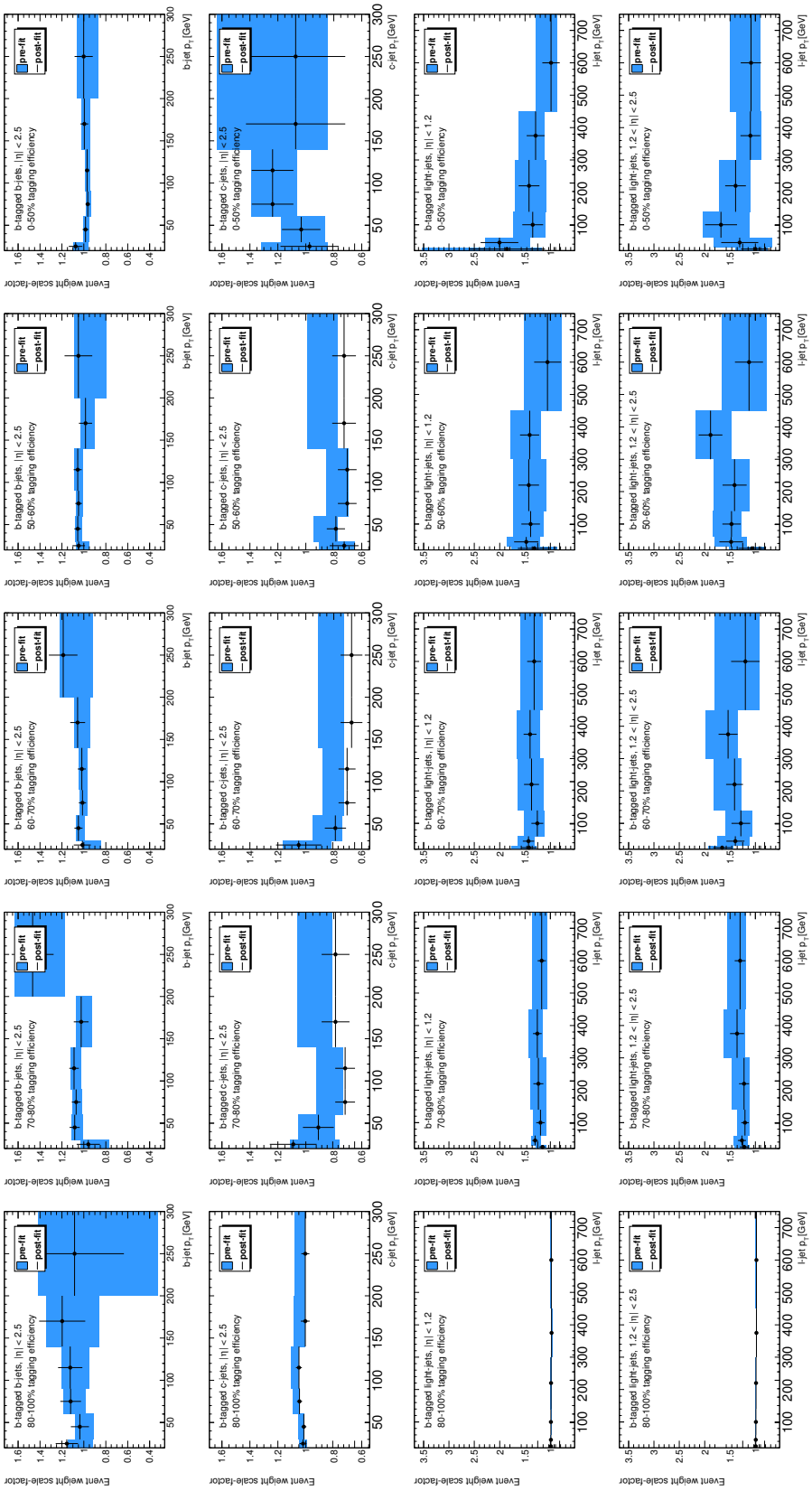

Figure 4.1: Monte-Carlo-to-data scale factors, before global fits to data (see section 4.7 for details of the global fit), and unfolded from distributions after global fits to data, for corrections to MV1c b-tagging efficiencies. Scale factors are binned in jet MC-truth-flavour, p_{T}, η, and w. Combined statistical and systematic uncertainties are shown.

4.3.6 Overlap Removal

To avoid double counting physics objects, identifying something as both a lepton and a jet for example, 'overlap removal' criteria are applied. Firstly all leptons and jets are identified independently. If a jet and an electron are separated by $\Delta R < 0.4$ then the jet is discarded. If a jet and a muon are separated by $\Delta R < 0.4$ then the jet is discarded if it has less than four particle tracks associated with it, otherwise the muon is discarded. If a muon and an electron are separated by $\Delta R < 0.2$ then the electron is discarded, unless the muon has only been identified in the ATLAS calorimeters in which case the muon is discarded instead.

4.3.7 Missing Transverse Energy

To account for energy from collisions that is not detected by the ATLAS detector, such as energy from neutrinos, the vector sum of transverse momenta associated with energy clusters in the calorimeters, with $|\eta| < 4.9$, is calculated, and the negative of this vector is taken to be the non-detected 'missing' transverse momentum vector sum, $\boldsymbol{E}_{\mathbf{T}}^{\mathbf{Miss}}$ [81]. This $\boldsymbol{E}_{\mathbf{T}}^{\mathbf{Miss}}$ is additionally corrected for calibrations of reconstructed physics objects in the event. A track-based missing transverse momentum vector is also calculated, $\boldsymbol{p}_{\mathbf{T}}^{\mathbf{Miss}}$. It is the negative of the vector sum of the transverse momenta of tracks associated with the primary vertex with $|\eta| < 2.4$.

4.3.8 Physics Object Corrections

Monte Carlo samples are also corrected in the analysis for differences between those samples and data in trigger efficiencies, lepton reconstruction and identification efficiencies, and lepton energy and momentum resolutions.

4.4 Event Selection

The choice of event selection criteria used in this analysis is optimised for the search of a Higgs boson with $m_H = 125$ GeV. Events in the 0-lepton channel must pass $E_{\mathrm{T}}^{\mathrm{Miss}}$ triggers. For the 1-lepton channel, single-lepton triggers are used. For the 2-lepton channel, either single lepton, di-electron, or di-muon triggers are used. Triggers used are listed in table 4.4. Requirements on different variables in these different channels and p_{T}^{V} bins are shown in table 4.5. Items in bold refer to the four-vector of the item. Items not in bold refer to scalar quantities: $E_{\mathrm{T}}^{\mathrm{Miss}} = |\boldsymbol{E}_{\mathbf{T}}^{\mathbf{Miss}}|$.

Trigger	Data period	Trigger selection requirements	ATLAS trigger name	Integrated luminosity collected [fb^{-1}]
$E_{\mathrm{T}}^{\mathrm{Miss}} < 160$ GeV	A-B5	$E_{\mathrm{T}}^{\mathrm{Miss}} > 80$ GeV	EF_xe80T_tclew_loose	1.9
$E_{\mathrm{T}}^{\mathrm{Miss}} > 160$ GeV	A-B5	$E_{\mathrm{T}}^{\mathrm{Miss}} > 80$ GeV	EF_xe80T_tclew	2.1
$E_{\mathrm{T}}^{\mathrm{Miss}}$	B6-L	$E_{\mathrm{T}}^{\mathrm{Miss}} > 80$ GeV	EF_xe80_tclew_loose	18.1
Single electron	A-L	$p_{\mathrm{T}}^{e} > 24$ GeV	EF_e24vhi_medium1	20.3
		$p_{\mathrm{T}}^{e} > 60$ GeV	EF_e60_medium1	
Single muon		$p_{\mathrm{T}}^{\mu} > 24$ GeV	EF_mu24i_tight	
		$p_{\mathrm{T}}^{\mu} > 60$ GeV	EF_mu60_tight	
Di-electron	A-L	$p_{\mathrm{T}}^{e_1} > 12$ GeV, $p_{\mathrm{T}}^{e_2} > 12$ GeV	EF_2e12Tvh_loose1	20.3
Di-muon		$p_{\mathrm{T}}^{\mu_1} > 13$ GeV, $p_{\mathrm{T}}^{\mu_2} > 13$ GeV	EF_2mu13	

Table 4.4: Triggers used for event selection in the $VH \to b\bar{b}$ analysis. The data period A started on the 4th of April 2012. The data period B5 ended on the 20th of May 2012. The data period B6 started on the 21st of May 2012. The data period L ended on the 6th of December 2012. Events in the 0-lepton channel must pass $E_{\mathrm{T}}^{\mathrm{Miss}}$ triggers. For the 1-lepton channel, single-lepton triggers are used. For the 2-lepton channel, either single lepton, di-electron, or di-muon triggers are used.

Variable	Analysis cuts				
Common selection					
p_{T}^{V} [GeV]	$0-90^{(*)}$	$90^{(*)}-120$	$120-160$	$160-200$	>200
$\Delta R(\boldsymbol{p}_{\mathrm{jet}_1}, \boldsymbol{p}_{\mathrm{jet}_2})$	$0.7-3.4$	$0.7-3.0$	$0.7-2.3$	$0.7-1.8$	<1.4
0-lepton channel selection					
$p_{\mathrm{T}}^{\mathrm{Miss}}$ [GeV]	NU	>30			
$\Delta\phi(\boldsymbol{E}_{\mathbf{T}}^{\mathbf{Miss}}, \boldsymbol{p}_{\mathbf{T}}^{\mathbf{Miss}})$		$<\pi/2$			
$\min[\Delta\phi(\boldsymbol{E}_{\mathbf{T}}^{\mathbf{Miss}}, \boldsymbol{p}_{\mathrm{jet}})]$		$-$	>1.5		
$\Delta\phi(\boldsymbol{E}_{\mathbf{T}}^{\mathbf{Miss}}, \boldsymbol{p}_{\mathrm{dijet}})$		>2.2	>2.8		
$\sum_{i=1}^{N_{\mathrm{jets}}=2(3)} p_{\mathrm{T}}^{\mathrm{jet}_i}$ [GeV]		>120 (NU)	>120 (150)		
1-lepton channel selection					
m_{T}^{W} [GeV]	<120				
ℓ accepted	μ only		μ or e		
H_{T} [GeV]	>180		$-$		
$E_{\mathrm{T}}^{\mathrm{Miss}}$ [GeV]	$-$		>20		>50
2-lepton channel selection					
$m_{\ell\ell}$ [GeV]	$83-99$				
$E_{\mathrm{T}}^{\mathrm{Miss}}$ [GeV]	<60				

Table 4.5: Event selection criteria of the $VH \to b\bar{b}$ analysis. Sections marked 'NU' are **N**ot **U**sed in the analysis. (*) For the 0-lepton channel, the bin edge separating the first and second p_{T}^{V} bins is set to 100 GeV rather than 90 GeV. In all channels, the highest-p_{T} b-tagged jet must also have a $p_{\mathrm{T}} > 45$ GeV.

The variables in table 4.5 not defined elsewhere in this chapter are as follows:

- $\Delta R(\boldsymbol{p}_{\mathrm{jet}_1}, \boldsymbol{p}_{\mathrm{jet}_2})$ is the separation ΔR between the two highest-p_{T} jets in the event.
- $\Delta\phi(\boldsymbol{E}_{\mathbf{T}}^{\mathbf{Miss}}, \boldsymbol{p}_{\mathbf{T}}^{\mathbf{Miss}})$ is the separation in ϕ between the $\boldsymbol{E}_{\mathrm{T}}^{\mathrm{Miss}}$ vector and the $\boldsymbol{p}_{\mathbf{T}}^{\mathrm{Miss}}$ vector.
- $\min[\Delta\phi(\boldsymbol{E}_{\mathbf{T}}^{\mathbf{Miss}}, \boldsymbol{p}_{\mathrm{jet}})]$ is the separation in ϕ between the $\boldsymbol{E}_{\mathrm{T}}^{\mathrm{Miss}}$ vector and the closest jet.
- $\Delta\phi(\boldsymbol{E}_{\mathbf{T}}^{\mathbf{Miss}}, \boldsymbol{p}_{\mathrm{dijet}})$ is the separation in ϕ between the $\boldsymbol{E}_{\mathrm{T}}^{\mathrm{Miss}}$ vector and the dijet system.
- $\sum_{i=1}^{N_{\mathrm{jets}}=2(3)} p_{\mathrm{T}}^{\mathrm{jet}_i}$ is the scalar sum of the transverse momenta of the jets in the event.

- m_{T}^{W} is the transverse mass of the W boson candidate, defined to be $m_{\mathrm{T}}^{W} = \sqrt{2p_{\mathrm{T}}^{\ell} \times E_{\mathrm{T}}^{\mathrm{Miss}} \times \left(1 - \cos\left(\phi_{\ell} - \phi_{E_{\mathrm{T}}^{\mathrm{Miss}}}\right)\right)}$.

- H_{T} is the scalar sum of $E_{\mathrm{T}}^{\mathrm{Miss}}$, the transverse momenta of the two highest-p_{T} jets in the event, and the transverse momentum of the charged lepton in the 1-lepton event.

- $m_{\ell\ell}$ is the invariant mass of the lepton pair in the 2-lepton channel. If these two leptons have come from the decay of a Z boson, then $m_{\ell\ell}$ should be close to the Z mass.

Each selected event must have either two or three jets. These jets must have $|\eta| < 2.5$ since this is the range in which b-jet tagging can be performed. Exactly two of these jets must be tagged as having come from b-quarks for the event to be considered as a potential signal event. The 'leading' b-tagged jet (the b-tagged jet with the highest p_{T}) must have $p_{\mathrm{T}} > 45$ GeV. Plots of $\Delta R(\boldsymbol{p}_{b\text{-jet}_1}, \boldsymbol{p}_{b\text{-jet}_2})$, the separation ΔR between the two b-tagged jets in an event, against the dijet mass $m_{b\bar{b}}$ are shown in figure 4.2. Events where only one, or none of the three jets are tagged as having come from b-quarks are also retained, but are used as 'control regions' to help constrain backgrounds. These b-tagging regions are shown in table 4.6.

<table>
<tr><td></td><td></td><td colspan="4">1st jet</td></tr>
<tr><td></td><td></td><td>Not b-tagged</td><td>Loose</td><td>Medium</td><td>Tight</td></tr>
<tr><td rowspan="4">2nd jet</td><td>Not b-tagged</td><td>0-tag</td><td colspan="3">1-tag</td></tr>
<tr><td>Loose</td><td rowspan="3">1-tag</td><td colspan="3">LL</td></tr>
<tr><td>Medium</td><td colspan="2">MM</td></tr>
<tr><td>Tight</td><td>TT</td></tr>
</table>

Table 4.6: b-jet tagging regions used in the $VH \to b\bar{b}$ analysis. The 'Loose', 'Medium', and 'Tight' terms refer to the b-tagging operating points discussed in section 4.3.5, corresponding to b-tagging efficiencies of 50%, 70%, and 80%, respectively.

In the signal regions in table 4.6, TT, MM, and LL, also known as the '2-tag' regions, the 4-vectors of the two b-tagged jets are summed to calculate the dijet mass. This is the mass of a Higgs boson candidate. The '1-tag' and '0-tag' regions are used as control regions. In the '1-tag' regions a dijet mass is formed from

the b-tagged jet and the highest p_{T} non-b-tagged jet. In the '0-tag' region a dijet mass is formed from the two highest p_{T} jets. By splitting the 2-tag region into TT, MM, and LL, the overall sensitivity of the analysis is improved.

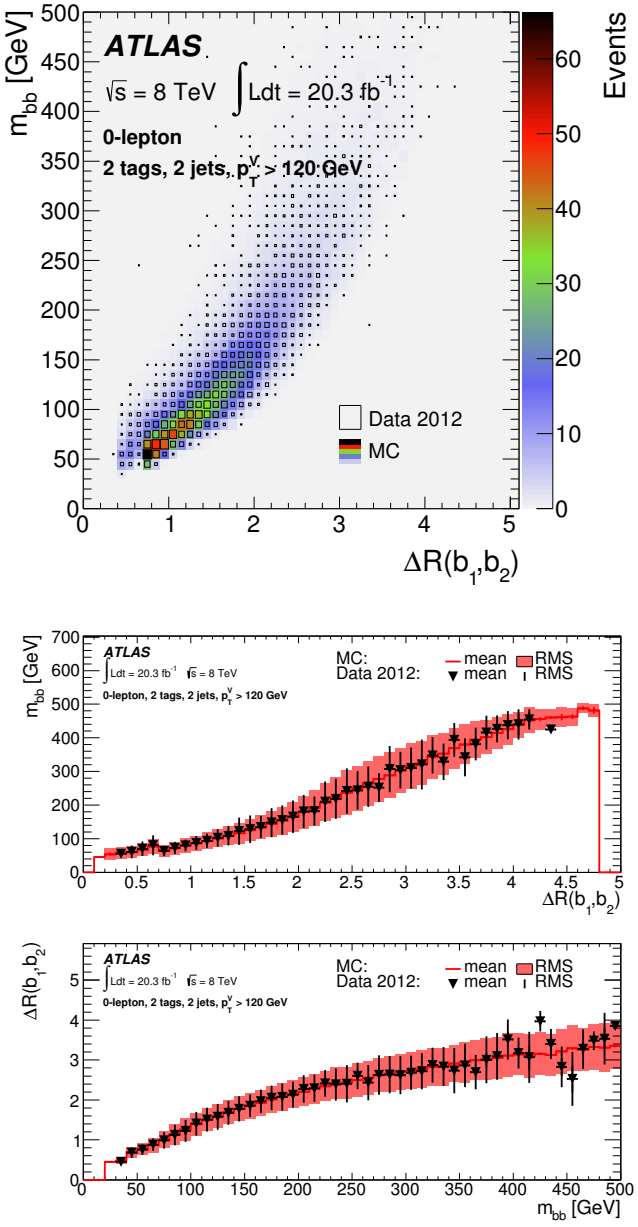

Figure 4.2: Plots showing the correlation between the dijet mass $m_{b\bar{b}}$ and $\Delta R(b_1, b_2) = \Delta R(\boldsymbol{p}_{b\text{-jet}_1}, \boldsymbol{p}_{b\text{-jet}_2})$, the separation ΔR between the two b-tagged jets in an event. The middle and lower plots show the mean values and variances of the total expected background (in red) and data (in black) when projected onto the $\Delta R(b_1, b_2)$ and $m_{b\bar{b}}$ axes, respectively, showing good agreement between simulated samples and data.

Events that pass all selection criteria have additional corrections applied to the energies of b-jets: Firstly, a p_{T}-dependent resolution correction. Secondly, if there is a muon (that has been rejected by overlap removal) within $\Delta R = 0.4$ of a jet, the four-momentum of that rejected muon (minus energy in the calorimeters associated with that muon) is added to the four-momentum of the b-jet. These corrections lead to a 14% improvement in dijet mass resolution [65], as shown in the upper plot of figure 4.3. In the 2-lepton channel a kinematic likelihood fit to the transverse momenta of the $\ell\ell b\bar{b}$ system and the dilepton mass $m_{\ell\ell}$ is performed. This provides corrections to the b-jet transverse momenta, leading to an overall improvement in the dijet mass resolution of 30% in this channel [65], as shown in the lower plot of figure 4.3.

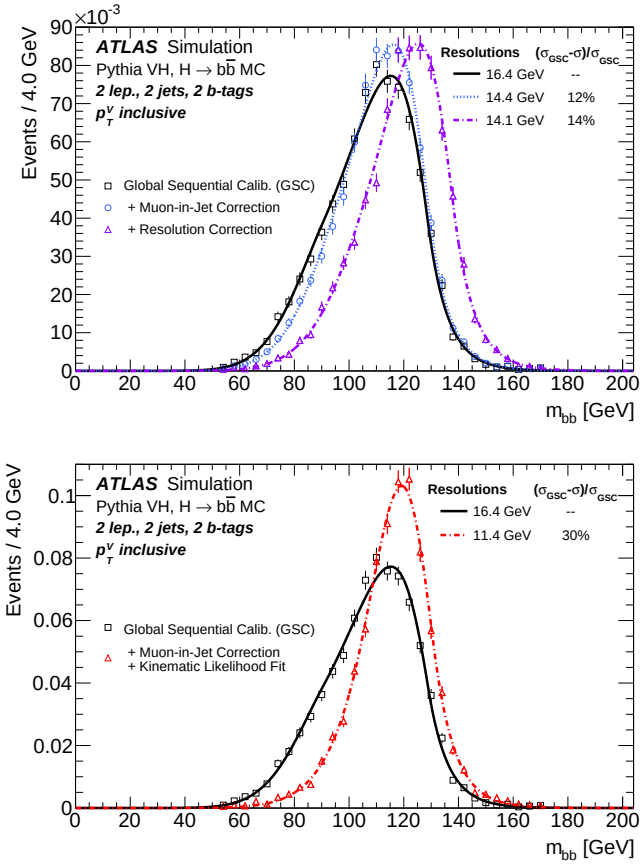

Figure 4.3: Improvement in dijet mass resolution for simulated $m_H = 125$ GeV $VH \to b\bar{b}$ signal, before and after muon-in-jet and p_{T}-dependent resolution corrections are applied (top), and before and after muon-in-jet and p_{T}-dependent resolution corrections and the kinematic likelihood fit are applied (bottom), in the 2-lepton channel of the $VH \to b\bar{b}$ analysis. From [65].

4.5 Background Modelling

Background and signal processes are modelled by Monte Carlo simulations, apart from the multijet QCD background which is determined from data, as described below. Corrections are applied, as also described below, to the vector-boson-plus-jets (V+jets) backgrounds, and to the $t\bar{t}$ background. Backgrounds and signal are then simultaneously fitted to data, allowing for the determination of signal yield. In this fit the normalisations of the corrected V+jets and $t\bar{t}$ backgrounds are allowed to float.

QCD multijet backgrounds can come from hadronic jets or photons that have converted into e^+e^- pairs being misidentified as electrons originating from the primary vertex. QCD multijet backgrounds can also come from semileptonic heavy-flavour decays. Additionally, QCD multijet backgrounds can come from hadronic jet energy mismeasurements that result in 'fake' $E_{\mathrm{T}}^{\mathrm{Miss}}$. These sources of background can not be easily modelled by Monte Carlo event generators, and are therefore estimated from data. This is done separately in different analysis channels and regions. In the 0-lepton channel, the QCD multijet background is estimated using an 'ABCD' method, using the variables $\Delta\phi(\boldsymbol{E}_{\mathbf{T}}^{\mathbf{Miss}}, \boldsymbol{p}_{\mathbf{T}}^{\mathbf{Miss}})$ and $\Delta\phi(\boldsymbol{E}_{\mathbf{T}}^{\mathbf{Miss}}, \boldsymbol{p}_{\mathrm{jet}})$ as shown in figure 4.4. Region A is signal-dominated, whereas regions B, C, and D are background dominated. In each of the regions B, C, and D the QCD multijet background is determined by subtracting other backgrounds (estimated using Monte Carlo samples) from data. b-tagging is not applied in regions B, C, and D in order to decrease statistical errors. However, the fraction of events in region D tagged as having originated from a b-quark, $\frac{N_{\mathrm{D}}(b\text{-tagged})}{N_{\mathrm{D}}}$, is determined. The shape of the QCD multijet background in region A is taken to be the same as the shape of the QCD multijet background in region C. The normalisation of the QCD multijet background in region A, N_{A}, is given by $N_{\mathrm{A}} = N_{\mathrm{C}} \times \frac{N_{\mathrm{B}}}{N_{\mathrm{D}}}$, where N_{B}, N_{C}, and N_{D} are the (background-subtracted) normalisations in the regions B, C, and D, respectively. The normalisation of the QCD multijet background in region A after b-tagging, $N_{\mathrm{A}}(b\text{-tagged})$, is given by $N_{\mathrm{A}}(b\text{-tagged}) = N_{\mathrm{A}} \times \frac{N_{\mathrm{D}}(b\text{-tagged})}{N_{\mathrm{D}}}$.

In the 1-lepton and 2-lepton channels, QCD multijet backgrounds are determined from background-dominated control regions, with other backgrounds (estimated using Monte Carlo samples) subtracted from data. The normalisations of these QCD multijet backgrounds are then allowed to float in the fit of

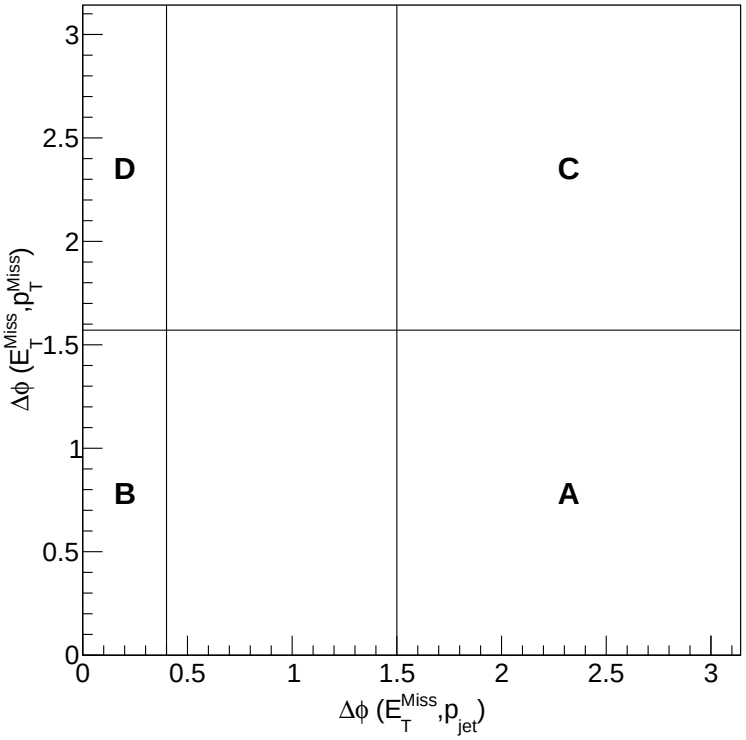

Figure 4.4: The 'ABCD' method regions used in the estimation of QCD multijet background in the 0-lepton channel of the $VH \to b\bar{b}$ search.

all backgrounds and signal to data. In the 1-lepton channel, QCD multijet backgrounds are determined separately for the electron and muon channels. It is found that the QCD multijet background in the electron channel is very large for $p_{\mathrm{T}}^{V} < 120$ GeV. The electron channel is therefore not used in the 1-lepton channel for $p_{\mathrm{T}}^{V} < 120$ GeV, as shown in table 4.5.

The V+jets background Monte Carlo samples are found to mismodel the p_{T}^{V} spectrum, with the samples being harder in p_{T}^{V} than data. This mismodelling is found to be highly correlated with $\Delta\phi(\boldsymbol{p}_{\mathrm{jet}_1}, \boldsymbol{p}_{\mathrm{jet}_2})$, the separation in ϕ between the two highest-p_{T} jets in the event. The V+jets Monte Carlo samples are therefore reweighted by the ratio of data to Monte Carlo samples in either $\Delta\phi(\boldsymbol{p}_{\mathrm{jet}_1}, \boldsymbol{p}_{\mathrm{jet}_2})$ or p_{T}^{V}, depending on which variable is found to be the most appropriate in each analysis category. Distributions of p_{T}^{V} and $\Delta\phi(\boldsymbol{p}_{\mathrm{jet}_1}, \boldsymbol{p}_{\mathrm{jet}_2})$, before and after reweighting, are shown in figures 4.5 and 4.6, respectively. A generator-level correction is applied to top-quarks in the $t\bar{t}$ background Monte Carlo sample.

This is due to Monte Carlo samples generated with Powheg_Box+PYTHIA6 being found to be too hard in the p_{T} spectrum of top quarks from pair production [82]. Plots of p_{T}^{V} distributions after fits to data (see section 4.7) are shown in figure 4.7, demonstrating good agreement between expected distributions and data.

Plots showing comparisons of expected distributions to data after fits to data (see section 4.7), for variables relevant to this analysis, are shown in figure 4.8, demonstrating good agreement between expected distributions and data.

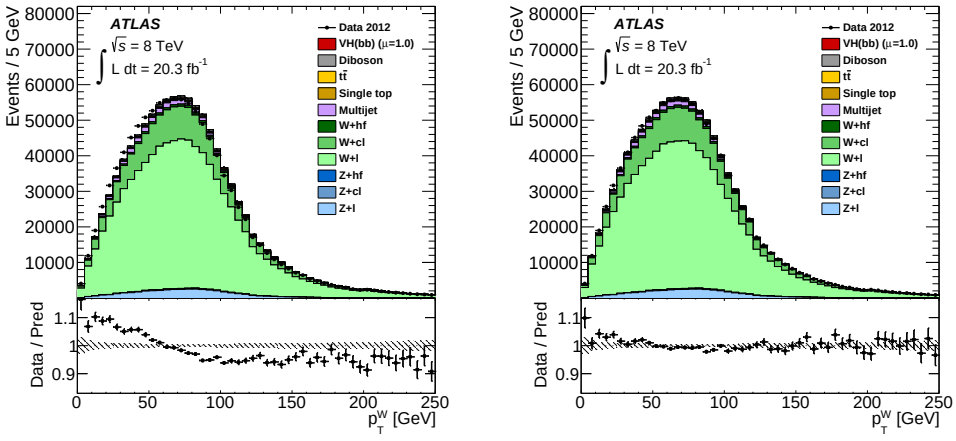

Figure 4.5: Plots showing p_{T}^{V}, before (left) and after (right) reweighting to correct the mismodelled p_{T}^{V} spectrum in V+jets background Monte Carlo samples, in the $VH \to b\bar{b}$ analysis. From [65].

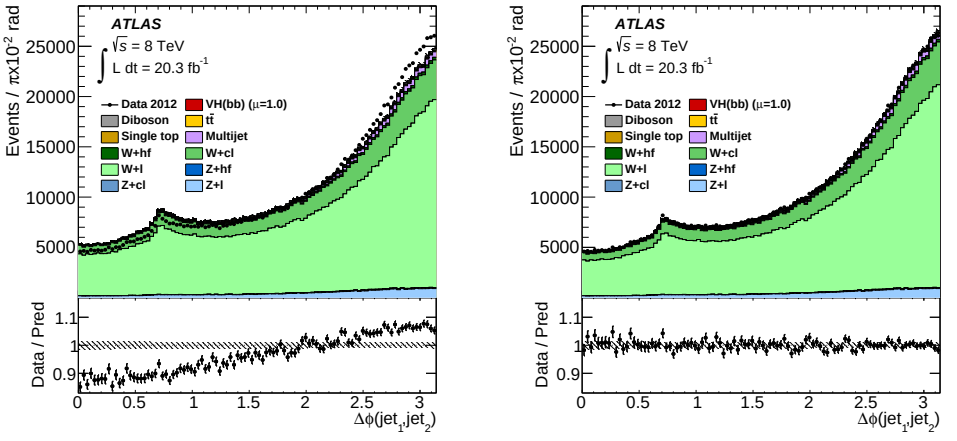

Figure 4.6: Plots showing $\Delta\phi(\boldsymbol{p}_{\mathrm{jet}_1}, \boldsymbol{p}_{\mathrm{jet}_2})$, before (left) and after (right) reweighting to correct the mismodelled p_{T}^{V} spectrum in V+jets background Monte Carlo samples, in the $VH \to b\bar{b}$ analysis. From [65].

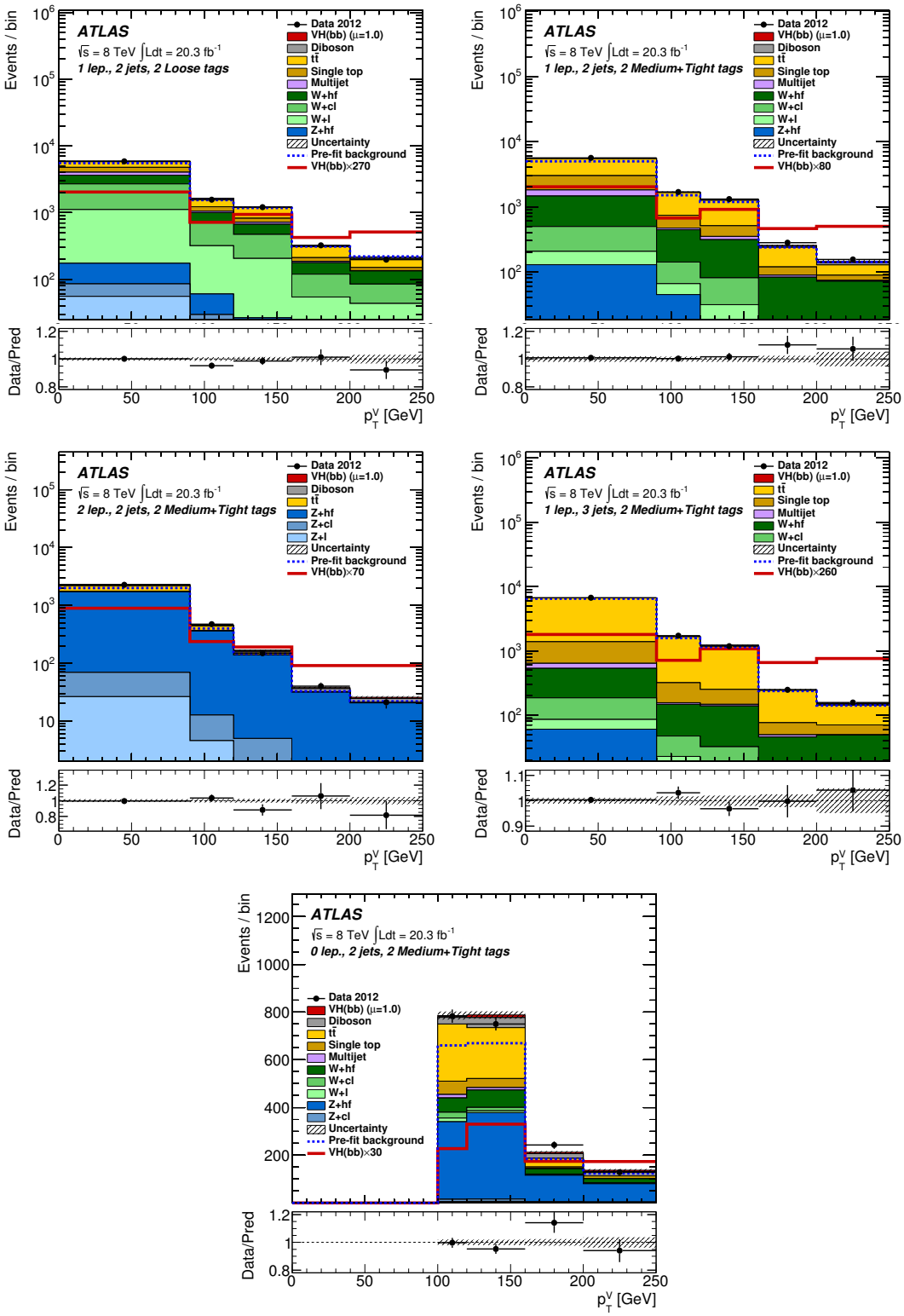

Figure 4.7: Plots of p_{T}^{V} distributions after fits to data (see section 4.7) for different number of leptons and jets in the final state, and different b-jet tagging regions, in the $VH \rightarrow b\bar{b}$ analysis, demonstrating good agreement between expected distributions and data. From [65].

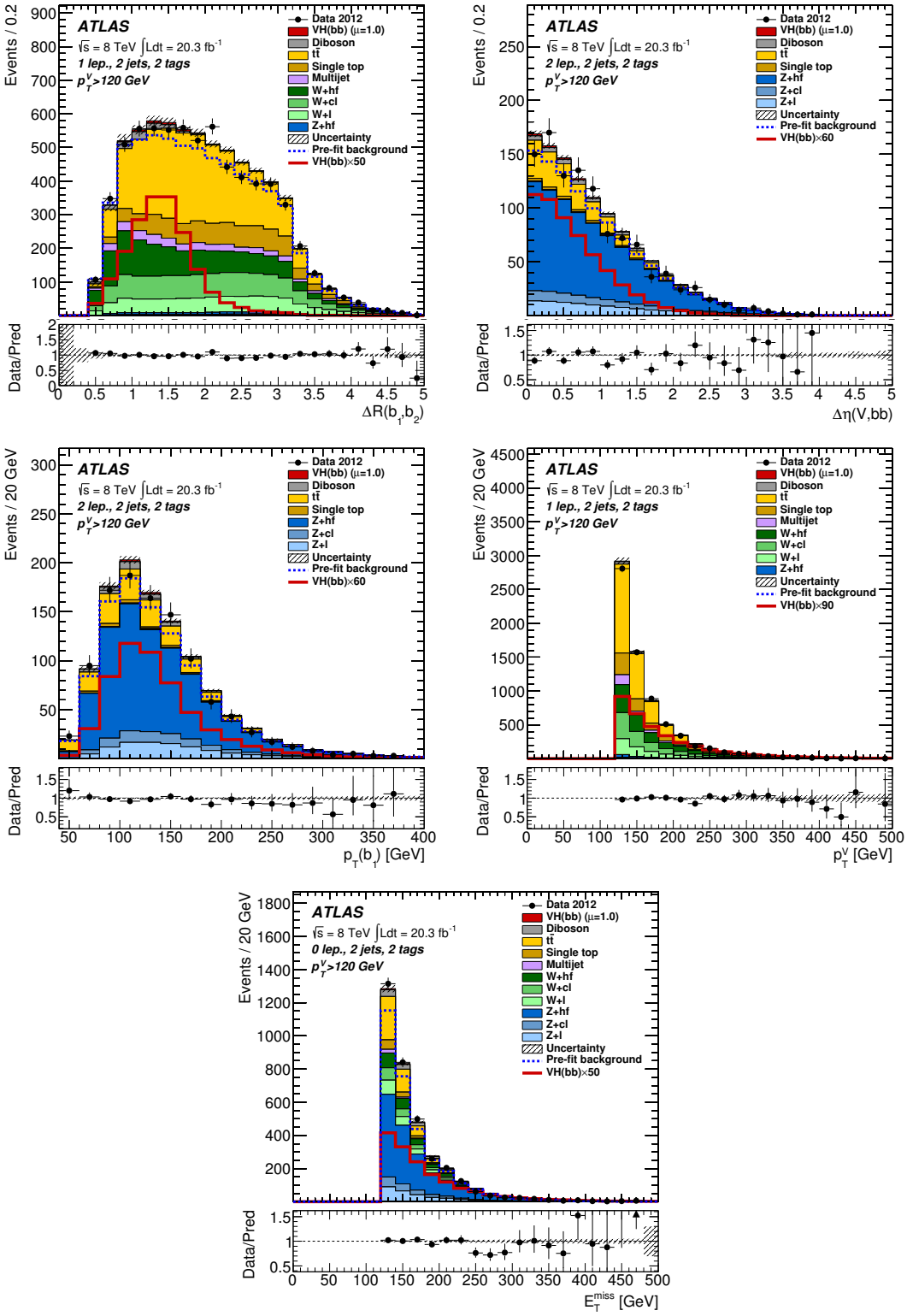

Figure 4.8: Plots showing comparisons of expected distributions to data, after fits to data (see section 4.7), for variables relevant to the $VH \to b\bar{b}$ analysis. From [65].

4.6 Systematic Uncertainties

Systematic uncertainties arise from a number of sources, but can be categorised as those coming from experimental sources, those coming from background modelling, and those coming from the modelling of signal processes. Sources of uncertainty coming from background modelling can further be split into those arising from QCD multijet background modelling from data, and those arising from backgrounds modelled using Monte Carlo simulations.

Experimental sources of systematic uncertainty considered include triggering, physics object reconstruction and identification, and physics object energy and momentum calibration and resolution.

For $E_{\mathrm{T}}^{\mathrm{Miss}}$ triggers, efficiency correction factors are computed from $W \to \mu\nu +$ jets and $Z \to \mu^{+}\mu^{-} +$ jets events. Uncertainties associated with these triggers are estimated from the statistical uncertainties associated with the calculation of the correction factors, and the differences in correction factors computed using the two different processes, $W \to \mu\nu +$ jets and $Z \to \mu^{+}\mu^{-} +$ jets.

Uncertainties associated with electrons and muons are found to be very small. Combining uncertainties from electron and muon triggering, identification, isolation, reconstruction, as well as from electron and muon energy and resolution correction factors, is found to give a total systematic uncertainty due to these sources of less than 1 %.

Uncertainties related to hadronic jets arise from uncertainties on the jet energy scale [74], the jet energy resolution [83], and also from the corrections applied to improve the dijet mass resolution. An eigenvector decomposition is performed on uncertainties arising from the jet energy scale, resulting in 56 orthogonal components, or nuisance parameters, associated with uncertainties arising from the jet energy scale. Two systematic uncertainties are associated with the jet energy resolution: one applied to all jets, and one additionally applied to only b-tagged jets.

Monte Carlo samples are corrected for differences between b-tagging efficiencies in data and in the Monte Carlo samples, and also for differences in b-tagging efficiencies between different Monte Carlo samples. This has been detailed in section 4.3.5, with plots of the scale factors used for the Monte-Carlo-to-date corrections shown in figure 4.1. For each scale factor, a value of half of the scale factor is taken as the systematic uncertainty associated with that scale

factor. An eigenvector decomposition is performed on uncertainties arising from b-tagging, resulting in 88 orthogonal components, or nuisance parameters. To make these uncertainties more manageable, these components are ranked in order of uncertainty size. The 10 largest b-jet related components are kept, as are the 15 largest c-jet related components, and the 10 largest light-jet related components. All other components are found to collectively contribute no more than a 1% uncertainty on final analysis results, and are discarded.

The uncertainty on the integrated luminosity is calculated, as described in [66], from luminosity scale calibrations derived from beam-separation scans performed in November 2012.

For the QCD multijet background in the 0-lepton channel, uncertainties on the predicted background are determined by varying the ratio $\frac{N_{\mathrm{B}}}{N_{\mathrm{D}}}$ in the ABCD method, and also by replacing the ratio $\frac{N_{\mathrm{D}}(b\text{-tagged})}{N_{\mathrm{D}}}$ with the ratio $\frac{N_{\mathrm{B}}(b\text{-tagged})}{N_{\mathrm{B}}}$. For the 1-lepton channel, uncertainties associated with the QCD multijet background are estimated by varying the control regions used to determine the QCD multijet background. In the 2-lepton channel, the QCD multijet background is small ($\sim 1\%$) and a 100% uncertainty on this is assigned.

Uncertainties on backgrounds modelled with Monte Carlo simulations are assessed separately for each background. Where possible, background-dominated control regions are used to constrain backgrounds as well as their associated uncertainties. The full details of all variations and comparisons used in the estimation of uncertainties on backgrounds modelled with Monte Carlo simulations will not be discussed here, but are documented in [65].

A summary of systematic uncertainties on background modelling is shown in table 4.7.

Uncertainties on $H \to b\bar{b}$ signal samples are treated in a similar manner to uncertainties on backgrounds modelled with Monte Carlo simulations, except that control regions can not be used to constrain signal models or the associated uncertainties. Uncertainties on $H \to b\bar{b}$ signal are calculated for $m_H = 125$ GeV. These uncertainties are used for all Higgs boson mass points in the fit (section 4.7). For the estimation of systematic uncertainties on $WH \to \ell\nu b\bar{b}$ Monte Carlo signal samples see chapter 5.

Systematic uncertainties are included as 'nuisance parameters' in a 'global fit' of all background and signal distributions to data, in order to extract final analysis

Z+jets	
Zl normalisation, 3/2-jet ratio	5%
Zcl 3/2-jet ratio	26%
Z+hf 3/2-jet ratio	20%
Z+hf/$Zb\bar{b}$ ratio	12%
$\Delta\phi(\boldsymbol{p}_{\text{jet}_1}, \boldsymbol{p}_{\text{jet}_2})$, p_{T}^{V} , $m_{b\bar{b}}$	S
W+jets	
Wl normalisation, 3/2-jet ratio	10%
Wcl, W+hf 3/2-jet ratio	10%
$Wbl/Wb\bar{b}$ ratio	35%
$Wbc/Wb\bar{b}$, $Wc\bar{c}/Wb\bar{b}$ ratio	12%
$\Delta\phi(\boldsymbol{p}_{\text{jet}_1}, \boldsymbol{p}_{\text{jet}_2})$, p_{T}^{V} , $m_{b\bar{b}}$	S
$t\bar{t}$	
3/2-jet ratio	20%
High/low-p_{T}^{V} ratio	7.5%
Top-quark p_{T} , $m_{b\bar{b}}$, $E_{\text{T}}^{\text{Miss}}$	S
Single top	
Cross section	4% (s and t-channels), 7% (Wt)
Acceptance (generator)	3%–52%
$m_{b\bar{b}}$, $p_{\text{T}}^{b_2}$	S
Diboson	
Cross section and acceptance (scale)	3%–29%
Cross section and acceptance (PDF)	2%–4%
$m_{b\bar{b}}$	S
Multijet	
0 and 2-lepton channels normalisation	100%
1-lepton channel normalisation	2%–60%
Template variations, reweighting	S

Table 4.7: A summary of systematic uncertainties on background modelling in the $VH \to b\bar{b}$ analysis. 'S' means shape-dependent uncertainties were applied. l, b, and c refer to light (u, d, or s-quark, or gluon), b-quark, and c-quark jets. hf refers to heavy flavour (c, b, or t-quark) jets.

results such as signal strength and limits on cross-sections. This is detailed in section 4.7. Final analysis results are given in chapter 6.

4.7 Fitting Procedure

Backgrounds and signal distributions are simultaneously fitted to those distributions in data, allowing for the determination of signal yield. This fit, referred to as the 'global' fit, is performed simultaneously for all three lepton channels, 0-lepton, 1-lepton, and 2-lepton. The distributions used as inputs to the fit are the $m_{b\bar{b}}$ distributions in the 2-tag regions, LL, MM, and TT, and also the MV1c b-tagging distributions in the 1-tag regions (section 4.4 and table 4.6). These input distributions are further split into bins of p_{T}^{V} and number of jets in the final state (section 4.4 and table 4.5). Figures 4.9, 4.10, and 4.11 show $m_{b\bar{b}}$ distributions, before and after the global fit has been performed, respectively for the 0, 1, and 2-lepton channels. They show the TT b-tagging regions with two jets in the final state and 200 GeV $< p_{\mathrm{T}}^{V}$. Figures 4.12, 4.13, and 4.14 show MV1c distributions, before and after the global fit has been performed, respectively for the 0, 1, and 2-lepton channels. Additional $m_{b\bar{b}}$ and MV1c distributions are shown in Appendix H.1.

A Roostats [84, 85] framework is used to perform the fit, using a binned likelihood function based on the input distributions, and taking into account both normalisations allowed to float in the fit and systematic uncertainties. For each normalisation allowed to float in the fit and each systematic uncertainty, a 'nuisance parameter' variable is used in the likelihood function. The nuisance parameters, $\boldsymbol{\theta}$, have Gaussian (for uncertainties) or log-normal (for normalisations, to prevent them becoming negative) probability density functions. The signal yield extracted by the fit is the parameter μ, the multiple found in data of the Standard Model Higgs boson cross-section.

Systematic uncertainties discussed in section 4.6, as well as final uncertainties on $H \to b\bar{b}$ signal given in chapter 5, are included as nuisance parameters in the global fit.

Once a fit has been performed, the fit returns an error on the given result which is a combination of all errors inputted into and adjusted by the fit. The fitting framework additionally then decomposes this total error into systematic and statistical components.

Dominant post-fit systematic uncertainties for $m_H = 125$ GeV are given in appendix J.

The likelihood function for a given μ and set of nuisance parameters $\boldsymbol{\theta}$ is $\mathcal{L}(\mu, \boldsymbol{\theta})$:

$$\mathcal{L}(\mu, \boldsymbol{\theta}) = \mathrm{P}(n|\mu S(\boldsymbol{\theta}) + B(\boldsymbol{\theta})) \left[\prod_{b \in \mathrm{bins}}^{N} \frac{\mu v(\boldsymbol{\theta})_b^{\mathrm{sig}} + v(\boldsymbol{\theta})_b^{\mathrm{bkg}}}{\mu S(\boldsymbol{\theta}) + B(\boldsymbol{\theta})} \right] \mathrm{P}(m|B_{CR}) \qquad (4.2)$$

where,

- N is the total number of bins from all regions.
- $v(\boldsymbol{\theta})_b^{\mathrm{sig}}$ is the expected number of signal events (signal yield) in bin b, given the prescribed nuisance parameters $\boldsymbol{\theta}$.
- $v(\boldsymbol{\theta})_b^{\mathrm{bkg}}$ is the expected number of background events in bin b, given the nuisance parameters $\boldsymbol{\theta}$.
- $S(\boldsymbol{\theta})$ is the expected total number of signal events in all bins, given the nuisance parameters $\boldsymbol{\theta}$. $S(\boldsymbol{\theta}) = \sum_{b \in \mathrm{bins}}^{N} v(\boldsymbol{\theta})_b^{\mathrm{sig}}$
- $B(\boldsymbol{\theta})$ is the expected total number of background events in all bins, given the nuisance parameters $\boldsymbol{\theta}$. $B(\boldsymbol{\theta}) = \sum_{b \in \mathrm{bins}}^{N} v(\boldsymbol{\theta})_b^{\mathrm{bkg}}$
- n is the number of events observed in the signal regions.
- m is the number of events observed in the control regions.
- B_{CR} is the expected total number of events in the control regions.
- $\mathrm{P}(x|y)$ is a Poisson probability term: The Poissonian probability of y given x: $\mathrm{P}(x|y) = \prod_{b \in \mathrm{bins}}^{N} \frac{y_b}{x_b!} e^{-y_b}$

The maximum value of $\mathcal{L}(\mu, \boldsymbol{\theta})$ is found: $\mathcal{L}(\hat{\mu}, \hat{\boldsymbol{\theta}}_{\hat{\mu}})$. $\hat{\mu}$ and $\hat{\boldsymbol{\theta}}_{\hat{\mu}}$ are the values of μ and $\boldsymbol{\theta}$ that maximise the likelihood. $\hat{\boldsymbol{\theta}}_{\mu}$ are the nuisance parameters that maximise the likelihood for a given μ. Practically, this is done by constructing a test statistic $p_\mu = -2 \ln \mathcal{L}(\mu, \boldsymbol{\theta})$, which is then minimised using minimisation tools by varying μ and $\boldsymbol{\theta}$, thus maximising $\mathcal{L}(\mu, \boldsymbol{\theta})$.

To find the standard deviation on the most likely value of μ, $\hat{\mu}$, the profile likelihood ratio $\Lambda_\mu = \mathcal{L}(\mu, \hat{\boldsymbol{\theta}}_{\mu}) / \mathcal{L}(\hat{\mu}, \hat{\boldsymbol{\theta}}_{\hat{\mu}})$ is constructed, as well as the test statistic $q_\mu = -2 \ln \Lambda_\mu$. The test statistic q_μ, in the limit of infinite data, is $-\chi^2$-distributed

[86, 87]. A range of μ are then tested. For each value of μ, q_μ is minimised by varying $\boldsymbol{\theta}$, thus maximising Λ_μ. The value of μ that results in $q_\mu = 1$ corresponds to one standard deviation on $\hat{\mu}$, the value of μ that results in $q_\mu = 4$ corresponds to two standard deviations on $\hat{\mu}$, and so on. Similarly, The value of μ corresponding to a 95% confidence interval ($q_\mu = 3.84$) can be found.

To set limits on the cross section of a process, the largest value of μ is found (so $\hat{\mu} \leq \mu$) that corresponds to $q_\mu = 3.84$ (for a 95% confidence interval limit). Let this μ be defined as $\mu_{95\%}$. Then it can be said, with 95% confidence, that the cross-section for this channel is no more than $\mu_{95\%}$ times the Standard Model prediction.

Values of μ such that $\hat{\mu} \geq \mu$ are not considered in the search for $\mu_{95\%}$, as although there will be a value of μ such that $\hat{\mu} \geq \mu$ and $q_\mu = 3.84$, since this value of μ is less than $\hat{\mu}$ it can not be considered an upper limit on the signal strength.

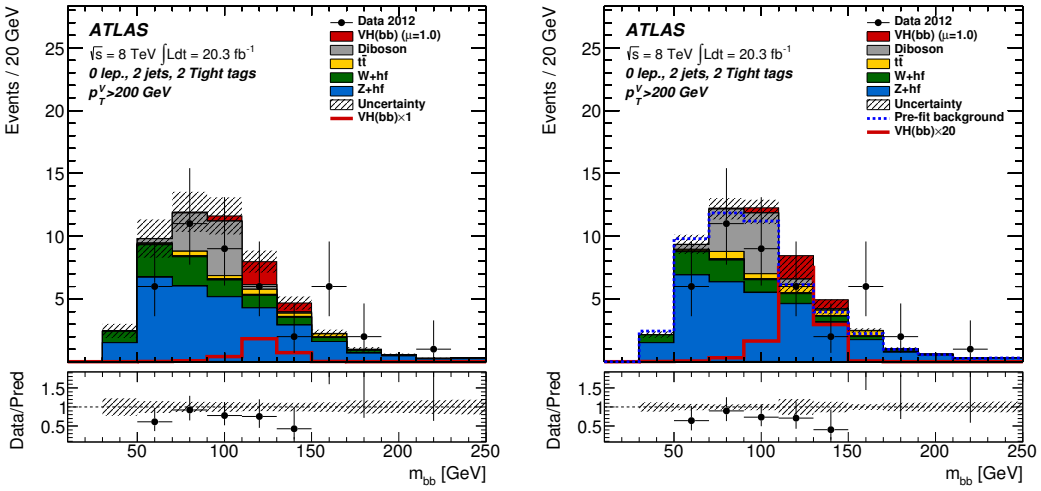

Figure 4.9: $m_{b\bar{b}}$ distributions in the 0-lepton channel, 200 GeV $< p_{\mathrm{T}}^V$ bin, before (left) and after (right) the global fit. The two-jet, TT b-tagging region is shown.

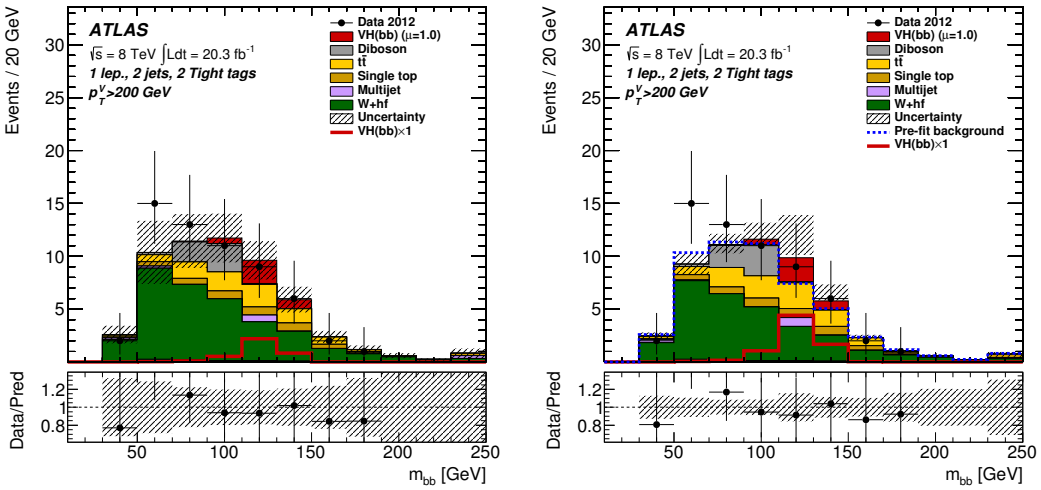

Figure 4.10: $m_{b\bar{b}}$ distributions in the 1-lepton channel, 200 GeV $< p_{\mathrm{T}}^{V}$ bin, before (left) and after (right) the global fit. The two-jet, TT b-tagging region is shown.

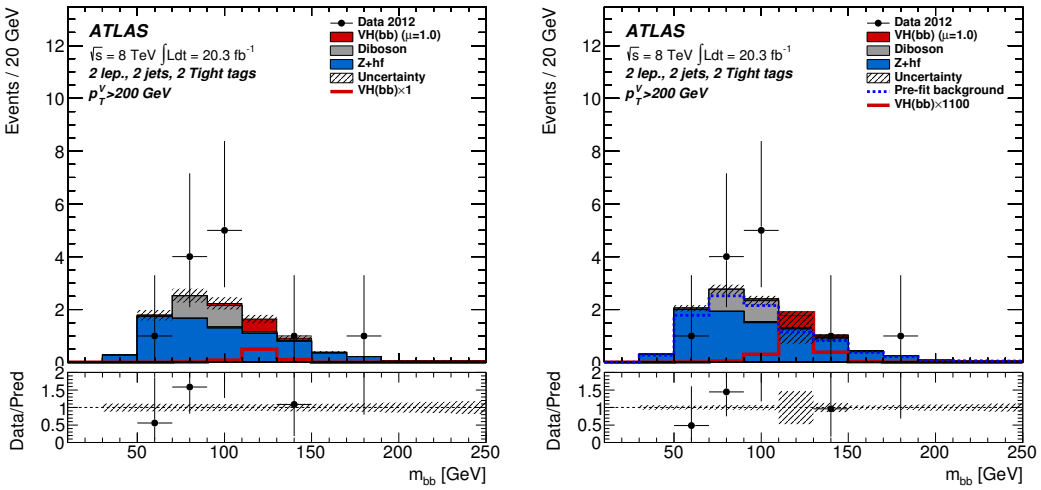

Figure 4.11: $m_{b\bar{b}}$ distributions in the 2-lepton channel, 200 GeV $< p_{\mathrm{T}}^{V}$ bin, before (left) and after (right) the global fit. The two-jet, TT b-tagging region is shown.

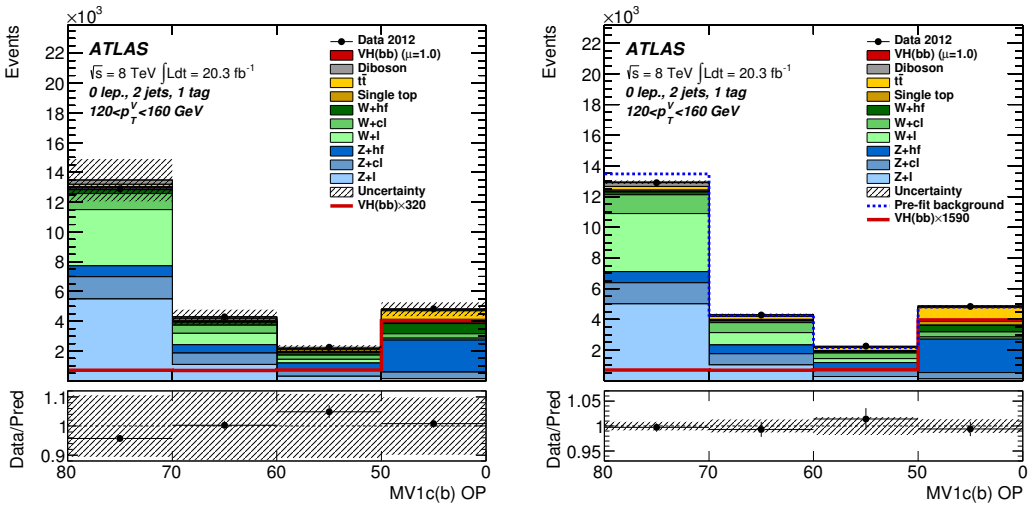

Figure 4.12: MV1c distributions in the 0-lepton channel, 120 GeV $< p_{\mathrm{T}}^{V} <$ 160 GeV bin, before (left) and after (right) the global fit. The two-jet, one-tag b-tagging region is shown.

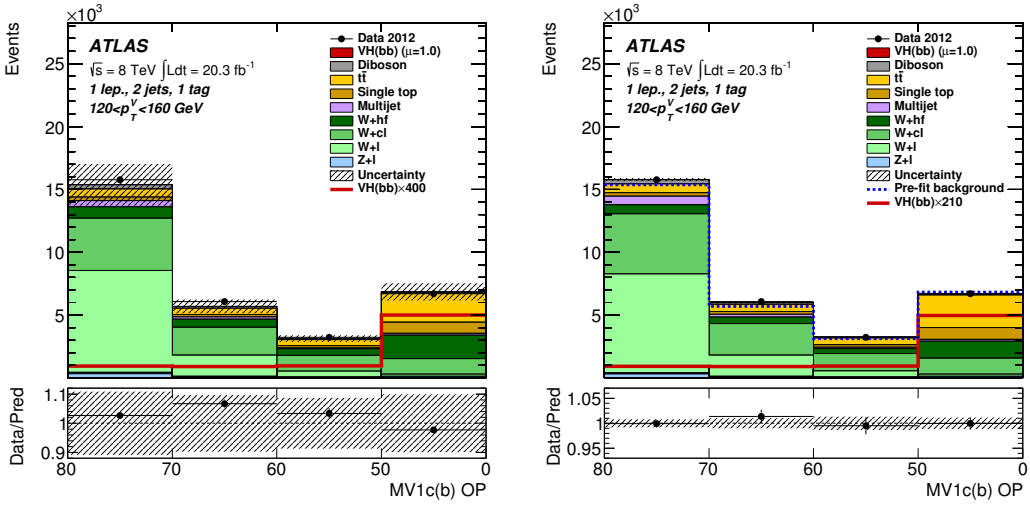

Figure 4.13: MV1c distributions in the 1-lepton channel, 120 GeV $< p_{\mathrm{T}}^{V} <$ 160 GeV bin, before (left) and after (right) the global fit. The two-jet, one-tag b-tagging region is shown.

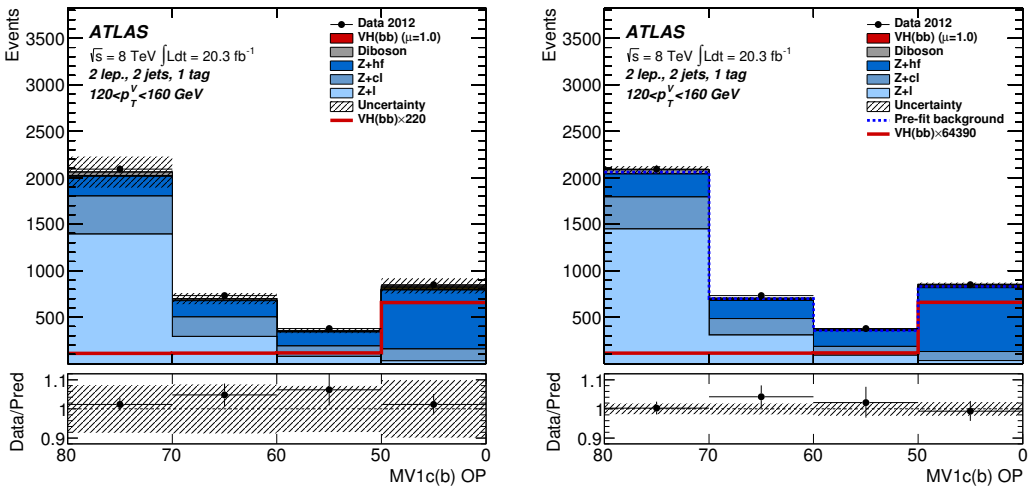

Figure 4.14: MV1c distributions in the 2-lepton channel, 120 GeV $< p_{\mathrm{T}}^{V} <$ 160 GeV bin, before (left) and after (right) the global fit. The two-jet, one-tag b-tagging region is shown.

4.8 Results

Results of the search for the Higgs boson in the $WH \to \ell\nu b\bar{b}$ channel, using the theoretical systematic uncertainties calculated in chapter 5, are presented in chapter 6. The combination of these results with the results of the searches in the $ZH \to \nu\bar{\nu}b\bar{b}$ and $ZH \to \ell\bar{\ell}b\bar{b}$ channels is also presented in chapter 6.

Chapter 5

Theoretical Uncertainties Of $WH \to \ell\nu b\bar{b}$ Production

5.1 Introduction

To search for a physics process in high energy particle collisions, it is necessary to know what the process will look like in those collisions, in order to know what to look for. Monte Carlo simulation can be used to model processes for this purpose, but the resulting simulations will have systematic uncertainties associated with them. In order to search for a process and understand the results, the systematic uncertainties associated with the Monte Carlo simulations used must be understood and accounted for.

Monte Carlo simulations of high energy particle collisions are performed by computer programs called 'event generators'. These simulations are factorised into different stages depending on the physics and energy-scales involved. Ideally all stages of these simulations would be calculated analytically, however at present humanity does not have sufficient knowledge and computational power to perform such calculations. Only part of a high energy particle collision simulation can be performed analytically, hence the factorisation of the simulation into stages, with the remaining non-analytical stages being modelled synthetically. A schematic diagram of a proton-proton collision showing the different stages of a Monte Carlo generated event is shown in figure 5.1.

In proton-proton collisions such as those at the LHC one parton from each proton will contribute to the high-energy particle-particle interaction of interest

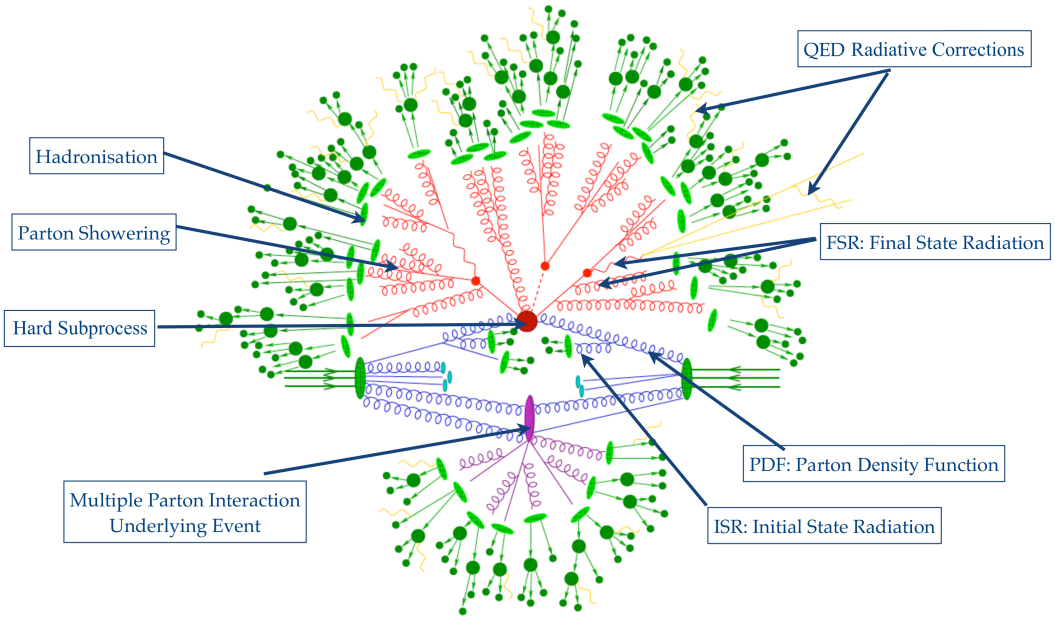

Figure 5.1: A proton-proton collision showing the different stages of Monte Carlo event generation. From [88].

(the 'hard subprocess'). How likely any given parton in each proton is to take part in this hard subprocess is required for Monte Carlo event generation. This information is contained within 'Parton Density Functions' (PDFs) (section 2.3.4).

The hard subprocess of interest can be calculated analytically and is often referred to as the 'matrix element' calculation, as it involves the calculation of Feynman diagram matrix elements. Current theoretical knowledge and computational ability limits this calculation to typically only two interacting partons going to N outgoing partons, where N is typically a single digit number. The further simulation of these N outgoing partons is performed by modelling known as 'parton showering', or simply 'showering'.

Initial-state radiation (ISR) and final-state radiation (FSR) are both processes modelled with parton showering.

The energy scale at which the analytical calculation of the hard subprocess stops and the parton showering modelling takes over is the 'factorisation scale' μ_F.

In the analytical calculation of the hard subprocess, corrections due to the appearance of loops in the associated Feynman diagrams will typically be

included. In order for these corrections to be finite the calculations must be renormalised. This renormalisation requires the definition of a 'renormalisation scale' μ_R.

Electromagnetic showers are modelled using parton showering. QED radiative corrections in particle decays can also be modelled separately, typically using 'bolt-on' software such as Photos [89] incorporated into event generators.

Once partons reach energies of about 1 GeV, colour confinement processes become dominant and the partons will become confined together to form hadrons. This process is known as 'hadronisation'. Currently hadronisation can not be described from first principles, and must be modelled.

Finally, from each of the protons, partons not involved in the hard subprocess can interact with each other. This will contribute lower-energy activity to an event, collectively known as 'the underlying event' (UE) or 'multi-parton interactions' (MPI).

This chapter deals with the systematic uncertainties arising from the theoretical predictions of Monte Carlo event generation for the $WH \to \ell\nu b\bar{b}$ process.

Event generators used in this chapter include Pythia6 [90], Pythia8 [91], and Herwig++ [92]. They are capable of performing all stages of Monte Carlo event generation. They can calculate hard subprocesses to leading order (LO) in the perturbative expansion of QCD. The programs Powheg_Box [93, 94, 95] and aMC@NLO [96] calculate hard subprocesses to next to leading order (NLO) in the perturbative expansion of QCD. However these NLO hard subprocesses, once generated, must be passed in an LHE file [97] to other event generators such as Pythia6, Pythia8 or Herwig++ to perform the remaining stages of Monte Carlo event generation. Herwig++ is also capable of calculating hard subprocesses to NLO in QCD using its own internal implementation of the Powheg method [94].

Event generators have adjustable parameters that control the output of their Monte Carlo simulations. These parameters are adjusted so that the resulting Monte Carlo simulations match data as closely as possible for certain variables. This process of adjusting these variables is known as 'tuning'. Typically, underlying event sensitive-variables are used for this tuning process.

5.1.1 A Note On Notation

In this text, unless otherwise noted, absolute uncertainties will be noted by Δ_X and fractional uncertainties will be noted by δ_X, where $\delta_X = \frac{\Delta_X}{X}$.

5.1.2 Systematic Uncertainty Estimation - General Method

For a given source of systematic uncertainty, parameters in event generators related to this source are varied. Through this, different Monte Carlo simulation samples are produced. These samples are then compared in order to determine the variation on a variable of interest, X. This variation is used to estimate the systematic uncertainty on X due to the given source.

In order to analyse Monte Carlo samples, a custom-written program has been created by the author of this thesis. It reads in Monte Carlo simulation samples, identifies and constructs analysis objects, optionally applies analysis selection criteria, and produces resulting distributions of interest. The selection criteria it applies are consistent with those described in chapter 4. It uses truth-level hadron matching for b-tagging of jets. All Monte Carlo samples generated as part of the studies presented in this chapter use $m_H = 125$ GeV.

X is either chosen to be the cross-section σ, either with or without analysis selection criteria applied (σ_{asc} and $\sigma_{\text{inclusive}}$, respectively), or X is chosen to be the signal acceptance, $A = \frac{\sigma_{\text{asc}}}{\sigma_{\text{inclusive}}}$.

In this chapter, where inclusive cross-sections are given, they are the cross-sections as reported by the relevant event generators used.

X is considered separately in each bin of the $m_{b\bar{b}}$ distribution. To calculate the overall uncertainty on X, if no dependence on the $m_{b\bar{b}}$ mass is found, the uncertainty is averaged over bins of the $m_{b\bar{b}}$ distribution. However, since the $m_{b\bar{b}}$ distribution is peaked around the simulated Higgs mass $m_H = 125$ GeV, bins of the $m_{b\bar{b}}$ distribution further from $m_H = 125$ GeV will have fewer events. Uncertainties calculated in these bins may have large statistical fluctuations. Careful choice of which bins to include in the calculation of an average uncertainty value is therefore made.

Additionally, the analysis is binned in number of hadronic jets in the final state. Distributions and uncertainties are calculated either in the two-jet bin, the three-jet bin, or the inclusive two-and-three-jet bin. If an uncertainty is found to

be independent of number of jets, then the uncertainty taken from the inclusive bin is used, otherwise separate uncertainties are used for the two and three jet bins.

σ_{asc}, $\sigma_{\text{inclusive}}$, and the acceptance A are related by:

$$\sigma_{\text{asc}} = \sigma_{\text{inclusive}} \times A \tag{5.1}$$

The uncertainty on σ_{asc}, $\sigma_{\text{inclusive}}$, and A, $\Delta_{\sigma_{\text{asc}}}$, $\Delta_{\sigma_{\text{inclusive}}}$, and Δ_A respectively, are therefore related by:

$$\left(\frac{\Delta_{\sigma_{\text{asc}}}}{\sigma_{\text{asc}}}\right)^2 = \left(\frac{\Delta_{\sigma_{\text{inclusive}}}}{\sigma_{\text{inclusive}}}\right)^2 + \left(\frac{\Delta_A}{A}\right)^2 + \frac{2\Delta_{\sigma_{\text{inclusive}}}\Delta_A \ \rho_{(\sigma_{\text{inclusive}} \ A)}}{\sigma_{\text{inclusive}} \ A} \tag{5.2}$$

where $\rho_{(\sigma_{\text{inclusive}} \ A)}$ is the correlation between $\sigma_{\text{inclusive}}$ and A. $\sigma_{\text{inclusive}}$ and A are expected to be largely uncorrelated. As a result of this, the correlation term in equation 5.2 is ignored. Additionally, where possible and appropriate, more accurately calculated values of $\Delta_{\sigma_{\text{inclusive}}}$ are used, for example from [98], as $\sigma_{\text{inclusive}}$ and $\Delta_{\sigma_{\text{inclusive}}}$ are analysis-independent.

5.2 Uncertainties Arising From Scale Factors

5.2.1 Introduction

The factorisation scale μ_F can be adjusted within an event generator. However, as it is an artefact of Monte Carlo simulation methods and does not have a physical parallel in nature, simulations should ideally not depend on the value chosen for it. In reality there is some dependence, and as such there is a systematic uncertainty associated with the factorisation scale.

In the analytical calculation of the hard subprocess, the renormalisation scale μ_R effectively defines the theory at that energy scale. For any momentum transfer q in the calculations, if $\frac{q^2}{\mu_R^2}$ is very small or very large then the perturbative theory and calculations may become unstable. While μ_R is chosen such that the analytical calculations will remain stable, there is still a dependence of the results on μ_R. There is therefore a systematic uncertainty associated with the renormalisation scale μ_R.

To estimate the systematic uncertainties associated with these scales, these scales are varied by factors of $\frac{1}{2}$ and 2. The resulting overall change in a variable of interest X is taken as twice the uncertainty on X due to these scale factors:

$$X^+ = \max\left[\ X(\mu_F,\mu_R)\ ,\ X(2\times\mu_F,2\times\mu_R)\ ,\ X(\frac{1}{2}\times\mu_F,\frac{1}{2}\times\mu_R)\ \right] \tag{5.3}$$

$$X^- = \min\left[\ X(\mu_F,\mu_R)\ ,\ X(2\times\mu_F,2\times\mu_R)\ ,\ X(\frac{1}{2}\times\mu_F,\frac{1}{2}\times\mu_R)\ \right] \tag{5.4}$$

$$\Delta_X = \frac{X^+ - X^-}{2} \tag{5.5}$$

To calculate scale uncertainties for final states containing specific numbers of jets, the effects of jet binning are considered. The inclusive cross-section can be written as an expansion in α_s neglecting PDF effects and other effects not relevant to this discussion:

$$\sigma_{\text{inclusive}} \simeq \sigma_{\text{B}}\left(1+\alpha_s+\alpha_s^2+\mathcal{O}\left(\alpha_s^3\right)\right) \tag{5.6}$$

where σ_{B} is the Born-level cross-section.

Introducing a lower bound on the number of jets in the final state is the same as requiring all jets in the final state to be above a certain p_{T} threshold. This p_{T} threshold brings in Sudakov logarithms of the form $L = ln(p_{\mathrm{T}}/\mu_F)$ [99]. The cross-section of events with one or more jets in the final state is then:

$$\sigma_{\geq 1} \simeq \sigma_{\mathrm{B}} \left(\alpha_s \left(L^2 + L + 1\right) + \alpha_s^2 \left(L^4 + L^3 + L^2 + L + 1\right) + \mathcal{O}\left(\alpha_s^3 L^6\right)\right) \tag{5.7}$$

The zero-jet cross-section σ_0 can be written as $\sigma_0 = \sigma_{\mathrm{inclusive}} - \sigma_{\geq 1}$, therefore,

$$\begin{aligned}\sigma_0 \simeq \sigma_{\mathrm{B}} \big(1 + \alpha_s + \alpha_s^2 + \mathcal{O}\left(\alpha_s^3\right) \\ - \alpha_s \left(L^2 + L + 1\right) - \alpha_s^2 \left(L^4 + L^3 + L^2 + L + 1\right) - \mathcal{O}\left(\alpha_s^3 L^6\right)\big)\end{aligned} \tag{5.8}$$

This can, depending on the value of p_{T} used, lead to large cancellations between the positive α_s terms and the negative logarithmic terms [99]. If the scale μ_F is varied, then these cancellations will result in a reduction in the variation of a variable X. If the scale μ_F is varied, and the variation in a variable X is used to estimate the systematic uncertainty on that variable due to μ_F scale variations, then that calculated uncertainty will underestimate the true uncertainty due to μ_F scale variations.

More generally, for N or more jets, where $N > 0$,

$$\sigma_{\geq N} \simeq \sigma_{\mathrm{B}} \left(\alpha_s^N \left(\sum_{i=0}^{2N} L^i\right) + \alpha_s^{N+1} \left(\sum_{i=0}^{2(N+1)} L^i\right) + \mathcal{O}\left(\alpha_s^{N+2} L^{2(N+2)}\right)\right) \tag{5.9}$$

and $\sigma_N = \sigma_{\geq N} - \sigma_{\geq N+1}$. Since the leading term for $\sigma_{\geq N}$ is proportional to α_s^N, cross-sections with different N can be considered, to first order, to be uncorrelated. Using this, the uncertainty on σ_N, Δ_{σ_N}, is then given by:

$$\Delta_{\sigma_N}^2 = \Delta_{\sigma_{\geq N}}^2 + \Delta_{\sigma_{\geq N+1}}^2 \tag{5.10}$$

If $\Delta_{\sigma_{\geq N}}$ and $\Delta_{\sigma_{\geq N+1}}$ are calculated separately, and equation 5.10 used to calculate Δ_{σ_N}, then the logarithmic cancellations of the kind found in equation 5.8 are thus avoided.

Samples Generated And Tested

Three Monte Carlo simulation samples were generated of $pp \to WH \to \ell\nu b\bar{b}$, where $\ell = e$ or μ. Powheg_Box was used to generate hard subprocesses at next to leading order (NLO). These were then showered using Pythia8. 100000 events were generated for each sample. For each sample, the values of μ_F and μ_R used are given in table 5.1.

Sample	μ_F	μ_R
Powheg_Box+Pythia8 Scale Normal	$(\mu_F)_0$	$(\mu_R)_0$
Powheg_Box+Pythia8 Scale Up	$2 \times (\mu_F)_0$	$2 \times (\mu_R)_0$
Powheg_Box+Pythia8 Scale Down	$\frac{1}{2} \times (\mu_F)_0$	$\frac{1}{2} \times (\mu_R)_0$

Table 5.1: Scale factors used in each of the three samples generated for the estimation of systematic uncertainties arising from scale factors.

For the $pp \to WH \to \ell\nu$ process, generated with Powheg_Box to NLO, the normal values of μ_F and μ_R used, $(\mu_F)_0$ and $(\mu_R)_0$, are set equal to the p_{T} of the off-shell W^* boson [100].

5.2.2 Results

The $m_{b\bar{b}}$ distributions for the three samples listed in table 5.1 are shown without analysis selection criteria applied in figure 5.2.

For the inclusive jet bin, the $m_{b\bar{b}}$ distributions for these three samples are shown with analysis selection criteria applied in figure 5.3. The signal acceptance is shown in figure 5.4. The $m_{b\bar{b}}$ distributions for these samples with analysis selection criteria applied, and the signal acceptance, are shown separately for the two-jet and three-jet bins in appendix A.1.1.

For the $N_{\mathrm{jets}} \geq 2$ jet bin, the $m_{b\bar{b}}$ distributions with analysis selection criteria applied, and the signal acceptance, are shown in figures 5.5 and 5.6. For the $N_{\mathrm{jets}} \geq 3$ jet, and the $N_{\mathrm{jets}} \geq 4$ jet bins, the equivalent plots are shown in appendix A.1.1.

The uncertainties on the cross sections σ_{asc} and $\sigma_{\mathrm{inclusive}}$, and the acceptance A, not taking account of logarithmic cancellations, are shown in figure 5.7 for the inclusive jet bin. These uncertainties, taking account of logarithmic cancellations,

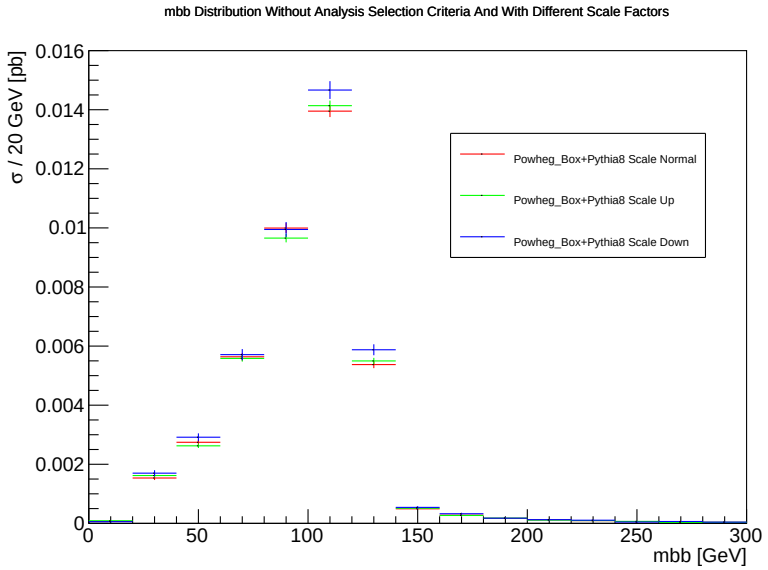

Figure 5.2: $m_{b\bar{b}}$ distributions, for the $WH \to \ell\nu b\bar{b}$ analysis, with $m_H = 125$ GeV, without analysis selection criteria applied and with different scale factors. Two and three-jet final states are included. Error bars show statistical uncertainty.

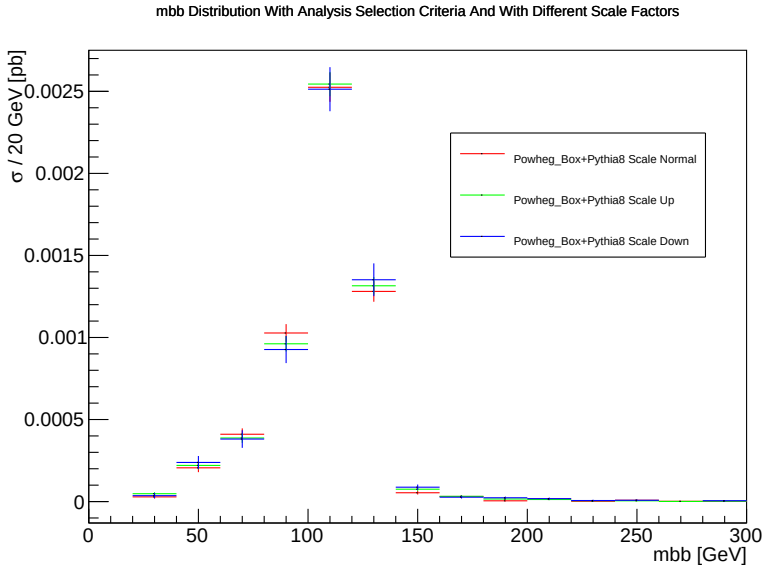

Figure 5.3: $m_{b\bar{b}}$ distributions, for the $WH \to \ell\nu b\bar{b}$ analysis, with $m_H = 125$ GeV, with analysis selection criteria applied and different scale factors. Two and three-jet final states are included. Error bars show statistical uncertainty.

are shown in figure 5.8 for the inclusive jet bin. Equivalent distributions for two-jet and three-jet final states are shown in appendix A.1.2.

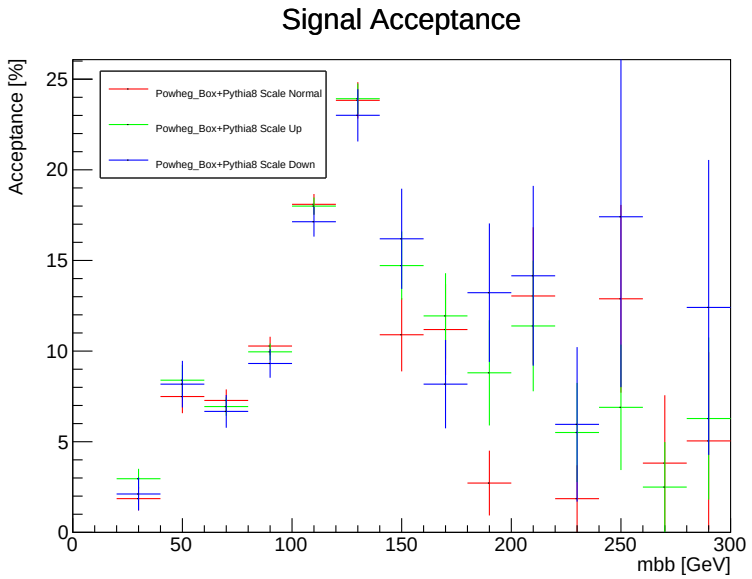

Figure 5.4: Signal acceptance, for the $WH \to \ell\nu b\bar{b}$ analysis, with $m_H = 125$ GeV, with different scale factors. Two and three-jet final states are included. Error bars show statistical uncertainty.

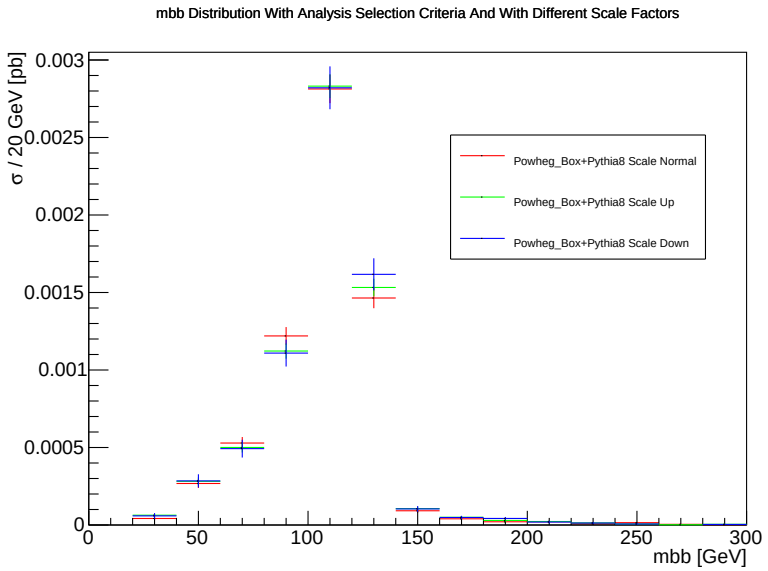

Figure 5.5: $m_{b\bar{b}}$ distributions, for the $WH \to \ell\nu b\bar{b}$ analysis, with $m_H = 125$ GeV, with analysis selection criteria applied and different scale factors. $N_{\text{jets}} \geq 2$ final states are included. Error bars show statistical uncertainty.

When considering uncertainties, only a region with a large number of events is chosen: the $m_{b\bar{b}}$ range of 60 GeV to 140 GeV around the Higgs mass peak.

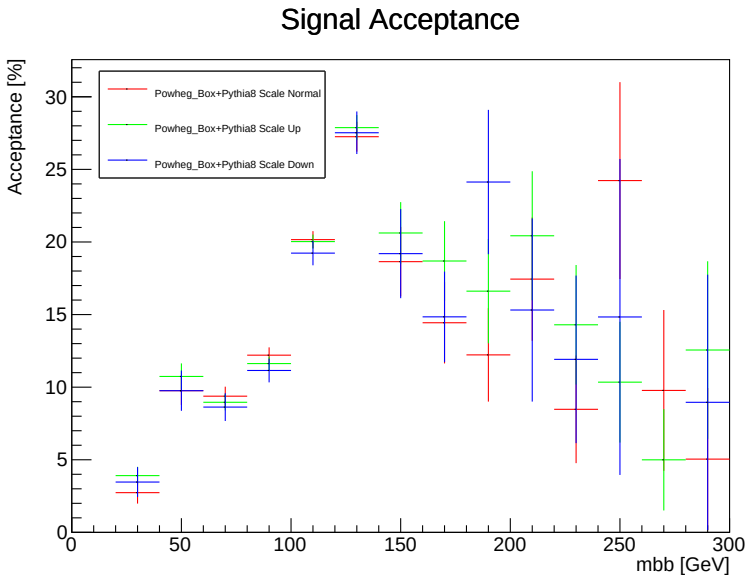

Figure 5.6: Signal acceptance, for the $WH \to \ell\nu b\bar{b}$ analysis, with $m_H = 125$ GeV, with different scale factors. $N_{\text{jets}} \geq 2$ final states are included. Error bars show statistical uncertainty.

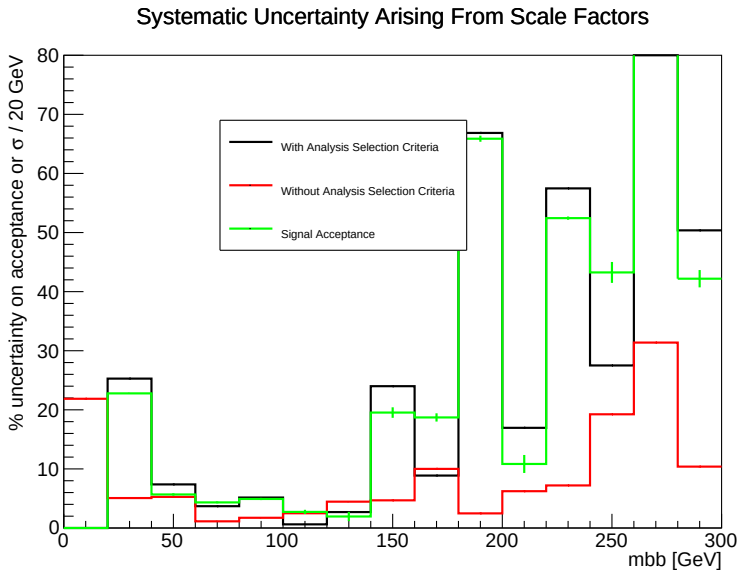

Figure 5.7: Systematic uncertainties arising from scale factors, for the $WH \to \ell\nu b\bar{b}$ analysis, with $m_H = 125$ GeV, not taking account of logarithmic cancellations, on the cross sections σ_{asc} and $\sigma_{\text{inclusive}}$, and the acceptance A. Two and three-jet final states are included. Error bars show statistical uncertainty.

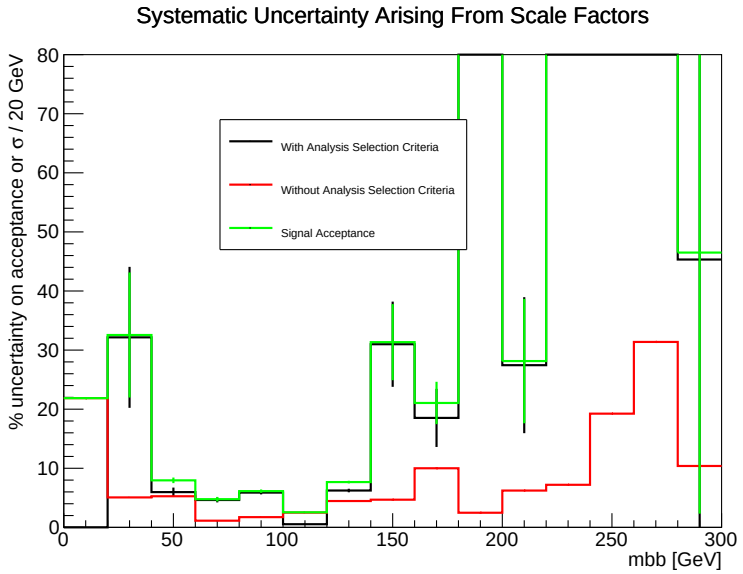

Figure 5.8: Systematic uncertainties arising from scale factors, for the $WH \to \ell\nu b\bar{b}$ analysis, with $m_H = 125$ GeV, taking account of logarithmic cancellations, on the cross sections σ_{asc} and $\sigma_{\text{inclusive}}$, and the acceptance A. Two and three-jet final states are included. Error bars show statistical uncertainty.

This can be seen to be the region with the largest number of events, for example, figure 5.2. It excludes regions with few events that result in, for example, the large statistical errors on the signal acceptance with $m_{b\bar{b}} > 140$ GeV seen in figure 5.4. In this region, no clear dependence of the uncertainties due to scale factors on $m_{b\bar{b}}$ is seen in figure 5.8. An average value for each uncertainty is therefore calculated within the range of 60 GeV $\geq m_{b\bar{b}} \geq 140$ GeV.

Two sets of results are presented. One, not taking account of logarithmic cancellations, are the uncertainties calculated when only varying the scale factors within a given jet bin. The other set, taking account of logarithmic cancellations, make use of the relation $\sigma_N = \sigma_{\geq N} - \sigma_{\geq N+1}$ and equation 5.10. The latter results are taken to be the correct uncertainties due to scale variation, as they avoid the issues of logarithmic cancellations, however the former results are also presented for comparison. By comparing the two sets of results, the effects of the logarithmic cancellations can be seen.

The averages of the uncertainties due to scale factors, not taking account of logarithmic cancellations, are shown in table 5.2. The averages of the uncertainties due to scale factors, taking account of logarithmic cancellations,

are shown in table 5.3. Statistical uncertainties on the calculated systematic uncertainties arising from scale factors are found to be at the sub-percent level, and are therefore neglected.

N_{jets} bin	$\sigma_{\text{inclusive}}$ $[pb]$	$\delta_{\sigma_{\text{inclusive}}}$ [%]	σ_{asc} $[pb]$	$\delta_{\sigma_{\text{asc}}}$ [%]	A [%]	δ_A [% of A]
2 and 3	0.0350	2.5	0.00524	3.0	15.0	3.5
2	0.0350	2.5	0.00356	6.6	10.2	6.3
3	0.0350	2.5	0.00169	7.1	4.8	6.9

Table 5.2: Systematic uncertainties arising from scale factors, for the $WH \to \ell\nu b\bar{b}$ analysis, with $m_H = 125$ GeV, not taking account of logarithmic cancellations.

N_{jets} bin	$\sigma_{\text{inclusive}}$ $[pb]$	$\delta_{\sigma_{\text{inclusive}}}$ [%]	σ_{asc} $[pb]$	$\delta_{\sigma_{\text{asc}}}$ [%]	A [%]	δ_A [% of A]
2 and 3	0.0350	2.5	0.00524	4.3	15.0	5.3
2	0.0350	2.5	0.00356	9.8	10.2	10.4
3	0.0350	2.5	0.00169	10.9	4.8	11.2

Table 5.3: Systematic uncertainties arising from scale factors, for the $WH \to \ell\nu b\bar{b}$ analysis, with $m_H = 125$ GeV, taking account of logarithmic cancellations.

5.2.3 Conclusion

Systematic uncertainties arising from scale factors have been calculated and are shown in table 5.3. Results that take account of logarithmic cancellations are taken to be the correct estimation of the true systematic uncertainties arising from scale factors. By comparing results that take account of logarithmic cancellations to results that do not, logarithmic cancellations are seen to have large effects on the final results. As $\sigma_{\text{inclusive}}$ and $\delta_{\sigma_{\text{inclusive}}}$ are unaffected by jet-bin choice (by definition), a more accurate calculation of the uncertainty $\delta_{\sigma_{\text{inclusive}}}$ can be used. In [98] the uncertainty on the inclusive WH cross section is calculated to NNLO in QCD and NLO in electroweak perturbative expansion, and is given as $\delta_{\sigma_{\text{inclusive}}} = 1.0\%$. This is compared to the results presented in this chapter, which have been calculated to NLO in QCD perturbative expansion.

For two and three-jet final states, the uncertainty on the inclusive cross-section $\delta_{\sigma_{\text{inclusive}}} = 1.0\%$, the uncertainty on the cross section after analysis selection criteria have been applied $\delta_{\sigma_{\text{asc}}} = 4.3\%$, and the uncertainty on signal acceptance $\delta_A = 5.3\%$.

5.3 Uncertainties Arising From Parton Distribution Functions

5.3.1 Introduction

Available PDFs are approximations of nature, and as such have systematic uncertainties associated with them. In order to estimate these uncertainties we would ideally regenerate all our Monte Carlo generated events for a given process with every PDF available. We would then be able to see how different PDFs affect our variables of interest, and calculate the associated uncertainty on our final results. However, given that the number of different PDFs that we would wish to generate our samples with is typically on the order of hundreds, generating a separate sample for each PDF would be prohibitively computationally expensive. An alternative method is to use a reweighting scheme. Say we have generated our sample with $\mathrm{PDF}_{\mathbf{1}}$ and we wish to see how our sample would differ if it were generated with $\mathrm{PDF}_{\mathbf{2}}$. Starting from equation 2.32 we then have for any given variable X:

$$X(pp \to WH)_{\mathrm{PDF}\boldsymbol{i}} = \sum_{events} \Big(\mathrm{PDF}_{\boldsymbol{i}}(x_1, Q^2, f_1)\ \mathrm{PDF}_{\boldsymbol{i}}(x_2, Q^2, f_2) \times\ X(q\bar{q} \to WH) \Big) \tag{5.11}$$

where the variables in equation 5.11 are the same as in equation 2.32, $X(pp \to WH)_{\mathrm{PDF}\boldsymbol{i}}$ is the variable X calculated using $\mathrm{PDF}_{\boldsymbol{i}}$, and where we have used $pp \to WH$ to denote 'proton-proton $\to WH$', and $q\bar{q} \to WH$ to denote 'parton-parton $\to WH$'.

We can then write,

$$\begin{aligned} X(pp \to WH)_{\mathrm{PDF}\mathbf{2}} &= \sum_{events} \Bigg(\frac{\mathrm{PDF}_{\mathbf{2}}(x_1, Q^2, f_1)\ \mathrm{PDF}_{\mathbf{2}}(x_2, Q^2, f_2)}{\mathrm{PDF}_{\mathbf{1}}(x_1, Q^2, f_1)\ \mathrm{PDF}_{\mathbf{1}}(x_2, Q^2, f_2)} \\ &\quad \times\ \mathrm{PDF}_{\mathbf{1}}(x_1, Q^2, f_1)\ \mathrm{PDF}_{\mathbf{1}}(x_2, Q^2, f_2) \\ &\quad \times\ X(q\bar{q} \to WH) \Bigg) \\ &= \sum_{events} \Bigg(\frac{\mathrm{PDF}_{\mathbf{2}}(x_1, Q^2, f_1)\ \mathrm{PDF}_{\mathbf{2}}(x_2, Q^2, f_2)}{\mathrm{PDF}_{\mathbf{1}}(x_1, Q^2, f_1)\ \mathrm{PDF}_{\mathbf{1}}(x_2, Q^2, f_2)} \\ &\quad \times\ X(pp \to WH)_{\mathrm{PDF}\mathbf{1}} \Bigg) \\ &= \sum_{events} w_i X(pp \to WH)_{\mathrm{PDF}\mathbf{1}} \end{aligned} \tag{5.12}$$

Thus for each event i generated with $\mathrm{PDF}_{\mathbf{1}}$ we can reweight that event's contribution to X by the factor w_i, where,

$$w_i = \frac{\mathrm{PDF}_{\mathbf{2}}(x_1, Q^2, f_1)\ \mathrm{PDF}_{\mathbf{2}}(x_2, Q^2, f_2)}{\mathrm{PDF}_{\mathbf{1}}(x_1, Q^2, f_1)\ \mathrm{PDF}_{\mathbf{1}}(x_2, Q^2, f_2)} \tag{5.13}$$

This will then give the variable X that we would have obtained had the Monte Carlo sample been generated with $\mathrm{PDF}_{\mathbf{2}}$. Generating a sample once and then reweighting the events of that sample in this manner is typically less computationally expensive and faster than regenerating the events for each PDF. PDFs do also enter into $X(q\bar{q} \to WH)$ through ISR parton showers. However, their contributions there are taken to be independent of the PDF type used, and as such the effect on $X(q\bar{q} \to WH)$ from changing PDFs is taken to be negligible [101, 102]. Thus reweighting events using the equation 5.12 is taken as a valid approximation.

In order to calculate values for the PDF functions $\mathrm{PDF}(x, Q^2, f)$, the LHAPDF software package can be used [103, 104]. It requires the input variables x_1, x_2, f_1, f_2, and Q^2 to be made available for each event by the event generator used.

Equation 2.32 however is only valid when the hard subprocess is calculated to leading order (LO) in the perturbative expansion of QCD. If the calculation is done to next to leading order (NLO) in QCD, then the definition of the reweighting weight w_i becomes more complicated [105], however the reweighting

scheme using the weight defined in equation 5.13 is still a reasonable and useful approximation in this scenario. The programs Pythia8, Powheg_Box and aMC@NLO can output the required variables for LHAPDF, however at time of writing Powheg_Box outputs values for these variables corresponding to LO calculations [95]. These values then do not match the NLO hard subprocesses, and as such Powheg_Box can not be used with LHAPDF to perform valid PDF reweighting using equation 2.32. aMC@NLO on the other hand outputs variables for LHAPDF that are corrected for the NLO hard subprocesses, and are able to be used with LHAPDF to perform PDF reweighting using equation 2.32. aMC@NLO is also capable of internally calculating NLO PDF reweighting weights as per [105].

PDF reweighting can thus be performed and studied for several different event generator setups:

Setup 1

A single event generator such as Pythia6, Pythia8, or Herwig++ is used to generate a Monte Carlo sample that contains corresponding variables for LHAPDF for each event. This sample is then analysed in a custom-written program that uses LHAPDF to calculate PDF functions and perform 'LO' PDF reweighting as per equation 5.13. This is illustrated in figure 5.9.

Setup 2

A program such as Powheg_Box or aMC@NLO is used to generate NLO hard subprocesses and associated variables for LHAPDF. These hard subprocesses and variables are passed to an event generator such as Pythia6, Pythia8, or Herwig++ to perform the remaining stages of Monte Carlo event generation. These event generators are able to handle the variables for LHAPDF, passed to them by the hard subprocess generating programs, such that these variables will be stored in the final Monte Carlo sample. This sample is then analysed in a custom-written program that uses LHAPDF to calculate PDF functions and perform 'LO' PDF reweighting as per equation 5.13. This is illustrated in figure 5.10.

Setup 3

aMC@NLO is used to generate NLO hard subprocesses, and also internally perform NLO PDF-reweighting calculations as per [105]. The reweighted event weights it produces are stored in the LHE file that must be passed

to an event generator such as Pythia6, Pythia8, or Herwig++ to perform the remaining stages of Monte Carlo event generation. At time of writing, these generators are not able to handle these extra event weights being present in the LHE file, and will not store these weights in the resulting Monte Carlo sample output file, or more typically will simply crash if the extra event weights are present in the LHE file. The event weights are therefore removed from the LHE file and stored in a separate file along with sufficient event kinematics information so that the weights for each event can be matched to the correct corresponding event in the final Monte Carlo sample file. This information for event matching is required as an event generator may not perform all the remaining stages of Monte Carlo event generation for every event in an LHE file: if the event generator finds an event in an LHE file that it is unable to process for whatever reason (it may be unable to handle the event kinematics and still conserve energy and momentum in the event) then it will skip that event. The modified LHE file, without the extra event weights, is then passed to an event generator to perform the remaining stages of Monte Carlo event generation. A custom-written program is used to read in the resulting Monte Carlo sample, as well as the extra file containing the NLO PDF-reweighting weights. This program is used to match the correct NLO PDF-reweighting weights to the corresponding events in the Monte Carlo sample using the stored event kinematics. The events in the Monte Carlo sample are then reweighted using these NLO PDF-reweighting weights. This is illustrated in figure 5.11.

It was found in the course of this study that aMC@NLO is only capable of internally reweighting to PDF members that are in the same PDF set as the PDF member used to generate the NLO hard subprocesses. Thus for each PDF set being considered, NLO hard subprocesses must be generated with the PDF set central member. These events can then be internally reweighted with aMC@NLO to the error set members of that PDF set. When considering multiple PDF sets however, this method introduces additional statistical uncertainty into final results compared to the LHAPDF method. Even when random number generator seeds are set to the same values for all samples, generating hard subprocesses using

aMC@NLO with different PDF sets results in samples being statistically independent. The cause of this is unconfirmed, although it is speculated that when aMC@NLO generates hard subprocesses, the different PDF parameterisations of PDF sets created by different collaborations result in different numbers of calls to the random number generator service being made, depending on the PDF set used in the generation. Different numbers of calls to the random number generator service per event will result in the random number sequences being out of sync between different samples, resulting in the samples being effectively statistically independent.

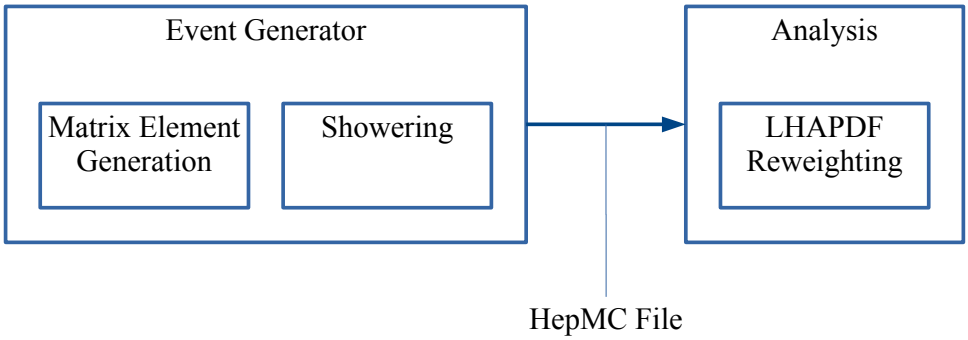

Figure 5.9: Setup 1 for event generation, PDF reweighting, and analysis. Programs are shown as larger blocks. Processes within programs are shown as smaller sub-blocks. File transfer of data between programs is shown as an arrow. As described in 5.3.1.

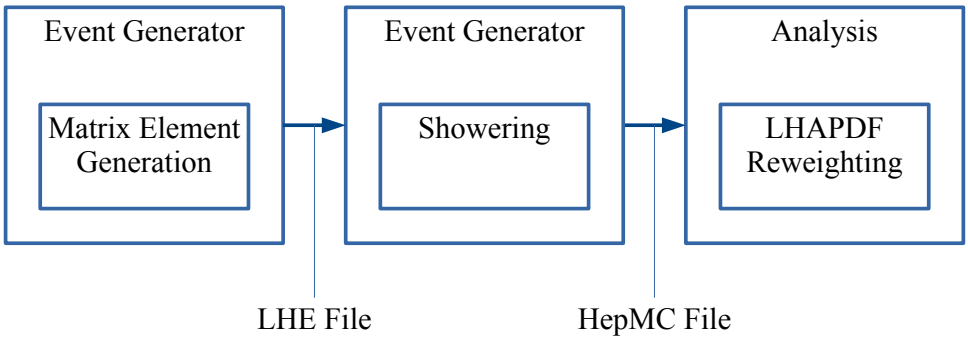

Figure 5.10: Setup 2 for event generation, PDF reweighting, and analysis. Programs are shown as larger blocks. Processes within programs are shown as smaller sub-blocks. File transfer of data between programs is shown as arrows. As described in 5.3.1.

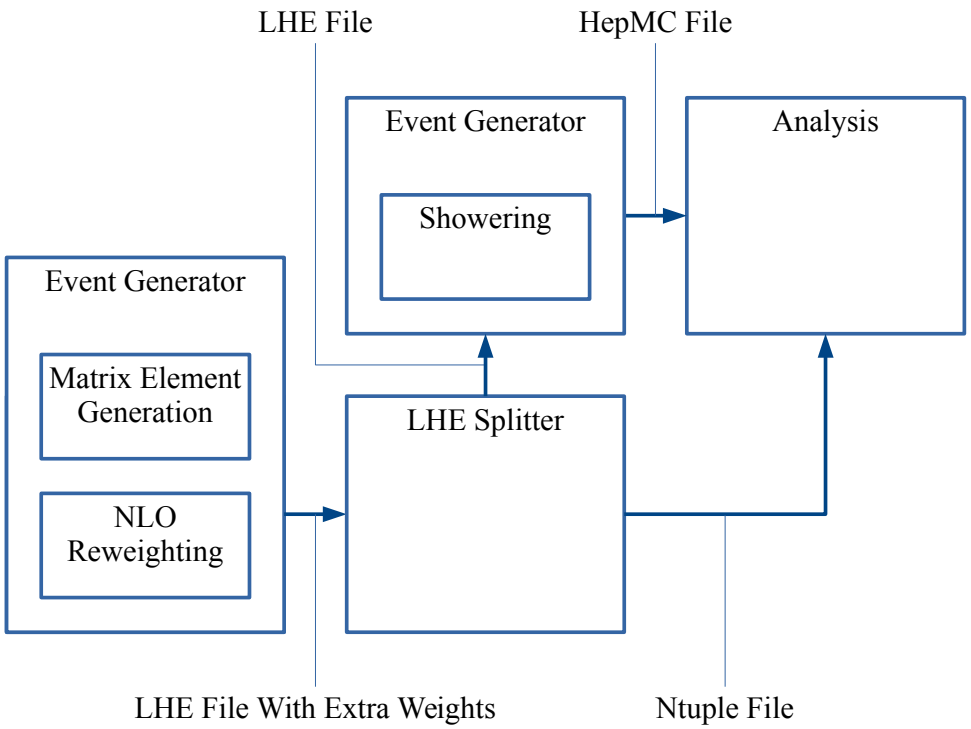

Figure 5.11: Setup 3 for event generation, PDF reweighting, and analysis. Programs are shown as larger blocks. Processes within programs are shown as smaller sub-blocks. File transfer of data between programs is shown as arrows. As described in 5.3.1.

The PDF sets used in this study are the CT10nlo, MSTW2008nlo68cl ('MSTW2008'), and NNPDF23_nlo_as_0119 ('NNPDF2.3') PDF sets, made, respectively, by the CTEQ [33], MSTW [34], and NNPDF [35] collaborations (section 2.3.4). How each error set is used depends on the design choices of the collaboration that has produced the PDF set.

CT10nlo And MSTW2008 PDF Sets

The error sets for the CT10nlo and MSTW2008 PDF sets are Hessian-type 2.3.4 error sets: the PDFs they contain form pairs, representing variations up and down of orthonormal PDF free parameter eigenvectors. For a given observable, a generated Monte Carlo sample is reweighted to each pair of PDFs. For each pair, the maximum increase and decrease in the observable is then computed. It should be noted that any eigenvector variation, up or down, may result in an increase or decrease in an observable. Since all PDF eigenvectors are orthogonal,

all maximum increases in an observable for the eigenvector pairs are summed in quadrature. This gives the overall upward variation for this observable. Likewise the maximum decreases in an observable for the eigenvector pairs is summed in quadrature to obtain the overall downward variation for this observable. These overall variations then correspond to the specified confidence level for that PDF set (a 68% C.L. for MSTW2008, 90% C.L. for CT10nlo).

It is assumed that the uncertainties for a PDF set are Gaussian in nature, and so each 90% C.L. uncertainty band is rescaled to a 68% C.L. uncertainty band (a $\pm 1\sigma$ uncertainty band) by multiplying the uncertainty by $\frac{1}{1.64485}$. In reality PDF set uncertainties are not perfectly Gaussian in nature, however this rescaling method is a valid approximation to first order.

The upper and lower uncertainty bands for the CT10nlo and MSTW2008 PDF sets, for a given variable X, are then given by:

$$\Delta_X^+ = S_F \sqrt{\sum_{i=1}^{N_{\text{Set}}/2} \max\left[\, X\left(\text{PDF}_{2i-1}\right) - X_0 \;,\; X\left(\text{PDF}_{2i}\right) - X_0 \;,\; 0 \,\right]^2} \tag{5.14}$$

$$\Delta_X^- = S_F \sqrt{\sum_{i=1}^{N_{\text{Set}}/2} \max\left[\, X_0 - X\left(\text{PDF}_{2i-1}\right) \;,\; X_0 - X\left(\text{PDF}_{2i}\right) \;,\; 0 \,\right]^2} \tag{5.15}$$

where X_0 is the variable X calculated with the central member PDF, S_F is a scale factor, and N_{Set} is the number of PDFs in the error set. $N_{\text{Set}} = 52$ and $S_F = \frac{1}{1.64485}$ for CT10nlo. $N_{\text{Set}} = 40$ and $S_F = 1$ for MSTW2008.

NNPDF2.3 PDF Set

The error set for the NNPDF2.3 PDF set is replica-type 2.3.4: it consists of 100 equally valid PDFs resulting from 100 fits to data. For a given observable X, to estimate the uncertainty due to the NNPDF2.3 PDF set, X is computed (or reweighted) for each PDF in the NNPDF2.3 error set. The standard deviation of this set of X values is then,

$$\Delta_X = \sqrt{\frac{1}{N_{\text{Set}} - 1} \sum_{i=1}^{N_{\text{Set}}} \left(X_i\left(\text{PDF}_i\right) - \langle X \rangle\right)^2} \tag{5.16}$$

where X_i is X computed using the ith PDF in the NNPDF2.3 error set, PDF_i, $N_{\mathrm{Set}} = 100$ is the number of PDFs in the error set, and the central value is,

$$\langle X \rangle = \frac{1}{N_{\mathrm{Set}}} \sum_{i=1}^{N_{\mathrm{Set}}} X_i \left(\mathrm{PDF}_i\right) \tag{5.17}$$

Combination Of PDF Sets

For a given sample set, the overall uncertainty Δ_X due to PDFs is calculated as follows [106]:

$$\begin{aligned} X_{\mathrm{Upper}} = \max\big[& \Delta_X^+(\mathrm{CT10nlo}) + X_0(\mathrm{CT10nlo}) \ , \\ & \Delta_X^+(\mathrm{MSTW2008}) + X_0(\mathrm{MSTW2008}) \ , \\ & \Delta_X(\mathrm{NNPDF2.3}) + X_0(\mathrm{NNPDF2.3}) \ \big] \end{aligned} \tag{5.18}$$

$$\begin{aligned} X_{\mathrm{Lower}} = \min\big[& X_0(\mathrm{CT10nlo}) - \Delta_X^-(\mathrm{CT10nlo}) \ , \\ & X_0(\mathrm{MSTW2008}) - \Delta_X^-(\mathrm{MSTW2008}) \ , \\ & X_0(\mathrm{NNPDF2.3}) - \Delta_X(\mathrm{NNPDF2.3}) \ \big] \end{aligned} \tag{5.19}$$

$$X_{\mathrm{Mid}} = \frac{X_{\mathrm{Upper}} + X_{\mathrm{Lower}}}{2} \tag{5.20}$$

and so,

$$\Delta_X = X_{\mathrm{Upper}} - X_{\mathrm{Mid}} \tag{5.21}$$

Samples Generated And Tested

$pp \to WH \to \ell\nu b\bar{b}$ samples, where $\ell = e$ or μ, were created and reweighted using the event generators and reweighting procedures listed in table 5.4. 100000 events were generated per sample. They are grouped into four sample sets: 'Pythia8', 'Powheg', 'aMC@NLO', and 'aMC@NLO-internal', where the aMC@NLO-internal set requires three separate samples to be generated.

Sample set	Hard subprocess event generator	Showering event generator	Generated with PDF	Reweighting method	PDF sets reweighted to
A	Pythia8	Pythia8	cteq6l1 CM	LHAPDF	CT10nlo, MSTW2008, NNPDF2.3
B	Powheg_Box	Pythia8	CT10nlo CM	LHAPDF	CT10nlo, MSTW2008, NNPDF2.3
C	aMC@NLO	Herwig++	CT10nlo CM	LHAPDF	CT10nlo, MSTW2008, NNPDF2.3
D	aMC@NLO	Herwig++	CT10nlo CM	aMC@NLO internal	CT10nlo
D	aMC@NLO	Herwig++	MSTW2008 CM	aMC@NLO internal	MSTW2008
D	aMC@NLO	Herwig++	NNPDF2.3 CM	aMC@NLO internal	NNPDF2.3

Table 5.4: Event generators and reweightings used in the estimation of systematic uncertainties arising from PDFs. Set A='Pythia8', B='Powheg', C='aMC@NLO', and D='aMC@NLO-internal'. 'CM' means the **C**entral **M**ember of the PDF set. 'MSTW2008' refers to the MSTW2008nlo68cl PDF set. 'NNPDF2.3' refers to the NNPDF23_nlo_as_0119 PDF set.

5.3.2 Results

Comparison Of Central Members

$pp \to WH \to \ell\nu b\bar{b}$ $m_{b\bar{b}}$ distributions for different event generator and PDF set central members, with no analysis event selection criteria applied, are shown in figure 5.12. Ratios of these distributions are shown in figure 5.13. The equivalent $m_{b\bar{b}}$ and ratio plots, with analysis event selection criteria applied, are shown for the combined two and three-jet bin in figures 5.14 and 5.15. Further plots are found in appendix B.1.1.

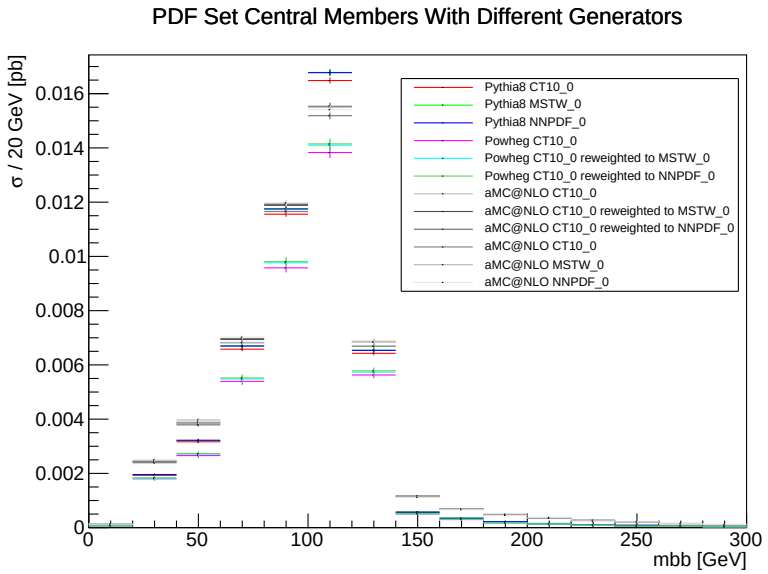

Figure 5.12: $m_{b\bar{b}}$ distributions, for the $WH \to \ell\nu b\bar{b}$ analysis, with $m_H = 125$ GeV, with different event generator and PDF set central members. Analysis event selection criteria have not been applied. Error bars show statistical uncertainty.

From figures 5.13 and 5.15 it can be seen that for Pythia8, Powheg (Powheg_Box+Pythia8), and aMC@NLO reweighted with LHAPDF, the ratios between the MSTW2008 central member distributions to the CT10nlo central member distributions, and the NNPDF2.3 central member distributions to the CT10nlo central member distribution, are all roughly equal to 1. For aMC@NLO samples, separately generated for the CT10nlo, MSTW2008, and NNPDF2.3 central members, the ratios between these distributions deviate considerably from 1, with large statistical fluctuations.

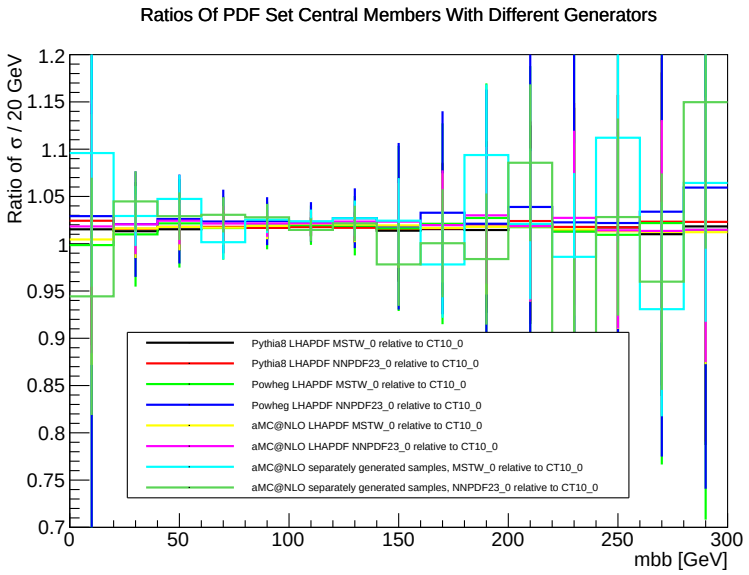

Figure 5.13: Ratios of $m_{b\bar{b}}$ distributions, for the $WH \to \ell\nu b\bar{b}$ analysis, with $m_H = 125$ GeV, with different event generator and PDF set central members. Analysis event selection criteria have not been applied. Error bars show statistical uncertainty.

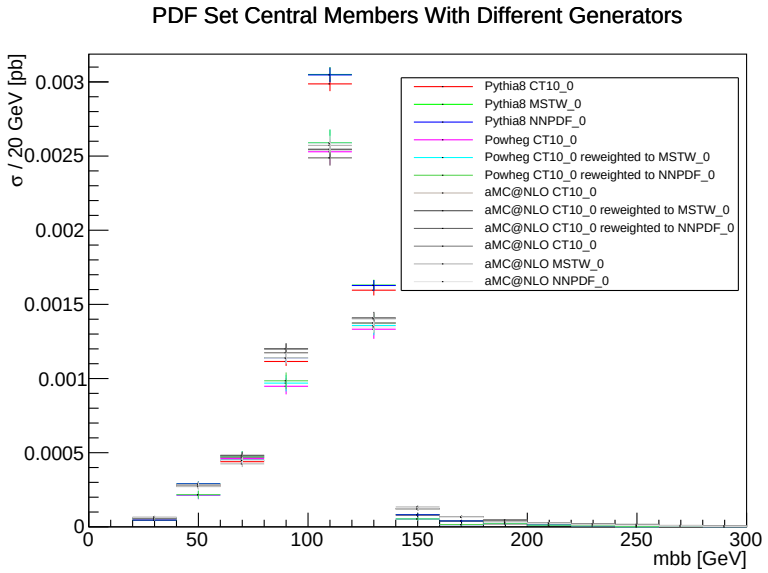

Figure 5.14: $m_{b\bar{b}}$ distributions, for the $WH \to \ell\nu b\bar{b}$ analysis, with $m_H = 125$ GeV, with different event generator and PDF set central members. Analysis event selection criteria have been applied. Two and three-jet final states are included. Error bars show statistical uncertainty.

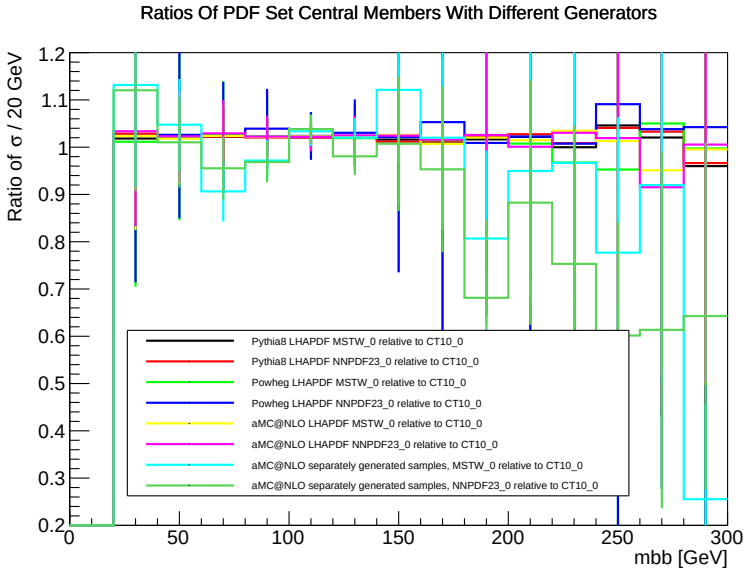

Figure 5.15: Ratios of $m_{b\bar{b}}$ distributions, for the $WH \rightarrow \ell\nu b\bar{b}$ analysis, with $m_H = 125$ GeV, with different event generator and PDF set central members. Analysis event selection criteria have been applied. Two and three-jet final states are included. Error bars show statistical uncertainty.

Cross-Sections And Acceptances

The $m_{b\bar{b}}$ distributions for the four sample sets listed in table 5.4 are shown without analysis selection criteria applied in figure 5.16. The systematic uncertainty arising from PDFs is shown as a band for each set. The equivalent plot after analysis selection criteria have been applied is shown in figure 5.17 for two and three-jet final states combined. Signal acceptance is shown, with systematic uncertainty bands from each PDF set, for 'Pythia8', 'Powheg', 'aMC@NLO', and 'aMC@NLO-internal' in figures 5.18 5.19 5.20 5.21 respectively, again for two and three-jet final states combined. Further cross-section and acceptance plots are found in appendix B.1.2.

Fractional Uncertainties

Fractional uncertainties on the signal cross-section without analysis selection criteria applied, the signal cross-section with analysis selection criteria applied, and signal acceptance are shown in figures 5.22, 5.23, and 5.24 respectively.

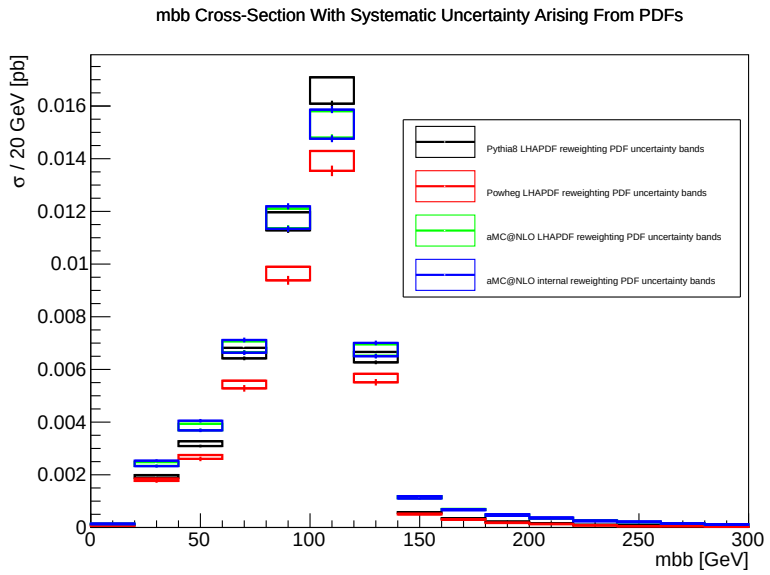

Figure 5.16: $m_{b\bar{b}}$ distributions, for the $WH \to \ell\nu b\bar{b}$ analysis, with $m_H = 125$ GeV, without analysis selection criteria applied, for different samples sets. The systematic uncertainty arising from PDFs is shown as a band for each sample set. Error bars on each band show the statistical uncertainty.

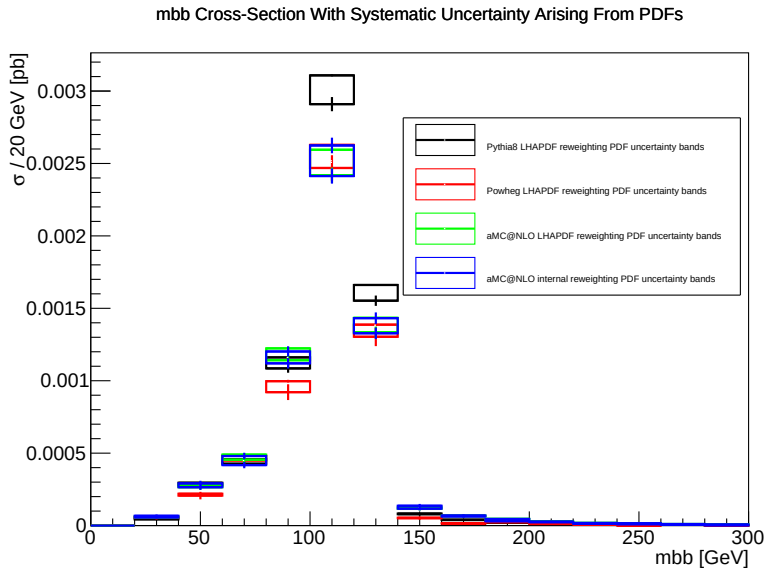

Figure 5.17: $m_{b\bar{b}}$ distributions, for the $WH \to \ell\nu b\bar{b}$ analysis, with $m_H = 125$ GeV, with analysis selection criteria applied, for different samples sets. Two and three-jet final states are included. The systematic uncertainty arising from PDFs is shown as a band for each sample set. Error bars on each band show the statistical uncertainty.

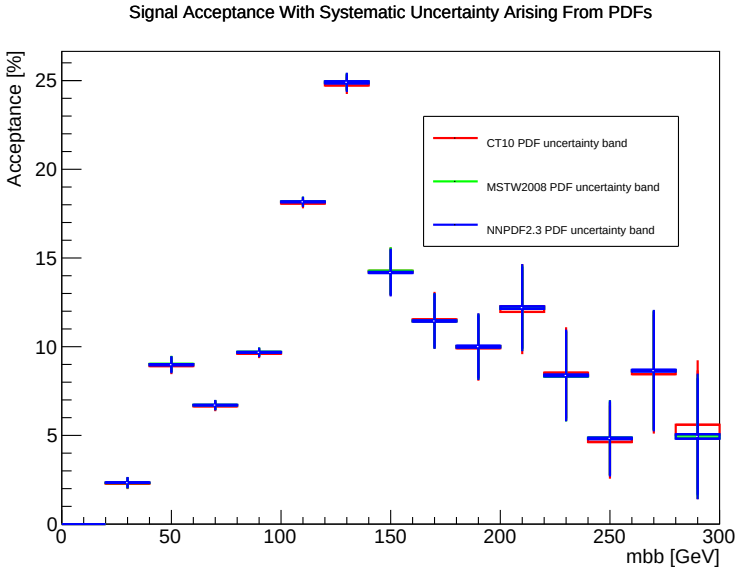

Figure 5.18: Signal acceptance, for the $WH \to \ell\nu b\bar{b}$ analysis, with $m_H = 125$ GeV, for the 'Pythia8' samples set. Two and three-jet final states are included. Systematic uncertainty is shown as a band for each PDF set. Error bars on each band show the statistical uncertainty.

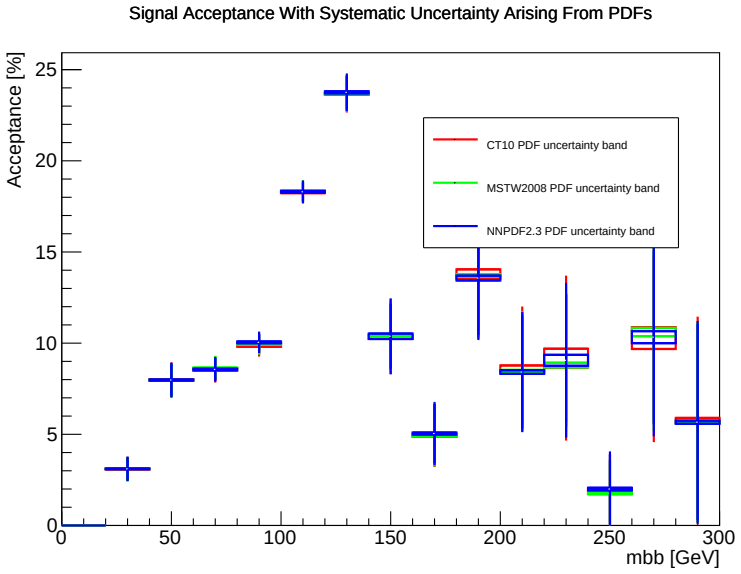

Figure 5.19: Signal acceptance, for the $WH \to \ell\nu b\bar{b}$ analysis, with $m_H = 125$ GeV, for the 'Powheg' samples set. Two and three-jet final states are included. Systematic uncertainty is shown as a band for each PDF set. Error bars on each band show the statistical uncertainty.

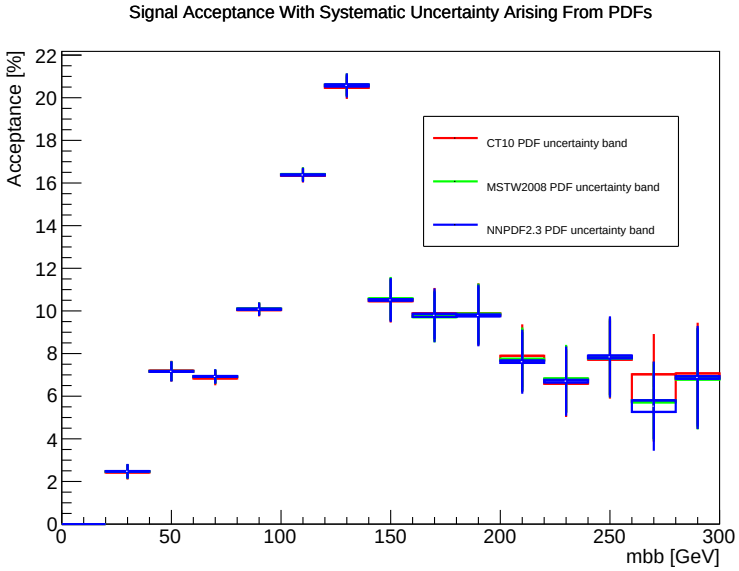

Figure 5.20: Signal acceptance, for the $WH \to \ell\nu b\bar{b}$ analysis, with $m_H = 125$ GeV, for the 'aMC@NLO' samples set. Two and three-jet final states are included. Systematic uncertainty is shown as a band for each PDF set. Error bars on each band show the statistical uncertainty.

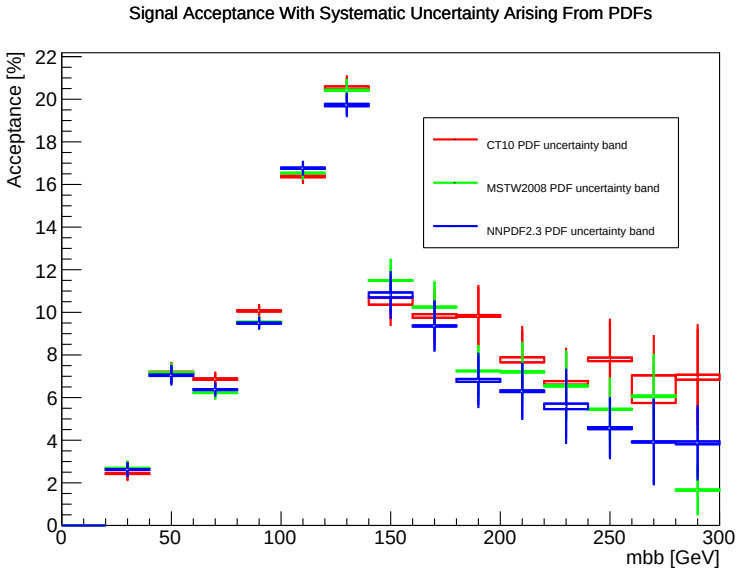

Figure 5.21: Signal acceptance, for the $WH \to \ell\nu b\bar{b}$ analysis, with $m_H = 125$ GeV, for the 'aMC@NLO-internal' samples set. Two and three-jet final states are included. Systematic uncertainty is shown as a band for each PDF set. Error bars on each band show the statistical uncertainty.

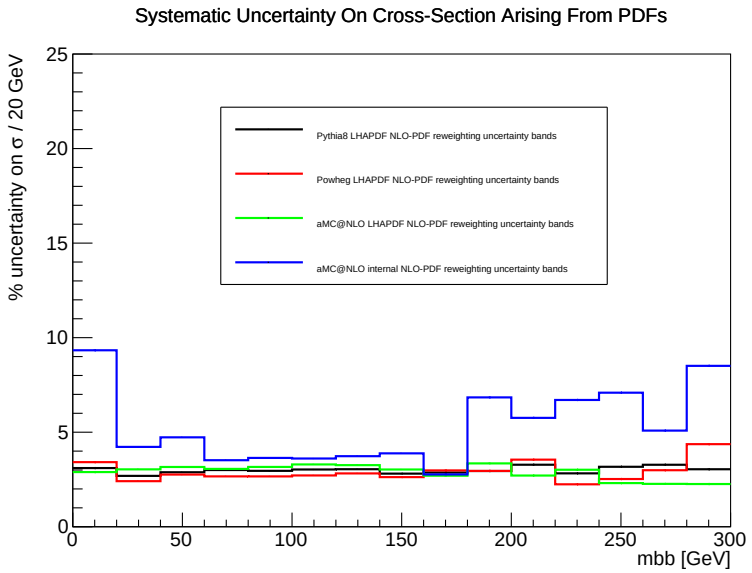

Figure 5.22: Systematic uncertainties on signal cross-section, for the $WH \to \ell\nu b\bar{b}$ analysis, with $m_H = 125$ GeV, without analysis selection criteria applied, for different sample sets. Error bars show statistical uncertainty.

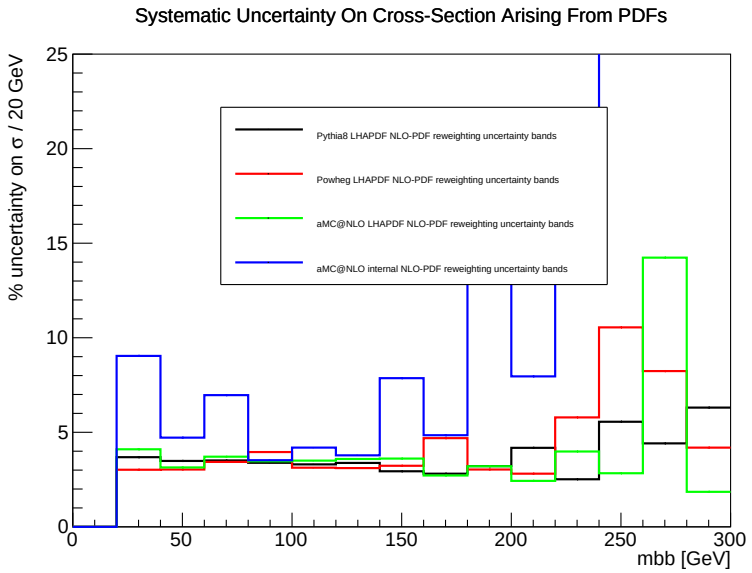

Figure 5.23: Systematic uncertainties on signal cross-section, for the $WH \to \ell\nu b\bar{b}$ analysis, with $m_H = 125$ GeV, with analysis selection criteria applied, for different sample sets. Two and three-jet final states are included. Error bars show statistical uncertainty.

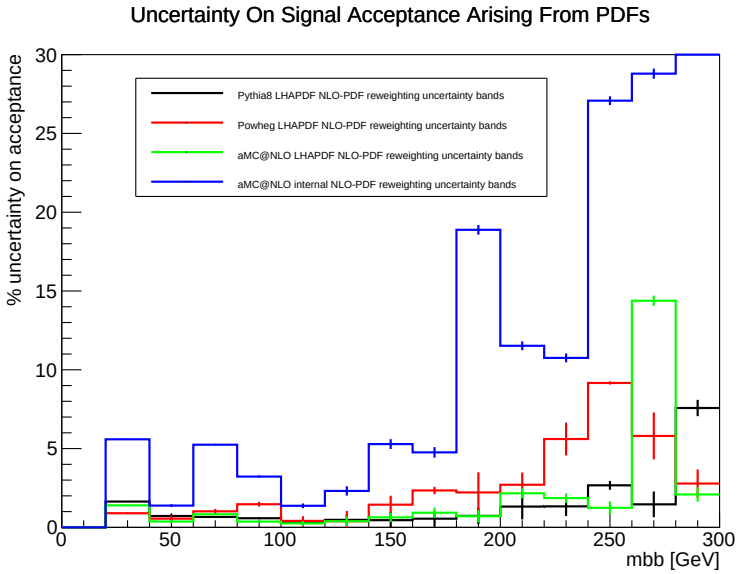

Figure 5.24: Systematic uncertainties on signal acceptance, for the $WH \to \ell\nu b\bar{b}$ analysis, with $m_H = 125$ GeV, for different sample sets. Two and three-jet final states are included. Error bars show statistical uncertainty.

Study Of aMC@NLO Internal Reweighting Results

Figures 5.13 and 5.15 show large statistical fluctuations between separately-generated aMC@NLO samples using different PDFs. Figure 5.25 shows the uncertainties on the inclusive cross-section for the CT10nlo PDF set, both for aMC@NLO reweighted with LHAPDF and for aMC@NLO internally reweighted. Figures 5.26 and 5.27 show the equivalent distributions for the MSTW2008 and NNPDF2.3 PDF sets, respectively. Further comparative plots are found in appendix B.1.4.

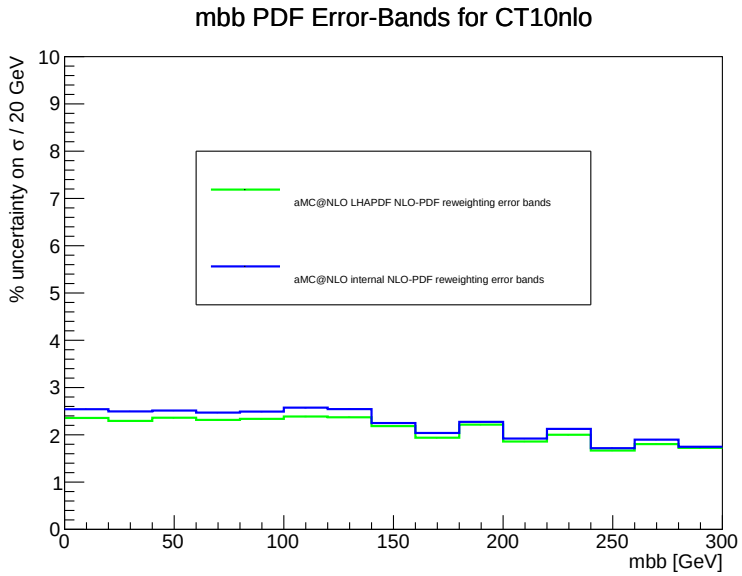

Figure 5.25: Systematic uncertainties on signal cross-section, for the $WH \to \ell\nu b\bar{b}$ analysis, with $m_H = 125$ GeV, without analysis selection criteria applied, for the CT10nlo PDF set. Distributions for aMC@NLO reweighted with LHAPDF, and for aMC@NLO internally reweighted, are shown. Two and three-jet final states are included. Error bars show statistical uncertainty.

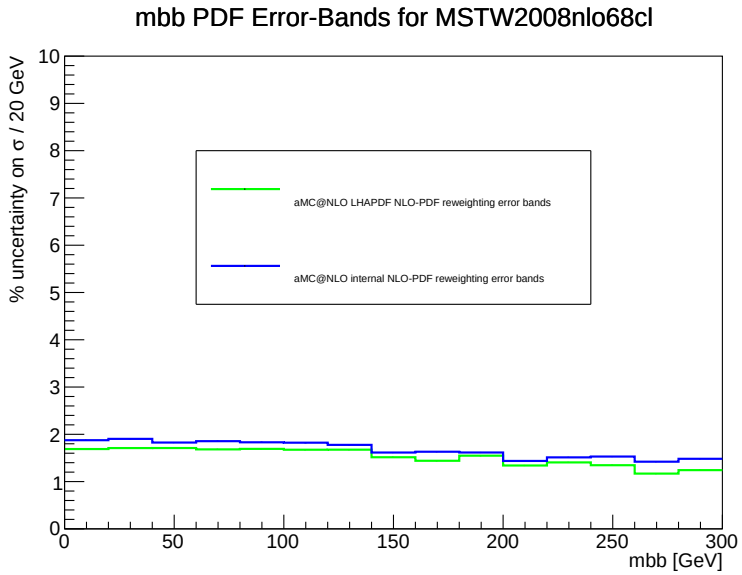

Figure 5.26: Systematic uncertainties on signal cross-section, for the $WH \to \ell\nu b\bar{b}$ analysis, with $m_H = 125$ GeV, without analysis selection criteria applied, for the MSTW2008nlo68cl PDF set. Distributions for aMC@NLO reweighted with LHAPDF, and for aMC@NLO internally reweighted, are shown. Two and three-jet final states are included. Error bars show statistical uncertainty.

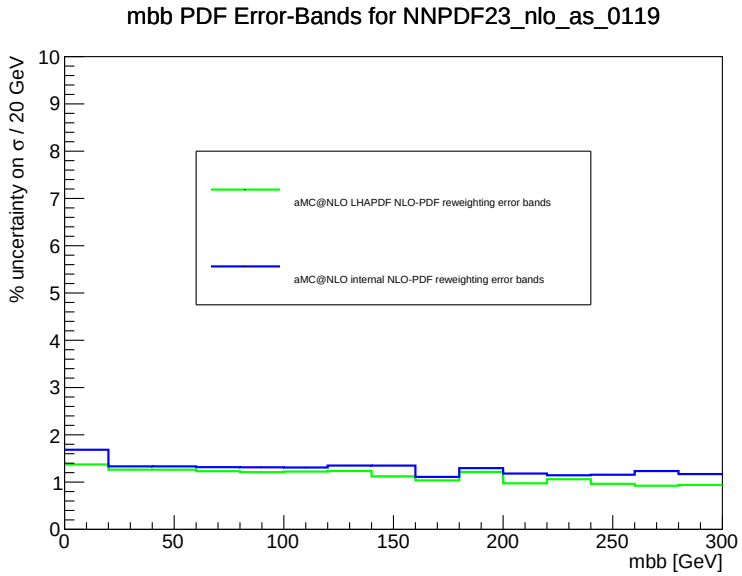

Figure 5.27: Systematic uncertainties on signal cross-section, for the $WH \to \ell\nu b\bar{b}$ analysis, with $m_H = 125$ GeV, without analysis selection criteria applied, for the NNPDF23_nlo_as_0119 PDF set. Distributions for aMC@NLO reweighted with LHAPDF, and for aMC@NLO internally reweighted, are shown. Two and three-jet final states are included. Error bars show statistical uncertainty.

Figures 5.25, 5.26, and 5.27 show that for a given PDF set, the aMC@NLO internal reweighting method produces similar results to the LHAPDF method. The large uncertainties seen in figure 5.22, 5.23, and 5.24 are therefore not due to the aMC@NLO internal reweighting calculations, but are instead due to the large statistical uncertainties between the separately generated aMC@NLO samples. The large uncertainties seen in figure 5.22, 5.23, and 5.24 are therefore not due to systematic PDF uncertainties, but are due to statistical uncertainties introduced by the need to generate separate samples when considering multiple PDF sets with the aMC@NLO internal reweighting method. The systematic uncertainties arising from PDFs as estimated using the aMC@NLO internal reweighting method can not therefore be taken as accurate estimations of the true PDF systematic uncertainties.

Averaged Uncertainties

When considering uncertainties, only a region with a large number of events is chosen: the $m_{b\bar{b}}$ range of 60 GeV to 140 GeV around the Higgs mass peak. In this region, no clear dependence of the uncertainties on $m_{b\bar{b}}$ is seen in figures 5.22, 5.23, and 5.24. An average value for each uncertainty, for each sample set, is therefore calculated within the range of 60 GeV $\geq m_{b\bar{b}} \geq$ 140 GeV.

Figures 5.28, 5.29, and 5.30, show for each sample set, respectively the averaged uncertainty set on the signal cross-section without analysis selection criteria applied, with analysis selection criteria applied, and on signal acceptance. These figures are for two and three-jet final states combined. Equivalent distributions for two-jet and three-jet final states are shown in appendix B.1.5. The averaged uncertainties are shown for sample sets 'Pythia8', 'Powheg', 'aMC@NLO', and 'aMC@NLO-internal' in tables 5.5, 5.6, 5.7, and 5.8 respectively.

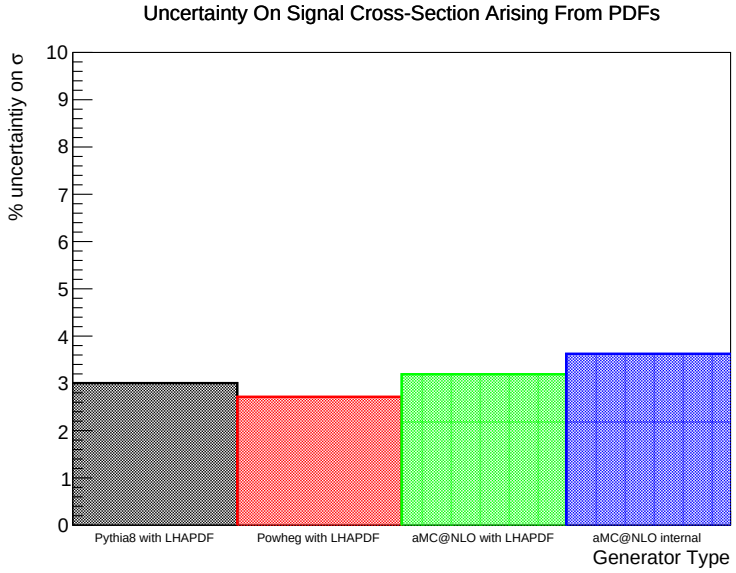

Figure 5.28: Systematic uncertainties on signal cross-section, for the $WH \to \ell\nu b\bar{b}$ analysis, with $m_H = 125$ GeV, without analysis selection criteria applied, for different sample sets.

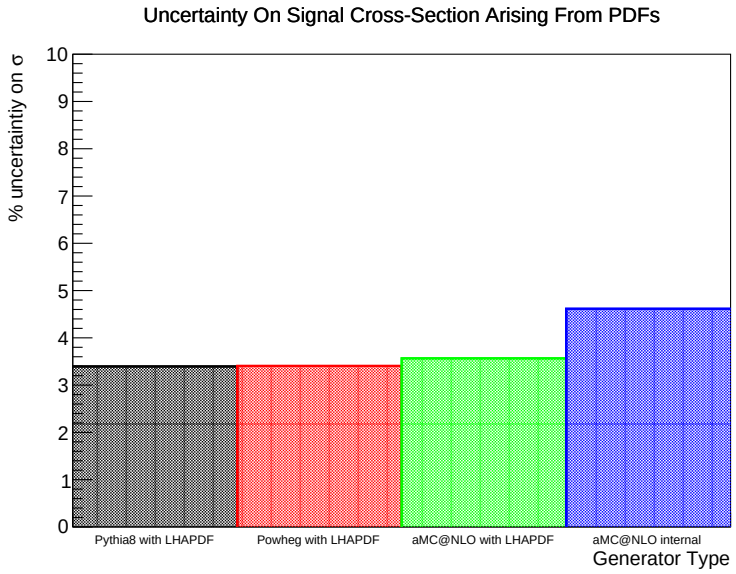

Figure 5.29: Systematic uncertainties on signal cross-section, for the $WH \to \ell\nu b\bar{b}$ analysis, with $m_H = 125$ GeV, with analysis selection criteria applied, for different sample sets. Two and three-jet final states are included.

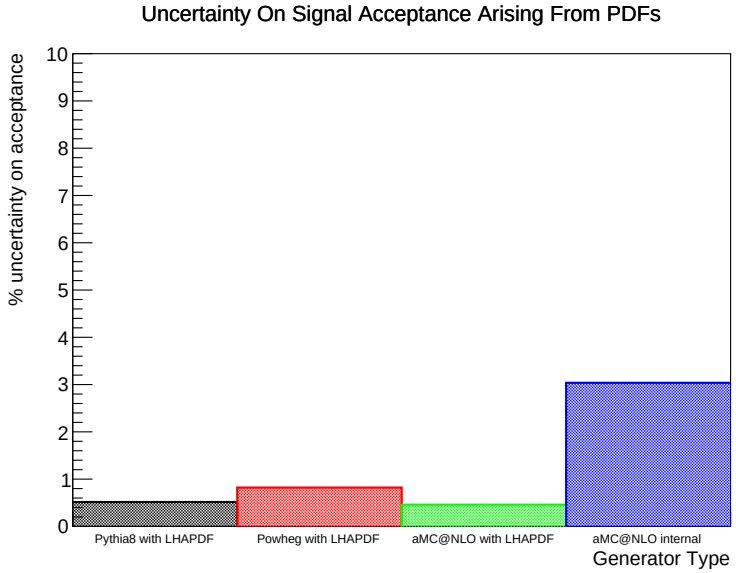

Figure 5.30: Systematic uncertainties on signal acceptance, for the $WH \to \ell\nu b\bar{b}$ analysis, with $m_H = 125$ GeV, for different sample sets. Two and three-jet final states are included.

N_{jets} bin	$\sigma_{\text{inclusive}}$ $[pb]$	$\delta_{\sigma_{\text{inclusive}}}$ [%]	σ_{asc} $[pb]$	$\delta_{\sigma_{\text{asc}}}$ [%]	A [%]	δ_A [% of A]
2 and 3	0.0410	3.0	0.00614	3.4	15.0	0.5
2	0.0410	3.0	0.00415	3.4	10.1	0.5
3	0.0410	3.0	0.00198	3.4	4.8	0.7

Table 5.5: Systematic uncertainties arising from PDFs, for the $WH \to \ell\nu b\bar{b}$ analysis, with $m_H = 125$ GeV, calculated using the 'Pythia8' sample set.

N_{jets} bin	$\sigma_{\text{inclusive}}$ $[pb]$	$\delta_{\sigma_{\text{inclusive}}}$ [%]	σ_{asc} $[pb]$	$\delta_{\sigma_{\text{asc}}}$ [%]	A [%]	δ_A [% of A]
2 and 3	0.0344	2.7	0.00527	3.4	15.3	0.8
2	0.0344	2.7	0.00360	3.5	10.5	1.0
3	0.0344	2.7	0.00167	3.2	4.9	0.9

Table 5.6: Systematic uncertainties arising from PDFs, for the $WH \to \ell\nu b\bar{b}$ analysis, with $m_H = 125$ GeV, calculated using the 'Powheg' sample set.

N_{jets} bin	$\sigma_{\text{inclusive}}$ $[pb]$	$\delta_{\sigma_{\text{inclusive}}}$ [%]	σ_{asc} $[pb]$	$\delta_{\sigma_{\text{asc}}}$ [%]	A [%]	δ_A [% of A]
2 and 3	0.0404	3.2	0.00551	3.6	13.6	0.5
2	0.0404	3.2	0.00354	3.6	8.8	0.6
3	0.0404	3.2	0.00197	3.4	4.9	0.5

Table 5.7: Systematic uncertainties arising from PDFs, for the $WH \to \ell\nu b\bar{b}$ analysis, with $m_H = 125$ GeV, calculated using the 'aMC@NLO' sample set.

N_{jets} bin	$\sigma_{\text{inclusive}}$ $[pb]$	$\delta_{\sigma_{\text{inclusive}}}$ [%]	σ_{asc} $[pb]$	$\delta_{\sigma_{\text{asc}}}$ [%]	A [%]	δ_A [% of A]
2 and 3	0.0403	3.6	0.00551	4.6	13.6	3.0
2	0.0403	3.6	0.00353	4.4	8.8	2.3
3	0.0403	3.6	0.00197	7.4	4.9	6.2

Table 5.8: Systematic uncertainties arising from PDFs, for the $WH \to \ell\nu b\bar{b}$ analysis, with $m_H = 125$ GeV, calculated using the 'aMC@NLO-internal' sample set.

5.3.3 Conclusion

Systematic uncertainties arising from PDFs have been calculated and are shown in tables 5.5, 5.6, 5.7, and 5.8. The choice then remains as to which set of systematic uncertainties to take as the final results. Pythia8 generates hard subprocesses to leading order in QCD. All other samples used in this study generate hard subprocesses to next-to-leading order in QCD. On this basis, the 'Pythia8' results are discarded. Powheg_Box has known issues when reweighting with LHAPDF, as discussed in the introduction, section 5.3.1. Results using the 'Powheg' sample can therefore not be taken to be correct, and as a result are discarded. aMC@NLO reweighted using aMC@NLO's internal reweighting method, while more advanced in its reweighting calculations, brings in additional statistical uncertainties into the results, as seen in section 5.3.2. These are introduced by the need to generate separate samples when considering multiple PDF sets. Results using the 'aMC@NLO-internal' sample can therefore not be taken as accurate estimations of the true PDF systematic uncertainties, and as a result are discarded. This leaves only the 'aMC@NLO' results shown in table 5.7. These are therefore taken as the best estimates of systematic uncertainties arising from parton distribution functions.

For two and three-jet final states, the uncertainty on the inclusive cross-section $\delta_{\sigma_{\text{inclusive}}} = 3.2\%$, the uncertainty on the cross section after analysis selection criteria have been applied $\delta_{\sigma_{\text{asc}}} = 3.6\%$, and the uncertainty on signal acceptance $\delta_A = 0.5\%$.

5.4 Uncertainties Arising From α_s

5.4.1 Introduction

The most recent world average of $\alpha_s(m_Z) = 0.1184 \pm 0.0007$ [16]. Since there is an uncertainty on $\alpha_s(m_Z)$, there will be a systematic uncertainty on our final results arising from α_s. For the purposes of the estimation of theoretical systematic uncertainties in Monte Carlo samples however, it has been decided to use a more conservative 1σ variation of $\Delta\alpha_s = 0.0012$ [106].

In order to estimate the uncertainty on our final results due to α_s, $\alpha_s(m_Z)$ is adjusted by $\pm 1\sigma$ while using the most accurate order of the $\alpha_s(Q^2)$ function available. In the Monte Carlo samples used in this study, a two-loop $\alpha_s(Q^2)$ evolution function is used. The resulting changes in our final results are then taken as $\pm 1\sigma$ systematic uncertainties arising from α_s.

α_s is involved in several stages of Monte Carlo generation: PDFs, the hard subprocess, and parton showering. It is important to ensure that α_s is consistent across different stages of Monte Carlo event generation. To ensure consistency, each Monte Carlo sample used in this study is generated with PDFs corresponding to the chosen value of $\alpha_s(m_Z)$ for that sample. The event generators used then read in this value of $\alpha_s(m_Z)$ from the PDFs, and use this value in all other calculations.

Due to the need to vary PDFs in order to estimate the systematic uncertainties arising from α_s, and the fact that different PDF sets are defined differently (section 5.3), calculating the systematic uncertainties arising from α_s must be performed differently for PDFs from different collaborations, and then subsequently combined. For each PDF collaboration's PDF sets used in this study, the method of calculation of systematic uncertainties arising from α_s is described in the following:

CT10nlo PDF Sets

For the CT10nlo PDF sets, PDF sets are available that correspond to the $\alpha_s(m_Z)$ values of 0.117, 0.118, and 0.119. $\alpha_s(m_Z) = 0.118$ is used as the central value of $\alpha_s(m_Z)$ around which it is varied by $\pm 1\sigma$. The $\alpha_s(m_Z)$ values of 0.119 and 0.117 are used as the variations of $+$ and $-$ 1σ respectively.

The upper and lower uncertainties on a variable X of interest are then given

by:

$$\Delta_X^+ = \frac{6}{5}\max\Big(X\left(\alpha_s\left(m_Z\right)=0.119\right) - X\left(\alpha_s\left(m_Z\right)=0.118\right), \\ X\left(\alpha_s\left(m_Z\right)=0.117\right) - X\left(\alpha_s\left(m_Z\right)=0.118\right), \\ 0\Big) \tag{5.22}$$

$$\Delta_X^- = \frac{6}{5}\max\Big(X\left(\alpha_s\left(m_Z\right)=0.118\right) - X\left(\alpha_s\left(m_Z\right)=0.119\right), \\ X\left(\alpha_s\left(m_Z\right)=0.118\right) - X\left(\alpha_s\left(m_Z\right)=0.117\right), \\ 0\Big) \tag{5.23}$$

where the factor of $\frac{6}{5}$ $(= \frac{0.0012}{0.001})$ is used to scale for the $\Delta\alpha_s(m_Z) = 0.001$ variation used in the construction of the CT10nlo PDF sets, such that the resulting uncertainties on the variable X are consistent with a 1σ uncertainty band on $\alpha_s(m_Z)$ of $\Delta\alpha_s = 0.0012$.

MSTW2008 PDF Sets

For the MSTW2008 PDF sets, PDF sets are available that correspond to the $\alpha_s(m_Z)$ values of 0.11867, 0.120179, and 0.12140. $\alpha_s(m_Z) = 0.120179$ is used as the central value of $\alpha_s(m_Z)$ around which it is varied by $\pm 1\sigma$. The $\alpha_s(m_Z)$ values of $\alpha_s(m_Z) = 0.120179 + 0.001221 = 0.12140$ and $\alpha_s(m_Z) = 0.120179 - 0.001509 = 0.11867$ are used as the variations of $+1\sigma$ and -1σ respectively.

The upper and lower uncertainties on a variable X of interest are then given by:

$$\Delta_X^+ = \max\Big(X\left(\alpha_s\left(m_Z\right)=0.12140\right) - X\left(\alpha_s\left(m_Z\right)=0.120179\right), \\ X\left(\alpha_s\left(m_Z\right)=0.11867\right) - X\left(\alpha_s\left(m_Z\right)=0.120179\right), \\ 0\Big) \tag{5.24}$$

$$\Delta_X^- = \frac{4}{5}\max\Big(X\left(\alpha_s\left(m_Z\right) = 0.120179\right) - X\left(\alpha_s\left(m_Z\right) = 0.12140\right), \\ X\left(\alpha_s\left(m_Z\right) = 0.120179\right) - X\left(\alpha_s\left(m_Z\right) = 0.11867\right), \\ 0\Big) \tag{5.25}$$

where the factor of $\frac{4}{5}$ ($\approx \frac{0.0012}{0.001509}$) is used to scale for the lower $\Delta\alpha_s(m_Z) = 0.001509$ variation used in the construction of the MSTW2008 PDF sets, such that the resulting uncertainties on the variable X are consistent with a 1σ uncertainty band on $\alpha_s(m_Z)$ of $\Delta\alpha_s = 0.0012$. No scale factor is applied in the calculation of the upper uncertainty as $\Delta\alpha_s = 0.001221 \approx 0.0012$.

NNPDF2.3 PDF sets

For the NNPDF2.3 PDF sets, PDF sets are available that correspond to the $\alpha_s(m_Z)$ values of 0.118, 0.119, and 0.120. $\alpha_s(m_Z) = 0.119$ is used as the central value of $\alpha_s(m_Z)$ around which it is varied by $\pm 1\sigma$. The $\alpha_s(m_Z)$ values of 0.120 and 0.118 are used as the variations of $+$ and $-$ 1σ respectively.

The upper and lower uncertainties on a variable X of interest are then given by:

$$\Delta_X^+ = \frac{6}{5}\max\Big(X\left(\alpha_s\left(m_Z\right) = 0.120\right) - X\left(\alpha_s\left(m_Z\right) = 0.119\right), \\ X\left(\alpha_s\left(m_Z\right) = 0.118\right) - X\left(\alpha_s\left(m_Z\right) = 0.119\right), \\ 0\Big) \tag{5.26}$$

$$\Delta_X^- = \frac{6}{5}\max\Big(X\left(\alpha_s\left(m_Z\right) = 0.119\right) - X\left(\alpha_s\left(m_Z\right) = 0.120\right), \\ X\left(\alpha_s\left(m_Z\right) = 0.119\right) - X\left(\alpha_s\left(m_Z\right) = 0.118\right), \\ 0\Big) \tag{5.27}$$

where the factor of $\frac{6}{5}$ ($= \frac{0.0012}{0.001}$) is used to scale for the $\Delta\alpha_s(m_Z) = 0.001$ variation used in the construction of the NNPDF2.3 PDF sets, such that the resulting uncertainties on the variable X are consistent with a 1σ uncertainty

band on $\alpha_s(m_Z)$ of $\Delta\alpha_s = 0.0012$.

Combination Of PDF Sets

For a given sample set, the overall uncertainty Δ_X due to α_s is calculated as follows:

$$\begin{aligned} X_{\text{Upper}} = \max\big[& \Delta_X^+(\text{CT10nlo}) + X(\text{CT10nlo}, \alpha_s(m_Z) = 0.118) \ , \\ & \Delta_X^+(\text{MSTW2008}) + X(\text{MSTW2008}, \alpha_s(m_Z) = 0.120179) \ , \\ & \Delta_X(\text{NNPDF2.3}) + X(\text{NNPDF2.3}, \alpha_s(m_Z) = 0.119) \ \big] \end{aligned} \tag{5.28}$$

$$\begin{aligned} X_{\text{Lower}} = \min\big[& X(\text{CT10nlo}, \alpha_s(m_Z) = 0.118) - \Delta_X^-(\text{CT10nlo}) \ , \\ & X(\text{MSTW2008}, \alpha_s(m_Z) = 0.120179) - \Delta_X^-(\text{MSTW2008}) \ , \\ & X(\text{NNPDF2.3}, \alpha_s(m_Z) = 0.119) - \Delta_X(\text{NNPDF2.3}) \ \big] \end{aligned} \tag{5.29}$$

$$X_{\text{Mid}} = \frac{X_{\text{Upper}} + X_{\text{Lower}}}{2} \tag{5.30}$$

and so,

$$\Delta_X = X_{\text{Upper}} - X_{\text{Mid}} \tag{5.31}$$

Samples Generated And Tested

$pp \to WH \to \ell\nu b\bar{b}$ Monte Carlo samples, where $\ell = e$ or μ, were generated as listed in table 5.9. 100000 events were generated per sample. Samples were generated for each of the central members of the PDF sets CT10nlo, MSTW2008nlo68cl, and NNPDF23_nlo_as_0119, as well as for the PDFs corresponding to $+1\sigma$ and -1σ for those PDF sets.

Sample set	Hard subprocess event generator	Showering event generator	Generated with PDF	$\alpha_s(m_Z)$
'Powheg'	Powheg_Box	Pythia8	CT10nlo CM	0.118
'Powheg'	Powheg_Box	Pythia8	CT10as	0.117
'Powheg'	Powheg_Box	Pythia8	CT10as	0.119
'Powheg'	Powheg_Box	Pythia8	MSTW2008nlo68cl CM	0.120179
'Powheg'	Powheg_Box	Pythia8	MSTW2008nlo68cl_asmz-68cl CM	0.11867
'Powheg'	Powheg_Box	Pythia8	MSTW2008nlo68cl_asmz+68cl CM	0.121
'Powheg'	Powheg_Box	Pythia8	NNPDF23_nlo_as_0119 CM	0.119
'Powheg'	Powheg_Box	Pythia8	NNPDF23_nlo_as_0118 CM	0.118
'Powheg'	Powheg_Box	Pythia8	NNPDF23_nlo_as_0120 CM	0.120
'aMC@NLO'	aMC@NLO	Herwig++	CT10nlo CM	0.118
'aMC@NLO'	aMC@NLO	Herwig++	CT10as	0.117
'aMC@NLO'	aMC@NLO	Herwig++	CT10as	0.119
'aMC@NLO'	aMC@NLO	Herwig++	MSTW2008nlo68cl CM	0.120179
'aMC@NLO'	aMC@NLO	Herwig++	MSTW2008nlo68cl_asmz-68cl CM	0.11867
'aMC@NLO'	aMC@NLO	Herwig++	MSTW2008nlo68cl_asmz+68cl CM	0.12140
'aMC@NLO'	aMC@NLO	Herwig++	NNPDF23_nlo_as_0119 CM	0.119
'aMC@NLO'	aMC@NLO	Herwig++	NNPDF23_nlo_as_0118 CM	0.118
'aMC@NLO'	aMC@NLO	Herwig++	NNPDF23_nlo_as_0120 CM	0.120

Table 5.9: Monte Carlo samples generated for the estimation of systematic uncertainties arising from α_s. 'CM' means the **C**entral **M**ember of the PDF set.

5.4.2 Results

Cross-Sections And Acceptances

Figure 5.31 shows signal cross-section $m_{b\bar{b}}$ distributions without analysis selection criteria applied. Figure 5.32 shows the equivalent distributions with analysis selection criteria applied for two and three-jet final states combined. Figure 5.33 shows signal acceptance for two and three-jet final states combined. Further cross-section and acceptance plots are found in appendix C.1.1.

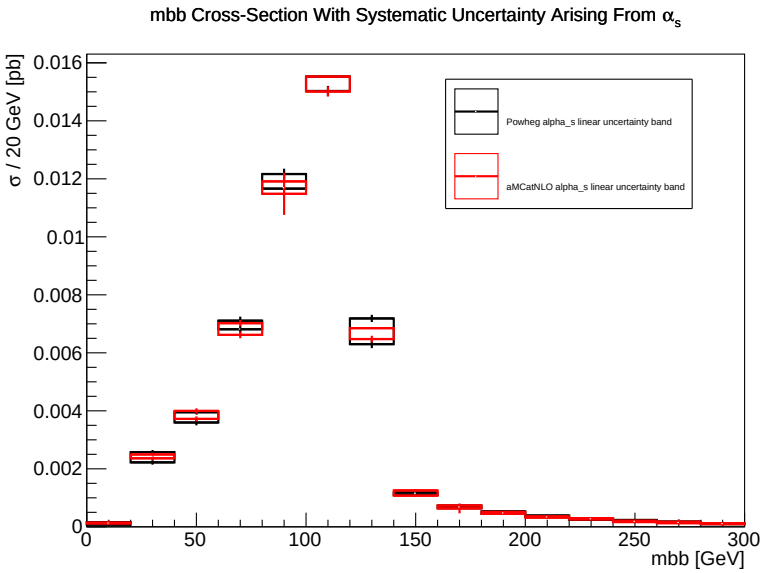

Figure 5.31: $m_{b\bar{b}}$ distributions, for the $WH \to \ell\nu b\bar{b}$ analysis, with $m_H = 125$ GeV, without analysis selection criteria applied, for different samples sets. Systematic uncertainty is shown as a band for each sample set. Error bars on each band show the statistical uncertainty.

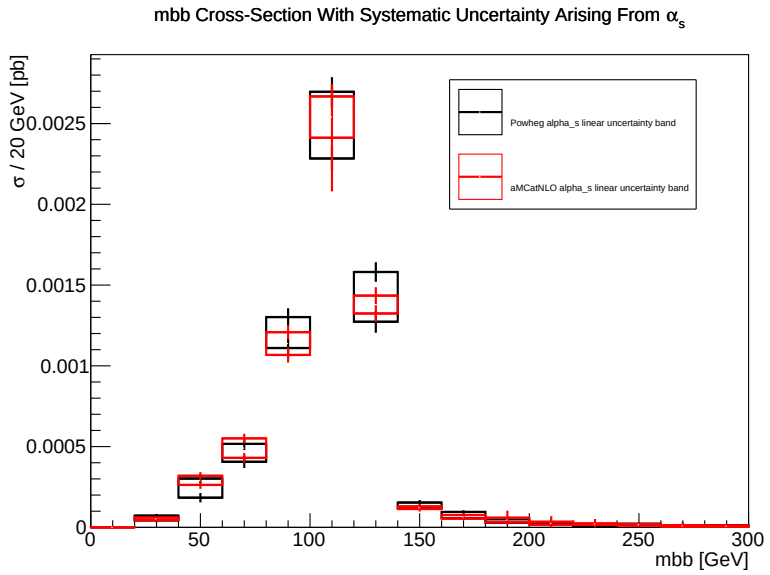

Figure 5.32: $m_{b\bar{b}}$ distributions, for the $WH \to \ell\nu b\bar{b}$ analysis, with $m_H = 125$ GeV, with analysis selection criteria applied, for different samples sets. Two and three-jet final states are included. Systematic uncertainty is shown as a band for each sample set. Error bars on each band show the statistical uncertainty.

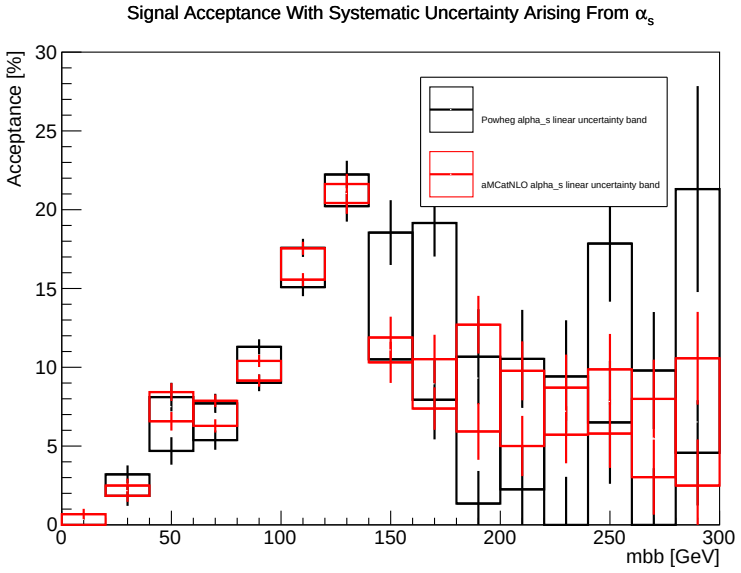

Figure 5.33: Signal acceptance, for the $WH \to \ell\nu b\bar{b}$ analysis, with $m_H = 125$ GeV, for different samples sets. Two and three-jet final states are included. Systematic uncertainty is shown as a band for each sample set. Error bars on each band show the statistical uncertainty.

Uncertainties

Figure 5.34 shows systematic uncertainties on signal cross-section $m_{b\bar{b}}$ distributions without analysis selection criteria applied. Figure 5.35 shows the equivalent distributions with analysis selection criteria applied. Figure 5.36 shows systematic uncertainties on signal acceptance. These figures are for the inclusive jet bin. Equivalent distributions for two-jet and three-jet final states are shown in appendix C.1.2.

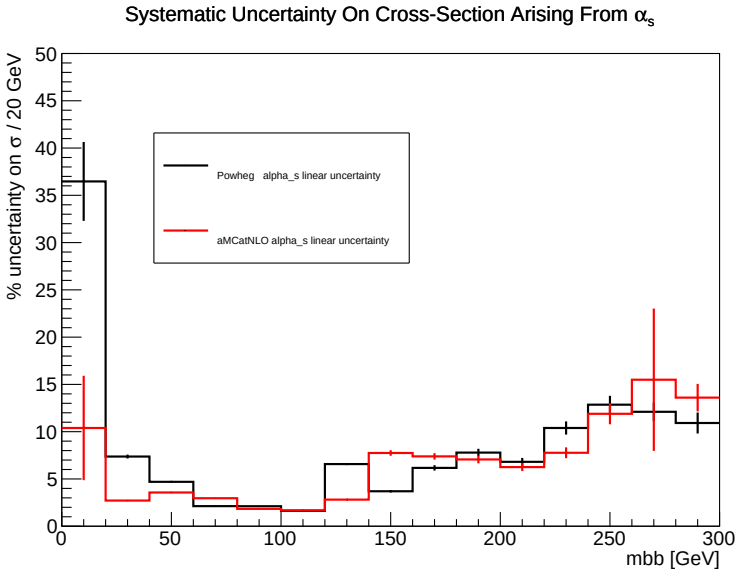

Figure 5.34: Systematic uncertainties on signal cross-section, for the $WH \to \ell\nu b\bar{b}$ analysis, with $m_H = 125$ GeV, without analysis selection criteria applied, for different sample sets. Error bars show statistical uncertainty.

When considering uncertainties, only a region with a large number of events is chosen: the $m_{b\bar{b}}$ range of 60 GeV to 140 GeV around the Higgs mass peak. In this region, no clear dependence of the uncertainties on $m_{b\bar{b}}$ is seen. An average value for each uncertainty, for each sample set, is therefore calculated within the range of 60 GeV $\geq m_{b\bar{b}} \geq$ 140 GeV.

Averaged systematic uncertainties are shown for the 'Powheg' sample set in table 5.10, and for the 'aMC@NLO' sample set in table 5.11.

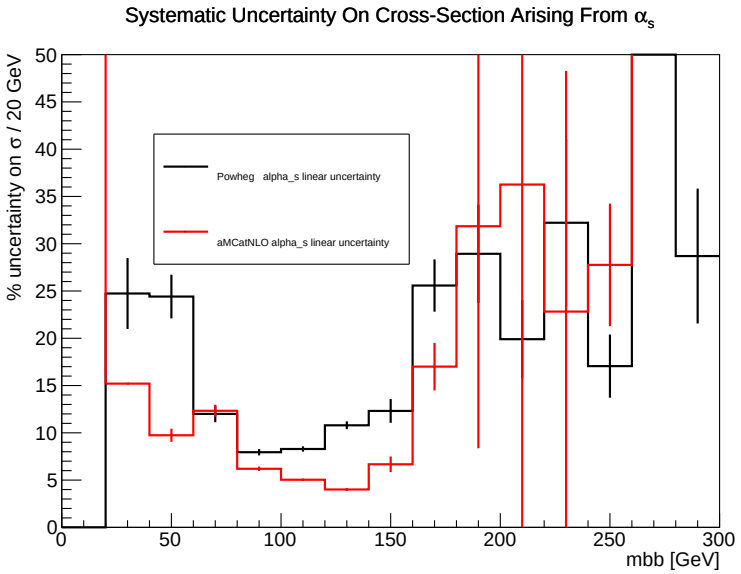

Figure 5.35: Systematic uncertainties on signal cross-section, for the $WH \to \ell\nu b\bar{b}$ analysis, with $m_H = 125$ GeV, with analysis selection criteria applied, for different sample sets. Two and three-jet final states are included. Error bars show statistical uncertainty.

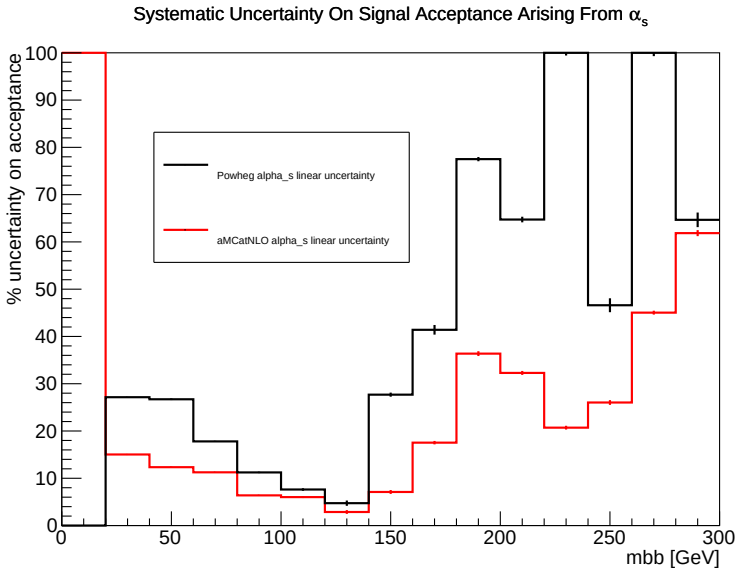

Figure 5.36: Systematic uncertainties on signal acceptance, for the $WH \to \ell\nu b\bar{b}$ analysis, with $m_H = 125$ GeV, for different sample sets. Two and three-jet final states are included. Error bars show statistical uncertainty.

N_{jets} bin	$\sigma_{\text{inclusive}}$ $[pb]$	$\delta_{\sigma_{\text{inclusive}}}$ [%]	σ_{asc} $[pb]$	$\delta_{\sigma_{\text{asc}}}$ [%]	A [%]	δ_A [% of A]
2 and 3	0.0344	3.1	0.00527	9.8	15.3	10.3
2	0.0344	3.1	0.00360	12.0	10.5	13.5
3	0.0344	3.1	0.00167	15.9	4.9	18.6

Table 5.10: Systematic uncertainties arising from α_s, for the $WH \rightarrow \ell\nu b\bar{b}$ analysis, with $m_H = 125$ GeV, calculated using the 'Powheg' sample set.

N_{jets} bin	$\sigma_{\text{inclusive}}$ $[pb]$	$\delta_{\sigma_{\text{inclusive}}}$ [%]	σ_{asc} $[pb]$	$\delta_{\sigma_{\text{asc}}}$ [%]	A [%]	δ_A [% of A]
2 and 3	0.0403	2.3	0.00551	6.9	13.6	6.6
2	0.0403	2.3	0.00353	9.2	8.8	8.9
3	0.0403	2.3	0.00197	8.5	4.9	7.9

Table 5.11: Systematic uncertainties arising from α_s, for the $WH \rightarrow \ell\nu b\bar{b}$ analysis, with $m_H = 125$ GeV, calculated using the 'aMC@NLO' sample set.

5.4.3 Conclusion

Systematic uncertainties arising from α_s have been calculated and are shown in tables 5.10 and 5.11. Both sets of results are equally valid, however if the results are to be combined with the aMC@NLO PDF systematic uncertainties calculated in section 5.3 then for consistency the aMC@NLO α_s systematic uncertainties should be used. This allows, for example, non-linear estimation methods to be used with the NNPDF PDF sets, when estimating combined uncertainties from PDFs and α_s. The combination of PDF and α_s systematic uncertainties is discussed in section 5.5.

For two and three-jet final states, the uncertainty on the inclusive cross-section $\delta_{\sigma_{\text{inclusive}}} = 2.3\%$, the uncertainty on the cross section after analysis selection criteria have been applied $\delta_{\sigma_{\text{asc}}} = 6.9\%$, and the uncertainty on signal acceptance $\delta_A = 6.6\%$.

5.5 Combination Of Uncertainties Arising From Parton Distribution Functions And α_s

5.5.1 Introduction

If we assume that systematic uncertainties arising from PDFs (section 5.3) are independent of systematic uncertainties arising from α_s (section 5.4), then we can combine these uncertainties by summing them in quadrature. For a variable X then,

$$\Delta_X\left(\text{PDF}, \alpha_s\right) = \sqrt{\left(\Delta_X\left(\text{PDF}\right)\right)^2 + \left(\Delta_X\left(\alpha_s\right)\right)^2} \tag{5.32}$$

where $\Delta_X\left(\text{PDF}\right)$ has been evaluated at a fixed value of $\alpha_s(m_Z)$, and $\Delta_X\left(\alpha_s\right)$ has been evaluated using a fixed PDF set type.

In sections 5.3 and 5.4, asymmetric uncertainties for $\Delta_X\left(\text{PDF}\right)$ and $\Delta_X\left(\alpha_s\right)$ have been calculated. The appropriate asymmetric quadratic combinations are then:

$$\Delta_X^+\left(\text{PDF}, \alpha_s\right) = \sqrt{\left(\Delta_X^+\left(\text{PDF}\right)\right)^2 + \left(\Delta_X^+\left(\alpha_s\right)\right)^2} \tag{5.33}$$

and

$$\Delta_X^-\left(\text{PDF}, \alpha_s\right) = \sqrt{\left(\Delta_X^-\left(\text{PDF}\right)\right)^2 + \left(\Delta_X^-\left(\alpha_s\right)\right)^2} \tag{5.34}$$

For the CT10nlo and MSTW2008 PDF sets, this method of PDF and α_s uncertainty combination is used. This is the only method available for the CT10nlo PDF sets, as a PDF error set (thus suitable for calculating $\Delta_X\left(\text{PDF}\right)$) is only available for one value of $\alpha_s(m_Z)$, and only central member PDFs are available for other values of $\alpha_s(m_Z)$ (this range of PDF sets, corresponding to a range of $\alpha_s(m_Z)$, being suitable for calculating $\Delta_X\left(\alpha_s\right)$). There is not sufficient information available to estimate the correlation between $\Delta_X\left(\text{PDF}\right)$ and $\Delta_X\left(\alpha_s\right)$.

If we do not make the assumption that $\Delta_X\left(\text{PDF}\right)$ and $\Delta_X\left(\alpha_s\right)$ are independent, then for the NNPDF2.3 PDF sets we can calculate $\Delta_X(\text{PDF}, \alpha_s)$ by the following method: NNPDF2.3 PDF sets are available for 11 different values of $\alpha_s(m_Z)$, and each PDF set contains a replica-type error-set (section 2.3.4).

A variable of interest X is calculated with (or reweighted to) each of the replica PDFs of the NNPDF2.3 PDF sets. These X values are then averaged, X with each value weighted depending to its corresponding $\alpha_s(m_Z)$ value, and the standard deviation on this average calculated. The average, $\langle X \rangle$, is,

$$\langle X \rangle = \frac{1}{S} \sum_{i=1}^{P} \sum_{j=1}^{n} W_i \; X\left(\mathrm{PDF}_{ij}, \alpha_s(m_Z)_i\right) \tag{5.35}$$

with,

$$S = \sum_{i=1}^{P} \sum_{j=1}^{n} W_i \tag{5.36}$$

where P is the number of PDF sets used. n is the number of PDFs in each error set. $P = 11$ and $n = 100$ for NNPDF2.3. $\alpha_s(m_Z)_i$ is the $\alpha_s(m_Z)$ value used in the construction of the ith PDF set. PDF_{ij} is the jth PDF in the error set of the ith PDF set. $X(\mathrm{PDF}_{ij}, \alpha_s(m_Z)_i)$ is the value of X calculated with (or reweighted to) PDF PDF_{ij}.

The weight W_i is the probability of $\alpha_s(m_Z)_i$ as given by the probability density function of $\alpha_s(m_Z)$. The probability density function of $\alpha_s(m_Z)$ is assumed to be a Gaussian centred around $\alpha_s(m_Z)_0$ with a standard deviation of $\Delta\alpha_s = 0.0012$. $\alpha_s(m_Z)_0 = 0.119$ for NNPDF2.3. The weight W_i is therefore equal to the probability density function of this Gaussian:

$$W_i = \exp\left(-\frac{\left(\alpha_s(m_Z)_i - \alpha_s(m_Z)_0\right)^2}{2\left(\Delta\alpha_s\right)^2} \right) \tag{5.37}$$

The standard deviation on $\langle X \rangle$ is then,

$$\Delta_X = \sqrt{\frac{1}{S-1} \sum_{i=1}^{P} \sum_{j=1}^{n} W_i \left(X\left(\mathrm{PDF}_{ij}, \alpha_s(m_Z)_i\right) - \langle X \rangle \right)^2} \tag{5.38}$$

This standard deviation is the $\pm 1\sigma$ uncertainty due to PDFs and α_s, $\Delta_X(\mathrm{PDF}, \alpha_s)$.

Both the linear and non-linear methods of estimating Δ_X can be calculated for NNPDF2.3. Differences between these results will indicate the extent of the

nonlinearity of the uncertainties due to Δ_X (PDF) and Δ_X (α_s) in NNPDF2.3.

Combination Of PDF Sets

For a given sample set, the overall combined uncertainty Δ_X due to PDFs and α_s is calculated as follows:

$$\begin{aligned} X_{\text{Upper}} = \max\big[& \Delta_X^+(\text{CT10nlo}) + X_0(\text{CT10nlo}) \ , \\ & \Delta_X^+(\text{MSTW2008}) + X_0(\text{MSTW2008}) \ , \\ & \Delta_X(\text{NNPDF2.3}) + X_0(\text{NNPDF2.3}) \ \big] \end{aligned} \tag{5.39}$$

$$\begin{aligned} X_{\text{Lower}} = \min\big[& X_0(\text{CT10nlo}) - \Delta_X^-(\text{CT10nlo}) \ , \\ & X_0(\text{MSTW2008}) - \Delta_X^-(\text{MSTW2008}) \ , \\ & X_0(\text{NNPDF2.3}) - \Delta_X(\text{NNPDF2.3}) \ \big] \end{aligned} \tag{5.40}$$

$$X_{\text{Mid}} = \frac{X_{\text{Upper}} + X_{\text{Lower}}}{2} \tag{5.41}$$

and so,

$$\Delta_X = X_{\text{Upper}} - X_{\text{Mid}} \tag{5.42}$$

Samples Generated And Tested

Combinations of samples used to calculate combined PDF and α_s systematic uncertainties are listed in table 5.12.

Sample set	PDF uncertainties event generators	α_s uncertainties event generators	NNPDF2.3 combination type	NNPDF2.3 nonlinear reweighting method
A	aMC@NLO + Herwig++	Powheg_Box + Pythia8	linear	N/A
B	aMC@NLO + Herwig++	aMC@NLO + Herwig++	linear	N/A
C	aMC@NLO + Herwig++	aMC@NLO + Herwig++	nonlinear	LHAPDF
D	aMC@NLO + Herwig++	aMC@NLO + Herwig++	nonlinear	aMC@NLO internal

Table 5.12: Samples used in the estimation of combined systematic uncertainties arising from PDFs and α_s. A='aMC@NLO PDF + Powheg α_s linear'. B='aMC@NLO PDF + aMC@NLO α_s linear'. C='aMC@NLO PDF + aMC@NLO α_s nonlinear LHAPDF'. D='aMC@NLO PDF + aMC@NLO α_s nonlinear internal'.

All sample sets use linear PDF and α_s combinations for the CT10nlo and MSTW2008 PDF sets, using results as derived in sections 5.3 and 5.4. The samples sets using linear NNPDF2.3 combination also use PDF and α_s NNPDF2.3 results as derived in sections 5.3 and 5.4. The sample sets using nonlinear NNPDF2.3 combination make use of equation 5.38 and its associated method, with either LHAPDF or aMC@NLO's internal reweighting method to reweight generated events to different NNPDF2.3 PDFs.

5.5.2 Results

Cross-Sections And Acceptances

Figure 5.37 shows signal cross-section $m_{b\bar{b}}$ distributions without analysis selection criteria applied. Figure 5.38 shows the equivalent distributions with analysis selection criteria applied for two and three-jet final states combined. Figure 5.39 shows signal acceptance for two and three-jet final states combined. Further cross-section and acceptance plots are found in appendix D.1.1.

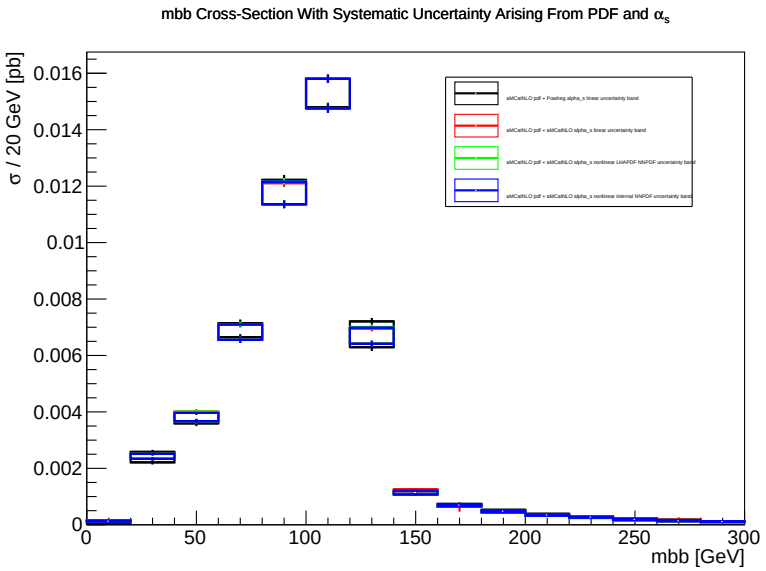

Figure 5.37: $m_{b\bar{b}}$ distributions, for the $WH \to \ell\nu b\bar{b}$ analysis, with $m_H = 125$ GeV, without analysis selection criteria applied, for different samples sets. Systematic uncertainty is shown as a band for each sample set. Error bars on each band show the statistical uncertainty.

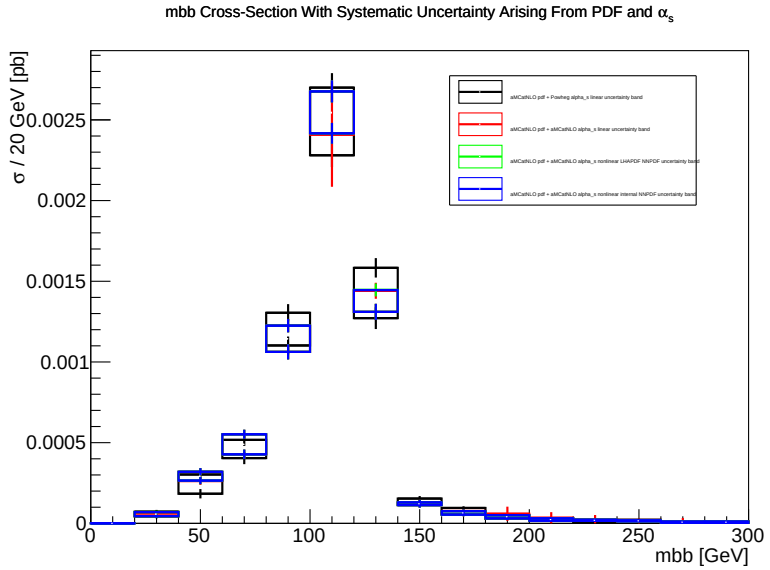

Figure 5.38: $m_{b\bar{b}}$ distributions, for the $WH \to \ell\nu b\bar{b}$ analysis, with $m_H = 125$ GeV, with analysis selection criteria applied, for different samples sets. Two and three-jet final states are included. Systematic uncertainty is shown as a band for each sample set. Error bars on each band show the statistical uncertainty.

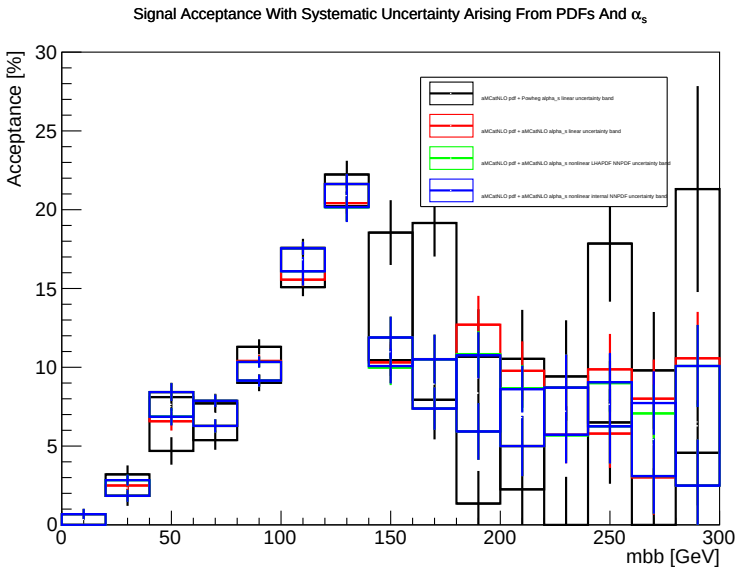

Figure 5.39: Signal acceptance, for the $WH \to \ell\nu b\bar{b}$ analysis, with $m_H = 125$ GeV, for different samples sets. Two and three-jet final states are included. Systematic uncertainty is shown as a band for each sample set. Error bars on each band show the statistical uncertainty.

Uncertainties

Figure 5.40 shows systematic uncertainties on signal cross-section $m_{b\bar{b}}$ distributions without analysis selection criteria applied. Figure 5.41 shows the equivalent distributions with analysis selection criteria applied. Figure 5.42 shows systematic uncertainties on signal acceptance. Equivalent distributions for two-jet and three-jet final states are shown in appendix D.1.2.

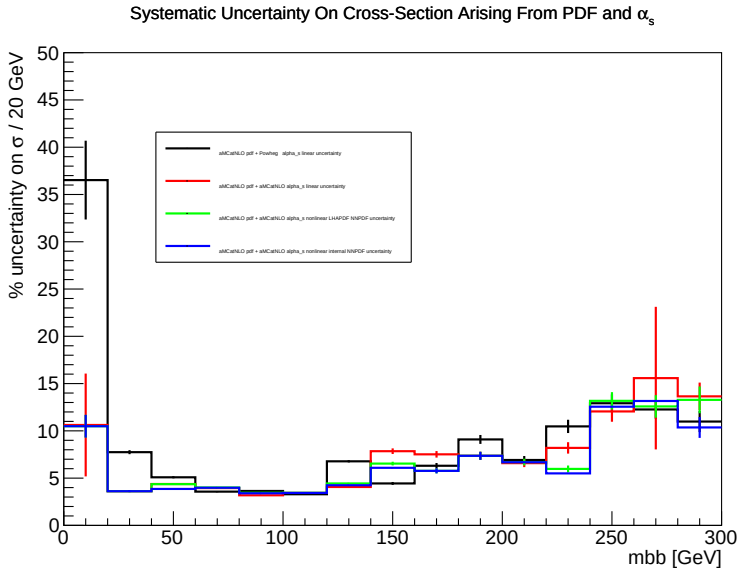

Figure 5.40: Systematic uncertainties on signal cross-section, for the $WH \to \ell\nu b\bar{b}$ analysis, with $m_H = 125$ GeV, without analysis selection criteria applied, for different sample sets. Error bars show statistical uncertainty.

When considering uncertainties, only a region with a large number of events is chosen: the $m_{b\bar{b}}$ range of 60 GeV to 140 GeV around the Higgs mass peak. In this region, no clear dependence of the uncertainties on $m_{b\bar{b}}$ is seen. An average value for each uncertainty, for each sample set, is therefore calculated within the range of 60 GeV $\geq m_{b\bar{b}} \geq$ 140 GeV.

Averaged systematic uncertainties are shown for the 'aMC@NLO PDF + Powheg α_s linear' sample set in table 5.13, for the 'aMC@NLO PDF + aMC@NLO α_s linear' sample set in table 5.14, the 'aMC@NLO PDF + aMC@NLO α_s nonlinear LHAPDF' sample set in table 5.15, and the 'aMC@NLO PDF + aMC@NLO α_s nonlinear internal' sample set in table 5.16.

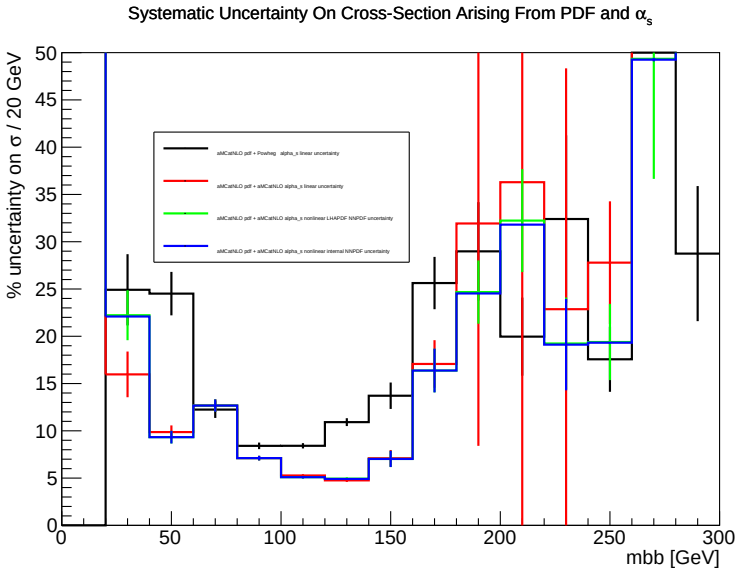

Figure 5.41: Systematic uncertainties on signal cross-section, for the $WH \to \ell\nu b\bar{b}$ analysis, with $m_H = 125$ GeV, with analysis selection criteria applied, for different sample sets. Two and three-jet final states are included. Error bars show statistical uncertainty.

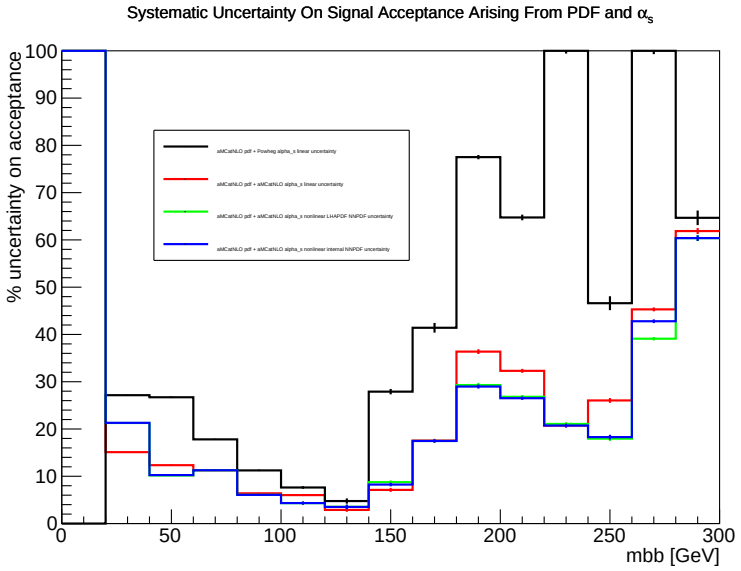

Figure 5.42: Systematic uncertainties on signal acceptance, for the $WH \to \ell\nu b\bar{b}$ analysis, with $m_H = 125$ GeV, for different sample sets. Two and three-jet final states are included. Error bars show statistical uncertainty.

N_{jets} bin	$\sigma_{\text{inclusive}}$ [pb]	$\delta_{\sigma_{\text{inclusive}}}$ [%]	σ_{asc} [pb]	$\delta_{\sigma_{\text{asc}}}$ [%]	A [%]	δ_A [% of A]
2 and 3	0.0344	4.3	0.00527	10.0	15.3	10.4
2	0.0344	4.3	0.00360	12.3	10.5	13.5
3	0.0344	4.3	0.00167	16.2	4.9	18.6

Table 5.13: Systematic uncertainties arising from PDFs and α_s combined, for the $WH \to \ell\nu b\bar{b}$ analysis, with $m_H = 125$ GeV, calculated using the 'aMC@NLO PDF + Powheg α_s linear' sample set.

N_{jets} bin	$\sigma_{\text{inclusive}}$ [pb]	$\delta_{\sigma_{\text{inclusive}}}$ [%]	σ_{asc} [pb]	$\delta_{\sigma_{\text{asc}}}$ [%]	A [%]	δ_A [% of A]
2 and 3	0.0403	3.7	0.00551	7.5	13.6	6.6
2	0.0403	3.7	0.00353	9.9	8.8	8.9
3	0.0403	3.7	0.00197	9.1	4.9	7.9

Table 5.14: Systematic uncertainties arising from PDFs and α_s combined, for the $WH \to \ell\nu b\bar{b}$ analysis, with $m_H = 125$ GeV, calculated using the 'aMC@NLO PDF + aMC@NLO α_s linear' sample set.

N_{jets} bin	$\sigma_{\text{inclusive}}$ [pb]	$\delta_{\sigma_{\text{inclusive}}}$ [%]	σ_{asc} [pb]	$\delta_{\sigma_{\text{asc}}}$ [%]	A [%]	δ_A [% of A]
2 and 3	0.0403	3.8	0.00551	7.5	13.6	6.3
2	0.0403	3.8	0.00353	9.4	8.8	7.9
3	0.0403	3.8	0.00197	7.7	4.9	7.3

Table 5.15: Systematic uncertainties arising from PDFs and α_s combined, for the $WH \to \ell\nu b\bar{b}$ analysis, with $m_H = 125$ GeV, calculated using the 'aMC@NLO PDF + aMC@NLO α_s nonlinear LHAPDF' sample set.

N_{jets} bin	$\sigma_{\text{inclusive}}$ [pb]	$\delta_{\sigma_{\text{inclusive}}}$ [%]	σ_{asc} [pb]	$\delta_{\sigma_{\text{asc}}}$ [%]	A [%]	δ_A [% of A]
2 and 3	0.0403	3.8	0.00551	7.4	13.6	6.3
2	0.0403	3.8	0.00353	9.4	8.8	7.9
3	0.0403	3.8	0.00197	7.6	4.9	7.3

Table 5.16: Systematic uncertainties arising from PDFs and α_s combined, for the $WH \to \ell\nu b\bar{b}$ analysis, with $m_H = 125$ GeV, calculated using the 'aMC@NLO PDF + aMC@NLO α_s nonlinear internal' sample set.

5.5.3 Conclusion

Combined systematic uncertainties arising from PDFs and α_s have been calculated and are shown in tables 5.13, 5.14, 5.15, 5.16. For consistency in using the same event generator for both PDFs and α_s uncertainty calculations, the 'aMC@NLO PDF + Powheg α_s linear' sample set results are discarded. Small differences are seen between the 'aMC@NLO PDF + aMC@NLO α_s linear' results

that use linear NNPDF2.3 combination, and the 'aMC@NLO PDF + aMC@NLO α_s nonlinear LHAPDF' and 'aMC@NLO PDF + aMC@NLO α_s nonlinear internal' results that use linear NNPDF2.3 combination. This indicates that systematic uncertainties arising from PDFs and α_s are not linearly independent. The results that use linear NNPDF2.3 combination are therefore discarded.

For the 'aMC@NLO PDF + aMC@NLO α_s nonlinear internal' sample set results, all reweighted events were generated in the same sample, since reweighting is only done for the NNPDF2.3 PDF set. This avoids introducing statistical uncertainties into the results as seen in section 5.3. Either the 'aMC@NLO PDF + aMC@NLO α_s nonlinear LHAPDF' or the 'aMC@NLO PDF + aMC@NLO α_s nonlinear internal' results can therefore be used. For consistency in reweighting methods, since the PDF results calculated in section 5.3 use LHAPDF reweighting, so the results here that use LHAPDF reweighting for the nonlinear NNPDF2.3 combination shall be used. The results shown for the 'aMC@NLO PDF + aMC@NLO α_s nonlinear LHAPDF' sample set in table 5.15 are therefore taken to be the best estimates of the true combined systematic uncertainties arising from PDFs and α_s.

As $\sigma_{\text{inclusive}}$ and $\delta_{\sigma_{\text{inclusive}}}$ are unaffected by jet-bin choice (by definition), a more accurate calculation of the uncertainty $\delta_{\sigma_{\text{inclusive}}}$ can be used. In [98] the uncertainty on the inclusive WH cross section is calculated to NNLO in QCD and NLO in electroweak perturbative expansion, and is given as $\delta_{\sigma_{\text{inclusive}}} = 2.3\%$. This is compared to the results presented in this chapter, which have been calculated to NLO in QCD and electroweak perturbative expansion.

For two and three-jet final states, the uncertainty on the inclusive cross-section $\delta_{\sigma_{\text{inclusive}}} = 2.3\%$, the uncertainty on the cross section after analysis selection criteria have been applied $\delta_{\sigma_{\text{asc}}} = 7.5\%$, and the uncertainty on signal acceptance $\delta_A = 6.3\%$.

5.6 Uncertainties Arising From Parton Showering And Hadronisation

5.6.1 Introduction

Initial And Final-State Radiation Parton Showering

Initial-state radiation (ISR) and final-state radiation (FSR) are both processes modelled with parton showering. These modelling processes have systematic uncertainties associated with them. Uncertainties arising from ISR and FSR modelling can be estimated by comparing simulations with these processes switched on and off. However, switching off ISR and FSR will affect other processes in Monte Carlo simulations, such as hadronisation. To better understand the effects of parton shower modelling, one can consider different models available. The difference between the predictions of different models will give an indication of the uncertainty due to this modelling. Parton shower models can largely be divided into two types: angular-ordered models and $k_\perp$-ordered dipole models.

Angular-ordered models

These models consider the probability for any single parton to emit another parton in a $1 \rightarrow 2$ body process. They order emissions by emission angle θ, the angle between an emitted parton and the parton that has emitted it. For a given parton, the first parton that it emits will have the largest value of θ. These types of parton showering models are thus known as angular-ordered parton shower models.

$k_\perp$-ordered dipole models

These parton showering models consider colour connections between partons, where two partons connected by a colour line make up a colour 'dipole'. This colour line can emit partons, thus making this a $2 \rightarrow 3$ body process. The emitted parton will have a non-zero $k_\perp$, the momentum of the emitted parton perpendicular to the axis of the colour line that has emitted it. Since a gluon will be connected to two partons by colour lines, if one colour line emits a parton, which will cause the gluon to recoil, this may affect subsequent emissions from the other colour line. Due to this interconnection

between many partons through colour lines, the parton showering of the entire event must be evolved as one process. At any given point in the evolution of a parton shower by this method, the next emission will be the emission with the largest $k_\perp$. These types of parton showering models are thus known as $k_\perp$-ordered dipole parton shower models.

α_s effects on parton showering

Parton showers are affected by variations in α_s. If α_s is increased (decreased) then the probability of emission of colour-charged particles is increased (decreased), thus emissions will occur more (less) frequently. Additionally, varying α_s will have non-trivial effects on the energy and momentum of an emitted particle. However, the uncertainty on parton showering due to α_s variation is included in uncertainties due to α_s (sections 5.4 and 5.5). Further parton shower modelling effects are therefore dealt with separately.

Hadronisation

All hadronisation models can be sorted into one of two categories: models based on the Lund string model [107, 108], and models based on colour clustering [108, 109]. If these two types of models are considered to be equally valid, then by comparing results using different types of models, an estimate of the systematic uncertainties arising from hadronisation modelling can be obtained. Two Monte Carlo samples are generated, one using a Lund string model for hadronisation, and the other using a colour clustering model for hadronisation. Results between the two samples are then compared.

Samples Generated And Tested

Systematic uncertainties arising from parton showering and hadronisation are considered together, to allow for possible correlation. To do this, the samples listed in table 5.17 were generated. 100000 events were generated for each sample. Both samples use the Powheg method for NLO hard subprocess generation, one with Powheg_Box, and the other with Herwig++'s internal implementation of the Powheg method.

Sample set	Hard subprocess event generator	Showering event generator	Generated with PDF	Parton shower model used	Hadronisation model used
'Powheg+Pythia8'	Powheg_Box	Pythia8	CT10nlo CM	Dipole	Lund string
'Herwig++'	Herwig++ (internal NLO Powheg method)	Herwig++	CT10nlo CM	Angular-ordered	Colour-clustering

Table 5.17: Monte Carlo samples generated for the estimation of systematic uncertainties arising from parton showering and hadronisation. 'CM' means the **C**entral **M**ember of the PDF set.

For a variable X, we can compute the uncertainty,

$$\Delta X = \frac{|X(\text{Powheg+Pythia8}) \; - \; X(\text{Herwig++})|}{2} \tag{5.43}$$

5.6.2 Results

Cross-Sections And Acceptances

Figure 5.43 shows signal cross-section $m_{b\bar{b}}$ distributions without analysis selection criteria applied. Figure 5.44 shows the equivalent distributions with analysis selection criteria applied for two and three-jet final states combined. Figure 5.45 shows signal acceptance for two and three-jet final states combined. Further cross-section and acceptance plots are found in appendix E.1.1.

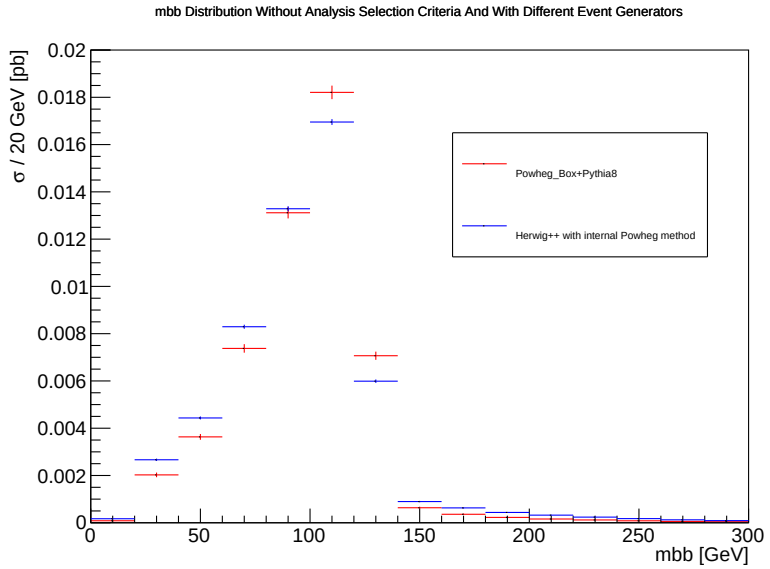

Figure 5.43: $m_{b\bar{b}}$ distributions, for the $WH \to \ell\nu b\bar{b}$ analysis, with $m_H = 125$ GeV, without analysis selection criteria applied, for different samples sets. Error bars show statistical uncertainty.

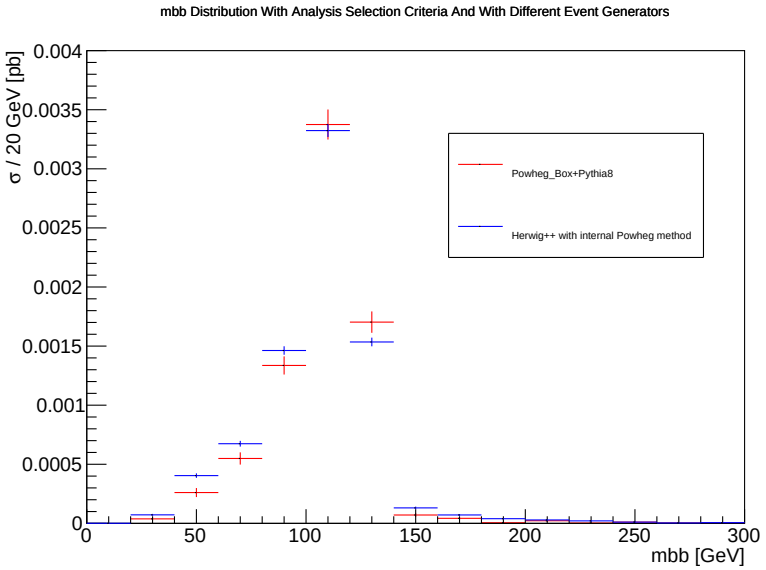

Figure 5.44: $m_{b\bar{b}}$ distributions, for the $WH \to \ell\nu b\bar{b}$ analysis, with $m_H = 125$ GeV, with analysis selection criteria applied, for different samples sets. Two and three-jet final states are included. Error bars show statistical uncertainty.

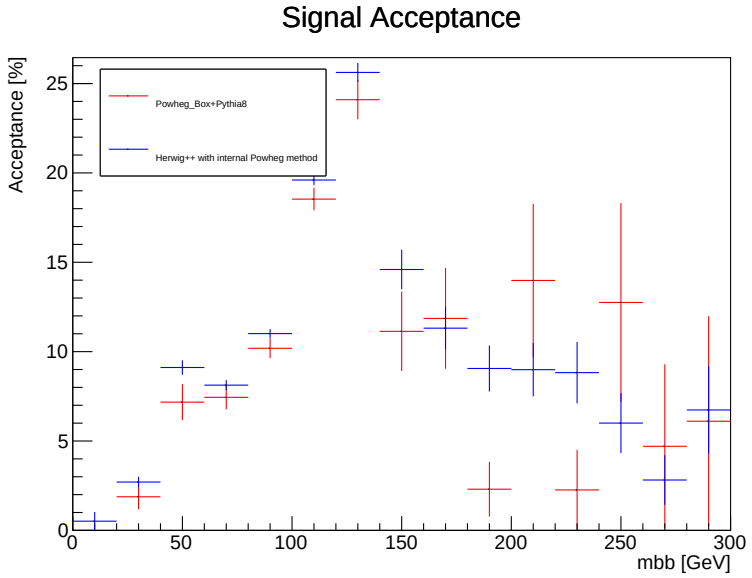

Figure 5.45: Signal acceptance, for the $WH \to \ell\nu b\bar{b}$ analysis, with $m_H = 125$ GeV, for different samples sets. Two and three-jet final states are included. Error bars show statistical uncertainty.

Uncertainties

For two and three-jet final states, figure 5.46 shows systematic uncertainties on signal cross-section with and without analysis selection criteria applied, as well

as systematic uncertainties on signal acceptance. Equivalent distributions for two-jet and three-jet final states are shown in appendix E.1.2.

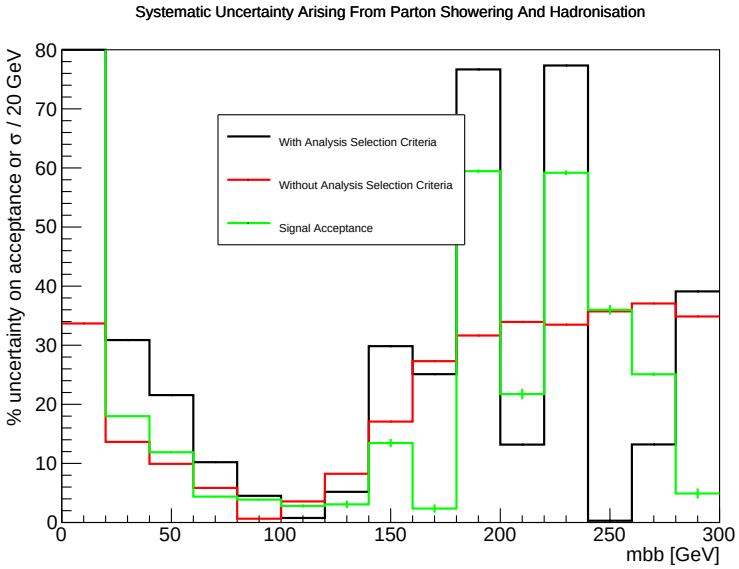

Figure 5.46: Systematic uncertainties on signal cross-section, for the $WH \to \ell\nu b\bar{b}$ analysis, with $m_H = 125$ GeV, with and without analysis selection criteria applied, and acceptance. Two and three-jet final states are included. Error bars show statistical uncertainty.

When considering uncertainties, only a region with a large number of events is chosen: the $m_{b\bar{b}}$ range of 60 GeV to 140 GeV around the Higgs mass peak. In this region, no clear dependence of the uncertainties on $m_{b\bar{b}}$ is seen. An average value for each uncertainty, for each sample set, is therefore calculated within the range of 60 GeV $\geq m_{b\bar{b}} \geq$ 140 GeV.

Averaged systematic uncertainties are shown in table 5.18.

N_{jets} bin	$\sigma_{\text{inclusive}}$ $[pb]$	$\delta_{\sigma_{\text{inclusive}}}$ [%]	σ_{asc} $[pb]$	$\delta_{\sigma_{\text{asc}}}$ [%]	A [%]	δ_A [% of A]
2 and 3	0.0458	4.6	0.00696	5.2	15.1	3.5
2	0.0458	4.6	0.00472	7.9	10.1	6.6
3	0.0458	4.6	0.00224	2.7	5.0	2.4

Table 5.18: Systematic uncertainties arising from parton showering and hadronisation, for the $WH \to \ell\nu b\bar{b}$ analysis, with $m_H = 125$ GeV.

5.6.3 Conclusion

Combined systematic uncertainties arising from parton showering and hadronisation have been calculated and are shown in table 5.18. These results are taken to be the best estimates of the true combined systematic uncertainties arising from parton showering and hadronisation.

For two and three-jet final states, the uncertainty on the inclusive cross-section $\delta_{\sigma_{\text{inclusive}}} = 4.6\%$, the uncertainty on the cross section after analysis selection criteria have been applied $\delta_{\sigma_{\text{asc}}} = 5.2\%$, and the uncertainty on signal acceptance $\delta_A = 3.5\%$.

5.7 Uncertainties Arising From The Underlying Event

5.7.1 Introduction

The underlying event, also known as multi-parton interactions (MPI), adds low-energy activity to an event. We must therefore understand how MPI modelling affects our final results, and estimate systematic uncertainties on our final results due to this modelling.

Scaling MPI Uncertainty Estimation Method

One way to investigate the effects of MPI modelling is to vary the MPI activity, and observe the effects of these variations on variables of interest. In Pythia 8, MPI activity can be adjusted by varying the `MultipartonInteractions:ecmPow` (`ecmPow` for short) parameter. Increasing (decreasing) `ecmPow` decreases (increases) MPI activity in the generated events. In the AU2 (**A**TLAS **U**nderlying Event Tune **2**) tune used in this analysis, the default value for `ecmPow` = 0.16.

To estimate the systematic uncertainties arising from MPI, `ecmPow` is varied by factors of $\frac{1}{2}$ and 2. Three samples are produced: one with 'normal' MPI activity (`ecmPow` = 0.16), one with increased ('scaled up') MPI activity (`ecmPow` = 0.08), and one with decreased ('scaled down') MPI activity (`ecmPow` = 0.32). The resulting overall change in a variable of interest X is taken as twice the uncertainty on X due to these variations in MPI activity:

$$X^{+} = \max\left[\, X(\text{MPI Scale Up}) \,,\; X(\text{MPI Scale Normal}) \,,\; X(\text{MPI Scale Down}) \,\right] \tag{5.44}$$

$$X^{-} = \min\left[\, X(\text{MPI Scale Up}) \,,\; X(\text{MPI Scale Normal}) \,,\; X(\text{MPI Scale Down}) \,\right] \tag{5.45}$$

$$\Delta_X = \frac{X^{+} - X^{-}}{2} \tag{5.46}$$

On-Off MPI Uncertainty Estimation Method

A simple way to investigate the effects of MPI modelling is to switch this modelling on and off. Due to the extreme nature of entirely switching off MPI modelling in event generation, this method can only be used to set conservative upper limits on the systematic uncertainties arising from MPI. The on-off method has been used to estimate systematic uncertainties arising from MPI, and this is detailed in appendix F.2, allowing for comparison with the MPI scaling method.

Plateau Height Retuning MPI Uncertainty Estimation Method

A more robust method for estimating systematic uncertainties arising from MPI is the plateau-height retuning method. Due to the added complexity of this method, requiring event generator tuning, it has not been employed in the following results. It is, however, described in appendix F.1.

Samples Generated And Tested

The plateau-height retuning method, due to the added complexity of retuning, has not been employed in the following results. The MPI scaling method is a more robust method for estimating systematic uncertainties arising from the underlying event than the on-off method. The MPI scaling method is therefore used in the following results. Three samples were generated in order to study systematic uncertainties arising from the underlying event. They are listed in table 5.19. Uncertainties are calculated according to equation 5.46.

Sample set	Hard subprocess event generator	Showering event generator	Generated with PDF	`ecmPow`
'MPI Scale Normal'	Powheg_Box	Pythia8	CT10nlo CM	0.16
'MPI Scale Up'	Powheg_Box	Pythia8	CT10nlo CM	0.08
'MPI Scale Down'	Powheg_Box	Pythia8	CT10nlo CM	0.32

Table 5.19: Monte Carlo samples generated for the estimation of systematic uncertainties arising from the underlying event with the MPI scaling method. 'CM' means the **C**entral **M**ember of the PDF set.

5.7.2 Results

Cross-Sections And Acceptances

Figure 5.47 shows signal cross-section $m_{b\bar{b}}$ distributions without analysis selection criteria applied. Figure 5.48 shows the equivalent distributions with analysis selection criteria applied for two and three-jet final states combined. Figure 5.49 shows signal acceptance for two and three-jet final states combined. Further cross-section and acceptance plots are found in appendix F.3.1.

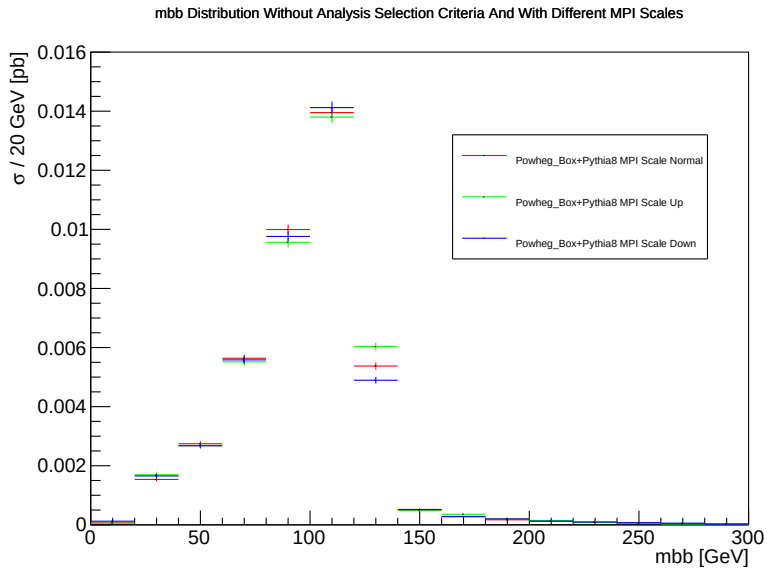

Figure 5.47: $m_{b\bar{b}}$ distributions, for the $WH \to \ell\nu b\bar{b}$ analysis, with $m_H = 125$ GeV, without analysis selection criteria applied, for different samples sets. Error bars show statistical uncertainty.

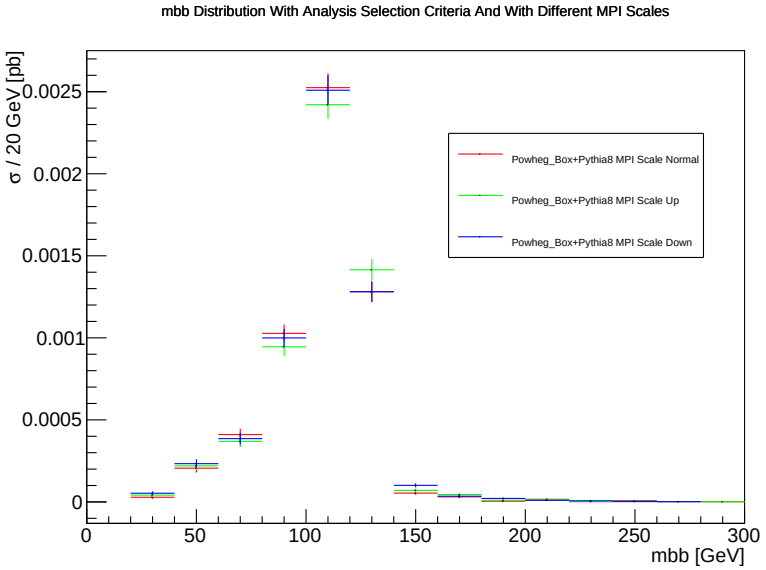

Figure 5.48: $m_{b\bar{b}}$ distributions, for the $WH \to \ell\nu b\bar{b}$ analysis, with $m_H = 125$ GeV, with analysis selection criteria applied, for different samples sets. Two and three-jet final states are included. Error bars show statistical uncertainty.

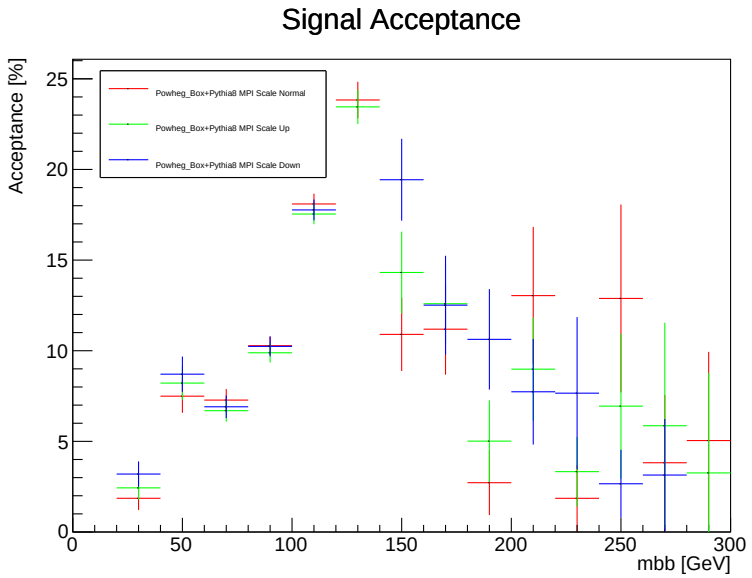

Figure 5.49: Signal acceptance, for the $WH \to \ell\nu b\bar{b}$ analysis, with $m_H = 125$ GeV, for different samples sets. Two and three-jet final states are included. Error bars show statistical uncertainty.

Uncertainties

For two and three-jet final states, figure 5.50 shows systematic uncertainties on signal cross-section with and without analysis selection criteria applied, as well as systematic uncertainties on signal acceptance. Equivalent distributions for two-jet and three-jet final states are shown in appendix F.3.2.

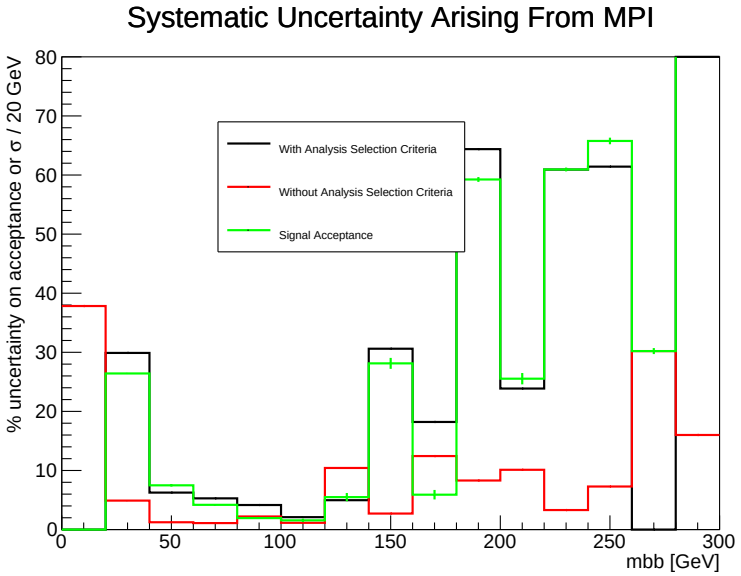

Figure 5.50: Systematic uncertainties on signal cross-section, for the $WH \rightarrow \ell\nu b\bar{b}$ analysis, with $m_H = 125$ GeV, with and without analysis selection criteria applied, and acceptance. Two and three-jet final states are included. Error bars show statistical uncertainty.

When considering uncertainties, only a region with a large number of events is chosen: the $m_{b\bar{b}}$ range of 60 GeV to 140 GeV around the Higgs mass peak. In this region, no clear dependence of the uncertainties on $m_{b\bar{b}}$ is seen. An average value for each uncertainty, for each sample set, is therefore calculated within the range of 60 GeV $\geq m_{b\bar{b}} \geq$ 140 GeV.

Averaged systematic uncertainties are shown in table 5.20.

N_{jets} bin	$\sigma_{\text{inclusive}}$ $[pb]$	$\delta_{\sigma_{\text{inclusive}}}$ [%]	σ_{asc} $[pb]$	$\delta_{\sigma_{\text{asc}}}$ [%]	A [%]	δ_A [% of A]
2 and 3	0.0350	3.7	0.00524	4.1	15.0	3.3
2	0.0350	3.7	0.00356	4.4	10.2	4.6
3	0.0350	3.7	0.00169	6.5	4.8	4.2

Table 5.20: Systematic uncertainties arising from the underlying event, calculated using the MPI scaling method, for the $WH \to \ell\nu b\bar{b}$ analysis, with $m_H = 125$ GeV.

5.7.3 Conclusion

Systematic uncertainties arising from the underlying event have been calculated and are shown in table 5.20. They have been calculated using the MPI scaling method. They are taken to be, for this analysis, the best estimates of the true systematic uncertainties due the underlying event.

For two and three-jet final states, the uncertainty on the inclusive cross-section $\delta_{\sigma_{\text{inclusive}}} = 3.7\%$, the uncertainty on the cross section after analysis selection criteria have been applied $\delta_{\sigma_{\text{asc}}} = 4.3\%$, and the uncertainty on signal acceptance $\delta_A = 3.3\%$.

5.8 Uncertainties Arising From Next To Leading Order Matching

Care must be taken in Monte Carlo particle physics simulations when combining matrix elements of hard subprocesses with parton shower modelling to avoid double counting partonic states, double counting regions of simulation phase space, or under-counting other regions. For example, when calculating matrix elements to NLO in QCD, the matrix element will contain one extra emission, the NLO emission. This extra emission could also be simulated by the parton shower. Care must therefore be taken to not double-count this extra emission parton configuration. Some corrections to the Monte Carlo simulations must therefore be performed in order to match the hard subprocess calculations to the parton shower modelling. With NLO hard subprocess calculations this is referred to as NLO matching. The question then arises as to whether there are systematic uncertainties on our final results arising from this NLO matching process.

Both the Powheg_Box and aMC@NLO programs calculate hard subprocesses to NLO accuracy (and thus have NLO-accurate event kinematics). They also perform NLO matching process in a way that is accurate to $\mathcal{O}(\alpha_s)$ for the cross-section [108]. During the development of the $WH \to \ell\nu b\bar{b}$ analysis (described in chapter 4), different options were considered for which event generators to use to generate $WH \to \ell\nu b\bar{b}$ signal Monte Carlo samples. Both the use of just Pythia 8 (LO), and the use of Powheg_Box combined with Pythia 8 (NLO), were considered. Due to more generated Monte Carlo events being available, Pythia 8 (LO) was used in the final results. As Pythia 8 generates events to LO in QCD, there is no NLO matching, and thus no uncertainty on the final results from NLO matching. For the NLO Monte Carlo samples generated as part of the work presented in this thesis, since they use either Powheg_Box or aMC@NLO, any systematic uncertainties on these samples arising from NLO matching, being of order $\mathcal{O}(\alpha_s)$, are contained within the systematic uncertainties arising from α_s, and therefore do not need to be considered as additional systematic uncertainties on results. Likewise, had Powheg_Box combined with Pythia 8 been chosen to generate the signal samples for the $WH \to \ell\nu b\bar{b}$ analysis, systematic uncertainties arising from NLO matching on these samples would also have been contained within systematic uncertainties arising from α_s.

5.9 Uncertainties Arising From QED Corrections

5.9.1 Introduction

Radiative QED corrections to particle decays - the emission of electromagnetic radiation from leptons - can be modelled by bolt-on programs such as Photos [89], used within Monte Carlo simulations in event generators. Photos is used within the Monte Carlo simulation of the $WH \to \ell\nu b\bar{b}$ process samples used in the analysis described in chapter 4. This modelling of radiative QED corrections will bring with it systematic uncertainties on final results. To investigate this, different QED correction are considered in order to determine their effect on final results. In the case of the $WH \to \ell\nu b\bar{b}$ samples used in the analysis described in chapter 4, Photos is used within the Pythia8 event generator. In order to include Photos in Pythia8, Pythia8's own modelling of radiative QED corrections to particle decays must be switched off. This provides two different models of radiative QED corrections to particle decays: Photos, and Pythia8's internal modelling of radiative QED corrections.

Samples Generated And Tested

Two samples were generated for this study. They are listed in table 5.21. The 'Photos' sample uses the Photos QED corrections. The 'Pythia8' sample uses Pythia8's QED corrections. For a variable X, the value $\Delta X = |X(\text{Photos QED corrections}) - X(\text{Pythia8 QED corrections})|/2$ is computed and taken as an estimate of the systematic uncertainty arising from radiative QED corrections to particle decays.

Sample set	Hard subprocess event generator	Showering event generator	Photos QED corrections	Pythia8's QED corrections
'Photos'	Powheg_Box	Pythia8	Switched on	Switched off
'Pythia8'	Powheg_Box	Pythia8	Switched off	Switched on

Table 5.21: Monte Carlo samples generated for the estimation of systematic uncertainties arising from QED corrections.

5.9.2 Results

Cross-Sections And Acceptances

Figure 5.51 shows signal cross-section $m_{b\bar{b}}$ distributions without analysis selection criteria applied. Figure 5.52 shows the equivalent distributions with analysis selection criteria applied for two and three-jet final states combined. Figure 5.53 shows signal acceptance for two and three-jet final states combined. Further cross-section and acceptance plots are found in appendix G.1.1.

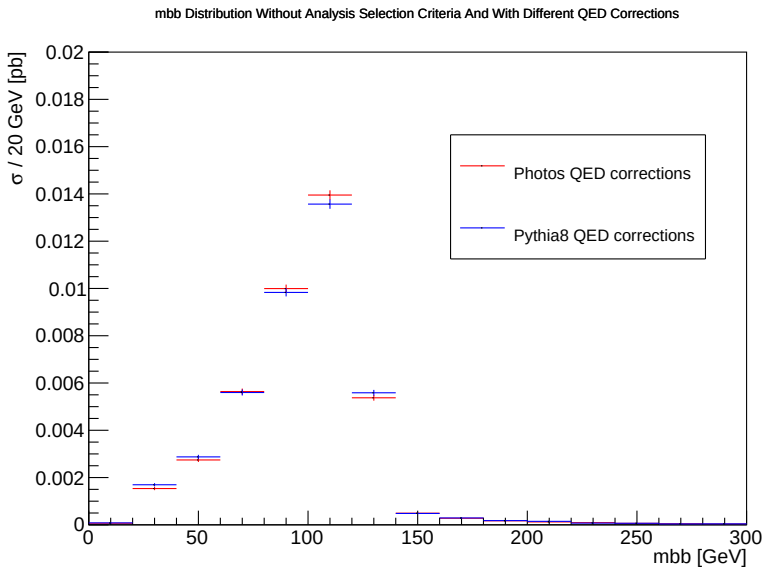

Figure 5.51: $m_{b\bar{b}}$ distributions, for the $WH \to \ell\nu b\bar{b}$ analysis, with $m_H = 125$ GeV, without analysis selection criteria applied, for different samples sets. Error bars show statistical uncertainty.

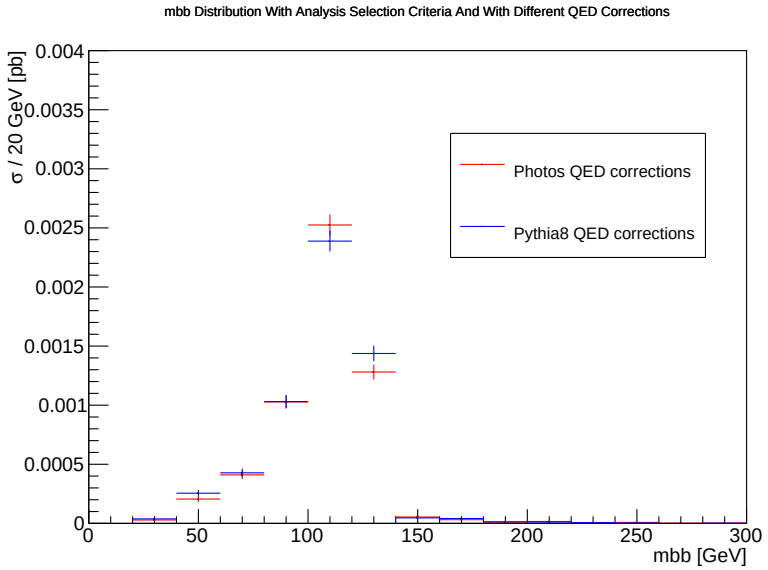

Figure 5.52: $m_{b\bar{b}}$ distributions, for the $WH \to \ell\nu b\bar{b}$ analysis, with $m_H = 125$ GeV, with analysis selection criteria applied, for different samples sets. Two and three-jet final states are included. Error bars show statistical uncertainty.

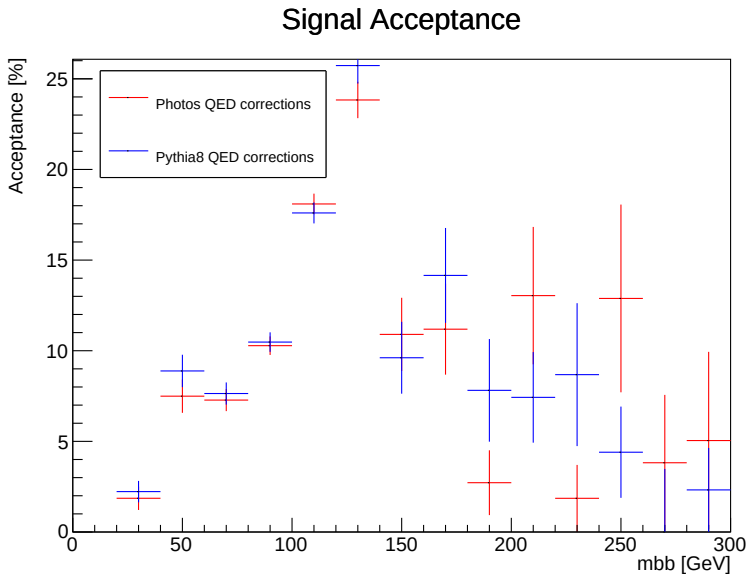

Figure 5.53: Signal acceptance, for the $WH \to \ell\nu b\bar{b}$ analysis, with $m_H = 125$ GeV, for different samples sets. Two and three-jet final states are included. Error bars show statistical uncertainty.

Uncertainties

For two and three-jet final states, figure 5.54 shows systematic uncertainties on signal cross-section with and without analysis selection criteria applied, as well as systematic uncertainties on signal acceptance. Equivalent distributions for two-jet and three-jet final states are shown in appendix G.1.2.

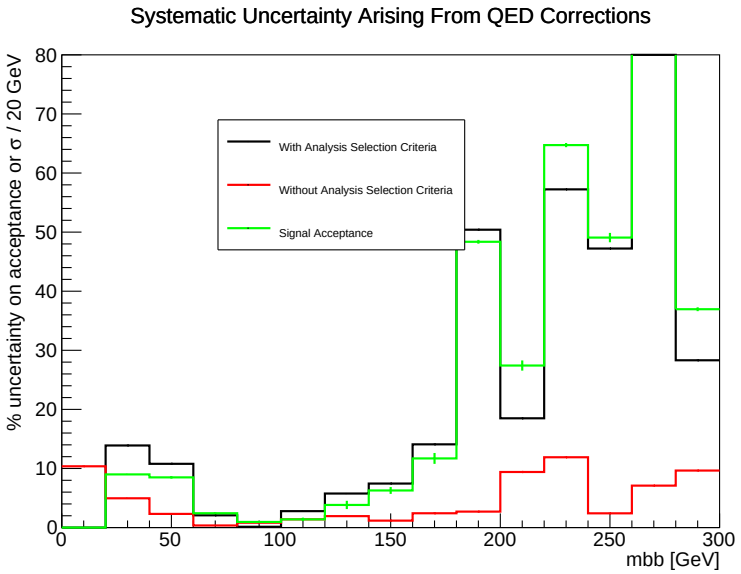

Figure 5.54: Systematic uncertainties on signal cross-section, for the $WH \rightarrow \ell\nu b\bar{b}$ analysis, with $m_H = 125$ GeV, with and without analysis selection criteria applied, and acceptance. Two and three-jet final states are included. Error bars show statistical uncertainty.

When considering uncertainties, only a region with a large number of events is chosen: the $m_{b\bar{b}}$ range of 60 GeV to 140 GeV around the Higgs mass peak. In this region, no clear dependence of the uncertainties on $m_{b\bar{b}}$ is seen. An average value for each uncertainty, for each sample set, is therefore calculated within the range of 60 GeV $\geq m_{b\bar{b}} \geq$ 140 GeV.

Averaged systematic uncertainties are shown in table 5.22.

N_{jets} bin	$\sigma_{\text{inclusive}}$ $[pb]$	$\delta_{\sigma_{\text{inclusive}}}$ [%]	σ_{asc} $[pb]$	$\delta_{\sigma_{\text{asc}}}$ [%]	A [%]	δ_A [% of A]
2 and 3	0.0350	1.1	0.00524	2.7	15.0	2.1
2	0.0350	1.1	0.00356	3.8	10.2	2.9
3	0.0350	1.1	0.00169	4.8	4.8	4.1

Table 5.22: Systematic uncertainties arising from radiative QED corrections, for the $WH \to \ell\nu b\bar{b}$ analysis, with $m_H = 125$ GeV.

5.9.3 Conclusion

Systematic uncertainties arising from radiative QED corrections to particle decays have been calculated and are shown in table 5.22. These results are taken to be the best estimates of the true systematic uncertainties arising from radiative QED corrections to particle decays.

For two and three-jet final states, the uncertainty on the inclusive cross-section $\delta_{\sigma_{\text{inclusive}}} = 1.1\%$, the uncertainty on the cross section after analysis selection criteria have been applied $\delta_{\sigma_{\text{asc}}} = 2.7\%$, and the uncertainty on signal acceptance $\delta_A = 2.1\%$.

5.10 Combination Of Theoretical Uncertainties

The following source of systematic uncertainty is neglected:

- Next to leading order (NLO) matching

as Monte Carlo samples generated as part of this study either do not contain NLO matching, or, where they do, systematic uncertainties arising from this source are contained within systematic uncertainties arising from α_s uncertainty.

The remaining sources of systematic uncertainty are:

- Scale factors
- Parton distribution functions and α_s combined
- Initial and final-state radiation parton showering, and hadronisation, combined
- The underlying event
- Radiative QED corrections to particle decays

The estimates of these uncertainties, as discussed in this chapter, are repeated here for clarity.

Uncertainties arising from scale factors, from section 5.2:

N_{jets} bin	$\sigma_{\text{inclusive}}$ $[pb]$	$\delta_{\sigma_{\text{inclusive}}}$ [%]	σ_{asc} $[pb]$	$\delta_{\sigma_{\text{asc}}}$ [%]	A [%]	δ_A [% of A]
2 and 3	0.0350	2.5	0.00524	4.3	15.0	5.3
2	0.0350	2.5	0.00356	9.8	10.2	10.4
3	0.0350	2.5	0.00169	10.9	4.8	11.2

Table 5.23: Systematic uncertainties arising from scale factors, for the $WH \to \ell\nu b\bar{b}$ analysis, with $m_H = 125$ GeV, taking account of logarithmic cancellations.

Combined uncertainties arising from parton distribution functions and α_s, from section 5.5:

N_{jets} bin	$\sigma_{\text{inclusive}}$ $[pb]$	$\delta_{\sigma_{\text{inclusive}}}$ [%]	σ_{asc} $[pb]$	$\delta_{\sigma_{\text{asc}}}$ [%]	A [%]	δ_A [% of A]
2 and 3	0.0403	3.8	0.00551	7.5	13.6	6.3
2	0.0403	3.8	0.00353	9.4	8.8	7.9
3	0.0403	3.8	0.00197	7.7	4.9	7.3

Table 5.24: Systematic uncertainties arising from PDFs and α_s combined, for the $WH \to \ell\nu b\bar{b}$ analysis, with $m_H = 125$ GeV, calculated using the 'aMC@NLO PDF + aMC@NLO α_s nonlinear LHAPDF' sample set.

Combined uncertainties arising from parton showering and hadronisation, from section 5.6:

N_{jets} bin	$\sigma_{\text{inclusive}}$ $[pb]$	$\delta_{\sigma_{\text{inclusive}}}$ [%]	σ_{asc} $[pb]$	$\delta_{\sigma_{\text{asc}}}$ [%]	A [%]	δ_A [% of A]
2 and 3	0.0458	4.6	0.00696	5.2	15.1	3.5
2	0.0458	4.6	0.00472	7.9	10.1	6.6
3	0.0458	4.6	0.00224	2.7	5.0	2.4

Table 5.25: Systematic uncertainties arising from parton showering and hadronisation, for the $WH \to \ell\nu b\bar{b}$ analysis, with $m_H = 125$ GeV.

Uncertainties arising from the underlying event, from section 5.7:

N_{jets} bin	$\sigma_{\text{inclusive}}$ $[pb]$	$\delta_{\sigma_{\text{inclusive}}}$ [%]	σ_{asc} $[pb]$	$\delta_{\sigma_{\text{asc}}}$ [%]	A [%]	δ_A [% of A]
2 and 3	0.0350	3.7	0.00524	4.1	15.0	3.3
2	0.0350	3.7	0.00356	4.4	10.2	4.6
3	0.0350	3.7	0.00169	6.5	4.8	4.2

Table 5.26: Systematic uncertainties arising from the underlying event, calculated using the MPI scaling method, for the $WH \to \ell\nu b\bar{b}$ analysis, with $m_H = 125$ GeV.

Uncertainties arising from radiative QED corrections, from section 5.9:

N_{jets} bin	$\sigma_{\text{inclusive}}$ $[pb]$	$\delta_{\sigma_{\text{inclusive}}}$ [%]	σ_{asc} $[pb]$	$\delta_{\sigma_{\text{asc}}}$ [%]	A [%]	δ_A [% of A]
2 and 3	0.0350	1.1	0.00524	2.7	15.0	2.1
2	0.0350	1.1	0.00356	3.8	10.2	2.9
3	0.0350	1.1	0.00169	4.8	4.8	4.1

Table 5.27: Systematic uncertainties arising from radiative QED corrections, for the $WH \to \ell\nu b\bar{b}$ analysis, with $m_H = 125$ GeV.

These uncertainties are summed in quadrature to obtain overall systematic uncertainties on the cross-section of $pp \to WH \to \ell\nu b\bar{b}$ production, and its acceptance by the analysis:

$$\begin{aligned}\Delta^2_{pp\to WH\to\ell\nu b\bar{b}} =& \Delta^2_{\text{Scale factors}} \\ &+ \Delta^2_{\text{Parton distribution functions and } \alpha_s \text{ combined}} \\ &+ \Delta^2_{\text{Parton showering and Hadronisation combined}} \\ &+ \Delta^2_{\text{The underlying event}} \\ &+ \Delta^2_{\text{Radiative QED corrections to particle decays}}\end{aligned} \tag{5.47}$$

These combined uncertainties are shown in table 5.29

N_{jets} bin	$\sigma_{\text{inclusive}}$ $[pb]$	$\delta_{\sigma_{\text{inclusive}}}$ [%]	σ_{asc} $[pb]$	$\delta_{\sigma_{\text{asc}}}$ [%]	A [%]	δ_A [% of A]
2 and 3	0.0350	8.8	0.00524	12.3	15.0	9.4
2	0.0350	8.8	0.00356	18.1	10.2	15.0
3	0.0350	8.8	0.00169	16.6	4.8	14.8

Table 5.28: Combined theoretical systematic uncertainties on $WH \to b\bar{b}$ signal, for the $WH \to \ell\nu b\bar{b}$ analysis, with $m_H = 125$ GeV.

Table 5.28 presents the combined results using only the uncertainty values calculated in this chapter.

In the cases of scale factor uncertainties, and parton distribution functions and α_s combined uncertainties, more accurate values of these uncertainties on the inclusive signal cross section are given in [98]. These values are $\delta_{\sigma_{\text{inclusive}}} = 1.0\%$ for scale factors, and $\delta_{\sigma_{\text{inclusive}}} = 2.3\%$ for parton distribution functions and α_s combined. These values have been used in the results presented in table 5.29.

N_{jets} bin	$\sigma_{\text{inclusive}}$ $[pb]$	$\delta_{\sigma_{\text{inclusive}}}$ [%]	σ_{asc} $[pb]$	$\delta_{\sigma_{\text{asc}}}$ [%]	A [%]	δ_A [% of A]
2 and 3	0.0350	7.7	0.00524	12.3	15.0	9.4
2	0.0350	7.7	0.00356	18.1	10.2	15.0
3	0.0350	7.7	0.00169	16.6	4.8	14.8

Table 5.29: Combined theoretical systematic uncertainties on $WH \to b\bar{b}$ signal, for the $WH \to \ell\nu b\bar{b}$ analysis, with $m_H = 125$ GeV.

5.11 Conclusions

Sources of theoretical uncertainty on $WH \to \ell\nu b\bar{b}$ Monte Carlo signal samples, for $m_H = 125$ GeV, have been considered and estimated. The combined theoretical uncertainties given in table 5.29 are taken to be the best estimates of the true uncertainties, as they use renormalisation and factorisation scale factor uncertainties, and combined PDF and α_s uncertainties, on the inclusive signal cross section from [98]. These uncertainties from [98] are considered to be more accurate estimates than the equivalent values calculated in this chapter.

For two and three-jet final states, the uncertainty on the inclusive cross-section $\delta_{\sigma_{\text{inclusive}}} = 7.7\%$, the uncertainty on the cross section after analysis selection criteria have been applied $\delta_{\sigma_{\text{asc}}} = 12.3\%$, and the uncertainty on signal acceptance $\delta_A = 9.4\%$.

For two and three-jet final states, the largest uncertainty on the inclusive cross-section N_{jets} is due to the combination of parton showering and hadronisation. The largest uncertainties on the cross section after analysis selection criteria have been applied σ_{asc}, and signal acceptance A, come from the combination of uncertainties arising from parton distribution functions and α_s.

Future estimates of uncertainties arising from the underlying event could be improved through the use of the plateau-height retuning method, described in appendix F.1. Future estimates of uncertainties arising from the combination of parton showering and hadronisation could be improved through new event generator tuning to the latest LHC data. They could also be improved through comparisons of additional event generator setups, to better estimate the true standard deviation on results due to parton showering and hadronisation. Future estimates of uncertainties arising from scale factors could be improved through the use of higher-order calculations.

Chapter 6

Results Of The Search For The Higgs Boson In The $WH \to b\bar{b}$ And $VH \to b\bar{b}$ Channels

6.1 Introduction

The procedures of the search for the Higgs boson in the $WH \to \ell\nu b\bar{b}$, $ZH \to \nu\bar{\nu}b\bar{b}$ and $ZH \to \ell\bar{\ell}b\bar{b}$ channels at the ATLAS detector have been presented in chapter 4, including systematic uncertainties on backgrounds. Systematic uncertainties on the $WH \to \ell\nu b\bar{b}$ signal process have been estimated and discussed in chapter 5. For convenience, the final uncertainties on the the $WH \to \ell\nu b\bar{b}$ signal process are summarised in section 5.10. These uncertainties have been applied as nuisance parameters in the global fit, as described in chapter 4 section 4.7, in order to produce the results presented in this chapter. For inclusive cross-sections of Higgs boson production, values used in the global fit are taken from [32], as these values have been calculated to next-to-next-to-leading order (NNLO) in the perturbative expansion of QCD, and to next-to-leading order (NLO) in the perturbative expansion of electroweak corrections. The results of this global fit is presented here for the 1-lepton channel, designed to target the $WH \to \ell\nu b\bar{b}$ process, as well as the results of this this channel combined with the 0 and 2-lepton channels, which are designed to target the $ZH \to \nu\bar{\nu}b\bar{b}$ and $ZH \to \ell\bar{\ell}b\bar{b}$ processes respectively.

For each channel, and the combination of the channels, upper limits are set on

the signal strength $\mu = \sigma/\sigma_{\mathrm{SM}}$, as described in chapter 4. μ is the cross-sections of the processes as measured in data (σ) compared to the cross-sections predicted by the Standard Model (σ_{SM}). These limits are presented with a confidence level of 95% for a range of possible Higgs boson masses. Both the expected and observed limits are presented. Expected limits show the expected sensitivity of the analysis, given the available data. They say that, given the available data, the analysis should be sensitive enough to set 95% confidence upper limits on the ratios of $\sigma/\sigma_{\mathrm{SM}}$, corresponding to the expected limits. They are shown with 1σ (green) and 2σ (yellow) uncertainty bands. The observed limits are the limits obtained with data.

If an observed 95% confidence upper limit on the ratio of $\sigma/\sigma_{\mathrm{SM}}$ is found to be less than 1 for a given Higgs boson mass, then is can be concluded with 95% confidence that a Higgs boson with that mass does not exist in the channel corresponding to the limit.

6.2 Input $m_{b\bar{b}}$ And b-Tagging Distributions

$m_{b\bar{b}}$ distributions, and distributions of the MV1c b-tagging algorithm output, are used as inputs to the global fit, as described in chapter 4. $m_{b\bar{b}}$ distributions are used in the signal regions of the analysis, where two hadronic jets have been b-tagged. In regions where only one hadronic jets has been b-tagged, MV1c distributions are used.

For all input distributions, separate histograms are used as inputs for each of the different lepton-number channels (0-lepton, 1-lepton, and 2-lepton), as well as for each of the different p_{T}^{V} bins within each lepton-number channels, and the number of hadronic jets in the final state (two or three). Furthermore, separate input distributions are used for each of the three signal b-tagging regions: LL, MM, and TT. For each input distribution, the bins of the histogram making up that distribution are used as the bins for the liklihood fit 4.2, with each background and signal in that bin allowed to float according to the nuisance parameters of the fit.

Figures 6.1, 6.2, and 6.3 show $m_{b\bar{b}}$ distributions, before and after the global fit has been performed, respectively for the 0, 1, and 2-lepton channels. They show the TT b-tagging regions with two jets in the final state and 200 GeV $< p_{\mathrm{T}}^{V}$.

Figures 6.4, 6.5, and 6.6 show MV1c distributions, before and after the global fit has been performed, respectively for the 0, 1, and 2-lepton channels.

Additional $m_{b\bar{b}}$ and MV1c distributions are shown in Appendix H.1.

$m_{b\bar{b}}$ distributions after the global fit, with all backgrounds except diboson subtracted, are shown in figure 6.7.

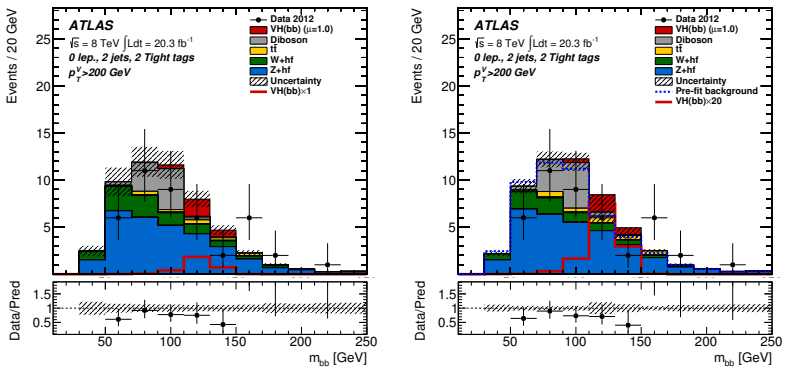

Figure 6.1: $m_{b\bar{b}}$ distributions in the 0-lepton channel, 200 GeV $< p_{\mathrm{T}}^{V}$ bin, before (left) and after (right) the global fit. The two-jet, TT b-tagging region is shown.

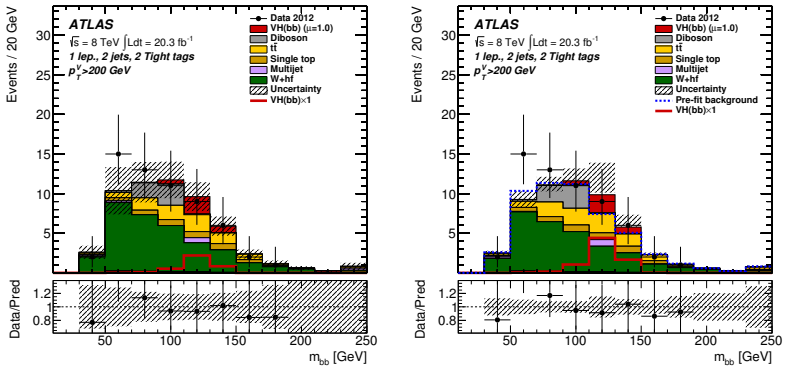

Figure 6.2: $m_{b\bar{b}}$ distributions in the 1-lepton channel, 200 GeV $< p_{\mathrm{T}}^{V}$ bin, before (left) and after (right) the global fit. The two-jet, TT b-tagging region is shown.

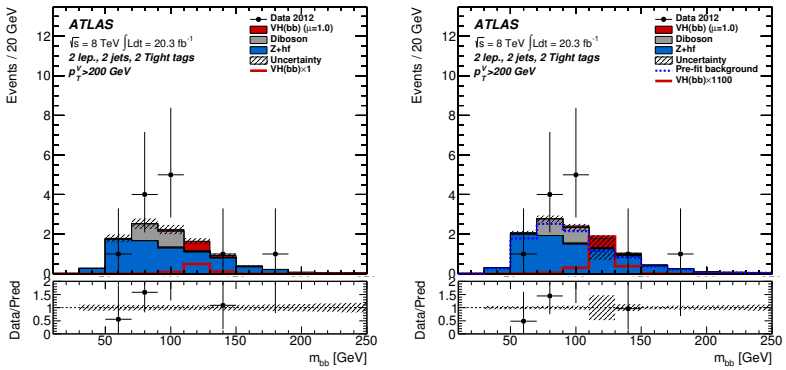

Figure 6.3: $m_{b\bar{b}}$ distributions in the 2-lepton channel, 200 GeV $< p_{\mathrm{T}}^{V}$ bin, before (left) and after (right) the global fit. The two-jet, TT b-tagging region is shown.

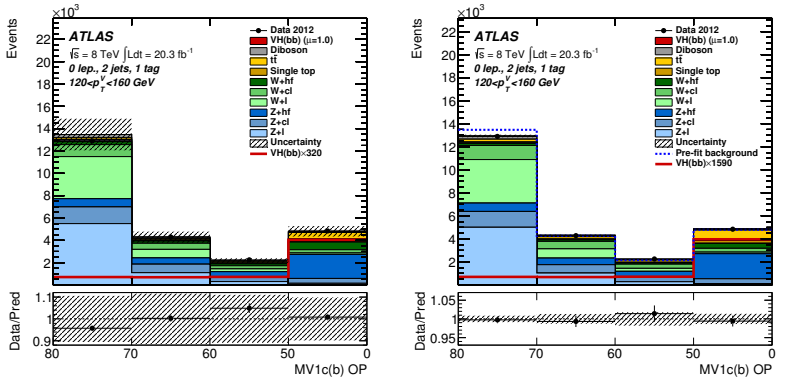

Figure 6.4: MV1c distributions in the 0-lepton channel, 120 GeV $< p_{\mathrm{T}}^{V} <$ 160 GeV bin, before (left) and after (right) the global fit. The two-jet, one-tag b-tagging region is shown.

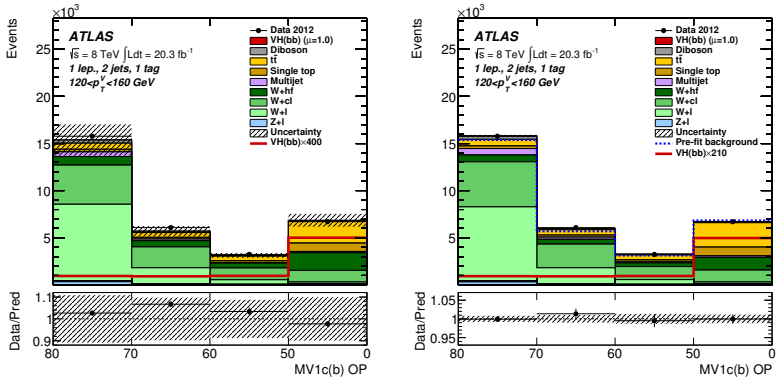

Figure 6.5: MV1c distributions in the 1-lepton channel, 120 GeV $< p_{\mathrm{T}}^{V} <$ 160 GeV bin, before (left) and after (right) the global fit. The two-jet, one-tag b-tagging region is shown.

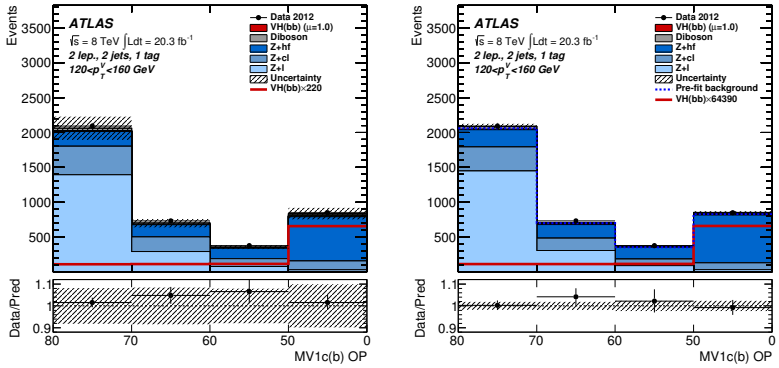

Figure 6.6: MV1c distributions in the 2-lepton channel, 120 GeV $< p_{\mathrm{T}}^{V} <$ 160 GeV bin, before (left) and after (right) the global fit. The two-jet, one-tag b-tagging region is shown.

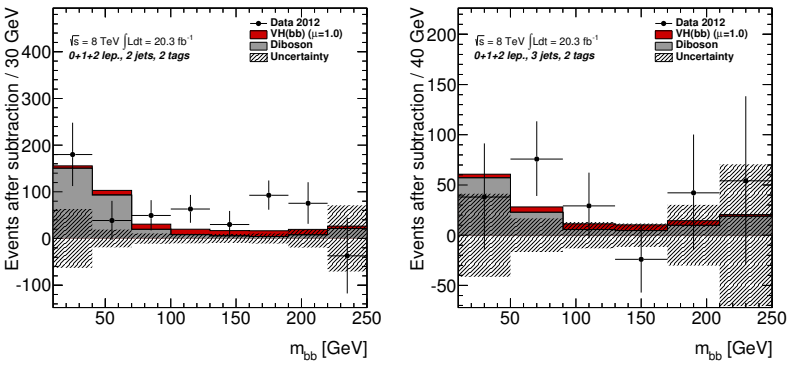

Figure 6.7: $m_{b\bar{b}}$ distributions after the global fit, with all backgrounds except diboson subtracted, for the two-jet (left) and three-jet (right) final states.

6.3 1-Lepton Channel Results

For the 1-lepton channel, designed to target the $WH \to \ell\nu b\bar{b}$ process, the 95% confidence upper limit on the ratio of $\sigma/\sigma_{\mathrm{SM}}$ is shown in figure 6.8. The limits for each of the tested Higgs boson masses are listed in table 6.1. Dominant post-fit systematic uncertainties for the $m_H = 125$ GeV mass point are given in appendix J.

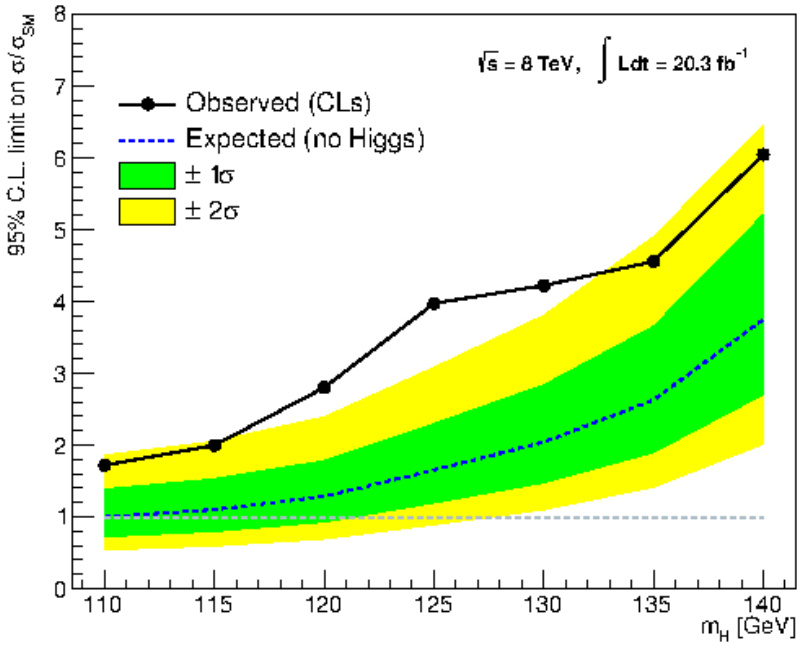

Figure 6.8: 95% confidence upper limit on the ratio of $\sigma/\sigma_{\mathrm{SM}}$ for the 1-lepton channel for a range of possible Higgs boson masses.

Higgs boson mass [GeV]	Exp.	$+2\sigma$	$+1\sigma$	-1σ	-2σ	Obs.
110	1.00	1.86	1.39	0.72	0.54	1.72
115	1.10	2.06	1.53	0.79	0.59	2.00
120	1.28	2.39	1.79	0.92	0.69	2.80
125	1.65	3.09	2.30	1.19	0.89	3.97
130	2.04	3.81	2.84	1.47	1.10	4.22
135	2.63	4.90	3.66	1.89	1.41	4.56
140	3.75	6.99	5.22	2.70	2.01	6.05

Table 6.1: 95% confidence upper limit on the ratio of $\sigma/\sigma_{\mathrm{SM}}$ for the 1-lepton channel for a range of possible Higgs boson masses.

The 1-lepton channel results show the observed 95% confidence upper limit on the ratio of $\sigma/\sigma_{\mathrm{SM}}$ being in excess of the expeccted limit for all tested Higgs boson masses. This indicates an excess of events in data compated to the Standard Model prediction. It can be noted however that there is a larger excess of events centred around a Higgs boson mass of 125 GeV.

For a Standard Model Higgs boson with a mass of 125 GeV, the observed (expected) 95% confidence upper limit on the ratio of $\sigma/\sigma_{\mathrm{SM}}$ in the 1-lepton channel is 3.97 (1.65).

6.4 Combined Results

For the 0 and 2-lepton channels, designed to target the $ZH \to \nu\bar{\nu}b\bar{b}$ and $ZH \to \ell\bar{\ell}b\bar{b}$ processes respectively, the 95% confidence upper limits on the ratios of $\sigma/\sigma_{\mathrm{SM}}$ are shown in figures 6.9 and 6.10. The limits for each of the tested Higgs boson masses are listed in tables 6.2 and 6.3. Dominant post-fit systematic uncertainties for the $m_H = 125$ GeV mass point are given in appendix J.

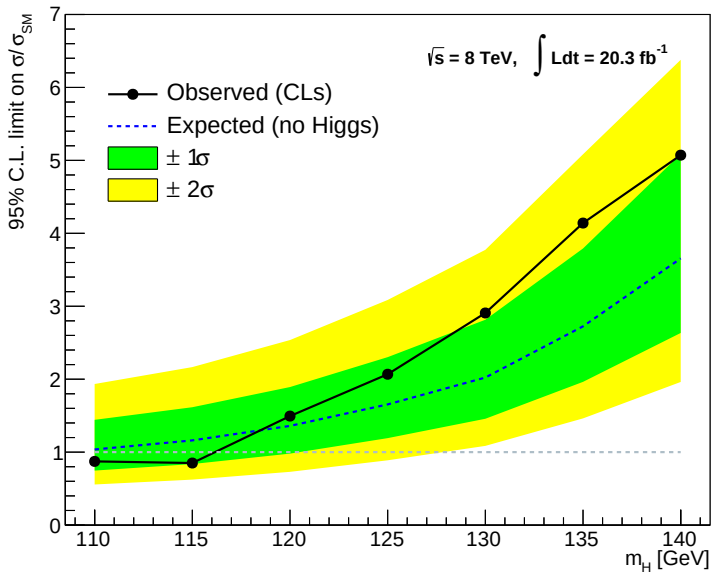

Figure 6.9: 95% confidence upper limit on the ratio of $\sigma/\sigma_{\mathrm{SM}}$ for the 0-lepton channel for a range of possible Higgs boson masses.

Higgs boson mass [GeV]	Exp.	$+2\sigma$	$+1\sigma$	-1σ	-2σ	Obs.
110	1.04	1.93	1.44	0.75	0.56	0.87
115	1.16	2.17	1.62	0.84	0.62	0.85
120	1.36	2.54	1.89	0.98	0.73	1.49
125	1.65	3.09	2.30	1.19	0.89	2.07
130	2.02	3.77	2.81	1.46	1.09	2.91
135	2.72	5.08	3.79	1.96	1.46	4.14
140	3.66	6.82	5.09	2.63	1.96	5.07

Table 6.2: 95% confidence upper limit on the ratio of $\sigma/\sigma_{\mathrm{SM}}$ for the 0-lepton channel for a range of possible Higgs boson masses.

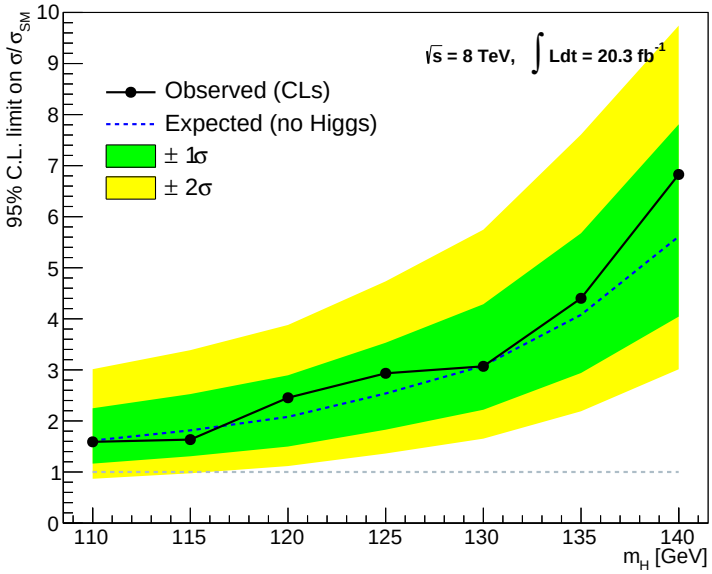

Figure 6.10: 95% confidence upper limit on the ratio of $\sigma/\sigma_{\mathrm{SM}}$ for the 2-lepton channel for a range of possible Higgs boson masses.

Higgs boson mass [GeV]	Exp.	$+2\sigma$	$+1\sigma$	-1σ	-2σ	Obs.
110	1.62	3.01	2.25	1.16	0.87	1.59
115	1.82	3.39	2.53	1.31	0.97	1.63
120	2.08	3.88	2.89	1.50	1.12	2.45
125	2.54	4.73	3.53	1.83	1.36	2.93
130	3.08	5.75	4.29	2.22	1.65	3.07
135	4.08	7.61	5.68	2.94	2.19	4.40
140	5.61	10.47	7.81	4.04	3.01	6.83

Table 6.3: 95% confidence upper limit on the ratio of $\sigma/\sigma_{\mathrm{SM}}$ for the 2-lepton channel for a range of possible Higgs boson masses.

When all three $VH \to b\bar{b}$ channels are combined, the overall 95% confidence upper limit on the ratio of $\sigma/\sigma_{\mathrm{SM}}$ is calculated, and is shown in figure 6.11. The limits for each of the tested Higgs boson masses are listed in table 6.4. The number of events in data and for each background, in the signal regions after the global fit has been performed, are listed in table 6.5. Dominant post-fit systematic uncertainties for the $m_H = 125$ GeV mass point are given in appendix J.

The combined 0, 1, and 2-lepton results show an excess of events in data, compared to the expected Standard Model prediction. The largest excess,

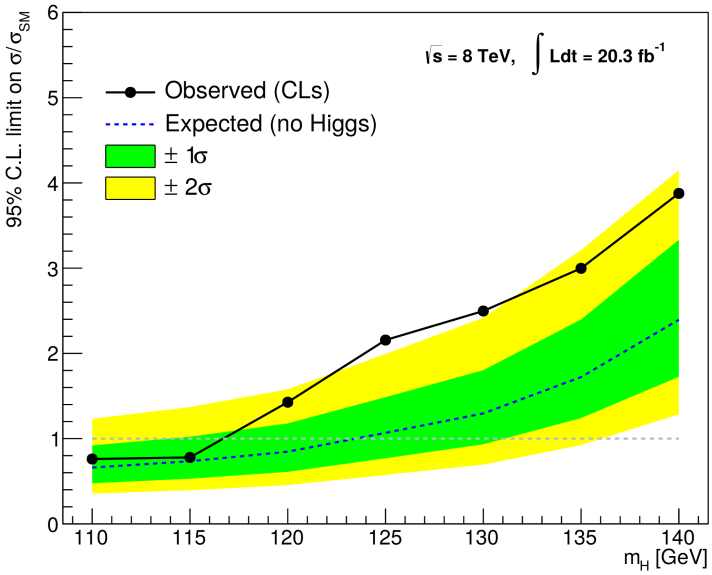

Figure 6.11: 95% confidence upper limit on the ratio of $\sigma/\sigma_{\mathrm{SM}}$ for the 0, 1, and 2-lepton channels combined for a range of possible Higgs boson masses.

Higgs boson mass [GeV]	Exp.	$+2\sigma$	$+1\sigma$	-1σ	-2σ	Obs.
110	0.66	1.23	0.92	0.48	0.35	0.76
115	0.73	1.37	1.02	0.53	0.39	0.78
120	0.85	1.58	1.18	0.61	0.45	1.43
125	1.07	1.99	1.49	0.77	0.57	2.16
130	1.30	2.42	1.80	0.93	0.70	2.50
135	1.72	3.21	2.40	1.24	0.92	3.00
140	2.39	4.47	3.33	1.73	1.29	3.88

Table 6.4: 95% confidence upper limit on the ratio of $\sigma/\sigma_{\mathrm{SM}}$ for the 0, 1, and 2-lepton channels combined for a range of possible Higgs boson masses.

compared to the expected Standard Model prediction, occurs with a Higgs boson mass of 125 GeV. Additionally, a Standard model Higgs boson with a mass between 110 GeV and 115 GeV has been excluded.

For a Standard Model Higgs boson with a mass of 125 GeV, the observed (expected) 95% confidence upper limit on the ratio of $\sigma/\sigma_{\mathrm{SM}}$ in the combination of the 0, 1, and 2-lepton channels is 2.16 (1.07).

The best fit value of the signal strength $\mu = \sigma/\sigma_{\mathrm{SM}}$, where σ_{SM} is the predicted cross section of a Standard Model Higgs boson with a mass of $m_H = 125$ GeV,

is shown is figure 6.12. The best fit signal strength in the 1-lepton channel is $\mu = 2.22\ ^{+0.66}_{-0.64}\ (\text{stat})\ ^{+0.76}_{-0.60}\ (\text{syst}) = 2.22\ ^{+1.01}_{-0.88}$. The best fit signal strength in the combination of the 0, 1, and 2-lepton channels is $\mu = 1.09\ ^{+0.43}_{-0.42}\ (\text{stat})\ ^{+0.44}_{-0.37}\ (\text{syst}) = 1.09\ ^{+0.61}_{-0.56}$. The combined results are consistent with a Standard Model Higgs boson ($\mu = 1$).

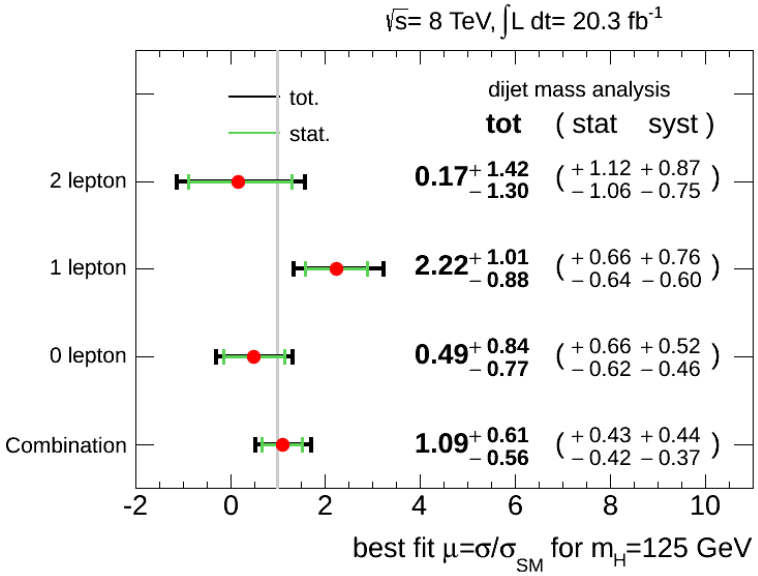

Figure 6.12: Best fit value of the signal strength $\mu = \sigma/\sigma_{\text{SM}}$, where σ_{SM} is the predicted cross section of a Standard Model Higgs boson with a mass of $m_H = 125$ GeV.

Process	Number of Events		
Data	9787.0	±	98.9
$q\bar{q} \to WH$	37.9	±	4.9
$q\bar{q} \to ZH$	26.0	±	9.4
$gg \to ZH$	3.6	±	1.7
W + jets	2523.9	±	79.1
Z + jets	1678.2	±	244.4
WW	40.3	±	2.5
WZ	105.8	±	9.8
ZZ	103.9	±	31.7
QCD multijet	164.0	±	8.2
Top-quark:			
$t\bar{t}$	3654.6	±	219.8
t-channel	227.9	±	12.1
s-channel	116.9	±	8.2
Wt-channel	338.4	±	21.8
Total background	8953.89	±	12.85
Total signal	67.53	±	10.74

Table 6.5: Number of events in data, and in signal and background models, in signal regions after final data selection, post-fit. These numbers are for the combined 0, 1, and 2-lepton results. Errors shown are the combination of statistical and systematic.

6.5 Conclusions

A Standard Model Higgs boson has not been observed being produced in association with a vector boson and decaying to a pair of b-quarks.

For a Standard Model Higgs boson with a mass of 125 GeV, the observed (expected) 95% confidence upper limit on the ratio of $\sigma/\sigma_{\mathrm{SM}}$ in the 1-lepton channel is 3.97 (1.65), and in the combination of the 0, 1, and 2-lepton channels is 2.16 (1.07).

A Standard Model Higgs boson with a mass between 110 GeV and 115 GeV has been excluded.

For a Standard Model Higgs boson with a mass of 125 GeV, the best fit signal strength in the 1-lepton channel is $\mu = 2.22\ ^{+0.66}_{-0.64}\ (\mathrm{stat})\ ^{+0.76}_{-0.60}\ (\mathrm{syst}) = 2.22\ ^{+1.01}_{-0.88}$, and the best fit signal strength in the combination of the 0, 1, and 2-lepton channels is $\mu = 1.09\ ^{+0.43}_{-0.42}\ (\mathrm{stat})\ ^{+0.44}_{-0.37}\ (\mathrm{syst}) = 1.09\ ^{+0.61}_{-0.56}$. The combined results are consistent with a Standard Model Higgs boson with a mass of 125 GeV.

Chapter 7

WH Triggers For Run 2

7.1 Introduction

When the LHC begins colliding protons in 2015 (referred to as 'Run 2') it will do so at higher energy and with higher luminosity than ever before. This will result in more collisions per bunch crossing ('pile-up') than ever before. These increases will make triggering on charged leptons with the ATLAS detector more challenging. In order to maintain the 2012 lepton trigger p_{T} thresholds at ATLAS an upgrade to the triggers would be required, costing roughly 1M CHF. Without this upgrade the single lepton trigger p_{T} thresholds will have to be set higher. The effects on the ATLAS WH $H \to b\bar{b}$ analysis of such higher thresholds is presented in section 7.2. If the triggers are not upgraded and the ATLAS WH $H \to b\bar{b}$ analysis can not be performed with the resulting single lepton triggers, then alternative triggering strategies must be developed. Such alternatives are discussed in section 7.3.

7.2 Single Lepton Trigger Thresholds

7.2.1 Method

The analysis framework used for [110] was modified to include a minimum p_{T} cut on all signal leptons in order to emulate a minimum lepton trigger p_{T} threshold. The full WH $H \to b\bar{b}$ analysis was then rerun with this code, with different values for the signal lepton minimum p_{T} cut; 25 GeV to 50 GeV in 5 GeV increments.

The standard 2012 analysis [110] (without the additional signal lepton minimum p_{T} cut) was also run for comparison.

One caveat in this approach is that applying an analysis level lepton p_{T} cut is not the same as having a trigger level p_{T} cut, but is comparable to within lepton p_{T} resolution at trigger and analysis level.

By comparing the cross-sections of Monte Carlo samples after all analysis cuts between a given analysis with a signal lepton minimum p_{T} cut and the control analysis, it is possible to discern the effects of that signal lepton minimum p_{T} cut. The fraction of signal events remaining, the fraction of background events remaining and the change in significance were calculated for each value of signal lepton minimum p_{T} cut. Significances were calculated in each $m_{b\bar{b}}$ (reconstructed Higgs candidate mass / di-jet mass) bin and then summed in quadrature.

Control tests were performed by setting the signal lepton minimum p_{T} cut to 0 GeV and comparing results to the default analysis that does not contain emulated triggers [110].

Data Used

Monte Carlo samples listed in table 7.1 were used in this analysis. These are the same samples used in [110]. 20.3 fb^{-1} of $\sqrt{s} = 8$ TeV proton proton collision data was analysed in this analysis. The collisions were provided by the LHC in 2012 with stable beam conditions. The data was collected with the ATLAS detector where all subsystems were running and providing high-quality data. This is the same 2012 data used in [110].

Calculation Of Uncertainties

Acceptance

For both both signal and background acceptance, the following is used to calculate the uncertainty on an acceptance value.

The Acceptance (A) is given by,

$$A = \frac{N_{Cut}}{N_{Control}} \tag{7.1}$$

where $N_{Control}$ is the number of events passing the standard analysis being used as a control, hereafter referred to as the 'control analysis', and N_{Cut} is the

Process	Generator Used	Sample Size (number of events)	$\sigma \times BR$
WH	Pythia 8.160	300 k	
ZH	Pythia 8.160	300 k	
$W \to \ell\nu$	Sherpa 1.4.1	168 M	10.97 nb
$Z/\gamma \to \ell^+\ell^-$	Sherpa 1.4.1	42 M	1.24 nb
$Z/\gamma \to \nu\bar{\nu}$	Sherpa 1.4.1	77 M	6.71 nb
WW	Herwig 6.510	10 M	55.43 pb
WZ	Herwig 6.510	20 M	22.69 pb
ZZ	Herwig 6.510	7.5 M	77.70 pb
Top-quark:			
$t\bar{t}$	Powheg_Box+PYTHIA6	75 M	238.06 pb
t-channel	AcerMC	9 M	87.76 pb
s-channel	Powheg_Box+PYTHIA6	6 M	5.61 pb
Wt-channel	Powheg_Box+PYTHIA6	20 M	22.37 pb

Table 7.1: Monte Carlo samples used in trigger studies presented in this thesis. For signal samples, $m_H = 125$ GeV.

number of events passing the analysis when an additional signal lepton p_{T} cut is applied, hereafter referred to as the 'cut analysis'.

We wish to calculate the uncertainty on A (Δ_A). For this we can use the binomial error,

$$\Delta_A = \sqrt{\frac{A(1-A)}{N_{Control}}} \tag{7.2}$$

Significance

A significance (Ω) is defined as,

$$\Omega = \frac{S}{\sqrt{S+B}} \tag{7.3}$$

When data is binned, then the overall significance is summed in quadrature over all bins:

$$\Omega^2 = \sum_{i=1}^{N} \Omega_i^2 \tag{7.4}$$

where Ω_i is the significance for bin i, and the sum is over all N bins.

Then,

$$\Omega_i = \frac{S_i}{\sqrt{S_i + B_i}} \tag{7.5}$$

Where S_i is the number of signal events in $m_{b\bar{b}}$ bin i, B_i is the number of background events in bin i. If $S_j = 0$ and $B_j = 0$ for any bin j, then Ω_j is taken to be equal to 0.

The uncertainty on the significance, σ_Ω, can then be written as,

$$\sigma_\Omega^2 = \sum_{i=1}^{N} \left(\frac{\partial \Omega}{\partial \Omega_i} \right)^2 \sigma_{\Omega_i}^2 \tag{7.6}$$

where σ_{Ω_i} is the error on the significance for bin i, given by,

$$\sigma_{\Omega_i}^2 = \left(\frac{\partial \Omega_i}{\partial S_i} \right)^2 \sigma_{S_i}^2 + \left(\frac{\partial \Omega_i}{\partial B_i} \right)^2 \sigma_{B_i}^2 \tag{7.7}$$

since S_i and B_i are independent of one another. From equation 7.5 we can compute,

$$\frac{\partial \Omega_i}{\partial S_i} = \frac{S + 2B}{2(S+B)^{3/2}} = \Omega_i \frac{S + 2B}{2S(S+B)} \tag{7.8}$$

and,

$$\frac{\partial \Omega_i}{\partial B_i} = \frac{-S}{2(S+B)^{3/2}} = \Omega_i \frac{-1}{2(S+B)} \tag{7.9}$$

We can then write,

$$\sigma_{\Omega_i}^2 = \Omega_i^2 \left(\left(\frac{S + 2B}{2S(S+B)} \right)^2 \sigma_{S_i}^2 + \left(\frac{-1}{2(S+B)} \right)^2 \sigma_{B_i}^2 \right) \tag{7.10}$$

Furthermore,

$$\frac{\partial \Omega}{\partial \Omega_i} = \frac{\Omega_i}{\Omega} \tag{7.11}$$

such that,

$$\sigma_\Omega^2 = \frac{1}{\Omega^2} \sum_{i=1}^{N} \Omega_i^2 \sigma_{\Omega_i}^2 \tag{7.12}$$

leading to,

$$\sigma_{\Omega}^{2} = \frac{1}{\Omega^{2}} \sum_{i=1}^{N} \Omega_{i}^{4} \left(\left(\frac{S+2B}{2S(S+B)} \right)^{2} \sigma_{S_i}^{2} + \left(\frac{-1}{2(S+B)} \right)^{2} \sigma_{B_i}^{2} \right) \tag{7.13}$$

7.2.2 Results

Results are presented split into different bins of p_{T}^{W} as in the analysis [110]. This p_{T}^{W} binning allows the analysis to be optimised separately in each p_{T}^{W} bin, leading to an increase in overall analysis sensitivity.

Control

Control tests were performed by setting the signal lepton minimum p_{T} cut to 0 GeV and comparing results to the default analysis that does not contain emulated triggers [110]. The control results were found to be identical to the results of the default analysis, showing that the trigger emulation was not introducing any unexpected or unwanted behaviour.

Figures 7.1 and 7.2 show the $m_{b\bar{b}}$ distributions for the control analyses in, respectively, the electron and muon channels.

Effects On Signal

Tables 7.2 and 7.3 show the effects on signal acceptance of different signal lepton p_{T} cuts.

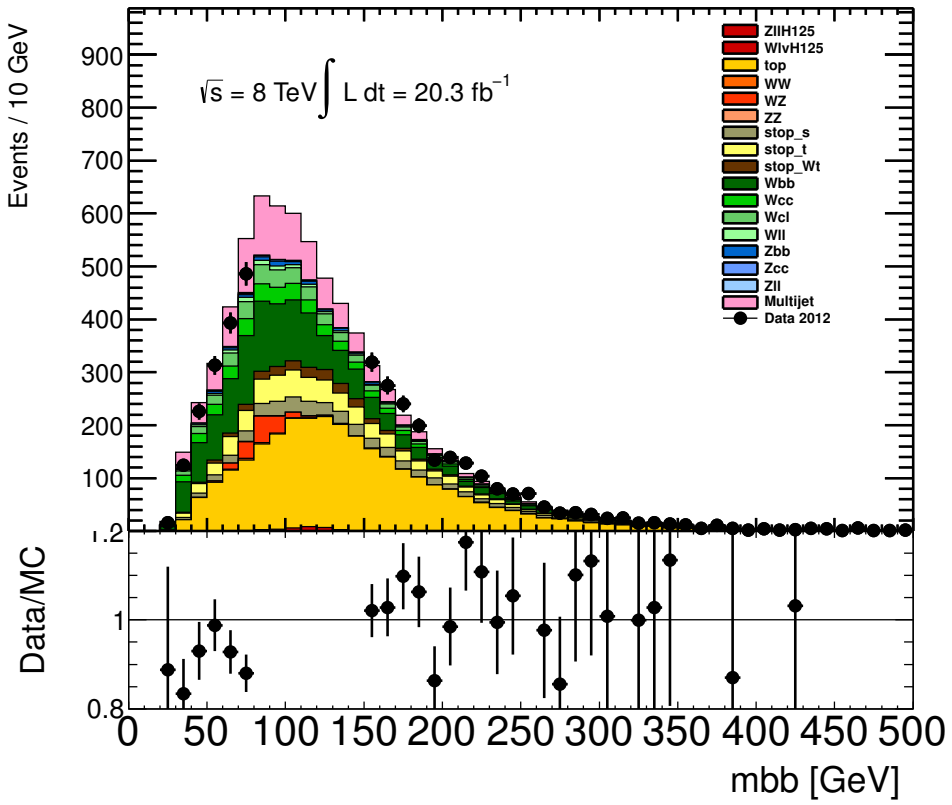

Figure 7.1: $m_{b\bar{b}}$ distribution, for $m_H = 125$ GeV, for control analysis in the electron channel.

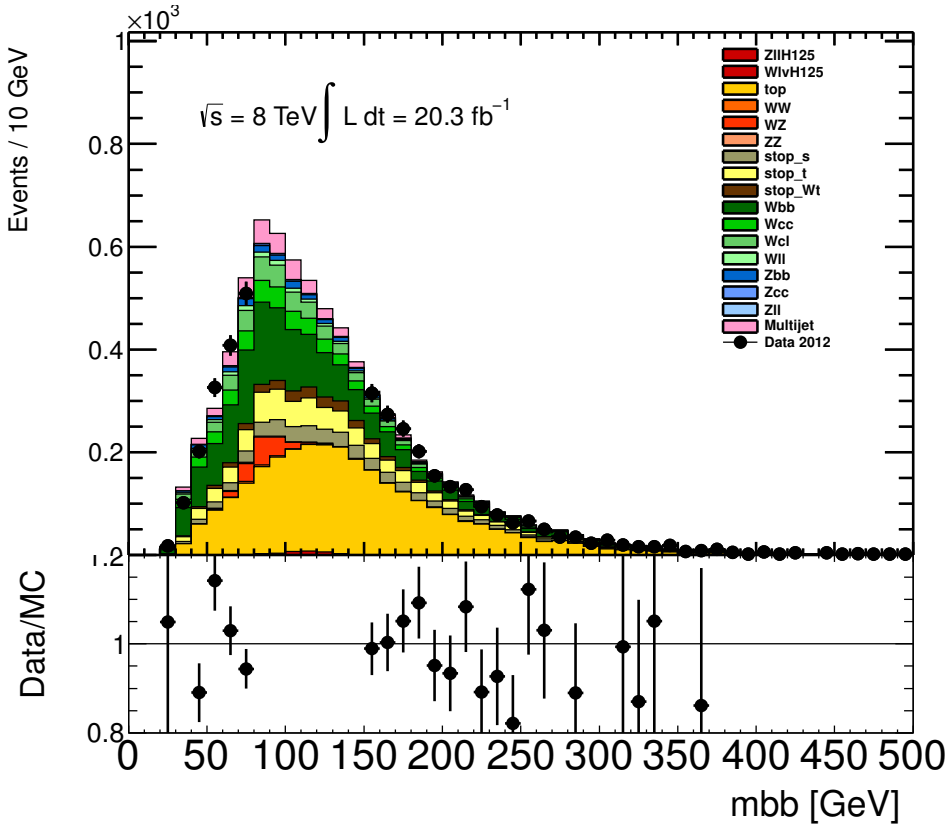

Figure 7.2: $m_{b\bar{b}}$ distribution, for $m_H = 125$ GeV, for control analysis in the muon channel.

	p_{T}^{W} [GeV]					
Lepton p_{T} cut [GeV]	Combined (All p_{T}^{W})	0-60	60-120	120-160	160-200	>200
25	1 ± 0	1 ± 0	1 ± 0	1 ± 0	1 ± 0	1 ± 0
30	0.93 ± 0.04	0.88 ± 0.08	$0.97 - 0.08 + 0.03$	$0.99 - 0.06 + 0.01$	$0.98 - 0.09 + 0.02$	$0.99 - 0.06 + 0.01$
35	0.83 ± 0.06	0.74 ± 0.10	$0.93 - 0.12 + 0.07$	$0.95 - 0.12 + 0.05$	$0.95 - 0.13 + 0.05$	$0.96 - 0.11 + 0.04$
40	0.74 ± 0.07	0.61 ± 0.11	$0.87 - 0.15 + 0.13$	$0.92 - 0.15 + 0.08$	$0.93 - 0.14 + 0.07$	$0.93 - 0.15 + 0.07$
45	0.66 ± 0.07	0.50 ± 0.12	0.80 ± 0.18	$0.87 - 0.18 + 0.13$	$0.90 - 0.17 + 0.10$	$0.92 - 0.16 + 0.08$
50	0.57 ± 0.08	0.39 ± 0.11	0.72 ± 0.21	$0.82 - 0.21 + 0.18$	$0.86 - 0.20 + 0.14$	$0.89 - 0.18 + 0.11$

Table 7.2: Fraction of 1-lepton electron channel signal events remaining, for $m_H = 125$ GeV, after signal lepton p_{T} cut compared to 2012 analysis [110] (25 GeV) signal lepton p_{T} cut.

	p_{T}^{W} [GeV]					
Lepton p_{T} cut [GeV]	Combined (All p_{T}^{W})	0-60	60-120	120-160	160-200	>200
25	1 ± 0	1 ± 0	1 ± 0	1 ± 0	1 ± 0	1 ± 0
30	0.90 ± 0.05	0.87 ± 0.08	$0.95 - 0.10 + 0.05$	$0.95 - 0.13 + 0.05$	$0.97 - 0.11 + 0.03$	$0.98 - 0.08 + 0.02$
35	0.79 ± 0.06	0.72 ± 0.10	$0.91 - 0.14 + 0.09$	$0.91 - 0.18 + 0.09$	$0.92 - 0.17 + 0.08$	$0.94 - 0.15 + 0.06$
40	0.68 ± 0.07	0.58 ± 0.11	$0.83 - 0.18 + 0.17$	$0.83 - 0.23 + 0.17$	$0.88 - 0.21 + 0.12$	$0.90 - 0.20 + 0.10$
45	0.59 ± 0.08	0.46 ± 0.11	0.76 ± 0.21	$0.80 - 0.25 + 0.20$	$0.84 - 0.23 + 0.16$	$0.87 - 0.22 + 0.13$
50	0.51 ± 0.08	0.37 ± 0.11	0.69 ± 0.23	$0.74 - 0.27 + 0.26$	$0.79 - 0.26 + 0.21$	$0.84 - 0.24 + 0.16$

Table 7.3: Fraction of 1-lepton muon channel signal events remaining, for $m_H = 125$ GeV, after signal lepton p_{T} cut compared to 2012 analysis [110] (25 GeV) signal lepton p_{T} cut.

Effects On Background

Tables 7.4 and 7.5 show the effects on background acceptance of different signal lepton p_{T} cuts.

	p_{T}^{W} [GeV]					
Lepton p_{T} cut [GeV]	Combined (All p_{T}^{W})	0-60	60-120	120-160	160-200	>200
25	1 ± 0	1 ± 0	1 ± 0	1 ± 0	1 ± 0	1 ± 0
30	0.88 ± 0.00	0.87 ± 0.00	0.91 ± 0.01	0.93 ± 0.01	0.95 ± 0.02	0.96 ± 0.02
35	0.76 ± 0.00	0.74 ± 0.01	0.82 ± 0.01	0.86 ± 0.02	0.90 ± 0.02	0.92 ± 0.03
40	0.63 ± 0.01	0.59 ± 0.01	0.72 ± 0.01	0.78 ± 0.02	0.83 ± 0.03	0.86 ± 0.04
45	0.53 ± 0.01	0.48 ± 0.01	0.64 ± 0.01	0.70 ± 0.02	0.78 ± 0.03	0.80 ± 0.04
50	0.43 ± 0.01	0.38 ± 0.01	0.56 ± 0.01	0.63 ± 0.02	0.73 ± 0.04	0.76 ± 0.05

Table 7.4: Fraction of 1-lepton electron channel background events remaining after signal lepton p_{T} cut compared to 2012 analysis [110] (25 GeV) signal lepton p_{T} cut.

	p_{T}^{W} [GeV]					
Lepton p_{T} cut [GeV]	Combined (All p_{T}^{W})	0-60	60-120	120-160	160-200	>200
25	1 ± 0	1 ± 0	1 ± 0	1 ± 0	1 ± 0	1 ± 0
30	0.85 ± 0.00	0.84 ± 0.00	0.88 ± 0.01	0.90 ± 0.01	0.93 ± 0.02	0.95 ± 0.03
35	0.72 ± 0.01	0.69 ± 0.01	0.79 ± 0.01	0.84 ± 0.02	0.90 ± 0.03	0.93 ± 0.03
40	0.59 ± 0.01	0.55 ± 0.01	0.70 ± 0.01	0.78 ± 0.02	0.85 ± 0.03	0.90 ± 0.04
45	0.48 ± 0.01	0.43 ± 0.01	0.62 ± 0.01	0.70 ± 0.02	0.80 ± 0.04	0.85 ± 0.04
50	0.39 ± 0.01	0.33 ± 0.01	0.54 ± 0.02	0.64 ± 0.02	0.75 ± 0.04	0.82 ± 0.05

Table 7.5: Fraction of 1-lepton muon channel background events remaining after signal lepton p_{T} cut compared to 2012 analysis [110] (25 GeV) signal lepton p_{T} cut.

Effects On Significance

Figures 7.3, 7.4, 7.5, 7.6, 7.7, 7.8, and 7.9 show the effects on $m_{b\bar{b}}$ distributions of different signal lepton p_{T} cuts.

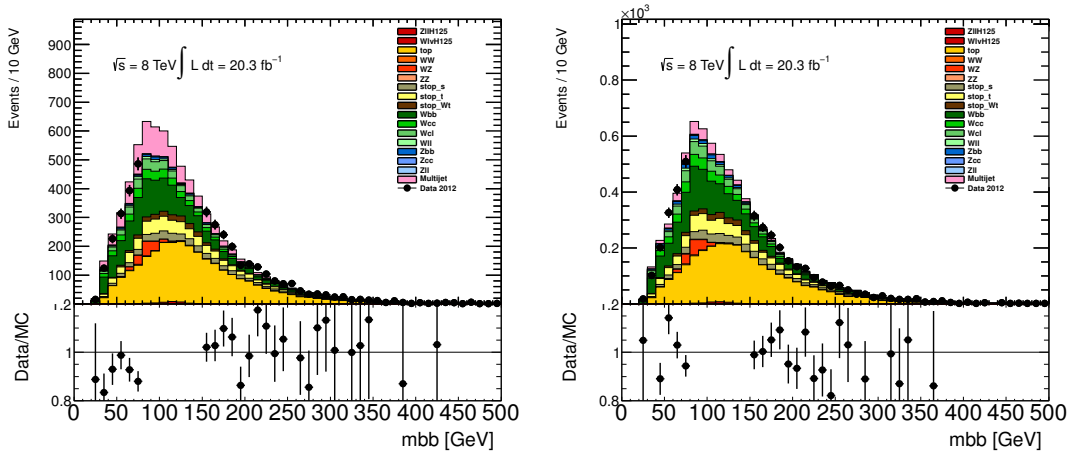

Figure 7.3: $m_{b\bar{b}}$ distributions, for $m_H = 125$ GeV, for control analysis in the electron (left) and muon (right) channels.

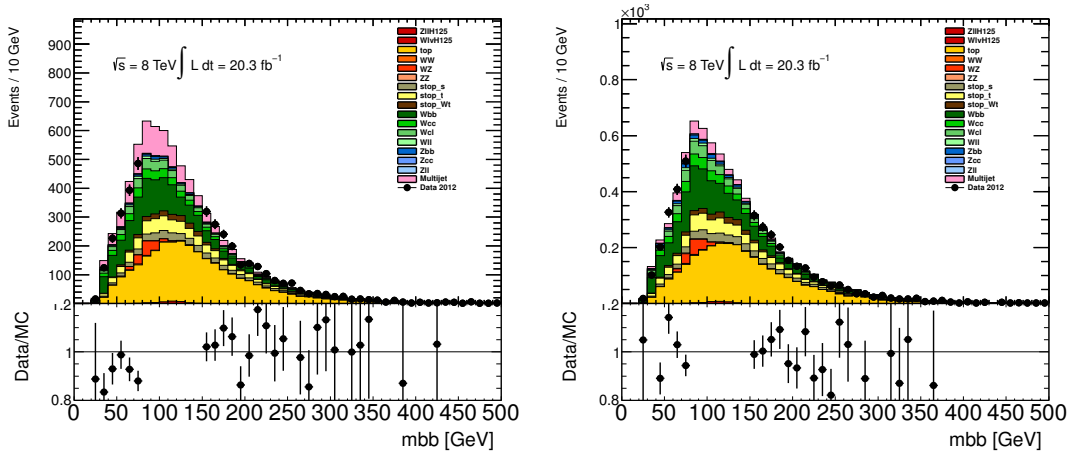

Figure 7.4: $m_{b\bar{b}}$ distributions, for $m_H = 125$ GeV, for an analysis with a 25 GeV minimum signal lepton p_{T} cut, in the electron (left) and muon (right) channels.

Tables 7.6 and 7.7 show the effects on significance of different signal lepton p_{T} cuts.

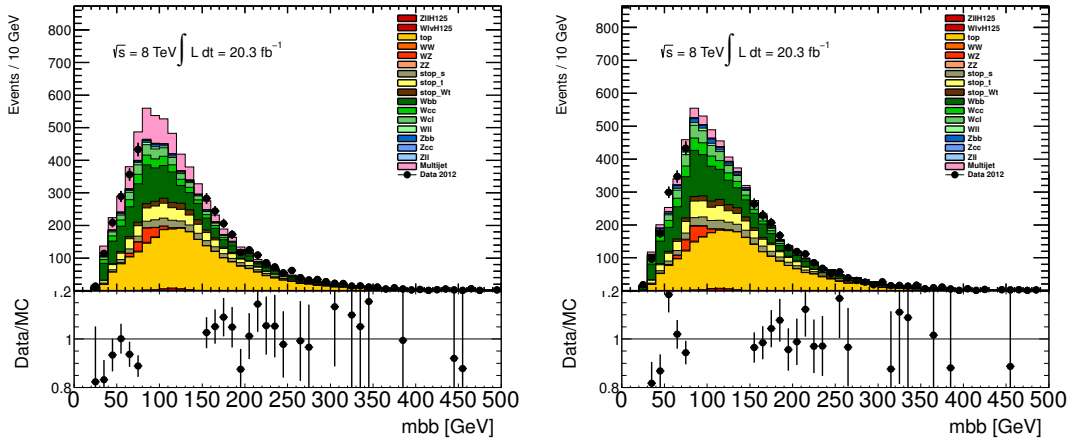

Figure 7.5: $m_{b\bar{b}}$ distributions, for $m_H = 125$ GeV, for an analysis with a 30 GeV minimum signal lepton p_{T} cut, in the electron (left) and muon (right) channels.

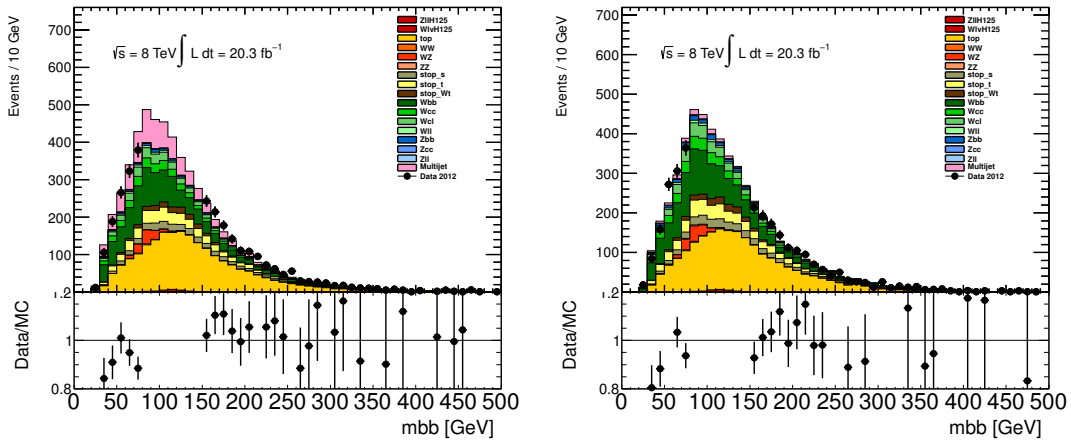

Figure 7.6: $m_{b\bar{b}}$ distributions, for $m_H = 125$ GeV, for an analysis with a 35 GeV minimum signal lepton p_{T} cut, in the electron (left) and muon (right) channels.

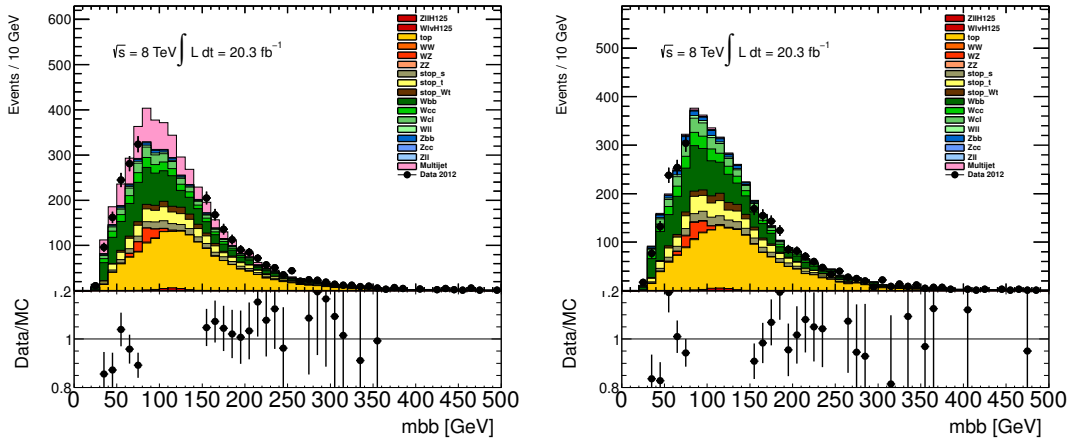

Figure 7.7: $m_{b\bar{b}}$ distributions, for $m_H = 125$ GeV, for an analysis with a 40 GeV minimum signal lepton p_{T} cut, in the electron (left) and muon (right) channels.

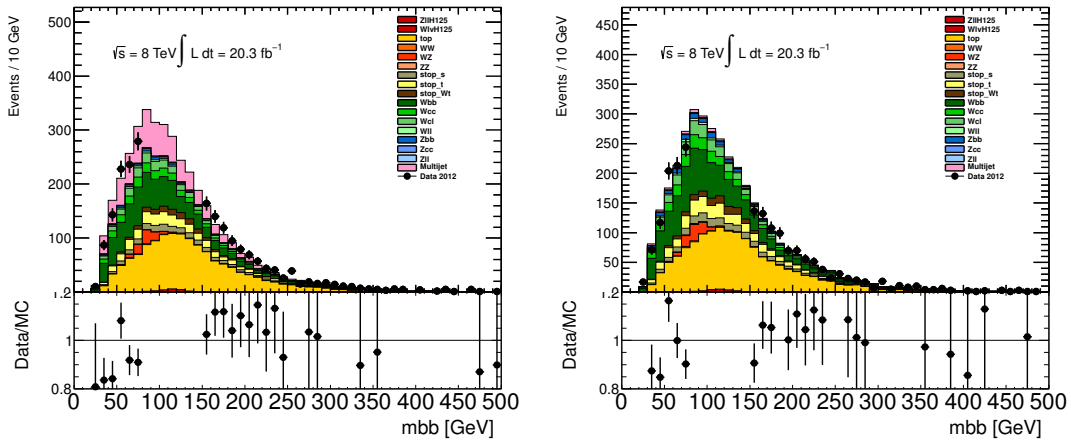

Figure 7.8: $m_{b\bar{b}}$ distributions, for $m_H = 125$ GeV, for an analysis with a 45 GeV minimum signal lepton p_{T} cut, in the electron (left) and muon (right) channels.

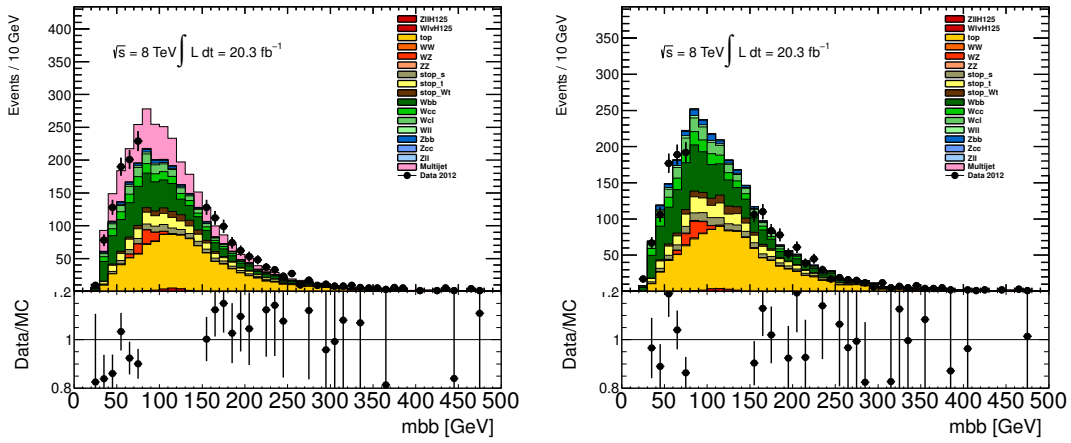

Figure 7.9: $m_{b\bar{b}}$ distributions, for $m_H = 125$ GeV, for an analysis with a 50 GeV minimum signal lepton p_{T} cut, in the electron (left) and muon (right) channels.

		p_{T}^{W} [GeV]				
Lepton p_{T} cut [GeV]	Combined (All p_{T}^{W})	0-60	60-120	120-160	160-200	>200
2012 analysis	0.95 ± 0.04	0.39 ± 0.01	0.25 ± 0.02	0.27 ± 0.02	0.42 ± 0.04	0.66 ± 0.06
25	0.95 ± 0.04	0.39 ± 0.01	0.25 ± 0.02	0.27 ± 0.02	0.42 ± 0.04	0.66 ± 0.06
30	0.94 ± 0.04	0.36 ± 0.01	0.25 ± 0.02	0.28 ± 0.02	0.42 ± 0.04	0.66 ± 0.06
35	0.93 ± 0.05	0.34 ± 0.01	0.26 ± 0.02	0.28 ± 0.02	0.42 ± 0.04	0.66 ± 0.06
40	0.92 ± 0.05	0.31 ± 0.01	0.26 ± 0.02	0.29 ± 0.03	0.43 ± 0.04	0.65 ± 0.06
45	0.93 ± 0.05	0.29 ± 0.01	0.25 ± 0.02	0.28 ± 0.02	0.43 ± 0.04	0.68 ± 0.06
50	0.92 ± 0.05	0.26 ± 0.01	0.24 ± 0.02	0.28 ± 0.02	0.42 ± 0.04	0.68 ± 0.06

Table 7.6: Significance in the 1-lepton electron channel for different values of signal lepton p_{T} cut, for $m_H = 125$ GeV. The 2012 analysis is documented in [110].

		p_{T}^{W} [GeV]				
Lepton p_{T} cut [GeV]	Combined (All p_{T}^{W})	0-60	60-120	120-160	160-200	>200
2012 analysis	0.92 ± 0.05	0.43 ± 0.01	0.23 ± 0.02	0.23 ± 0.02	0.39 ± 0.04	0.64 ± 0.07
25	0.92 ± 0.05	0.43 ± 0.01	0.23 ± 0.02	0.23 ± 0.02	0.39 ± 0.04	0.64 ± 0.07
30	0.92 ± 0.05	0.41 ± 0.01	0.24 ± 0.02	0.23 ± 0.02	0.40 ± 0.04	0.64 ± 0.07
35	0.86 ± 0.05	0.37 ± 0.01	0.24 ± 0.02	0.23 ± 0.02	0.38 ± 0.04	0.59 ± 0.06
40	0.84 ± 0.05	0.34 ± 0.01	0.24 ± 0.02	0.22 ± 0.02	0.38 ± 0.04	0.58 ± 0.06
45	0.83 ± 0.05	0.31 ± 0.01	0.23 ± 0.02	0.23 ± 0.02	0.38 ± 0.04	0.58 ± 0.07
50	0.80 ± 0.05	0.28 ± 0.01	0.23 ± 0.02	0.22 ± 0.02	0.37 ± 0.04	0.56 ± 0.07

Table 7.7: Significance in the 1-lepton muon channel for different values of signal lepton p_{T} cut, for $m_H = 125$ GeV. The 2012 analysis is documented in [110].

7.3 Lepton Plus Jets Triggers

7.3.1 Introduction

If the ATLAS $WH\ H \to b\bar{b}$ analysis can not be performed with the single lepton triggers available in run 2, then alternative triggering strategies will be required.

Lepton plus jet triggers present a possible alternative to single lepton triggers for the $WH\ H \to b\bar{b}$ analysis as the $WH\ H \to b\bar{b}$ final state contains two jets coming from the Higgs decay in addition to the lepton from the decay of the W, resulting in a certain fraction of signal events passing lepton plus jets triggers. Also, by requiring jets with p_{T} above a certain threshold, the p_{T} threshold requirement on the lepton can be lowered, while still maintaining a manageable trigger rate.

7.3.2 Method

The analysis framework used for [110] was modified to include a minimum p_{T} cut on all signal leptons in order to emulate a minimum lepton trigger p_{T} threshold. It was also modified to include a minimum p_{T} cut on all jets in order to emulate a minimum jet trigger p_{T} threshold. The full $WH\ H \to b\bar{b}$ analysis was then rerun with this code, with different values for the signal lepton and jet minimum p_{T} cuts in order to emulate different Run 2 trigger options. In addition to emulating single Run 2 triggers, logical ORs of Run 2 triggers were also implemented and tested. The standard analysis (without the additional signal lepton and jet minimum p_{T} cuts) was also run for comparison. Run 2 lepton plus jets triggers considered are listed in table 7.8.

Run 2 Trigger Emulated	Minimum number of electrons	Electron p_{T} requirement	Minimum number of muons	Muon p_{T} requirement	Minimum number of jets	Jet p_{T} requirement
e28_j70	1	$\geq$ 28 GeV			1	$\geq$ 70 GeV
e28_2j55	1	$\geq$ 28 GeV			2	$\geq$ 55 GeV on both jets
mu24_j50			1	$\geq$ 24 GeV	1	$\geq$ 50 GeV
mu24_2j30			1	$\geq$ 24 GeV	2	$\geq$ 30 GeV on both jets

Table 7.8: Lepton plus jets triggers considered for Run 2. Blanks indicate no requirement is applied. Where there is a p_{T} requirement on a type of object, only the N highest-p_{T} objects of that type in an event are required to pass the p_{T} requirement, where N is the minimum number of that type of object required by the trigger.

One caveat in this approach is that applying an analysis level lepton p_{T} cut is not the same as having a trigger level p_{T} cut, but is comparable to within lepton p_{T} resolution at trigger and analysis level. Likewise, applying an analysis level jet p_{T} cut is not the same as having a trigger level p_{T} cut, but is comparable to within jet p_{T} resolution at trigger and analysis level.

In order to better estimate the effects on signal acceptance of the proposed Run 2 triggers, 14 TeV WH $H \to b\bar{b}$ signal Monte Carlo samples were used. These samples also included high pile-up ($\mu = 80$) as is expected in LHC conditions during Run 2.

Unfortunately no background 14 TeV Monte Carlo samples with high ($\mu = 80$, where μ is the average number of proton-proton collisions per bunch-crossing.) pile-up were available. For significance estimations, the 8 TeV samples listed in table 7.1 were therefore used. Significances were calculated in each $m_{b\bar{b}}$ (reconstructed Higgs candidate mass / di-jet mass) bin and then summed in quadrature.

Control tests were performed by setting the signal lepton and jet minimum p_{T} cuts to 0 GeV and comparing results to the default analysis that does not contain emulated triggers [110].

7.3.3 Results

Tables 7.9 and 7.10, respectively for the electron and muon channels, show the fraction of 14 TeV WH $H \to b\bar{b}$ signal events remaining, for $m_H = 125$ GeV, after applying emulated Run 2 triggers, compared to the 2012 analysis [110].

	p_{T}^{W} [GeV]					
Run 2 Trigger Emulated	Combined (All p_{T}^{W})	0-60	60-120	120-160	160-200	>200
e28_j70	0.646 ± 0.002	0.338 ± 0.003	0.880 ± 0.004	0.882 ± 0.006	1.000 ± 0.000	1.000 ± 0.000
e28_2j55	0.401 ± 0.002	0.211 ± 0.002	0.320 ± 0.009	0.647 ± 0.013	0.778 ± 0.010	0.688 ± 0.013
e28_j70 OR e28_2j55	0.673 ± 0.001	0.366 ± 0.003	0.920 ± 0.003	0.941 ± 0.003	1.000 ± 0.000	1.000 ± 0.000

Table 7.9: Fraction of 14 TeV WH $H \to b\bar{b}$ electron channel signal events remaining, for $m_H = 125$ GeV, after applying emulated Run 2 triggers, compared to the 2012 analysis [110].

	p_{T}^{W} [GeV]					
Run 2 Trigger Emulated	Combined (All p_{T}^{W})	0-60	60-120	120-160	160-200	>200
mu24_j50	0.947 ± 0.000	0.926 ± 0.001	0.957 ± 0.002	0.923 ± 0.005	1.000 ± 0.000	1.000 ± 0.000
mu24_2j30	0.809 ± 0.001	0.779 ± 0.003	0.652 ± 0.010	0.846 ± 0.010	1.000 ± 0.000	1.000 ± 0.000
mu24_j50 OR mu24_2j30	0.977 ± 0.000	0.971 ± 0.000	1.000 ± 0.000	0.923 ± 0.005	1.000 ± 0.000	1.000 ± 0.000

Table 7.10: Fraction of 14 TeV WH $H \to b\bar{b}$ muon channel signal events remaining, for $m_H = 125$ GeV, after applying emulated Run 2 triggers, compared to the 2012 analysis [110].

Tables 7.11 and 7.12 show the effects on significance of different emulated Run 2 trigger combinations, using 8 TeV samples for both signal and backgrounds.

		p_{T}^{W} [GeV]				
Run 2 Trigger Emulated	Combined (All p_{T}^{W})	0-60	60-120	120-160	160-200	>200
2012 analysis	1.65 ± 0.389	0.370 ± 0.0153	0.240 ± 0.0212	0.273 ± 0.0333	0.363 ± 0.0435	1.52 ± 0.596
e28_j70	1.63 ± 0.392	0.278 ± 0.0180	0.224 ± 0.0211	0.290 ± 0.0362	0.364 ± 0.0440	1.52 ± 0.594
e28_2j55	1.59 ± 0.402	0.169 ± 0.0239	0.163 ± 0.0295	0.285 ± 0.0727	0.466 ± 0.0899	1.47 ± 0.613
e28_j70 OR e28_2j55	1.63 ± 0.391	0.290 ± 0.0177	0.233 ± 0.0213	0.290 ± 0.0361	0.364 ± 0.0439	1.52 ± 0.594

Table 7.11: 8 TeV WH $H \to b\bar{b}$ significance for emulated Run 2 triggers in the electron channel. The 2012 analysis is documented in [110].

		p_{T}^{W} [GeV]				
Run 2 Trigger Emulated	Combined (All p_{T}^{W})	0-60	60-120	120-160	160-200	>200
2012 analysis	1.29 ± 0.137	0.434 ± 0.0165	0.242 ± 0.0233	0.268 ± 0.0321	0.459 ± 0.0990	1.06 ± 0.231
mu24_j50	1.28 ± 0.138	0.419 ± 0.0166	0.242 ± 0.0233	0.269 ± 0.0321	0.459 ± 0.0989	1.06 ± 0.231
mu24_2j30	1.26 ± 0.138	0.414 ± 0.0170	0.216 ± 0.0222	0.259 ± 0.0337	0.457 ± 0.0997	1.05 ± 0.230
mu24_j50 OR mu24_2j30	1.29 ± 0.137	0.432 ± 0.0165	0.242 ± 0.0233	0.268 ± 0.0321	0.459 ± 0.0989	1.06 ± 0.231

Table 7.12: 8 TeV WH $H \to b\bar{b}$ significance for emulated Run 2 triggers in the muon channel. The 2012 analysis is documented in [110].

7.4 Conclusion

From studies into single lepton trigger thresholds (Section 7.2) we see that as the single lepton trigger thresholds are increased, signal and background acceptances decrease. We also see that signal acceptance decreases more in the lower p_{T}^{W} bins than in the higher p_{T}^{W} bins as single lepton trigger thresholds are increased. Significance increases as p_{T}^{W} increases, for all single lepton trigger thresholds. As single lepton trigger thresholds increase, sensitivity decreases. The sensitivity decreases more in lower p_{T}^{W} bins than in higher p_{T}^{W} bins. Increasing the single lepton trigger thresholds appears to have a small effect on sensitivity in the higher p_{T}^{W} bins. Sensitivity even appears to increase for some data points, when compared to the 2012 analysis [110], however these increases are within statistical uncertainty and so can not be assumed to be anything more than statistical fluctuations.

Since the overall sensitivity for the analysis [110] can be found by combining the sensitivity of all bins in quadrature, bins with higher sensitivity contribute more to the overall sensitivity of the analysis. As such, although there is larger signal and sensitivity loss in lower p_{T}^{W} bins as single lepton trigger thresholds increase, this has a smaller impact on overall sensitivity since these are the lower sensitivity bins of the analysis.

What level of signal loss is acceptable is a subjective question, but a reasonable choice would be to have no more than a 20% loss of signal in high-sensitivity analysis bins. From this we see that a single lepton trigger thresholds of 50 GeV seem reasonable. If we also prescribe a loss in overall sensitivity of no more than 20% then we also see that in the muon channel a single lepton trigger threshold of 50 GeV is at the limit of what is acceptable. In the electron channel a single lepton trigger threshold of 50 GeV gives an acceptable sensitivity. From the trend of changing overall sensitivity with changing single lepton trigger threshold in the electron channel, it is possible that in this channel a single lepton trigger threshold of more than 50 GeV may also give an acceptable sensitivity. Further study would be required to determine this though.

Studies of proposed Run 2 Lepton Plus Jets Triggers (section 7.3) also show that signal acceptance and significance increase with increased p_{T}^{W}. As would be expected, doing a logical OR of multiple triggers increases signal acceptance compared to the individual triggers.

Proposed Run 2 triggers allow for 2 scenarios: One where the EF trigger output rate is limited to 500 Hz, and another (more expensive to implement, costing roughly 1M CHF) scenario where the EF trigger output rate is limited to 1 kHz.

In the 1 kHz scenario, the lowest-p_{T} trigger thresholds for unprescaled single lepton triggers are 28 GeV for electrons and 24 GeV for muons. Clearly these thresholds are suitably low for the $WH\ H \to b\bar{b}$ analysis.

The questions then remains as to whether the 500 Hz scenario is also suitable, or whether more money will need to be spent to implement the 1 kHz scenario.

In the 500 Hz scenario, the lowest-p_{T} trigger thresholds for unprescaled single lepton triggers are 60 GeV for electrons and 50 GeV for muons. These thresholds are on the limit of what is acceptable for the $WH\ H \to b\bar{b}$ analysis. In the 500 Hz scenario it would therefore be useful to include lepton-plus-jet triggers in the $WH\ H \to b\bar{b}$ analysis for increased sensitivity and signal acceptance.

Ultimately the choice of which triggers to use in the Run 2 $WH\ H \to b\bar{b}$ analysis will be based on the relevant costs and benefits. The benefits will be increased sensitivity and signal acceptance. The main cost will be the added complexity to the analysis; primarily the $2^{n_{\mathrm{ElTrig}}} + 2^{n_{\mathrm{MuTrig}}} - 1$ trigger scale factors that will be required (where n_{ElTrig} and n_{MuTrig} are the number of electron-channel and muon-channel triggers used in the analysis). In a scenario where the available single lepton triggers will not, or cannot be guaranteed to, allow sufficient signal acceptance and significance, then the benefits of using extra triggers will outweigh the costs. However if available single lepton triggers will allow sufficient signal acceptance and significance, then it could well be argued that the costs of including extra triggers will outweigh the benefits. In both cases, the definition of 'sufficient' signal acceptance and significance is subjective, but could be reasonably take to be 'sufficient to allow an observation of a 125 GeV Higgs boson decaying to a b-quark pair'.

Another way to look at the problem here is to consider that the choice of which triggers will be available (including the choice of their p_{T} thresholds) in Run 2 will decide what selection of triggers will be required to achieve sufficient signal acceptance and significance in the $WH\ H \to b\bar{b}$ analysis. The choice will then be (when considering the choice between the 500 Hz and 1 kHz trigger scenarios) a choice between spending extra money or introducing extra analysis complexity.

Chapter 8

Conclusion

$pp \rightarrow WH \rightarrow \ell\nu b\bar{b}$ is an important channel in the search for a Higgs boson decaying to a b-quark pair with the ATLAS detector. Systematic uncertainties on the $pp \rightarrow WH \rightarrow \ell\nu b\bar{b}$ signal process have been calculated and presented in chapter 5, and used in setting upper limits on $VH \rightarrow b\bar{b}$ production rate, as presented in chapter 6.

A Standard Model Higgs boson is not observed decaying to b-quark pairs, and a Standard Model Higgs boson with a mass of between 110 GeV and 115 GeV is excluded. For a Standard Model Higgs boson with a mass of 125 GeV, the observed (expected) upper limit on the cross-section times the branching ratio is found to be 2.16 (1.07) times the Standard Model prediction, and the best fit signal strength is $\mu = 1.09\ ^{+0.43}_{-0.42}\ (\text{stat})\ ^{+0.44}_{-0.37}\ (\text{syst}) = 1.09\ ^{+0.61}_{-0.56}$. These results are consistent with a Standard Model Higgs boson with a mass of 125 GeV.

Determining whether the recently discovered Higgs boson does decay to b-quark pairs will require further study, and the collection of more data with the ATLAS detector. In order to collect suitable data for this purpose, suitable triggers will be required. This has been studied, and suitable future triggering strategies have been presented in chapter 7.

This work combines with the work of others in the ATLAS collaboration and particle physics community-wide effort to determine whether the recently discovered boson with a mass of about 125 GeV [3, 4] is the Standard Model Higgs boson.

It is just one part too of the larger ongoing effort by particle physics and science in general to further human understanding.

It is part of mankind's continuing quest to know what Timaeus claimed is known only by the creator, to understand the underlying laws of the universe.

Appendix A

Systematic Uncertainties Arising From Scale Factors - Additional Information

A.1 Results

A.1.1 Cross-Sections And Acceptances

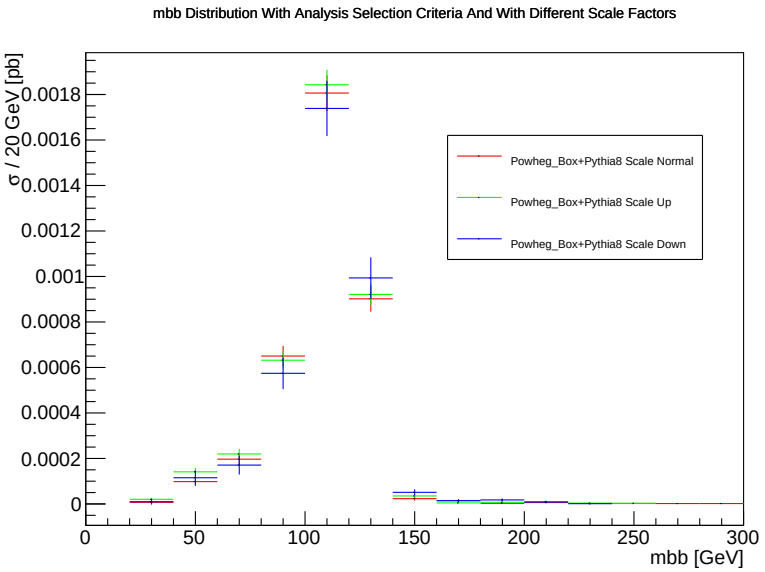

Figure A.1: $m_{b\bar{b}}$ distributions, for the $WH \to \ell\nu b\bar{b}$ analysis, with $m_H = 125$ GeV, with analysis selection criteria applied and different scale factors. Two-jet final states are included. Error bars show statistical uncertainty.

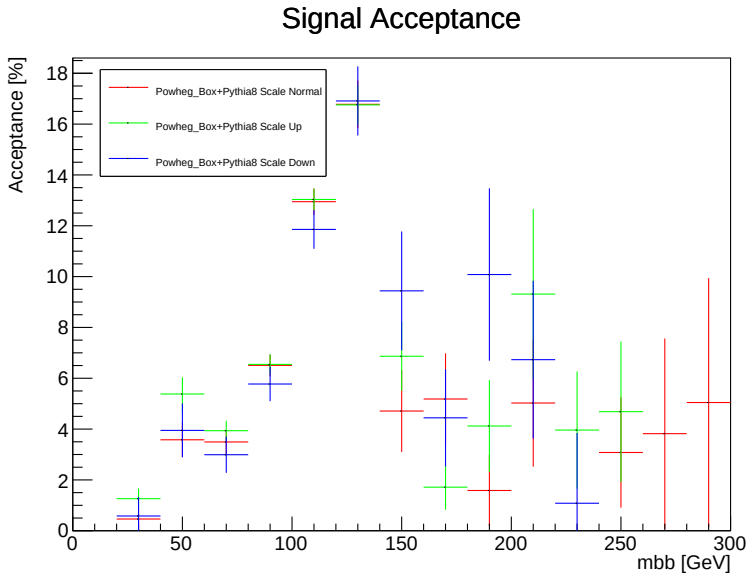

Figure A.2: Signal acceptance, for the $WH \to \ell\nu b\bar{b}$ analysis, with $m_H = 125$ GeV, with different scale factors. Two-jet final states are included. Error bars show statistical uncertainty.

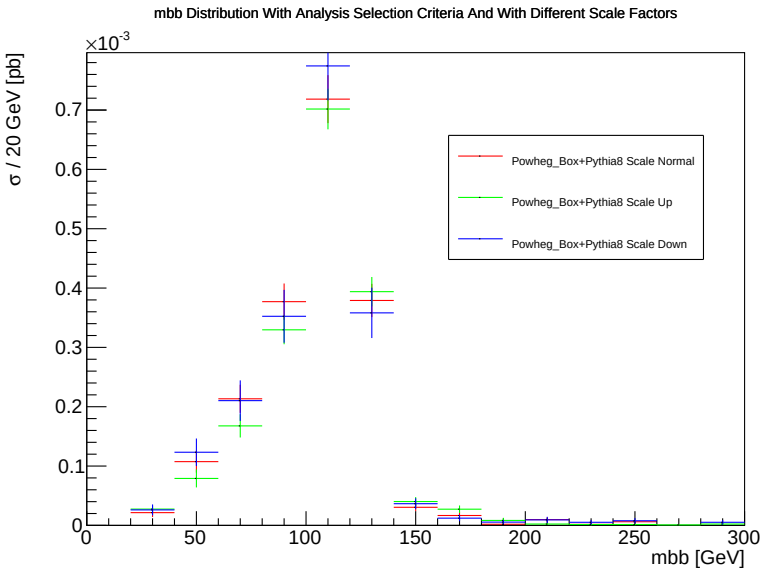

Figure A.3: $m_{b\bar{b}}$ distributions, for the $WH \to \ell\nu b\bar{b}$ analysis, with $m_H = 125$ GeV, with analysis selection criteria applied and different scale factors. Three-jet final states are included. Error bars show statistical uncertainty.

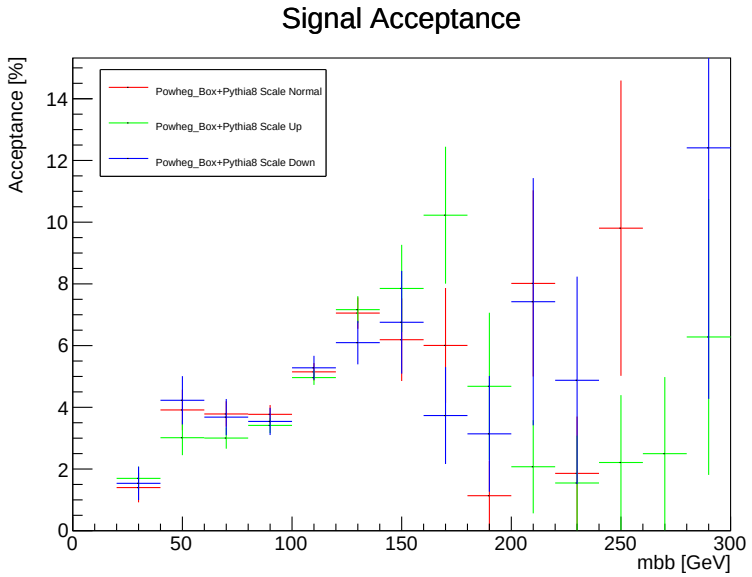

Figure A.4: Signal acceptance, for the $WH \to \ell\nu b\bar{b}$ analysis, with $m_H = 125$ GeV, with different scale factors. Three-jet final states are included. Error bars show statistical uncertainty.

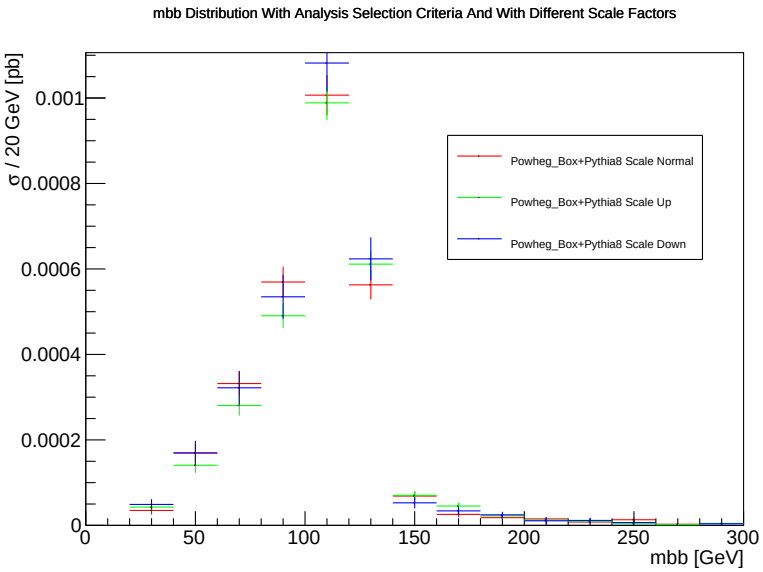

Figure A.5: $m_{b\bar{b}}$ distributions, for the $WH \to \ell\nu b\bar{b}$ analysis, with $m_H = 125$ GeV, with analysis selection criteria applied and different scale factors. $N_{\text{jets}} \geq 3$ final states are included. Error bars show statistical uncertainty.

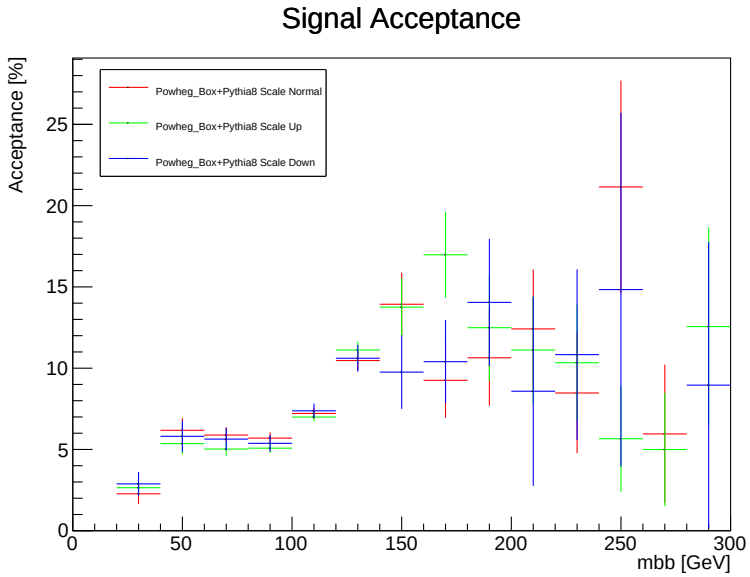

Figure A.6: Signal acceptance, for the $WH \to \ell\nu b\bar{b}$ analysis, with $m_H = 125$ GeV, with different scale factors. $N_{\text{jets}} \geq 3$ final states are included. Error bars show statistical uncertainty.

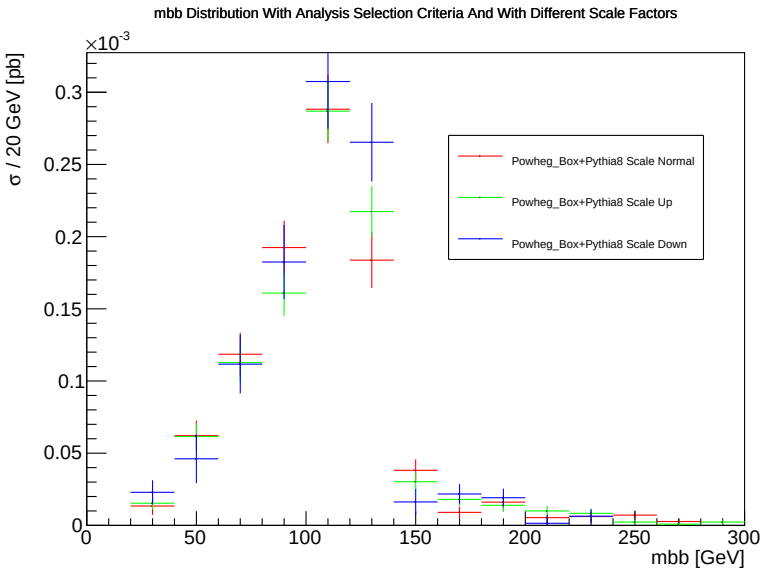

Figure A.7: $m_{b\bar{b}}$ distributions, for the $WH \to \ell\nu b\bar{b}$ analysis, with $m_H = 125$ GeV, with analysis selection criteria applied and different scale factors. $N_{\text{jets}} \geq 4$ final states are included. Error bars show statistical uncertainty.

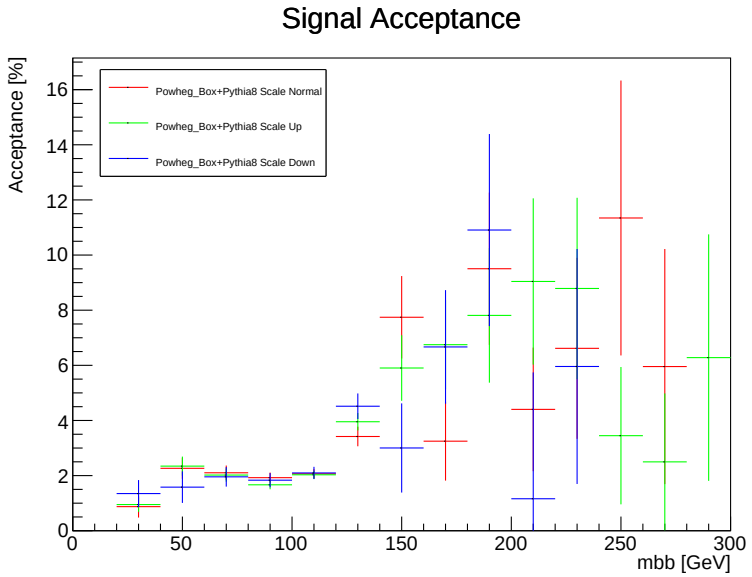

Figure A.8: Signal acceptance, for the $WH \to \ell\nu b\bar{b}$ analysis, with $m_H = 125$ GeV, with different scale factors. $N_{\text{jets}} \geq 4$ final states are included. Error bars show statistical uncertainty.

A.1.2 Uncertainties

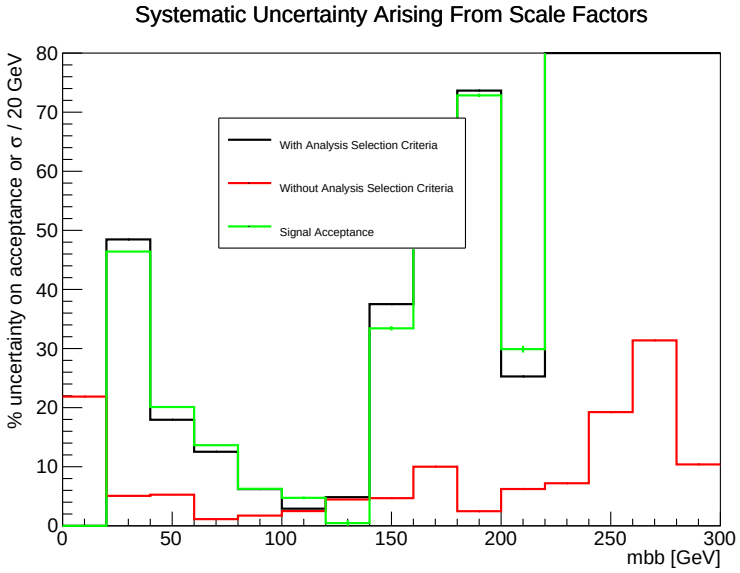

Figure A.9: Systematic uncertainties arising from scale factors, for the $WH \to \ell\nu b\bar{b}$ analysis, with $m_H = 125$ GeV, not taking account of logarithmic cancellations, on the cross sections σ_{asc} and $\sigma_{\text{inclusive}}$, and the acceptance A. Two-jet final states are included. Error bars show statistical uncertainty.

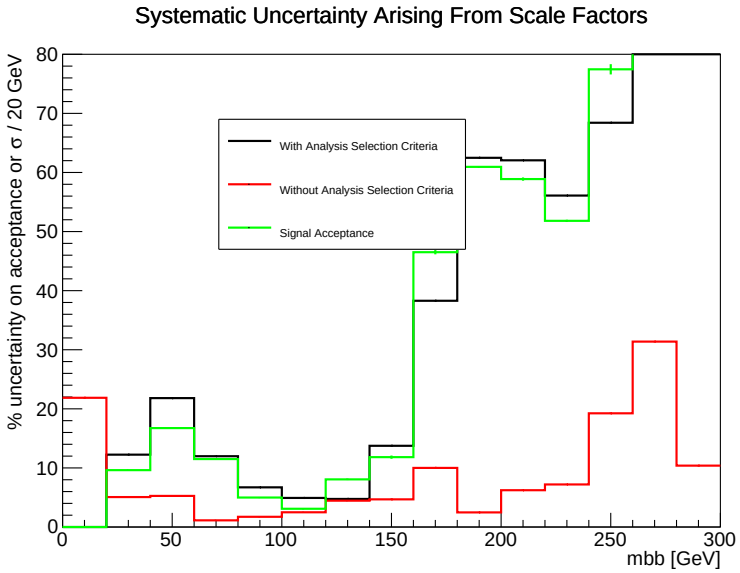

Figure A.10: Systematic uncertainties arising from scale factors, for the $WH \to \ell\nu b\bar{b}$ analysis, with $m_H = 125$ GeV, not taking account of logarithmic cancellations, on the cross sections σ_{asc} and $\sigma_{\text{inclusive}}$, and the acceptance A. Three-jet final states are included. Error bars show statistical uncertainty.

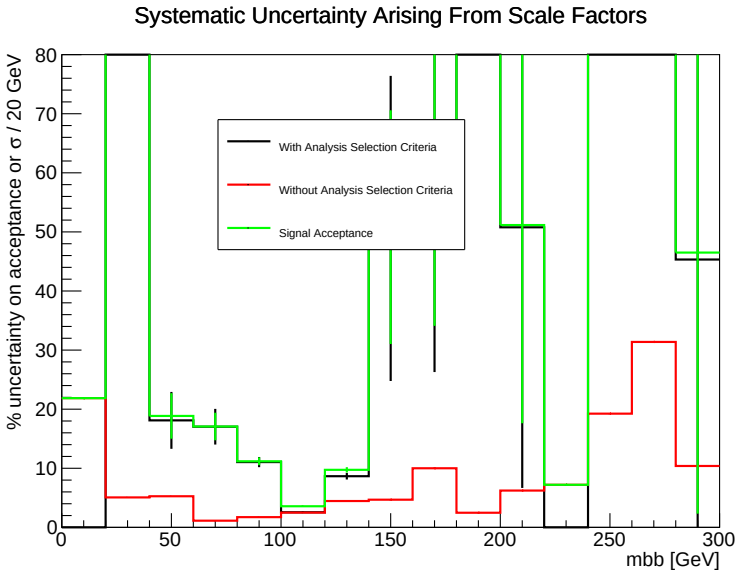

Figure A.11: Systematic uncertainties arising from scale factors, for the $WH \to \ell\nu b\bar{b}$ analysis, with $m_H = 125$ GeV, taking account of logarithmic cancellations, on the cross sections σ_{asc} and $\sigma_{\text{inclusive}}$, and the acceptance A. Two-jet final states are included. Error bars show statistical uncertainty.

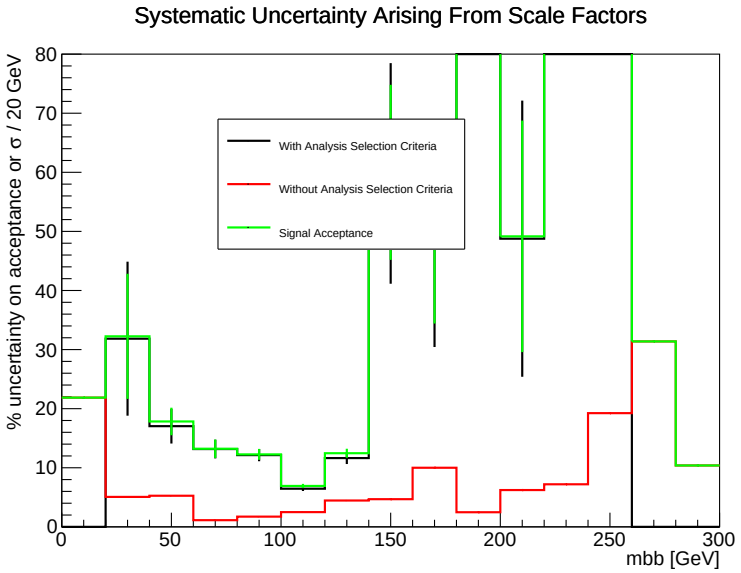

Figure A.12: Systematic uncertainties arising from scale factors, for the $WH \to \ell\nu b\bar{b}$ analysis, with $m_H = 125$ GeV, taking account of logarithmic cancellations, on the cross sections σ_{asc} and $\sigma_{\text{inclusive}}$, and the acceptance A. Three-jet final states are included. Error bars show statistical uncertainty.

Appendix B

Systematic Uncertainties Arising From Parton Distribution Functions - Additional Information

B.1 Results

B.1.1 Comparison Of Central Members

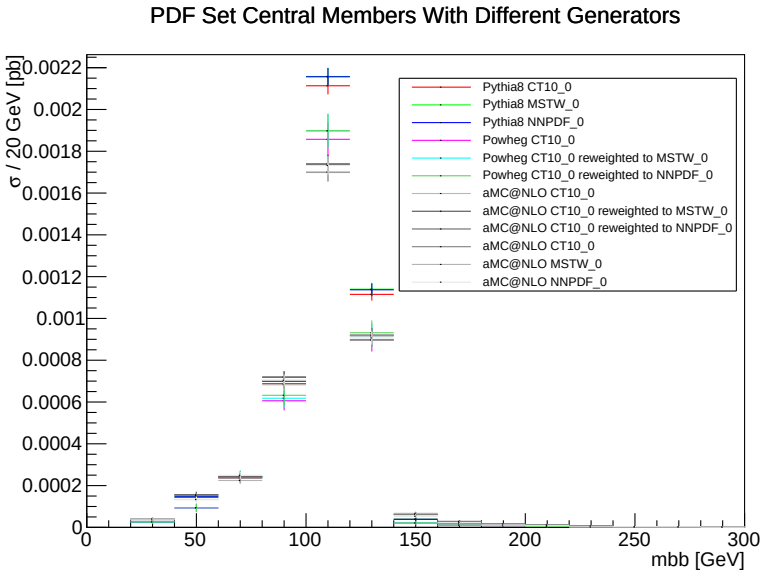

Figure B.1: $m_{b\bar{b}}$ distributions, for $m_H = 125$ GeV, with different event generator and PDF set central members. Analysis event selection criteria have been applied. Two-jet final states are included. Error bars show statistical uncertainty.

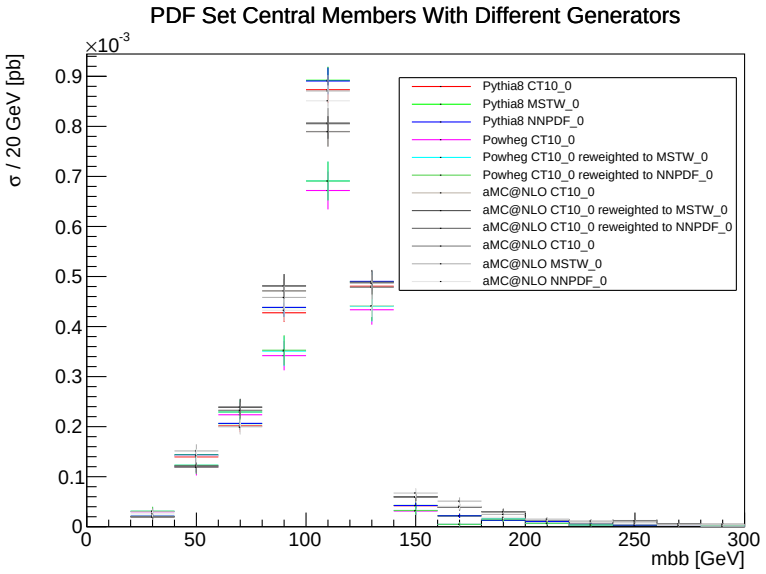

Figure B.2: $m_{b\bar{b}}$ distributions, for $m_H = 125$ GeV, with different event generator and PDF set central members. Analysis event selection criteria have been applied. Three-jet final states are included. Error bars show statistical uncertainty.

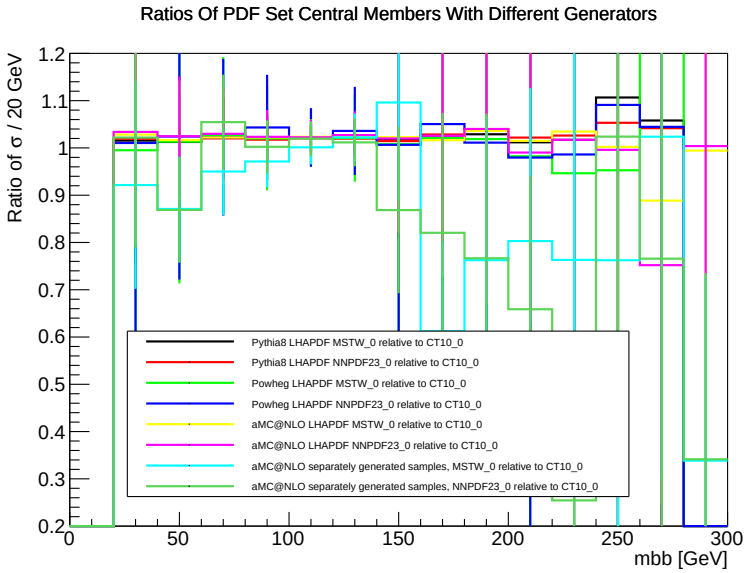

Figure B.3: Ratios of $m_{b\bar{b}}$ distributions, for $m_H = 125$ GeV, with different event generator and PDF set central members. Analysis event selection criteria have been applied. Two-jet final states are included. Error bars show statistical uncertainty.

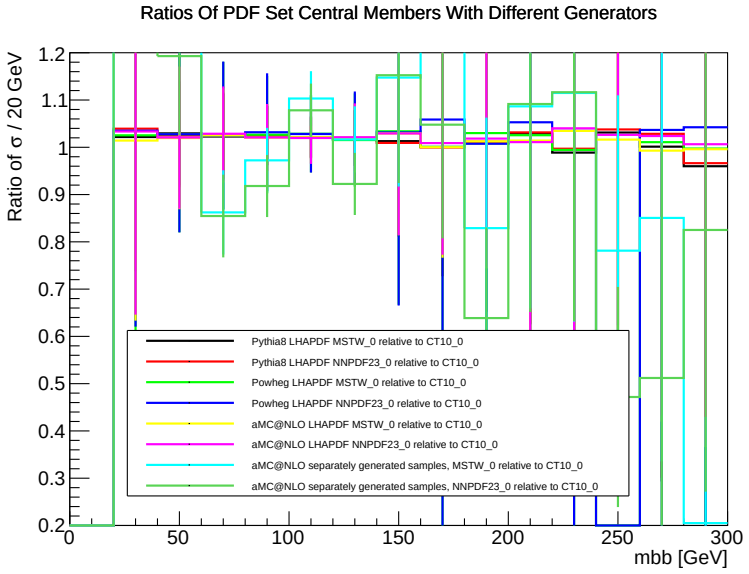

Figure B.4: Ratios of $m_{b\bar{b}}$ distributions, for $m_H = 125$ GeV, with different event generator and PDF set central members. Analysis event selection criteria have been applied. Three-jet final states are included. Error bars show statistical uncertainty.

B.1.2 Cross-Sections And Acceptances

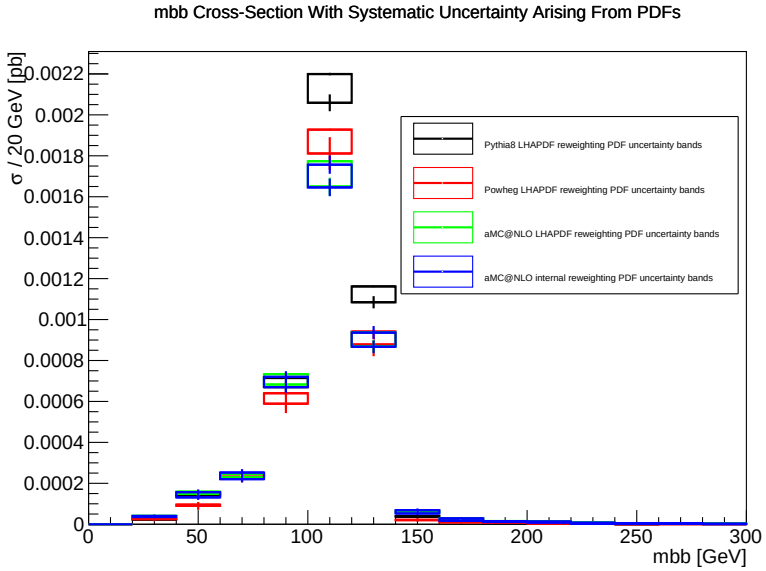

Figure B.5: $m_{b\bar{b}}$ distributions, with analysis selection criteria applied, for different samples sets. Two-jet final states are included. Systematic uncertainty is shown as a band for each PDF set. Error bars on each band show the statistical uncertainty.

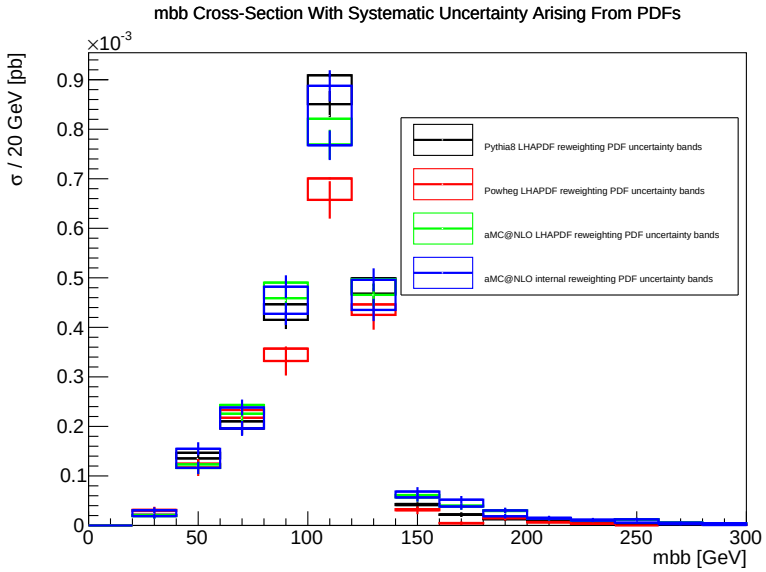

Figure B.6: $m_{b\bar{b}}$ distributions, with analysis selection criteria applied, for different samples sets. Three-jet final states are included. Systematic uncertainty is shown as a band for each PDF set. Error bars on each band show the statistical uncertainty.

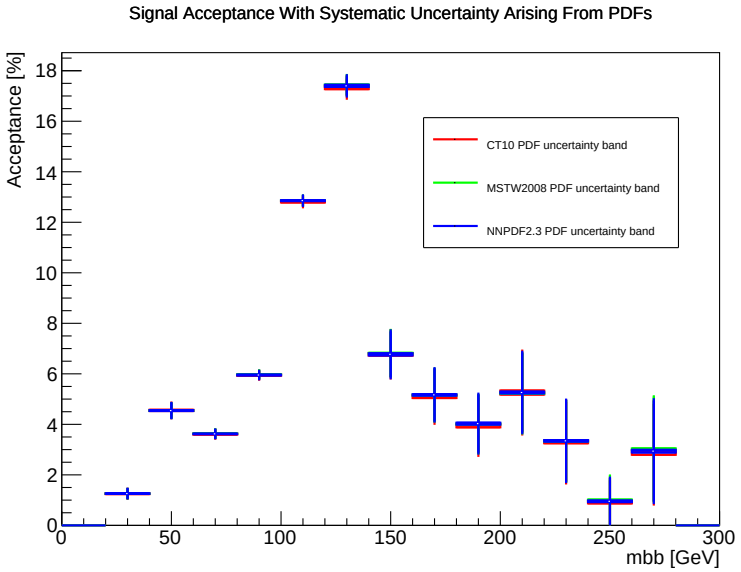

Figure B.7: Signal acceptance for the 'Pythia8' samples set. Two-jet final states are included. Systematic uncertainty is shown as a band for each PDF set. Error bars on each band show the statistical uncertainty.

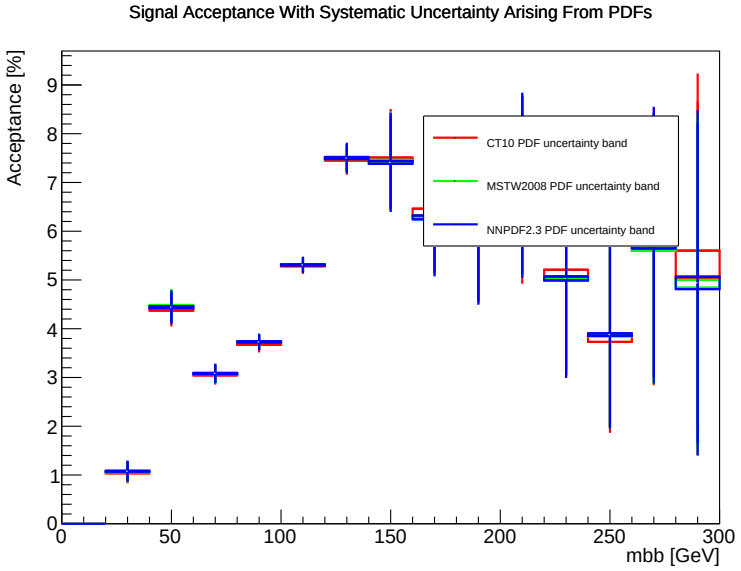

Figure B.8: Signal acceptance for the 'Pythia8' samples set. Three-jet final states are included. Systematic uncertainty is shown as a band for each PDF set. Error bars on each band show the statistical uncertainty.

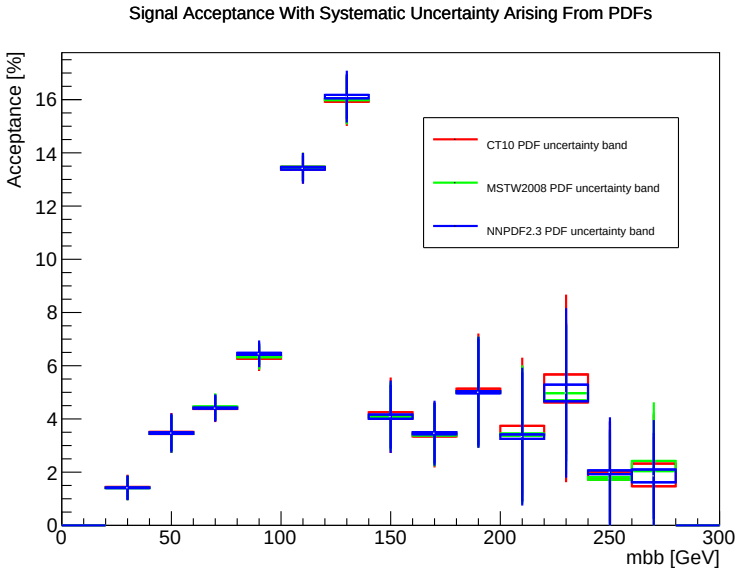

Figure B.9: Signal acceptance for the 'Powheg' samples set. Two-jet final states are included. Systematic uncertainty is shown as a band for each PDF set. Error bars on each band show the statistical uncertainty.

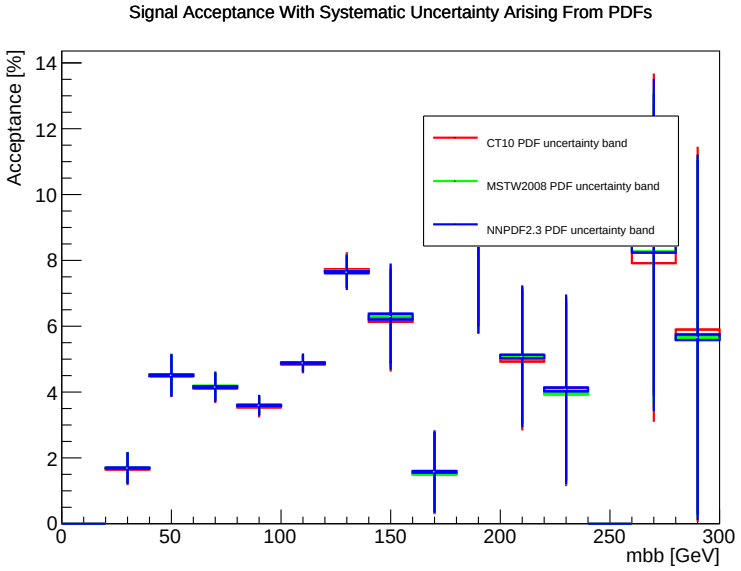

Figure B.10: Signal acceptance for the 'Powheg' samples set. Three-jet final states are included. Systematic uncertainty is shown as a band for each PDF set. Error bars on each band show the statistical uncertainty.

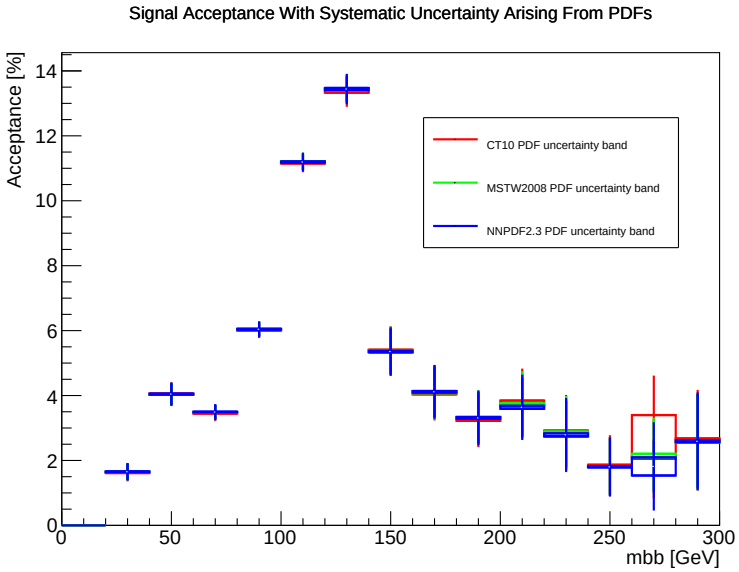

Figure B.11: Signal acceptance for the 'aMC@NLO' samples set. Two-jet final states are included. Systematic uncertainty is shown as a band for each PDF set. Error bars on each band show the statistical uncertainty.

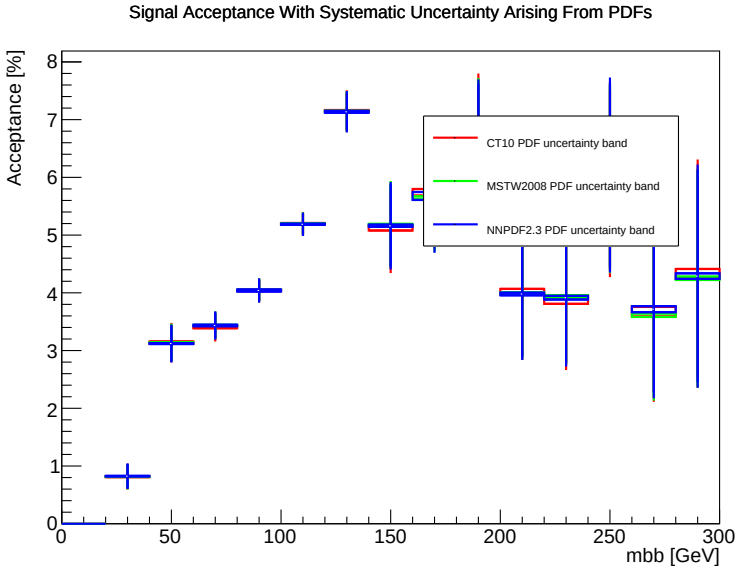

Figure B.12: Signal acceptance for the 'aMC@NLO' samples set. Three-jet final states are included. Systematic uncertainty is shown as a band for each PDF set. Error bars on each band show the statistical uncertainty.

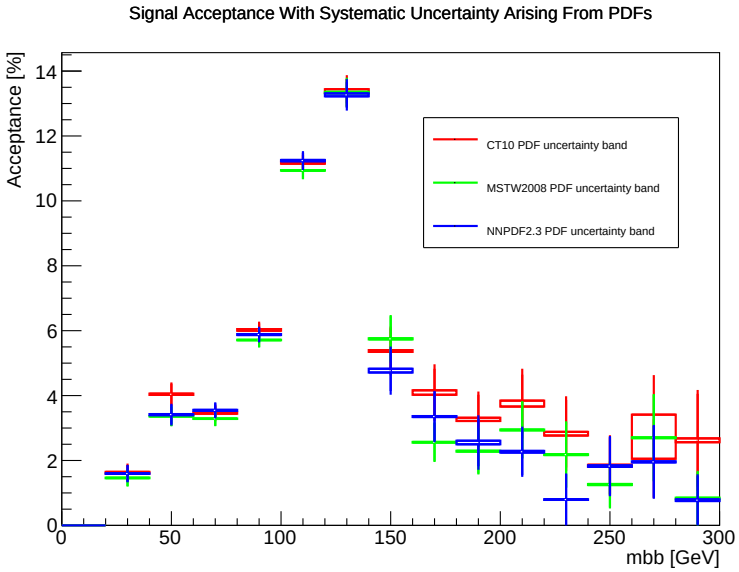

Figure B.13: Signal acceptance for the 'aMC@NLO-internal' samples set. Two-jet final states are included. Systematic uncertainty is shown as a band for each PDF set. Error bars on each band show the statistical uncertainty.

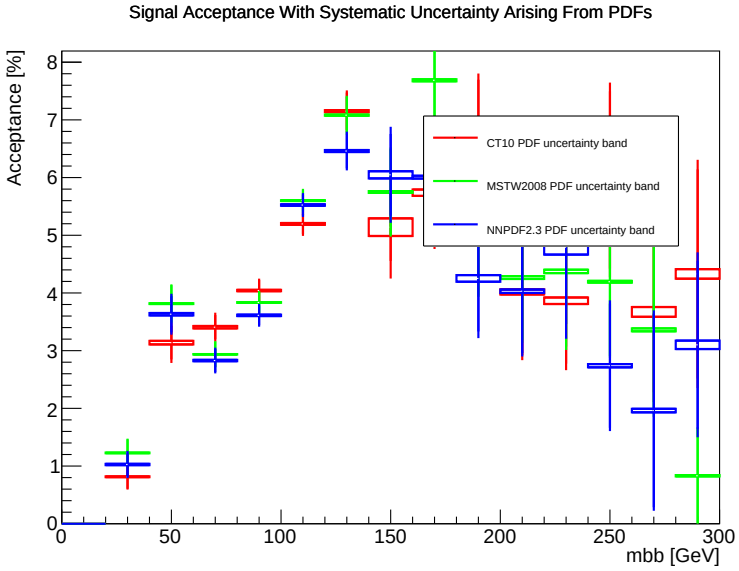

Figure B.14: Signal acceptance for the 'aMC@NLO-internal' samples set. Three-jet final states are included. Systematic uncertainty is shown as a band for each PDF set. Error bars on each band show the statistical uncertainty.

B.1.3 Fractional Uncertainties

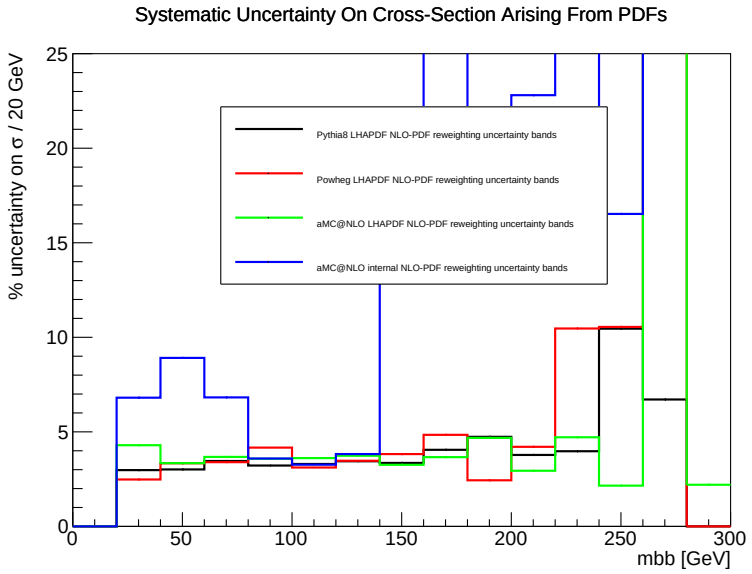

Figure B.15: Systematic uncertainties on signal cross-section, with analysis selection criteria applied, for different sample sets. Two-jet final states are included. Error bars show statistical uncertainty.

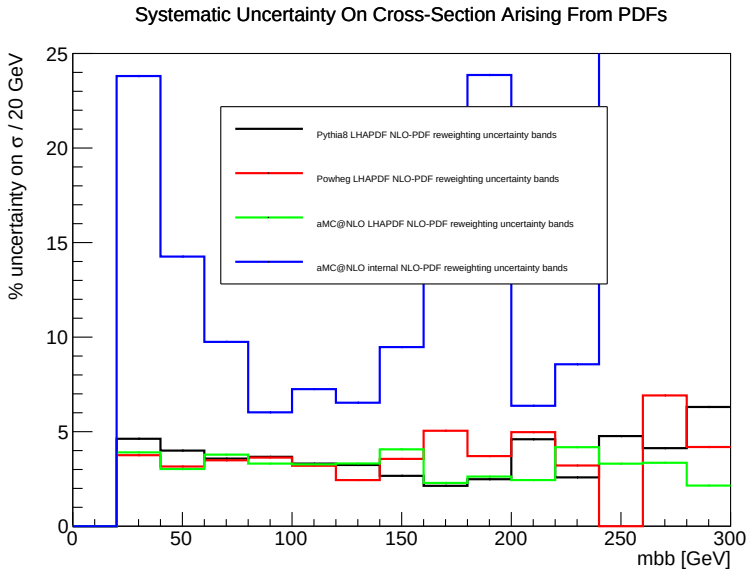

Figure B.16: Systematic uncertainties on signal cross-section, with analysis selection criteria applied, for different sample sets. Three-jet final states are included. Error bars show statistical uncertainty.

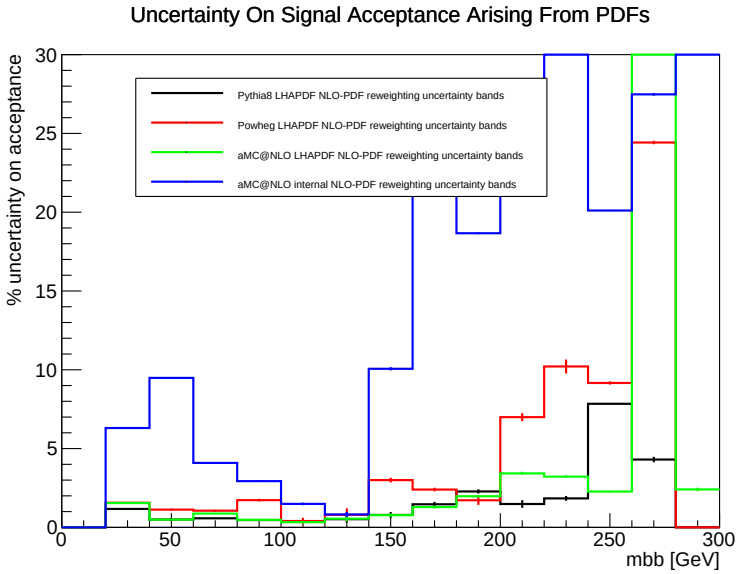

Figure B.17: Systematic uncertainties on signal acceptance for different sample sets. Two-jet final states are included. Error bars show statistical uncertainty.

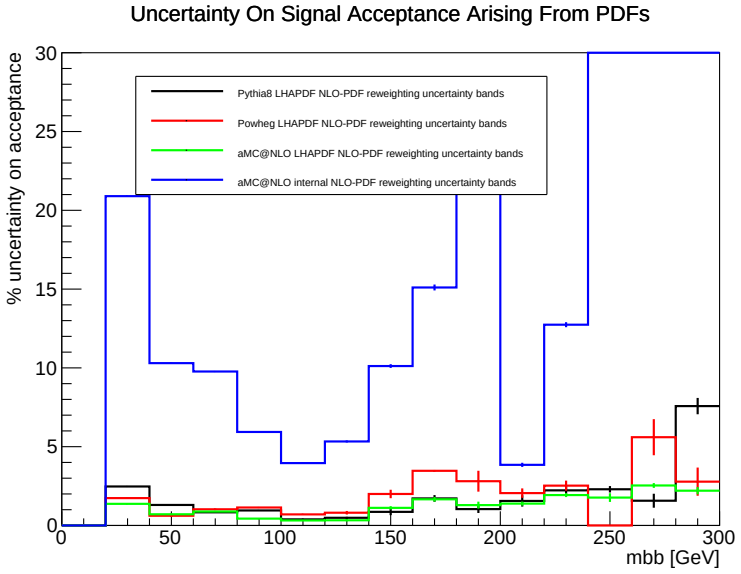

Figure B.18: Systematic uncertainties on signal acceptance for different sample sets. Three-jet final states are included. Error bars show statistical uncertainty.

B.1.4 Study Of aMC@NLO Internal Reweighting Results

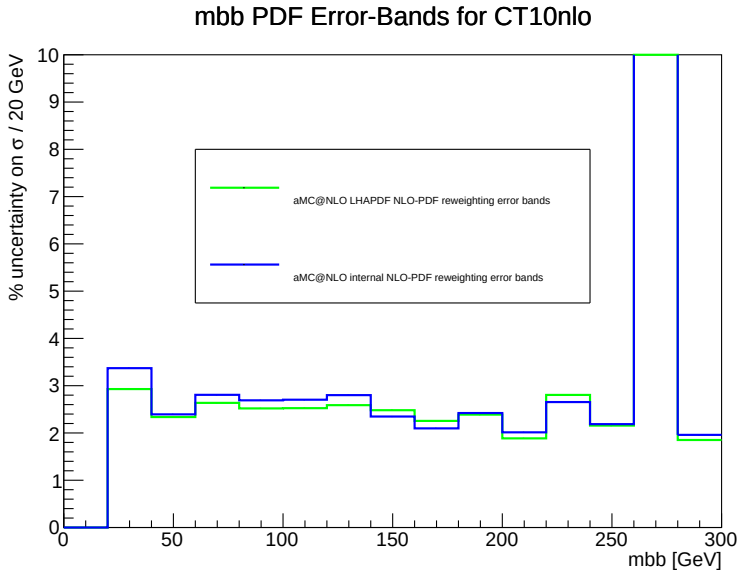

Figure B.19: Systematic uncertainties on signal cross-section, with analysis selection criteria applied, for the CT10nlo PDF set. Distributions for aMC@NLO reweighted with LHAPDF, and for aMC@NLO internally reweighted, are shown. Two and three-jet final states are included. Error bars show statistical uncertainty.

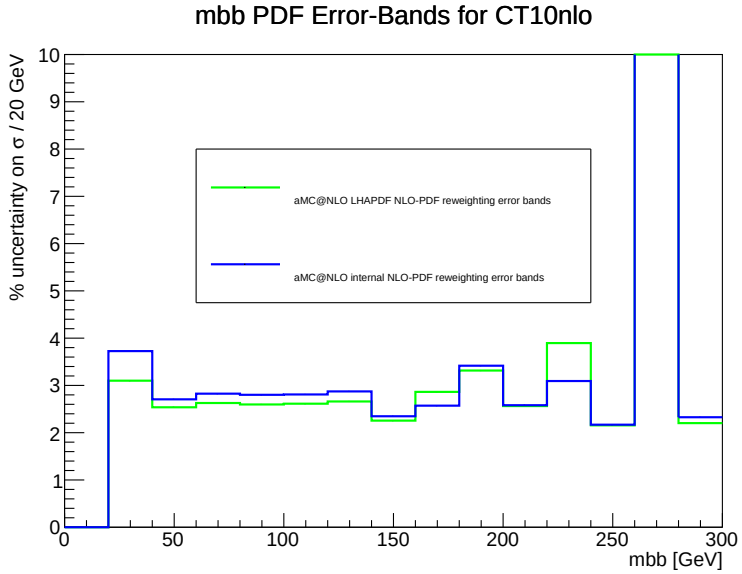

Figure B.20: Systematic uncertainties on signal cross-section, with analysis selection criteria applied, for the CT10nlo PDF set. Distributions for aMC@NLO reweighted with LHAPDF, and for aMC@NLO internally reweighted, are shown. Two-jet final states are included. Error bars show statistical uncertainty.

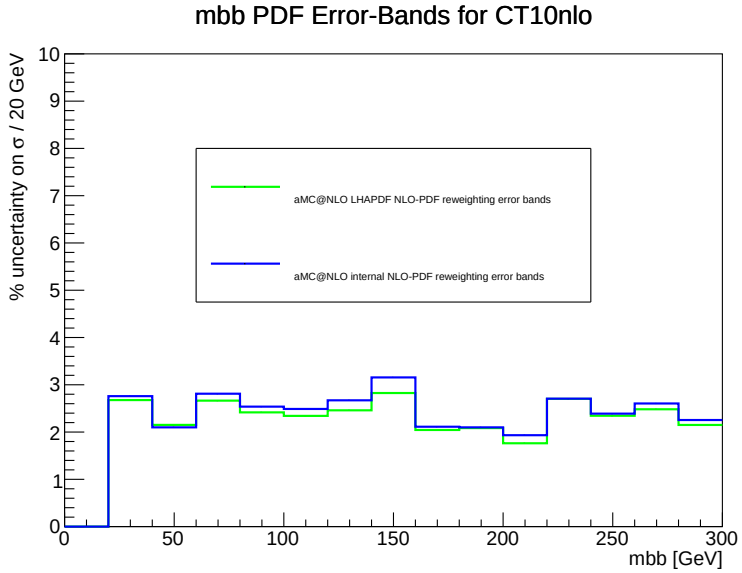

Figure B.21: Systematic uncertainties on signal cross-section, with analysis selection criteria applied, for the CT10nlo PDF set. Distributions for aMC@NLO reweighted with LHAPDF, and for aMC@NLO internally reweighted, are shown. Three-jet final states are included. Error bars show statistical uncertainty.

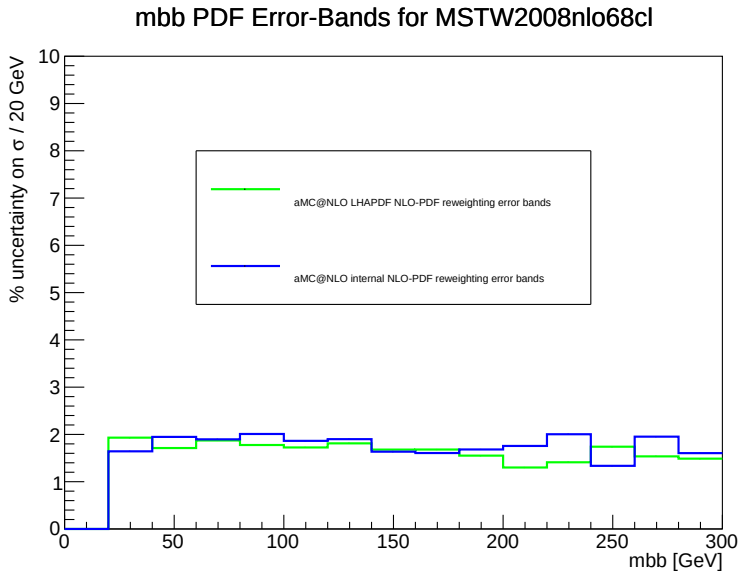

Figure B.22: Systematic uncertainties on signal cross-section, with analysis selection criteria applied, for the MSTW2008nlo68cl PDF set. Distributions for aMC@NLO reweighted with LHAPDF, and for aMC@NLO internally reweighted, are shown. Two and three-jet final states are included. Error bars show statistical uncertainty.

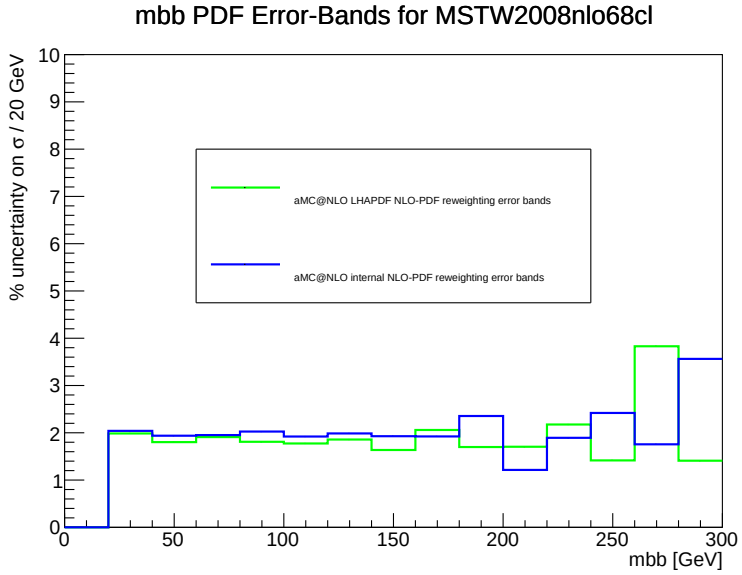

Figure B.23: Systematic uncertainties on signal cross-section, with analysis selection criteria applied, for the MSTW2008nlo68cl PDF set. Distributions for aMC@NLO reweighted with LHAPDF, and for aMC@NLO internally reweighted, are shown. Two-jet final states are included. Error bars show statistical uncertainty.

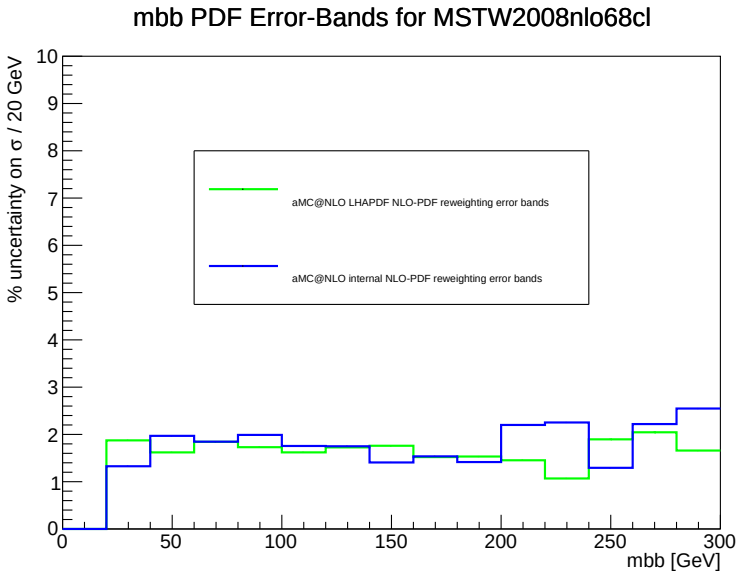

Figure B.24: Systematic uncertainties on signal cross-section, with analysis selection criteria applied, for the MSTW2008nlo68cl PDF set. Distributions for aMC@NLO reweighted with LHAPDF, and for aMC@NLO internally reweighted, are shown. Three-jet final states are included. Error bars show statistical uncertainty.

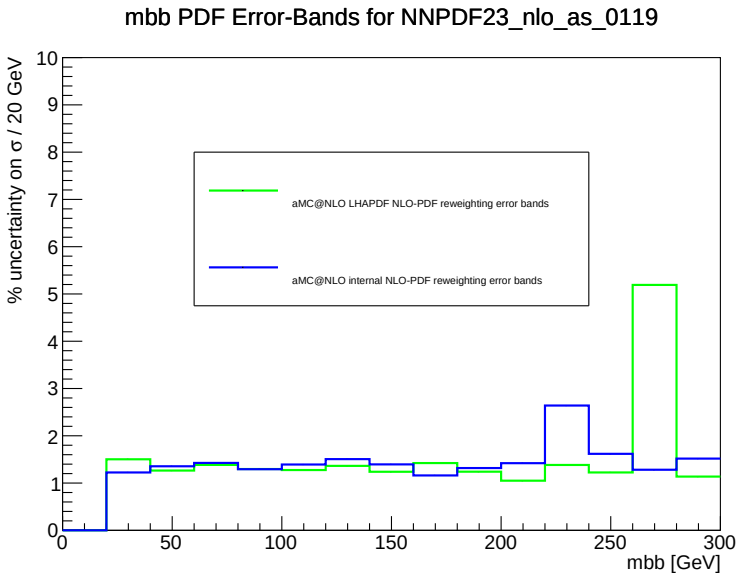

Figure B.25: Systematic uncertainties on signal cross-section, with analysis selection criteria applied, for the NNPDF23_nlo_as_0119 PDF set. Distributions for aMC@NLO reweighted with LHAPDF, and for aMC@NLO internally reweighted, are shown. Two and three-jet final states are included. Error bars show statistical uncertainty.

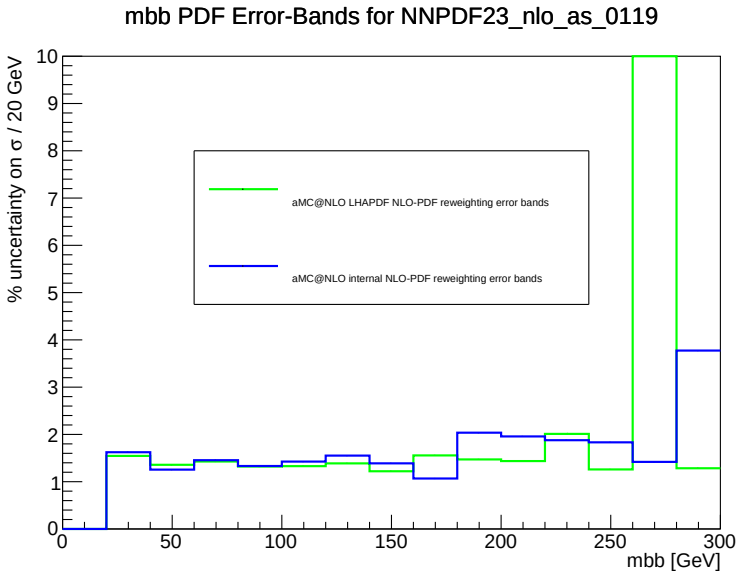

Figure B.26: Systematic uncertainties on signal cross-section, with analysis selection criteria applied, for the NNPDF23_nlo_as_0119 PDF set. Distributions for aMC@NLO reweighted with LHAPDF, and for aMC@NLO internally reweighted, are shown. Two-jet final states are included. Error bars show statistical uncertainty.

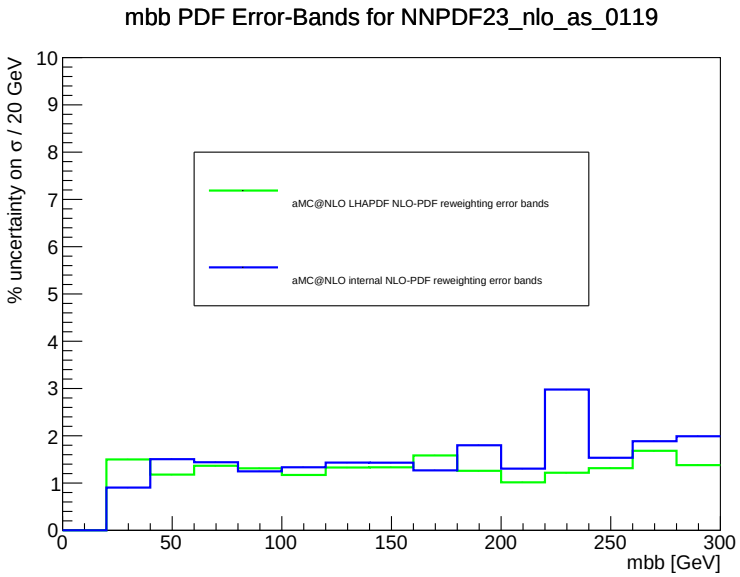

Figure B.27: Systematic uncertainties on signal cross-section, with analysis selection criteria applied, for the NNPDF23_nlo_as_0119 PDF set. Distributions for aMC@NLO reweighted with LHAPDF, and for aMC@NLO internally reweighted, are shown. Three-jet final states are included. Error bars show statistical uncertainty.

B.1.5 Averaged Uncertainties

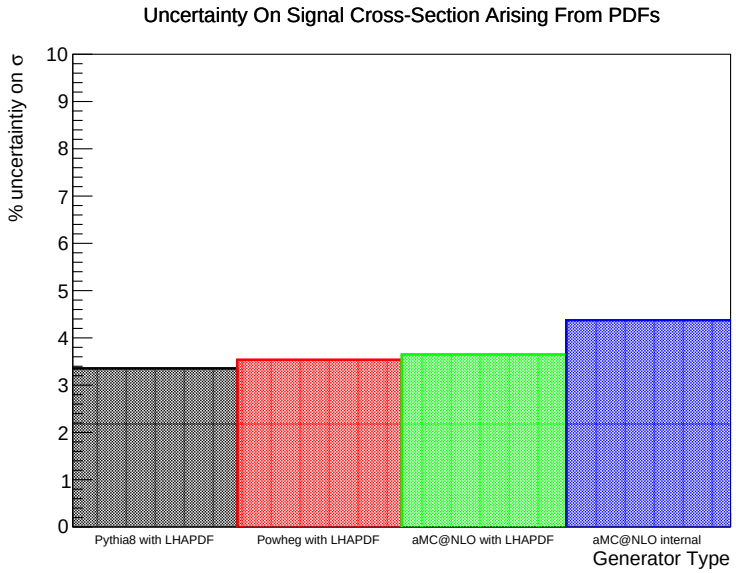

Figure B.28: Systematic uncertainties on signal cross-section, for the $WH \to \ell\nu b\bar{b}$ analysis, with $m_H = 125$ GeV, with analysis selection criteria applied, for different sample sets. Two-jet final states are included.

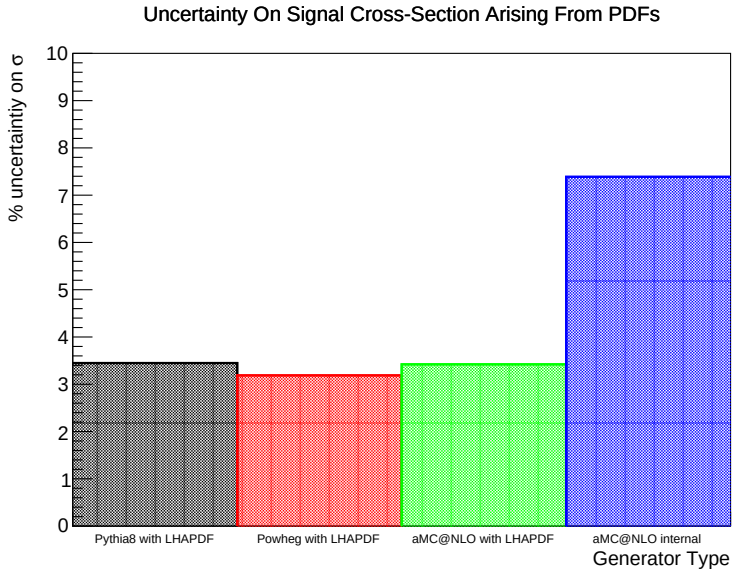

Figure B.29: Systematic uncertainties on signal cross-section, for the $WH \to \ell\nu b\bar{b}$ analysis, with $m_H = 125$ GeV, with analysis selection criteria applied, for different sample sets. Three-jet final states are included.

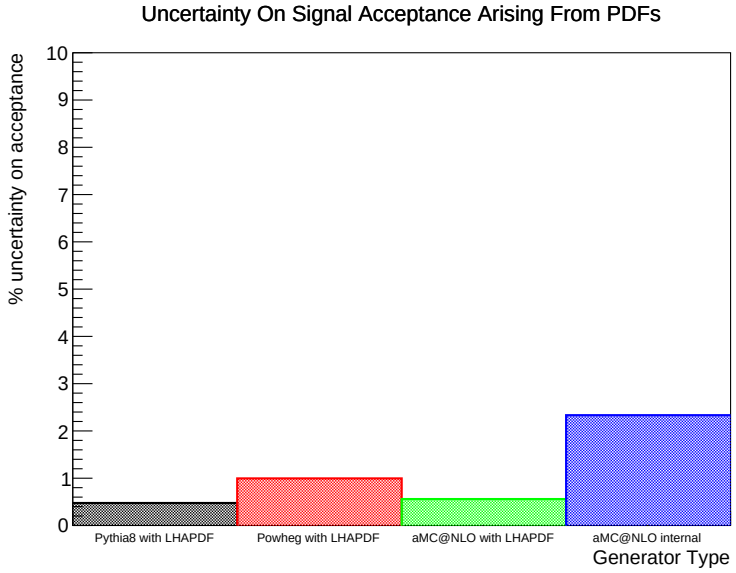

Figure B.30: Systematic uncertainties on signal acceptance, for the $WH \to \ell\nu b\bar{b}$ analysis, with $m_H = 125$ GeV, for different sample sets. Two-jet final states are included.

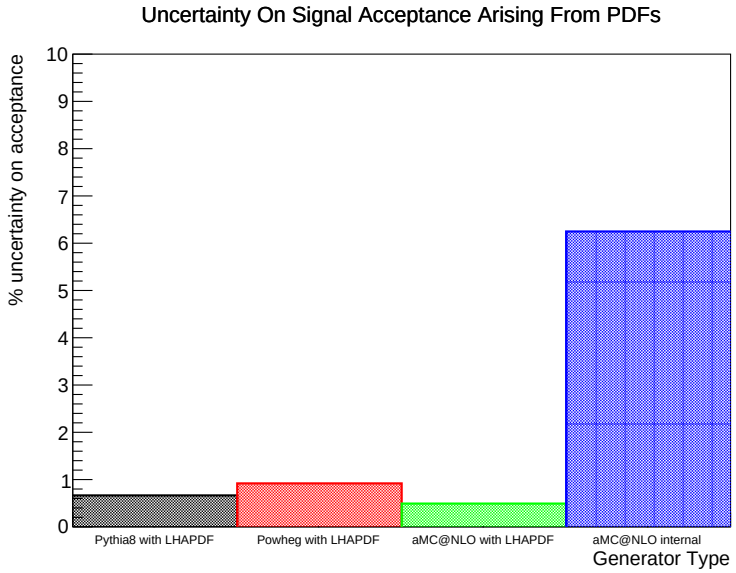

Figure B.31: Systematic uncertainties on signal acceptance, for the $WH \to \ell\nu b\bar{b}$ analysis, with $m_H = 125$ GeV, for different sample sets. Three-jet final states are included.

Appendix C

Systematic Uncertainties Arising From α_s - Additional Information

C.1 Results

C.1.1 Cross-Sections And Acceptances

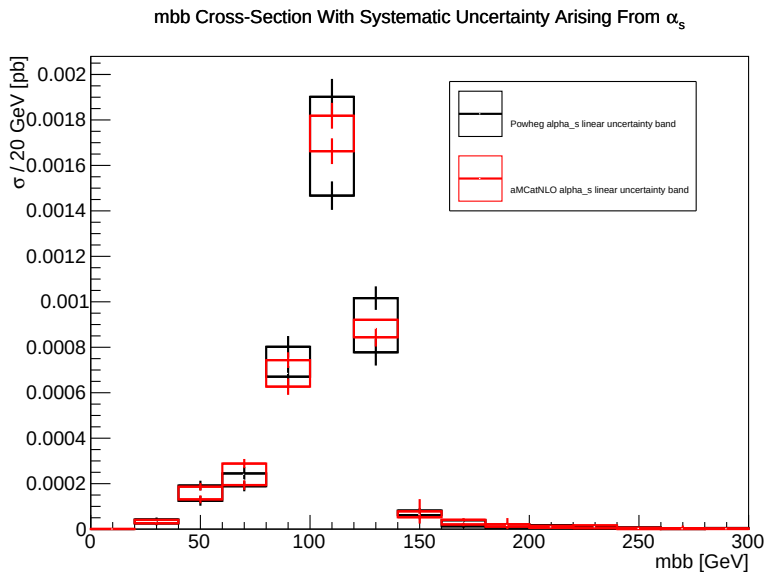

Figure C.1: $m_{b\bar{b}}$ distributions, with analysis selection criteria applied, for different samples sets. Two-jet final states are included. Systematic uncertainty is shown as a band for each sample set. Error bars on each band show the statistical uncertainty.

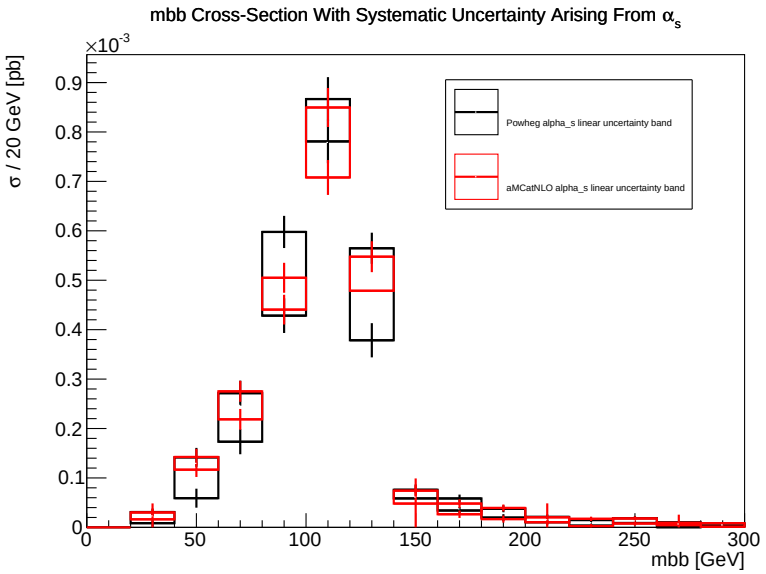

Figure C.2: $m_{b\bar{b}}$ distributions, with analysis selection criteria applied, for different samples sets. Three-jet final states are included. Systematic uncertainty is shown as a band for each sample set. Error bars on each band show the statistical uncertainty.

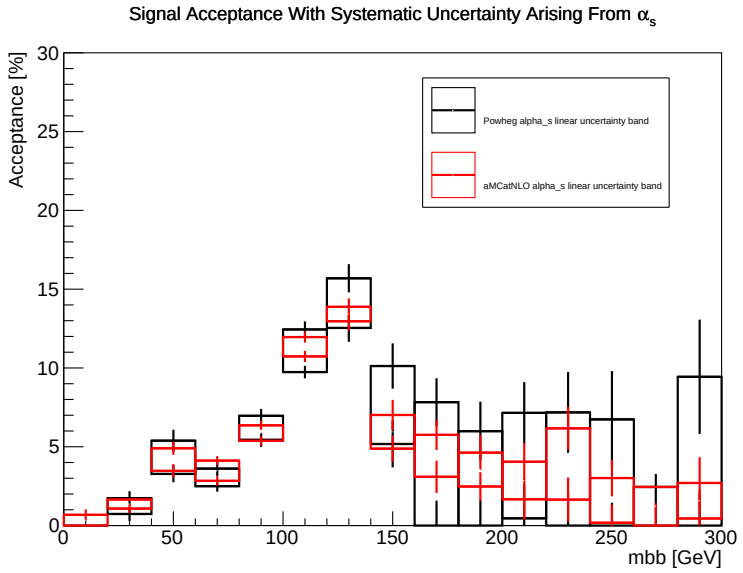

Figure C.3: Signal acceptance, for different samples sets. Two-jet final states are included. Systematic uncertainty is shown as a band for each sample set. Error bars on each band show the statistical uncertainty.

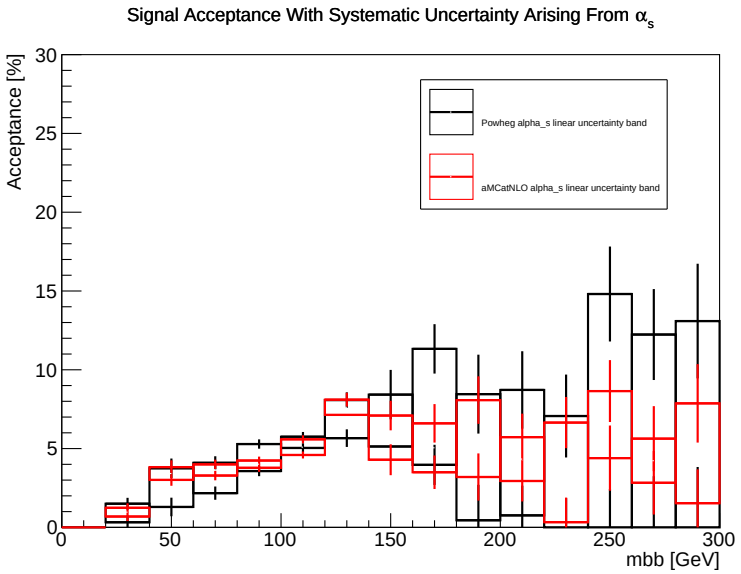

Figure C.4: Signal acceptance, for different samples sets. Three-jet final states are included. Systematic uncertainty is shown as a band for each sample set. Error bars on each band show the statistical uncertainty.

C.1.2 Uncertainties

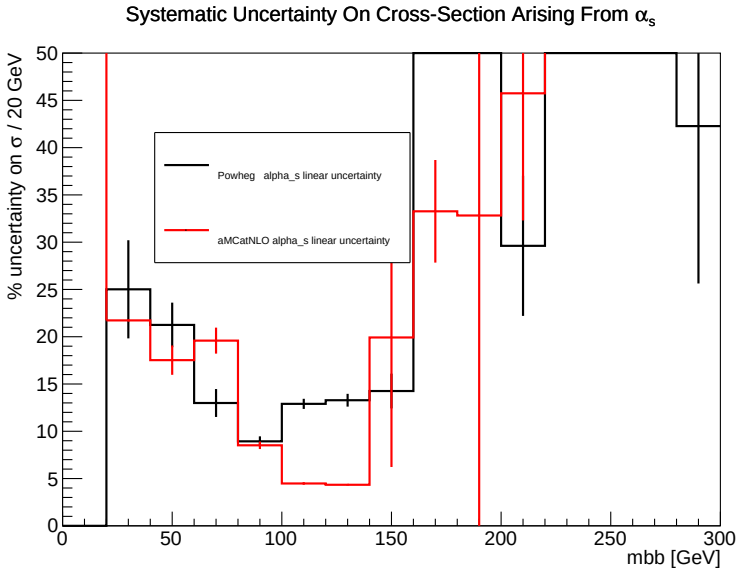

Figure C.5: Systematic uncertainties on signal cross-section, for the $WH \to \ell\nu b\bar{b}$ analysis, with $m_H = 125$ GeV, with analysis selection criteria applied, for different sample sets. Two-jet final states are included. Error bars show statistical uncertainty.

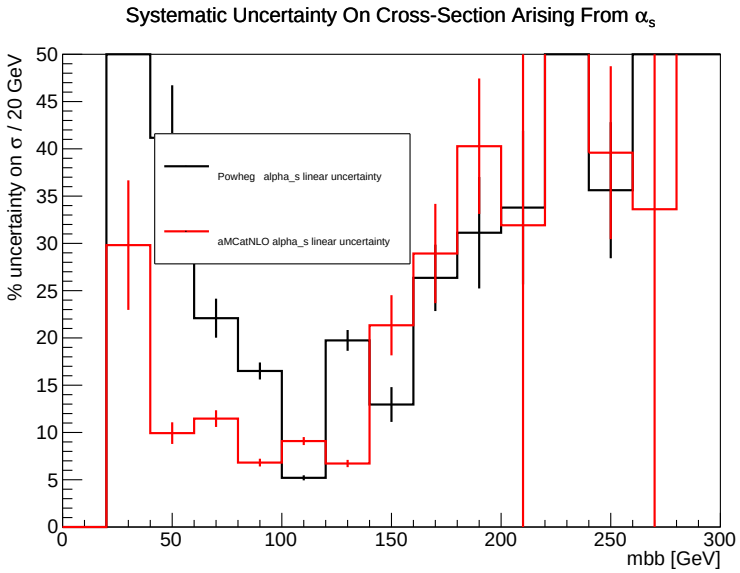

Figure C.6: Systematic uncertainties on signal cross-section, for the $WH \to \ell\nu b\bar{b}$ analysis, with $m_H = 125$ GeV, with analysis selection criteria applied, for different sample sets. Three-jet final states are included. Error bars show statistical uncertainty.

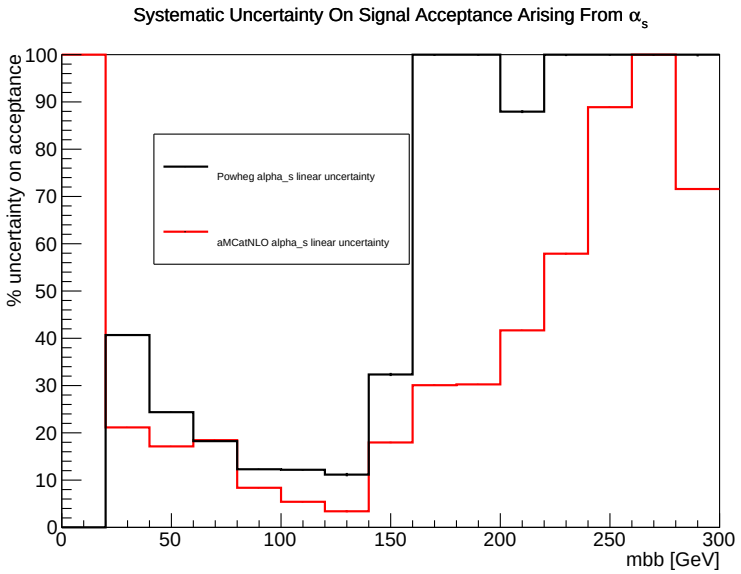

Figure C.7: Systematic uncertainties on signal acceptance, for the $WH \to \ell\nu b\bar{b}$ analysis, with $m_H = 125$ GeV, for different sample sets. Two-jet final states are included. Error bars show statistical uncertainty.

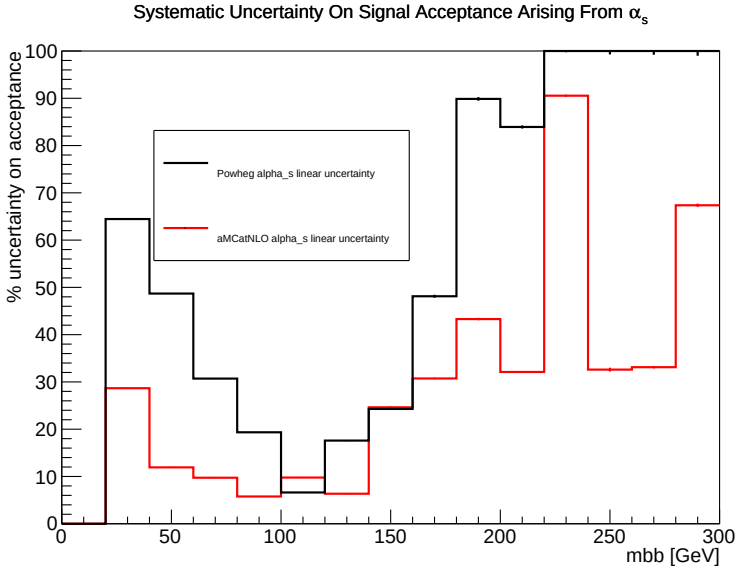

Figure C.8: Systematic uncertainties on signal acceptance, for the $WH \to \ell\nu b\bar{b}$ analysis, with $m_H = 125$ GeV, for different sample sets. Three-jet final states are included. Error bars show statistical uncertainty.

Appendix D

Combination Of Systematic Uncertainties Arising From Parton Distribution Functions And α_s - Additional Information

D.1 Results

D.1.1 Cross-Sections And Acceptances

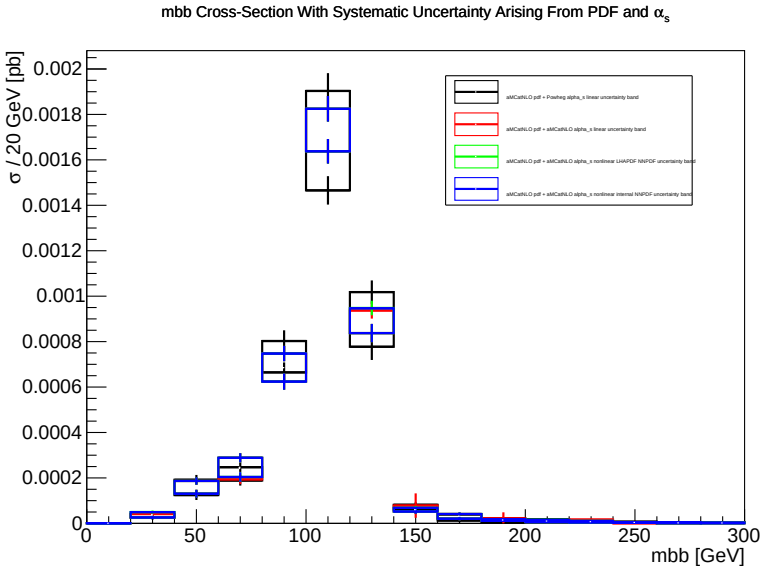

Figure D.1: $m_{b\bar{b}}$ distributions, with analysis selection criteria applied, for different samples sets. Two-jet final states are included. Systematic uncertainty is shown as a band for each sample set. Error bars on each band show the statistical uncertainty.

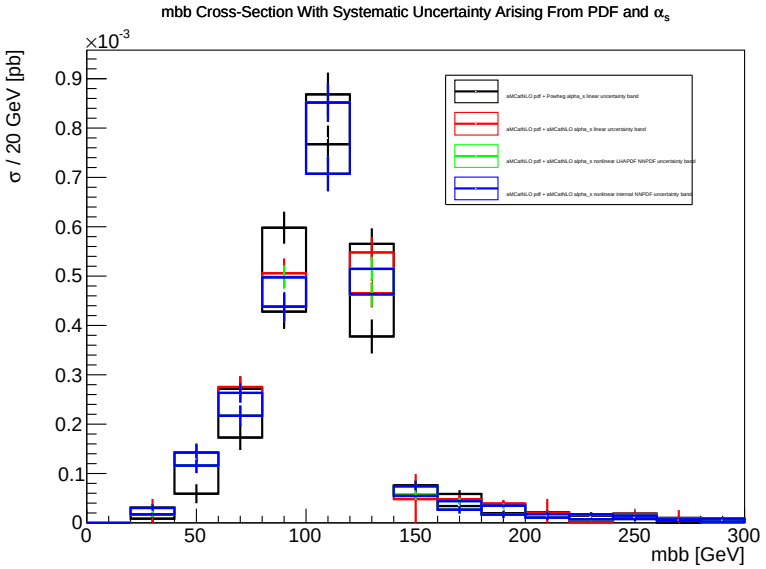

Figure D.2: $m_{b\bar{b}}$ distributions, with analysis selection criteria applied, for different samples sets. Three-jet final states are included. Systematic uncertainty is shown as a band for each sample set. Error bars on each band show the statistical uncertainty.

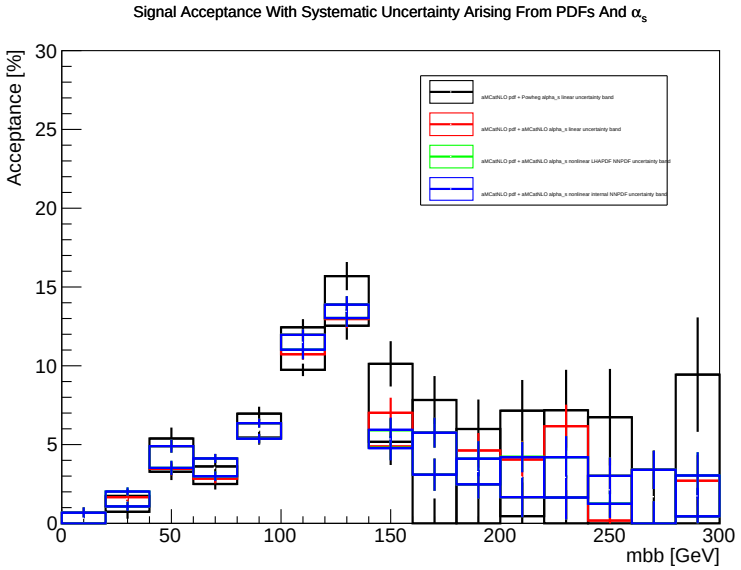

Figure D.3: Signal acceptance, for different samples sets. Two-jet final states are included. Systematic uncertainty is shown as a band for each sample set. Error bars on each band show the statistical uncertainty.

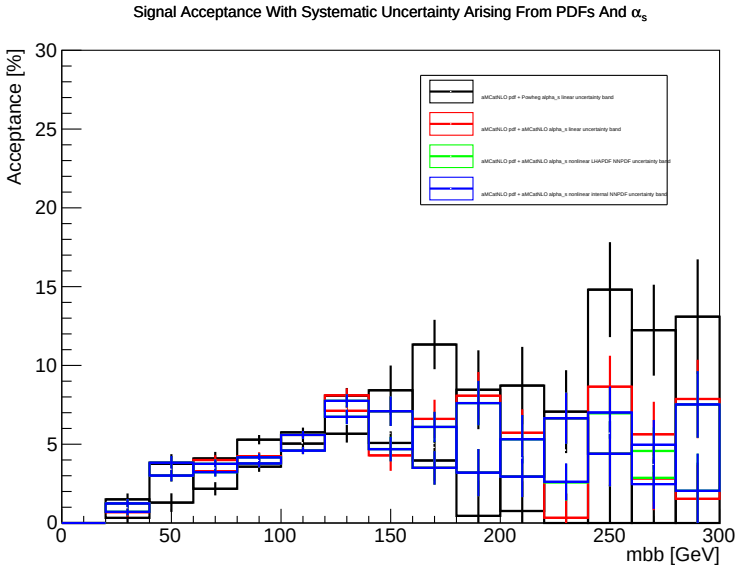

Figure D.4: Signal acceptance, for different samples sets. Three-jet final states are included. Systematic uncertainty is shown as a band for each sample set. Error bars on each band show the statistical uncertainty.

D.1.2 Uncertainties

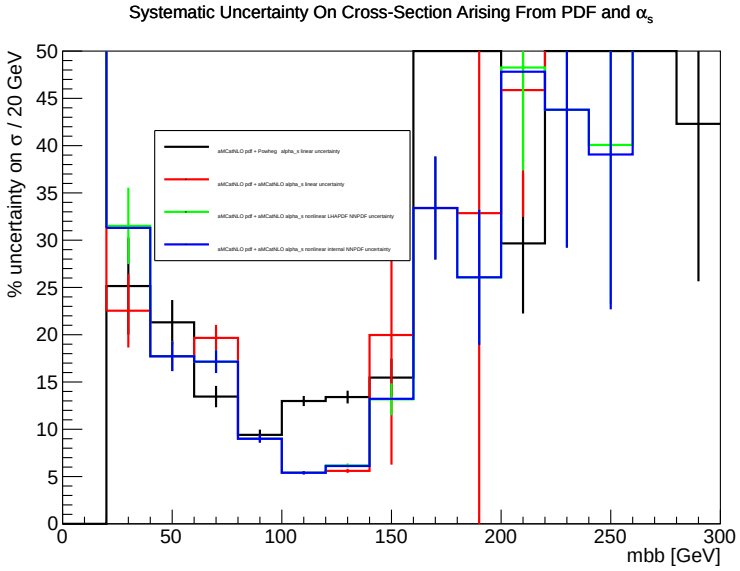

Figure D.5: Systematic uncertainties on signal cross-section, for the $WH \to \ell\nu b\bar{b}$ analysis, with $m_H = 125$ GeV, with analysis selection criteria applied, for different sample sets. Two-jet final states are included. Error bars show statistical uncertainty.

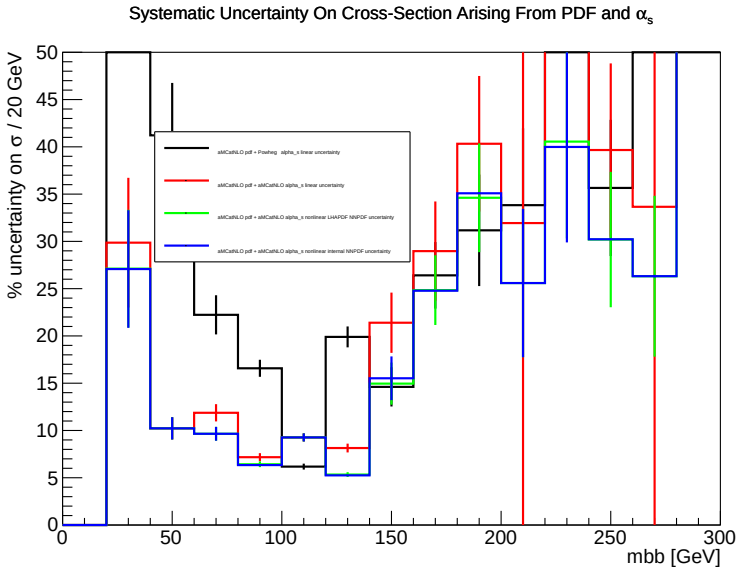

Figure D.6: Systematic uncertainties on signal cross-section, for the $WH \to \ell\nu b\bar{b}$ analysis, with $m_H = 125$ GeV, with analysis selection criteria applied, for different sample sets. Three-jet final states are included. Error bars show statistical uncertainty.

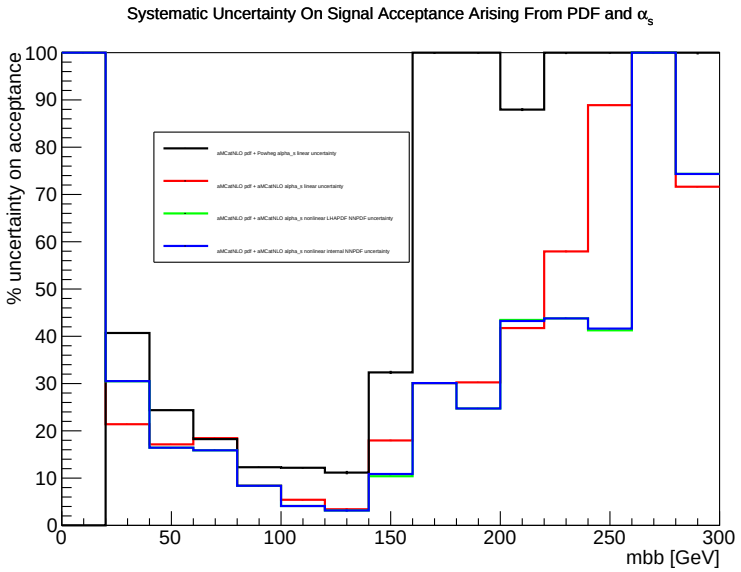

Figure D.7: Systematic uncertainties on signal acceptance, for the $WH \to \ell\nu b\bar{b}$ analysis, with $m_H = 125$ GeV, for different sample sets. Two-jet final states are included. Error bars show statistical uncertainty.

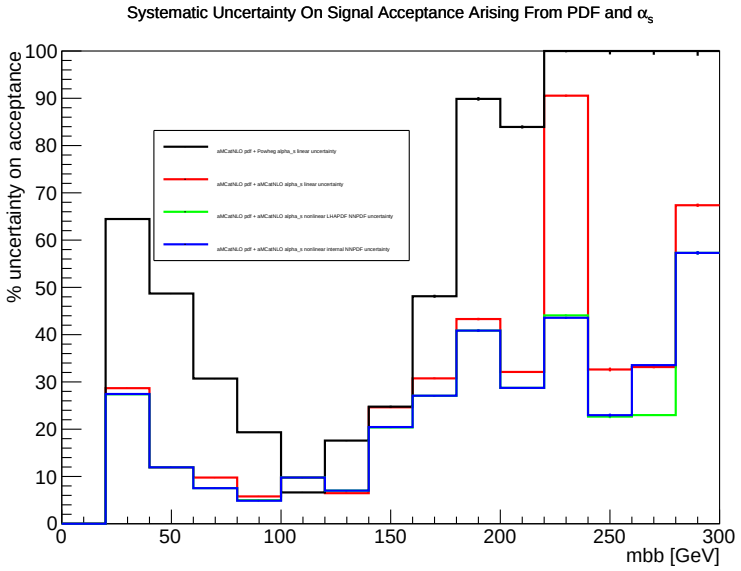

Figure D.8: Systematic uncertainties on signal acceptance, for the $WH \to \ell\nu b\bar{b}$ analysis, with $m_H = 125$ GeV, for different sample sets. Three-jet final states are included. Error bars show statistical uncertainty.

Appendix E

Systematic Uncertainties Arising From Parton Showering And Hadronisation - Additional Information

E.1 Results

E.1.1 Cross-Sections And Acceptances

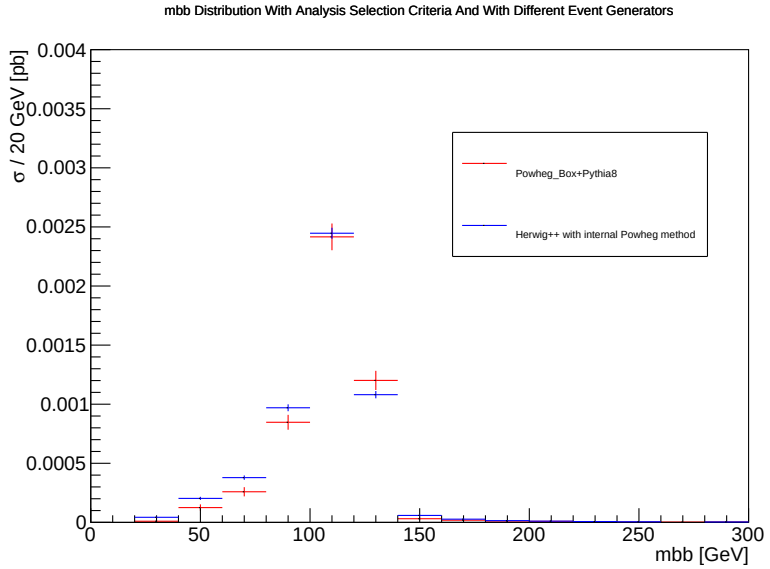

Figure E.1: $m_{b\bar{b}}$ distributions, with analysis selection criteria applied, for different samples sets. Two-jet final states are included. Error bars show statistical uncertainty.

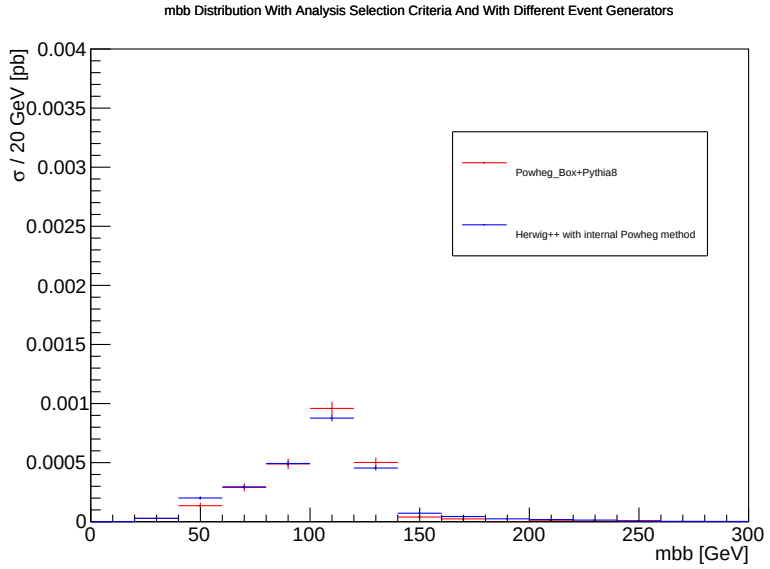

Figure E.2: $m_{b\bar{b}}$ distributions, with analysis selection criteria applied, for different samples sets. Three-jet final states are included. Error bars show statistical uncertainty.

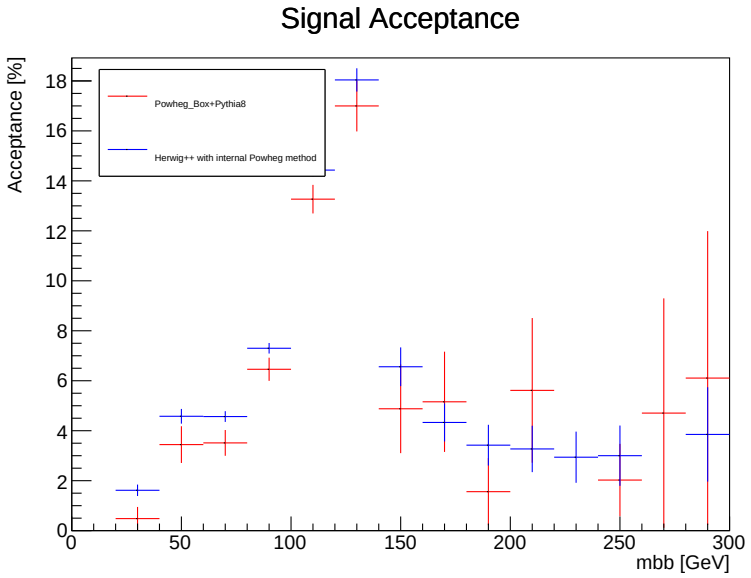

Figure E.3: Signal acceptance, for different samples sets. Two-jet final states are included. Error bars show statistical uncertainty.

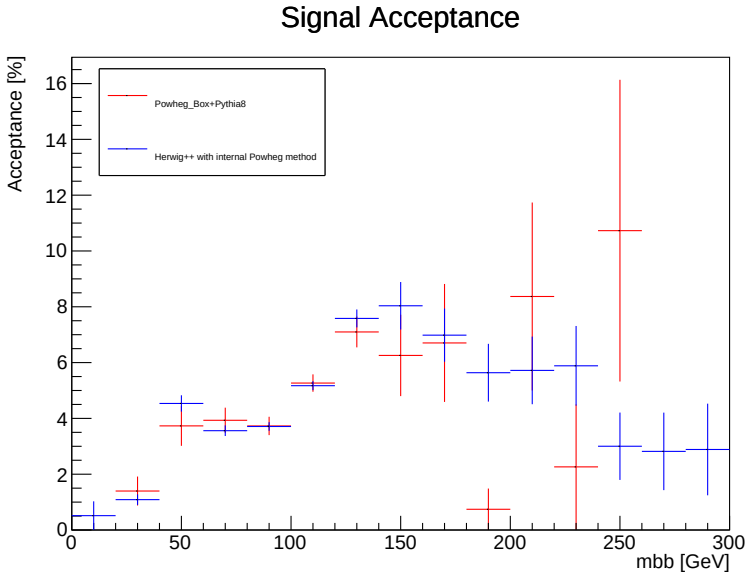

Figure E.4: Signal acceptance, for different samples sets. Three-jet final states are included. Error bars show statistical uncertainty.

E.1.2 Uncertainties

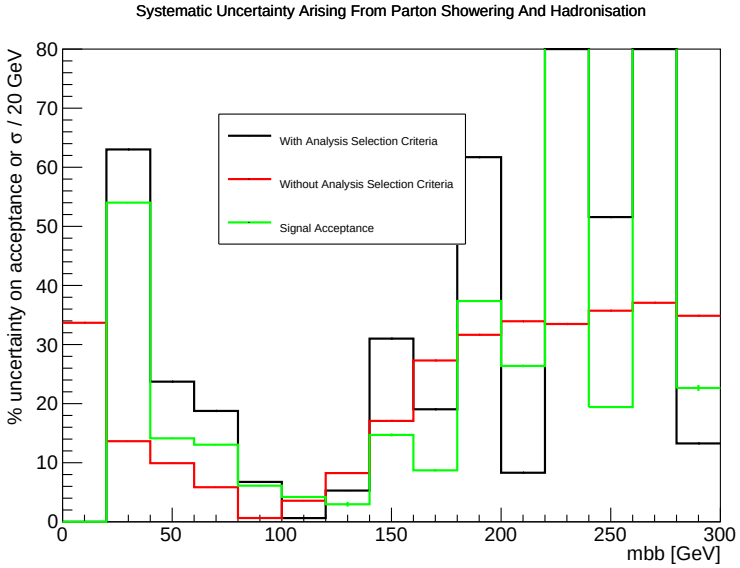

Figure E.5: Systematic uncertainties on signal cross-section, for the $WH \to \ell\nu b\bar{b}$ analysis, with $m_H = 125$ GeV, with and without analysis selection criteria applied, and acceptance. Two-jet final states are included. Error bars show statistical uncertainty.

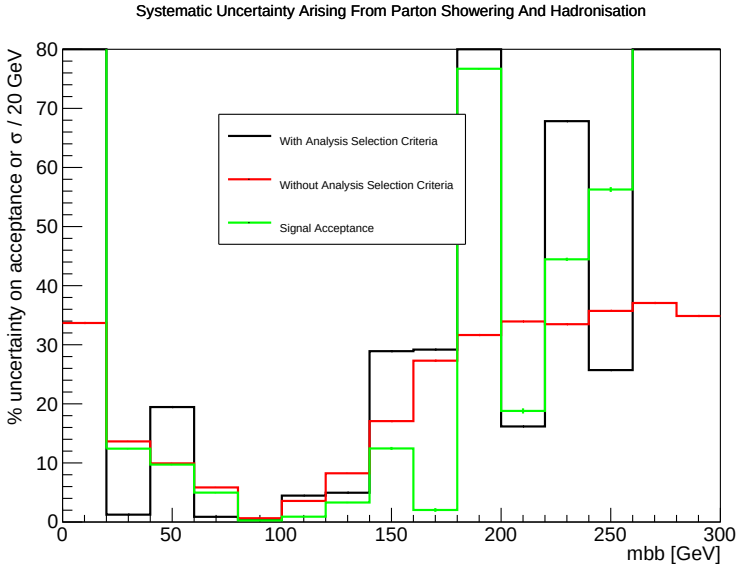

Figure E.6: Systematic uncertainties on signal cross-section, for the $WH \to \ell\nu b\bar{b}$ analysis, with $m_H = 125$ GeV, with and without analysis selection criteria applied, and acceptance. Three-jet final states are included. Error bars show statistical uncertainty.

Appendix F

Systematic Uncertainties Arising From The Underlying Event - Additional Information

F.1 Plateau Height Retuning MPI Uncertainty Estimation Method

For different MPI-sensitive variables, a plateau is typically observed: as event activity and hard subprocess energy increase, MPI activity and energy plateau at a certain level. This is shown in figure F.1.

A more robust method for estimating systematic uncertainties arising from MPI is to take the height of the underlying event plateau in real-world data, adjust it by $\pm 1\sigma$, and then retune a Monte Carlo generator to these adjusted underlying event plateau heights. Monte Carlo samples generated with this retuned generator can then be compared to a standard (non-retuned) Monte Carlo sample. The difference in a variable of interest between these samples is then an estimate of the systematic uncertainty arising from MPI. The plateau height should be raised by a factor of $F^+ > 1$, and lowered by a factor of $F^- < 1$, to correspond to variations of $\pm 1\sigma$. Conservative values of $F^+ = 2$ and $F^- = \frac{1}{2}$ can be used. From underlying event studies in data [111] the $\pm 1\sigma$ standard deviation on the plateau height corresponds to $F^+ \simeq 1.05$ and $F^- \simeq 0.95$.

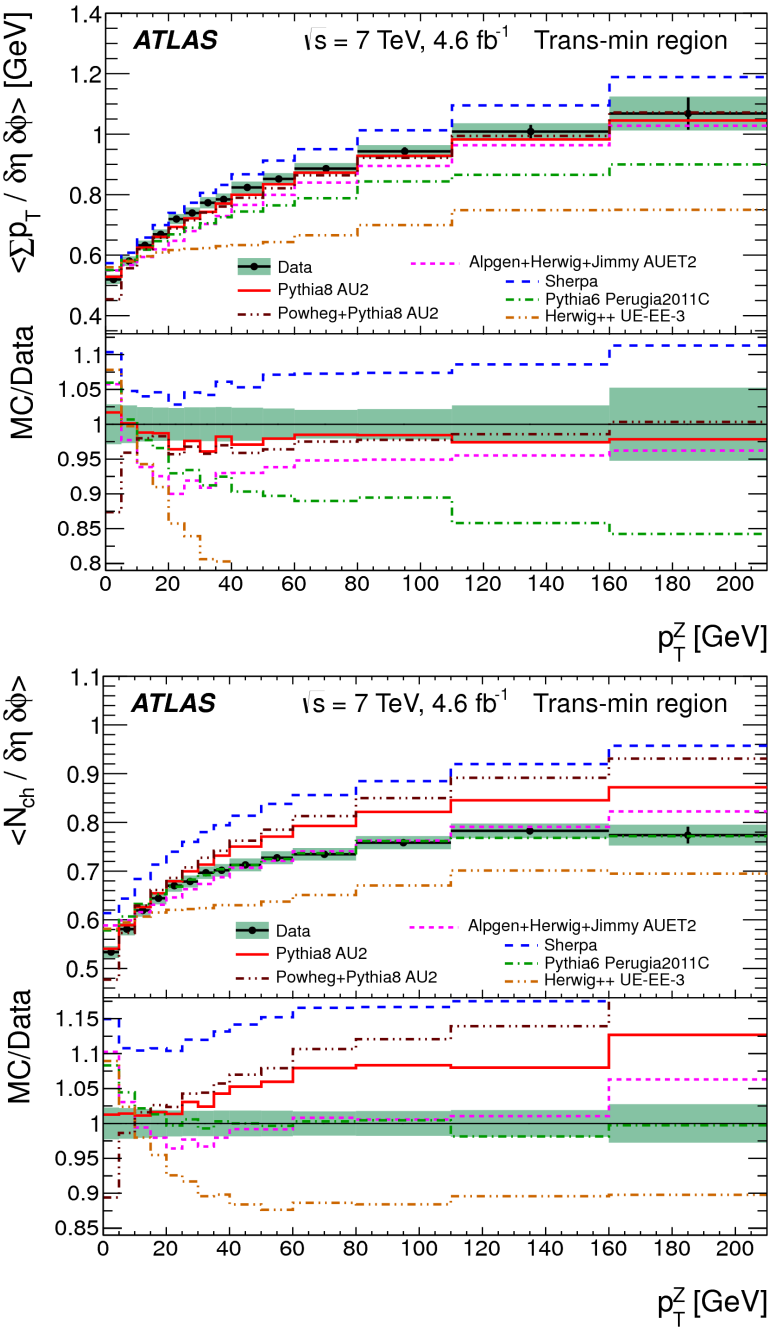

Figure F.1: Plots of underlying event, MPI, activity for different underlying event-sensitive variables, in regions sensitive to the underlying event. Top: charged particle scalar $\sum p_{\mathrm{T}}$ density, $\langle \sum p_{\mathrm{T}} / \delta\eta\delta\phi \rangle$, as a function of Z-boson transverse momentum, p_{T}^{Z}. Bottom: charged particle multiplicity density, $\langle \mathrm{N_{ch}} / \delta\eta\delta\phi \rangle$, as a function of Z-boson transverse momentum, p_{T}^{Z}. From [111].

For a variable X, the systematic uncertainty arising from MPI is then:

$$\Delta_X = \sqrt{\max\left(\left(X^+ - X_0\right)^2, \left(X^- - X_0\right)^2\right)} \tag{F.1}$$

where X_0 is the value of X in the Monte Carlo sample tuned to the normal UE plateau height. X^+ is the value of X in the Monte Carlo sample tuned to the UE plateau height $\times F^+$. X^- is the value of X in the Monte Carlo sample tuned to the UE plateau height $\times F^-$

Asymmetric uncertainties can also be computed:

$$\Delta_X^+ = \max\left(X^+ - X_0, X^- - X_0, 0\right) \tag{F.2}$$

$$\Delta_X^- = \max\left(X_0 - X^+, X_0 - X^-, 0\right) \tag{F.3}$$

F.2 On-Off MPI Uncertainty Estimation Method

F.2.1 Introduction

A simple way to investigate the effects of MPI modelling is to switch this modelling on and off. By comparing a variable of interest X generated with MPI on (X(MPI on)) and MPI off (X(MPI off)), effects of MPI on X can be inferred, and upper limits on the systematic uncertainties arising from MPI can be set. For a variable X, the uncertainty is then given by,

$$\Delta X = \frac{|X(\text{MPI on}) - X(\text{MPI off})|}{2} \tag{F.4}$$

Samples Generated And Tested

Two samples were generated in order to study systematic uncertainties arising from the underlying event with the on-off method. They are listed in table F.1. Uncertainties are calculated according to equation F.4.

Sample set	Hard subprocess event generator	Showering event generator	Generated with PDF	MPI
'MPI on'	Powheg_Box	Pythia8	CT10nlo CM	Switched on
'MPI off'	Powheg_Box	Pythia8	CT10nlo CM	Switched off

Table F.1: Monte Carlo samples generated for the estimation of systematic uncertainties arising from the underlying event with the on-off method. 'CM' means the **C**entral **M**ember of the PDF set.

F.2.2 Results

Cross-Sections And Acceptances

Figure F.2 shows signal cross-section $m_{b\bar{b}}$ distributions without analysis selection criteria applied. Figure F.3 shows the equivalent distributions with analysis selection criteria applied for two and three-jet final states combined. Figure F.4 shows signal acceptance for two and three-jet final states combined. Further cross-section and acceptance plots are found in appendix F.3.1.

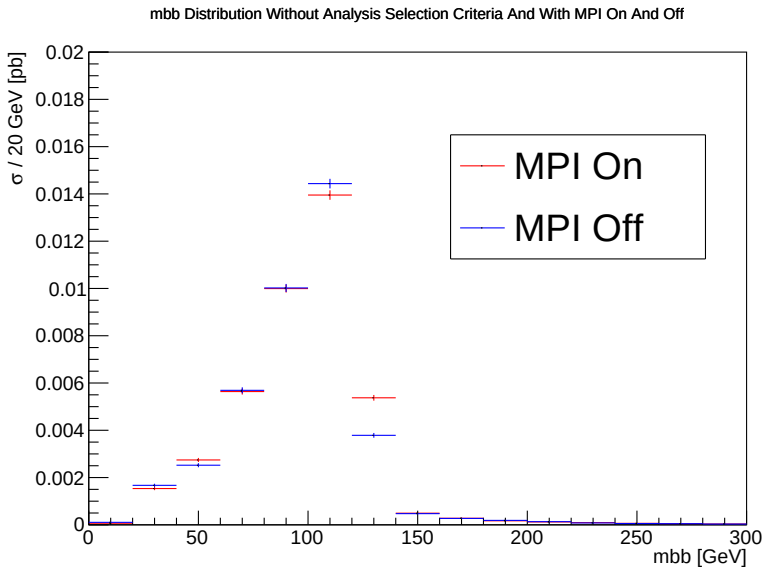

Figure F.2: $m_{b\bar{b}}$ distributions, for the $WH \to \ell\nu b\bar{b}$ analysis, with $m_H = 125$ GeV, without analysis selection criteria applied, for different samples sets. Error bars show statistical uncertainty.

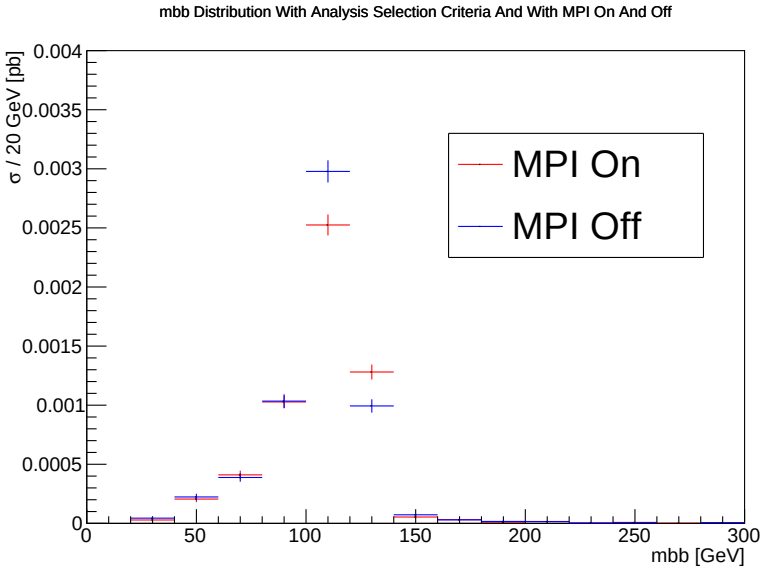

Figure F.3: $m_{b\bar{b}}$ distributions, for the $WH \to \ell\nu b\bar{b}$ analysis, with $m_H = 125$ GeV, with analysis selection criteria applied, for different samples sets. Two and three-jet final states are included. Error bars show statistical uncertainty.

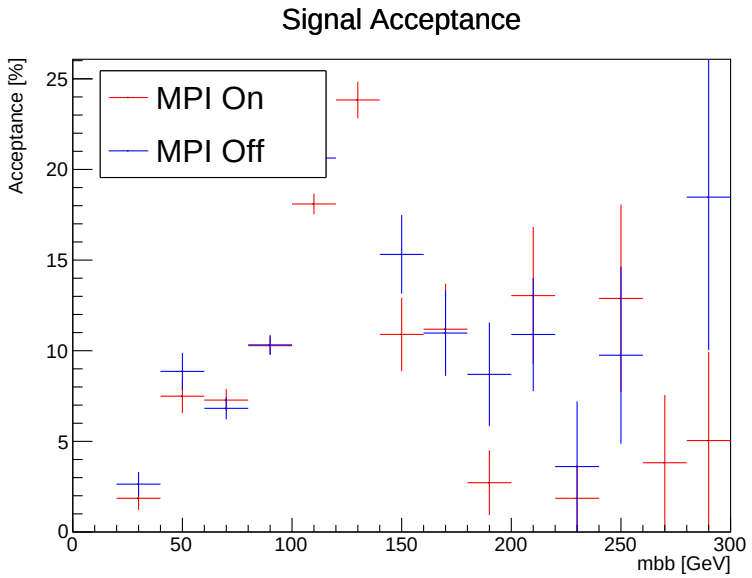

Figure F.4: Signal acceptance, for the $WH \to \ell\nu b\bar{b}$ analysis, with $m_H = 125$ GeV, for different samples sets. Two and three-jet final states are included. Error bars show statistical uncertainty.

Uncertainties

For two and three-jet final states, figure F.5 shows systematic uncertainties on signal cross-section with and without analysis selection criteria applied, as well as systematic uncertainties on signal acceptance. Equivalent distributions for two-jet and three-jet final states are shown in appendix F.3.2.

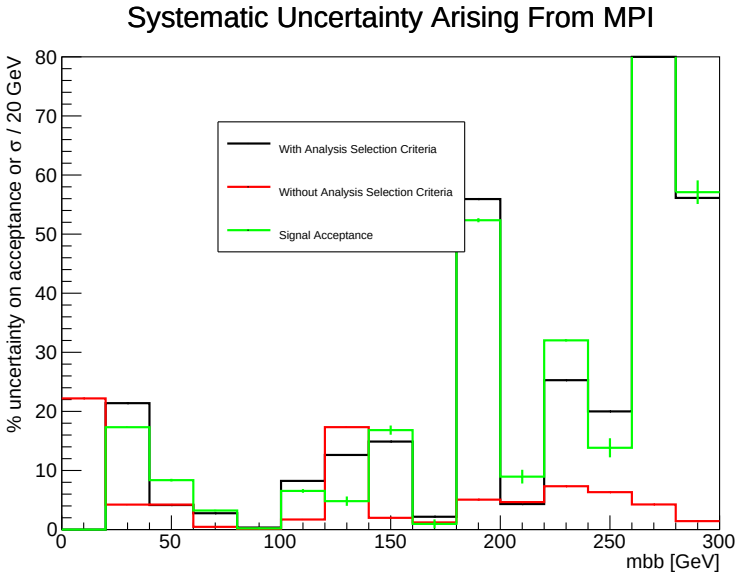

Figure F.5: Systematic uncertainties on signal cross-section, for the $WH \rightarrow \ell\nu b\bar{b}$ analysis, with $m_H = 125$ GeV, with and without analysis selection criteria applied, and acceptance. Two and three-jet final states are included. Error bars show statistical uncertainty.

When considering uncertainties, only a region with a large number of events is chosen: the $m_{b\bar{b}}$ range of 60 GeV to 140 GeV around the Higgs mass peak. In this region, no clear dependence of the uncertainties on $m_{b\bar{b}}$ is seen. An average value for each uncertainty, for each sample set, is therefore calculated within the range of 60 GeV $\geq m_{b\bar{b}} \geq$ 140 GeV.

Averaged systematic uncertainties are shown in table F.2.

N_{jets} bin	$\sigma_{\text{inclusive}}$ $[pb]$	$\delta_{\sigma_{\text{inclusive}}}$ [%]	σ_{asc} $[pb]$	$\delta_{\sigma_{\text{asc}}}$ [%]	A [%]	δ_A [% of A]
2 and 3	0.0350	4.9	0.00524	6.0	15.0	3.7
2	0.0350	4.9	0.00356	6.3	10.2	3.2
3	0.0350	4.9	0.00169	5.6	4.8	4.5

Table F.2: Systematic uncertainties arising from the underlying event, calculated using the on-off method, for the $WH \to \ell\nu b\bar{b}$ analysis, with $m_H = 125$ GeV.

F.2.3 Conclusion

Systematic uncertainties arising from the underlying event have been calculated using the on-off method and are shown in table F.2. These results can be taken as upper limits on the systematic uncertainties due the underlying event.

For two and three-jet final states, the uncertainty on the inclusive cross-section $\delta_{\sigma_{\text{inclusive}}} = 4.9\%$, the uncertainty on the cross section after analysis selection criteria have been applied $\delta_{\sigma_{\text{asc}}} = 6.0\%$, and the uncertainty on signal acceptance $\delta_A = 3.7\%$.

It should be noted that the MPI scaling method is a more robust method for estimating systematic uncertainties arising from the underlying event than the on-off method. The results from the MPI scaling method, as given in table 5.20, are therefore used in the analysis presented in this thesis. The on-off method is presented here for comparison.

F.3 Additional Results For The On-Off Method

F.3.1 Cross-Sections And Acceptances

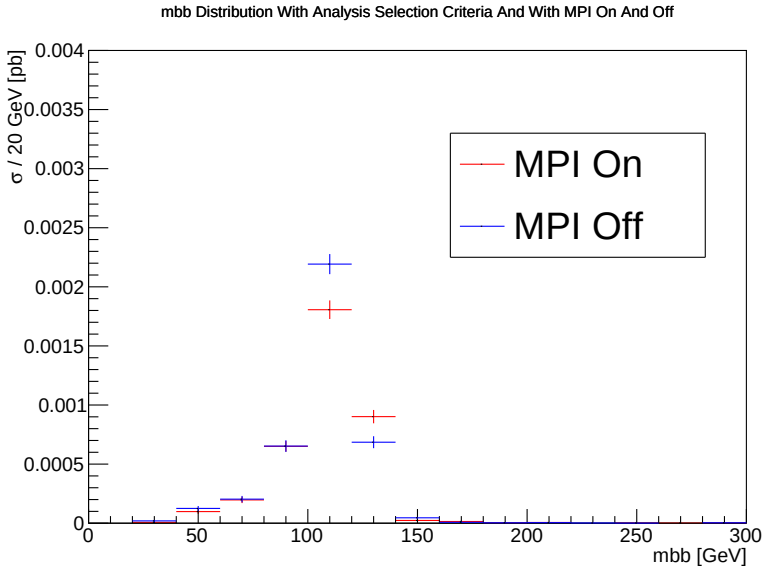

Figure F.6: $m_{b\bar{b}}$ distributions, with analysis selection criteria applied, for different samples sets. Two-jet final states are included. Error bars show statistical uncertainty.

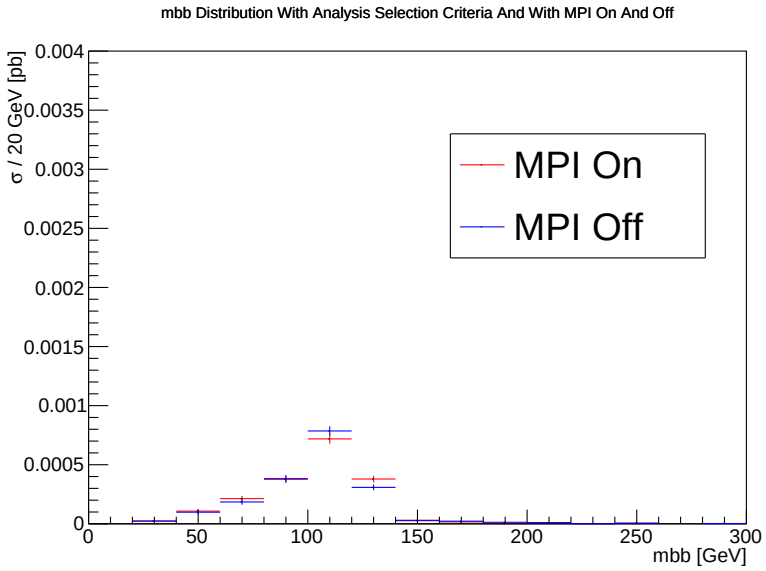

Figure F.7: $m_{b\bar{b}}$ distributions, with analysis selection criteria applied, for different samples sets. Three-jet final states are included. Error bars show statistical uncertainty.

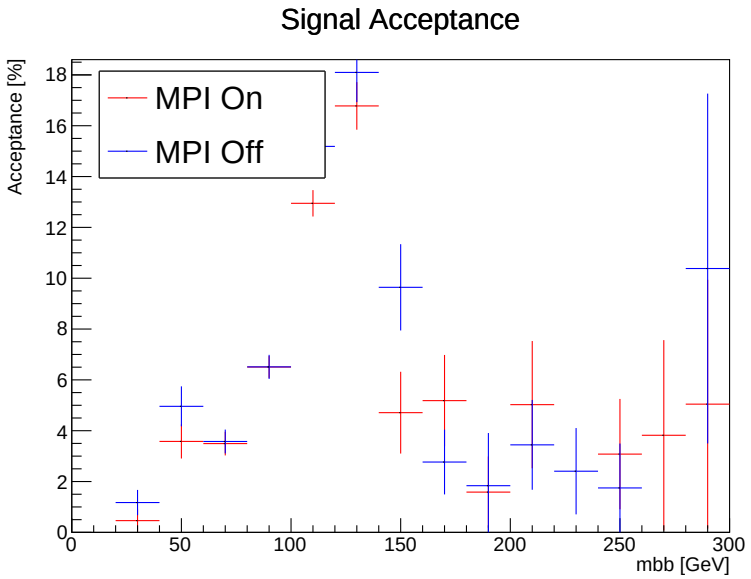

Figure F.8: Signal acceptance, for different samples sets. Two-jet final states are included. Error bars show statistical uncertainty.

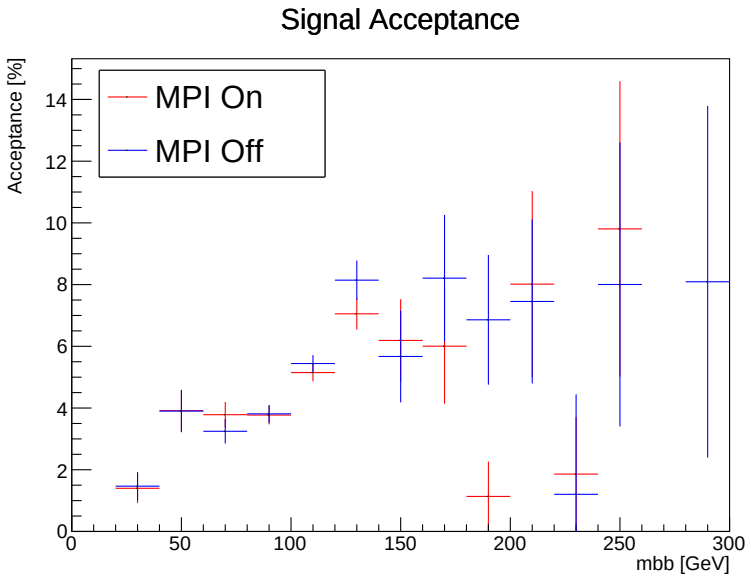

Figure F.9: Signal acceptance, for different samples sets. Three-jet final states are included. Error bars show statistical uncertainty.

F.3.2 Uncertainties

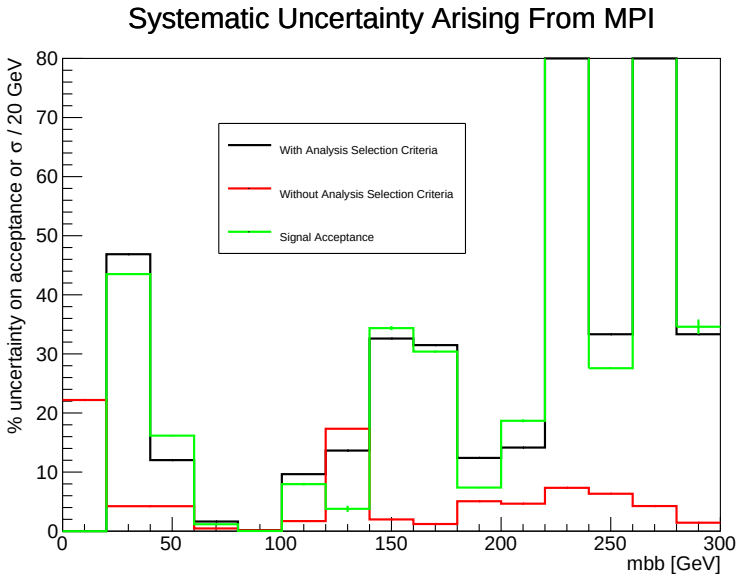

Figure F.10: Systematic uncertainties on signal cross-section, for the $WH \to \ell\nu b\bar{b}$ analysis, with $m_H = 125$ GeV, with and without analysis selection criteria applied, and acceptance. Two-jet final states are included. Error bars show statistical uncertainty.

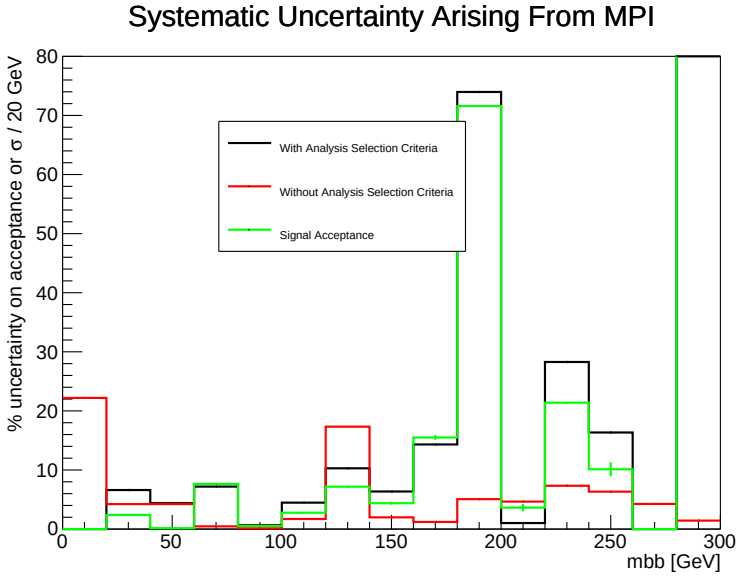

Figure F.11: Systematic uncertainties on signal cross-section, for the $WH \to \ell\nu b\bar{b}$ analysis, with $m_H = 125$ GeV, with and without analysis selection criteria applied, and acceptance. Three-jet final states are included. Error bars show statistical uncertainty.

F.4 Additional Results For The MPI Scaling Method

F.4.1 Cross-Sections And Acceptances

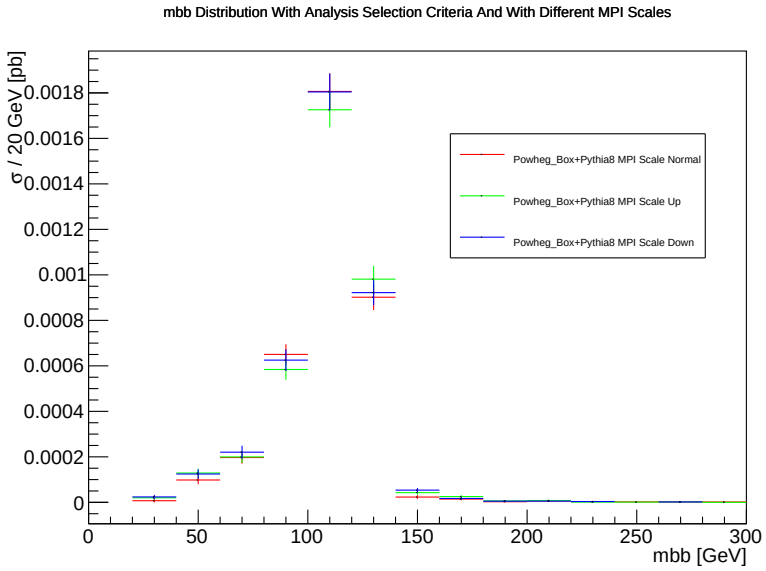

Figure F.12: $m_{b\bar{b}}$ distributions, with analysis selection criteria applied, for different samples sets. Two-jet final states are included. Error bars show statistical uncertainty.

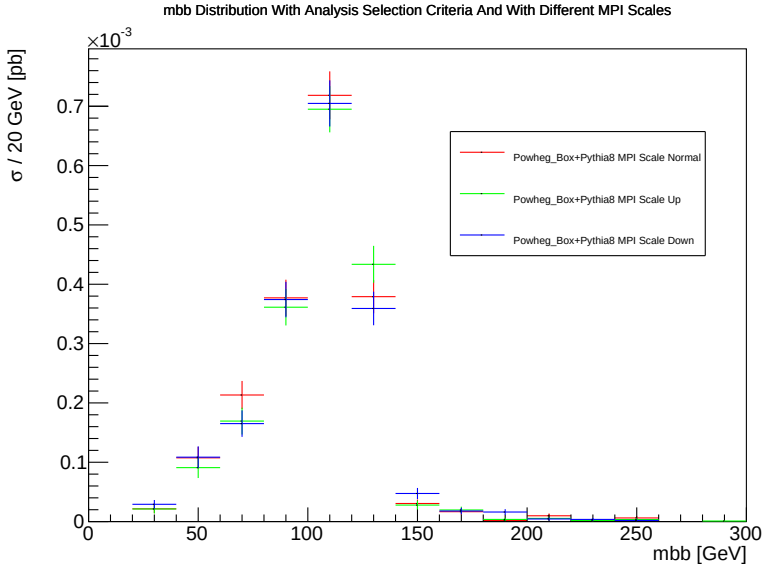

Figure F.13: $m_{b\bar{b}}$ distributions, with analysis selection criteria applied, for different samples sets. Three-jet final states are included. Error bars show statistical uncertainty.

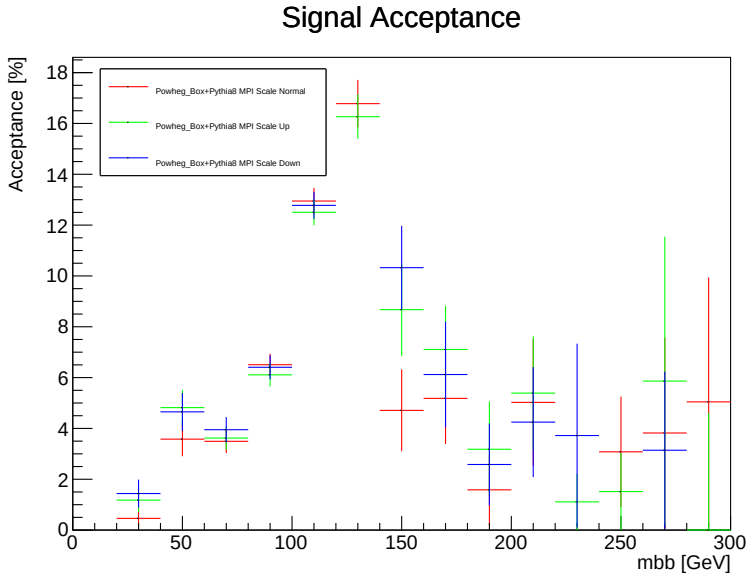

Figure F.14: Signal acceptance, for different samples sets. Two-jet final states are included. Error bars show statistical uncertainty.

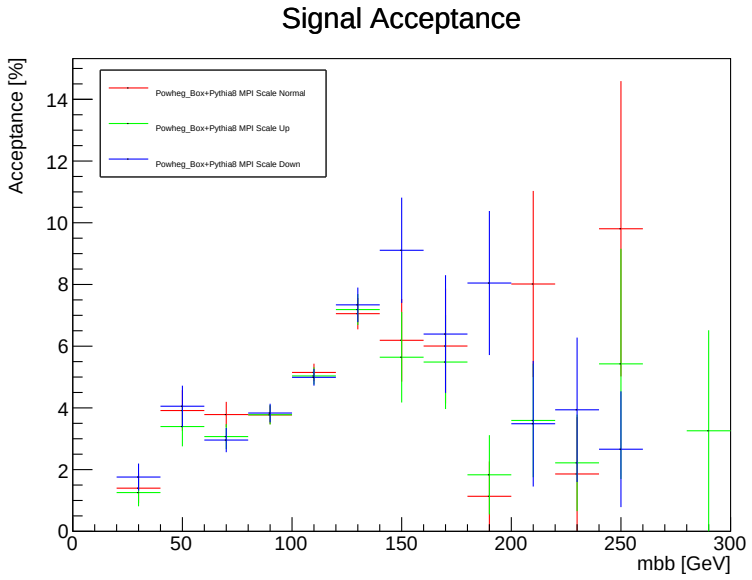

Figure F.15: Signal acceptance, for different samples sets. Three-jet final states are included. Error bars show statistical uncertainty.

F.4.2 Uncertainties

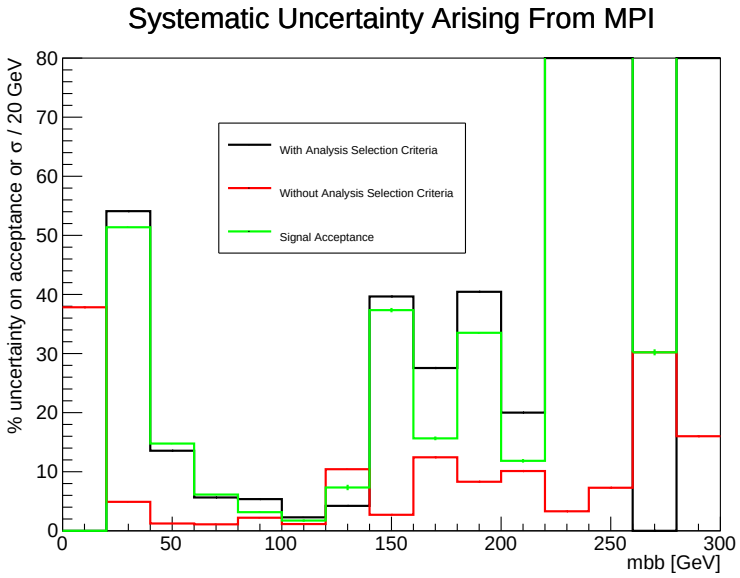

Figure F.16: Systematic uncertainties on signal cross-section, for the $WH \to \ell\nu b\bar{b}$ analysis, with $m_H = 125$ GeV, with and without analysis selection criteria applied, and acceptance. Two-jet final states are included. Error bars show statistical uncertainty.

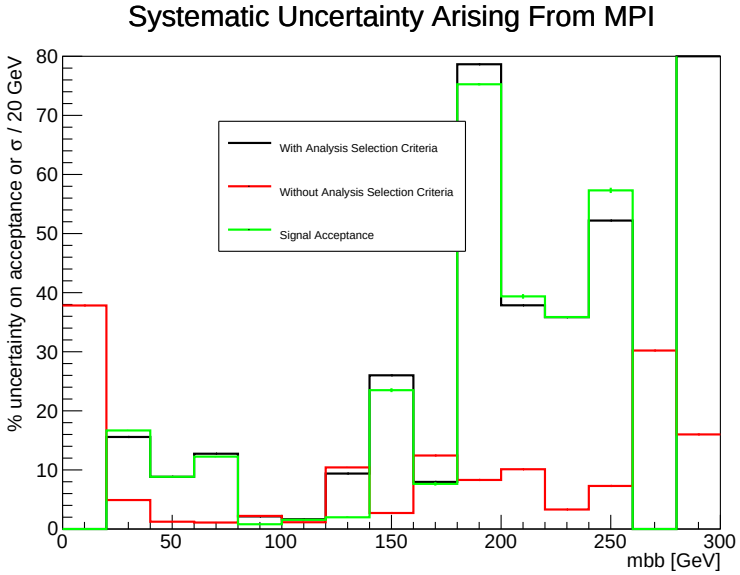

Figure F.17: Systematic uncertainties on signal cross-section, for the $WH \to \ell\nu b\bar{b}$ analysis, with $m_H = 125$ GeV, with and without analysis selection criteria applied, and acceptance. Three-jet final states are included. Error bars show statistical uncertainty.

Appendix G

Systematic Uncertainties Arising From QED Corrections - Additional Information

G.1 Results

G.1.1 Cross-Sections And Acceptances

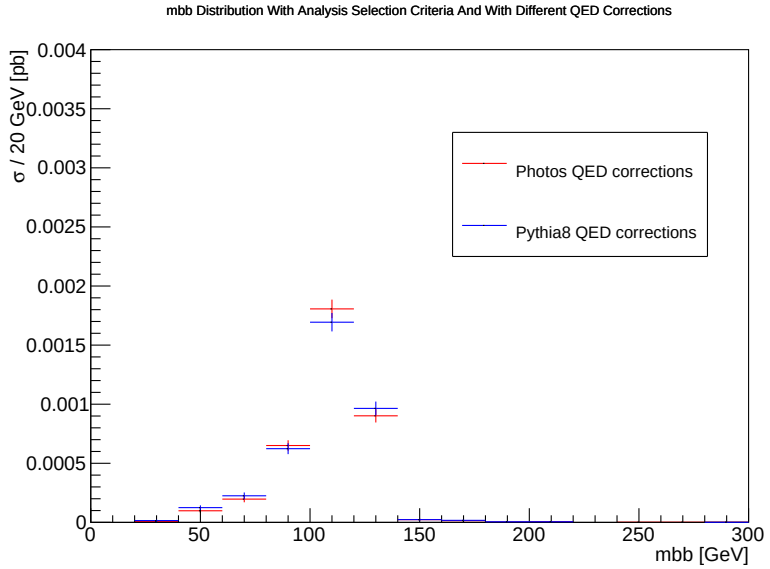

Figure G.1: $m_{b\bar{b}}$ distributions, with analysis selection criteria applied, for different samples sets. Two-jet final states are included. Error bars show statistical uncertainty.

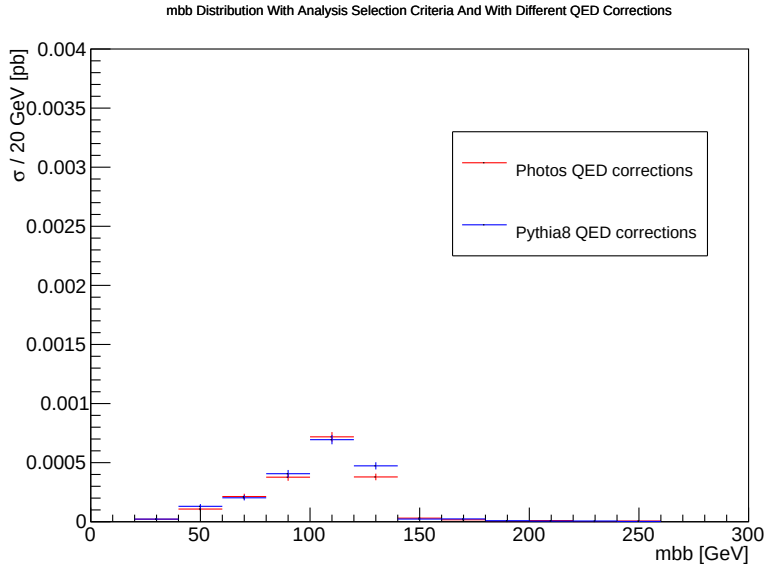

Figure G.2: $m_{b\bar{b}}$ distributions, with analysis selection criteria applied, for different samples sets. Three-jet final states are included. Error bars show statistical uncertainty.

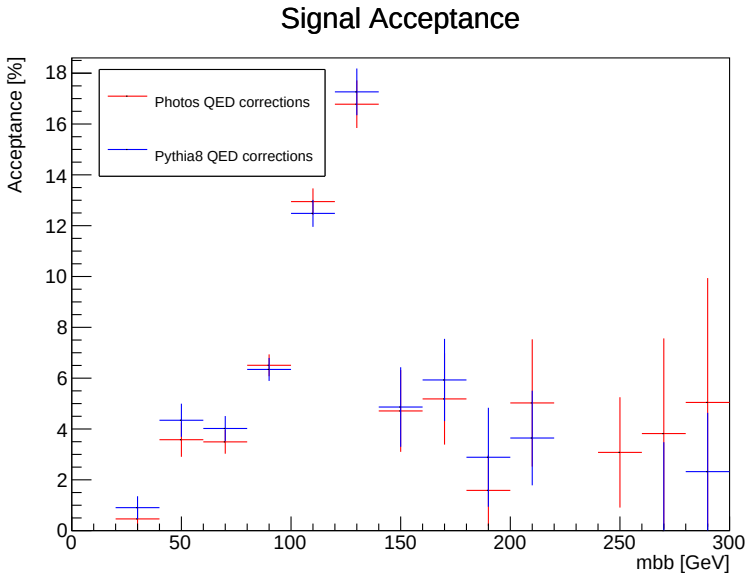

Figure G.3: Signal acceptance, for different samples sets. Two-jet final states are included. Error bars show statistical uncertainty.

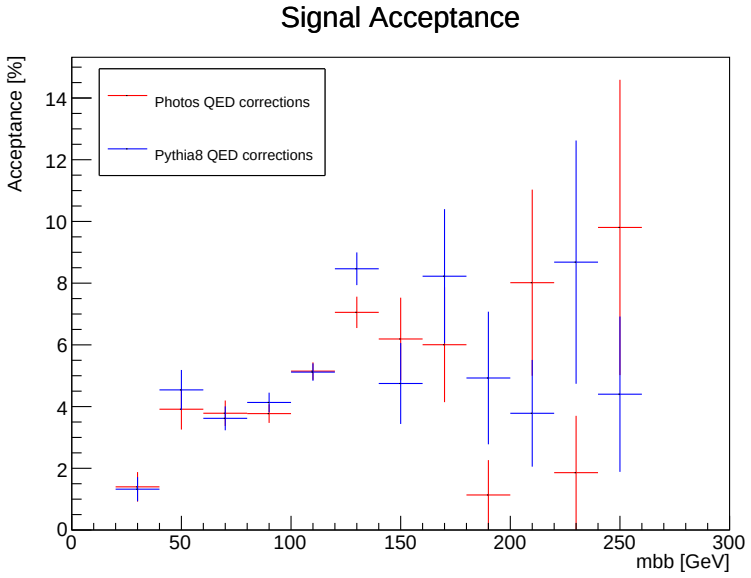

Figure G.4: Signal acceptance, for different samples sets. Three-jet final states are included. Error bars show statistical uncertainty.

G.1.2 Uncertainties

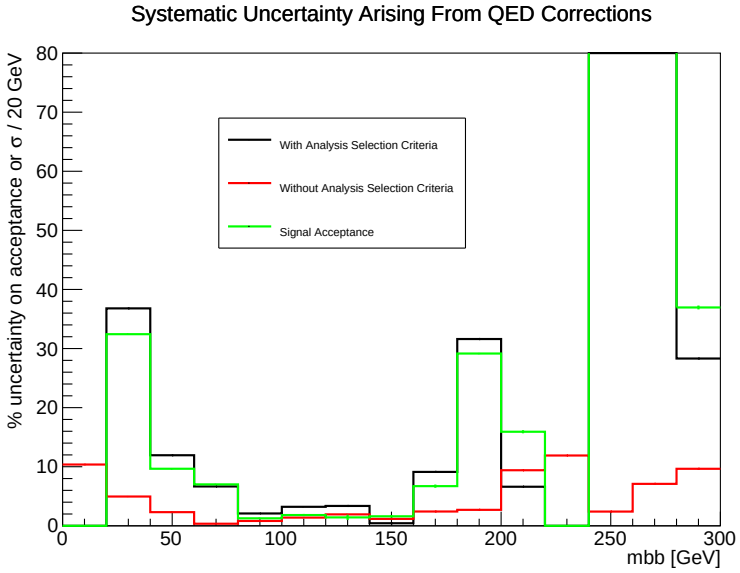

Figure G.5: Systematic uncertainties on signal cross-section, for the $WH \to \ell\nu b\bar{b}$ analysis, with $m_H = 125$ GeV, with and without analysis selection criteria applied, and acceptance. Two-jet final states are included. Error bars show statistical uncertainty.

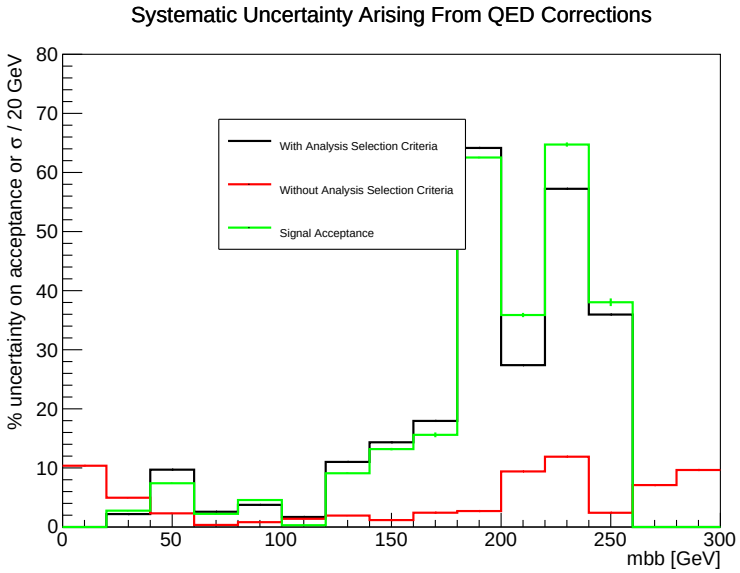

Figure G.6: Systematic uncertainties on signal cross-section, for the $WH \to \ell\nu b\bar{b}$ analysis, with $m_H = 125$ GeV, with and without analysis selection criteria applied, and acceptance. Three-jet final states are included. Error bars show statistical uncertainty.

Appendix H

Results Of The Search For The Higgs Boson In The $WH \to b\bar{b}$ And $VH \to b\bar{b}$ Channels - Additional Information

H.1 $m_{b\bar{b}}$ Distributions

Figures H.1, H.2, and H.3 show $m_{b\bar{b}}$ distributions, before and after the global fit has been performed, respectively for the 0, 1, and 2-lepton channels. They show the TT b-tagging regions with two jets in the final state and 90(100) GeV $< p_{\mathrm{T}}^{V} <$ 120 GeV (where the 100 GeV lower bound is only in the 0-lepton channel, as discussed in table 4.5).

Figures H.4, H.5, and H.6 show MV1c distributions, before and after the global fit has been performed, respectively for the 0, 1, and 2-lepton channels. They show the one-tag b-tagging regions with two jets in the final state and $p_{\mathrm{T}}^{V} <$ 90(100) GeV (where the 100 GeV upper bound is only in the 0-lepton channel, as discussed in table 4.5).

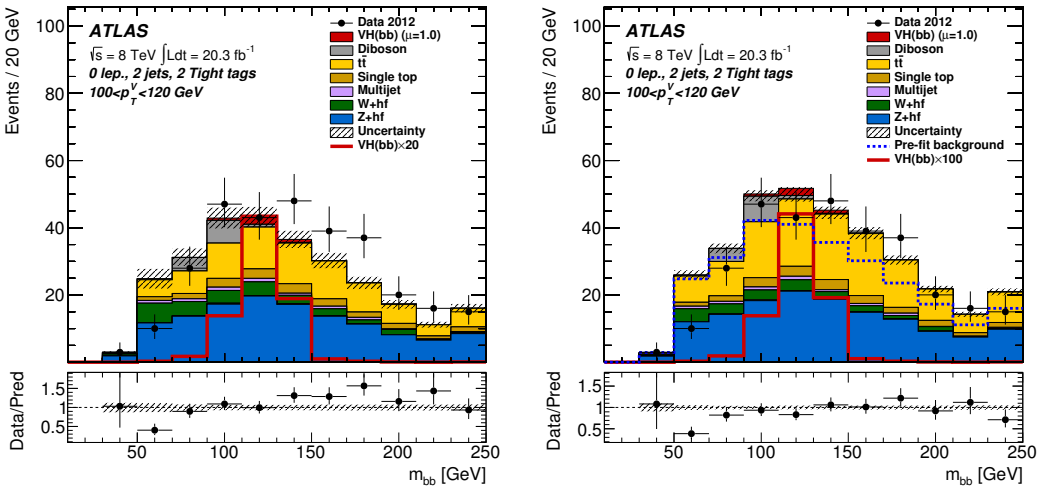

Figure H.1: $m_{b\bar{b}}$ distributions in the 0-lepton channel, 100 GeV $< p_{\mathrm{T}}^{V} <$ 120 GeV bin, before and after the global fit. The two-jet, TT b-tagging region is shown.

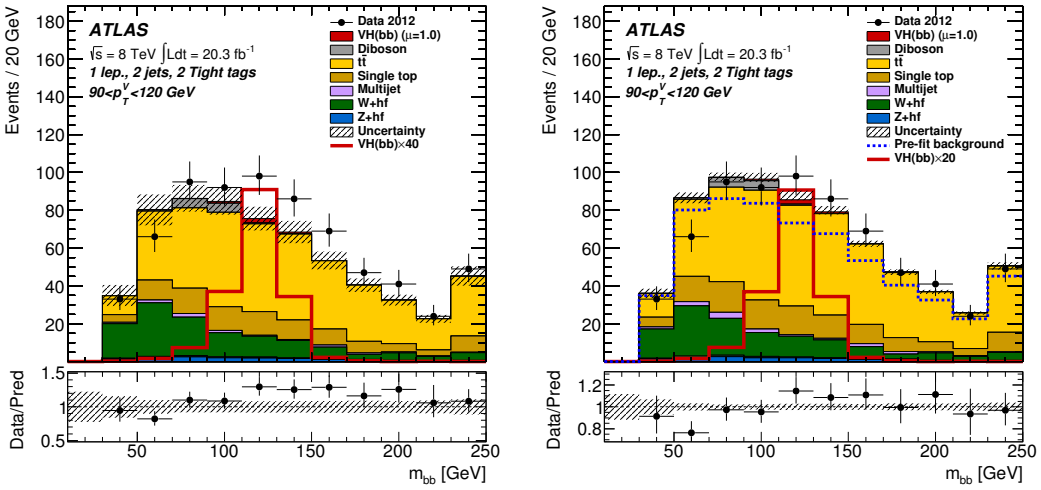

Figure H.2: $m_{b\bar{b}}$ distributions in the 1-lepton channel, 90 GeV $< p_{\mathrm{T}}^{V} <$ 120 GeV bin, before and after the global fit. The two-jet, TT b-tagging region is shown.

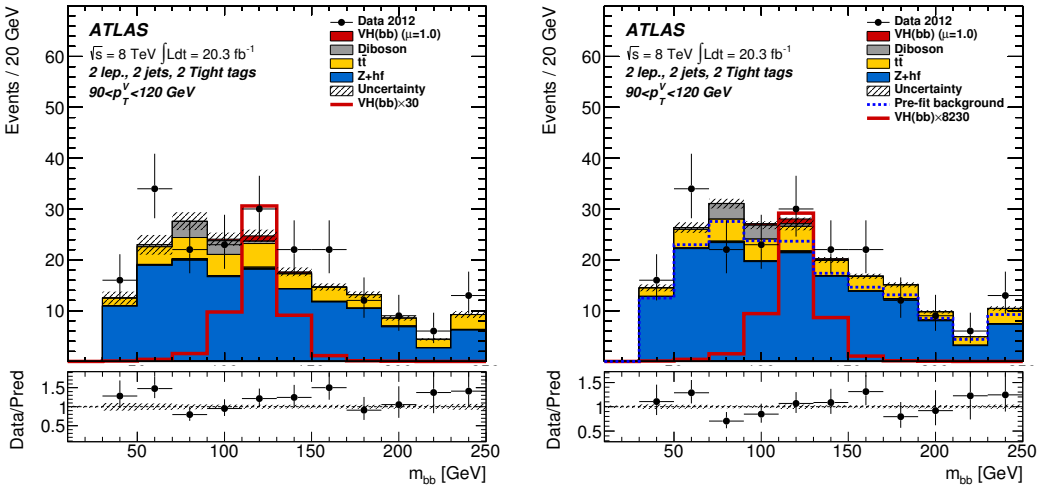

Figure H.3: $m_{b\bar{b}}$ distributions in the 2-lepton channel, 90 GeV $< p_{\mathrm{T}}^{V} <$ 120 GeV bin, before and after the global fit. The two-jet, TT b-tagging region is shown.

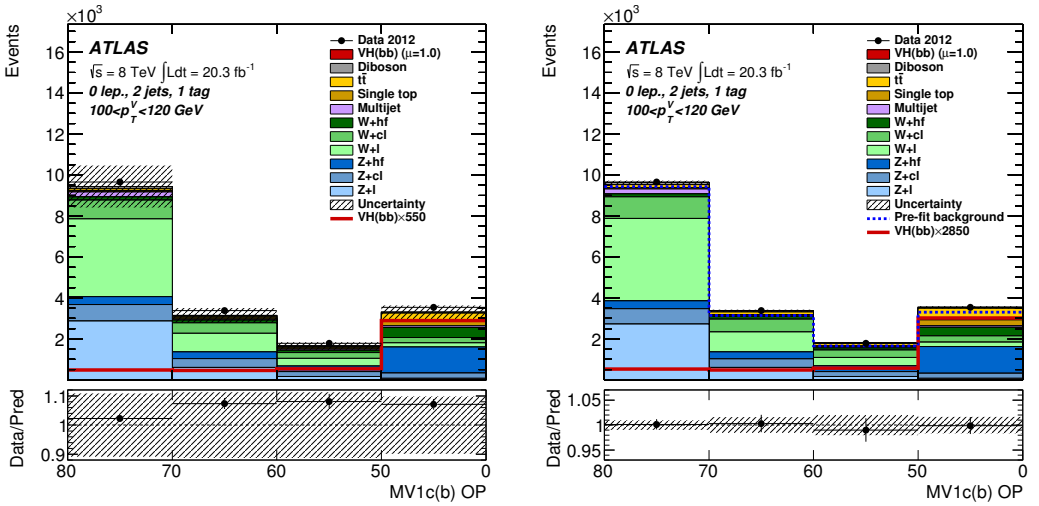

Figure H.4: MV1c distributions in the 0-lepton channel, 100 GeV $< p_{\mathrm{T}}^{V} <$ 120 GeV bin, before (left) and after (right) the global fit. The two-jet, one-tag b-tagging region is shown.

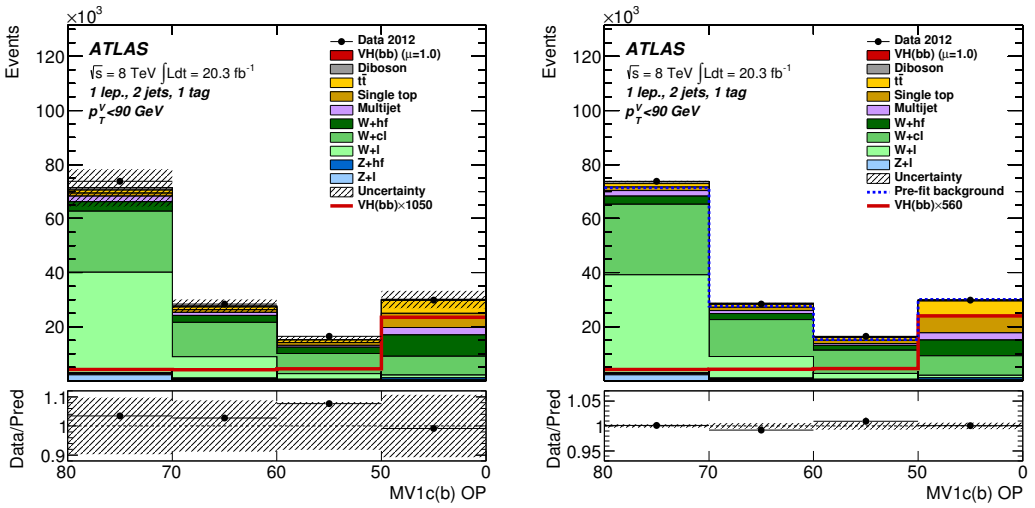

Figure H.5: MV1c distributions in the 1-lepton channel, $p_{\mathrm{T}}^{V} < 90$ GeV bin, before (left) and after (right) the global fit. The two-jet, one-tag b-tagging region is shown.

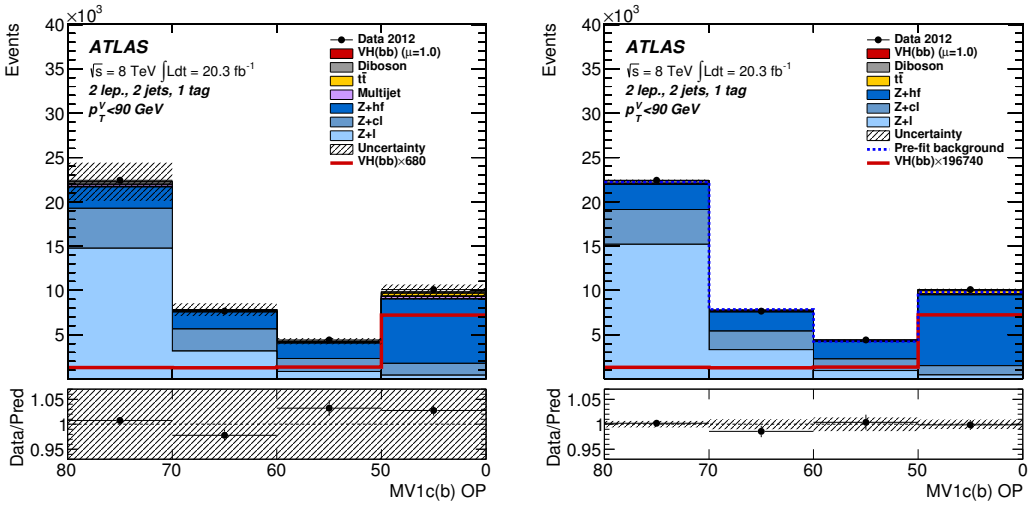

Figure H.6: MV1c distributions in the 2-lepton channel, $p_{\mathrm{T}}^{V} < 90$ GeV bin, before (left) and after (right) the global fit. The two-jet, one-tag b-tagging region is shown.

Appendix I

Global Fit Nuisance Parameter Pulls

Nuisance parameter pulls after the global fit, as defined in [110, 65], are shown in figure I.1 for the 1-lepton channel, and figure I.2 for the combination of the 0, 1, and 2-lepton channels.

The nuisance parameter pulls corresponding to the theoretical systematic uncertainties detailed in chapter 5 are shown to be close to zero. This indicates that the theoretical systematic uncertainties detailed in chapter 5 were not significantly altered by the fit, indicating that the values given in chapter 5 are reasonable estimates of the true uncertainties.

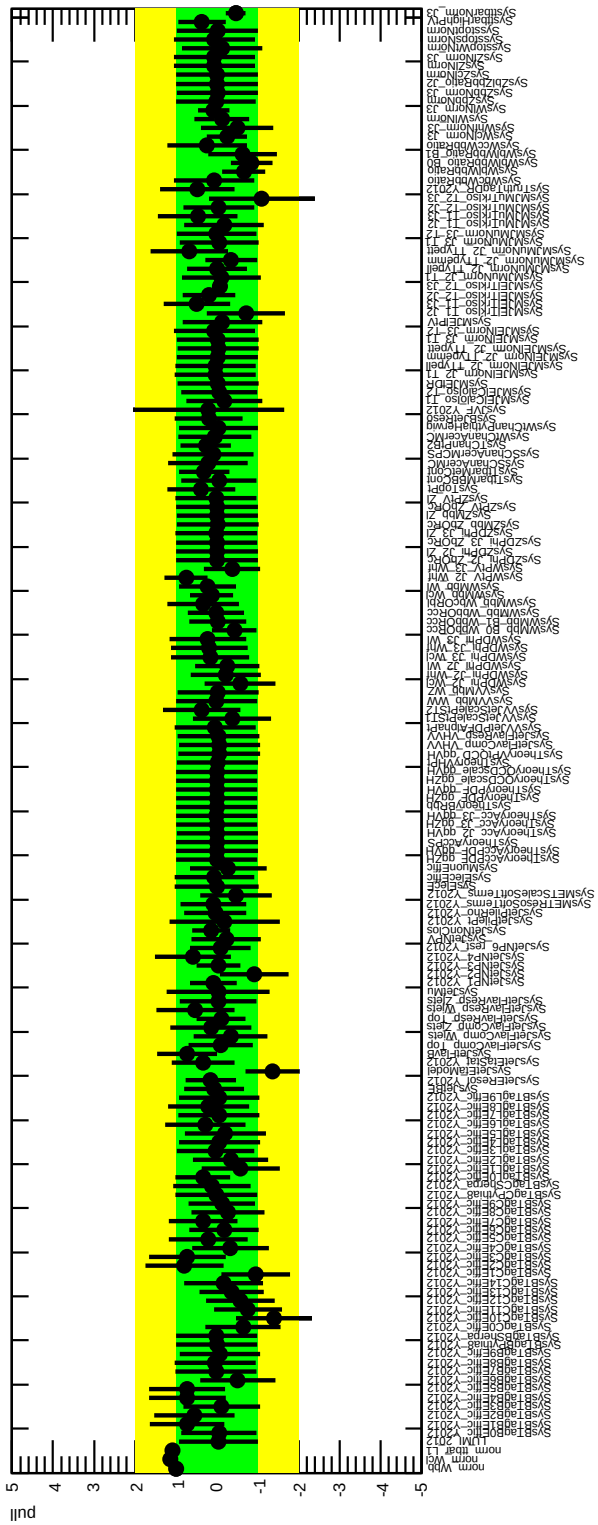
pull
5
4
3
2
1
0
-1
-2
-3
-4
-5
norm_WbbCR
norm_WeiCR
norm_ttbarCR_13
LUMI_2012
SysBtagBEffic_Y2012
SysBtagBEffic_Y2012
SysBtagBEffic_Y

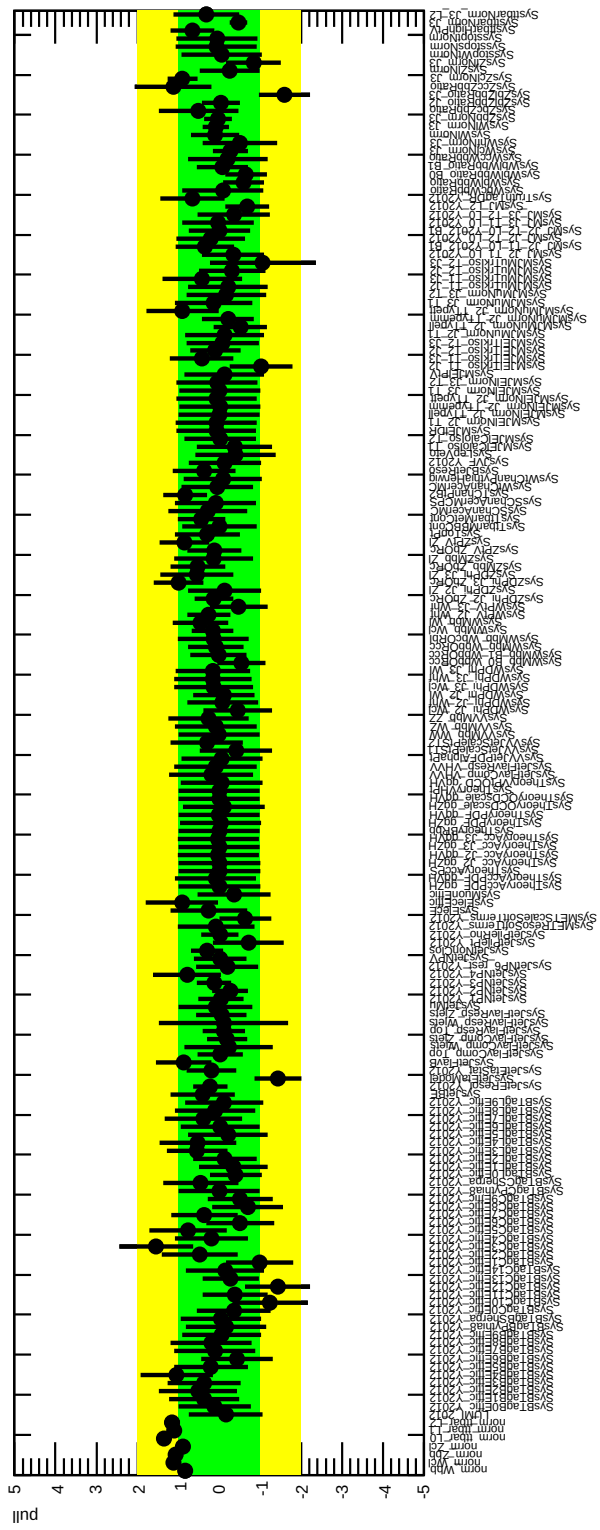

Figure I.2: Nuisance parameter pulls after the global fit for the combination of the 0, 1, and 2-lepton channels, for $m_H = 125$ GeV.

Appendix J

Dominant Post-Global Fit Systematic Uncertainties

Dominant systematic uncertainties and normalisation corrections factors, after the global fit, as defined in [110, 65] and chapter 5, for $m_H = 125$ GeV, are shown in figure J.1 for the 0-lepton channel, figure J.2 for the 1-lepton channel, figure J.3 for the 2-lepton channel, and figure J.4 for the combination of the 0, 1, and 2-lepton channels. For each uncertainty and normalisation, the contributed uncertainty on the fitted signal-strength parameter $\hat{\mu}$ is shown. The systematic uncertainties are listed top to bottom in decreasing order of their contributed uncertainty on $\hat{\mu}$ on the y-axis. The blue boxes show the variations of $\hat{\mu}$, referring to the top x-axis, when fixing the corresponding individual nuisance parameter θ to its post-fit value $\hat{\theta}$ modified upwards or downwards by its post-fit one-σ uncertainty, and repeating the global fit. The hatched and open blue boxes correspond to the upwards and downwards variations, respectively. The filled circles, referring to the bottom x-axis, show the deviations of the fitted nuisance parameters $\hat{\theta}$ from their pre-fit values θ_0, expressed in terms of standard deviations with respect to their pre-fit uncertainties $\Delta\theta = \Delta\theta_0$. The associated error bars show $\frac{\sigma_{\hat{\theta}}}{\sigma_{\theta_0}}$, the ratio of the post-fit uncertainties of the nuisance parameters to their pre-fit uncertainties. The open circles with their error bars, also referring to the bottom x-axis, show the fitted values and uncertainties of the normalisation corrections factors that are allowed to float freely in the global fit. The normalisation corrections factors have pre-fit values of one. For further details of the global fit, $\hat{\mu}$, and nuisance parameters, see chapter 5 section 4.7.

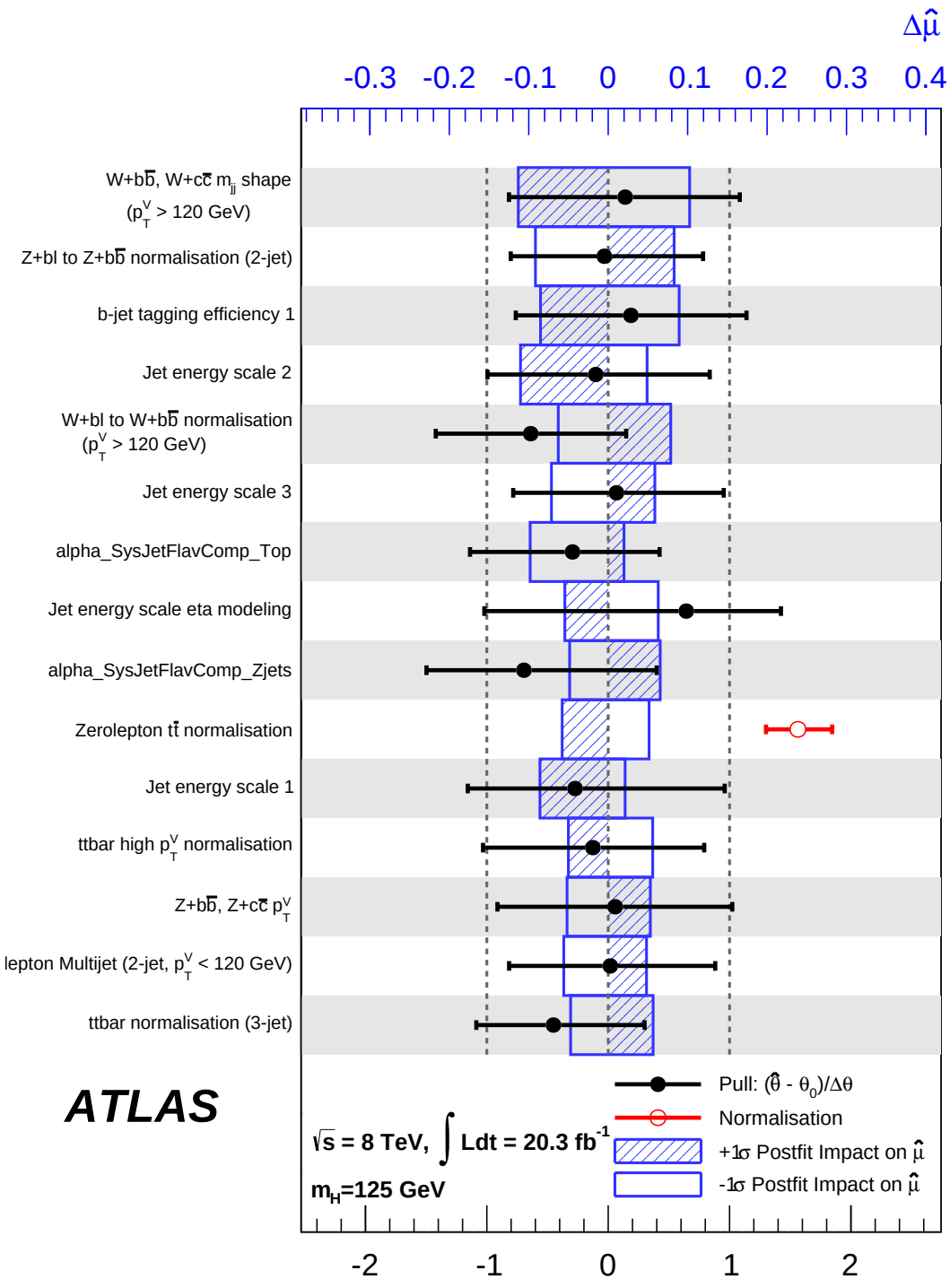

Figure J.1: Dominant systematic uncertainties and normalisation corrections factors, after the global fit, for $m_H = 125$ GeV, for the 0-lepton channel.

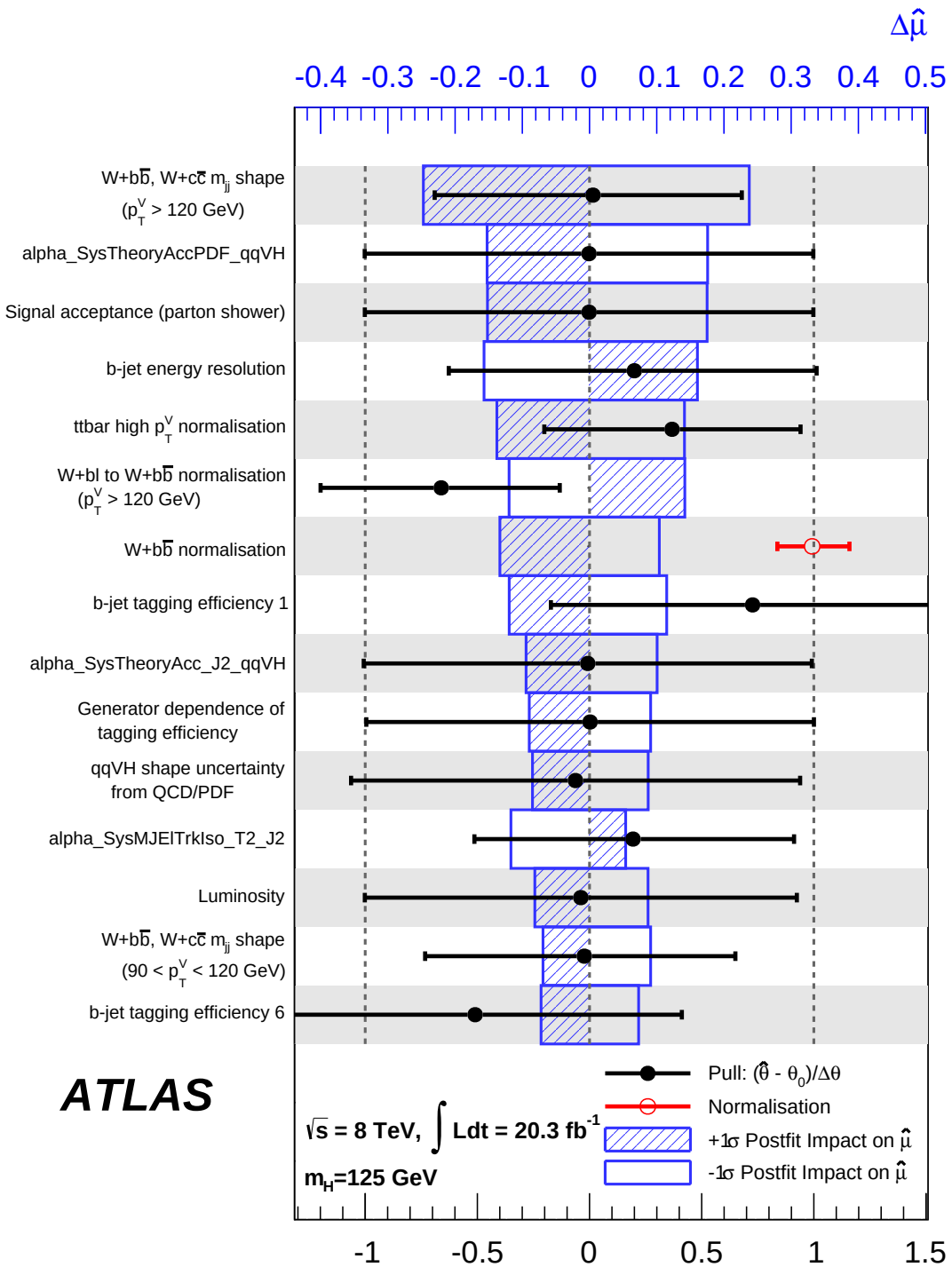

Figure J.2: Dominant systematic uncertainties and normalisation corrections factors, after the global fit, for $m_H = 125$ GeV, for the 1-lepton channel.

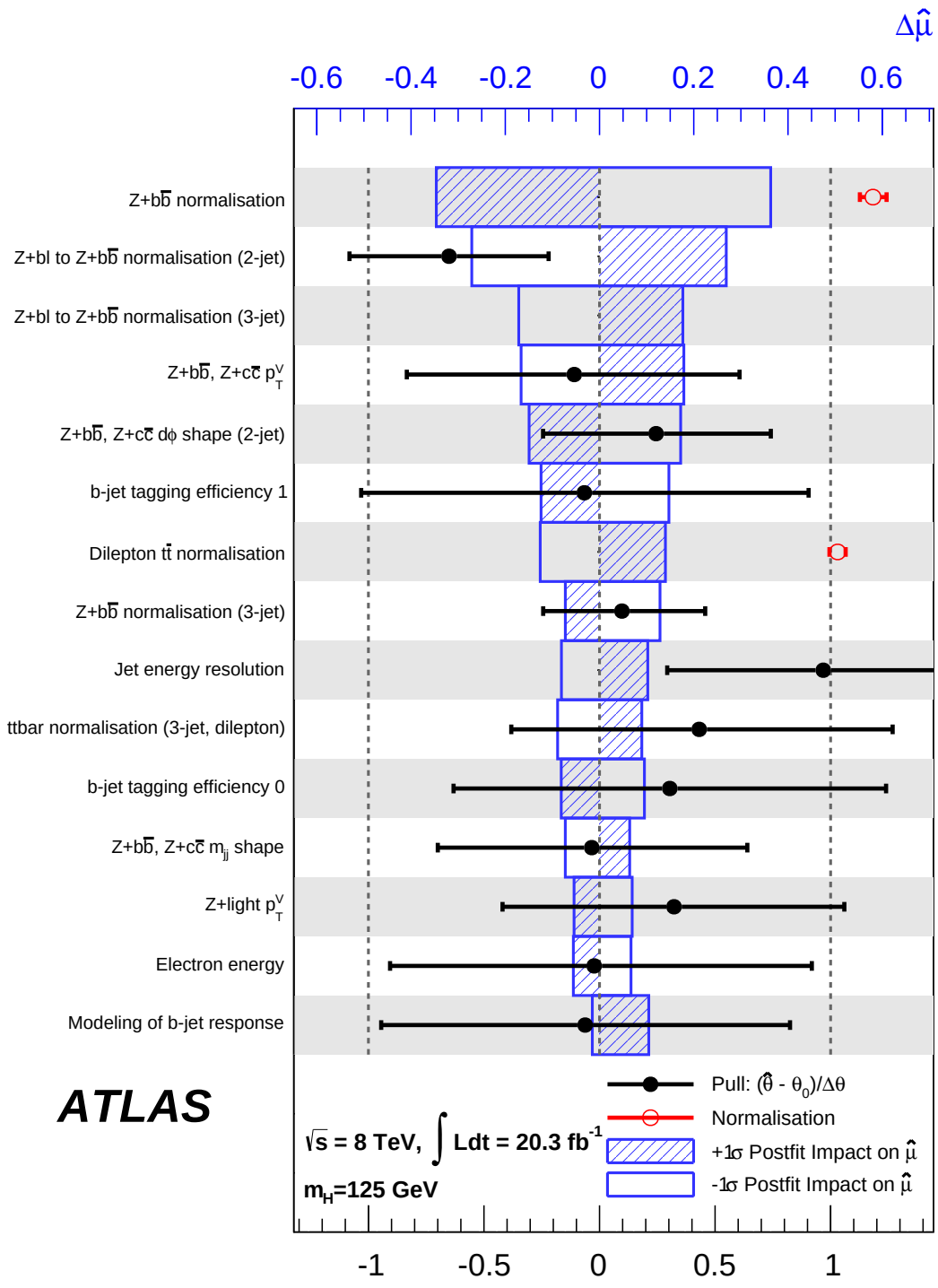

Figure J.3: Dominant systematic uncertainties and normalisation corrections factors, after the global fit, for $m_H = 125$ GeV, for the 2-lepton channel.

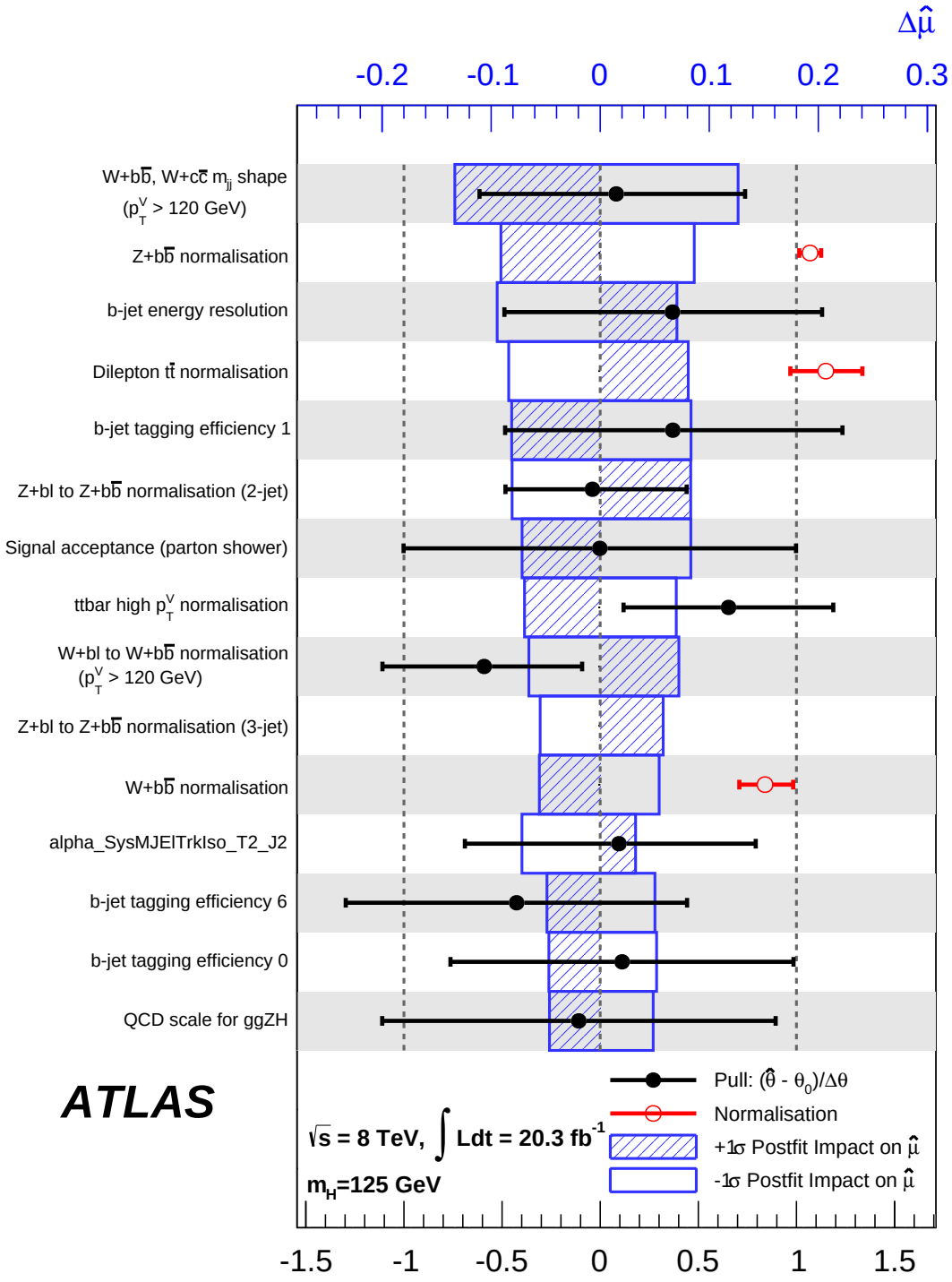

Figure J.4: Dominant systematic uncertainties and normalisation corrections factors, after the global fit, for $m_H = 125$ GeV, for the combination of the 0, 1, and 2-lepton channels.

Bibliography

[1] Plato. *Timeaus*. Circa 360 BC. (Cited on page 1.)

[2] Steven Weinberg. A model of leptons. *Phys. Rev. Lett.*, 19:1264–1266, Nov 1967. (Cited on pages 1 and 79.)

[3] Georges Aad et al. Observation of a new particle in the search for the Standard Model Higgs boson with the ATLAS detector at the LHC. *Phys.Lett.*, B716:1–29, 2012. (Cited on pages 1, 12, 79, and 225.)

[4] Serguei Chatrchyan et al. Observation of a new boson at a mass of 125 GeV with the CMS experiment at the LHC. *Phys.Lett.*, B716:30–61, 2012. (Cited on pages 1, 12, 79, and 225.)

[5] Peter W. Higgs. Broken symmetries and the masses of gauge bosons. *Phys. Rev. Lett.*, 13:508–509, Oct 1964. (Cited on pages 1, 12, and 79.)

[6] Andy Buckley et al. Rivet user manual. 2010. (Cited on page 2.)

[7] Author: MissMJ. Table of particles - The Standard Model of Particle Physics, 2014. (Cited on page 5.)

[8] Paul A.M. Dirac. Nobel Lecture: Theory of Electrons and Positrons. (Cited on page 5.)

[9] Ettore Majorana. Teoria simmetrica dellelettrone e del positrone. *Il Nuovo Cimento*, 14(4):171–184, 1937. (Cited on page 5.)

[10] Roel Aaij et al. Precision measurement of CP violation in $B_s^0 \to J/\psi K^+K^-$ decays. *Phys.Rev.Lett.*, 114:041801, 2015. (Cited on page 5.)

[11] R Aaij et al. First measurement of the CP-violating phase in $B_s^0 \to \phi\phi$ decays. *Phys.Rev.Lett.*, 110(24):241802, 2013. (Cited on page 5.)

[12] Roel Aaij et al. Measurement of polarization amplitudes and CP asymmetries in $B^0 \to \phi K^*(892)^0$. *JHEP*, 1405:069, 2014. (Cited on page 5.)

[13] S. Schael et al. Precision electroweak measurements on the Z resonance. *Phys.Rept.*, 427:257–454, 2006. (Cited on page 5.)

[14] A. Einstein. Die Feldgleichungen der Gravitation. *Sitzungsberichte der Königlich Preußischen Akademie der Wissenschaften (Berlin), Seite 844-847.*, pages 844–847, 1915. (Cited on page 6.)

[15] "The Nobel Prize in Physics 2004". nobelprize.org. nobel media ab 2014. web. (Cited on page 7.)

[16] Siegfried Bethke. The 2009 World Average of alpha(s). *Eur.Phys.J.*, C64:689–703, 2009. (Cited on pages 8 and 146.)

[17] F. Englert and R. Brout. Broken symmetry and the mass of gauge vector mesons. *Phys. Rev. Lett.*, 13:321–323, Aug 1964. (Cited on page 12.)

[18] Peter W. Higgs. Broken symmetries, massless particles and gauge fields. *Phys.Lett.*, 12:132–133, 1964. (Cited on page 12.)

[19] G. S. Guralnik, C. R. Hagen, and T. W. B. Kibble. Global conservation laws and massless particles. *Phys. Rev. Lett.*, 13:585–587, Nov 1964. (Cited on page 12.)

[20] Peter W. Higgs. Spontaneous symmetry breakdown without massless bosons. *Phys. Rev.*, 145:1156–1163, May 1966. (Cited on page 12.)

[21] T. W. B. Kibble. Symmetry breaking in non-abelian gauge theories. *Phys. Rev.*, 155:1554–1561, Mar 1967. (Cited on page 12.)

[22] "the nobel prize in physics 2013". nobelprize.org. nobel media ab 2014. web. (Cited on page 12.)

[23] Sara Alderweireldt. Private communication. (Cited on page 13.)

[24] Jeffrey Goldstone, Abdus Salam, and Steven Weinberg. Broken symmetries. *Phys. Rev.*, 127:965–970, Aug 1962. (Cited on page 14.)

[25] Timo van Ritbergen and Robin G. Stuart. Complete two loop quantum electrodynamic contributions to the muon lifetime in the Fermi model. *Phys.Rev.Lett.*, 82:488–491, 1999. (Cited on page 17.)

[26] Timo van Ritbergen and Robin G. Stuart. On the precise determination of the Fermi coupling constant from the muon lifetime. *Nucl.Phys.*, B564:343–390, 2000. (Cited on page 17.)

[27] M. Steinhauser and T. Seidensticker. Second order corrections to the muon lifetime and the semileptonic B decay. *Phys.Lett.*, B467:271–278, 1999. (Cited on page 17.)

[28] K.A. Olive and Particle Data Group. Review of particle physics. *Chinese Physics C*, 38(9):090001, 2014. (Cited on pages 17, 19, 42, 43, and 51.)

[29] Georges Aad et al. Measurement of the Higgs boson mass from the $H \to \gamma\gamma$ and $H \to ZZ^* \to 4\ell$ channels with the ATLAS detector using 25 fb^{-1} of pp collision data. *Phys.Rev.*, D90:052004, 2014. (Cited on pages 18 and 79.)

[30] Vardan Khachatryan et al. Precise determination of the mass of the Higgs boson and tests of compatibility of its couplings with the standard model predictions using proton collisions at 7 and 8 TeV. 2014. (Cited on pages 18 and 79.)

[31] K.S. Kumar, Sonny Mantry, W.J. Marciano, and P.A. Souder. Low Energy Measurements of the Weak Mixing Angle. *Ann.Rev.Nucl.Part.Sci.*, 63:237–267, 2013. (Cited on page 19.)

[32] S. Dittmaier et al. Handbook of LHC Higgs Cross Sections: 1. Inclusive Observables. 2011. (Cited on pages 20, 21, 22, 50, 56, 79, and 189.)

[33] The Coordinated Theoretical-Experimental Project on QCD . users.phys.psu.edu/∼cteq. (Cited on pages 24, 26, and 128.)

[34] Martin-stirling-thorne-watt parton distribution functions. mstwpdf.hepforge.org. (Cited on pages 24, 27, and 128.)

[35] Neural network parton distribution functions. nnpdf.hepforge.org. (Cited on pages 24, 27, and 128.)

[36] Hung-Liang Lai, Marco Guzzi, Joey Huston, Zhao Li, Pavel M. Nadolsky, et al. New parton distributions for collider physics. *Phys.Rev.*, D82:074024, 2010. (Cited on pages 24 and 26.)

[37] A.D. Martin, W.J. Stirling, R.S. Thorne, and G. Watt. Parton distributions for the LHC. *Eur.Phys.J.*, C63:189–285, 2009. (Cited on page 24.)

[38] Richard D. Ball, Valerio Bertone, Stefano Carrazza, Christopher S. Deans, Luigi Del Debbio, et al. Parton distributions with LHC data. *Nucl.Phys.*, B867:244–289, 2013. (Cited on page 24.)

[39] Michael Edward Peskin and Daniel V. Schroeder. *An introduction to quantum field theory*. Advanced book program. Westview Press Reading (Mass.), Boulder (Colo.), 1995. (Cited on pages 30 and 35.)

[40] Gordon L. Kane, editor. *Perspectives on Higgs physics*. 1993. (Cited on pages 48 and 49.)

[41] John F. Gunion, Howard E. Haber, Gordon L. Kane, and Sally Dawson. The Higgs Hunter's Guide. *Front. Phys.*, 80:1–448, 2000. (Cited on pages 48 and 49.)

[42] Jorge C. Romao and Sofia Andringa. Vector boson decays of the Higgs boson. *Eur. Phys. J.*, C7:631–642, 1999. (Cited on pages 48 and 49.)

[43] V. Del Duca, W. Kilgore, C. Oleari, C. R. Schmidt, and D. Zeppenfeld. Kinematical limits on Higgs boson production via gluon fusion in association with jets. *Phys. Rev.*, D67:073003, 2003. (Cited on page 49.)

[44] The ATLAS Collaboration and G Aad *et al.* The ATLAS Experiment at the CERN Large Hadron Collider. *Journal of Instrumentation*, 3(08):S08003, 2008. (Cited on pages 57, 68, 69, 75, and 83.)

[45] Oliver Sim Brning, Paul Collier, P Lebrun, Stephen Myers, Ranko Ostojic, John Poole, and Paul Proudlock. *LHC Design Report, Vol. 1.* Number CERN-2004-003-V-1. CERN, Geneva, 2004. (Cited on pages 57 and 58.)

[46] Oliver Sim Brning, Paul Collier, P Lebrun, Stephen Myers, Ranko Ostojic, John Poole, and Paul Proudlock. *LHC Design Report, Vol. 2.* Number CERN-2004-003-V-3. CERN, Geneva, 2004. (Cited on pages 57 and 58.)

[47] Michael Benedikt, Paul Collier, V Mertens, John Poole, and Karlheinz Schindl. *LHC Design Report, Vol. 3.* Number CERN-2004-003-V-3. CERN, Geneva, 2004. (Cited on pages 57 and 58.)

[48] *LEP design report, Vol. 1.* Number CERN-LEP-TH 83-29. CERN, Geneva, 1983. By the LEP Injector Study Group. (Cited on page 58.)

[49] *LEP design report, Vol. 2.* Number CERN-LEP 84-01. CERN, Geneva, 1984. By the LEP Injector Study Group. (Cited on page 58.)

[50] The ATLAS website, 2015. atlas.ch. (Cited on pages 58, 61, 63, 68, 70, 72, 75, and 76.)

[51] Peter Jenni, Marzio Nessi, Markus Nordberg, and Kenway Smith. *ATLAS high-level trigger, data-acquisition and controls: Technical Design Report.* Technical Design Report ATLAS. CERN, Geneva, 2003. (Cited on pages 60 and 80.)

[52] CERN Accelerators and Technology Sector, 2009. espace.cern.ch/acc-tec-sector. (Cited on page 62.)

[53] The LHC Collimation Project website. lhc-collimation-project.web.cern.ch/lhc-collimation-project. (Cited on page 62.)

[54] LHC Beam Dumping System Project, 2005. proj-lbds.web.cern.ch/proj-lbds. (Cited on page 64.)

[55] The ATLAS Experiment - Luminosity Public Results, 2013. twiki.cern.ch/twiki/bin/view/AtlasPublic/LuminosityPublicResults. (Cited on pages 65, 66, and 67.)

[56] J. Liouville. Note sur la thorie de la variation des constantes arbitraires. *Journal de Mathmatiques Pures et Appliques*, I(3):342–349, 1838. (Cited on page 67.)

[57] A. Ahmad et al. The silicon microstrip sensors of the ATLAS semiconductor tracker. *Nuclear Instruments and Methods in Physics Research Section A: Accelerators, Spectrometers, Detectors and Associated Equipment*, 578(1):98 – 118, 2007. (Cited on page 71.)

[58] D Robinson. The ATLAS Semi-Conductor Tracker Operation and Performance. Technical Report ATL-INDET-PROC-2012-002, CERN, Geneva, Jan 2012. (Cited on page 71.)

[59] The ATLAS collaboration. Alignment of the ATLAS Inner Detector and its Performance in 2012. Jul 2014. (Cited on page 75.)

[60] Georges Aad et al. Measurement of the muon reconstruction performance of the ATLAS detector using 2011 and 2012 LHC proton-proton collision data. *Eur.Phys.J.*, C74(11):3130, 2014. (Cited on page 76.)

[61] R. Barate et al. Search for the standard model Higgs boson at LEP. *Phys.Lett.*, B565:61–75, 2003. (Cited on page 79.)

[62] T. Aaltonen et al. Higgs Boson Studies at the Tevatron. *Phys.Rev.*, D88(5):052014, 2013. (Cited on page 79.)

[63] Evidence for Higgs Boson Decays to the $\tau^+\tau^-$ Final State with the ATLAS Detector. Technical Report ATLAS-CONF-2013-108, CERN, Geneva, Nov 2013. (Cited on page 79.)

[64] James Stirling. Private communication, 2014. (Cited on page 80.)

[65] Georges Aad et al. Search for the $b\bar{b}$ decay of the Standard Model Higgs boson in associated $(W/Z)H$ production with the ATLAS detector. 2014. (Cited on pages 80, 94, 97, 98, 99, 101, 287, and 290.)

[66] Georges Aad et al. Improved luminosity determination in pp collisions at $\sqrt{s} = 7$ TeV using the ATLAS detector at the LHC. *Eur.Phys.J.*, C73:2518, 2013. (Cited on pages 82 and 101.)

[67] Georges Aad et al. Electron reconstruction and identification efficiency measurements with the ATLAS detector using the 2011 LHC proton-proton collision data. *Eur.Phys.J.*, C74:2941, 2014. (Cited on page 83.)

[68] The ATLAS collaboration. Electron efficiency measurements with the ATLAS detector using the 2012 LHC proton-proton collision data. 2014. (Cited on pages 83 and 84.)

[69] Georges Aad et al. Muon reconstruction efficiency and momentum resolution of the ATLAS experiment in proton-proton collisions at $\sqrt{s}$=7 TeV in 2010. *Eur.Phys.J.*, C74:3034, 2014. (Cited on page 83.)

[70] W. Lampl, S. Laplace, D. Lelas, P. Loch, H. Ma, et al. Calorimeter clustering algorithms: Description and performance. 2008. (Cited on page 84.)

[71] Matteo Cacciari, Gavin P. Salam, and Gregory Soyez. The Anti-k(t) jet clustering algorithm. *JHEP*, 0804:063, 2008. (Cited on page 84.)

[72] Matteo Cacciari and Gavin P. Salam. Pileup subtraction using jet areas. *Phys.Lett.*, B659:119–126, 2008. (Cited on page 84.)

[73] Georges Aad et al. Jet energy measurement with the ATLAS detector in proton-proton collisions at $\sqrt{s} = 7$ TeV. *Eur.Phys.J.*, C73:2304, 2013. (Cited on page 84.)

[74] Georges Aad et al. Jet energy measurement and its systematic uncertainty in proton-proton collisions at $\sqrt{s} = 7$ TeV with the ATLAS detector. 2014. (Cited on pages 84 and 100.)

[75] Commissioning of the ATLAS high-performance b-tagging algorithms in the 7 TeV collision data. Technical Report ATLAS-CONF-2011-102, CERN, Geneva, Jul 2011. (Cited on page 84.)

[76] Calibration of b-tagging using dileptonic top pair events in a combinatorial likelihood approach with the ATLAS experiment. Technical Report ATLAS-CONF-2014-004, CERN, Geneva, Feb 2014. (Cited on pages 84 and 85.)

[77] Calibration of the performance of b-tagging for c and light-flavour jets in the 2012 ATLAS data. Technical Report ATLAS-CONF-2014-046, CERN, Geneva, Jul 2014. (Cited on page 84.)

[78] G Piacquadio. Calibration of b-tagging using di-leptonic top pair events applying the combinatorial likelihood approach to 2011 data. Technical Report ATL-COM-PHYS-2013-1083, CERN, Geneva, Aug 2013. (Cited on page 85.)

[79] G Aad, H Arnold, and C Weiser. b-jet tagging calibration on c-jets produced in association with $W^{\pm}$ bosons. Technical Report ATL-COM-PHYS-2013-1365, CERN, Geneva, Sep 2013. (Cited on page 85.)

[80] I Burmeister, I Connelly, A Ferretto, F Filthaut, R Goncalo, R Hawkings, H Esch, F Parodi, D Sidorov, C Schiavi, J Thomas-Wilsker, J Yu, and M Zur Nedden. Measurement of the b-tagging performance in the 2012 ATLAS data. Technical Report ATL-COM-PHYS-2013-456, CERN, Geneva, Apr 2013. (Cited on page 85.)

[81] Performance of Missing Transverse Momentum Reconstruction in ATLAS studied in Proton-Proton Collisions recorded in 2012 at 8 TeV. Technical Report ATLAS-CONF-2013-082, CERN, Geneva, Aug 2013. (Cited on page 88.)

[82] Georges Aad et al. Measurements of normalized differential cross-sections for ttbar production in pp collisions at sqrt(s) = 7 TeV using the ATLAS detector. *Phys.Rev.*, D90:072004, 2014. (Cited on page 97.)

[83] Georges Aad et al. Jet energy resolution in proton-proton collisions at $\sqrt{s} = 7$ TeV recorded in 2010 with the ATLAS detector. *Eur.Phys.J.*, C73:2306, 2013. (Cited on page 100.)

[84] L. Moneta, K. Cranmer, G. Schott, and W. Verkerke. The RooStats project. In *Proceedings of the 13th International Workshop on Advanced Computing and Analysis Techniques in Physics Research. February 22-27, 2010, Jaipur, India.*, page 57, 2010. (Cited on page 103.)

[85] W. Verkerke and D. Kirkby. The RooFit toolkit for data modeling. *ArXiv Physics e-prints*, June 2003. (Cited on page 103.)

[86] Glen Cowan, Kyle Cranmer, Eilam Gross, and Ofer Vitells. Asymptotic formulae for likelihood-based tests of new physics. *The European Physical Journal C*, 71(2), 2011. (Cited on page 105.)

[87] S. S. Wilks. The large-sample distribution of the likelihood ratio for testing composite hypotheses. *The Annals of Mathematical Statistics*, 9(1):pp. 60–62, 1938. (Cited on page 105.)

[88] A. Schaelicke, T. Gleisberg, Stefan. Hoeche, S. Schumann, J. Winter, et al. Event generator for particle production in high-energy collisions. *Prog.Part.Nucl.Phys.*, 53:329–338, 2004. (Cited on page 111.)

[89] C++ Interface to PHOTOS. photospp.web.cern.ch/photospp/index.html. (Cited on pages 112 and 180.)

[90] The PYTHIA 6.4 website. pythia6.hepforge.org. (Cited on page 112.)

[91] The Pythia 8 website. home.thep.lu.se/∼torbjorn/Pythia.html. (Cited on page 112.)

[92] The Herwig++ Event Generator. herwig.hepforge.org. (Cited on page 112.)

[93] Paolo Nason. A New method for combining NLO QCD with shower Monte Carlo algorithms. *JHEP*, 0411:040, 2004. (Cited on page 112.)

[94] Stefano Frixione, Paolo Nason, and Carlo Oleari. Matching NLO QCD computations with Parton Shower simulations: the POWHEG method. *JHEP*, 0711:070, 2007. (Cited on page 112.)

[95] Simone Alioli, Paolo Nason, Carlo Oleari, and Emanuele Re. A general framework for implementing NLO calculations in shower Monte Carlo programs: the POWHEG BOX. *JHEP*, 1006:043, 2010. (Cited on pages 112 and 125.)

[96] J. Alwall, R. Frederix, S. Frixione, V. Hirschi, F. Maltoni, et al. The automated computation of tree-level and next-to-leading order differential cross sections, and their matching to parton shower simulations. *JHEP*, 1407:079, 2014. (Cited on page 112.)

[97] Johan Alwall, A. Ballestrero, P. Bartalini, S. Belov, E. Boos, et al. A Standard format for Les Houches event files. *Comput.Phys.Commun.*, 176:300–304, 2007. (Cited on page 112.)

[98] S Heinemeyer et al. Handbook of LHC Higgs Cross Sections: 3. Higgs Properties. 2013. (Cited on pages 114, 122, 165, 187, and 188.)

[99] Iain W. Stewart and Frank J. Tackmann. Theory Uncertainties for Higgs and Other Searches Using Jet Bins. *Phys.Rev.*, D85:034011, 2012. (Cited on page 116.)

[100] Gionata Luisoni, Paolo Nason, Carlo Oleari, and Francesco Tramontano. $HW^{\pm}$/HZ + 0 and 1 jet at NLO with the POWHEG BOX interfaced to GoSam and their merging within MiNLO. *JHEP*, 1310:083, 2013. (Cited on page 117.)

[101] Stefan Gieseke. Uncertainties of Sudakov form-factors. *JHEP*, 01:058, 2005. (Cited on page 124.)

[102] Simone Alioli, Paolo Nason, Carlo Oleari, and Emanuele Re. The POWHEG BOX user manual: common features. 2011. (Cited on page 124.)

[103] Andy Buckley, James Ferrando, Stephen Lloyd, Karl Nordstrom, Ben Page, Martin Rufenacht, Marek Schonherr, and Graeme Watt. LHAPDF6: parton density access in the LHC precision era. *Eur. Phys. J.*, C75(3):132, 2015. (Cited on page 124.)

[104] J. Butterworth, G. Dissertori, S. Dittmaier, D. de Florian, N. Glover, et al. Les Houches 2013: Physics at TeV Colliders: Standard Model Working Group Report. 2014. (Cited on page 124.)

[105] Rikkert Frederix, Stefano Frixione, Valentin Hirschi, Fabio Maltoni, Roberto Pittau, et al. Four-lepton production at hadron colliders: aMC@NLO predictions with theoretical uncertainties. *JHEP*, 1202:099, 2012. (Cited on pages 124 and 125.)

[106] Sergey Alekhin, Simone Alioli, Richard D. Ball, Valerio Bertone, Johannes Blumlein, et al. The PDF4LHC Working Group Interim Report. 2011. (Cited on pages 130 and 146.)

[107] Bo Andersson, G. Gustafson, G. Ingelman, and T. Sjostrand. Parton Fragmentation and String Dynamics. *Phys.Rept.*, 97:31–145, 1983. (Cited on page 167.)

[108] Andy Buckley, Jonathan Butterworth, Stefan Gieseke, David Grellscheid, Stefan Hoche, et al. General-purpose event generators for LHC physics. *Phys.Rept.*, 504:145–233, 2011. (Cited on pages 167 and 179.)

[109] Jan-Christopher Winter, Frank Krauss, and Gerhard Soff. A Modified cluster hadronization model. *Eur.Phys.J.*, C36:381–395, 2004. (Cited on page 167.)

[110] 5 HSG. Common supporting documentation for multivariate and cut-based searches for the production of a standard model higgs boson produced in association with a vector boson. Technical Report ATL-COM-PHYS-2013-465, CERN, Geneva, Apr 2013. (Cited on pages xxvii, 202, 203, 206, 209, 211, 216, 217, 219, 220, 222, 223, 287, and 290.)

[111] Georges Aad et al. Measurement of distributions sensitive to the underlying event in inclusive Z-boson production in pp collisions at $\sqrt{s} = 7$ TeV with the ATLAS detector. 2014. (Cited on pages 264 and 265.)

Publications

1. **"Measurement of transverse energy-energy correlations in multi-jet events in pp collisions at $\sqrt{s} = 7$ TeV using the ATLAS detector and determination of the strong coupling constant $\alpha_s(m_Z)$"**
   G. Aad *et al.* [ATLAS Collaboration].
   arXiv:1508.01579 [hep-ex]
   10.1016/j.physletb.2015.09.050
   Phys. Lett. B **750**, 427 (2015)
   (Aug 6, 2015) [HEP entry link]

2. **"Search for photonic signatures of gauge-mediated supersymmetry in 8 TeV pp collisions with the ATLAS detector"**
   G. Aad *et al.* [ATLAS Collaboration].
   arXiv:1507.05493 [hep-ex]
   10.1103/PhysRevD.92.072001
   Phys. Rev. D **92**, no. 7, 072001 (2015)
   (Jul 20, 2015) [HEP entry link]

3. **"Measurement of exclusive $\gamma\gamma \to \ell^+\ell^-$ production in proton-proton collisions at $\sqrt{s} = 7$ TeV with the ATLAS detector"**
   G. Aad *et al.* [ATLAS Collaboration].
   arXiv:1506.07098 [hep-ex]
   10.1016/j.physletb.2015.07.069
   Phys. Lett. B **749**, 242 (2015)
   (Jun 23, 2015) [HEP entry link]

4. **"Study of (W/Z)H production and Higgs boson couplings using $H \to WW^*$ decays with the ATLAS detector"**
   G. Aad *et al.* [ATLAS Collaboration].
   arXiv:1506.06641 [hep-ex]
   10.1007/JHEP08(2015)137
   JHEP **1508**, 137 (2015)
   (Jun 22, 2015) [HEP entry link]

5. **"Search for heavy Majorana neutrinos with the ATLAS detector in pp collisions at $\sqrt{s} = 8$ TeV"**
   G. Aad *et al.* [ATLAS Collaboration].
   arXiv:1506.06020 [hep-ex]

10.1007/JHEP07(2015)162
JHEP **1507**, 162 (2015)
(Jun 19, 2015) [HEP entry link]

6. **"Search for the associated production of the Higgs boson with a top quark pair in multilepton final states with the ATLAS detector"**
G. Aad *et al.* [ATLAS Collaboration].
arXiv:1506.05988 [hep-ex]
10.1016/j.physletb.2015.07.079
Phys. Lett. B **749**, 519 (2015)
(Jun 19, 2015) [HEP entry link]

7. **"Study of the spin and parity of the Higgs boson in diboson decays with the ATLAS detector"**
G. Aad *et al.* [ATLAS Collaboration].
arXiv:1506.05669 [hep-ex]
10.1140/epjc/s10052-015-3685-1
Eur. Phys. J. C **75**, no. 10, 476 (2015)
(Jun 18, 2015) [HEP entry link]

8. **"Measurement of colour flow with the jet pull angle in $t\bar{t}$ events using the ATLAS detector at $\sqrt{s} = 8$ TeV"**
G. Aad *et al.* [ATLAS Collaboration].
arXiv:1506.05629 [hep-ex]
10.1016/j.physletb.2015.09.051
Physics Letters B (2015) 475-493
(Jun 18, 2015) [HEP entry link]

9. **"Modelling $Z \to \tau\tau$ processes in ATLAS with τ-embedded $Z \to \mu\mu$ data"**
G. Aad *et al.* [ATLAS Collaboration].
arXiv:1506.05623 [hep-ex]
10.1088/1748-0221/10/09/P09018, 10.1088/1748-0221/2015/9/P09018
JINST **10**, no. 09, P09018 (2015)
(Jun 18, 2015) [HEP entry link]

10. **"Search for metastable heavy charged particles with large ionisation energy loss in pp collisions at $\sqrt{s} = 8$ TeV using the ATLAS experiment"**
G. Aad *et al.* [ATLAS Collaboration].
arXiv:1506.05332 [hep-ex]
10.1140/epjc/s10052-015-3609-0
Eur. Phys. J. C **75**, no. 9, 407 (2015)
(Jun 17, 2015) [HEP entry link]

11. **"Search for type-III Seesaw heavy leptons in pp collisions at $\sqrt{s} = 8$ TeV with the ATLAS Detector"**
G. Aad *et al.* [ATLAS Collaboration].

arXiv:1506.01839 [hep-ex]
10.1103/PhysRevD.92.032001
Phys. Rev. D **92**, no. 3, 032001 (2015)
(Jun 5, 2015) [HEP entry link]

12. **"Search for heavy lepton resonances decaying to a Z boson and a lepton in pp collisions at $\sqrt{s} = 8$ TeV with the ATLAS detector"**
G. Aad *et al.* [ATLAS Collaboration].
arXiv:1506.01291 [hep-ex]
10.1007/JHEP09(2015)108
JHEP **1509**, 108 (2015)
(Jun 3, 2015) [HEP entry link]

13. **"Search for Dark Matter in Events with Missing Transverse Momentum and a Higgs Boson Decaying to Two Photons in pp Collisions at $\sqrt{s} = 8$ TeV with the ATLAS Detector"**
G. Aad *et al.* [ATLAS Collaboration].
arXiv:1506.01081 [hep-ex]
10.1103/PhysRevLett.115.131801
Phys. Rev. Lett. **115**, no. 13, 131801 (2015)
(Jun 2, 2015) [HEP entry link]

14. **"Search for Higgs boson pair production in the $b\bar{b}b\bar{b}$ final state from pp collisions at $\sqrt{s} = 8$ TeV with the ATLAS detector"**
G. Aad *et al.* [ATLAS Collaboration].
arXiv:1506.00285 [hep-ex]
10.1140/epjc/s10052-015-3628-x
Eur. Phys. J. C **75**, no. 9, 412 (2015)
(May 31, 2015) [HEP entry link]

15. **"Measurement of differential J/ψ production cross sections and forward-backward ratios in p+Pb collisions with the ATLAS detector"**
G. Aad *et al.* [ATLAS Collaboration].
arXiv:1505.08141 [hep-ex]
10.1103/PhysRevC.92.034904
Phys. Rev. C **92**, no. 3, 034904 (2015)
(May 29, 2015) [HEP entry link]

16. **"A search for $t\bar{t}$ resonances using lepton-plus-jets events in proton-proton collisions at $\sqrt{s} = 8$ TeV with the ATLAS detector"**
G. Aad *et al.* [ATLAS Collaboration].
arXiv:1505.07018 [hep-ex]
10.1007/JHEP08(2015)148
JHEP **1508**, 148 (2015)
(May 26, 2015) [HEP entry link]

17. **"Search for production of vector-like quark pairs and of four top quarks in the lepton-plus-jets final state in pp collisions at $\sqrt{s} = 8$ TeV with**

the ATLAS detector"
G. Aad *et al.* [ATLAS Collaboration].
arXiv:1505.04306 [hep-ex]
10.1007/JHEP08(2015)105
JHEP **1508**, 105 (2015)
(May 16, 2015) [HEP entry link]

18. **"Search for Higgs bosons decaying to aa in the $\mu\mu\tau\tau$ final state in pp collisions at $\sqrt{s} = 8$ TeV with the ATLAS experiment"**
G. Aad *et al.* [ATLAS Collaboration].
arXiv:1505.01609 [hep-ex]
10.1103/PhysRevD.92.052002
Phys. Rev. D **92**, no. 5, 052002 (2015)
(May 7, 2015) [HEP entry link]

19. **"Measurements of the Total and Differential Higgs Boson Production Cross Sections Combining the H and HZZ*4 Decay Channels at $\sqrt{s}$=8TeV with the ATLAS Detector"**
G. Aad *et al.* [ATLAS Collaboration].
arXiv:1504.05833 [hep-ex]
10.1103/PhysRevLett.115.091801
Phys. Rev. Lett. **115**, no. 9, 091801 (2015)
(Apr 21, 2015) [HEP entry link]

20. **"Search for high-mass diphoton resonances in pp collisions at $\sqrt{s} = 8$ TeV with the ATLAS detector"**
G. Aad *et al.* [ATLAS Collaboration].
arXiv:1504.05511 [hep-ex]
10.1103/PhysRevD.92.032004
Phys. Rev. D **92**, no. 3, 032004 (2015)
(Apr 21, 2015) [HEP entry link]

21. **"Measurement of charged-particle spectra in Pb+Pb collisions at $\sqrt{s_{\mathrm{NN}}} = 2.76$ TeV with the ATLAS detector at the LHC"**
G. Aad *et al.* [ATLAS Collaboration].
arXiv:1504.04337 [hep-ex]
10.1007/JHEP09(2015)050
JHEP **1509**, 050 (2015)
(Apr 16, 2015) [HEP entry link]

22. **"Search for invisible decays of the Higgs boson produced in association with a hadronically decaying vector boson in pp collisions at $\sqrt{s} = 8$ TeV with the ATLAS detector"**
G. Aad *et al.* [ATLAS Collaboration].
arXiv:1504.04324 [hep-ex]
10.1140/epjc/s10052-015-3551-1
Eur. Phys. J. C **75**, no. 7, 337 (2015)
(Apr 16, 2015) [HEP entry link]

23. **"Measurement of the top pair production cross section in 8TeV proton-proton collisions using kinematic information in the lepton+jets final state with ATLAS"**
G. Aad *et al.* [ATLAS Collaboration].
arXiv:1504.04251 [hep-ex]
10.1103/PhysRevD.91.112013
Phys. Rev. D **91**, no. 11, 112013 (2015)
(Apr 16, 2015) [HEP entry link]

24. **"Search for heavy long-lived multi-charged particles in pp collisions at $\sqrt{s} = 8$ TeV using the ATLAS detector"**
G. Aad *et al.* [ATLAS Collaboration].
arXiv:1504.04188 [hep-ex]
10.1140/epjc/s10052-015-3534-2
Eur. Phys. J. C **75**, no. 8, 362 (2015)
(Apr 16, 2015) [HEP entry link]

25. **"Search for long-lived, weakly interacting particles that decay to displaced hadronic jets in proton-proton collisions at $\sqrt{s} = 8$ TeV with the ATLAS detector"**
G. Aad *et al.* [ATLAS Collaboration].
arXiv:1504.03634 [hep-ex]
10.1103/PhysRevD.92.012010
Phys. Rev. D **92**, no. 1, 012010 (2015)
(Apr 14, 2015) [HEP entry link]

26. **"Measurement of the correlation between flow harmonics of different order in lead-lead collisions at $\sqrt{s_{NN}}$=2.76 TeV with the ATLAS detector"**
G. Aad *et al.* [ATLAS Collaboration].
arXiv:1504.01289 [hep-ex]
10.1103/PhysRevC.92.034903
Phys. Rev. C **92**, no. 3, 034903 (2015)
(Apr 6, 2015) [HEP entry link]

27. **"Search for New Phenomena in Dijet Angular Distributions in Proton-Proton Collisions at $\sqrt{s} = 8$ TeV Measured with the ATLAS Detector"**
G. Aad *et al.* [ATLAS Collaboration].
arXiv:1504.00357 [hep-ex]
10.1103/PhysRevLett.114.221802
Phys. Rev. Lett. **114**, no. 22, 221802 (2015)
(Apr 1, 2015) [HEP entry link]

28. **"Search for low-scale gravity signatures in multi-jet final states with the ATLAS detector at $\sqrt{s} = 8$ TeV"**
G. Aad *et al.* [ATLAS Collaboration].
arXiv:1503.08988 [hep-ex]

10.1007/JHEP07(2015)032
JHEP **1507**, 032 (2015)
(Mar 31, 2015) [HEP entry link]

29. **"Search for a new resonance decaying to a W or Z boson and a Higgs boson in the $\ell\ell/\ell\nu/\nu\nu + b\bar{b}$ final states with the ATLAS detector"**
G. Aad *et al.* [ATLAS Collaboration].
arXiv:1503.08089 [hep-ex]
10.1140/epjc/s10052-015-3474-x
Eur. Phys. J. C **75**, no. 6, 263 (2015)
(Mar 27, 2015) [HEP entry link]

30. **"Combined Measurement of the Higgs Boson Mass in pp Collisions at $\sqrt{s} = 7$ and 8 TeV with the ATLAS and CMS Experiments"**
G. Aad *et al.* [ATLAS and CMS Collaborations].
arXiv:1503.07589 [hep-ex]
10.1103/PhysRevLett.114.191803
Phys. Rev. Lett. **114**, 191803 (2015)
(Mar 26, 2015) [HEP entry link]

31. **"Measurement of the top quark mass in the $t\bar{t} \to$ lepton+jets and $t\bar{t} \to$ dilepton channels using $\sqrt{s} = 7$ TeV ATLAS data"**
G. Aad *et al.* [ATLAS Collaboration].
arXiv:1503.05427 [hep-ex]
10.1140/epjc/s10052-015-3544-0
Eur. Phys. J. C **75**, no. 7, 330 (2015)
(Mar 18, 2015) [HEP entry link]

32. **"Search for vectorlike B quarks in events with one isolated lepton, missing transverse momentum and jets at $\sqrt{s} = 8$ TeV with the ATLAS detector"**
G. Aad *et al.* [ATLAS Collaboration].
arXiv:1503.05425 [hep-ex]
10.1103/PhysRevD.91.112011
Phys. Rev. D **91**, no. 11, 112011 (2015)
(Mar 18, 2015) [HEP entry link]

33. **"Search for the Standard Model Higgs boson produced in association with top quarks and decaying into $b\bar{b}$ in pp collisions at $\sqrt{s} = 8$ TeV with the ATLAS detector"**
G. Aad *et al.* [ATLAS Collaboration].
arXiv:1503.05066 [hep-ex]
10.1140/epjc/s10052-015-3543-1
Eur. Phys. J. C **75**, no. 7, 349 (2015)
(Mar 17, 2015) [HEP entry link]

34. **"Search for production of WW/WZ resonances decaying to a lepton, neutrino and jets in pp collisions at $\sqrt{s} = 8$ TeV with the ATLAS**

detector"
G. Aad *et al.* [ATLAS Collaboration].
arXiv:1503.04677 [hep-ex]
10.1140/epjc/s10052-015-3593-4, 10.1140/epjc/s10052-015-3425-6
Eur. Phys. J. C **75**, no. 5, 209 (2015), [Eur. Phys. J. C **75**, 370 (2015)]
(Mar 16, 2015) [HEP entry link]

35. **"Search for a Heavy Neutral Particle Decaying to $e\mu$, $e\tau$, or $\mu\tau$ in pp Collisions at $\sqrt{s} = 8$ TeV with the ATLAS Detector"**
G. Aad *et al.* [ATLAS Collaboration].
arXiv:1503.04430 [hep-ex]
10.1103/PhysRevLett.115.031801
Phys. Rev. Lett. **115**, no. 3, 031801 (2015)
(Mar 15, 2015) [HEP entry link]

36. **"Search for a Charged Higgs Boson Produced in the Vector-Boson Fusion Mode with Decay $H^{\pm} \to W^{\pm}Z$ using pp Collisions at $\sqrt{s} = 8$TeV with the ATLAS Experiment"**
G. Aad *et al.* [ATLAS Collaboration].
arXiv:1503.04233 [hep-ex]
10.1103/PhysRevLett.114.231801
Phys. Rev. Lett. **114**, no. 23, 231801 (2015)
(Mar 13, 2015) [HEP entry link]

37. **"Measurement of the forward-backward asymmetry of electron and muon pair-production in pp collisions at $\sqrt{s} = 7$ TeV with the ATLAS detector"**
G. Aad *et al.* [ATLAS Collaboration].
arXiv:1503.03709 [hep-ex]
10.1007/JHEP09(2015)049
JHEP **1509**, 049 (2015)
(Mar 12, 2015) [HEP entry link]

38. **"Determination of spin and parity of the Higgs boson in the $WW^* \to e\nu\mu\nu$ decay channel with the ATLAS detector"**
G. Aad *et al.* [ATLAS Collaboration].
arXiv:1503.03643 [hep-ex]
10.1140/epjc/s10052-015-3436-3
Eur. Phys. J. C **75**, no. 5, 231 (2015)
(Mar 12, 2015) [HEP entry link]

39. **"Search for supersymmetry in events containing a same-flavour opposite-sign dilepton pair, jets, and large missing transverse momentum in $\sqrt{s} = 8$ TeV pp collisions with the ATLAS detector"**
G. Aad *et al.* [ATLAS Collaboration].
arXiv:1503.03290 [hep-ex]
10.1140/epjc/s10052-015-3661-9, 10.1140/epjc/s10052-015-3518-2

Eur. Phys. J. C **75**, no. 7, 318 (2015), [Eur. Phys. J. C **75**, no. 10, 463 (2015)]
(Mar 11, 2015) [HEP entry link]

40. **"Evidence of W Production in pp Collisions at s=8TeV and Limits on Anomalous Quartic Gauge Couplings with the ATLAS Detector"**
G. Aad *et al.* [ATLAS Collaboration].
arXiv:1503.03243 [hep-ex]
10.1103/PhysRevLett.115.031802
Phys. Rev. Lett. **115**, no. 3, 031802 (2015)
(Mar 11, 2015) [HEP entry link]

41. **"Constraints on the off-shell Higgs boson signal strength in the high-mass ZZ and WW final states with the ATLAS detector"**
G. Aad *et al.* [ATLAS Collaboration].
arXiv:1503.01060 [hep-ex]
10.1140/epjc/s10052-015-3542-2
Eur. Phys. J. C **75**, no. 7, 335 (2015)
(Mar 3, 2015) [HEP entry link]

42. **"Two-particle BoseEinstein correlations in pp collisions at $\sqrt{s} = 0.9$ and 7 TeV measured with the ATLAS detector"**
G. Aad *et al.* [ATLAS Collaboration].
arXiv:1502.07947 [hep-ex]
10.1140/epjc/s10052-015-3644-x
Eur. Phys. J. C **75**, no. 10, 466 (2015)
(Feb 27, 2015) [HEP entry link]

43. **"A search for high-mass resonances decaying to $\tau^+\tau^-$ in pp collisions at $\sqrt{s} = 8$ TeV with the ATLAS detector"**
G. Aad *et al.* [ATLAS Collaboration].
arXiv:1502.07177 [hep-ex]
10.1007/JHEP07(2015)157
JHEP **1507**, 157 (2015)
(Feb 25, 2015) [HEP entry link]

44. **"Differential top-antitop cross-section measurements as a function of observables constructed from final-state particles using pp collisions at $\sqrt{s} = 7$ TeV in the ATLAS detector"**
G. Aad *et al.* [ATLAS Collaboration].
arXiv:1502.05923 [hep-ex]
10.1007/JHEP06(2015)100
JHEP **1506**, 100 (2015)
(Feb 20, 2015) [HEP entry link]

45. **"Search for massive supersymmetric particles decaying to many jets using the ATLAS detector in pp collisions at $\sqrt{s} = 8$ TeV"**
G. Aad *et al.* [ATLAS Collaboration].
arXiv:1502.05686 [hep-ex]

10.1103/PhysRevD.91.112016
Phys. Rev. D **91**, no. 11, 112016 (2015)
(Feb 19, 2015) [HEP entry link]

46. **"Search for a CP-odd Higgs boson decaying to Zh in pp collisions at $\sqrt{s} = 8$TeV with the ATLAS detector"**
G. Aad *et al.* [ATLAS Collaboration].
arXiv:1502.04478 [hep-ex]
10.1016/j.physletb.2015.03.054
Phys. Lett. B **744**, 163 (2015)
(Feb 16, 2015) [HEP entry link]

47. **"Search for new phenomena in final states with an energetic jet and large missing transverse momentum in pp collisions at $\sqrt{s}$ =8 TeV with the ATLAS detector"**
G. Aad *et al.* [ATLAS Collaboration].
arXiv:1502.01518 [hep-ex]
10.1140/epjc/s10052-015-3517-3, 10.1140/epjc/s10052-015-3639-7
Eur. Phys. J. C **75**, no. 7, 299 (2015), [Eur. Phys. J. C **75**, no. 9, 408 (2015)]
(Feb 5, 2015) [HEP entry link]

48. **"Observation of top-quark pair production in association with a photon and measurement of the $t\bar{t}\gamma$ production cross section in pp collisions at $\sqrt{s} = 7$ TeV using the ATLAS detector"**
G. Aad *et al.* [ATLAS Collaboration].
arXiv:1502.00586 [hep-ex]
10.1103/PhysRevD.91.072007
Phys. Rev. D **91**, no. 7, 072007 (2015)
(Feb 2, 2015) [HEP entry link]

49. **"Measurement of the charge asymmetry in dileptonic decays of top quark pairs in pp collisions at $\sqrt{s} = 7$ TeV using the ATLAS detector"**
G. Aad *et al.* [ATLAS Collaboration].
arXiv:1501.07383 [hep-ex]
10.1007/JHEP05(2015)061
JHEP **05**, 061 (2015)
(Jan 29, 2015) [HEP entry link]

50. **"Search for direct pair production of a chargino and a neutralino decaying to the 125GeV Higgs boson in $\sqrt{s} = 8$ TeV pp collisions with the ATLAS detector"**
G. Aad *et al.* [ATLAS Collaboration].
arXiv:1501.07110 [hep-ex]
10.1140/epjc/s10052-015-3408-7
Eur. Phys. J. C **75**, no. 5, 208 (2015)
(Jan 28, 2015) [HEP entry link]

51. **"Evidence for the Higgs-boson Yukawa coupling to tau leptons with the ATLAS detector"**
G. Aad *et al.* [ATLAS Collaboration].
arXiv:1501.04943 [hep-ex]
10.1007/JHEP04(2015)117
JHEP **1504**, 117 (2015)
(Jan 20, 2015) [HEP entry link]

52. **"Search for pair-produced long-lived neutral particles decaying in the ATLAS hadronic calorimeter in pp collisions at $\sqrt{s} = 8$ TeV"**
G. Aad *et al.* [ATLAS Collaboration].
arXiv:1501.04020 [hep-ex]
10.1016/j.physletb.2015.02.015
Phys. Lett. B **743**, 15 (2015)
(Jan 16, 2015) [HEP entry link]

53. **"Search for squarks and gluinos in events with isolated leptons, jets and missing transverse momentum at $\sqrt{s} = 8$ TeV with the ATLAS detector"**
G. Aad *et al.* [ATLAS Collaboration].
arXiv:1501.03555 [hep-ex]
10.1007/JHEP04(2015)116
JHEP **1504**, 116 (2015)
(Jan 14, 2015) [HEP entry link]

54. **"Search for Higgs and Z Boson Decays to J/ and (nS) with the ATLAS Detector"**
G. Aad *et al.* [ATLAS Collaboration].
arXiv:1501.03276 [hep-ex]
10.1103/PhysRevLett.114.121801
Phys. Rev. Lett. **114**, no. 12, 121801 (2015)
(Jan 14, 2015) [HEP entry link]

55. **"Search for Scalar Charm Quark Pair Production in pp Collisions at $\sqrt{s} = 8$TeV with the ATLAS Detector"**
G. Aad *et al.* [ATLAS Collaboration].
arXiv:1501.01325 [hep-ex]
10.1103/PhysRevLett.114.161801
Phys. Rev. Lett. **114**, no. 16, 161801 (2015)
(Jan 6, 2015) [HEP entry link]

56. **"Identification and energy calibration of hadronically decaying tau leptons with the ATLAS experiment in pp collisions at $\sqrt{s}$=8 TeV"**
G. Aad *et al.* [ATLAS Collaboration].
arXiv:1412.7086 [hep-ex]
10.1140/epjc/s10052-015-3500-z
Eur. Phys. J. C **75**, no. 7, 303 (2015)
(Dec 22, 2014) [HEP entry link]

57. **"Search for charged Higgs bosons decaying via $H^{\pm} \to \tau^{\pm}\nu$ in fully hadronic final states using pp collision data at $\sqrt{s} = 8$ TeV with the ATLAS detector"**
G. Aad *et al.* [ATLAS Collaboration].
arXiv:1412.6663 [hep-ex]
10.1007/JHEP03(2015)088
JHEP **1503**, 088 (2015)
(Dec 20, 2014) [HEP entry link]

58. **"Observation and measurements of the production of prompt and non-prompt J/ψ mesons in association with a Z boson in pp collisions at $\sqrt{s} = 8$ TeV with the ATLAS detector"**
G. Aad *et al.* [ATLAS Collaboration].
arXiv:1412.6428 [hep-ex]
10.1140/epjc/s10052-015-3406-9
Eur. Phys. J. C **75**, no. 5, 229 (2015)
(Dec 19, 2014) [HEP entry link]

59. **"Measurement of Spin Correlation in Top-Antitop Quark Events and Search for Top Squark Pair Production in pp Collisions at $\sqrt{s} = 8$ TeV Using the ATLAS Detector"**
G. Aad *et al.* [ATLAS Collaboration].
arXiv:1412.4742 [hep-ex]
10.1103/PhysRevLett.114.142001
Phys. Rev. Lett. **114**, no. 14, 142001 (2015)
(Dec 15, 2014) [HEP entry link]

60. **"Centrality and rapidity dependence of inclusive jet production in $\sqrt{s_{\mathrm{NN}}} = 5.02$ TeV proton-lead collisions with the ATLAS detector"**
G. Aad *et al.* [ATLAS Collaboration].
arXiv:1412.4092 [hep-ex]
10.1016/j.physletb.2015.07.023
Phys. Lett. B **748**, 392 (2015)
(Dec 12, 2014) [HEP entry link]

61. **"Observation and measurement of Higgs boson decays to WW* with the ATLAS detector"**
G. Aad *et al.* [ATLAS Collaboration].
arXiv:1412.2641 [hep-ex]
10.1103/PhysRevD.92.012006
Phys. Rev. D **92**, no. 1, 012006 (2015)
(Dec 8, 2014) [HEP entry link]

62. **"Measurement of the transverse polarization of Λ and $\bar{\Lambda}$ hyperons produced in proton-proton collisions at $\sqrt{s} = 7$ TeV using the ATLAS detector"**
G. Aad *et al.* [ATLAS Collaboration].

arXiv:1412.1692 [hep-ex]
10.1103/PhysRevD.91.032004
Phys. Rev. D **91**, no. 3, 032004 (2015)
(Dec 4, 2014) [HEP entry link]

63. **"Search for anomalous production of prompt same-sign lepton pairs and pair-produced doubly charged Higgs bosons with $\sqrt{s} = 8$ TeV pp collisions using the ATLAS detector"**
G. Aad *et al.* [ATLAS Collaboration].
arXiv:1412.0237 [hep-ex]
10.1007/JHEP03(2015)041
JHEP **1503**, 041 (2015)
(Nov 30, 2014) [HEP entry link]

64. **"Searches for heavy long-lived charged particles with the ATLAS detector in proton-proton collisions at $\sqrt{s} = 8$ TeV"**
G. Aad *et al.* [ATLAS Collaboration].
arXiv:1411.6795 [hep-ex]
10.1007/JHEP01(2015)068
JHEP **1501**, 068 (2015)
(Nov 25, 2014) [HEP entry link]

65. **"Search for new phenomena in events with three or more charged leptons in pp collisions at $\sqrt{s} = 8$ TeV with the ATLAS detector"**
G. Aad *et al.* [ATLAS Collaboration].
arXiv:1411.2921 [hep-ex]
10.1007/JHEP08(2015)138
JHEP **1508**, 138 (2015)
(Nov 11, 2014) [HEP entry link]

66. **"Measurements of the Nuclear Modification Factor for Jets in Pb+Pb Collisions at $\sqrt{s_{\mathrm{NN}}} = 2.76$ TeV with the ATLAS Detector"**
G. Aad *et al.* [ATLAS Collaboration].
arXiv:1411.2357 [hep-ex]
10.1103/PhysRevLett.114.072302
Phys. Rev. Lett. **114**, no. 7, 072302 (2015)
(Nov 10, 2014) [HEP entry link]

67. **"Measurement of three-jet production cross-sections in pp collisions at 7 TeV centre-of-mass energy using the ATLAS detector"**
G. Aad *et al.* [ATLAS Collaboration].
arXiv:1411.1855 [hep-ex]
10.1140/epjc/s10052-015-3363-3
Eur. Phys. J. C **75**, no. 5, 228 (2015)
(Nov 7, 2014) [HEP entry link]

68. **"Search for new phenomena in events with a photon and missing transverse momentum in pp collisions at $\sqrt{s} = 8$ TeV with the ATLAS**

detector"
G. Aad *et al.* [ATLAS Collaboration].
arXiv:1411.1559 [hep-ex]
10.1103/PhysRevD.92.059903, 10.1103/PhysRevD.91.012008
Phys. Rev. D **91**, no. 1, 012008 (2015), [Phys. Rev. D **92**, no. 5, 059903 (2015)]
(Nov 6, 2014) [HEP entry link]

69. **"Measurement of the inclusive jet cross-section in proton-proton collisions at $\sqrt{s} = 7$ TeV using 4.5 fb^1 of data with the ATLAS detector"**
G. Aad *et al.* [ATLAS Collaboration].
arXiv:1410.8857 [hep-ex]
10.1007/JHEP02(2015)153, 10.1007/JHEP09(2015)141
JHEP **1502**, 153 (2015), [JHEP **1509**, 141 (2015)]
(Oct 31, 2014) [HEP entry link]

70. **"Measurement of the $WW + WZ$ cross section and limits on anomalous triple gauge couplings using final states with one lepton, missing transverse momentum, and two jets with the ATLAS detector at $\sqrt{\mathrm{s}} = 7$ TeV"**
G. Aad *et al.* [ATLAS Collaboration].
arXiv:1410.7238 [hep-ex]
10.1007/JHEP01(2015)049
JHEP **1501**, 049 (2015)
(Oct 27, 2014) [HEP entry link]

71. **"Search for invisible particles produced in association with single-top-quarks in proton-proton collisions at $\sqrt{s} = 8$ TeV with the ATLAS detector"**
G. Aad *et al.* [ATLAS Collaboration].
arXiv:1410.5404 [hep-ex]
10.1140/epjc/s10052-014-3233-4
Eur. Phys. J. C **75**, no. 2, 79 (2015)
(Oct 20, 2014) [HEP entry link]

72. **"Search for the X_b and other hidden-beauty states in the $\pi^+\pi^-\Upsilon(1\mathrm{S})$ channel at ATLAS"**
G. Aad *et al.* [ATLAS Collaboration].
arXiv:1410.4409 [hep-ex]
10.1016/j.physletb.2014.11.055
Phys. Lett. B **740**, 199 (2015)
(Oct 16, 2014) [HEP entry link]

73. **"Search for $W' \to t\bar{b}$ in the lepton plus jets final state in proton-proton collisions at a centre-of-mass energy of $\sqrt{s} = 8$ TeV with the ATLAS detector"**
G. Aad *et al.* [ATLAS Collaboration].
arXiv:1410.4103 [hep-ex]

10.1016/j.physletb.2015.02.051
Phys. Lett. B **743**, 235 (2015)
(Oct 15, 2014) [HEP entry link]

74. **"Search for dark matter in events with heavy quarks and missing transverse momentum in *pp* collisions with the ATLAS detector"**
G. Aad *et al.* [ATLAS Collaboration].
arXiv:1410.4031 [hep-ex]
10.1140/epjc/s10052-015-3306-z
Eur. Phys. J. C **75**, no. 2, 92 (2015)
(Oct 15, 2014) [HEP entry link]

75. **"Search for *s*-channel single top-quark production in protonproton collisions at $\sqrt{s} = 8$TeV with the ATLAS detector"**
G. Aad *et al.* [ATLAS Collaboration].
arXiv:1410.0647 [hep-ex]
10.1016/j.physletb.2014.11.042
Phys. Lett. B **740**, 118 (2015)
(Oct 2, 2014) [HEP entry link]

76. **"Measurements of the W production cross sections in association with jets with the ATLAS detector"**
G. Aad *et al.* [ATLAS Collaboration].
arXiv:1409.8639 [hep-ex]
10.1140/epjc/s10052-015-3262-7
Eur. Phys. J. C **75**, no. 2, 82 (2015)
(Sep 30, 2014) [HEP entry link]

77. **"Search for the $b\bar{b}$ decay of the Standard Model Higgs boson in associated $(W/Z)H$ production with the ATLAS detector"**
G. Aad *et al.* [ATLAS Collaboration].
arXiv:1409.6212 [hep-ex]
10.1007/JHEP01(2015)069
JHEP **1501**, 069 (2015)
(Sep 22, 2014) [HEP entry link]

78. **"Search for resonant diboson production in the $\ell\ell q\bar{q}$ final state in *pp* collisions at $\sqrt{s} = 8$ TeV with the ATLAS detector"**
G. Aad *et al.* [ATLAS Collaboration].
arXiv:1409.6190 [hep-ex]
10.1140/epjc/s10052-015-3261-8
Eur. Phys. J. C **75**, no. 2, 69 (2015)
(Sep 22, 2014) [HEP entry link]

79. **"Search for neutral Higgs bosons of the minimal supersymmetric standard model in pp collisions at $\sqrt{s} = 8$ TeV with the ATLAS detector"**
G. Aad *et al.* [ATLAS Collaboration].

arXiv:1409.6064 [hep-ex]
10.1007/JHEP11(2014)056
JHEP **1411**, 056 (2014)
(Sep 21, 2014) [HEP entry link]

80. **"Search for nonpointing and delayed photons in the diphoton and missing transverse momentum final state in 8TeV *pp* collisions at the LHC using the ATLAS detector"**
G. Aad *et al.* [ATLAS Collaboration].
arXiv:1409.5542 [hep-ex]
10.1103/PhysRevD.90.112005
Phys. Rev. D **90**, no. 11, 112005 (2014)
(Sep 19, 2014) [HEP entry link]

81. **"Search for pair and single production of new heavy quarks that decay to a Z boson and a third-generation quark in *pp* collisions at $\sqrt{s} = 8$ TeV with the ATLAS detector"**
G. Aad *et al.* [ATLAS Collaboration].
arXiv:1409.5500 [hep-ex]
10.1007/JHEP11(2014)104
JHEP **1411**, 104 (2014)
(Sep 18, 2014) [HEP entry link]

82. **"Measurement of distributions sensitive to the underlying event in inclusive Z-boson production in *pp* collisions at $\sqrt{s} = 7$ TeV with the ATLAS detector"**
G. Aad *et al.* [ATLAS Collaboration].
arXiv:1409.3433 [hep-ex]
10.1140/epjc/s10052-014-3195-6
Eur. Phys. J. C **74**, no. 12, 3195 (2014)
(Sep 11, 2014) [HEP entry link]

83. **"Search for $H \to \gamma\gamma$ produced in association with top quarks and constraints on the Yukawa coupling between the top quark and the Higgs boson using data taken at 7 TeV and 8 TeV with the ATLAS detector"**
G. Aad *et al.* [ATLAS Collaboration].
arXiv:1409.3122 [hep-ex]
10.1016/j.physletb.2014.11.049
Phys. Lett. B **740**, 222 (2015)
(Sep 10, 2014) [HEP entry link]

84. **"Measurement of long-range pseudorapidity correlations and azimuthal harmonics in $\sqrt{s_{NN}} = 5.02$ TeV proton-lead collisions with the ATLAS detector"**
G. Aad *et al.* [ATLAS Collaboration].
arXiv:1409.1792 [hep-ex]

10.1103/PhysRevC.90.044906
Phys. Rev. C **90**, no. 4, 044906 (2014)
(Sep 5, 2014) [HEP entry link]

85. **"Measurement of the top-quark mass in the fully hadronic decay channel from ATLAS data at $\sqrt{s} = 7\,\mathrm{TeV}$"**
G. Aad *et al.* [ATLAS Collaboration].
arXiv:1409.0832 [hep-ex]
10.1140/epjc/s10052-015-3373-1
Eur. Phys. J. C **75**, no. 4, 158 (2015)
(Sep 2, 2014) [HEP entry link]

86. **"Search for long-lived neutral particles decaying into lepton jets in proton-proton collisions at $\sqrt{s} = 8$ TeV with the ATLAS detector"**
G. Aad *et al.* [ATLAS Collaboration].
arXiv:1409.0746 [hep-ex]
10.1007/JHEP11(2014)088
JHEP **1411**, 088 (2014)
(Sep 2, 2014) [HEP entry link]

87. **"Measurement of Higgs boson production in the diphoton decay channel in pp collisions at center-of-mass energies of 7 and 8TeV with the ATLAS detector"**
G. Aad *et al.* [ATLAS Collaboration].
arXiv:1408.7084 [hep-ex]
10.1103/PhysRevD.90.112015
Phys. Rev. D **90**, no. 11, 112015 (2014)
(Aug 29, 2014) [HEP entry link]

88. **"A measurement of the ratio of the production cross sections for W and Z bosons in association with jets with the ATLAS detector"**
G. Aad *et al.* [ATLAS Collaboration].
arXiv:1408.6510 [hep-ex]
10.1140/epjc/s10052-014-3168-9
Eur. Phys. J. C **74**, no. 12, 3168 (2014)
(Aug 27, 2014) [HEP entry link]

89. **"Measurement of the total cross section from elastic scattering in pp collisions at $\sqrt{s} = 7$TeV with the ATLAS detector"**
G. Aad *et al.* [ATLAS Collaboration].
arXiv:1408.5778 [hep-ex]
10.1016/j.nuclphysb.2014.10.019
Nucl. Phys. B **889**, 486 (2014)
(Aug 25, 2014) [HEP entry link]

90. **"Search for the lepton flavor violating decay Ze in pp collisions at $\sqrt{s}$TeV with the ATLAS detector"**
G. Aad *et al.* [ATLAS Collaboration].

arXiv:1408.5774 [hep-ex]
10.1103/PhysRevD.90.072010
Phys. Rev. D **90**, no. 7, 072010 (2014)
(Aug 25, 2014) [HEP entry link]

91. **"Measurements of Higgs boson production and couplings in the four-lepton channel in pp collisions at center-of-mass energies of 7 and 8TeV with the ATLAS detector"**
G. Aad *et al.* [ATLAS Collaboration].
arXiv:1408.5191 [hep-ex]
10.1103/PhysRevD.91.012006
Phys. Rev. D **91**, no. 1, 012006 (2015)
(Aug 21, 2014) [HEP entry link]

92. **"Measurement of the production and lepton charge asymmetry of W bosons in Pb+Pb collisions at $\sqrt{s_{\rm NN}} = 2.76$ TeV with the ATLAS detector"**
G. Aad *et al.* [ATLAS Collaboration].
arXiv:1408.4674 [hep-ex]
10.1140/epjc/s10052-014-3231-6
Eur. Phys. J. C **75**, no. 1, 23 (2015)
(Aug 20, 2014) [HEP entry link]

93. **"Measurement of flow harmonics with multi-particle cumulants in Pb+Pb collisions at $\sqrt{s_{\rm NN}} = 2.76$ TeV with the ATLAS detector"**
G. Aad *et al.* [ATLAS Collaboration].
arXiv:1408.4342 [hep-ex]
10.1140/epjc/s10052-014-3157-z
Eur. Phys. J. C **74**, no. 11, 3157 (2014)
(Aug 19, 2014) [HEP entry link]

94. **"Fiducial and differential cross sections of Higgs boson production measured in the four-lepton decay channel in pp collisions at $\sqrt{s}$=8 TeV with the ATLAS detector"**
G. Aad *et al.* [ATLAS Collaboration].
arXiv:1408.3226 [hep-ex]
10.1016/j.physletb.2014.09.054
Phys. Lett. B **738**, 234 (2014)
(Aug 14, 2014) [HEP entry link]

95. **"Performance of the ATLAS muon trigger in pp collisions at $\sqrt{s} = 8$ TeV"**
G. Aad *et al.* [ATLAS Collaboration].
arXiv:1408.3179 [hep-ex]
10.1140/epjc/s10052-015-3325-9
Eur. Phys. J. C **75**, no. 3, 120 (2015)
(Aug 13, 2014) [HEP entry link]

96. **"Search for $W' \to tb \to qqbb$ decays in pp collisions at $\sqrt{s}$ =8TeV with the ATLAS detector"**
G. Aad *et al.* [ATLAS Collaboration].
arXiv:1408.0886 [hep-ex]
10.1140/epjc/s10052-015-3372-2
Eur. Phys. J. C **75**, no. 4, 165 (2015)
(Aug 5, 2014) [HEP entry link]

97. **"Search for new resonances in $W\gamma$ and $Z\gamma$ final states in pp collisions at $\sqrt{s} = 8$ TeV with the ATLAS detector"**
G. Aad *et al.* [ATLAS Collaboration].
arXiv:1407.8150 [hep-ex]
10.1016/j.physletb.2014.10.002
Phys. Lett. B **738**, 428 (2014)
(Jul 30, 2014) [HEP entry link]

98. **"Search for new particles in events with one lepton and missing transverse momentum in pp collisions at $\sqrt{s} = 8$ TeV with the ATLAS detector"**
G. Aad *et al.* [ATLAS Collaboration].
arXiv:1407.7494 [hep-ex]
10.1007/JHEP09(2014)037
JHEP **1409**, 037 (2014)
(Jul 28, 2014) [HEP entry link]

99. **"Search for Scalar Diphoton Resonances in the Mass Range** $65 - 600$ **GeV with the ATLAS Detector in pp Collision Data at $\sqrt{s} = 8$ TeV"**
G. Aad *et al.* [ATLAS Collaboration].
arXiv:1407.6583 [hep-ex]
10.1103/PhysRevLett.113.171801
Phys. Rev. Lett. **113**, no. 17, 171801 (2014)
(Jul 24, 2014) [HEP entry link]

100. **"Measurements of jet vetoes and azimuthal decorrelations in dijet events produced in pp collisions at $\sqrt{s} = 7\,\mathrm{TeV}$ using the ATLAS detector"**
G. Aad *et al.* [ATLAS Collaboration].
arXiv:1407.5756 [hep-ex]
10.1140/epjc/s10052-014-3117-7
Eur. Phys. J. C **74**, no. 11, 3117 (2014)
(Jul 22, 2014) [HEP entry link]

101. **"Measurement of the production cross-section of $\psi(2S) \to J/\psi(\to \mu^+\mu^-)\pi^+\pi^-$ in pp collisions at $\sqrt{s} = 7$ TeV at ATLAS"**
G. Aad *et al.* [ATLAS Collaboration].
arXiv:1407.5532 [hep-ex]
10.1007/JHEP09(2014)079

JHEP **1409**, 079 (2014)
(Jul 21, 2014) [HEP entry link]

102. **"Electron and photon energy calibration with the ATLAS detector using LHC Run 1 data"**
G. Aad *et al.* [ATLAS Collaboration].
arXiv:1407.5063 [hep-ex]
10.1140/epjc/s10052-014-3071-4
Eur. Phys. J. C **74**, no. 10, 3071 (2014)
(Jul 18, 2014) [HEP entry link]

103. **"Measurements of spin correlation in top-antitop quark events from proton-proton collisions at $\sqrt{s} = 7$ TeV using the ATLAS detector"**
G. Aad *et al.* [ATLAS Collaboration].
arXiv:1407.4314 [hep-ex]
10.1103/PhysRevD.90.112016
Phys. Rev. D **90**, no. 11, 112016 (2014)
(Jul 16, 2014) [HEP entry link]

104. **"Measurements of fiducial and differential cross sections for Higgs boson production in the diphoton decay channel at $\sqrt{s} = 8$ TeV with ATLAS"**
G. Aad *et al.* [ATLAS Collaboration].
arXiv:1407.4222 [hep-ex]
10.1007/JHEP09(2014)112
JHEP **1409**, 112 (2014)
(Jul 16, 2014) [HEP entry link]

105. **"Measurement of the muon reconstruction performance of the ATLAS detector using 2011 and 2012 LHC protonproton collision data"**
G. Aad *et al.* [ATLAS Collaboration].
arXiv:1407.3935 [hep-ex]
10.1140/epjc/s10052-014-3130-x
Eur. Phys. J. C **74**, no. 11, 3130 (2014)
(Jul 15, 2014) [HEP entry link]

106. **"Measurement of differential production cross-sections for a Z boson in association with b-jets in 7 TeV proton-proton collisions with the ATLAS detector"**
G. Aad *et al.* [ATLAS Collaboration].
arXiv:1407.3643 [hep-ex]
10.1007/JHEP10(2014)141
JHEP **1410**, 141 (2014)
(Jul 14, 2014) [HEP entry link]

107. **"Search for contact interactions and large extra dimensions in the dilepton channel using proton-proton collisions at $\sqrt{s} = 8$ TeV with the ATLAS detector"**

G. Aad *et al.* [ATLAS Collaboration].
arXiv:1407.2410 [hep-ex]
10.1140/epjc/s10052-014-3134-6
Eur. Phys. J. C **74**, no. 12, 3134 (2014)
(Jul 9, 2014) [HEP entry link]

108. **"Flavor tagged time-dependent angular analysis of the $B_s \to J/\psi\phi$ decay and extraction of $\Delta\Gamma$s and the weak phase ϕ_s in ATLAS"**
G. Aad *et al.* [ATLAS Collaboration].
arXiv:1407.1796 [hep-ex]
10.1103/PhysRevD.90.052007
Phys. Rev. D **90**, no. 5, 052007 (2014)
(Jul 7, 2014) [HEP entry link]

109. **"Search for new phenomena in the dijet mass distribution using $p-p$ collision data at $\sqrt{s} = 8$ TeV with the ATLAS detector"**
G. Aad *et al.* [ATLAS Collaboration].
arXiv:1407.1376 [hep-ex]
10.1103/PhysRevD.91.052007
Phys. Rev. D **91**, no. 5, 052007 (2015)
(Jul 5, 2014) [HEP entry link]

110. **"Observation of an Excited $B_c^{\pm}$ Meson State with the ATLAS Detector"**
G. Aad *et al.* [ATLAS Collaboration].
arXiv:1407.1032 [hep-ex]
10.1103/PhysRevLett.113.212004
Phys. Rev. Lett. **113**, no. 21, 212004 (2014)
(Jul 3, 2014) [HEP entry link]

111. **"Measurement of the $t\bar{t}$ production cross-section as a function of jet multiplicity and jet transverse momentum in 7 TeV proton-proton collisions with the ATLAS detector"**
G. Aad *et al.* [ATLAS Collaboration].
arXiv:1407.0891 [hep-ex]
10.1007/JHEP01(2015)020
JHEP **1501**, 020 (2015)
(Jul 3, 2014) [HEP entry link]

112. **"Measurement of the cross-section of high transverse momentum vector bosons reconstructed as single jets and studies of jet substructure in pp collisions at $\sqrt{s} = 7$ TeV with the ATLAS detector"**
G. Aad *et al.* [ATLAS Collaboration].
arXiv:1407.0800 [hep-ex]
10.1088/1367-2630/16/11/113013
New J. Phys. **16**, no. 11, 113013 (2014)
(Jul 3, 2014) [HEP entry link]

113. **"Search for pair-produced third-generation squarks decaying via charm quarks or in compressed supersymmetric scenarios in pp collisions at $\sqrt{s} = 8$ TeV with the ATLAS detector"**
G. Aad *et al.* [ATLAS Collaboration].
arXiv:1407.0608 [hep-ex]
10.1103/PhysRevD.90.052008
Phys. Rev. D **90**, no. 5, 052008 (2014)
(Jul 2, 2014) [HEP entry link]

114. **"Search for supersymmetry in events with large missing transverse momentum, jets, and at least one tau lepton in 20 fb^{-1} of $\sqrt{s} = 8$ TeV proton-proton collision data with the ATLAS detector"**
G. Aad *et al.* [ATLAS Collaboration].
arXiv:1407.0603 [hep-ex]
10.1007/JHEP09(2014)103
JHEP **1409**, 103 (2014)
(Jul 2, 2014) [HEP entry link]

115. **"Search for strong production of supersymmetric particles in final states with missing transverse momentum and at least three b-jets at $\sqrt{s}$= 8 TeV proton-proton collisions with the ATLAS detector"**
G. Aad *et al.* [ATLAS Collaboration].
arXiv:1407.0600 [hep-ex]
10.1007/JHEP10(2014)024
JHEP **1410**, 24 (2014)
(Jul 2, 2014) [HEP entry link]

116. **"Search for top squark pair production in final states with one isolated lepton, jets, and missing transverse momentum in $\sqrt{s}$ =8 TeV pp collisions with the ATLAS detector"**
G. Aad *et al.* [ATLAS Collaboration].
arXiv:1407.0583 [hep-ex]
10.1007/JHEP11(2014)118
JHEP **1411**, 118 (2014)
(Jul 2, 2014) [HEP entry link]

117. **"Simultaneous measurements of the $t\bar{t}$, W^+W^-, and $Z/\gamma^* \to \tau\tau$ production cross-sections in pp collisions at $\sqrt{s} = 7$ TeV with the ATLAS detector"**
G. Aad *et al.* [ATLAS Collaboration].
arXiv:1407.0573 [hep-ex]
10.1103/PhysRevD.91.052005
Phys. Rev. D **91**, no. 5, 052005 (2015)
(Jul 2, 2014) [HEP entry link]

118. **"Measurements of normalized differential cross sections for $t\bar{t}$ production in pp collisions at $\sqrt{s} = 7$TeV using the ATLAS detector"**

G. Aad *et al.* [ATLAS Collaboration].
arXiv:1407.0371 [hep-ex]
10.1103/PhysRevD.90.072004
Phys. Rev. D **90**, no. 7, 072004 (2014)
(Jul 1, 2014) [HEP entry link]

119. **"Search for the direct production of charginos, neutralinos and staus in final states with at least two hadronically decaying taus and missing transverse momentum in pp collisions at $\sqrt{s} = 8$ TeV with the ATLAS detector"**
G. Aad *et al.* [ATLAS Collaboration].
arXiv:1407.0350 [hep-ex]
10.1007/JHEP10(2014)096
JHEP **1410**, 96 (2014)
(Jul 1, 2014) [HEP entry link]

120. **"Comprehensive measurements of t-channel single top-quark production cross sections at $\sqrt{s} = 7$ TeV with the ATLAS detector"**
G. Aad *et al.* [ATLAS Collaboration].
arXiv:1406.7844 [hep-ex]
10.1103/PhysRevD.90.112006
Phys. Rev. D **90**, no. 11, 112006 (2014)
(Jun 30, 2014) [HEP entry link]

121. **"A neural network clustering algorithm for the ATLAS silicon pixel detector"**
G. Aad *et al.* [ATLAS Collaboration].
arXiv:1406.7690 [hep-ex]
10.1088/1748-0221/9/09/P09009
JINST **9**, P09009 (2014)
(Jun 30, 2014) [HEP entry link]

122. **"Search for the Standard Model Higgs boson decay to $\mu^+\mu^-$ with the ATLAS detector"**
G. Aad *et al.* [ATLAS Collaboration].
arXiv:1406.7663 [hep-ex]
10.1016/j.physletb.2014.09.008
Phys. Lett. B **738**, 68 (2014)
(Jun 30, 2014) [HEP entry link]

123. **"Measurement of the $t\bar{t}$ production cross-section using $e\mu$ events with b -tagged jets in pp collisions at $\sqrt{s} = 7$ and 8 TeV with the ATLAS detector"**
G. Aad *et al.* [ATLAS Collaboration].
arXiv:1406.5375 [hep-ex]
10.1140/epjc/s10052-014-3109-7
Eur. Phys. J. C **74**, no. 10, 3109 (2014)
(Jun 20, 2014) [HEP entry link]

124. **"Search For Higgs Boson Pair Production in the $\gamma\gamma b\bar{b}$ Final State using pp Collision Data at $\sqrt{s} = 8$ TeV from the ATLAS Detector"**
G. Aad *et al.* [ATLAS Collaboration].
arXiv:1406.5053 [hep-ex]
10.1103/PhysRevLett.114.081802
Phys. Rev. Lett. **114**, no. 8, 081802 (2015)
(Jun 19, 2014) [HEP entry link]

125. **"Search for WZ resonances in the fully leptonic channel using pp collisions at $\sqrt{s} = 8$ TeV with the ATLAS detector"**
G. Aad *et al.* [ATLAS Collaboration].
arXiv:1406.4456 [hep-ex]
10.1016/j.physletb.2014.08.039
Phys. Lett. B **737**, 223 (2014)
(Jun 17, 2014) [HEP entry link]

126. **"Measurement of the Higgs boson mass from the $H \to \gamma\gamma$ and $H \to ZZ^* \to 4\ell$ channels with the ATLAS detector using 25 fb^{-1} of pp collision data"**
G. Aad *et al.* [ATLAS Collaboration].
arXiv:1406.3827 [hep-ex]
10.1103/PhysRevD.90.052004
Phys. Rev. D **90**, no. 5, 052004 (2014)
(Jun 15, 2014) [HEP entry link]

127. **"Measurement of the Z/γ^* boson transverse momentum distribution in pp collisions at $\sqrt{s} = 7$ TeV with the ATLAS detector"**
G. Aad *et al.* [ATLAS Collaboration].
arXiv:1406.3660 [hep-ex]
10.1007/JHEP09(2014)145
JHEP **1409**, 145 (2014)
(Jun 13, 2014) [HEP entry link]

128. **"Measurement of inclusive jet charged-particle fragmentation functions in Pb+Pb collisions at $\sqrt{s_{NN}} = 2.76$ TeV with the ATLAS detector"**
G. Aad *et al.* [ATLAS Collaboration].
arXiv:1406.2979 [hep-ex]
10.1016/j.physletb.2014.10.065
Phys. Lett. B **739**, 320 (2014)
(Jun 11, 2014) [HEP entry link]

129. **"Search for direct pair production of the top squark in all-hadronic final states in proton-proton collisions at $\sqrt{s} = 8$ TeV with the ATLAS detector"**
G. Aad *et al.* [ATLAS Collaboration].
arXiv:1406.1122 [hep-ex]

10.1007/JHEP09(2014)015
JHEP **1409**, 015 (2014)
(Jun 4, 2014) [HEP entry link]

130. **"Measurement of the underlying event in jet events from 7 TeV proton-proton collisions with the ATLAS detector"**
G. Aad *et al.* [ATLAS Collaboration].
arXiv:1406.0392 [hep-ex]
10.1140/epjc/s10052-014-2965-5
Eur. Phys. J. C **74**, no. 8, 2965 (2014)
(Jun 2, 2014) [HEP entry link]

131. **"Jet energy measurement and its systematic uncertainty in proton-proton collisions at $\sqrt{s} = 7$ TeV with the ATLAS detector"**
G. Aad *et al.* [ATLAS Collaboration].
arXiv:1406.0076 [hep-ex]
10.1140/epjc/s10052-014-3190-y
Eur. Phys. J. C **75**, 17 (2015)
(May 31, 2014) [HEP entry link]

132. **"Search for squarks and gluinos with the ATLAS detector in final states with jets and missing transverse momentum using $\sqrt{s} = 8$ TeV proton–proton collision data"**
G. Aad *et al.* [ATLAS Collaboration].
arXiv:1405.7875 [hep-ex]
10.1007/JHEP09(2014)176
JHEP **1409**, 176 (2014)
(May 30, 2014) [HEP entry link]

133. **"Light-quark and gluon jet discrimination in pp collisions at $\sqrt{s} = 7$ TeV with the ATLAS detector"**
G. Aad *et al.* [ATLAS Collaboration].
arXiv:1405.6583 [hep-ex]
10.1140/epjc/s10052-014-3023-z
Eur. Phys. J. C **74**, no. 8, 3023 (2014)
(May 26, 2014) [HEP entry link]

134. **"Evidence for Electroweak Production of $W^{\pm}W^{\pm}jj$ in pp Collisions at $\sqrt{s} = 8$ TeV with the ATLAS Detector"**
G. Aad *et al.* [ATLAS Collaboration].
arXiv:1405.6241 [hep-ex]
10.1103/PhysRevLett.113.141803
Phys. Rev. Lett. **113**, no. 14, 141803 (2014)
(May 23, 2014) [HEP entry link]

135. **"Search for supersymmetry in events with four or more leptons in $\sqrt{s}$ = 8 TeV pp collisions with the ATLAS detector"**
G. Aad *et al.* [ATLAS Collaboration].

arXiv:1405.5086 [hep-ex]
10.1103/PhysRevD.90.052001
Phys. Rev. D **90**, no. 5, 052001 (2014)
(May 20, 2014) [HEP entry link]

136. **"Search for microscopic black holes and string balls in final states with leptons and jets with the ATLAS detector at sqrt(s) = 8 TeV"**
G. Aad *et al.* [ATLAS Collaboration].
arXiv:1405.4254 [hep-ex]
10.1007/JHEP08(2014)103
JHEP **1408**, 103 (2014)
(May 16, 2014) [HEP entry link]

137. **"Search for high-mass dilepton resonances in pp collisions at $\sqrt{s}$ = 8TeV with the ATLAS detector"**
G. Aad *et al.* [ATLAS Collaboration].
arXiv:1405.4123 [hep-ex]
10.1103/PhysRevD.90.052005
Phys. Rev. D **90**, no. 5, 052005 (2014)
(May 16, 2014) [HEP entry link]

138. **"Measurement of the centrality and pseudorapidity dependence of the integrated elliptic flow in lead-lead collisions at $\sqrt{s_{\rm NN}} = 2.76$ TeV with the ATLAS detector"**
G. Aad *et al.* [ATLAS Collaboration].
arXiv:1405.3936 [hep-ex]
10.1140/epjc/s10052-014-2982-4
Eur. Phys. J. C **74**, no. 8, 2982 (2014)
(May 15, 2014) [HEP entry link]

139. **"Monitoring and data quality assessment of the ATLAS liquid argon calorimeter"**
G. Aad *et al.* [ATLAS Collaboration].
arXiv:1405.3768 [hep-ex]
10.1088/1748-0221/9/07/P07024
JINST **9**, P07024 (2014)
(May 15, 2014) [HEP entry link]

140. **"Operation and performance of the ATLAS semiconductor tracker"**
G. Aad *et al.* [ATLAS Collaboration].
arXiv:1404.7473 [hep-ex]
10.1088/1748-0221/9/08/P08009
JINST **9**, P08009 (2014)
(Apr 29, 2014) [HEP entry link]

141. **"Measurement of the cross section of high transverse momentum $Z \to b\bar{b}$ production in proton–proton collisions at $\sqrt{s} = 8TeV$ with the ATLAS Detector"**

G. Aad *et al.* [ATLAS Collaboration].
arXiv:1404.7042 [hep-ex]
10.1016/j.physletb.2014.09.020
Phys. Lett. B **738**, 25 (2014)
(Apr 28, 2014) [HEP entry link]

142. **"Measurement of χ_{c1} and χ_{c2} production with $\sqrt{s} = 7$ TeV pp collisions at ATLAS"**
G. Aad *et al.* [ATLAS Collaboration].
arXiv:1404.7035 [hep-ex]
10.1007/JHEP07(2014)154
JHEP **1407**, 154 (2014)
(Apr 28, 2014) [HEP entry link]

143. **"Muon reconstruction efficiency and momentum resolution of the ATLAS experiment in proton-proton collisions at $\sqrt{s} = 7$ TeV in 2010"**
G. Aad *et al.* [ATLAS Collaboration].
arXiv:1404.4562 [hep-ex]
10.1140/epjc/s10052-014-3034-9
Eur. Phys. J. C **74**, no. 9, 3034 (2014)
(Apr 17, 2014) [HEP entry link]

144. **"Search for supersymmetry at $\sqrt{s}$=8 TeV in final states with jets and two same-sign leptons or three leptons with the ATLAS detector"**
G. Aad *et al.* [ATLAS Collaboration].
arXiv:1404.2500 [hep-ex]
10.1007/JHEP06(2014)035
JHEP **1406**, 035 (2014)
(Apr 9, 2014) [HEP entry link]

145. **"Electron reconstruction and identification efficiency measurements with the ATLAS detector using the 2011 LHC proton-proton collision data"**
G. Aad *et al.* [ATLAS Collaboration].
arXiv:1404.2240 [hep-ex]
10.1140/epjc/s10052-014-2941-0
Eur. Phys. J. C **74**, no. 7, 2941 (2014)
(Apr 8, 2014) [HEP entry link]

146. **"Measurement of the low-mass Drell-Yan differential cross section at $\sqrt{s} = 7$ TeV using the ATLAS detector"**
G. Aad *et al.* [ATLAS Collaboration].
arXiv:1404.1212 [hep-ex]
10.1007/JHEP06(2014)112
JHEP **1406**, 112 (2014)
(Apr 4, 2014) [HEP entry link]

147. **"Measurement of the parity-violating asymmetry parameter α_b and the helicity amplitudes for the decay $\Lambda_b^0 \to J/\psi + \Lambda^0$ with the ATLAS detector"**
G. Aad *et al.* [ATLAS Collaboration].
arXiv:1404.1071 [hep-ex]
10.1103/PhysRevD.89.092009
Phys. Rev. D **89**, no. 9, 092009 (2014)
(Apr 3, 2014) [HEP entry link]

148. **"Search for dark matter in events with a Z boson and missing transverse momentum in pp collisions at $\sqrt{s}$=8 TeV with the ATLAS detector"**
G. Aad *et al.* [ATLAS Collaboration].
arXiv:1404.0051 [hep-ex]
10.1103/PhysRevD.90.012004
Phys. Rev. D **90**, no. 1, 012004 (2014)
(Mar 31, 2014) [HEP entry link]

149. **"Search for top quark decays $t \to qH$ with $H \to \gamma\gamma$ using the ATLAS detector"**
G. Aad *et al.* [ATLAS Collaboration].
arXiv:1403.6293 [hep-ex]
10.1007/JHEP06(2014)008
JHEP **1406**, 008 (2014)
(Mar 25, 2014) [HEP entry link]

150. **"Measurements of Four-Lepton Production at the Z Resonance in pp Collisions at $\sqrt{s}$ =7 and 8TeV with ATLAS"**
G. Aad *et al.* [ATLAS Collaboration].
arXiv:1403.5657 [hep-ex]
10.1103/PhysRevLett.112.231806
Phys. Rev. Lett. **112**, no. 23, 231806 (2014)
(Mar 22, 2014) [HEP entry link]

151. **"Search for direct production of charginos, neutralinos and sleptons in final states with two leptons and missing transverse momentum in pp collisions at $\sqrt{s}$ = 8 TeV with the ATLAS detector"**
G. Aad *et al.* [ATLAS Collaboration].
arXiv:1403.5294 [hep-ex]
10.1007/JHEP05(2014)071
JHEP **1405**, 071 (2014)
(Mar 20, 2014) [HEP entry link]

152. **"Search for direct top squark pair production in events with a Z boson, b-jets and missing transverse momentum in sqrt(s)=8 TeV pp collisions with the ATLAS detector"**
G. Aad *et al.* [ATLAS Collaboration].

arXiv:1403.5222 [hep-ex]
10.1140/epjc/s10052-014-2883-6
Eur. Phys. J. C **74**, no. 6, 2883 (2014)
(Mar 20, 2014) [HEP entry link]

153. **"Search for direct top-squark pair production in final states with two leptons in pp collisions at $\sqrt{s}$ = 8TeV with the ATLAS detector"**
G. Aad *et al.* [ATLAS Collaboration].
arXiv:1403.4853 [hep-ex]
10.1007/JHEP06(2014)124
JHEP **1406**, 124 (2014)
(Mar 19, 2014) [HEP entry link]

154. **"Measurement of event-plane correlations in $\sqrt{s_{NN}}$ = 2.76 TeV lead-lead collisions with the ATLAS detector"**
G. Aad *et al.* [ATLAS Collaboration].
arXiv:1403.0489 [hep-ex]
10.1103/PhysRevC.90.024905
Phys. Rev. C **90**, no. 2, 024905 (2014)
(Mar 3, 2014) [HEP entry link]

155. **"Search for direct production of charginos and neutralinos in events with three leptons and missing transverse momentum in $\sqrt{s}$ = 8TeV *pp* collisions with the ATLAS detector"**
G. Aad *et al.* [ATLAS Collaboration].
arXiv:1402.7029 [hep-ex]
10.1007/JHEP04(2014)169
JHEP **1404**, 169 (2014)
(Feb 27, 2014) [HEP entry link]

156. **"Measurement of the production of a W boson in association with a charm quark in *pp* collisions at $\sqrt{s}$ = 7 TeV with the ATLAS detector"**
G. Aad *et al.* [ATLAS Collaboration].
arXiv:1402.6263 [hep-ex]
10.1007/JHEP05(2014)068
JHEP **1405**, 068 (2014)
(Feb 25, 2014) [HEP entry link]

157. **"The differential production cross section of the ϕ (1020) meson in $\sqrt{s}$ = 7 TeV *pp* collisions measured with the ATLAS detector"**
G. Aad *et al.* [ATLAS Collaboration].
arXiv:1402.6162 [hep-ex]
10.1140/epjc/s10052-014-2895-2
Eur. Phys. J. C **74**, no. 7, 2895 (2014)
(Feb 25, 2014) [HEP entry link]

158. **"Search for Invisible Decays of a Higgs Boson Produced in Association with a Z Boson in ATLAS"**

G. Aad *et al.* [ATLAS Collaboration].
arXiv:1402.3244 [hep-ex]
10.1103/PhysRevLett.112.201802
Phys. Rev. Lett. **112**, 201802 (2014)
(Feb 13, 2014) [HEP entry link]

159. **"Search for Higgs boson decays to a photon and a Z boson in pp collisions at $\sqrt{s}$=7 and 8 TeV with the ATLAS detector"**
G. Aad *et al.* [ATLAS Collaboration].
arXiv:1402.3051 [hep-ex]
10.1016/j.physletb.2014.03.015
Phys. Lett. B **732**, 8 (2014)
(Feb 13, 2014) [HEP entry link]

160. **"Measurement of the electroweak production of dijets in association with a Z-boson and distributions sensitive to vector boson fusion in proton-proton collisions at $\sqrt{s}$ = 8 TeV using the ATLAS detector"**
G. Aad *et al.* [ATLAS Collaboration].
arXiv:1401.7610 [hep-ex]
10.1007/JHEP04(2014)031
JHEP **1404**, 031 (2014)
(Jan 29, 2014) [HEP entry link]

161. **"Measurement of the production cross section of prompt J/ψ mesons in association with a $W^{\pm}$ boson in pp collisions at $\sqrt{s}$ = 7 TeV with the ATLAS detector"**
G. Aad *et al.* [ATLAS Collaboration].
arXiv:1401.2831 [hep-ex]
10.1007/JHEP04(2014)172
JHEP **1404**, 172 (2014)
(Jan 13, 2014) [HEP entry link]

162. **"Measurement of dijet cross sections in pp collisions at 7 TeV centre-of-mass energy using the ATLAS detector"**
G. Aad *et al.* [ATLAS Collaboration].
arXiv:1312.3524 [hep-ex]
10.1007/JHEP05(2014)059
JHEP **1405**, 059 (2014)
(Dec 12, 2013) [HEP entry link]

163. **"Search for a multi-Higgs-boson cascade in $W^+Wb\bar{b}$ events with the ATLAS detector in pp collisions at $\sqrt{s} = 8$TeV"**
G. Aad *et al.* [ATLAS Collaboration].
arXiv:1312.1956 [hep-ex]
10.1103/PhysRevD.89.032002
Phys. Rev. D **89**, no. 3, 032002 (2014)
(Dec 6, 2013) [HEP entry link]

164. **"Standalone vertex finding in the ATLAS muon spectrometer"**
G. Aad *et al.* [ATLAS Collaboration].
arXiv:1311.7070 [physics.ins-det]
10.1088/1748-0221/9/02/P02001
JINST **9**, P02001 (2014)
(Nov 27, 2013) [HEP entry link]

165. **"Measurement of the top quark pair production charge asymmetry in proton-proton collisions at $\sqrt{s} = 7$ TeV using the ATLAS detector"**
G. Aad *et al.* [ATLAS Collaboration].
arXiv:1311.6724 [hep-ex]
10.1007/JHEP02(2014)107
JHEP **1402**, 107 (2014)
(Nov 26, 2013) [HEP entry link]

166. **"Search for Quantum Black Hole Production in High-Invariant-Mass Lepton+Jet Final States Using pp Collisions at $\sqrt{s} = 8$TeV and the ATLAS Detector"**
G. Aad *et al.* [ATLAS Collaboration].
arXiv:1311.2006 [hep-ex]
10.1103/PhysRevLett.112.091804
Phys. Rev. Lett. **112**, no. 9, 091804 (2014)
(Nov 8, 2013) [HEP entry link]

167. **"Measurement of the inclusive isolated prompt photons cross section in pp collisions at $\sqrt{s} = 7$TeV with the ATLAS detector using 4.6fb^{1}"**
G. Aad *et al.* [ATLAS Collaboration].
arXiv:1311.1440 [hep-ex]
10.1103/PhysRevD.89.052004
Phys. Rev. D **89**, no. 5, 052004 (2014)
(Nov 6, 2013) [HEP entry link]

168. **"Search for long-lived stopped R-hadrons decaying out-of-time with pp collisions using the ATLAS detector"**
G. Aad *et al.* [ATLAS Collaboration].
arXiv:1310.6584 [hep-ex]
10.1103/PhysRevD.88.112003
Phys. Rev. D **88**, no. 11, 112003 (2013)
(Oct 24, 2013) [HEP entry link]

169. **"Measurement of the mass difference between top and anti-top quarks in pp collisions at $\sqrt(s) = 7$ TeV using the ATLAS detector"**
G. Aad *et al.* [ATLAS Collaboration].
arXiv:1310.6527 [hep-ex]
10.1016/j.physletb.2013.12.010
Phys. Lett. B **728**, 363 (2014)
(Oct 24, 2013) [HEP entry link]

170. **"Search for charginos nearly mass degenerate with the lightest neutralino based on a disappearing-track signature in pp collisions at $\sqrt{(s)}$=8TeV with the ATLAS detector"**
G. Aad *et al.* [ATLAS Collaboration].
arXiv:1310.3675 [hep-ex]
10.1103/PhysRevD.88.112006
Phys. Rev. D **88**, no. 11, 112006 (2013)
(Oct 14, 2013) [HEP entry link]

171. **"Search for dark matter in events with a hadronically decaying W or Z boson and missing transverse momentum in pp collisions at $\sqrt{s}$ = 8 TeV with the ATLAS detector"**
G. Aad *et al.* [ATLAS Collaboration].
arXiv:1309.4017 [hep-ex]
10.1103/PhysRevLett.112.041802
Phys. Rev. Lett. **112**, no. 4, 041802 (2014)
(Sep 16, 2013) [HEP entry link]

172. **"Search for new phenomena in photon+jet events collected in proton–proton collisions at sqrt(s) = 8 TeV with the ATLAS detector"**
G. Aad *et al.* [ATLAS Collaboration].
arXiv:1309.3230 [hep-ex]
10.1016/j.physletb.2013.12.029
Phys. Lett. B **728**, 562 (2014)
(Sep 12, 2013) [HEP entry link]

173. **"Search for microscopic black holes in a like-sign dimuon final state using large track multiplicity with the ATLAS detector"**
G. Aad *et al.* [ATLAS Collaboration].
arXiv:1308.4075 [hep-ex]
10.1103/PhysRevD.88.072001
Phys. Rev. D **88**, no. 7, 072001 (2013)
(Aug 19, 2013) [HEP entry link]

174. **"Search for direct third-generation squark pair production in final states with missing transverse momentum and two b-jets in $\sqrt{s}$ = 8 TeV pp collisions with the ATLAS detector"**
G. Aad *et al.* [ATLAS Collaboration].
arXiv:1308.2631 [hep-ex]
10.1007/JHEP10(2013)189
JHEP **1310**, 189 (2013)
(Aug 12, 2013) [HEP entry link]

175. **"Search for new phenomena in final states with large jet multiplicities and missing transverse momentum at $\sqrt{s}$=8 TeV proton-proton collisions using the ATLAS experiment"**
G. Aad *et al.* [ATLAS Collaboration].

arXiv:1308.1841 [hep-ex]
10.1007/JHEP10(2013)130, 10.1007/JHEP01(2014)109
JHEP **1310**, 130 (2013), [JHEP **1401**, 109 (2014)]
(Aug 8, 2013) [HEP entry link]

176. **"Search for excited electrons and muons in $\sqrt{s}$=8 TeV proton-proton collisions with the ATLAS detector"**
G. Aad *et al.* [ATLAS Collaboration].
arXiv:1308.1364 [hep-ex]
10.1088/1367-2630/15/9/093011
New J. Phys. **15**, 093011 (2013)
(Aug 6, 2013) [HEP entry link]

177. **"Dynamics of isolated-photon plus jet production in pp collisions at $\sqrt(s) = 7$ TeV with the ATLAS detector"**
G. Aad *et al.* [ATLAS Collaboration].
arXiv:1307.6795 [hep-ex]
10.1016/j.nuclphysb.2013.07.025
Nucl. Phys. B **875**, 483 (2013)
(Jul 25, 2013) [HEP entry link]

178. **"Measurement of Top Quark Polarization in Top-Antitop Events from Proton-Proton Collisions at $\sqrt{s}$ = 7TeV Using the ATLAS Detector"**
G. Aad *et al.* [ATLAS Collaboration].
arXiv:1307.6511 [hep-ex]
10.1103/PhysRevLett.111.232002
Phys. Rev. Lett. **111**, no. 23, 232002 (2013)
(Jul 24, 2013) [HEP entry link]

179. **"Measurement of jet shapes in top-quark pair events at $\sqrt{s}$ = 7 TeV using the ATLAS detector"**
G. Aad *et al.* [ATLAS Collaboration].
arXiv:1307.5749 [hep-ex]
10.1140/epjc/s10052-013-2676-3
Eur. Phys. J. C **73**, no. 12, 2676 (2013)
(Jul 22, 2013) [HEP entry link]

180. **"Measurement of the top quark charge in pp collisions at $\sqrt{s}$ = 7 TeV with the ATLAS detector"**
G. Aad *et al.* [ATLAS Collaboration].
arXiv:1307.4568 [hep-ex]
10.1007/JHEP11(2013)031
JHEP **1311**, 031 (2013)
(Jul 17, 2013) [HEP entry link]

181. **"Evidence for the spin-0 nature of the Higgs boson using ATLAS data"**
G. Aad *et al.* [ATLAS Collaboration].
arXiv:1307.1432 [hep-ex]

10.1016/j.physletb.2013.08.026
Phys. Lett. B **726**, 120 (2013)
(Jul 4, 2013) [HEP entry link]

182. **"Measurements of Higgs boson production and couplings in diboson final states with the ATLAS detector at the LHC"**
G. Aad *et al.* [ATLAS Collaboration].
arXiv:1307.1427 [hep-ex]
10.1016/j.physletb.2014.05.011, 10.1016/j.physletb.2013.08.010
Phys. Lett. B **726**, 88 (2013), [Phys. Lett. B **734**, 406 (2014)]
(Jul 4, 2013) [HEP entry link]

183. **"Measurement of the differential cross-section of B^+ meson production in pp collisions at $\sqrt{s}$ = 7 TeV at ATLAS"**
G. Aad *et al.* [ATLAS Collaboration].
arXiv:1307.0126 [hep-ex]
10.1007/JHEP10(2013)042
JHEP **1310**, 042 (2013)
(Jun 29, 2013) [HEP entry link]

184. **"Measurement of the Azimuthal Angle Dependence of Inclusive Jet Yields in Pb+Pb Collisions at $\sqrt{s_{NN}}$ = 2.76 TeV with the ATLAS detector"**
G. Aad *et al.* [ATLAS Collaboration].
arXiv:1306.6469 [hep-ex]
10.1103/PhysRevLett.111.152301
Phys. Rev. Lett. **111**, no. 15, 152301 (2013)
(Jun 27, 2013) [HEP entry link]

185. **"Performance of jet substructure techniques for large-R jets in proton-proton collisions at $\sqrt{s}$ = 7 TeV using the ATLAS detector"**
G. Aad *et al.* [ATLAS Collaboration].
arXiv:1306.4945 [hep-ex]
10.1007/JHEP09(2013)076
JHEP **1309**, 076 (2013)
(Jun 20, 2013) [HEP entry link]

186. **"Measurement of the high-mass Drell–Yan differential cross-section in pp collisions at sqrt(s)=7 TeV with the ATLAS detector"**
G. Aad *et al.* [ATLAS Collaboration].
arXiv:1305.4192 [hep-ex]
10.1016/j.physletb.2013.07.049
Phys. Lett. B **725**, 223 (2013)
(May 17, 2013) [HEP entry link]

187. **"Measurement of the distributions of event-by-event flow harmonics in lead-lead collisions at = 2.76 TeV with the ATLAS detector at the LHC"**

G. Aad *et al.* [ATLAS Collaboration].
arXiv:1305.2942 [hep-ex]
10.1007/JHEP11(2013)183
JHEP **1311**, 183 (2013)
(May 13, 2013) [HEP entry link]

188. **"Search for $t\bar{t}$ resonances in the lepton plus jets final state with ATLAS using 4.7 fb^{-1} of pp collisions at $\sqrt{s} = 7$ TeV"**
G. Aad *et al.* [ATLAS Collaboration].
arXiv:1305.2756 [hep-ex]
10.1103/PhysRevD.88.012004
Phys. Rev. D **88**, no. 1, 012004 (2013)
(May 13, 2013) [HEP entry link]

189. **"Triggers for displaced decays of long-lived neutral particles in the ATLAS detector"**
G. Aad *et al.* [ATLAS Collaboration].
arXiv:1305.2284 [hep-ex]
10.1088/1748-0221/8/07/P07015
JINST **8**, P07015 (2013)
(May 10, 2013) [HEP entry link]

190. **"Search for resonant diboson production in the WW/WZjj decay channels with the ATLAS detector at $\sqrt{s}$ = 7TeV"**
G. Aad *et al.* [ATLAS Collaboration].
arXiv:1305.0125 [hep-ex]
10.1103/PhysRevD.87.112006
Phys. Rev. D **87**, no. 11, 112006 (2013)
(May 1, 2013) [HEP entry link]

191. **"Measurement of the production cross section of jets in association with a Z boson in pp collisions at $\sqrt{s}$ = 7 TeV with the ATLAS detector"**
G. Aad *et al.* [ATLAS Collaboration].
arXiv:1304.7098 [hep-ex]
10.1007/JHEP07(2013)032
JHEP **1307**, 032 (2013)
(Apr 26, 2013) [HEP entry link]

192. **"Study of heavy-flavor quarks produced in association with top-quark pairs at $\sqrt{s} = 7$TeV using the ATLAS detector"**
G. Aad *et al.* [ATLAS Collaboration].
arXiv:1304.6386 [hep-ex]
10.1103/PhysRevD.89.072012
Phys. Rev. D **89**, no. 7, 072012 (2014)
(Apr 23, 2013) [HEP entry link]

193. **"Search for nonpointing photons in the diphoton and E_T^{miss} final state in $\sqrt{s}$=7TeV proton-proton collisions using the ATLAS detector"**
G. Aad *et al.* [ATLAS Collaboration].
arXiv:1304.6310 [hep-ex]
10.1103/PhysRevD.88.012001
Phys. Rev. D **88**, no. 1, 012001 (2013)
(Apr 23, 2013) [HEP entry link]

194. **"Measurement of the inclusive jet cross section in pp collisions at sqrt(s)=2.76 TeV and comparison to the inclusive jet cross section at sqrt(s)=7 TeV using the ATLAS detector"**
G. Aad *et al.* [ATLAS Collaboration].
arXiv:1304.4739 [hep-ex]
10.1140/epjc/s10052-013-2509-4
Eur. Phys. J. C **73**, no. 8, 2509 (2013)
(Apr 17, 2013) [HEP entry link]

195. **"A particle consistent with the Higgs Boson observed with the ATLAS Detector at the Large Hadron Collider"**
G. Aad *et al.* [ATLAS Collaboration].
10.1126/science.1232005
Science **338**, 1576 (2012).
(2012) [HEP entry link]

196. **"Measurement with the ATLAS detector of multi-particle azimuthal correlations in p+Pb collisions at sqrt(s_NN)=5.02 TeV"**
G. Aad *et al.* [ATLAS Collaboration].
arXiv:1303.2084 [hep-ex]
10.1016/j.physletb.2013.06.057
Phys. Lett. B **725**, 60 (2013)
(Mar 8, 2013) [HEP entry link]

197. **"Search for third generation scalar leptoquarks in pp collisions at $\sqrt{s}$ = 7 TeV with the ATLAS detector"**
G. Aad *et al.* [ATLAS Collaboration].
arXiv:1303.0526 [hep-ex]
10.1007/JHEP06(2013)033
JHEP **1306**, 033 (2013)
(Mar 3, 2013) [HEP entry link]

198. **"Characterisation and mitigation of beam-induced backgrounds observed in the ATLAS detector during the 2011 proton-proton run"**
G. Aad *et al.* [ATLAS Collaboration].
arXiv:1303.0223 [hep-ex]
10.1088/1748-0221/8/07/P07004
JINST **8**, P07004 (2013)
(Mar 1, 2013) [HEP entry link]

199. **"Search for WH production with a light Higgs boson decaying to prompt electron-jets in proton-proton collisions at $\sqrt{s}$=7 TeV with the ATLAS detector"**
G. Aad *et al.* [ATLAS Collaboration].
arXiv:1302.4403 [hep-ex]
10.1088/1367-2630/15/4/043009
New J. Phys. **15**, 043009 (2013)
(Feb 18, 2013) [HEP entry link]

200. **"Improved luminosity determination in pp collisions at sqrt(s) = 7 TeV using the ATLAS detector at the LHC"**
G. Aad *et al.* [ATLAS Collaboration].
arXiv:1302.4393 [hep-ex]
10.1140/epjc/s10052-013-2518-3
Eur. Phys. J. C **73**, no. 8, 2518 (2013)
(Feb 18, 2013) [HEP entry link]

201. **"Search for a light charged Higgs boson in the decay channel $H^+ \to c\bar{s}$ in $t\bar{t}$ events using pp collisions at $\sqrt{s}$ = 7 TeV with the ATLAS detector"**
G. Aad *et al.* [ATLAS Collaboration].
arXiv:1302.3694 [hep-ex]
10.1140/epjc/s10052-013-2465-z
Eur. Phys. J. C **73**, no. 6, 2465 (2013)
(Feb 15, 2013) [HEP entry link]

202. **"Measurement of the cross-section for W boson production in association with b-jets in pp collisions at $\sqrt{s}$ = 7 TeV with the ATLAS detector"**
G. Aad *et al.* [ATLAS Collaboration].
arXiv:1302.2929 [hep-ex]
10.1007/JHEP06(2013)084
JHEP **1306**, 084 (2013)
(Feb 12, 2013) [HEP entry link]

203. **"Measurement of kT splitting scales in W-¿lv events at sqrt(s)=7 TeV with the ATLAS detector"**
G. Aad *et al.* [ATLAS Collaboration].
arXiv:1302.1415 [hep-ex]
10.1140/epjc/s10052-013-2432-8
Eur. Phys. J. C **73**, no. 5, 2432 (2013)
(Feb 6, 2013) [HEP entry link]

204. **"Measurements of $W\gamma$ and $Z\gamma$ production in pp collisions at $\sqrt{s}$=7TeV with the ATLAS detector at the LHC"**
G. Aad *et al.* [ATLAS Collaboration].
arXiv:1302.1283 [hep-ex]

10.1103/PhysRevD.87.112003, 10.1103/PhysRevD.91.119901
Phys. Rev. D **87**, no. 11, 112003 (2013), [Phys. Rev. D **91**, no. 11, 119901 (2015)]
(Feb 6, 2013) [HEP entry link]

205. **"Measurement of hard double-parton interactions in $W(\rightarrow l\nu)$+ 2 jet events at $\sqrt{s}$=7 TeV with the ATLAS detector"**
G. Aad *et al.* [ATLAS Collaboration].
arXiv:1301.6872 [hep-ex]
10.1088/1367-2630/15/3/033038
New J. Phys. **15**, 033038 (2013)
(Jan 29, 2013) [HEP entry link]

206. **"Search for long-lived, multi-charged particles in pp collisions at $\sqrt{s}$=7 TeV using the ATLAS detector"**
G. Aad *et al.* [ATLAS Collaboration].
arXiv:1301.5272 [hep-ex]
10.1016/j.physletb.2013.04.036
Phys. Lett. B **722**, 305 (2013)
(Jan 22, 2013) [HEP entry link]

207. **"Search for single b^*-quark production with the ATLAS detector at $\sqrt{s} = 7$ TeV"**
G. Aad *et al.* [ATLAS Collaboration].
arXiv:1301.1583 [hep-ex]
10.1016/j.physletb.2013.03.016
Phys. Lett. B **721**, 171 (2013)
(Jan 2013) [HEP entry link]

208. **"Multi-channel search for squarks and gluinos in $\sqrt{s} = 7$ TeV pp collisions with the ATLAS detector"**
G. Aad *et al.* [ATLAS Collaboration].
arXiv:1212.6149 [hep-ex]
10.1140/epjc/s10052-013-2362-5
Eur. Phys. J. C **73**, no. 3, 2362 (2013)
(Dec 2012) [HEP entry link]

209. **"A search for prompt lepton-jets in pp collisions at $\sqrt{s} = 7$ TeV with the ATLAS detector"**
G. Aad *et al.* [ATLAS Collaboration].
arXiv:1212.5409
10.1016/j.physletb.2013.01.034
Phys. Lett. B **719**, 299 (2013)
(Dec 2012) [HEP entry link]

210. **"Observation of Associated Near-Side and Away-Side Long-Range Correlations in $\sqrt{s_{NN}}$=5.02TeV Proton-Lead Collisions with the ATLAS Detector"**
G. Aad *et al.* [ATLAS Collaboration].

arXiv:1212.5198 [hep-ex]
10.1103/PhysRevLett.110.182302
Phys. Rev. Lett. **110**, no. 18, 182302 (2013)
(Dec 2012) [HEP entry link]

211. **"Search for charged Higgs bosons through the violation of lepton universality in $t\bar{t}$ events using pp collision data at $\sqrt{s} = 7$ TeV with the ATLAS experiment"**
G. Aad *et al.* [ATLAS Collaboration].
arXiv:1212.3572 [hep-ex]
10.1007/JHEP03(2013)076
JHEP **1303**, 076 (2013)
(Dec 2012) [HEP entry link]

212. **"Search for a heavy narrow resonance decaying to $e\mu$, $e\tau$, or $\mu\tau$ with the ATLAS detector in $\sqrt{s} = 7$ TeV pp collisions at the LHC"**
G. Aad *et al.* [ATLAS Collaboration].
arXiv:1212.1272
10.1016/j.physletb.2013.04.035
Phys. Lett. B **723**, 15 (2013)
(Dec 2012) [HEP entry link]

213. **"Measurement of Upsilon production in 7 TeV pp collisions at ATLAS"**
G. Aad *et al.* [ATLAS Collaboration].
arXiv:1211.7255 [hep-ex]
10.1103/PhysRevD.87.052004
Phys. Rev. D **87**, no. 5, 052004 (2013)
(Nov 2012) [HEP entry link]

214. **"Measurement of the ttbar production cross section in the tau+jets channel using the ATLAS detector"**
G. Aad *et al.* [ATLAS Collaboration].
arXiv:1211.7205 [hep-ex]
10.1140/epjc/s10052-013-2328-7
Eur. Phys. J. C **73**, no. 3, 2328 (2013)
(Nov 2012) [HEP entry link]

215. **"Search for the neutral Higgs bosons of the Minimal Supersymmetric Standard Model in pp collisions at $\sqrt{s} = 7$ TeV with the ATLAS detector"**
G. Aad *et al.* [ATLAS Collaboration].
arXiv:1211.6956 [hep-ex]
10.1007/JHEP02(2013)095
JHEP **1302**, 095 (2013)
(Nov 2012) [HEP entry link]

216. **"Measurement of angular correlations in Drell-Yan lepton pairs to probe Z/gamma* boson transverse momentum at sqrt(s)=7 TeV with**

the ATLAS detector"
G. Aad *et al.* [ATLAS Collaboration].
arXiv:1211.6899 [hep-ex]
10.1016/j.physletb.2013.01.054
Phys. Lett. B **720**, 32 (2013)
(Nov 29, 2012) [HEP entry link]

217. **"Search for new phenomena in events with three charged leptons at $/sqrts$ = 7 TeV with the ATLAS detector"**
G. Aad *et al.* [ATLAS Collaboration].
arXiv:1211.6312 [hep-ex]
10.1103/PhysRevD.87.052002
Phys. Rev. D **87**, no. 5, 052002 (2013)
(Nov 2012) [HEP entry link]

218. **"Measurement of ZZ production in pp collisions at $\sqrt{s}$ = 7 TeV and limits on anomalous ZZZ and $ZZ\gamma$ couplings with the ATLAS detector"**
G. Aad *et al.* [ATLAS Collaboration].
arXiv:1211.6096 [hep-ex]
10.1007/JHEP03(2013)128
JHEP **1303**, 128 (2013)
(Nov 2012) [HEP entry link]

219. **"Search for resonances decaying into top-quark pairs using fully hadronic decays in pp collisions with ATLAS at $\sqrt{s} = 7$ TeV"**
G. Aad *et al.* [ATLAS Collaboration].
arXiv:1211.2202 [hep-ex]
10.1007/JHEP01(2013)116
JHEP **1301**, 116 (2013)
(Nov 2012) [HEP entry link]

220. **"Measurement of isolated-photon pair production in pp collisions at $\sqrt{s} = 7$ TeV with the ATLAS detector"**
G. Aad *et al.* [ATLAS Collaboration].
arXiv:1211.1913 [hep-ex]
10.1007/JHEP01(2013)086
JHEP **1301**, 086 (2013)
(Nov 2012) [HEP entry link]

221. **"Searches for heavy long-lived sleptons and R-Hadrons with the ATLAS detector in pp collisions at $\sqrt{s} = 7$ TeV"**
G. Aad *et al.* [ATLAS Collaboration].
arXiv:1211.1597 [hep-ex]
10.1016/j.physletb.2013.02.015
Phys. Lett. B **720**, 277 (2013)
(Nov 2012) [HEP entry link]

222. **"Search for supersymmetry in events with photons, bottom quarks, and missing transverse momentum in proton-proton collisions at a centre-of-mass energy of 7 TeV with the ATLAS detector"**
G. Aad *et al.* [ATLAS Collaboration].
arXiv:1211.1167 [hep-ex]
10.1016/j.physletb.2013.01.041
Phys. Lett. B **719**, 261 (2013)
(Nov 2012) [HEP entry link]

223. **"Search for contact interactions and large extra dimensions in dilepton events from pp collisions at $\sqrt{s} = 7$ TeV with the ATLAS detector"**
G. Aad *et al.* [ATLAS Collaboration].
arXiv:1211.1150 [hep-ex]
10.1103/PhysRevD.87.015010
Phys. Rev. D **87**, no. 1, 015010 (2013)
(Nov 2012) [HEP entry link]

224. **"Search for Extra Dimensions in diphoton events using proton-proton collisions recorded at $\sqrt{s} = 7$ TeV with the ATLAS detector at the LHC"**
G. Aad *et al.* [ATLAS Collaboration].
arXiv:1210.8389 [hep-ex]
10.1088/1367-2630/15/4/043007
New J. Phys. **15**, 043007 (2013)
(Oct 2012) [HEP entry link]

225. **"Search for long-lived, heavy particles in final states with a muon and multi-track displaced vertex in proton-proton collisions at $\sqrt{s} = 7$ TeV with the ATLAS detector"**
G. Aad *et al.* [ATLAS Collaboration].
arXiv:1210.7451 [hep-ex]
10.1016/j.physletb.2013.01.042
Phys. Lett. B **719**, 280 (2013)
(Oct 2012) [HEP entry link]

226. **"A search for high-mass resonances decaying to $\tau^+\tau^-$ in pp collisions at $\sqrt{s} = 7$ TeV with the ATLAS detector"**
G. Aad *et al.* [ATLAS Collaboration].
arXiv:1210.6604 [hep-ex]
10.1016/j.physletb.2013.01.040
Phys. Lett. B **719**, 242 (2013)
(Oct 2012) [HEP entry link]

227. **"Measurement of Z boson Production in Pb+Pb Collisions at $\sqrt{s_{NN}} =$ 2.76 TeV with the ATLAS Detector"**
G. Aad *et al.* [ATLAS Collaboration].
arXiv:1210.6486 [hep-ex]

10.1103/PhysRevLett.110.022301
Phys. Rev. Lett. **110**, no. 2, 022301 (2013)
(Oct 2012) [HEP entry link]

228. **"Jet energy resolution in proton-proton collisions at $\sqrt{s} = 7$ TeV recorded in 2010 with the ATLAS detector"**
G. Aad *et al.* [ATLAS Collaboration].
arXiv:1210.6210 [hep-ex]
10.1140/epjc/s10052-013-2306-0
Eur. Phys. J. C **73**, no. 3, 2306 (2013)
(Oct 2012) [HEP entry link]

229. **"Search for pair production of heavy top-like quarks decaying to a high-pT W boson and a b quark in the lepton plus jets final state at $\sqrt{s}$=7 TeV with the ATLAS detector"**
G. Aad *et al.* [ATLAS Collaboration].
arXiv:1210.5468 [hep-ex]
10.1016/j.physletb.2012.11.071
Phys. Lett. B **718**, 1284 (2013)
(Oct 2012) [HEP entry link]

230. **"Search for doubly-charged Higgs bosons in like-sign dilepton final states at $\sqrt{s} = 7$ TeV with the ATLAS detector"**
G. Aad *et al.* [ATLAS Collaboration].
arXiv:1210.5070 [hep-ex]
10.1140/epjc/s10052-012-2244-2
Eur. Phys. J. C **72**, 2244 (2012)
(Oct 2012) [HEP entry link]

231. **"Search for pair-produced massive coloured scalars in four-jet final states with the ATLAS detector in proton-proton collisions at $\sqrt{s} = 7$ TeV"**
G. Aad *et al.* [ATLAS Collaboration].
arXiv:1210.4826 [hep-ex]
10.1140/epjc/s10052-012-2263-z
Eur. Phys. J. C **73**, no. 1, 2263 (2013)
(Oct 2012) [HEP entry link]

232. **"Search for pair production of massive particles decaying into three quarks with the ATLAS detector in $\sqrt{s} = 7$ TeV pp collisions at the LHC"**
G. Aad *et al.* [ATLAS Collaboration].
arXiv:1210.4813 [hep-ex]
10.1007/JHEP12(2012)086
JHEP **1212**, 086 (2012)
(Oct 2012) [HEP entry link]

233. **"Search for anomalous production of prompt like-sign lepton pairs at $\sqrt{s} = 7$ TeV with the ATLAS detector"**
G. Aad *et al.* [ATLAS Collaboration].
arXiv:1210.4538 [hep-ex]
10.1007/JHEP12(2012)007
JHEP **1212**, 007 (2012)
(Oct 2012) [HEP entry link]

234. **"Search for dark matter candidates and large extra dimensions in events with a jet and missing transverse momentum with the ATLAS detector"**
G. Aad *et al.* [ATLAS Collaboration].
arXiv:1210.4491 [hep-ex]
10.1007/JHEP04(2013)075
JHEP **1304**, 075 (2013)
(Oct 2012) [HEP entry link]

235. **"Search for R-parity-violating supersymmetry in events with four or more leptons in $\sqrt{s} = 7$ TeV pp collisions with the ATLAS detector"**
G. Aad *et al.* [ATLAS Collaboration].
arXiv:1210.4457 [hep-ex]
10.1007/JHEP12(2012)124
JHEP **1212**, 124 (2012)
(Oct 2012) [HEP entry link]

236. **"Measurement of W^+W^- production in pp collisions at $\sqrt{s}$=7TeV with the ATLAS detector and limits on anomalous WWZ and WW couplings"**
G. Aad *et al.* [ATLAS Collaboration].
arXiv:1210.2979 [hep-ex]
10.1103/PhysRevD.87.112001, 10.1103/PhysRevD.88.079906
Phys. Rev. D **87**, no. 11, 112001 (2013), [Phys. Rev. D **88**, no. 7, 079906 (2013)]
(Oct 2012) [HEP entry link]

237. **"Search for direct chargino production in anomaly-mediated supersymmetry breaking models based on a disappearing-track signature in pp collisions at $\sqrt{s} = 7$ TeV with the ATLAS detector"**
G. Aad *et al.* [ATLAS Collaboration].
arXiv:1210.2852 [hep-ex]
10.1007/JHEP01(2013)131
JHEP **1301**, 131 (2013)
(Oct 2012) [HEP entry link]

238. **"ATLAS search for new phenomena in dijet mass and angular distributions using pp collisions at $\sqrt{s} = 7$ TeV"**
G. Aad *et al.* [ATLAS Collaboration].
arXiv:1210.1718 [hep-ex]

10.1007/JHEP01(2013)029
JHEP **1301**, 029 (2013)
(Oct 2012) [HEP entry link]

239. **"Search for Supersymmetry in Events with Large Missing Transverse Momentum, Jets, and at Least One Tau Lepton in 7 TeV Proton-Proton Collision Data with the ATLAS Detector"**
G. Aad *et al.* [ATLAS Collaboration].
arXiv:1210.1314 [hep-ex]
10.1140/epjc/s10052-012-2215-7
Eur. Phys. J. C **72**, 2215 (2012)
(Oct 2012) [HEP entry link]

240. **"Measurement of the flavour composition of dijet events in pp collisions at $\sqrt{s} = 7$ TeV with the ATLAS detector"**
G. Aad *et al.* [ATLAS Collaboration].
arXiv:1210.0441 [hep-ex]
10.1140/epjc/s10052-013-2301-5
Eur. Phys. J. C **73**, no. 2, 2301 (2013)
(Oct 2012) [HEP entry link]

241. **"Search for displaced muonic lepton jets from light Higgs boson decay in proton-proton collisions at $\sqrt{s} = 7$ TeV with the ATLAS detector"**
G. Aad *et al.* [ATLAS Collaboration].
arXiv:1210.0435 [hep-ex]
10.1016/j.physletb.2013.02.058
Phys. Lett. B **721**, 32 (2013)
(Oct 2012) [HEP entry link]

242. **"Search for resonant top plus jet production in $t\bar{t}$ + jets events with the ATLAS detector in pp collisions at $\sqrt{s} = 7$ TeV"**
G. Aad *et al.* [ATLAS Collaboration].
arXiv:1209.6593 [hep-ex]
10.1103/PhysRevD.86.091103
Phys. Rev. D **86**, 091103 (2012)
(Sep 2012) [HEP entry link]

243. **"Search for dark matter candidates and large extra dimensions in events with a photon and missing transverse momentum in pp collision data at $\sqrt{s} = 7$ TeV with the ATLAS detector"**
G. Aad *et al.* [ATLAS Collaboration].
arXiv:1209.4625 [hep-ex]
10.1103/PhysRevLett.110.011802
Phys. Rev. Lett. **110**, no. 1, 011802 (2013)
(Sep 2012) [HEP entry link]

244. **"ATLAS search for a heavy gauge boson decaying to a charged lepton and a neutrino in pp collisions at $\sqrt{s} = 7$ TeV"**

G. Aad *et al.* [ATLAS Collaboration].
arXiv:1209.4446 [hep-ex]
10.1140/epjc/s10052-012-2241-5
Eur. Phys. J. C **72**, 2241 (2012)
(Sep 2012) [HEP entry link]

245. **"Search for a heavy top-quark partner in final states with two leptons with the ATLAS detector at the LHC"**
G. Aad *et al.* [ATLAS Collaboration].
arXiv:1209.4186 [hep-ex]
10.1007/JHEP11(2012)094
JHEP **1211**, 094 (2012)
(Sep 2012) [HEP entry link]

246. **"Search for high-mass resonances decaying to dilepton final states in pp collisions at s**(1/2) = 7-TeV with the ATLAS detector"**
G. Aad *et al.* [ATLAS Collaboration].
arXiv:1209.2535 [hep-ex]
10.1007/JHEP11(2012)138
JHEP **1211**, 138 (2012)
(Sep 2012) [HEP entry link]

247. **"Search for light top squark pair production in final states with leptons and b^- jets with the ATLAS detector in $\sqrt{s} = 7$ TeV proton-proton collisions"**
G. Aad *et al.* [ATLAS Collaboration].
arXiv:1209.2102 [hep-ex]
10.1016/j.physletb.2013.01.049
Phys. Lett. B **720**, 13 (2013)
(Sep 2012) [HEP entry link]

248. **"Search for diphoton events with large missing transverse momentum in 7 TeV proton-proton collision data with the ATLAS detector"**
G. Aad *et al.* [ATLAS Collaboration].
arXiv:1209.0753 [hep-ex]
10.1016/j.physletb.2012.10.069
Phys. Lett. B **718**, 411 (2012)
(Sep 2012) [HEP entry link]

249. **"Measurements of the pseudorapidity dependence of the total transverse energy in proton-proton collisions at $\sqrt{s} = 7$ TeV with ATLAS"**
G. Aad *et al.* [ATLAS Collaboration].
arXiv:1208.6256 [hep-ex]
10.1007/JHEP11(2012)033
JHEP **1211**, 033 (2012)
(Aug 2012) [HEP entry link]

250. **"Further search for supersymmetry at $\sqrt{s} = 7$ TeV in final states with jets, missing transverse momentum and isolated leptons with the ATLAS detector"**
G. Aad *et al.* [ATLAS Collaboration].
arXiv:1208.4688 [hep-ex]
10.1103/PhysRevD.86.092002
Phys. Rev. D **86**, 092002 (2012)
(Aug 2012) [HEP entry link]

251. **"Search for light scalar top quark pair production in final states with two leptons with the ATLAS detector in $\sqrt{s} = 7$ TeV proton-proton collisions"**
G. Aad *et al.* [ATLAS Collaboration].
arXiv:1208.4305 [hep-ex]
10.1140/epjc/s10052-012-2237-1
Eur. Phys. J. C **72**, 2237 (2012)
(Aug 2012) [HEP entry link]

252. **"Search for direct production of charginos and neutralinos in events with three leptons and missing transverse momentum in $\sqrt{s} = 7$ TeV pp collisions with the ATLAS detector"**
G. Aad *et al.* [ATLAS Collaboration].
arXiv:1208.3144 [hep-ex]
10.1016/j.physletb.2012.11.039
Phys. Lett. B **718**, 841 (2013)
(Aug 2012) [HEP entry link]

253. **"Search for direct slepton and gaugino production in final states with two leptons and missing transverse momentum with the ATLAS detector in pp collisions at $\sqrt{s} = 7$ TeV"**
G. Aad *et al.* [ATLAS Collaboration].
arXiv:1208.2884 [hep-ex]
10.1016/j.physletb.2012.11.058
Phys. Lett. B **718**, 879 (2013)
(Aug 2012) [HEP entry link]

254. **"Search for new phenomena in the WW to $\ell\nu\ell'\,\nu'$ final state in pp collisions at $\sqrt{s} = 7$ TeV with the ATLAS detector"**
G. Aad *et al.* [ATLAS Collaboration].
arXiv:1208.2880 [hep-ex]
10.1016/j.physletb.2012.11.040
Phys. Lett. B **718**, 860 (2013)
(Aug 2012) [HEP entry link]

255. **"Search for direct top squark pair production in final states with one isolated lepton, jets, and missing transverse momentum in $\sqrt{s} = 7$ TeV pp collisions using 4.7 fb^{-1} of ATLAS data"**

G. Aad *et al.* [ATLAS Collaboration].
arXiv:1208.2590 [hep-ex]
10.1103/PhysRevLett.109.211803
Phys. Rev. Lett. **109**, 211803 (2012)
(Aug 2012) [HEP entry link]

256. **"Measurement of the jet radius and transverse momentum dependence of inclusive jet suppression in lead-lead collisions at $\sqrt{s_{NN}}$= 2.76 TeV with the ATLAS detector"**
G. Aad *et al.* [ATLAS Collaboration].
arXiv:1208.1967 [hep-ex]
10.1016/j.physletb.2013.01.024
Phys. Lett. B **719**, 220 (2013)
(Aug 2012) [HEP entry link]

257. **"Search for a supersymmetric partner to the top quark in final states with jets and missing transverse momentum at $\sqrt{s} = 7$ TeV with the ATLAS detector"**
G. Aad *et al.* [ATLAS Collaboration].
arXiv:1208.1447 [hep-ex]
10.1103/PhysRevLett.109.211802
Phys. Rev. Lett. **109**, 211802 (2012)
(Aug 2012) [HEP entry link]

258. **"Measurement of WZ production in proton-proton collisions at $\sqrt{s} = 7$ TeV with the ATLAS detector"**
G. Aad *et al.* [ATLAS Collaboration].
arXiv:1208.1390 [hep-ex]
10.1140/epjc/s10052-012-2173-0
Eur. Phys. J. C **72**, 2173 (2012)
(Aug 2012) [HEP entry link]

259. **"Search for squarks and gluinos with the ATLAS detector in final states with jets and missing transverse momentum using 4.7 fb^{-1} of $\sqrt{s} = 7$ TeV proton-proton collision data"**
G. Aad *et al.* [ATLAS Collaboration].
arXiv:1208.0949 [hep-ex]
10.1103/PhysRevD.87.012008
Phys. Rev. D **87**, no. 1, 012008 (2013)
(Aug 2012) [HEP entry link]

260. **"Time-dependent angular analysis of the decay $B_s^0 \to J/\psi\phi$ and extraction of $\Delta\Gamma_s$ and the CP-violating weak phase ϕ_s by ATLAS"**
G. Aad *et al.* [ATLAS Collaboration].
arXiv:1208.0572 [hep-ex]
10.1007/JHEP12(2012)072
JHEP **1212**, 072 (2012)
(Aug 2012) [HEP entry link]

261. **"Underlying event characteristics and their dependence on jet size of charged-particle jet events in pp collisions at $\sqrt{s} = 7$ TeV with the ATLAS detector"**
G. Aad *et al.* [ATLAS Collaboration].
arXiv:1208.0563 [hep-ex]
10.1103/PhysRevD.86.072004
Phys. Rev. D **86**, 072004 (2012)
(Aug 2012) [HEP entry link]

262. **"Observation of a new particle in the search for the Standard Model Higgs boson with the ATLAS detector at the LHC"**
G. Aad *et al.* [ATLAS Collaboration].
arXiv:1207.7214 [hep-ex]
10.1016/j.physletb.2012.08.020
Phys. Lett. B **716**, 1 (2013)
(Jul 2012) [HEP entry link]

263. **"Measurement of charged-particle event shape variables in $\sqrt{s} = 7$ TeV proton-proton interactions with the ATLAS detector"**
G. Aad *et al.* [ATLAS Collaboration].
arXiv:1207.6915 [hep-ex]
10.1103/PhysRevD.88.032004
Phys. Rev. D **88**, no. 3, 032004 (2013)
(Jul 2012) [HEP entry link]

264. **"Search for magnetic monopoles in $\sqrt{s} = 7$ TeV pp collisions with the ATLAS detector"**
G. Aad *et al.* [ATLAS Collaboration].
arXiv:1207.6411 [hep-ex]
10.1103/PhysRevLett.109.261803
Phys. Rev. Lett. **109**, 261803 (2012)
(Jul 2012) [HEP entry link]

265. **"Measurements of top quark pair relative differential cross-sections with ATLAS in pp collisions at $\sqrt{s} = 7$ TeV"**
G. Aad *et al.* [ATLAS Collaboration].
arXiv:1207.5644 [hep-ex]
10.1140/epjc/s10052-012-2261-1
Eur. Phys. J. C **73**, no. 1, 2261 (2013)
(Jul 2012) [HEP entry link]

266. **"Search for top and bottom squarks from gluino pair production in final states with missing transverse energy and at least three b-jets with the ATLAS detector"**
G. Aad *et al.* [ATLAS Collaboration].
arXiv:1207.4686 [hep-ex]
10.1140/epjc/s10052-012-2174-z

Eur. Phys. J. C **72**, 2174 (2012)
(Jul 2012) [HEP entry link]

267. **"A search for $t\bar{t}$ resonances in lepton+jets events with highly boosted top quarks collected in pp collisions at $\sqrt{s} = 7$ TeV with the ATLAS detector"**
G. Aad *et al.* [ATLAS Collaboration].
arXiv:1207.2409 [hep-ex]
10.1007/JHEP09(2012)041
JHEP **1209**, 041 (2012)
(Jul 2012) [HEP entry link]

268. **"Measurement of the ^0_b lifetime and mass in the ATLAS experiment"**
G. Aad *et al.* [ATLAS Collaboration].
arXiv:1207.2284 [hep-ex]
10.1103/PhysRevD.87.032002
Phys. Rev. D **87**, no. 3, 032002 (2013)
(Jul 2012) [HEP entry link]

269. **"Combined search for the Standard Model Higgs boson in pp collisions at $\sqrt{s} = 7$ TeV with the ATLAS detector"**
G. Aad *et al.* [ATLAS Collaboration].
arXiv:1207.0319 [hep-ex]
10.1103/PhysRevD.86.032003
Phys. Rev. D **86**, 032003 (2012)
(Jul 2012) [HEP entry link]

270. **"Search for the Standard Model Higgs boson produced in association with a vector boson and decaying to a b-quark pair with the ATLAS detector"**
G. Aad *et al.* [ATLAS Collaboration].
arXiv:1207.0210 [hep-ex]
10.1016/j.physletb.2012.10.061
Phys. Lett. B **718**, 369 (2012)
(Jul 2012) [HEP entry link]

271. **"Search for the Higgs boson in the $H \to WW \to$ lnujj decay channel at $\sqrt{s} = 7$ TeV with the ATLAS detector"**
G. Aad *et al.* [ATLAS Collaboration].
arXiv:1206.6074 [hep-ex]
10.1016/j.physletb.2012.10.066
Phys. Lett. B **718**, 391 (2012)
(Jun 2012) [HEP entry link]

272. **"Search for the Standard Model Higgs boson in the H to $\tau^+\tau^-$ decay mode in $\sqrt{s} = 7$ TeV pp collisions with ATLAS"**
G. Aad *et al.* [ATLAS Collaboration].
arXiv:1206.5971 [hep-ex]

10.1007/JHEP09(2012)070
JHEP **1209**, 070 (2012)
(Jun 2012) [HEP entry link]

273. **"ATLAS measurements of the properties of jets for boosted particle searches"**
G. Aad *et al.* [ATLAS Collaboration].
arXiv:1206.5369 [hep-ex]
10.1103/PhysRevD.86.072006
Phys. Rev. D **86**, 072006 (2012)
(Jun 2012) [HEP entry link]

274. **"Measurement of the b-hadron production cross section using decays to $D^*\mu^- X$ final states in pp collisions at sqrt(s) = 7 TeV with the ATLAS detector"**
G. Aad *et al.* [ATLAS Collaboration].
arXiv:1206.3122 [hep-ex]
10.1016/j.nuclphysb.2012.07.009
Nucl. Phys. B **864**, 341 (2012)
(Jun 2012) [HEP entry link]

275. **"Search for a standard model Higgs boson in the mass range 200-600 GeV in the $H \to ZZ \to \ell^+\ell^- q\bar{q}$ decay channel with the ATLAS detector"**
G. Aad *et al.* [ATLAS Collaboration].
arXiv:1206.2443 [hep-ex]
10.1016/j.physletb.2012.09.020
Phys. Lett. B **717**, 70 (2013)
(Jun 2012) [HEP entry link]

276. **"Measurement of event shapes at large momentum transfer with the ATLAS detector in pp collisions at $\sqrt{s} = 7$ TeV"**
G. Aad *et al.* [ATLAS Collaboration].
arXiv:1206.2135 [hep-ex]
10.1140/epjc/s10052-012-2211-y
Eur. Phys. J. C **72**, 2211 (2012)
(Jun 2012) [HEP entry link]

277. **"Hunt for new phenomena using large jet multiplicities and missing transverse momentum with ATLAS in 4.7 fb^{-1} of $\sqrt{s} = 7$ TeV proton-proton collisions"**
G. Aad *et al.* [ATLAS Collaboration].
arXiv:1206.1760 [hep-ex]
10.1007/JHEP07(2012)167
JHEP **1207**, 167 (2012)
(Jun 2012) [HEP entry link]

278. **"Search for the Standard Model Higgs boson in the $H \to$ WW(*) $\to \ell\nu\ell\nu$ decay mode with 4.7 /fb of ATLAS data at $\sqrt{s} = 7$ TeV"**

G. Aad *et al.* [ATLAS Collaboration].
arXiv:1206.0756 [hep-ex]
10.1016/j.physletb.2012.08.010
Phys. Lett. B **716**, 62 (2013)
(Jun 2012) [HEP entry link]

279. **"A search for flavour changing neutral currents in top-quark decays in pp collision data collected with the ATLAS detector at $\sqrt{s} = 7$ TeV"**
G. Aad *et al.* [ATLAS Collaboration].
arXiv:1206.0257 [hep-ex]
10.1007/JHEP09(2012)139
JHEP **1209**, 139 (2012)
(Jun 2012) [HEP entry link]

280. **"Search for a standard sodel Higgs boson in the H $\to$ ZZ $\to \ell^+\ell^-\nu\bar{\nu}$ decay channel using 4.7 fb^{-1} of $\sqrt{s} = 7$ TeV data with the ATLAS detector"**
G. Aad *et al.* [ATLAS Collaboration].
arXiv:1205.6744 [hep-ex]
10.1016/j.physletb.2012.09.016
Phys. Lett. B **717**, 29 (2013)
(May 2012) [HEP entry link]

281. **"Evidence for the associated production of a W boson and a top quark in ATLAS at $\sqrt{s} = 7$ TeV"**
G. Aad *et al.* [ATLAS Collaboration].
arXiv:1205.5764 [hep-ex]
10.1016/j.physletb.2012.08.011
Phys. Lett. B **716**, 142 (2013)
(May 2012) [HEP entry link]

282. **"A search for $t\bar{t}$ resonances with the ATLAS detector in 2.05 fb^{-1} of proton-proton collisions at $\sqrt{s} = 7$ TeV"**
G. Aad *et al.* [ATLAS Collaboration].
arXiv:1205.5371 [hep-ex]
10.1140/epjc/s10052-012-2083-1
Eur. Phys. J. C **72**, 2083 (2012)
(May 2012) [HEP entry link]

283. **"Measurement of the t-channel single top-quark production cross section in pp collisions at $\sqrt{s} = 7$ TeV with the ATLAS detector"**
G. Aad *et al.* [ATLAS Collaboration].
arXiv:1205.3130 [hep-ex]
10.1016/j.physletb.2012.09.031
Phys. Lett. B **717**, 330 (2013)
(May 2012) [HEP entry link]

284. **"Measurement of $W\gamma$ and $Z\gamma$ production cross sections in pp collisions at $\sqrt{s} = 7$ TeV and limits on anomalous triple gauge couplings with the ATLAS detector"**
G. Aad *et al.* [ATLAS Collaboration].
arXiv:1205.2531 [hep-ex]
10.1016/j.physletb.2012.09.017
Phys. Lett. B **717**, 49 (2013)
(May 2012) [HEP entry link]

285. **"Measurement of the W boson polarization in top quark decays with the ATLAS detector"**
G. Aad *et al.* [ATLAS Collaboration].
arXiv:1205.2484 [hep-ex]
10.1007/JHEP06(2012)088
JHEP **1206**, 088 (2012)
(May 2012) [HEP entry link]

286. **"Measurement of the top quark pair cross section with ATLAS in pp collisions at $\sqrt{s} = 7$ TeV using final states with an electron or a muon and a hadronically decaying τ lepton"**
G. Aad *et al.* [ATLAS Collaboration].
arXiv:1205.2067 [hep-ex]
10.1016/j.physletb.2012.09.032
Phys. Lett. B **717**, 89 (2013)
(May 2012) [HEP entry link]

287. **"Search for tb resonances in proton-proton collisions at $\sqrt{s} = 7$ TeV with the ATLAS detector"**
G. Aad *et al.* [ATLAS Collaboration].
arXiv:1205.1016 [hep-ex]
10.1103/PhysRevLett.109.081801
Phys. Rev. Lett. **109**, 081801 (2012)
(May 2012) [HEP entry link]

288. **"Search for a fermiophobic Higgs boson in the diphoton decay channel with the ATLAS detector"**
G. Aad *et al.* [ATLAS Collaboration].
arXiv:1205.0701 [hep-ex]
10.1140/epjc/s10052-012-2157-0
Eur. Phys. J. C **72**, 2157 (2012)
(May 2012) [HEP entry link]

289. **"Search for scalar top quark pair production in natural gauge mediated supersymmetry models with the ATLAS detector in pp collisions at $\sqrt{s} = 7$ TeV"**
G. Aad *et al.* [ATLAS Collaboration].
arXiv:1204.6736 [hep-ex]

10.1016/j.physletb.2012.07.010
Phys. Lett. B **715**, 44 (2013)
(Apr 2012) [HEP entry link]

290. **"Measurement of τ polarization in $W- > \tau\nu$ decays with the ATLAS detector in pp collisions at sqrt(s) = 7 TeV"**
G. Aad *et al.* [ATLAS Collaboration].
arXiv:1204.6720 [hep-ex]
10.1140/epjc/s10052-012-2062-6
Eur. Phys. J. C **72**, 2062 (2012)
(Apr 2012) [HEP entry link]

291. **"Search for supersymmetry in events with three leptons and missing transverse momentum in $\sqrt{s} = 7$ TeV pp collisions with the ATLAS detector"**
G. Aad *et al.* [ATLAS Collaboration].
arXiv:1204.5638 [hep-ex]
10.1103/PhysRevLett.108.261804
Phys. Rev. Lett. **108**, 261804 (2012)
(Apr 2012) [HEP entry link]

292. **"Search for TeV-scale gravity signatures in final states with leptons and jets with the ATLAS detector at $\sqrt{s} = 7$ TeV"**
G. Aad *et al.* [ATLAS Collaboration].
arXiv:1204.4646 [hep-ex]
10.1016/j.physletb.2012.08.009
Phys. Lett. B **716**, 122 (2013)
(Apr 2012) [HEP entry link]

293. **"Search for supersymmetry with jets, missing transverse momentum and at least one hadronically decaying τ lepton in proton-proton collisions at $\sqrt{s} = 7$ TeV with the ATLAS detector"**
G. Aad *et al.* [ATLAS Collaboration].
arXiv:1204.3852 [hep-ex]
10.1016/j.physletb.2012.06.061
Phys. Lett. B **714**, 197 (2013)
(Apr 2012) [HEP entry link]

294. **"Search for charged Higgs bosons decaying via $H^+ \to \tau\nu$ in top quark pair events using pp collision data at $\sqrt{s} = 7$ TeV with the ATLAS detector"**
G. Aad *et al.* [ATLAS Collaboration].
arXiv:1204.2760 [hep-ex]
10.1007/JHEP06(2012)039
JHEP **1206**, 039 (2012)
(Apr 2012) [HEP entry link]

295. **"Search for resonant WZ production in the $WZ \to \ell\nu\ell'\ell'$ channel in $\sqrt{s} = 7$ TeV pp collisions with the ATLAS detector"**
G. Aad *et al.* [ATLAS Collaboration].
arXiv:1204.1648 [hep-ex]
10.1103/PhysRevD.85.112012
Phys. Rev. D **85**, 112012 (2012)
(Apr 2012) [HEP entry link]

296. **"Search for pair production of a new quark that decays to a Z boson and a bottom quark with the ATLAS detector"**
G. Aad *et al.* [ATLAS Collaboration].
arXiv:1204.1265 [hep-ex]
10.1103/PhysRevLett.109.071801
Phys. Rev. Lett. **109**, 071801 (2012)
(Apr 2012) [HEP entry link]

297. **"Search for the decay Bs0 -¿ mu mu with the ATLAS detector"**
G. Aad *et al.* [ATLAS Collaboration].
arXiv:1204.0735 [hep-ex]
10.1016/j.physletb.2012.06.013
Phys. Lett. B **713**, 387 (2013)
(Apr 2012) [HEP entry link]

298. **"Search for events with large missing transverse momentum, jets, and at least two tau leptons in 7 TeV protonproton collision data with the ATLAS detector"**
G. Aad *et al.* [ATLAS Collaboration].
arXiv:1203.6580 [hep-ex]
10.1016/j.physletb.2012.06.055
Phys. Lett. B **714**, 180 (2013)
(Mar 2012) [HEP entry link]

299. **"Measurement of the WW cross section in $\sqrt{s} = 7$ TeV pp collisions with the ATLAS detector and limits on anomalous gauge couplings"**
G. Aad *et al.* [ATLAS Collaboration].
arXiv:1203.6232 [hep-ex]
10.1016/j.physletb.2012.05.003
Phys. Lett. B **712**, 289 (2013)
(Mar 2012) [HEP entry link]

300. **"Search for supersymmetry in pp collisions at $\sqrt{s} = 7$ TeV in final states with missing transverse momentum and b^- jets with the ATLAS detector"**
G. Aad *et al.* [ATLAS Collaboration].
arXiv:1203.6193 [hep-ex]
10.1103/PhysRevD.85.112006
Phys. Rev. D **85**, 112006 (2012)
(Mar 2012) [HEP entry link]

301. **"Search for gluinos in events with two same-sign leptons, jets and missing transverse momentum with the ATLAS detector in pp collisions at $\sqrt{s} = 7$ TeV"**
G. Aad *et al.* [ATLAS Collaboration].
arXiv:1203.5763 [hep-ex]
10.1103/PhysRevLett.108.241802
Phys. Rev. Lett. **108**, 241802 (2012)
(Mar 2012) [HEP entry link]

302. **"Search for heavy neutrinos and right-handed W bosons in events with two leptons and jets in pp collisions at $\sqrt{s} = 7$ TeV with the ATLAS detector"**
G. Aad *et al.* [ATLAS Collaboration].
arXiv:1203.5420 [hep-ex]
10.1140/epjc/s10052-012-2056-4
Eur. Phys. J. C **72**, 2056 (2012)
(Mar 2012) [HEP entry link]

303. **"Measurement of $t\bar{t}$ production with a veto on additional central jet activity in pp collisions at sqrt(s) = 7 TeV using the ATLAS detector"**
G. Aad *et al.* [ATLAS Collaboration].
arXiv:1203.5015 [hep-ex]
10.1140/epjc/s10052-012-2043-9
Eur. Phys. J. C **72**, 2043 (2012)
(Mar 2012) [HEP entry link]

304. **"Jet mass and substructure of inclusive jets in $\sqrt{s} = 7$ TeV pp collisions with the ATLAS experiment"**
G. Aad *et al.* [ATLAS Collaboration].
arXiv:1203.4606 [hep-ex]
10.1007/JHEP05(2012)128
JHEP **1205**, 128 (2012)
(Mar 2012) [HEP entry link]

305. **"Observation of spin correlation in $t\bar{t}$ events from pp collisions at sqrt(s) = 7 TeV using the ATLAS detector"**
G. Aad *et al.* [ATLAS Collaboration].
arXiv:1203.4081 [hep-ex]
10.1103/PhysRevLett.108.212001
Phys. Rev. Lett. **108**, 212001 (2012)
(Mar 2012) [HEP entry link]

306. **"Determination of the strange quark density of the proton from ATLAS measurements of the $W \to \ell\nu$ and $Z \to \ell\ell$ cross sections"**
G. Aad *et al.* [ATLAS Collaboration].
arXiv:1203.4051 [hep-ex]
10.1103/PhysRevLett.109.012001

Phys. Rev. Lett. **109**, 012001 (2012)
(Mar 2012) [HEP entry link]

307. **"Measurement of inclusive two-particle angular correlations in pp collisions with the ATLAS detector at the LHC"**
G. Aad *et al.* [ATLAS Collaboration].
arXiv:1203.3549 [hep-ex]
10.1007/JHEP05(2012)157
JHEP **1205**, 157 (2012)
(Mar 2012) [HEP entry link]

308. **"Search for second generation scalar leptoquarks in pp collisions at $\sqrt{s} = 7$ TeV with the ATLAS detector"**
G. Aad *et al.* [ATLAS Collaboration].
arXiv:1203.3172 [hep-ex]
10.1140/epjc/s10052-012-2151-6
Eur. Phys. J. C **72**, 2151 (2012)
(Mar 2012) [HEP entry link]

309. **"Measurement of the production cross section of an isolated photon associated with jets in proton-proton collisions at $\sqrt{s} = 7$ TeV with the ATLAS detector"**
G. Aad *et al.* [ATLAS Collaboration].
arXiv:1203.3161 [hep-ex]
10.1103/PhysRevD.85.092014
Phys. Rev. D **85**, 092014 (2012)
(Mar 2012) [HEP entry link]

310. **"Forward-backward correlations and charged-particle azimuthal distributions in pp interactions using the ATLAS detector"**
G. Aad *et al.* [ATLAS Collaboration].
arXiv:1203.3100 [hep-ex]
10.1007/JHEP07(2012)019
JHEP **1207**, 019 (2012)
(Mar 2012) [HEP entry link]

311. **"Measurement of the azimuthal anisotropy for charged particle production in $\sqrt{s_{NN}} = 2.76$ TeV lead-lead collisions with the ATLAS detector"**
G. Aad *et al.* [ATLAS Collaboration].
arXiv:1203.3087 [hep-ex]
10.1103/PhysRevC.86.014907
Phys. Rev. C **86**, 014907 (2012)
(Mar 2012) [HEP entry link]

312. **"Measurement of the polarisation of W bosons produced with large transverse momentum in pp collisions at $\sqrt{s} = 7$ TeV with the ATLAS experiment"**

G. Aad *et al.* [ATLAS Collaboration].
arXiv:1203.2165 [hep-ex]
10.1140/epjc/s10052-012-2001-6
Eur. Phys. J. C **72**, 2001 (2012)
(Mar 2012) [HEP entry link]

313. **"Single hadron response measurement and calorimeter jet energy scale uncertainty with the ATLAS detector at the LHC"**
G. Aad *et al.* [ATLAS Collaboration].
arXiv:1203.1302 [hep-ex]
10.1140/epjc/s10052-013-2305-1
Eur. Phys. J. C **73**, no. 3, 2305 (2013)
(Mar 2012) [HEP entry link]

314. **"Search for new particles decaying to ZZ using final states with leptons and jets with the ATLAS detector in $\sqrt{s} = 7$ TeV proton-proton collisions"**
G. Aad *et al.* [ATLAS Collaboration].
arXiv:1203.0718 [hep-ex]
10.1016/j.physletb.2012.05.020
Phys. Lett. B **712**, 331 (2013)
(Mar 2012) [HEP entry link]

315. **"Search for FCNC single top-quark production at $\sqrt{s} = 7$ TeV with the ATLAS detector"**
G. Aad *et al.* [ATLAS Collaboration].
arXiv:1203.0529 [hep-ex]
10.1016/j.physletb.2012.05.022
Phys. Lett. B **712**, 351 (2013)
(Mar 2012) [HEP entry link]

316. **"Search for down-type fourth generation quarks with the ATLAS detector in events with one lepton and hadronically decaying W bosons"**
G. Aad *et al.* [ATLAS Collaboration].
arXiv:1202.6540 [hep-ex]
10.1103/PhysRevLett.109.032001
Phys. Rev. Lett. **109**, 032001 (2012)
(Feb 2012) [HEP entry link]

317. **"Search for same-sign top-quark production and fourth-generation down-type quarks in pp collisions at $\sqrt{s} = 7$ TeV with the ATLAS detector"**
G. Aad *et al.* [ATLAS Collaboration].
arXiv:1202.5520 [hep-ex]
10.1007/JHEP04(2012)069
JHEP **1204**, 069 (2012)
(Feb 2012) [HEP entry link]

318. **"Search for pair-produced heavy quarks decaying to Wq in the two-lepton channel at $\sqrt{s} = 7$ TeV with the ATLAS detector"**
G. Aad *et al.* [ATLAS Collaboration].
arXiv:1202.3389 [hep-ex]
10.1103/PhysRevD.86.012007
Phys. Rev. D **86**, 012007 (2012)
(Feb 2012) [HEP entry link]

319. **"Search for pair production of a heavy up-type quark decaying to a W boson and a b quark in the lepton+jets channel with the ATLAS detector"**
G. Aad *et al.* [ATLAS Collaboration].
arXiv:1202.3076 [hep-ex]
10.1103/PhysRevLett.108.261802
Phys. Rev. Lett. **108**, 261802 (2012)
(Feb 2012) [HEP entry link]

320. **"Search for the Standard Model Higgs boson in the decay channel $H \to$ ZZ(*) $\to 4\ell$ with 4.8 fb-1 of pp collision data at $\sqrt{s} = 7$ TeV with ATLAS"**
G. Aad *et al.* [ATLAS Collaboration].
arXiv:1202.1415 [hep-ex]
10.1016/j.physletb.2012.03.005
Phys. Lett. B **710**, 383 (2013)
(Feb 2012) [HEP entry link]

321. **"Search for the Standard Model Higgs boson in the diphoton decay channel with 4.9 fb^{-1} of pp collisions at $\sqrt{s} = 7$ TeV with ATLAS"**
G. Aad *et al.* [ATLAS Collaboration].
arXiv:1202.1414 [hep-ex]
10.1103/PhysRevLett.108.111803
Phys. Rev. Lett. **108**, 111803 (2012)
(Feb 2012) [HEP entry link]

322. **"Combined search for the Standard Model Higgs boson using up to 4.9 fb^{-1} of pp collision data at $\sqrt{s} = 7$ TeV with the ATLAS detector at the LHC"**
G. Aad *et al.* [ATLAS Collaboration].
arXiv:1202.1408 [hep-ex]
10.1016/j.physletb.2012.02.044
Phys. Lett. B **710**, 49 (2013)
(Feb 2012) [HEP entry link]

323. **"Search for excited leptons in proton-proton collisions at $\sqrt{s} = 7$ TeV with the ATLAS detector"**
G. Aad *et al.* [ATLAS Collaboration].
arXiv:1201.3293 [hep-ex]

10.1103/PhysRevD.85.072003
Phys. Rev. D **85**, 072003 (2012)
(Jan 2012) [HEP entry link]

324. **"Observation of a new χ_b state in radiative transitions to $\Upsilon(1S)$ and $\Upsilon(2S)$ at ATLAS"**
G. Aad *et al.* [ATLAS Collaboration].
arXiv:1112.5154 [hep-ex]
10.1103/PhysRevLett.108.152001
Phys. Rev. Lett. **108**, 152001 (2012)
(Dec 2011) [HEP entry link]